

Design and Development of New Zinc Porphyrin
Molecules as High Performing Photoacoustic
Contrast Agents



UNIVERSITI MALAYSIA PAHANG

UNIVERSITI MALAYSIA PAHANG

DECLARATION OF THESIS AND COPYRIGHT

Author's Full Name : Amina Yasin

Date of Birth : 06th July 1986

Title : Design and Development of New Zinc Porphyrin Molecules as High Performing Photoacoustic Contrast Agents

Academic Session : 2013/2018

I declare that this thesis is classified as:

- CONFIDENTIAL (Contains confidential information under the Official Secret Act 1997)*
- RESTRICTED (Contains restricted information as specified by the organization where research was done)*
- OPEN ACCESS I agree that my thesis to be published as online open access (Full Text)

I acknowledge that Universiti Malaysia Pahang reserves the following rights:

1. The Thesis is the Property of Universiti Malaysia Pahang
2. The Library of Universiti Malaysia Pahang has the right to make copies of the thesis for the purpose of research only.
3. The Library has the right to make copies of the thesis for academic exchange.

Certified by:

(Student's Signature)

(Supervisor's Signature)

FA6809702
New IC/Passport Number
Date: 10-06-2018

Prof. Dato' Dr. Mashitah M. Yusoff
Name of Supervisor
Date: 10-06-2018

NOTE : * If the thesis is CONFIDENTIAL or RESTRICTED, please attach a thesis declaration letter.

SUPERVISOR'S DECLARATION

We hereby declare that we have checked this thesis and in our opinion, this thesis is adequate in terms of scope and quality for the award of the degree of Doctor of Philosophy in Chemistry.

(Supervisor's Signature)

Full Name : PROFESSOR DATO' DR. MASHITAH MOHD YUSOFF
Position : PROFESSOR, DEPUTY VICE CHANCELLOR UMP
Date : 10-06-2018

(Co-supervisor's Signature)

Full Name : PROFESSOR DR. JOSE RAJAN
Position : PROFESSOR, DEAN OF RESEARCH UMP
Date : 10-06-2018

(Co-supervisor's Signature)

Full Name : DR. MD SHAHEEN SARKAR
Position : SENIOR LECTURER
Date : 10-06-2018

STUDENT'S DECLARATION

I hereby declare that the work in this thesis is based on my original work except for quotations and citations which have been duly acknowledged. I also declare that it has not been previously or concurrently submitted for any other degree at Universiti Malaysia Pahang or any other institutions.

(Student's Signature)

Full Name : AMINA YASIN

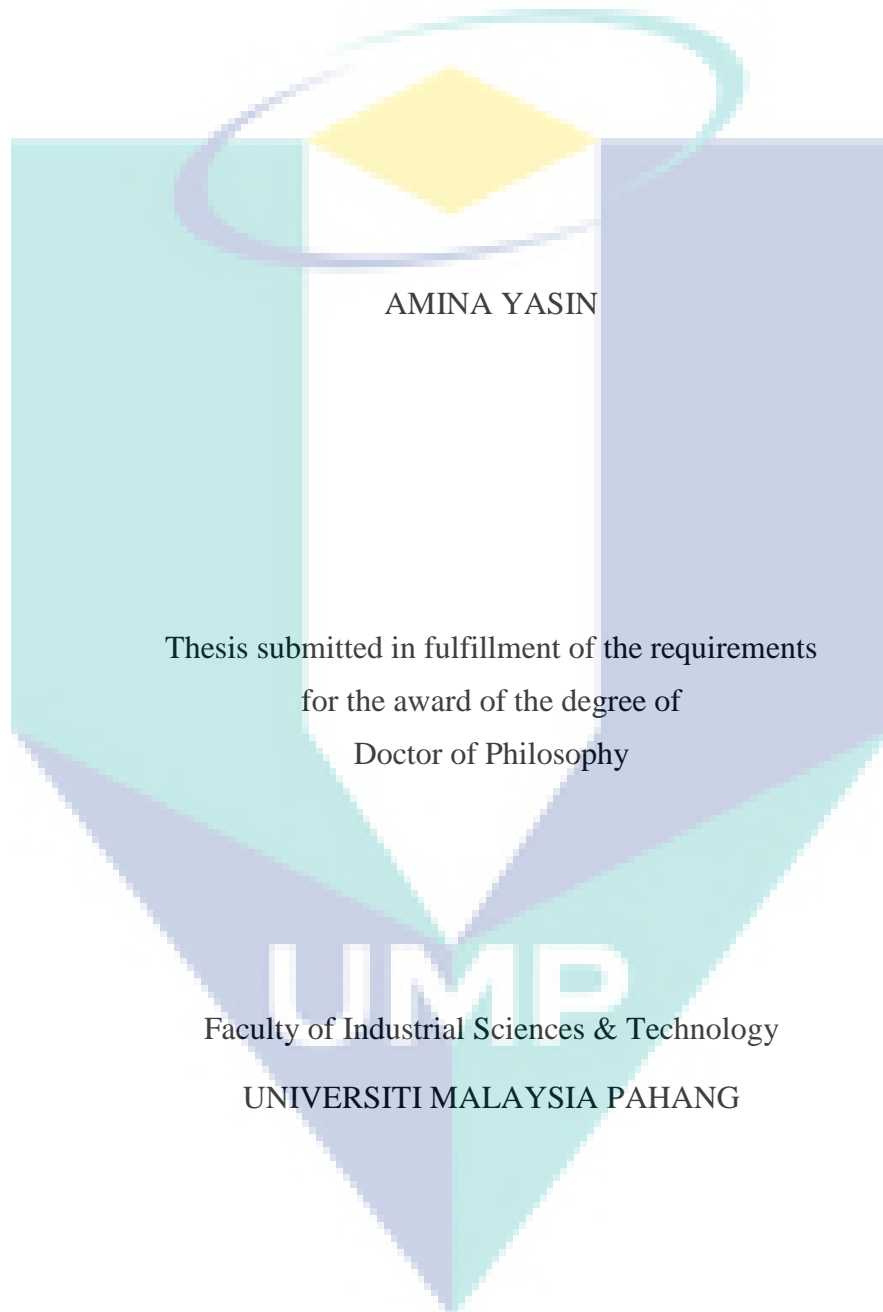
ID Number : PSK13002

Date : 10-06-2018



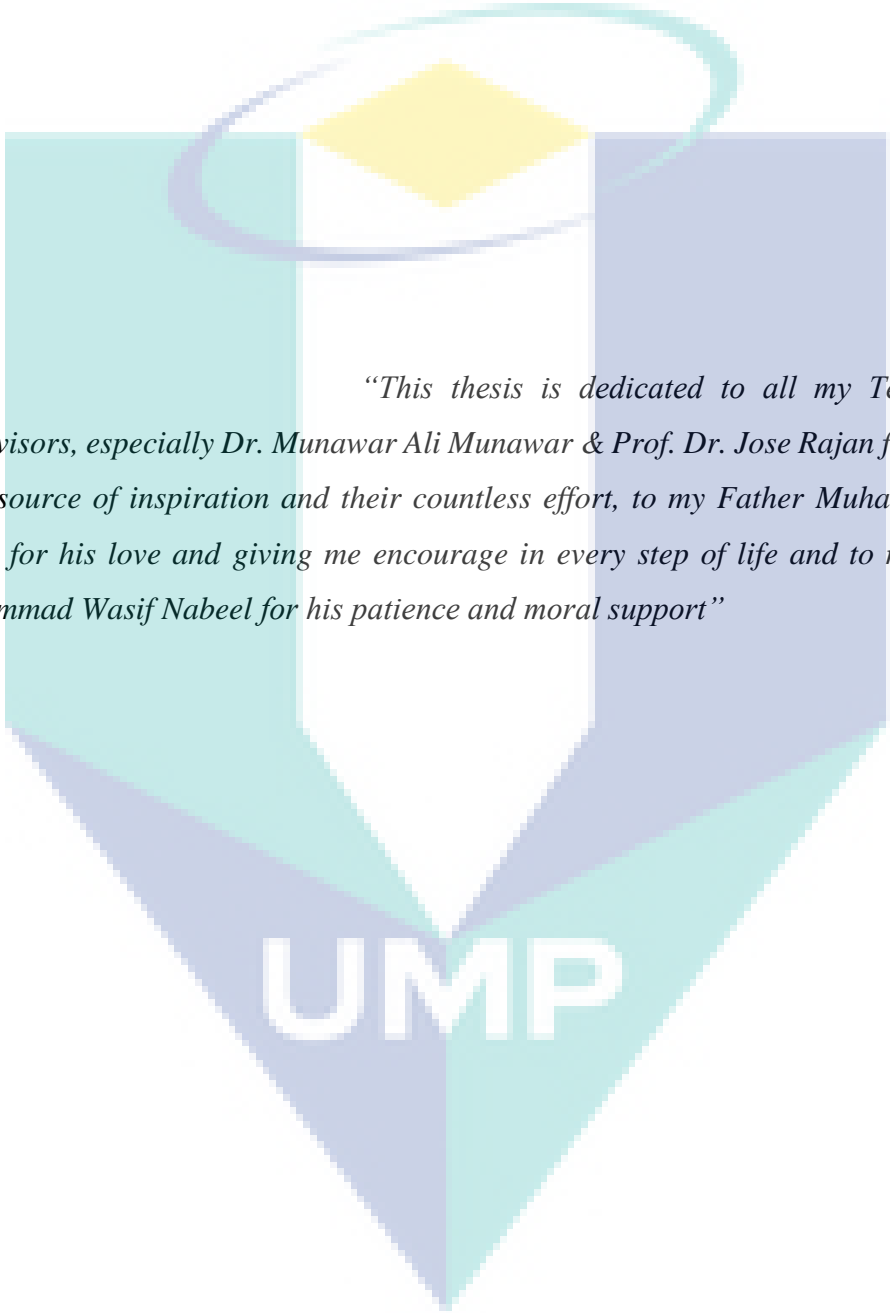
UMP

Design and Development of New Zinc Porphyrin Molecules as High Performing
Photoacoustic Contrast Agents



JUNE 2018

DEDICATION

The logo for Umpress is a shield-shaped emblem. It features a central white vertical band with a yellow diamond at the top. The shield is divided into four quadrants: top-left is teal, top-right is light blue, bottom-left is light blue, and bottom-right is teal. The letters 'UMP' are printed in white at the bottom of the shield. A stylized, glowing ring in teal and light blue encircles the top of the shield.

“This thesis is dedicated to all my Teachers and Supervisors, especially Dr. Munawar Ali Munawar & Prof. Dr. Jose Rajan for providing me a source of inspiration and their countless effort, to my Father Muhammad Yasin Bhatti for his love and giving me encourage in every step of life and to my Husband Muhammad Wasif Nabeel for his patience and moral support”

ACKNOWLEDGEMENTS

I am obliged and would like to express my sincere gratitude to my supervisors Professor Dato' Dr. Mashitah Mohd Yusoff; Professor Dr. Jose Rajan; and Dr. Md Shaheen Sarkar for their indispensable guidance, interminable encouragement and relentless support in making this research possible. I really appreciate their supervision from the beginning to the final level that empowered me to develop an understanding of this research thoroughly. Without their advice and kind assistance, it would be a lot tougher to accomplish. I also sincerely thanks for the time spent proofreading and correcting my mistakes.

I also would like to express very special thanks to Gaussian technical support team for their suggestions and co-operation. A special appreciation should be given to Fernando R. Clemente from Gaussian technical support team whom which gave me a brand new perception about my research.

Besides my advisors, I would like to thank Dr. Chandra S. Yelleswarapu from Department of Physics, University of Massachusetts Boston, United States and Dr. Iman S. Roqan from Physical Science and Engineering Division, King Abdullah University of Science and Technology, Kingdom of Saudia Arabia for their collaboration on this project that make us possible to complete this doctoral dissertation.

My sincere thanks go to all lecturers and members of the staff of the FSTI Department, UMP, who helped me in many ways and made my education journey at UMP pleasant and unforgettable. Many thanks go to Central Laboratory, Institute of Postgraduate Studies & International Office for their co-operation, and supports during this study. This experience will be remembered as important memory for me to face the new chapter of life.

I acknowledge my sincere indebtedness and gratitude to my parents for their love, dream and sacrifice throughout my life. I am thankful for their sacrifice, patience, and understanding that were inevitable to make this work possible. Their sacrifice had inspired me from the day I learned how to read and write until what I have become now. I cannot find the appropriate words that could properly describe my appreciation for their devotion, support and faith in my ability to achieve my dreams.

I am very grateful to my dearest husband who supported me in every possible way to fulfil my dream. Without his patience, I would not be able to complete my doctoral research. My deepest gratitude to my siblings and my family for the continuous prayers, encouragement and support, at every stage of my life. I also want to share this accomplishment with my friends for always being there for me.

Lastly, I would like to thanks any person, which contributes to my dissertation project directly or indirectly. I would like to acknowledge their comments and suggestions, which was crucial for the successful completion of this research.

AMINA YASIN, June 2018

ABSTRAK

Penyelidikan doktoral ini bertujuan untuk merekabentuk dan membangunkan molekul porfirin baru sebagai agen kontras dalam pengimejan fotoakustik (PA) seperti tomografi PA dan mikroskopi PA. Untuk kejayaan pelaksanaan teknik pengimejan PA, agen kontras yang mempamerkan koefisien PA yang besar adalah salah satu keperluan penting. Banyak bahan, sama ada biomolekul endogen seperti hemoglobin, deoxyhaemoglobin, melanin atau bahan-bahan eksogen seperti molekul organik, kluster atau nanokristal didapati menunjukkan kesan PA. Walau bagaimanapun, ia sama ada dihad oleh koefisien PA yang lemah, kedalaman penembusan yang lemah atau ketoksikan. Pengembangan molekul PA baru adalah terhad kerana faktor-faktor yang mempengaruhi kesan PA jarang diteliti secara sistematik, mengakibatkan kekurangan panduan untuk reka bentuk molekul agen kontras PA. Dalam tesis ini, hipotesis bahawa kesan PA yang besar boleh dicapai jika getaran kumpulan molekul atau berfungsi terletak di atas atom yang membentuk orbital molekul tidak dihuni paling rendah dapat dimanipulasi sedemikian rupa sehingga kekuatan pengayun dari getaran tersebut meningkat pada pengubahsuaian kimia yang sesuai, maka sebahagian besar foton yang teruja dapat disejukkan melalui pelepasan fonon. Dengan menggunakan Zn(II)porfirin sebagai sistem model, sebilangan besar molekul dimodelkan menggunakan teori berfungsi ketumpatan (DFT) semasa berdasarkan andaian di atas dan sifat asas dan keadaan teruja dikaji secara sistematik dengan menggunakan kaedah hibrid tiga parameter Becke dengan gradian korelasi berfungsi (B3LYP) Lee, Yang, dan Parr dan teras-teras berpotensi diperbetulkan yang berkesan menggunakan LANL2DZ dan 6-31G(d) dalam pakej program Gaussian 09W. Telah diperhatikan bahawa kumpulan-kumpulan berfungsi dalam kumpulan fenil kurang resonans yang melekat pada teras porfirin menguatkan kekuatan ayunan kelompok alkoksi – variasi sistematik dalam koefisien penyerapan mod C-H vibrational juga diperhatikan dengan perubahan relatif dalam resonans kumpulan molekul berlabuh. Dipengaruhi pemerhatian tersebut, empat molekul Zn(II)porfirin ($RJ-C_n-MY_m$, di mana $n= 12$ atau 8 dan $m= 1-4$) telah disintesis dengan hasil yang baik melalui pengoksidaan berasaskan asid, pemeluwapan Knoevenagel, pemeluwapan MacDonald (2+2), brominasi, logam, nyahlindung dan reaksi gandingan Sonogashira. Struktur molekul dikaji menggunakan spektroskopi NMR, MS, dan FTIR manakala ciri-ciri optik dikaji dengan kaedah spektroskopi penyerapan UV-Vis, spektroskopi fotopendarkilau dan pengiraan foton tunggal yang berkorelasi; sementara sifat-sifat PA dikaji dengan kaedah spektroskopi fotoakustik. Koefisien penyerapan menurun mengikut susunan $RJ-C_{12}-MY_1 > RJ-C_{12}-MY_2 > RJ-C_{12}-MY_3 > RJ-C_8-MY_4$; oleh itu variasi yang serupa dalam isyarat PA telah diramalkan. Ramalan teori telah disahkan oleh ukuran koefisien PA dengan tomografi PA. Koefisien PA dan keamatan tomografi menurun mengikut susunan $RJ-C_{12}-MY_1 > RJ-C_{12}-MY_2 > RJ-C_{12}-MY_3 > RJ-C_8-MY_4$, seperti yang diramalkan oleh DFT. Pengelasan molekul terperinci dalam menentukan ciri-ciri optoelektronik seperti kepupusan koefisien molar keadaan asas, kepupusan koefisien molar keadaan teruja, hasil kuantum pendarfluor dan masa hayat keadaan teruja molekul Zn(II)porfirin yang baru disintesis diperiksa bagi menunjukkan korelasi positif antara tahap tenaga getaran, koefisien kepupusan molar, keadaan pemancaran fonon dan kesan PA. Koefisien PA yang besar diperhatikan bagi $RJ-C_{12}-MY_1$ memberikan peningkatan PA sebanyak ~ 7 kali ganda berbanding dengan ZnTPP yang digunakan sebagai rujukan adalah lebih tinggi daripada molekul kecil sedia ada. Di samping menawarkan molekul unggul untuk tomografi PA tesis dan kriteria yang diterima pakai akan membolehkan rekabentuk molekul yang lebih mudah dengan ciri-ciri fotoakustik superior dan lain-lain ciri optik tidak linear.

ABSTRACT

This doctoral research aims to design and develop new porphyrin molecules as contrast agents in photoacoustic (PA) imaging (PAI) such as PA tomography and PA microscopy. For successful implementation of PAI techniques, contrast agents exhibiting large PA coefficients are one of the essential requirements. Many materials, either endogenous biomolecules such as haemoglobin, deoxyhaemoglobin, melanin or exogenous materials such as organic molecules, clusters or nanocrystals are shown to exhibit PA effects. However, they are either limited by poor PA coefficients, poor penetration depths or toxicity. Development of new PA molecules is limited because the factors influencing the PA effect have rarely been systematically studied, resulting in a lack of guidance for the design of molecular PA contrast agents. In this thesis, it is hypothesized that large PA effects could be achieved if vibrations of the molecular or functional groups lying above the atoms composing the lowest unoccupied molecular orbitals could be manipulated in such a way that the oscillator strength of those vibrations increase upon suitable chemical modification, then a large portion of the excited photons can be thermalized via phonon emission. By using Zn(II)porphyrin as a model system, a large number of molecules were modelled using state of the art density functional theory (DFT) based on the above assumption and their ground and excited state properties were studied systematically by using the Becke's three-parameter hybrid method with the Lee, Yang, and Parr gradient corrected correlation functional (B3LYP) with the effective core potential employing basis sets of LANL2DZ and 6-31G(d) using the Gaussian 09W program package. It was observed that less resonating functional groups in a phenyl group attached to the porphyrin core amplify the oscillation strengths of the alkoxy groups – a systematic variation in the absorption coefficients of the C-H vibrational modes was observed with relative change in the resonance of the molecular groups anchored. Motivated from this result, representative four Zn(II)porphyrin molecules (RJ-C_n-MY_m, where n = 12 or 8 and m = 1 – 4) were synthesized in good yields by acid-catalyzed oxidation, Knoevenagel condensation, MacDonald (2+2) condensation, bromination, metalation, deprotection, and Sonogashira coupling reactions. Structure of the molecules were studied by NMR, Mass Spectrometry, and FTIR spectroscopy; optical properties were studied by UV-Vis absorption spectroscopy, photoluminescence spectroscopy, and time-correlated single photon counting; and PA properties were studied by photoacoustic spectroscopy. The absorption coefficient decreased in the order of RJ-C₁₂-MY₁ > RJ-C₁₂-MY₂ > RJ-C₁₂-MY₃ > RJ-C₈-MY₄; and therefore, a similar variation in the PA signals was predicted. Theoretical predictions were validated by PA coefficients measurements and PA tomography. The PA coefficients and tomographic intensities decreased in the order RJ-C₁₂-MY₁ > RJ-C₁₂-MY₂ > RJ-C₁₂-MY₃ > RJ-C₈-MY₄, as predicted by DFT. The detailed molecular characterizations in determining the nature of optoelectronic properties i.e.; ground state molar extinction coefficients, excited state molar extinction coefficients, fluorescence quantum yields and excited state lifetimes of newly synthesized Zn(II)porphyrin molecules were examined in order to show the positive correlation between vibrational energy levels, molar extinction coefficients, phonon emitting states and PA effect. Large PA coefficients were observed for the RJ-C₁₂-MY₁, providing an up to ~7-fold PA enhancement over that of ZnTPP used as a reference, which is superior to that of the existing small molecules. Besides offering a superior molecule for PA tomography, the present thesis and criterion adopted here would enable to design simpler molecules with superior photoacoustic and other nonlinear optical properties.

TABLE OF CONTENT

DECLARATION	
TITLE PAGE	
DEDICATION	ii
ACKNOWLEDGEMENTS	iii
ABSTRAK	iv
ABSTRACT	v
TABLE OF CONTENT	vi
LIST OF TABLES	xi
LIST OF FIGURES	xii
LIST OF SYMBOLS	xviii
LIST OF ABBREVIATIONS	xxi
CHAPTER 1 INTRODUCTION	1
1.1 Problem Statement	2
1.2 Hypothesis	3
1.3 Research Objectives	4
1.4 Research Scope	5
1.5 Novelty of Research	7
1.6 Thesis Outline	7
CHAPTER 2 LITERATURE REVIEW	9
2.1 Introduction	9
2.2 Metalloporphyrins	11

2.3	Classification of Porphyrins	12
2.3.1	In-Plane Metalloporphyrins	13
2.3.2	SAT Metalloporphyrins	16
2.4	Photochemistry	19
2.4.1	Electronic Properties of Porphyrins	22
2.5	Synthetic Methodologies of Porphyrin	31
2.5.1	Pre-Functionalization	32
2.5.2	Post-Functionalization	41
2.5.3	Metalloporphyrins Synthesis	47
2.6	Density Functional Theory Calculations of Porphyrins	49
2.6.1	Ab-initio Quantum Chemical Methods	50
2.6.2	Density Functional Theory Calculations	51
2.6.3	DFT Calculations by Different Functionals	53
2.6.4	DFT Calculations by Different Basis Sets	55
2.6.5	Time Dependent DFT Calculations	57
2.7	Applications of Porphyrins	58
2.7.1	Photoacoustic Imaging:	59
2.7.2	Porphyrin as Photoacoustic Contrast Agent	62
2.8	Conclusions	65
CHAPTER 3 MATERIALS AND METHODS		66
3.1	Introduction	66
3.2	Research Methodology	66
3.3	Materials and Chemicals	68
3.4	Design of Porphyrins by DFT Calculation	69
3.4.1	Molecular Geometry Optimization	69

3.4.2	Molecular Structures and Nomenclatures	71
3.4.3	Frequency and Vibrational Energy Calculations	72
3.4.4	Excitation Energy Calculations	74
3.5	Synthesis of Newly Designed Zn(II)Porphyrins	76
3.5.1	Instrumentation	76
3.5.2	Synthesis of π -Conjugated Meso-Ethynyl-Zn(II)Porphyrins	76
3.5.3	Synthesis of Porphyrins RJ-C ₈ -MY ₄ :	87
3.6	Photoacoustic Measurements	92
3.7	Summary	93
CHAPTER 4 RESULTS AND DISCUSSION: SYNTHESIS AND OPTOELECTRONIC PROPERTIES OF π-CONJUGATED MESO-ETHYNYL-ZN(II)PORPHYRINS		94
4.1	Introduction	94
4.2	Synthesis of Meso-Ethynyl-Zn(II)porphyrins	94
4.2.1	Knoevenagel Condensation Reaction	99
4.2.2	Sonogashira Cross-Coupling Reaction	105
4.3	Steady State Absorption Spectral Studies	113
4.3.1	Absorption Spectral Studies Relates to PAI Signals	125
4.4	Steady State Emission Spectral Studies	131
4.4.1	Quantum Yield Studies	143
4.4.2	Time Resolved Photoluminescence Studies	148
4.4.3	PAI Signals Correlation with Emitting Excited States	149
4.5	IR-Vibrational Modes Studies	151
4.5.1	Phonon Emission Correlation with Extended-Conjugation	155
4.6	Thermogravimetric Thermal Analysis (TGA)	156
4.7	Conclusions	157

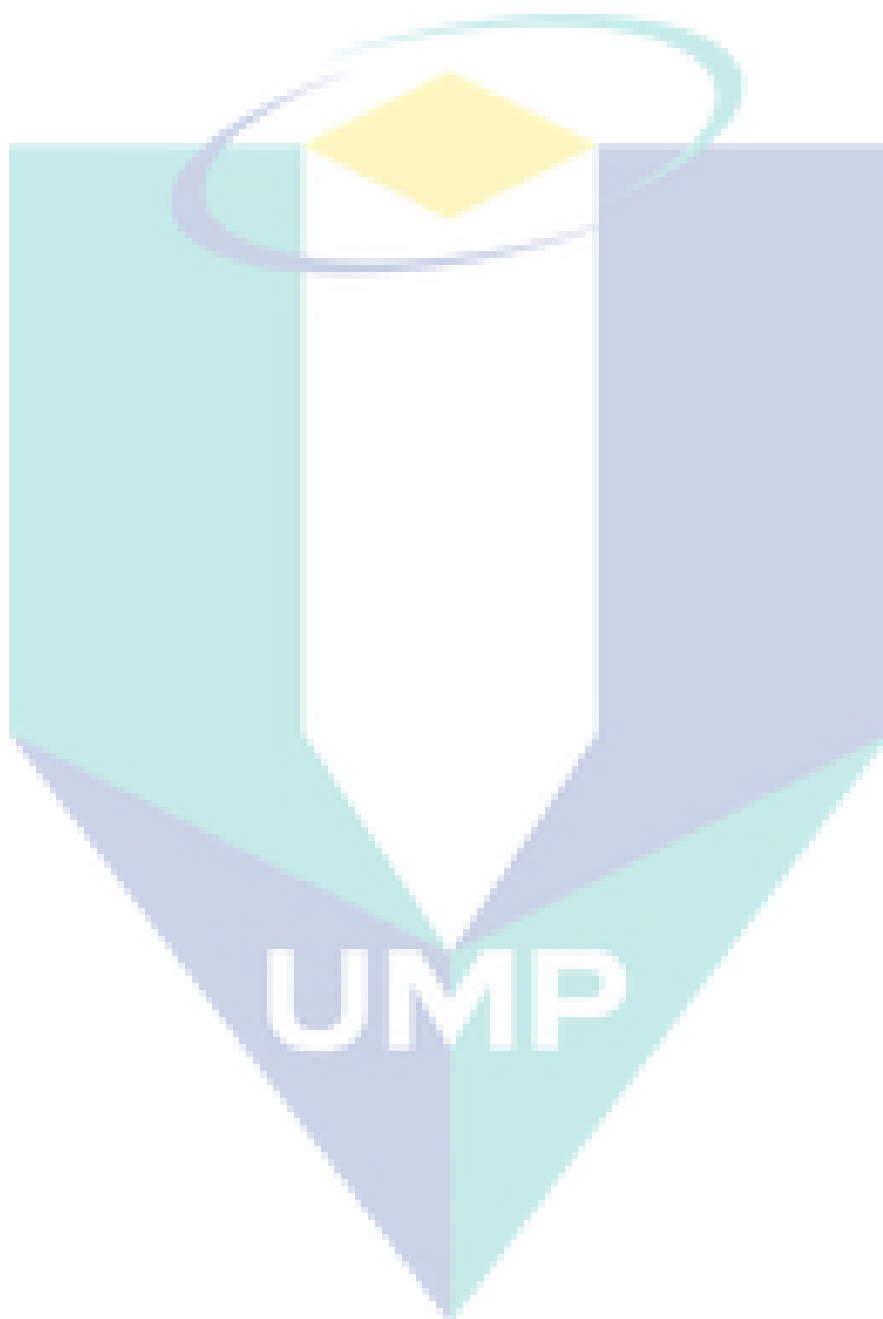
CHAPTER 5 RESULTS AND DISCUSSION: PHOTOACOUSTIC STUDIES OF π-CONJUGATED MESO-ETHYNYL-ZN(II)PORPHYRINS	159
5.1 Introduction	159
5.2 Photoacoustic Studies	159
5.3 Optical and Photoacoustic Z-Scan Studies	160
5.3.1 Dye Concentration Dependence – Low Laser Fluence	162
5.3.2 Dye Concentration Dependence – High Laser Fluence	163
5.4 Photoacoustic Tomography	166
5.5 Optical Photoacoustic Z-Scan Arrangement Details	168
5.6 Photoacoustic Tomography Experimental Details	169
5.7 Conclusions	170
CHAPTER 6 CONCLUSIONS AND RECOMMENDATIONS	171
6.1 Conclusions	171
6.2 Future Recommendations	175
REFERENCES	177
APPENDIX A PORPHYRINS IN NATURE	216
APPENDIX B PORPHYRINS AS PA CONTRAST AGENTS	224
APPENDIX C SCREEN SHORT OF OPTIMIZATION OF PORPHYRINS	232
APPENDIX D MOLECULAR STRUCTURES AND NOMENCLATURES OF DESIGNED PORPHYRINS	233
APPENDIX E UV-VIS SPECTRA OF ALL DESIGNED PORPHYRINS	245
APPENDIX F NMR OF THE SYNTHESIZED PORPHYRINS	248
APPENDIX G ENERGY-GAP LAW	292
APPENDIX H VISUALS OF OPTIMIZED STRUCTURES AND ALL VIBRATIONS OF RJ-C_n-MY_m COMPLEXES	294

**APPENDIX I MOLECULAR ORBITAL DIAGRAMS OF THE RJ-C_n-MY_m
SERIES**

295

LIST OF PUBLICATIONS

297



LIST OF TABLES

Table 3.1	Approaches used to optimize the porphyrin molecules	71
Table 4.1	Starting materials and the yields of porphyrin precursors and the meso-ethynyl-Zn(II)porphyrins	96
Table 4.2	Continued	97
Table 4.3	The absorbance spectral data for free-base and Zn(II)porphyrins	118
Table 4.4	Experimental and calculated absorption bands (λ) along with their molar extinction coefficients (ϵ) for RJ-C _n -MY _m series complexes	130
Table 4.5	The fluorescence spectral data for first series porphyrin complexes	135
Table 4.6	The fluorescence spectral data for second series porphyrin complexes	136
Table 4.7	The fluorescence spectral data for RJ-C _n -MY _m series porphyrin complexes	140
Table 4.8	The quantum yield data for RJ-C _n -MY _m series complexes	146
Table 5.1	Molar absorption coefficients (ϵ) of RJ-C _n -MY _m series of porphyrins at 532 nm & 680 nm	164

UMP

LIST OF FIGURES

Figure 1.1	Basic Structure of Porphyrin	1
Figure 1.2	Excited energy state of a molecule	4
Figure 1.3	The flow chart of research progress and a relationship between the chapters	8
Figure 2.1	Schematic representation of the two tautomers of porphyrin. 1) <i>cis</i> -NH tautomer and 2) <i>trans</i> -NH tautomer	9
Figure 2.2	Metalloporphyrins (adpoted from Gaussview); blue, light gray, dark gray and white colored atoms represents nitrogens, carbons, metal ion and hydrogens	11
Figure 2.3	The most common substitution patterns found in porphyrin macrocycle. 1) porphine; 2) β -substituted porphyrin; 3) meso-substituted porphyrin; 4) β - and meso-substituted (mixed) porphyrins	13
Figure 2.4	Representation of a) In-plane metalloporphyrins; b) Out-of-plane metalloporphyrin	14
Figure 2.5	Structure representation of In-plane metalloporphyrins; a) Top-view; b) Side-view	14
Figure 2.6	In-plane metalloporphyrin distortion; a) Saddle metalloporphyrin; b) Ruffled metalloporphyrin	15
Figure 2.7	Structure representation of Out-of-plane metalloporphyrin; a) Top-view; b) Side-view	17
Figure 2.8	SAT metalloporphyrin distortion (Dome distortion)	17
Figure 2.9	Formation of In-plane metalloporphyrin via Out-of-plan metallopor-phyrin as intermediate	18
Figure 2.10	Aromaticity in porphyrin: 18- π electrons out of 22- π electrons form the conjugation pathway (indicated in bold)	19
Figure 2.11	$^1\text{H-NMR}$ representation of porphyrin	20
Figure 2.12	Jablonski diagram showing the decay phenomena for singlet and triplet relaxation after absorption of photon. The solid lines represent the radiation decay and dashed lines for non-radiation decay	21
Figure 2.13	UV-Vis spectra for free-base porphyrins (D_{2h}) (top) and metalloporphyrin (D_{4h}) (bottom)	24
Figure 2.14	Q-bands absorption spectra for free-base porphyrins: a) etio-type; b) rhodo-type; c) oxo-rhodo-type and d) phyllo-types	24
Figure 2.15	Molecular orbital diagram of “regular” porphyrins	25
Figure 2.16	Molecular orbital diagram of hypso-porphyrins (irregular porphyrins). The notations a_{1u} and a_{2u} are singly degenerate and e_g is doubly degenerate orbitals	26

Figure 2.17	Molecular orbital diagram of hyper-porphyrins (irregular porphyrins)	26
Figure 2.18	Gouterman four-orbital model for D_{2h} symmetry (top) and D_{4h} symmetry porphyrins (bottom)	28
Figure 2.19	The HOMO and LUMO orbitals according to the Gouterman Four-Orbital Model	28
Figure 2.20	Emission spectra of metalloporphyrin, regular porphyrin represented in red (ZnTPP) and irregular porphyrin in purple (PtTPP)	29
Figure 2.21	Classification of porphyrin synthesis	31
Figure 2.22	General representation of pre-functionalization of porphyrins	32
Figure 2.23	General methodologies for porphyrin synthesis through tetramerization of mono-pyrrole; i) acid catalyzed condensation; ii) oxidation reaction	33
Figure 2.24	Methodologies for meso-porphyrin synthesis; i) Rothmund synthesis; ii) Adler and Longo synthesis; iii) Lindsey synthesis, acid catalyzed condensation; iiib) Lindsey synthesis, oxidation reaction	34
Figure 2.25	Methodologies for synthesis of unsymmetrical meso-porphyrin; i) acid catalyzed condensation; ii) oxidation reaction	35
Figure 2.26	Methodologies for β - porphyrin synthesis	36
Figure 2.27	Self-condensation of 2- substituted pyrrole for β - & meso-porphyrin synthesis	37
Figure 2.28	MacDonald (2+2) condensation for porphyrin synthesis	38
Figure 2.29	MacDonald (2+2) condensation for <i>trans</i> substituted meso-porphyrin synthesis	39
Figure 2.30	Tripyrrolic [3+1] route for β -unsymmetrical porphyrin synthesis	40
Figure 2.31	Cyclization of linear tetrapyrroles i) MeOH, HCl, RT; ii) MeOH, Cu(OAc) ₂ , reflux, 48 h; iii) H ₂ SO ₄	40
Figure 2.32	General representation of post-functionalization of porphyrins	41
Figure 2.33	Classification of post-functionalization by position	41
Figure 2.34	Various reaction types of post-functionalization of porphyrins	42
Figure 2.35	Post-functionalization for porphyrins synthesis	43
Figure 2.36	palladium-catalyzed cross-coupling reactions for porphyrins synthesis	45
Figure 2.37	Routes for inserting metal ions into the porphyrin ring through; a) coordination of metal; b) Reduction of metal; c) Oxidation of metal	48
Figure 2.38	Application domains of natural and synthetic porphyrins	59

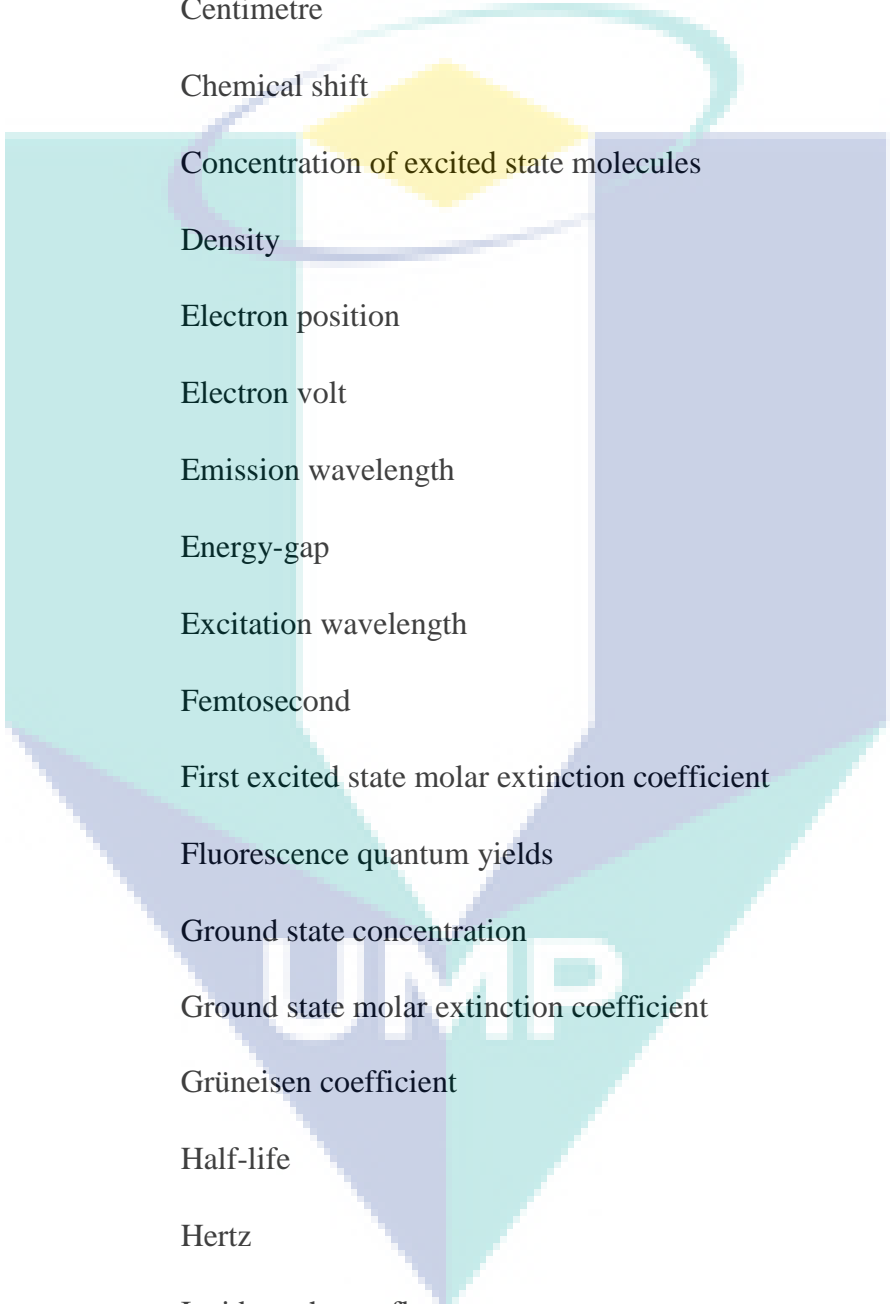
Figure 2.39	Structures of zinc phthalocyanine, protoporphyrin IX employed as PAI contrast agents	63
Figure 2.40	Structures of uranium porphyrinoid complex employed PAI contrast agents	63
Figure 2.41	Structures of quinoline-annulated porphyrins and bacteriochlorins employed as PAI contrast agents	64
Figure 2.42	Structures of quinoline-annulated porphyrin derivatives employed as PAI contrast agents	64
Figure 3.1	The flow chart of general research methodology	67
Figure 3.2	Geometry optimization steps for the global minimum energies a) compound RJ-C ₁₂ -MY ₁ ; b) compound RJ-C ₁₂ -MY ₂ ; c) compound RJ-C ₁₂ -MY ₃ ; d) compound RJ-C ₈ -MY ₄	70
Figure 3.3	Structures and IUPAC naming of porphyrin molecules. The left panel shows planer ChemDraw sketch and right panel are the computed geometry developed using Gauss View. a) compound RJ-C ₁₂ -MY ₁ ; b) compound RJ-C ₁₂ -MY ₂ ; c) compound RJ-C ₁₂ -MY ₃ ; d) compound RJ-C ₈ -MY ₄	72
Figure 3.4	IR spectra for a) compound RJ-C ₁₂ -MY ₁ ; b) compound RJ-C ₁₂ -MY ₂ ; c) compound RJ-C ₁₂ -MY ₃ ; d) compound RJ-C ₈ -MY ₄	74
Figure 3.5	UV-Vis spectra for a) compound RJ-C ₁₂ -MY ₁ ; b) compound RJ-C ₁₂ -MY ₂ ; c) compound RJ-C ₁₂ -MY ₃ ; d) compound RJ-C ₈ -MY ₄	75
Figure 3.6	Synthetic schemes for a) compound RJ-C ₁₂ -MY ₁ ; b) compound RJ-C ₁₂ -MY ₂ ; c) compound RJ-C ₁₂ -MY ₃	78
Figure 3.7	Synthesis of RJ-C ₈ -MY ₄	87
Figure 3.8	Schematic of experimental setup used to obtain nonlinear optical transmission and scattering, and photoacoustic data	93
Figure 4.1	Synthesis of meso-ethynyl-Zn(II)porphyrins	95
Figure 4.2	Reaction mechanism for 1,3-di(alkoxy)benzene (5-5a) and 2,6-bis(alkoxy)benzaldehyde (6-6a)	98
Figure 4.3	General mechanism of Knoevenagel condensation reaction	99
Figure 4.4	Reaction mechanism for 2-cyano-3-(4-iodophenyl)acrylic acid (3)	100
Figure 4.5	Reaction mechanism for di(1H-pyrrol-2-yl)methane (9)	101
Figure 4.6	Reaction mechanism for Free-base porphyrins (10-10b)	102
Figure 4.7	Reaction mechanism for Free-base bromo-porphyrins (11-11b)	104
Figure 4.8	Reaction mechanism for Zn(II) porphyrins (12-12b)	105
Figure 4.9	General mechanism of Sonogashira cross coupling reaction	106
Figure 4.10	General mechanism of copper-free Sonogashira cross coupling reaction	107
Figure 4.11	Reaction mechanism for Zn(II) porphyrins (13-13b)	108

Figure 4.12	Reaction mechanism for Zn(II) porphyrins (14-14b).	109
Figure 4.13	Reaction mechanism for RJ-C ₁₂ -MY ₁	110
Figure 4.14	Reaction mechanism for RJ-C ₁₂ -MY ₂ , RJ-C ₁₂ -MY ₃ and RJ-C ₈ -MY ₄	113
Figure 4.15	Absorption spectra of a) free-base porphyrin (10); b) bromo free-base porphyrin (11); c) bromo Zn(II)porphyrin (12); d) ethynyl-Zn(II)porphyrin (13)	115
Figure 4.16	Q-band absorption spectra of a) free-base porphyrin (10); b) bromo free-base porphyrin (11); c) bromo Zn(II)porphyrin (12); d) ethynyl-Zn(II)porphyrin (13)	116
Figure 4.17	Comparison absorption spectra of free-base porphyrin (10), bromo free-base porphyrin (11), bromo Zn(II)porphyrin (12) and ethynyl-Zn(II)porphyrin (13)	117
Figure 4.18	Absorption spectra of a) free-base porphyrin (10b); b) bromo free-base porphyrin (11b); c) bromo Zn(II)porphyrin (12b); d) ethynyl-Zn(II)porphyrin (13b)	120
Figure 4.19	Q-band absorption spectra of a) free-base porphyrin (10b); b) bromo free-base porphyrin (11b); c) bromo Zn(II)porphyrin (12b); d) ethynyl-Zn(II)porphyrin (13b)	121
Figure 4.20	Comparison absorption spectra of free-base porphyrin (10b), bromo free-base porphyrin (11b), bromo Zn(II)porphyrin (12b) and ethynyl-Zn(II)porphyrin (13b)	121
Figure 4.21	Comparison of absorption spectra between first & second series of porphyrins	122
Figure 4.22	Absorption spectra of RJ-C ₁₂ -MY ₁ , RJ-C ₁₂ -MY ₂ , RJ-C ₁₂ -MY ₃ and RJ-C ₈ -MY ₄	123
Figure 4.23	Comparison between absorption spectra of RJ-C ₁₂ -MY ₁ , RJ-C ₁₂ -MY ₂ , RJ-C ₁₂ -MY ₃ and RJ-C ₈ -MY ₄	124
Figure 4.24	Comparison between absorption spectra of a) RJ-C ₁₂ -MY ₁ ; b) RJ-C ₁₂ -MY ₂ ; c) RJ-C ₁₂ -MY ₃ and d) RJ-C ₈ -MY ₄ with their respective parent compounds	125
Figure 4.25	Comparison between experimental and calculated absorption spectra of a) RJ-C ₁₂ -MY ₁ ; b) RJ-C ₁₂ -MY ₂ ; c) RJ-C ₁₂ -MY ₃ and d) RJ-C ₈ -MY ₄	128
Figure 4.26	LUMO orbitals for a) RJ-C ₁₂ -MY ₁ ; b) RJ-C ₁₂ -MY ₂ ; c) RJ-C ₁₂ -MY ₃ and d) RJ-C ₈ -MY ₄	129
Figure 4.27	Emission spectra of a) free-base porphyrin (10); b) bromo free-base porphyrin (11); c) bromo Zn(II)porphyrin (12); d) ethynyl-Zn(II)porphyrin (13)	133
Figure 4.28	Comparison between absorption and emission spectra of a) free-base porphyrin (10); b) bromo free-base porphyrin (11); c) bromo Zn(II)porphyrin (12); and d) ethynyl-Zn(II)porphyrin (13)	134

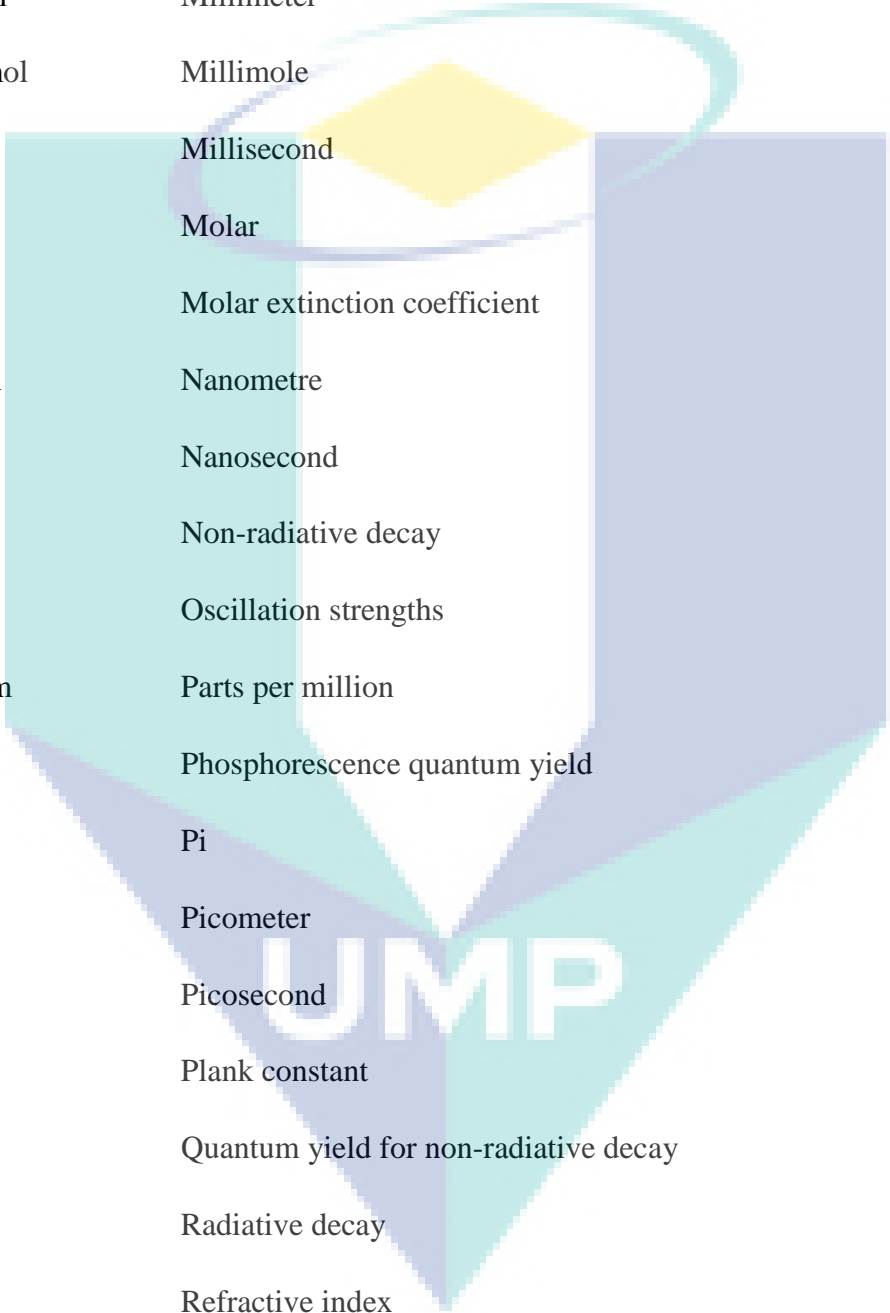
Figure 4.29	Comparison of emission spectra of free-base porphyrin (10), bromo free-base porphyrin (11), bromo Zn(II)porphyrin (12) and ethynyl-Zn(II)porphyrin (13)	135
Figure 4.30	Emission spectra of a) free-base porphyrin (10b); b) bromo free-base porphyrin (11b); c) bromo Zn(II)porphyrin (12b); d) ethynyl-Zn(II)porphyrin (13b)	137
Figure 4.31	Comparison absorption and emission spectra of a) free-base porphyrin (10b); b) bromo free-base porphyrin (11b); c) bromo Zn(II)porphyrin (12b); and d) ethynyl-Zn(II)porphyrin (13b)	138
Figure 4.32	Comparison of emission spectra of free-base porphyrin (10b), bromo free-base porphyrin (11b), bromo Zn(II)porphyrin (12b) and ethynyl-Zn(II)porphyrin (13b)	138
Figure 4.33	Emission spectra of RJ-C _n -MY _m series complexes a) RJ-C ₁₂ -MY ₁ ; b) RJ-C ₁₂ -MY ₂ ; c) RJ-C ₁₂ -MY ₃ ; d) RJ-C ₈ -MY ₄	139
Figure 4.34	Comparison between absorption and emission spectra of RJ-C _n -MY _m series complexes a) RJ-C ₁₂ -MY ₁ ; b) RJ-C ₁₂ -MY ₂ ; c) RJ-C ₁₂ -MY ₃ ; d) RJ-C ₈ -MY ₄	141
Figure 4.35	PL spectra of RJ-C _n -MY _m series complexes excited by femtosecond laser at 400 nm wavelength and having 1.4 mW power	142
Figure 4.36	Emission spectra of RJ-C _n -MY _m series complexes at different excitation wavelength a) RJ-C ₁₂ -MY ₁ ; b) RJ-C ₁₂ -MY ₂ ; c) RJ-C ₁₂ -MY ₃ ; d) RJ-C ₈ -MY ₄	143
Figure 4.37	Absorbance profile for Φ_f calculation of RJ-C _n -MY _m series of porphyrin complexes at different concentrations a) RJ-C ₁₂ -MY ₁ ; b) RJ-C ₁₂ -MY ₂ ; c) RJ-C ₁₂ -MY ₃ ; d) RJ-C ₈ -MY ₄	144
Figure 4.38	Emission profile for Φ_f calculation of RJ-C _n -MY _m series of porphyrin complexes at different concentrations a) RJ-C ₁₂ -MY ₁ ; b) RJ-C ₁₂ -MY ₂ ; c) RJ-C ₁₂ -MY ₃ ; d) RJ-C ₈ -MY ₄	145
Figure 4.39	Slopes of the line generated from plotting the absorbance against the integrated emission intensity at various wavelengths for RJ-C ₁₂ -MY ₁ complex	146
Figure 4.40	Slopes of the line generated from plotting the absorbance against the integrated emission intensity at various wavelengths for RJ-C ₁₂ -MY ₂ complex	147
Figure 4.41	Slopes of the line generated from plotting the absorbance against the integrated emission intensity at various wavelengths for RJ-C ₁₂ -MY ₃ complex	147
Figure 4.42	Slopes of the line generated from plotting the absorbance against the integrated emission intensity at various wavelengths for RJ-C ₈ -MY ₄ complex	148
Figure 4.43	a) Time-resolved photoluminescence spectra (TRPL) of RJ-C _n -MY _m series complexes b) the fast and slow time components for RJ-C _n -MY _m series complexes	149

Figure 4.44	The contribution from vibrational states in the absorption and emission spectra of a) RJ-C ₁₂ -MY ₁ ; b) RJ-C ₁₂ -MY ₂ ; c) RJ-C ₁₂ -MY ₃ ; d) RJ-C ₈ -MY ₄	151
Figure 4.45	Experimental FTIR spectra for RJ-C _n -MY _m series complexes; a) RJ-C ₁₂ -MY ₁ ; b) RJ-C ₁₂ -MY ₂ ; c) RJ-C ₁₂ -MY ₃ ; d) RJ-C ₈ -MY ₄	152
Figure 4.46	Computed FTIR spectra for RJ-C _n -MY _m series complexes; a) RJ-C ₁₂ -MY ₁ ; b) RJ-C ₁₂ -MY ₂ ; c) RJ-C ₁₂ -MY ₃ ; d) RJ-C ₈ -MY ₄	153
Figure 4.47	Vibrational spectra of a) RJ-C ₁₂ -MY ₁ ; b) RJ-C ₁₂ -MY ₂ ; c) RJ-C ₁₂ -MY ₃ and d) RJ-C ₈ -MY ₄	153
Figure 4.48	Comparison between vibrational modes of RJ-C ₁₂ -MY ₁ , RJ-C ₁₂ -MY ₂ , RJ-C ₁₂ -MY ₃ and RJ-C ₈ -MY ₄	154
Figure 4.49	TGA curve of a) RJ-C ₁₂ -MY ₁ ; b) RJ-C ₁₂ -MY ₂ ; c) RJ-C ₁₂ -MY ₃ and d) RJ-C ₈ -MY ₄	156
Figure 5.1	Optical absorption as a function of laser fluence for the RJ-C _n -MY _m series of porphyrins absorbing 0.1 OD in a 2 mm quartz cuvette at 532 nm	161
Figure 5.2	Photoacoustic response plotted with laser fluence. All the porphyrin samples were recorded at 0.1 OD in a 2 mm quartz cuvette at 532 nm	161
Figure 5.3	Optical Z-scan absorption (top) and photoacoustic emission (bottom) of all dyes as a function of optical density and concentration, respectively, measured at 20 mJ/cm ² fluence	163
Figure 5.4	Plots of optical Z-scan absorption and PA emission vs concentration recorded 400 mJ/cm ² laser fluence	164
Figure 5.5	Photoacoustic response plotted with laser fluence. All the porphyrin samples were recorded at 0.3 OD in a 2 mm quartz cuvette at 680 nm	165
Figure 5.6	Photoacoustic emission of all the RJ-C _n -MY _m series of porphyrin as a function of concentration, respectively, measured at 20 mJ/cm ² fluence	166
Figure 5.7	PAT image recorded at the low laser fluence of 20 mJ/cm ² and high laser fluence of 400 mJ/cm ² at $\lambda_{exc} = 532$ nm. All the RJ-C _n -MY _m samples had 0.1 O.D. at 532 nm in the 1 mm path length borosilicate capillary tubes. (top) Reconstructed WORD FOR WORD image at low laser fluence, normalized with the maximum PA signal strength of high laser fluence. The line plot is the PA signal strength for each sample. (bottom) Reconstructed PAT image obtained at high laser fluence and the corresponding line profile	167
Figure 5.8	PAT image recorded at $\lambda_{exc} = 680$ nm. All the RJ-C _n -MY _m samples had 0.1 O.D. at 680 nm in the 1 mm path length borosilicate capillary tubes	168

LIST OF SYMBOLS

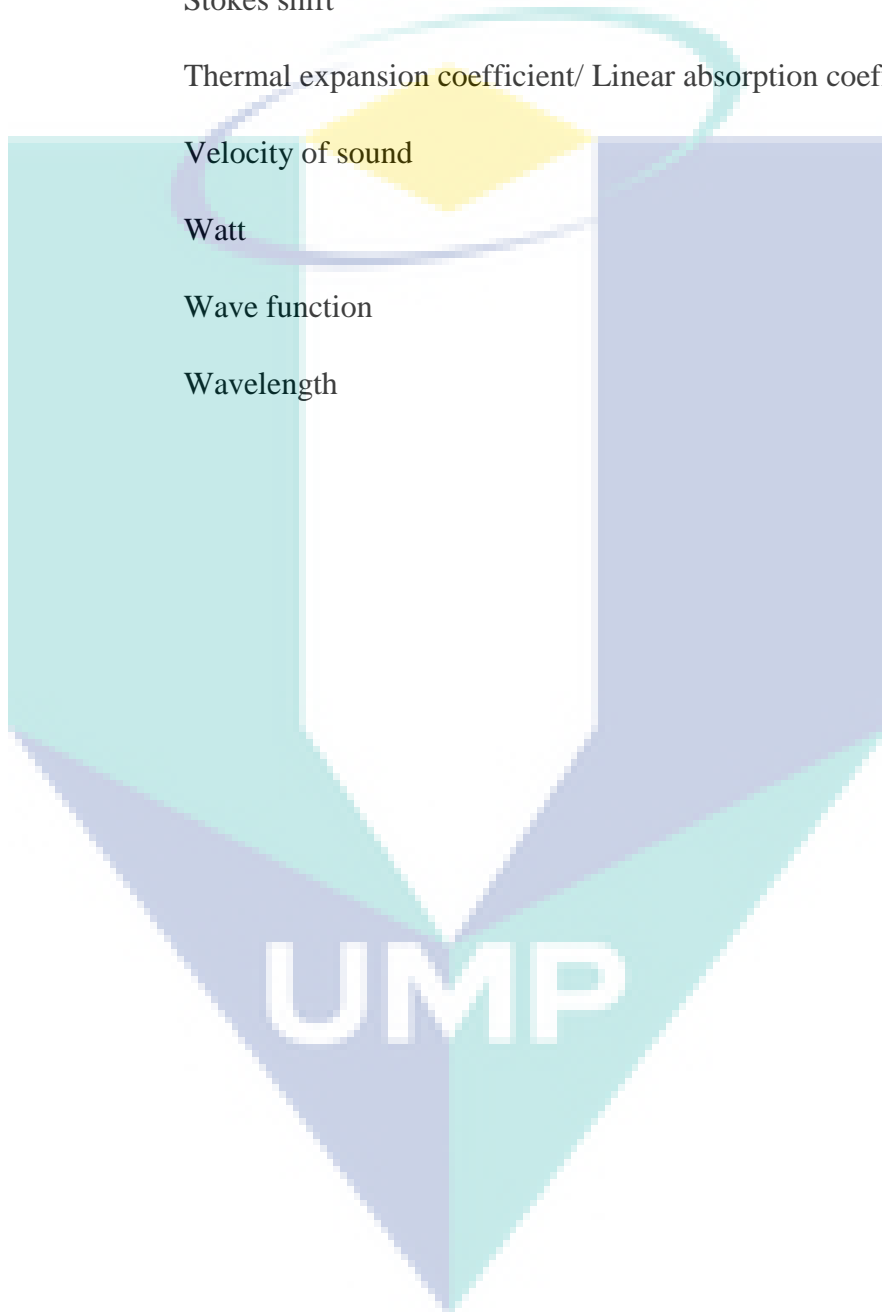


α	Alpha
β	Beta
cm	Centimetre
Δ	Chemical shift
C_e	Concentration of excited state molecules
ρ	Density
R	Electron position
eV	Electron volt
λ_{em}	Emission wavelength
E_g	Energy-gap
λ_{ex}	Excitation wavelength
Fs	Femtosecond
ϵ_e	First excited state molar extinction coefficient
Φ_f	Fluorescence quantum yields
C_g	Ground state concentration
ϵ_g	Ground state molar extinction coefficient
Γ	Grüneisen coefficient
$t_{1/2}$	Half-life
Hz	Hertz
I	Incident photon fluence
∇^2	Laplacian operator
MHz	Megahertz
μJ	Microjoules



μm	Micrometre
mJ	Millijoules
mL	Millilitre
Mm	Millimeter
mmol	Millimole
Ms	Millisecond
M	Molar
E	Molar extinction coefficient
Nm	Nanometre
Ns	Nanosecond
k_{nr}	Non-radiative decay
F	Oscillation strengths
Ppm	Parts per million
Φ_{ph}	Phosphorescence quantum yield
π	Pi
Pm	Picometer
Ps	Picosecond
\hbar	Plank constant
Φ_{nr}	Quantum yield for non-radiative decay
k_{r}	Radiative decay
N	Refractive index
${}^1\tau$	Singlet excited state life time
C_p	Specific heat of the medium at constant pressure
C_v	Specific heat of the medium at constant volume

C	Speed of light
$\Delta\nu_1$	Splitting between excited states Q(1,0) and Q(0,0) vibrational bands
$\Delta\nu_2$	Splitting between ground states Q(0,0) and Q(1,0) vibrational bands
$\Delta\nu$	Stokes shift
α	Thermal expansion coefficient/ Linear absorption coefficient
V_s	Velocity of sound
W	Watt
Ψ	Wave function
λ	Wavelength



LIST OF ABBREVIATIONS

B3LYP	Becke, 3-parameter, Lee-Yang-Parr
(Pd(PPh ₃) ₂ Cl ₂)	Bis(triphenylphosphine)palladium(II)chloride
BODIPY	Boron-Dipyrromethene
¹³ CNMR	Carbon Nuclear Magnetic Resonance
CHCl ₃	Chloroform
CI	Configuration Interaction
CuI	Copper iodide
CAMB3LYP	Coulomb attenuated-B3LYP
CC	Coupled-Cluster
CCSD	Coupled Cluster with single and double excitations
DFT	Density Functional Theory
CDCl ₃	Deuteriochloroform
CD ₃ OH	Deuteromethanol
DDQ	2,3-dichloro-5,6-dicyano-1,4-benzoquinone
CH ₂ Cl ₂ or DCM	Dichloromethane
DMF	Dimethylformamide
DZ	Double Zeta
E _{em}	Emission energy
EtOAc	Ethyl acetate
E _{ex}	Excitation energy
S ₁	Excited singlet state
FDA	Food and Drug Administration
FTIR	Fourier Transform Infrared
GTOs	Gaussian type orbitals
GUI	Graphical user interface

S ₀	Ground state
HF	Hartree-Fock
HOMO	Highest Occupied Molecular Orbital
HRMS	High Resonance Mass Spectroscopy
HK	Hohenberg-Kohn
HI	Hydriodic acid
HCl	Hydrochloric acid
HBr	Hydrogen bromide
H ₂ O ₂	Hydrogen peroxide
ICG	Indocyanine green
IR	Infrared
IEF-PCM	Integral Equation Formalism Polarizable Continuum Model
IC	Interconversion
IUPAC	International union for pure and applied chemistry
ISC	Intersystem crossing
LR-TD-DFT	Linear response Time-dependent Density Functional Theory
LANL2DZ	Los Alamos National Laboratory (LANL) ECP with Double Zeta valence
LUMO	Lowest Unoccupied Molecular Orbital
MgSO ₄	Magnesium sulfate
MATLAB	MATrix LABoratory
H ₂ TMP	meso-tetramethylporphyrin
H ₂ TPP	meso-tetraphenylporphyrin
M ^{II} (L)(CO)	Metal ligand cobalt
MX ₂	Metal salts
MLCT	Metal to ligand charge transfer
CH ₃ OH or MeOH	Methanol

MP2	Møller-Plesset Perturbation
NBS	<i>N</i> -bromosuccinimide
<i>n</i> BuLi	<i>n</i> -Butyllithium
NCS	<i>N</i> -chlorosuccinimide
NIR	Near-Infrared
Nd:YAG	Neodymium Yttrium Aluminum Garnet
NIS	<i>N</i> -iodosuccinimide
HNO ₃	Nitric acid
N ₂	Nitrogen gas
N ₂ O ₄	Nitrogen tetroxide
NO ₂ BF ₄	Nitrosonium borofluorate
NMR	Nuclear Magnetic Resonance
OPAZ	Optical and Photoacoustic Z-Scan
OD	Optical density
PhSeBr ₃	Phenylselenium tribromide
PhSeCl ₃	Phenylselenium trichloride
POCl ₃	Phosphoryl chloride
PA	Photoacoustic
PAI	Photoacoustic Imaging
PAM	Photoacoustic Microscopy
PAT	Photoacoustic Tomography
PCM	Polarizable Continuum Model
K ₂ CO ₃	Potassium carbonate
¹ HNMR	Proton Nuclear Magnetic Resonance
QZ	Quadruple Zeta
QC	Quantum chemical

RSA	Reverse saturable absorption
SCRf	Self-consistent reaction-field
SAT	Sitting at top
STOs	Slater type orbital
NaN ₃	Sodium azide
NaBH ₄	Sodium borohydride
NaOH	Sodium hydroxide
TBAF	Tetrabutylammonium fluoride
THF	Tetrahydrofuran
TMEDA	Tetramethylethylenediamine
TGA	Thermal Gravimetric Analysis
TLC	Thin-Layer Chromatograph
TD-DFT	Time-dependent Density Functional Theory
TRPL	Time-resolved Photoluminescence
SnCl ₂	Tin(II) chloride
NEt ₃	Triethylamine
TFA	Trifluoroacetic acid
TIPS	Triisopropylsilyl
AsPh ₃	Triphenylarsine
T ₁	Triplet excited state
T _n	Triplet excited states
TZ	Triple Zeta
Pd ₂ (dba) ₃	Tris(dibenzylideneacetone)dipalladium(0)
UV-Vis	UltraViolet-Visible
VR	Vibrational relaxation
Zn(OAc) ₂ •2H ₂ O	Zinc acetate dehydrate
ZnTPP	Zinc tetraphenylporphyrin

CHAPTER 1

INTRODUCTION

In short, this doctoral research thesis addresses design and synthesis of new porphyrin molecules for biomedical imaging, specifically photoacoustic imaging. Porphyrin plays an important role in many aspects of our lives including photosynthesis in green plants and oxygen sensing, transport and storage in living organisms. Porphyrins are a large family of macrocyclic aromatic molecules, its chemical structure can be visualized as four pyrrole-type rings, possessing two pyrrole (NH) and two pyrroline (=N) units, connected by methine groups as shown in Figure 1.1.

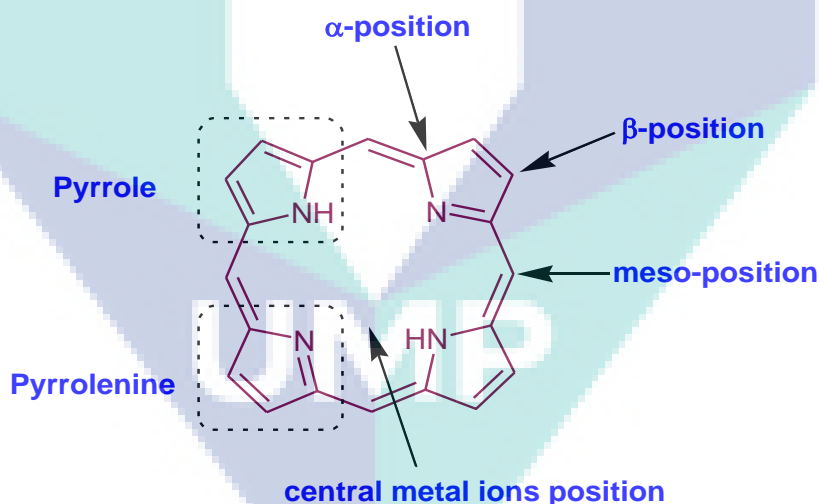


Figure 1.1 Basic Structure of Porphyrin

Besides, they are materials for an array of applications including Photodynamic Therapy, Chemotherapy, Magnetic Resonance Imaging, Supramolecules, Enzymes Catalysis, Dye-sensitized Solar Cells, Metal Ligands, Conductive Organic Materials, Nano-electronic Devices, Non-linear Optical Materials, and so on (Abrahamse & Hamblin, 2016; Jiang, Vairaprakash, et al., 2014; Jurow, Schuckman, Batteas & Drain, 2010; Mathew et al., 2014; Rybicka-Jasińska, Shan, Zawada, Kadish & Gryko, 2016;

Senge et al., 2007; Wróbel & Graja, 2006; Zhou, Liang & Dai, 2016). Porphyrin offers enormous possibilities in tailoring its optoelectronic properties by substitution of different functional groups at its α -, β -, and meso- positions as well as using varied choice of metal ions at the central position in its basic structure (Figure 1.1). Several stable structural moieties are known that would make an ideal point for further investigation of remarkable and tunable optical and electronic properties of a porphyrin molecule with slight modification in its basic core structure. This chapter summarizes the framework of this research that details the problem addressed, the objectives, and scope.

1.1 Problem Statement

Photoacoustic tomography (PAT) and photoacoustic microscopy (PAM) are emerging biomedical imaging techniques because of their high spatial resolution and ability for deeper in-vivo imaging (Schaberle et al., 2011; Zhang et al., 2011). In general, photoacoustic imaging (PAI) is a hybrid technique of ‘light in and sound out’ instead of ‘sound in and sound out’ as in ultrasound imaging and ‘light in and light out’ as in optical imaging. In PAI, laser pulses are utilized as a source of light to penetrate in tissues, which is either absorbed by endogenous biomolecules (hemoglobin, deoxyhemoglobin, melanin, and other biological molecules) or exogenous contrast agents (organic molecules, clusters or nanocrystals) and converted into heat. The released heat leads to thermal expansion, causing the generation of acoustic waves that are detected using an ultrasound transducer. Thus, PA signals are optically generated and ultrasonically detected; therefore, PAI combines the advantages of large optical window usable for imaging tissues, deep penetrating depth and spatial resolution of ultrasound. However, the endogenous biomolecules have limitations of deep tissue penetration; and therefore, exogenous contrast agents exhibiting large PA coefficients are one of the essential requirements for successful implementation of PAT and PAM. An ideal contrast agent should have high absorption cross-section, long lived S_1 excited state, rapid S_n-S_1 non radiative decay and relatively lower fluorescence such that the photoexcited electrons are rapidly relaxed through non-radiative pathways, causing a transient rise in temperature around its closest vicinity thereby leading to a localized thermoelastic expansion followed by acoustic waves.

In recent years, many micro- or nano- scale materials besides organic molecules, such as nanoparticles, nanofibers, nanorods, nanocages and nanotubes, have been introduced as contrast agents, some of which showed desirable photoacoustic properties (Chen et al., 2011; Maji et al., 2014; Sreejith, Huong, Borah & Zhao, 2015; Zhang et al., 2015). While nanostructures such as gold nanoparticles or carbon nanotubes offer high absorption cross-section and superior thermal effect than organic molecules, however they impose severe restrictions on clinical use due to toxicity and metabolism (Browning et al., 2009). Alternative approaches are the use of organic dyes assembled into vesicles, such as porphosomes, microbubbles, nanodroplets and photoacoustic probes generated in tissues (Filonov et al., 2012; Lovell et al., 2011). However, PAI applications are currently limited due to the lack of simple molecular contrast agents. Although, the organic dyes with a high absorption in the NIR range, such as cyanine, porphyrin and BODIPY derivatives, have been used as PA contrast agents, they are limited due to their poor PA effects (Frenette et al., 2014; Wang, Zhao, Barkey, Morse & Jiang, 2012). Among them, porphyrins are particularly interesting due to their high optical absorption, stability, and biocompatibility, long lifetimes and can be used for lifetime-base PA imaging to probe the molecular environment surrounding a sample. So far, dedicated efforts to develop common metalloporphyrins such as Zn(II)porphyrins as a molecular contrast agent by tailoring their absorption spectra have not been undertaken. Besides, correlation between structural and optoelectronic properties to PA signals has also not been undertaken systematically. The development of new PA molecules is limited because the factors influencing the PA effect have rarely been systematically studied, resulting in a lack of guidance for the design of molecular PA contrast agents. Conspicuously rare in the literature are small molecular porphyrin contrast agents designed for PAI. Therefore, the research described in this thesis is concerned with the design and synthesis of novel porphyrins using modern protocols for their applications as PAI contrast agents. Furthermore, the novel synthesized porphyrins are examined in the view of their potential optoelectronic properties.

1.2 Hypothesis

It is hypothesized that if the molecular structure is controlled in such a way that thermalization pathways (phonon emission) are provided near to the emitting states of

the molecules, photoexcited electrons will be rapidly thermalized than emitted as photons that could help the development of new PAI contrast agent with high PA signals.

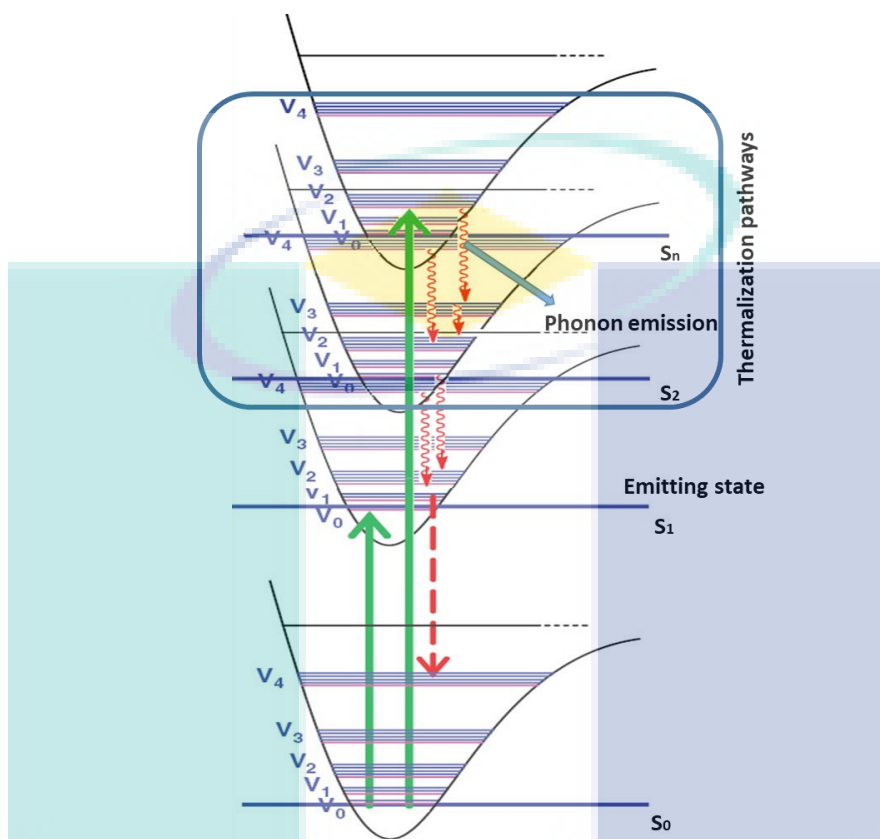


Figure 1.2 Excited energy state of a molecule

1.3 Research Objectives

The broad objective of this doctoral research is to develop a general design criterion based on the hypothesis for porphyrins to show large photoacoustic effects and its practical demonstration. This broad objective is supported by several more specific objectives, which include:

- i. To study the evolution of molecular vibration spectra of porphyrin from its basic moiety with systematic π -conjugation and correlate the emission states and the vibrational energies to the photoacoustic coefficient using density functional theory.

- ii. To study the feasibility of synthesizing the predicted Zn(II)porphyrin molecules and correlate the experimental data with that of theoretical results.
- iii. To validate the hypothesis by demonstrating a systematic variation in photoacoustic intensity using the newly synthesized porphyrin molecules.

1.4 Research Scope

The broad scope of this research is to design and synthesize new porphyrin molecules for evaluating various vibrational energies states as well as showing broader absorption spectra. Identifying a porphyrin molecule with the higher vibrational emitting states is considered important for strong PA signals generation. The scope of research to achieve the specific objectives mentioned above as follows:

Scope of objective 1:

As density functional theory calculations (DFT) has emerged as an excellent predictive tool with less computational cost in addition to minimize the materials cost and environmental risks, the state of the art theory will be used for designing the new molecules. The boundaries of this objectives are:

- i. Designing of new molecules is employed by quantum chemical calculations under the frame work of density functional theory.
- ii. Only organic and Zn(II)porphyrins are considered in this study.
- iii. Only hybrid functional (B3LYP and CAMB3LYP) and basic sets 3-21G, 6-31G and LANL2DZ are used for metal-free porphyrin molecules for geometry optimization and calculation of optoelectronic properties; the consistence of the data is verified only within B3LYP/3-21G, B3LYP/6-31G, B3LYP/LANL2DZ, CAMB3LYP/3-21G, CAMB3LYP/6-31G, and CAMB3LYP/LANL2DZ levels of the theory using Gaussian 09W software.
- iv. The geometry optimization and optoelectronic property calculations for metalloporphyrins are limited to B3LYP/3-21G, B3LYP/6-31G(d), B3LYP/LANL2DZ, CAMB3LYP/3-21G, CAMB3LYP/6-31G(d), and CAMB3LYP/LANL2DZ levels of the theory to account the d-orbital electrons.

- v. The optoelectronic property calculations are limited to FTIR and UV-Vis spectroscopy.
- vi. The effect of different solvents on optoelectronic properties of porphyrin molecules are studied by using polarizable continuum model (PCM). However, to correlate the theoretical data with experimental data, the optoelectronic spectra calculated in methanol (CH₃OH) are more preferable.
- vii. The energies of molecular orbitals HOMO, HOMO+1, LUMO, LUMO-1, etc. and the energy gaps of optimized structures are calculated under the framework solvent effect using B3LYP/LANL2DZ levels of the theory.
- viii. The vibrational spectra (FTIR) of optimized molecules are limited for B3LYP/LANL2DZ levels of the theory in gas state.
- ix. The absorption spectra (UV-Vis) of optimized molecules are limited for the 50 lowest singlet-singlet excitations by using Time dependent DFT (TD-DFT) calculations in gas state as well as in solution phase.

Scope of objective 2:

- i. The newly designed porphyrin molecules are synthesized by ten-step series of reactions, including acid catalyzed oxidation reaction, Knoevenagel condensation, MacDonald (2+2) condensation, bromination, metalation, deprotection reaction, and Sonogashira coupling with modifications.
- ii. The methodologies adopted for the synthesis of porphyrin macromolecules are optimized only for free-base and Zn(II)porphyrins.
- iii. The methods optimized for the various precursor synthesis are limited to synthesizing the di(alkoxy)benzene, bis(alkoxy)benzaldehyde, cyano-3-(4-iodophenyl)acrylic acid and di(1H-pyrrol-2-yl)methane precursors.
- iv. The synthesis of four novel metalloporphyrins are limited to Zn metal fragment attached to the central core of the porphyrin macromolecules and extended π -conjugated functional groups attached at the meso-positions.
- v. The synthetic porphyrins are characterized by Nuclear Magnetic Resonance (¹HNMR and ¹³CNMR), High resonance mass spectroscopy (HRMS), Fourier Transformer Infra-red (FTIR), UV-Vis and Thermal Gravimetric analysis (TGA) techniques.

Scope of objective 3:

- i. The absorption, emission and vibrational spectra of synthesized porphyrins are measured in solution phase and are compared with those of theoretical spectra.
- ii. The PA studies of synthesized porphyrins are done with optical and photoacoustic Z-scan (OPAZ) as well as photoacoustic tomography (PAT).
- iii. The optoelectronic properties of synthesized porphyrins are then correlated with that of PA studies.

1.5 Novelty of Research

The meso-substituted Zn(II)porphyrin macromolecules with various π -conjugated functional groups starting from the parent porphine have been designed and their optoelectronic properties have been studied by employing the hybrid functionals B3LYP and CAMB3LYP with basic sets 3-21G, 6-31G, 6-31G(d) and LANL2DZ using Gaussian 09W software. The four novel meso-substituted Zn(II)porphyrin macromolecules, namely as RJ-C_n-MY_m, have been synthesized and characterized. The PA studies of the synthesized Zn(II)porphyrins have been done by OPAZ-scan and PAT.

1.6 Thesis Outline

Organization of this thesis is summarized in Figure 1.3. Chapter 1 outlines the problem statement, objectives, scope and contribution of the research. Comprehensive review of the porphyrins, DFT calculations, their synthesis, their optoelectronic properties and PAI properties are discussed in chapter 2. Details of the methods used for DFT calculations as well as synthetic protocols used in this study are elaborated in the chapter 3. Chapter 4 explains the synthetic mechanism as well as optoelectronic properties in correlation with PA properties of synthesized porphyrins. In chapter 5, the discussion on PA studies of newly synthesized porphyrin molecules are highlighted in detail. Lastly, chapter 6 concludes the findings of the present research and provides recommendations for future progresses.

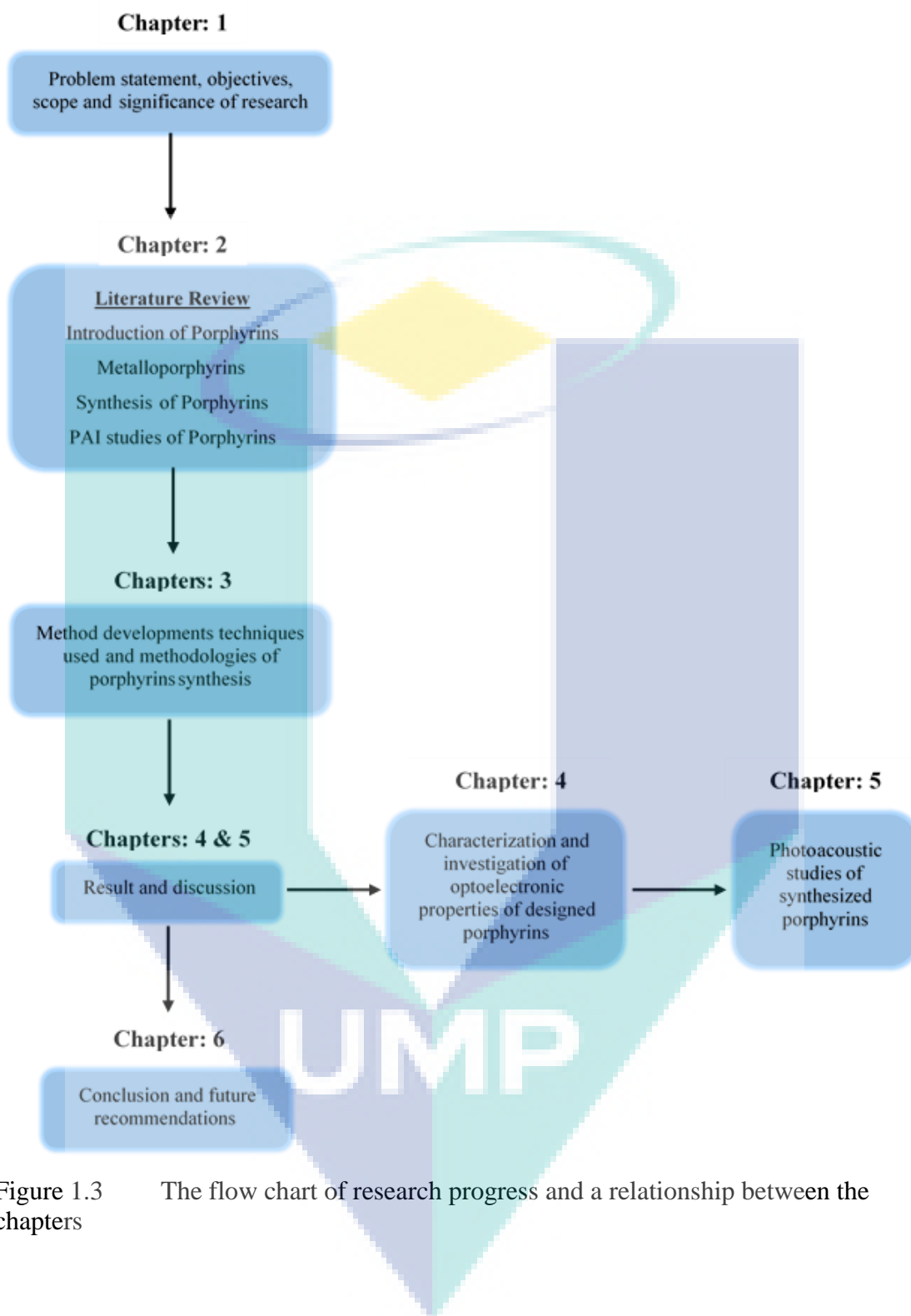


Figure 1.3 The flow chart of research progress and a relationship between the chapters

CHAPTER 2

LITERATURE REVIEW

2.1 Introduction

This chapter presents structure, properties and applications of porphyrins, and progress made in their synthesis. Porphyrin is derived from porphura, the Greek word for purple. Porphyrins are heterocyclic macromolecules, consisting of four pyrrole type subunits, viz. two pyrrole (NH) and two pyrrolenine (=N) units, which are connected via methine (=CH-) bridges as shown in Figure 2.1.

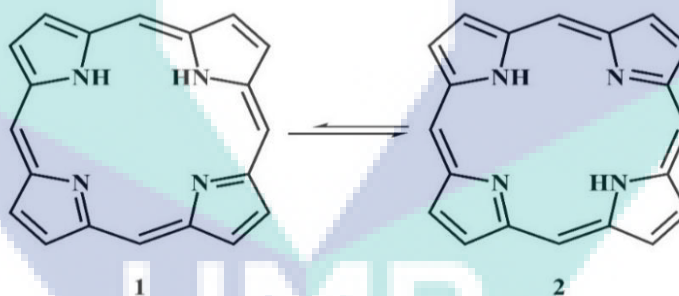


Figure 2.1 Schematic representation of the two tautomers of porphyrin. 1) *cis*-NH tautomer and 2) *trans*-NH tautomer

The porphyrins play a vital role in living organisms: as chlorophyll in green plants, as hemoglobin in red blood, as vitamin B₁₂ a cofactor involved in diversity of biochemical processes, cofactor F₄₃₀ the prosthetic group of the enzyme methyl coenzyme M reductase, as bacteriochlorophylls in various phototropic bacteria and as cytochromes in both animals and plants cells (See Appendix A). The structure can be visualized as existing in tautomeric equilibrium, where two protons are exchanged between four nitrogen atoms, forming four pyrrole rings equivalent to *cis*-NH tautomer and *trans*-NH tautomer (Figure 2.1). Among them the *trans* configuration is more stable

than the other as proved by spectroscopic and computational studies (Hynninen & Lötjönen, 1980).

Porphyrins and related tetrapyrrolic macromolecules are the fundamental molecules of all organisms; and therefore, are the intense area of research since the early 19th century. They play an essential part in many aspects of our lives including photosynthesis in green plants, oxygen transport and storage within living organisms. Porphyrins have been utilized in large number of applications in different fields such as catalysis (Pereira, Simões, Tomé & Almeida Paz, 2016; Rybicka-Jasińska et al., 2016; Sheldon, 1994), medicine (Abrahamse & Hamblin, 2016; Ol'shevskaya et al., 2007; Zhou et al., 2016), and optoelectronic (Ishihara et al., 2014; Jurow et al., 2010; Mathew et al., 2014; Senge et al., 2007; Zhan et al., 2011). The remarkable physical, optical, chemical, and coordinative properties of porphyrins have prompted countless efforts towards the synthesis of new porphyrins with various improved electronic, steric, and conformational environments.

Ever since the isolation of porphyrin (hematoporphyrin) from blood in 1867 by Thudichum, this unique macromolecules has fascinated researchers from all over the world because of their remarkable physical, chemical and spectroscopic properties and their essential biological functionalities. The history of porphyrins has been the subject of numerous reviews (Adler & Gouterman, 1985; Drabkin, 2012; Longo, 1979; Sheldon, 1994). The structure of porphyrin as a cyclic tetrapyrrole was first suggested by Küster in 191. Willstätter & Stoll (1913) firstly isolated the chlorophyll *a* and was awarded the Nobel Prize in Chemistry in 1915 for his research on plant pigments, especially chlorophyll. Milroy (1918) first synthesized the porphyrins from hematoporphyrin. Later, Fischer (1929), who is known as the father of porphyrin chemistry, confirmed the structure of porphyrins proposed by Küster through synthesis of porphyrins, including etioporphyrin-III, octamethylporphyrin and chlorohemin; and become recipient of Nobel Prize in 1930. The synthesis of meso-tetraphenyl-porphyrin, which emerged as the synthetic model for porphyrin complexes, was first described by Rothemund (1939). Moreover, the molecular structure elucidations of hemoglobin and myoglobin using X-ray crystallography were first reported by Perutz, Rossmann, Cullis, Muirhead, Will and North (1960) and Dickerson, Strandberg, Hart, Davies, Phillips and Shore (1960) respectively, in same year and shared the Nobel Prize in 1962. In short, at least nine Nobel

Prizes have been awarded on porphyrin chemistry. Till now, porphyrins have not dropped any attraction as expressed in the countless publications every year on porphyrin chemistry. The foundation of its own journal the “Journal of Porphyrins and Phthalocyanines” (JPP) in 1997 and also the foundation of “The Society of Porphyrins and Phthalocyanines” (SPP) in 2000 confirmed the sheer impact of this research topic. Moreover, twenty volumes of “The Porphyrin Handbook” have been published until now.

2.2 Metalloporphyrins

One of the important features of porphyrins is its ability to form complex with any of transition metal or semi metal atoms in its macrocyclic cavity (Figure 2.2). A number of metalloporphyrins are known by a metal atom coordinated with the porphyrin ring, having different oxidation of metals and possibility of further coordination at the axial position. Porphyrin acts as chelating ligands employing the transition metal ion in its macrocyclic plane. The macrocyclic cavity of the porphyrin can coordinate with metal ions having a maximum radius of 2 Å (Sessler & Tomat, 2007).

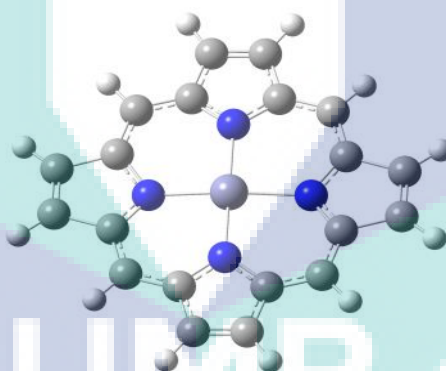


Figure 2.2 Metalloporphyrins (adpoted from Gaussview); blue, light gray, dark gray and white colored atoms represents nitrogens, carbons, metal ion and hydrogens

The geometry of these complexes and number of additional ligands in the axial position depends upon the metal ion (Liao, Watts & Huang, 2005; Nelson, Roberts & Berns, 1987; Shelby, Mara & Chen, 2014). The most common metal atoms in porphyrin ring are iron (Fujii, 2002; Grinstaff, Hill, Labinger & Gray, 1994; Luthra, Denisov & Sligar, 2011; Mittra, Singha & Dey, 2016; Nakamura, Ikezaki & Takahashi, 2013), magnesium (Abedian & Dehghani, 2013; Borah & Bhuyan, 2017; Ichiki, Matsuo & Nakamura, 2013; Jusélius & Sundholm, 2000; Lindsey & Woodford, 1995), copper (Chen, Zhang, He & Liu, 2002; Kruglik, Apanasevich, Chirvony, Kvach & Orlovich,

1995; Wang, Zhou, et al., 2014; Wang, Brugh, Rawson, Therien & Forbes, 2017), cobalt (Chizhova, Kumeev & Mamardashvili, 2013; Éll et al., 2006; Liao et al., 2005; Zhu et al., 2009), zinc (D'Souza & Ito, 2005; Mathew et al., 2014; Shoji, Tashiro & Aida, 2004; Yamaguchi, Kimura, Matsuda & Aida, 2004; Yella et al., 2011), nickel (Han et al., 2016; Kadish et al., 1993; Sharma, Ahuja & Sidhwani, 2009; Thies et al., 2010), manganese (Radon, 2015; Tovmasyan et al., 2013), Palladium (Amao, Asai, Miyakawa & Okura, 2000; To, Liu, Lau & Che, 2013), platinum (Naik, Rubbiani, Gasser & Spingler, 2014; Sommer et al., 2011; Zems, Moiseev & Perepichka, 2013) and vanadium (Márquez, Ysambertt & De La Cruz, 1999; Poncet et al., 1982). Although porphyrins are typically planar, the binding of metal atoms in the centre position or further protonation of the central nitrogen atoms can lead to structural distortions (Milgrom & Warren, 1997). Porphyrins have the ability to form complexes with a variety of geometries including in-plane, out-of-plane (in other words, sitting at top, SAT), and bimetallic complexes (Hoard & Smith, 1975; Smith 1975). Depending on the metal, they can form square planar (Cu^{2+} , Ni^{2+}), square-pyramidal (Mg^{2+} , Zn^{2+}) or octahedral (Fe^{2+} , Mn^{2+}) complexes. Almost all metal ions form a 1:1 complex with porphyrin. Upon coordination of metal, two protons on the inner nitrogen atoms leave and form neutral complexes with divalent metals (explain in section 2.6.2 in detail). These metalloporphyrins play vital roles in biological systems: hemo and myoglobins (Fe coordinated), chlorophyll (Mg coordinated), cytochromes (Fe coordinated), and catalases (Fe coordinated) are well known examples. Distortions of the macrocycle also occur with addition of substituents onto the β - and meso-carbon. The introduction of such variations to the porphyrin ring results in having a wide range of photo-physical properties and biochemical functions.

2.3 Classification of Porphyrins

Porphyrins are classified into (i) free-base porphyrins and metalloporphyrins depending upon whether a metal ion is coordinated in the core of the porphyrin ring; (ii) symmetrical and unsymmetrical depending on their molecular symmetry; (iii) β -substituted porphyrins, meso-substituted porphyrins and β - and meso-substituted porphyrins according to the position the substituent occupies in the porphyrin core. These structures are schematically shown in Figure 2.3.

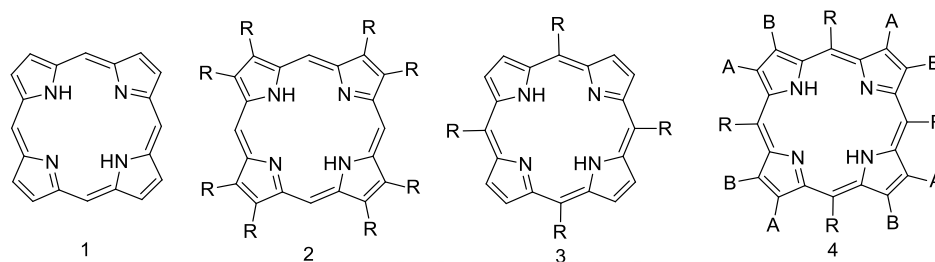


Figure 2.3 The most common substitution patterns found in porphyrin macrocycle. 1) porphine; 2) β -substituted porphyrin; 3) meso-substituted porphyrin; 4) β - and meso-substituted (mixed) porphyrins

Symmetry of a porphyrins mainly depends upon the starting material used for synthesis and are of the following types (Wijesekera & Dolphin, 1994); 1) un-substituted monopyrroles (Liu, Feng, Gu, Meng & Zhang, 2012; Neya, Yodo & Funasaki, 1993; Trova et al., 2003); 2) substituted monopyrroles (Neya, Quan, Hoshino, Hata & Funasaki, 2004); 3) dipyrromethane (Jiang, Gou & Jing, 2014; Jradi et al., 2015; Wiehe, Ryppa & Senge, 2002; Yella et al., 2011); 4) substituted dipyrromethane (Ambroise et al., 2001; Beyzavi, Lentz, Reissig & Wiehe, 2013; Dogutan, Ptaszek & Lindsey, 2007; Dogutan, Ptaszek & Lindsey, 2008; Fungo, Otero, Sereno, Silber & Durantini, 2000); 5) tripyrranes (Lash, 1996; Saltsman, Goldberg, Balasz & Gross, 2007; Taniguchi, Hasegawa, Nishimura & Takahashi, 1999); and 6) linear tetrapyrroles (Jackson, Kenner & Smith, 1971; Wijesekera & Dolphin, 1990) (explain in section 2.6 in detail).

Stability of metalloporphyrin depends upon the comparability in size of ionic radii of metal ions and the central cavity of porphyrin ligand. Based on the later consideration, the metalloporphyrin are described as In-plane (or coplanar) metalloporphyrins and out-of-plane or sitting-atop (SAT) metalloporphyrins.

2.3.1 In-Plane Metalloporphyrins

Upon coordination, the radius of the central cavity of deprotonated porphyrin ligand is from 0.6 to 0.7 Å (Hoard, 1971) and is ideally well matched to bind proximately all metal ions. The position of central metal and the symmetry of metalloporphyrin greatly depends upon the spin multiplicity, size and charge of metal ions. When the radius of coordinating metal ion is in the range of 55-80 pm, the subsequent metalloporphyrin is called in-plane (also called normal, regular or coplanar) metalloporphyrin. The metal

centres are situated within the plane of the porphyrin ring and fit properly into the porphyrin ligand cavity (Giovannetti, 2012) as shown in Figure 2.4a.

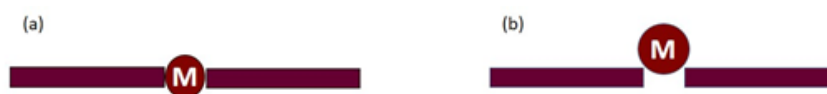


Figure 2.4 Representation of a) In-plane metalloporphyrins; b) Out-of-plane metalloporphyrin

Source: Giovannetti (2012)

Metal ions such as Co(III), Ni(II), Cu(II), Zn(II) can fit accurately into the cavity of porphyrin ligand to form the kinetically inert in-plane or regular metalloporphyrins. The structure representation of regular metalloporphyrin is shown in Figure 2.5. Most of the metalloporphyrins found in natural form are of regular types. The formation of regular metalloporphyrins is slow due to the rigidity of porphyrins. Some in-plane metalloporphyrins include $\text{Al}^{\text{III}}\text{TSP}^{3-}$ with radius of 53.5 pm for Al^{III} (Horváth, Huszánk, Valicsek & Lendvay, 2006), $\text{Fe}^{\text{III}}\text{TSP}^{3-}$ with radius of 60 pm for Fe^{III} (Huszánk & Horváth, 2005; Valicsek & Horváth, 2007) and $\text{Pd}^{\text{II}}\text{TSP}^{4-}$ with radius of 86 pm for Pd^{II} (Horváth et al., 2006; Horváth, Valicsek, Harrach, Lendvay & Fodor, 2012).

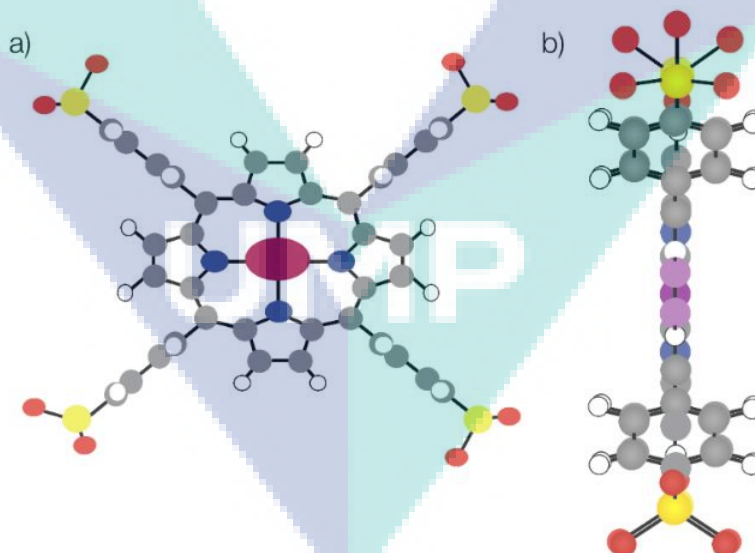


Figure 2.5 Structure representation of In-plane metalloporphyrins; a) Top-view; b) Side-view

Source: Horváth et al. (2006)

Porphyrins have the capability to produce stable metal complexes without any large change in the structure. The characteristic of non-planarity of porphyrin play vital

role in biological functions. For example, cytochromes and peroxidase (hemoproteins) have distorted structures (Jentzen, Ma & Shelnut, 1998; Shelnut & Medforth, 1998). Therefore, a significant consideration has been made on the of porphyrins distortion (Harada et al., 2005). Distortion in porphyrins affect their properties, relativities and their redox potential. As a result of distortion, symmetry decreases and modification in the absorption spectrum has been observed (Al-Karadaghi et al., 2006; Shelnut & Medforth, 1998).

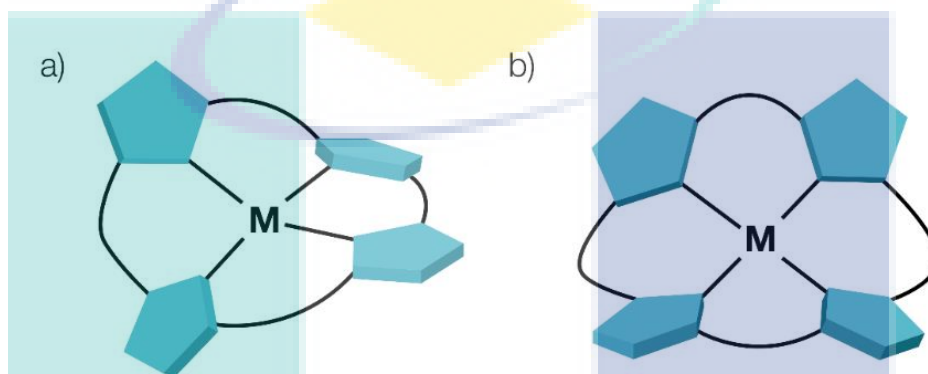


Figure 2.6 In-plane metalloporphyrin distortion; a) Saddle metalloporphyrin; b) Ruffled metalloporphyrin

Source: Harada et al. (2005)

In-Plane metalloporphyrins may display saddle type and ruffled type distortion as shown in Figure 2.6. Such kinds of distortions occur due to the overcrowded (bulky) substitutions on the periphery position, the protonation of alkylation of the pyrrolic nitrogen atoms and too short metal nitrogen bonds causing the contraction of the coordination cavity. The examples of such kinds of metalloporphyrins are nickel(II) (Brückner et al., 2005; Kaplan, Suslick & Scott, 1991), chromium(III), titanium(IV), and manganese(III) porphyrins (Dwyer, Puppe, Buchler & Scheidt, 1975; Galich, Hückstädt & Homborg, 1998). Saddle and ruffled type distortion result in strong deviation of metalloporphyrin from the plane and can be confirmed by the $N-C_{\alpha}-C_{meso}-C_{\alpha}$ dihedral angles (Valicsek & Horváth, 2013). Alteration in the planar geometry of metalloporphyrins modify their photochemical properties. Jentzen and other researchers have found the presence of saddle kind of distortion in zinc and nickel metalloporphyrins, explaining the change in photo-physical and photo-chemical properties (Drain et al., 1996; Horning, Fujita & Fajer, 1986). The non-planar distortion has spectroscopic significance which have been observed as a red shift in the absorption band. The magnitude of distortion decides the red shift in spectrum (Barkigia et al., 1990; Jentzen

et al., 1995; Shelnutt & Medforth, 1998). Many researchers have developed in-plane metal porphyrin complexes for many applications (Böhm & Gröger, 2015; Natali, Luisa, Iengo & Scandola, 2014; Vasil'ev & Lobanovskaya, 2015).

2.3.2 SAT Metalloporphyrins

Out-of-Plane metalloporphyrins are moulded when metal centres are not capable to fit into the porphyrin cavity as shown in Figure 2.4b. Central metal ions of ionic radii greater than 80-90 pm, are too big to fit into the central cavity of porphyrin and they are situated out of porphyrin ring plane, resulted in the formation of SAT (sitting-atop) metalloporphyrin. Different names like allo, exo-planar, dome metalloporphyrins, roof, and sitting above the plane of ligand have been applied by different researchers for SAT complexes (Abraham, Hawkes, Hudson & Smith, 1975; Barkigia, Fajer, Adler & Williams, 1980; Giovannetti, 2012; Horrocks Jr & Hove, 1978). These metal porphyrins display special characteristics originating from the non-planar structure due to the metallic size.

The out-of-plane metalloporphyrins are kinetically labile, thermodynamically less stable and has different structural and photo-induced features compared to in-plane metalloporphyrins. The formation rate of SAT metalloporphyrins is faster and more reactive than in-plane metalloporphyrins (Barnes & Dorough, 1950) because of their inflexibility. The out-of-plane position of the metal in SAT complexes induces superior photo-chemical and photo-physical properties to all of this class of compounds. The SAT complexes have C_{4v} to C_1 symmetry, lower than that of free-base porphyrins D_{2h} and in-plane complexes D_{4h} . Structure of out-of-plane metalloporphyrin is shown in Figure 2.7 indicates that metal ion lies in and out of plane position of porphyrin cavity (Giovannetti, 2012; Valicsek, Eller & Horváth, 2012).

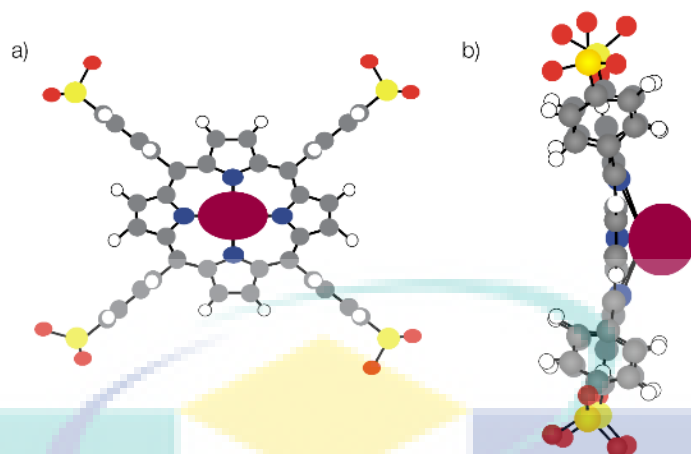


Figure 2.7 Structure representation of Out-of-plane metalloporphyrin; a) Top-view; b) Side-view

Source: Horváth et al. (2006)

In SAT metalloporphyrins, due to the metal ions of large radii or their coordination abilities may cause distortion in structures. Such type of distortion is known as dome distortion, shown in Figure 2.8. This distortion is observed when the M-N bond lengths are longer than half of the diagonal N-N bond distance. Dome distortion are also occurred in some special cases with small metal ions radii, if coordinated with a ligand at axial position (Horváth et al., 2006; Horváth et al., 2012).

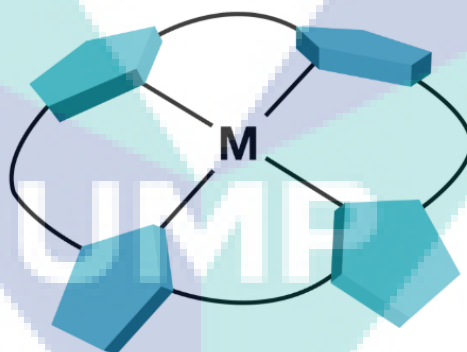


Figure 2.8 SAT metalloporphyrin distortion (Dome distortion)

Source: Harada et al. (2005)

This dome distorted structure exposes peculiar photochemical characteristics. They can endure the photo-induced charge transfer from porphyrin ligand towards the metal centre. The absorption and emission properties of SAT complexes are different than in-plane metalloporphyrins (Valicsek et al., 2012). Some heavy metal ions in out-of-plane metalloporphyrins like Pb^{2+} , Hg^{2+} , and Cd^{2+} are able to catalyze the synthesis of in-plane complexes via exchanging the metal ions through the formation of SAT as

intermediate, shown in Figure 2.9 (Horváth et al., 2006). A low amount of a large radius metal ion can speed up the inclusion of small metal ions into the porphyrin cavity. The SAT of different metals in porphyrin plane has been fully explained on the basis of X-ray analysis of structural data. Some reported examples of SAT metalloporphyrins are $\text{Ag}^{\text{II}}\text{TSPP}^{4-}$ with ionic radius of 94 pm (Harrach, Valicsek & Horváth, 2011), $\text{Hg}^{\text{II}}\text{TSPP}^{4-}$ with ionic radius of 102 pm (Horváth, Valicsek & Vogler, 2004; Valicsek, Lendvay & Horváth, 2008), and $\text{Bi}^{\text{III}}\text{TSPP}^{3-}$ with ionic radius of 103 pm (Valicsek, Horváth & Patonay, 2011).

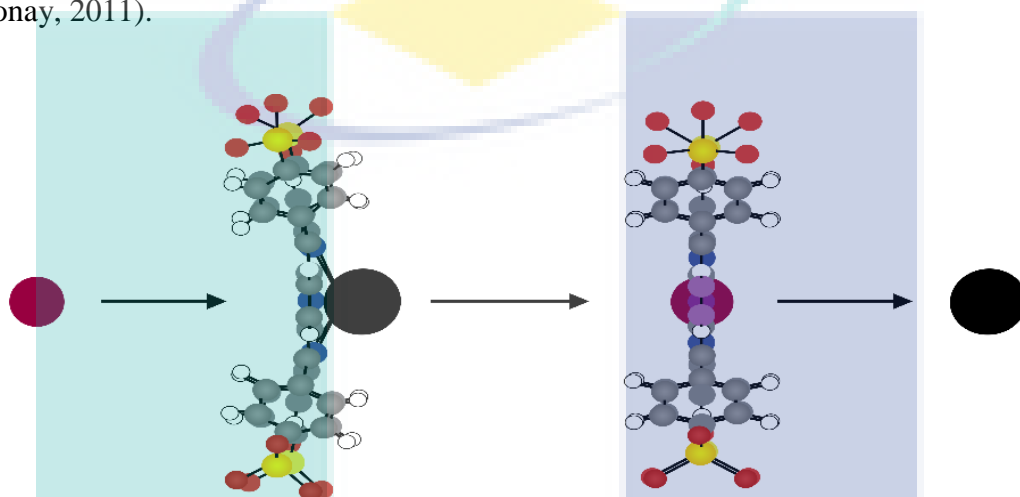


Figure 2.9 Formation of In-plane metalloporphyrin via Out-of-plan metalloporphyrin as intermediate

Source: Horváth et al. (2006)

The types of SAT complexes are also based upon number of porphyrin ligands and metal ions involved. One of its type is mononuclear monoporphyrin complexes. Examples of such complexes are Zirconium (IV) and hafnium (IV) porphyrins. The other type of complex is mononuclear bisporphyrins (Taylor & Tsutsui, 1975). Porphyrins have the capability to coordinate with two metal centres to form dinuclear monoporphyrins (Hambricht, 1970; Tsutsui & Hrungr, 1973). Furthermore, one out of plane metal ion may harmonize parallel to the cavities of two porphyrin macrocycle which result in the formation of sandwich style of structure (Akins, Zhu & Guo, 1994; Akins, Özçelik, Zhu & Guo, 1996; Hudson & Smith, 1974; Ricciardi, Rosa, Baerends & van Gisbergen, 2002). Trinuclear bisporphyrin mercury complex, also representing the third type of SAT complexes, is the example of sandwiched or stacked polymer type metalloporphyrins in which three metals ions are bonded with two macrocycles, representing the out of plane complexes. In these complexes the interactions between porphyrin macrocycles can

result in interesting electronic, steric as well as photo-physical and photochemical consequences (Liao, Watts & Huang, 2006; Taylor & Tsutsui, 1975).

2.4 Photochemistry

The porphyrin macromolecule is highly conjugated having 22π electrons in the ring. However, the aromaticity of porphyrins is arising by contribution of only 18π electrons in the delocalization of aromatic system and obeying the Hückel's $4n+2$ rule (Gouterman, 1978; Stepien & Latos-Grazynski, 2008; Wu, Fernández & Schleyer, 2012). Porphyrins follow the Hückel's rule of aromaticity ($n=4$), showing in Figure 2.10, and usually have planar geometry according to their crystal structures. Their aromaticity has been authenticated by heat of combustion, X-ray crystal structures (Aizawa et al., 1987) and chemical shifts in ^1H NMR spectroscopy (Sondheimer, Wolovsky & Amiel, 1962; Stepien & Latos-Grazynski, 2008).

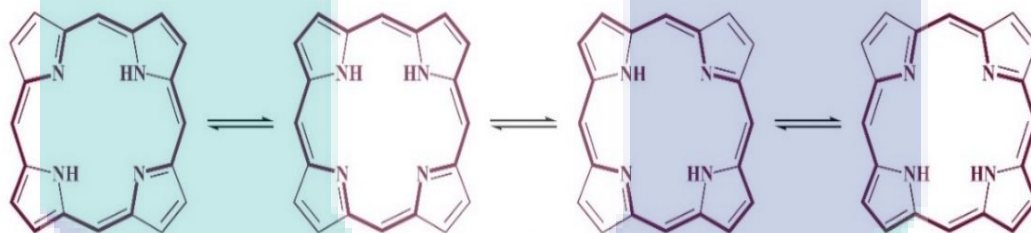


Figure 2.10 Aromaticity in porphyrin: 18π electrons out of 22π electrons form the conjugation pathway (indicated in bold)

The rigid 18π conjugation system in porphyrins convey their electronic properties. All the porphyrins and other related derivatives absorb in the visible region strongly; and therefore, are highly colored. All the free-based porphyrins show an intense absorption band at ~ 400 nm with extinction coefficient $\sim 1 \times 10^5 - 1 \times 10^6 \text{ M}^{-1}\text{cm}^{-1}$ called Soret band or B band, and show four less intense bands in the 450-700 nm spectra region with extinction coefficient $\sim 1 \times 10^4 \text{ M}^{-1}\text{cm}^{-1}$ called Q-bands. Both the Soret band and the Q-bands ascend from the $\pi\text{-}\pi^*$ transition and are explained by the Gouterman four-orbital model (explained in section 2.4.1.2) (Gouterman, 1961).

The chemical shifts in NMR spectra of porphyrin are one of their characteristic feature for identification. The NMR spectra of porphyrins show anisotropic effect and intensely influenced by the aromatic ring current (Smith, Goff & Abraham, 1984). In

$^1\text{H-NMR}$, the signals for the deshielded *meso*-protons tend to resonate to lower fields in spectrum ($\delta \sim 10$ ppm), likewise the pyrrolic protons are deshielded and their signals are appeared at low field ($\delta \sim 8$ ppm- 9 ppm). While the signals of the inner NH- protons are appeared at high field (between -2ppm to - 4 ppm) due to high shielding effect by the ring current (Figure 2.11).

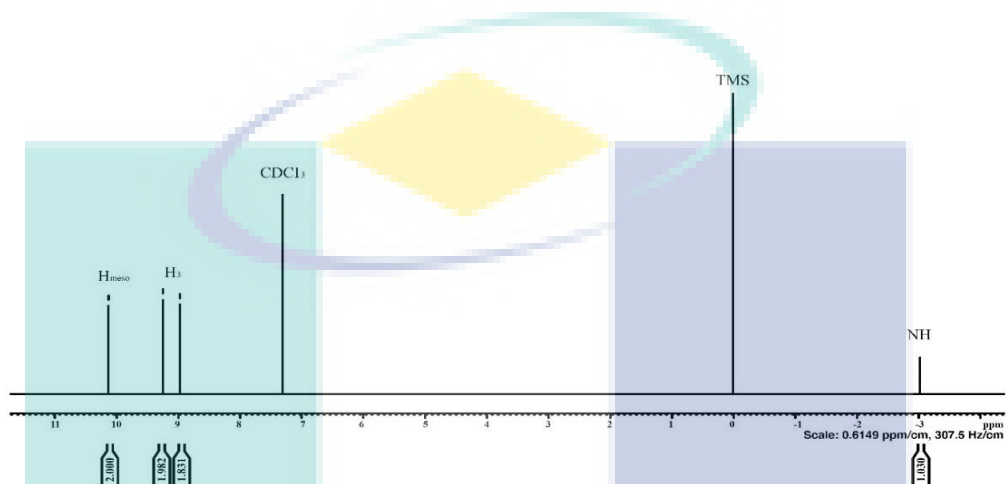


Figure 2.11 $^1\text{H-NMR}$ representation of porphyrin

When the light is fallen on a molecule, there are three possible pathways of a molecule to interact with light i.e; reflection, transmission or absorption. The photochemistry deals with the variety of processes that involve the absorption of light by a molecule. The Jablonski diagram (Figure 2.12) offers a well-known pathway to explain the phenomena of excitation and emissions (Jablonski, 1933). When a molecule absorbs a photon, the electrons are excited from their lower ground level S_0 to the higher energy levels S_n depending on the energy of a photon absorbed. Each energy level is also associated with a series of different vibrational states (Lakowicz, 1999a). When excitation occurs, the molecule is typically excited to a higher energy states of corresponding energy level, and according to Kasha's rules (Kasha, 1950) the excited electrons from any excited state S_n (S_2, S_3, S_4, \dots) lead to the radiation-less decay to the lowest singlet excited state S_1 (S_n-S_1) prior to emission of light. These types of decays are known as interconversion (IC) relaxation. The excited molecule may also undergo relaxation from higher vibrational levels ($v > 0$) to the lowest energy vibrational level ($v = 0$) of the corresponding excited state through non-radiative vibrational relaxation (VR). This process is completed by the release of thermal energy and by collision with other molecules.

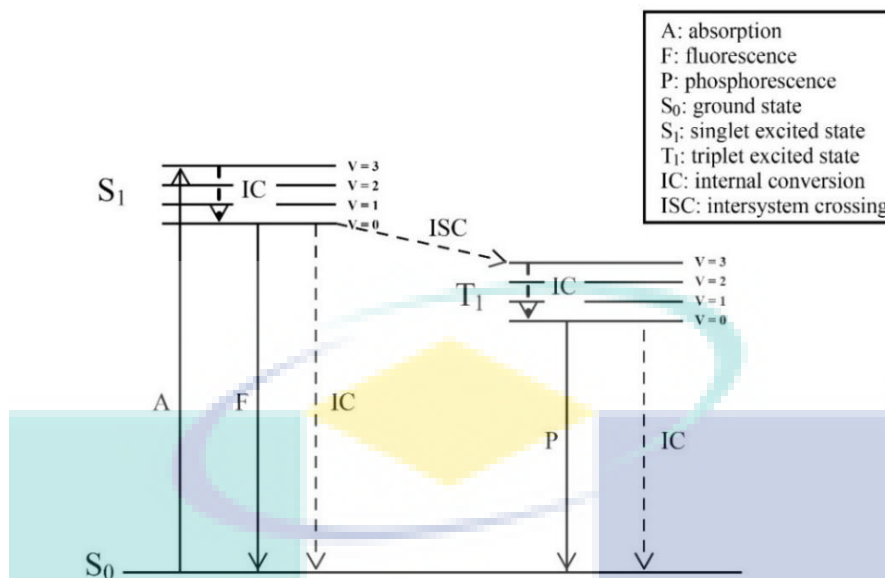


Figure 2.12 Jablonski diagram showing the decay phenomena for singlet and triplet relaxation after absorption of photon. The solid lines represent the radiation decay and dashed lines for non-radiation decay

From the excited singlet state (S_1), a molecule undergoes a radiative transition to any vibrational level of the ground state (S_0) with a rate k_f , accompanying the emission of photon. This phenomenon is called fluorescence. The energy of the emitted photons is typically less than that of the absorbed photons and can easily be measured from the wavelengths of the emission (λ_{ems}) and absorbance (λ_{abs}), where absorbance wavelength is generally shorter (Lakowicz, 1999a).

In addition to radiative fluorescence, photoexcited electrons from S_1 also undergo non-radiative decay S_1 - S_0 (IC) with rate k_1 through VR and/or intersystem crossing (ISC) with rate k_2 . When the electron is excited to the higher energy state, its spin is forbidden to change owing to the spin restrictions according to quantum mechanics; and therefore, is called as a singlet excited state (S_1). However, in some cases excited electron flips its spin; the process is termed as ISC, creating a situation where both electrons are of same spin. The nature of this excited state is known as triplet excited state (T_1). Therefore, ISC is a transition from a higher electronic energy level of one spin state to a lower energy level of a different spin state such as $S_1 \rightarrow T_1$. Similar to the singlet excited states, the triplet excited states (T_n) are associated with various vibrational energy levels and the fast non-radiation relaxations occur from higher vibrational levels ($v > 0$) to the lowest energy vibrational level ($v = 0$). The excited triplet state possesses a higher spin multiplicity than its corresponding singlet state. From the excited triplet state (T_1), an excited electron can

undergo a radiative transition from $T_1 \rightarrow S_0$, the phenomenon is termed as phosphorescence, non-radiative decay $T_1 \rightarrow S_0$ through VR, and/or be re-excited to singlet excited state again.

Although ISC is classified as a quantum-mechanically forbidden transition, it is thought that ISC is possible through spin-orbit coupling and is influenced by the electron's spin and orbital motions. The rate of ISC can be enhanced by the addition of heavy atoms in a process known as the heavy atom effect (McGlynn, Azumi & Kasha, 1964). The process of ISC involves the conservation of total orbital angular momentum and in heavy atoms the spin angular momentum and orbital angular momentum are not individually conserved. This facilitates spin-orbit coupling and increases the rate of the electron spin flip to form the triplet excited state. Additionally, the rate of non-radiative decay is governed by the energy gap law. This law states that as the gap between the excited and ground states becomes lower in energy the rate of non-radiative decay will increase exponentially. Simply, one could expect that a fluorophore emitting light at 450 nm would have a smaller non-radiative decay rate than a fluorophore emitting at 700 nm due to the smaller gap in energy between the excited and ground state (Caspar & Meyer, 1983).

2.4.1 Electronic Properties of Porphyrins

2.4.1.1 Light Absorption

Porphyrin molecules are the strongest light absorption complexes in nature. The bright purple color of porphyrins is the result of their unique absorption. The absorption spectroscopy is the most fundamental and suitable analytical technique to elucidate the electronic structure of porphyrins and metalloporphyrin. Understanding what gives rise to their fascinating optical absorption has been an exciting topic for researchers. The 18π -electrons system in the porphyrin ring are responsible for the general optical spectra observed. However various factors such as change in conjugation pathway, symmetry, external substituents, central substituents and other chemical variation cause to moderate to strong perturbation in absorption spectra of porphyrins (Gouterman, 1961; Hashimoto, Choe, Nakano & Hirao, 1999). The study of photo-physical, electronic nature, excited states and deactivation to ground states makes the porphyrins to be prime importance for

evaluating the potential applications (Cook, Brewer & Wong-Ng, 2017; Danquah, 2017; Senge et al., 2007; Urbani, Grätzel, Nazeeruddin & Torres, 2014; Zhou et al., 2016).

Porphyrins possess characteristic UV-Vis absorption spectra because of their 4-fold or 2-fold symmetry and their four central nitrogen atoms leading the centre of electronic heart. They help to distinguish between free-base porphyrins and metalloporphyrin. UV-Vis absorption bands consist of two distinct regions appearing in the near-UV and visible regions of the spectrum. In near-UV region, there is an extremely intense Soret band (B-band) (Adar, 1978; Soret, 1883) having typical extinction coefficients between 1×10^5 and $1 \times 10^6 \text{ M}^{-1}\text{cm}^{-1}$. In visible region, four less intense Q bands in free-base porphyrins are found 450 – 700 nm having extinction coefficients at $1 \times 10^4 \text{ M}^{-1}\text{cm}^{-1}$ (Valicsek & Horváth, 2013). Soret band corresponds to the electronic excitation from ground state to second singlet transition states (S_0 - S_2) while Q bands involve the electronic excitation from ground state to first singlet transition states (S_0 - S_1). The maximum wavelength and relative intensities of the bands are thus valuable evidences regarding the nature, possible substituents, their position and metalation of porphyrins, classification of porphyrin could also have been made on these bands.

On the basis of relative intensities of Q bands for free-base porphyrins, represented by roman number I, II, III and IV, the spectra could be categorized into etio, rhodo, oxo-rhodo and phyllo types (Prins, Reinhoudt & Timmerman, 2001), showing in Figure 2.14. If the relative intensities of Q bands are such that $IV > III > II > I$, the spectrum is etio-type and porphyrins are called as etioporphyrins. This type of spectrum is shown by the porphyrins in which all the β -positions are substituted by the groups possessing no π -electrons, e.g., alkyl groups. In the second case, if the substituents having π -electrons (such as carbonyl) are attached to the all β -positions, it gives rise to rhodo-type spectrum and the porphyrins are called rhodoporphyrins. In this spectrum, Q bands are in the order of $III > IV > II > I$. However, if two groups having π -electrons are attached on opposite pyrrole units, Q bands are in the order of $III > II > IV > I$ and the resulting spectra are called oxo-rhodo-type. This type of porphyrins is called oxo-rhodoporphyrins. At fourth type, meso positions are occupied by substituents giving the phyllo-type spectra, in which the Q bands are $IV > II > III > I$ (Giovannetti, 2012; Milgrom & Warren, 1997; Wijesekera & Dolphin, 1994).

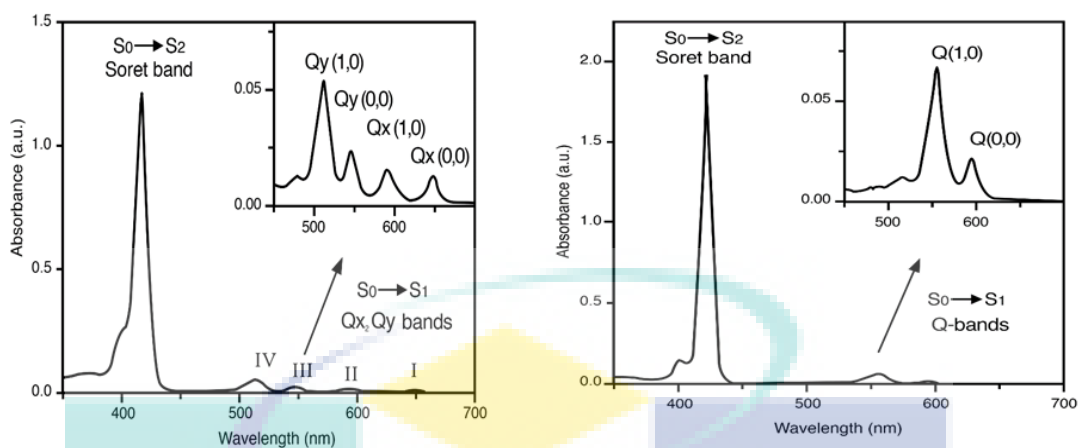


Figure 2.13 UV-Vis spectra for free-base porphyrins (D_{2h}) (top) and metalloporphyrin (D_{4h}) (bottom)

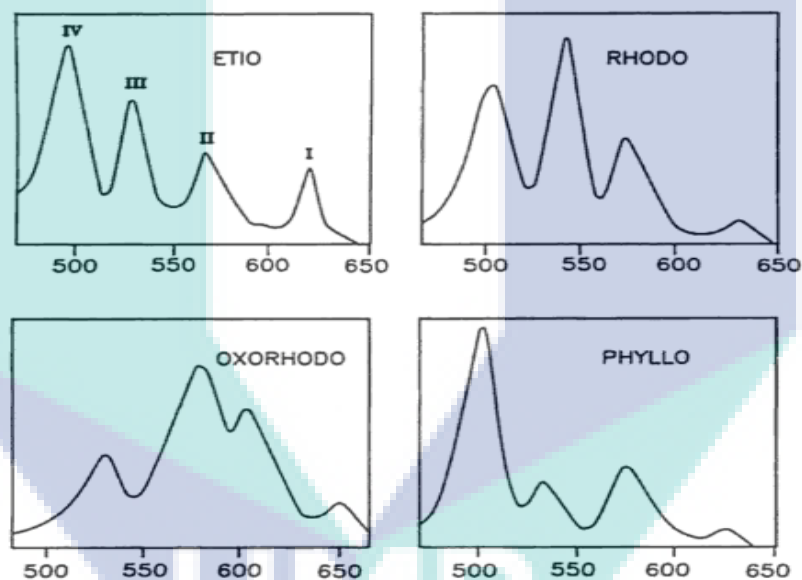


Figure 2.14 Q-bands absorption spectra for free-base porphyrins: a) etioid-type; b) rhodoid-type; c) oxo-rhodoid-type and d) phylloid-types

The general absorption spectrum for metalloporphyrin is shown in Figure 2.13—the number Q bands has been reduced from four to two when the metal atom is bonded with the free-base porphyrin, which has been described as due to reduction of symmetry to D_{4h} (metalloporphyrin) from the D_{2h} symmetry of free-base porphyrins (Gouterman, 1959). Based on the coordination of metal to the porphyrin, the metalloporphyrins are categorized into “regular” and “irregular” porphyrins (Duncan, 2001; Wang, Zhou, et al., 2014). The “regular” metalloporphyrins contain metal ion having closed-shell valence electrons (d^0 or d^{10}) and, consequently, the “irregular” one is one with open-shell valence

electrons ($d^1 - d^9$). As shown in Figure 2.15, the $d\pi$ energy of the metal ion having d^{10} orbital (e.g, Zn^{II}) is lower than that of porphyrin π orbital; therefore $d\pi$ (metal) - π^* (porphyrin) transition is forbidden energetically; i.e., the $d\pi$ orbitals of the metal ion have little or no effect on the porphyrin $\pi-\pi^*$ energy gap. Therefore, the normal absorption spectra are established from the π -electrons of porphyrin with very little interaction between the coordinated metal's atomic orbitals and the porphyrin's π -molecular orbitals.

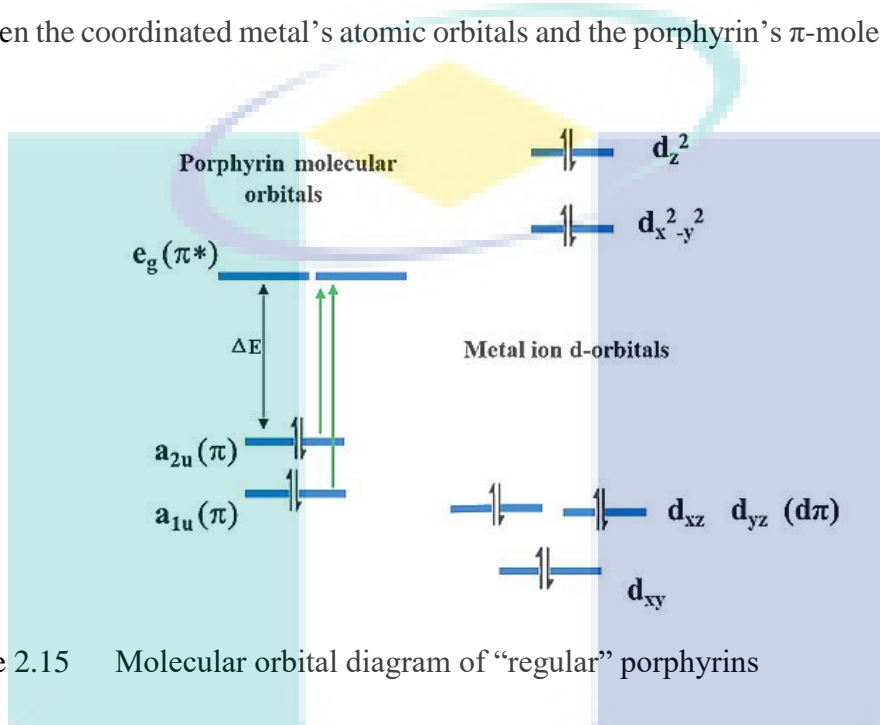


Figure 2.15 Molecular orbital diagram of “regular” porphyrins

On the other hand, in the irregular metalloporphyrins, the $d\pi$ orbitals of the chelated metals have much stronger effect on the absorption spectra because of strong mixing of orbitals with the porphyrins π -electrons. The irregular metalloporphyrins show spectra that are further classified into two types: hypso and hyper metalloporphyrins. Hypso porphyrins are metalloporphyrins in which the metal ions are of d^m ($m = 6-9$) electrons in their orbitals (e.g, Pd^{II} , Pt^{II} and Ni^{II}) having filled $d\pi$ (d_{xz} , d_{yz}) orbitals. The hypso-type spectra resemble the normal spectra but the Q bands are blue shifted compared to those of free-base porphyrins spectra. In hypso porphyrins there is significant interaction between metal $d\pi$ orbital to porphyrin π^* orbital leading to metal to ligand back bonding and metal to ligand charge transfer (MLCT) thereby (Suslick & Watson, 1992). This in turn stabilizes the metal $d\pi$ orbitals but rises the porphyrin π^* orbital energy as shown in Figure 2.16. This results in an increased π to π^* energy gap causing the hypsochromic shift in the absorption spectra for metalloporphyrins compared to normal spectra. The metal ions (d^m , $m=1-5$) with partially filled $d\pi$ (d_{xz} , d_{yz}) orbitals (e.g, Cr^{III} , Mn^{III} , and Fe^{III}) form the hyperporphyrins and the resulting spectra are more

complex because of extensive mixing of the metal $d\pi$ orbitals and the π^* orbital of the porphyrin. In hyperporphyrin, the partially filled $d\pi$ (d_{xz} , d_{yz}) orbitals make the porphyrin to metal transition possible and are characterized by red shifted Q bands and some additional absorbance compared to normal spectra as shown in Figure 2.17 (Duncan, 2001; Gouterman, 1978; Suslick & Watson, 1992).

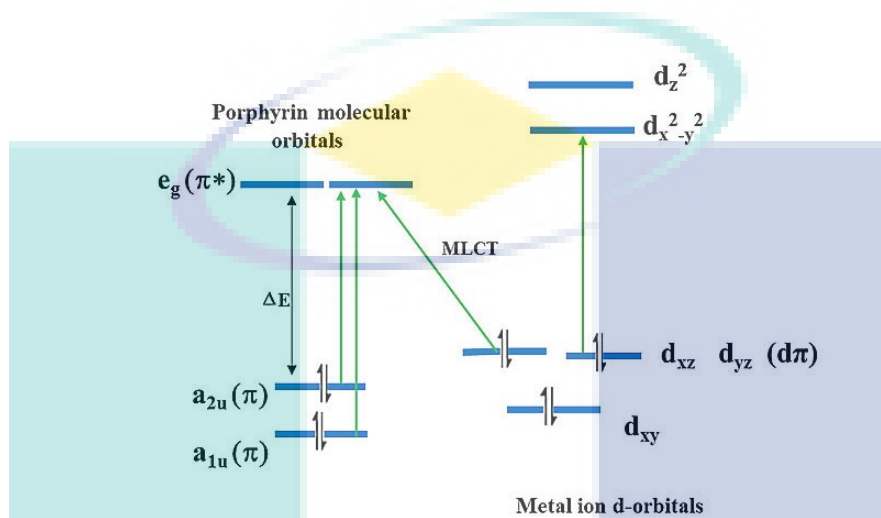


Figure 2.16 Molecular orbital diagram of hypso-porphyrins (irregular porphyrins). The notations a_{1u} and a_{2u} are singly degenerate and e_g is doubly degenerate orbitals

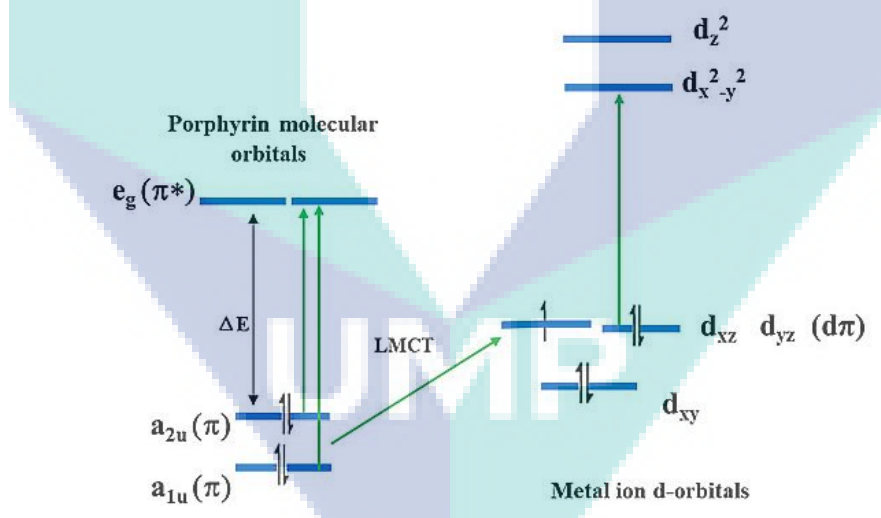


Figure 2.17 Molecular orbital diagram of hyper-porphyrins (irregular porphyrins)

2.4.1.2 Gouterman Four Orbital Theory

It has been well documented that changes in the conjugation pathway and symmetry of a porphyrin can affect its UV-Vis absorption spectrum (Gouterman, 1961; Gouterman, 1978; Nappa & Valentine, 1978; Rubio, Roos, Serrano-Andrés & Merchán, 1999). The absorption spectrum of porphyrins has long been understood in terms of the “four-orbital” model which first proposed in 1959 by Martin Gouterman as a general

theory and applied to explain the absorption spectra of porphyrins (Gouterman, 1959; Gouterman, 1961) in 1960s.

According to this theory, porphyrin have two HOMOs (HOMO & HOMO-1) and two LUMOs (LUMO & LUMO+1) that are responsible for the absorption bands of porphyrins. For the metalloporphyrins of D_{4h} symmetry, the HOMOs are singly degenerated as a_{1u} and a_{2u} orbitals, while LUMOs are doubly degenerated as e_g orbitals as shown in Figure 2.18. The a_{2u} orbital is localized on nitrogens and on meso-carbons, while the a_{1u} orbital is localized on C_α and C_β atoms, shown in Figure 2.19. On the other hand, anti-bonding orbitals e_g are on the whole molecule (Kalyanasundaram, 1991; Prushan, 2005). The bands seen in absorption spectra are due to the electron excitation from a_{1u} or a_{2u} to the e_g . As the a_{1u} and a_{2u} orbitals are of same energy, their consequent interaction with each other is favored. Constructive interaction leads to the more intense Soret bands whereas destructive combinations leads to the weaker Q-bands (Ham & Ruedenberg, 1956a; Ham & Ruedenberg, 1956b). The Q-bands are of two types, the lower energy Q-band, $Q(0,0)$ is assigned by electronic excitation to the first excitation state. The higher energy Q-band, $Q(1,0)$ is the vibrational excitation interacting with electronic transition of porphyrin, thus forming the vibronic overtone of $Q(0,0)$ band. The Soret band is assigned by electronic excitation to the second excitation state and vibronic overtone $B(1,0)$ may also be observed in well resolved spectra.

For free-base porphyrin having lower D_{2h} symmetry due to the presence of two inner hydrogens bonded with nitrogen atoms compared to metalloporphyrins, there is no degeneracy between the two HOMOs orbitals causing the transitions split into distinctive x- and y-polarized transition bands (Gouterman, 1961; Nemykin & Hadt, 2010) (Figure 2.18). In free-base absorption spectra, the transition between HOMO and π^* causes the appearance of four Q-bands in visible region, two from x- and two from y- component of the Q-band, represented as $Q_x(0,0)$, $Q_x(1,0)$, $Q_y(0,0)$ and $Q_y(1,0)$ (Gouterman, 1978). The $Q_x(1,0)$ and $Q_y(1,0)$ are the vibronic overtones for $Q_x(0,0)$ and $Q_y(0,0)$ respectively shown in Figure 2.13

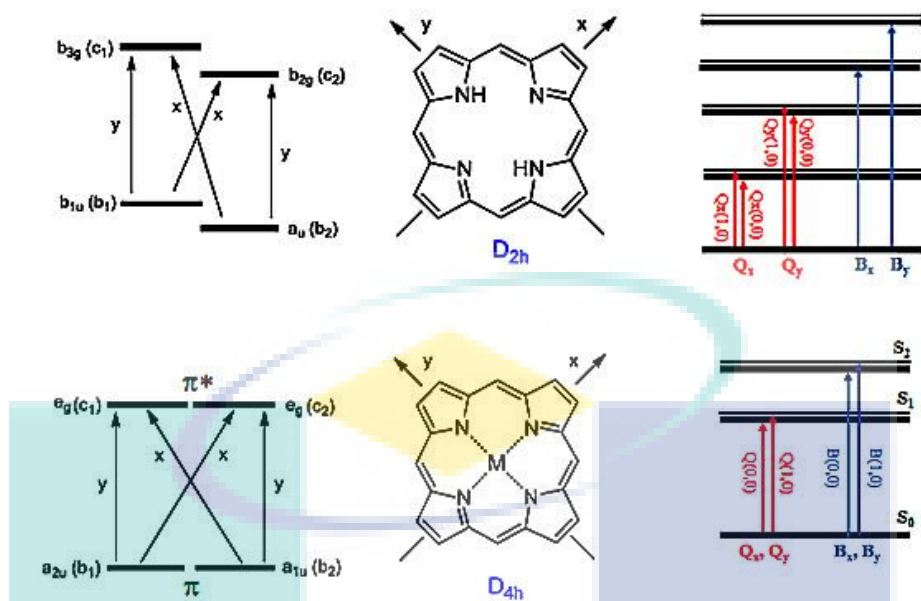


Figure 2.18 Gouterman four-orbital model for D_{2h} symmetry (top) and D_{4h} symmetry porphyrins (bottom)

Source: Nemykin & Hadt (2010).

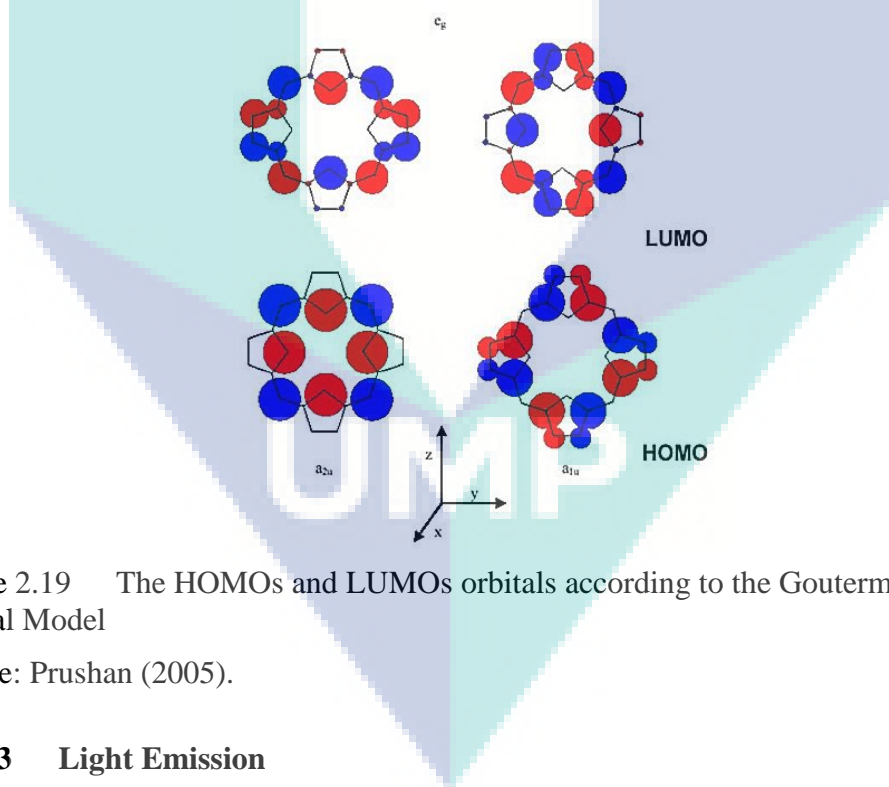


Figure 2.19 The HOMOs and LUMOs orbitals according to the Gouterman Four-Orbital Model

Source: Prushan (2005).

2.4.1.3 Light Emission

The first report of emission observed from porphyrin was from the reduced chlorophyll in 1834. The two most important properties observed from emission data of porphyrins include quantum yields and Stokes shift. Figure 2.20 shows the fluorescence spectra of porphyrins.

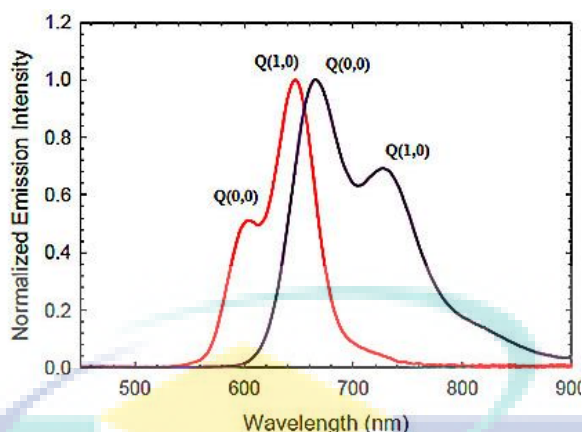


Figure 2.20 Emission spectra of metalloporphyrin, regular porphyrin represented in red (ZnTPP) and irregular porphyrin in purple (PtTPP)

The fluorescence spectra of porphyrins usually consist of two bands, the emission of singlet excited state Q(0,0) and a vibronic overtone Q(1,0) (Gouterman, 1978). The Stokes shift (Djelal & áGeorge Truscott, 1999) is the energy difference in electronic structure of the excited state and ground state. The energy difference “ ΔE ” can be calculated by the subtraction of emission energy (E_{em}) from the energy of excitation (E_{ex}) as shown in equation 2.1 (Guilbault, 1990)

$$\Delta E = E_{ex} - E_{em} \quad 2.1$$

$$\Delta E = \left[\frac{\hbar c}{\lambda_{ex}} - \frac{\hbar c}{\lambda_{em}} \right] * \frac{6.022 * 10^{23}}{1000} \text{ kJmol}^{-1} \quad 2.2$$

Where “ \hbar ” is the Planck constant, “ c ” is speed of light and “ λ_{ex} ” and “ λ_{em} ” are the excitation and emission wavelengths, respectively. The fluorescence quantum yield “ Φ ” (Djelal & áGeorge Truscott, 1999; Guilbault, 1990; Seybold & Gouterman, 1969) is defined as the ratio of the amount of emitted fluorescence photons to photons absorbed.

$$\Phi = \frac{\text{No of quanta emitted}}{\text{No of quanta absorbed}} \quad 2.3$$

“ Φ ” is determined by a quantitative comparison with the standard of known quantum yield.

$$\Phi = \Phi_R * \frac{I}{I_R} * \frac{A_R}{A} * \frac{\eta^2}{\eta_R^2}$$

Where “I” is the measured integrated emission intensity, “η” is the refractive index of the solvent, and “A” is the Absorbance. The subscript “R” refers to standard index.

Metalloporphyrins typically differ very little by optical absorption spectra; however, their emission spectra are appreciably different depending on the metal ion. For metalloporphyrins, the fluorescence and phosphorescence usually occur at shorter wavelengths compared to their free-base analogue as a consequence of higher singlet and triplet excitation energies. The insertion of a heavy metal to form a metalloporphyrin causes a decrease in the fluorescence quantum yield from the expected increase in the rate of intersystem crossing from the heavy atom effect (Seybold & Gouterman, 1969). The fluorescent quantum yields of regular metalloporphyrins are usually in the range 0.001 – 0.2 with singlet lifetime ~ 60 ns and phosphorescence quantum yield in the 0.0001 – 0.2 range with triplet lifetime 1 – 400 ms (Gouterman, 1978; Seybold & Gouterman, 1969). Emission from the excited states for regular porphyrins occurs from the π^* - π state of the porphyrin ring. The metal contributes small electronic perturbations resulting in small spectral changes or spin-orbit perturbations. Like free-base porphyrins, the regular metalloporphyrins give normal fluorescence spectra with two bands Q(0,0) and Q(1,0), as shown in Figure 2.20. The irregular metalloporphyrin which give hypso-type absorption spectra (platinum porphyrins), increases the rate of ISC, therefore phosphorescence is dominant. These type of metalloporphyrins are having no or weak observable fluorescence with quantum yields < 0.001. This leads the phosphorescent quantum yields being much higher up to 0.2 with the triplet lifetimes usually <3 msec. Some metalloporphyrins, considered as radiation-less porphyrins, show very weak emission, that is, the emission yields are in the range 10^{-4} - 10^{-6} with excited state lifetime from 60 ps to 60 fs, and any prompt emission may be from un-vibrationally relaxed excited states (Gouterman, 1978).

2.5 Synthetic Methodologies of Porphyrin

Porphyrin have many reaction sites; eight β -, four meso- and internal nitrogen – suitable substitutions at these sites lead to a large number of porphyrins. Consequently, a large number of synthetic routes have been developed for the preparation of symmetrical and unsymmetrical porphyrin derivatives. One of the viable synthetic protocol is to synthesize the porphyrins derivatives from the extracts of natural porphyrins. For example, chlorophylls, bacteriochlorophylls and heme can all be used to generate a variety of porphyrins derivatives. However, only β -porphyrins can be synthesized in this way from natural porphyrins. In order to obtain porphyrins with different patterns, it is necessary to start from a standard synthetic pattern, which in most cases start from pyrroles with aldehydes.

According to method adopted for the functionalization on porphyrin, the synthetic routes can be divided into two categories i.e., pre-functionalization and post functionalization as shown in Figure 2.21.

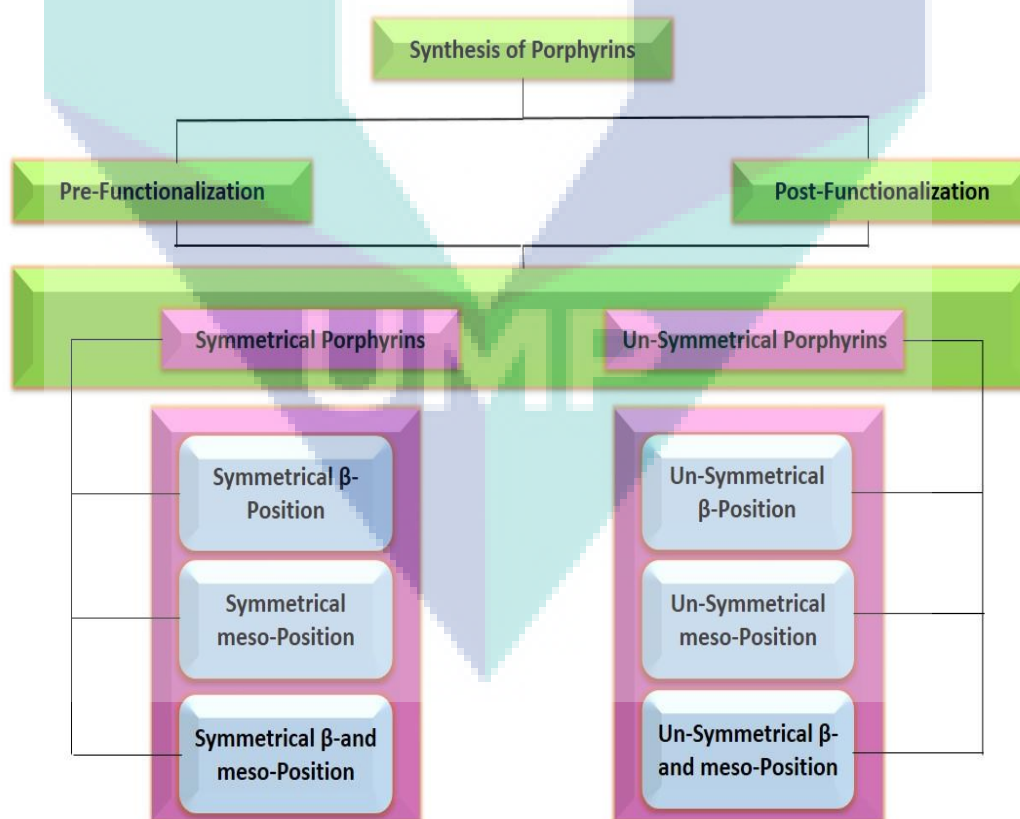


Figure 2.21 Classification of porphyrin synthesis

2.5.1 Pre-Functionalization

Synthesis of porphyrin by pre-functionalization involves the formation of porphyrin ring with built-in substitution on its meso- and/or β - positions (shown in Figure 2.22). These types of porphyrins could be symmetrical or un-symmetrical depending on the nature and type of starting materials. Generally, the porphyrins are synthesized by tetramerization of mono-pyrrole with aldehyde (Rothemund, 1935; Rothemund & Menotti, 1941), MacDonald (2+2) condensation (MacDonald, Arsenault & Bullock, 1960), Tripyrrolic [3+1] route (Boudif & Momenteau, 1994; Boudif & Momenteau, 1996) and cyclization of linear tetrapyrrolic compounds (Johnson & Kay, 1961; Smith et al., 2000).

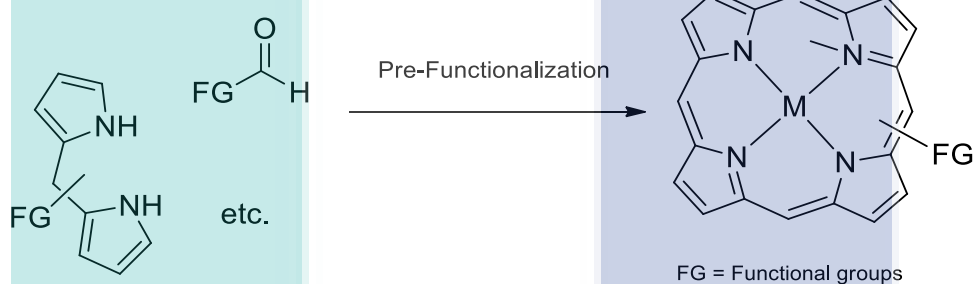


Figure 2.22 General representation of pre-functionalization of porphyrins

2.5.1.1 Tetramerization of Mono-pyrrole

Figure 2.23 shows a general methodology for the synthesis of meso-, β - and meso- & β -substituted porphyrins by tetramerization of mono-pyrrole. In the synthesis of meso-substituted porphyrins (e.g; meso-tetraphenylporphyrin, H_2TPP), the meso-carbons are given by the aldehyde group; therefore, a variety of meso-porphyrin could be synthesized by choosing a suitable aldehyde. Rothemund firstly synthesized meso-tetramethylporphyrin (H_2TMP) in 1935 (Rothemund, 1935) and later expanded this method for synthesizing a variety of porphyrins, including H_2TPP (Rothemund & Menotti, 1941). In 1941, Rothemund synthesized H_2TPP with yield up to 9% (which was considered a large yield during that time) by heating pyrrole and benzaldehyde in pyridine in a closed seal tube (Figure 2.24(i)). The highest yield of H_2TPP obtained from this reaction was at high pressure ~11% using $Zn(OAc)_2$ as a metal template (Calvin, Ball & Aronoff, 1943).

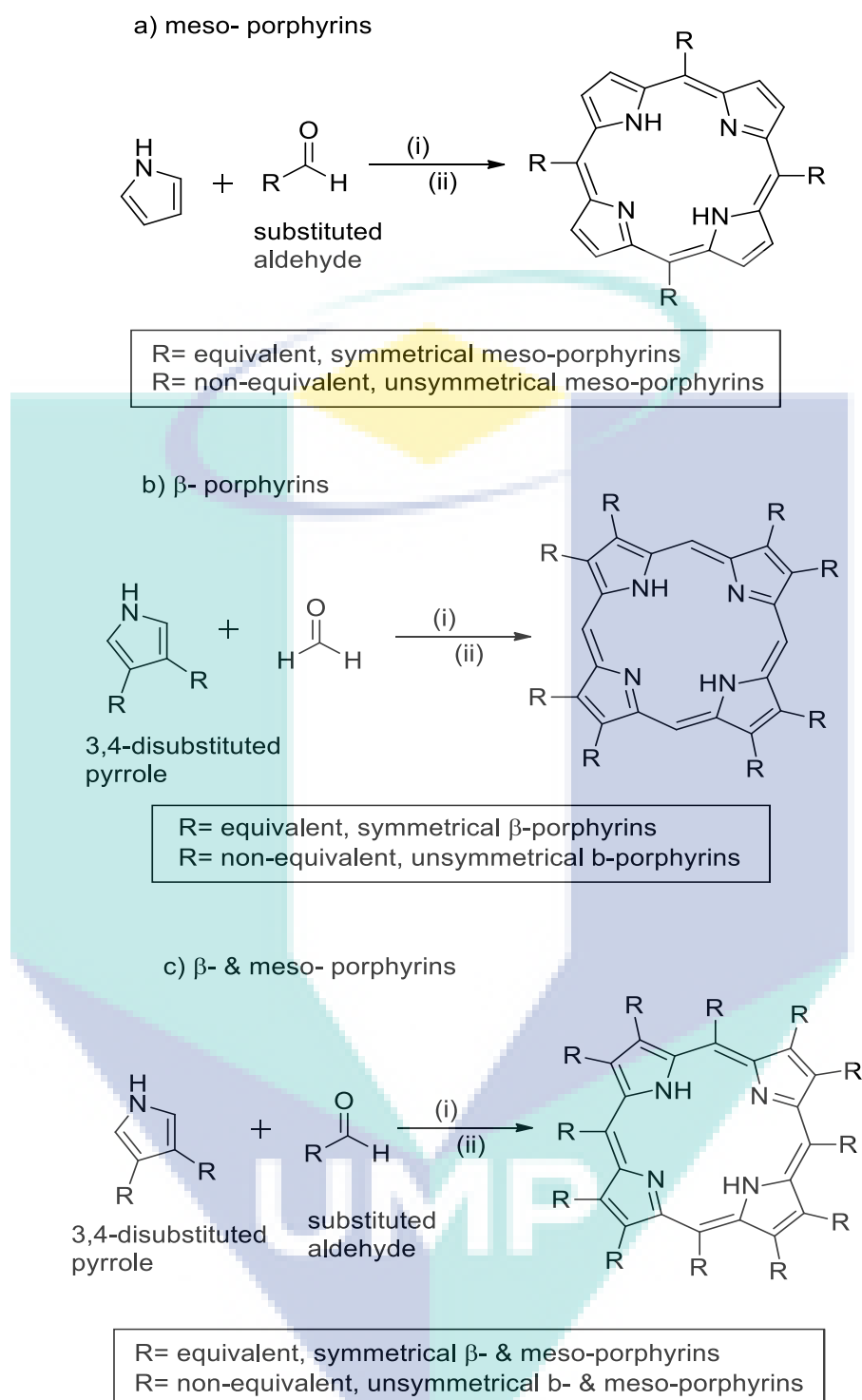


Figure 2.23 General methodologies for porphyrin synthesis through tetramerization of mono-pyrrole; i) acid catalyzed condensation; ii) oxidation reaction

During 1960s, Alder and Longo improved the Rothmund methodology using acid catalyzed pyrrole aldehyde condensation in air with yield up to 20% (Figure 2.24(ii)) (Adler et al., 1967). However, Alder and Longo's have the following limitations: (i) their reaction does not allow synthesis of porphyrin bearing sensitive functional group; (ii)

generation of tar at very high level made their purification cumbersome besides poor batch-to-batch reproducibility (Barnett, Hudson & Smith, 1975; Rousseau & Dolphin, 1974). In 1980s, Lindsey further revised this method by allowing a variety of substituted aldehydes for synthesis of meso-aryl substituted porphyrin with yield up to 40% (Lindsey, Schreiman, Hsu, Kearney & Marguerettaz, 1987). At first step, the acid catalyzed condensation is occurred to form the intermediate porphyrinogen, followed by the second step i.e., the addition of an external oxidant such as DDQ or chlorinal to form the porphyrin (Figure 2.24(iii)). A schematic summary of these methods is shown in Figure 2.24.

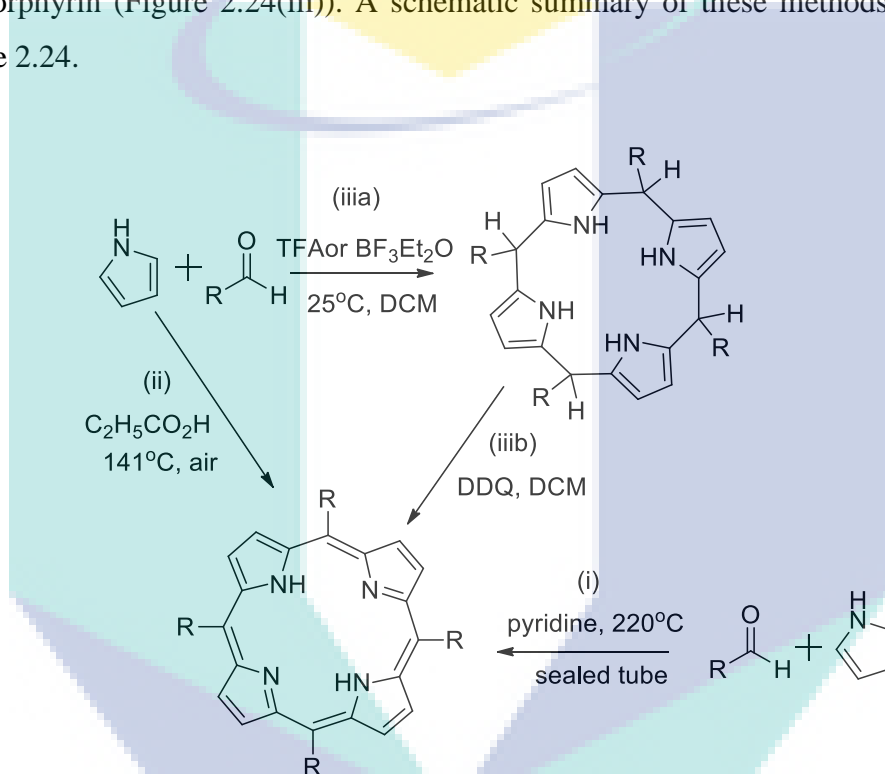


Figure 2.24 Methodologies for meso-porphyrin synthesis; i) Rothermund synthesis; ii) Adler and Longo synthesis; iii) Lindsey synthesis, acid catalyzed condensation; iii) Lindsey synthesis, oxidation reaction

The synthesis of unsymmetrical meso-substituted porphyrins has been carried out via mixed aldehyde condensations, which routinely results in the formation of a mixture of porphyrins which must be chromatographically separated to obtain the desired product. By utilizing two different aldehydes as preliminary materials in the Adler or Lindsey synthesis, a mixture of products is formed (Figure 2.25). These kinds of porphyrins are helpful precursors for constructing bio-conjugates and porphyrin arrays.

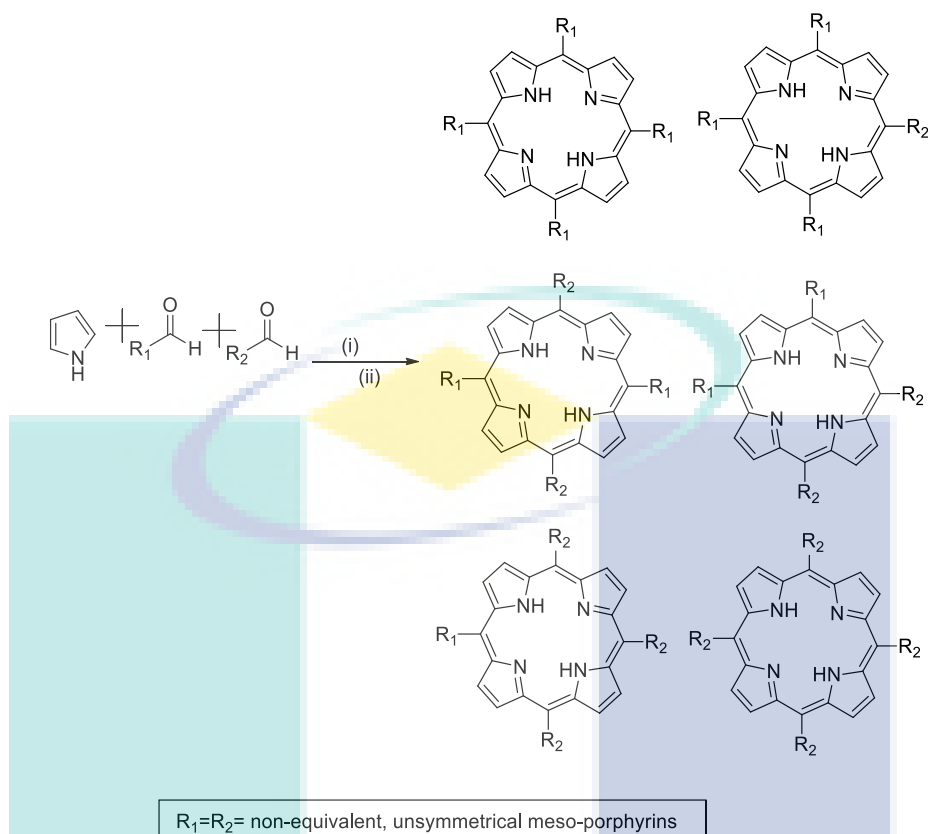


Figure 2.25 Methodologies for synthesis of unsymmetrical meso-porphyrin; i) acid catalyzed condensation; ii) oxidation reaction

Synthetic methods for β -substituted porphyrins are more complicated compared to the meso-substituted ones due to difficulties for preparing the 3,4-disubstituted pyrrole as the starting material. In the case of β -porphyrins, the meso-carbons can either be included separately by utilizing aldehydes or can already be present in the form of a 2-substituent on the pyrrole (Figure 2.26). It is vital that the synthesis of symmetrical β -substituted porphyrins through mono-pyrrole tetramerization can be carried out if the 3- and 4-substituents in the mono-pyrrole are identical.

There are three vital ways to synthesize β -porphyrins. First, tetramerization of 2,5-di-unsubstituted pyrroles in the presence of aldehyde which can provide the four meso methine carbons of the product (Figure 2.26 (i)) (Sessler, Mozaffari & Johnson, 1991). Secondly, tetramerization of pyrroles containing 2-CH₂R substituents; the “R” group on the “methylene” must be a good leaving group providing the methylene carbons as meso-carbons of the product after a nucleophilic attack on it (Figure 2.26 (iia & iib)) (Aoyagi et al., 1997; Dogutan et al., 2007; Dogutan et al., 2008; Ono, Kawamura, Bougauchi & Maruyama, 1990). Third way is the cyclotetramerization of 2,5-di-

substituted pyrroles where the meso-carbons are provided by 2 and 5 substituents on pyrroles (Figure 2.26 (iii)) (Inhoffen, Fuhrhop, Voigt & Brockmann, 1966; Paine III, Kirshner, Moskowitz & Dolphin, 1976; Wang & Chang, 1979). Once the condensation reaction occurred, an oxidation step is vital to afford yields of porphyrin from an intermediate porphyrinogen. Using the above procedures, a large number of β -substituted porphyrins could be produced just by altering the 3- and 4-substituents on pyrrole.

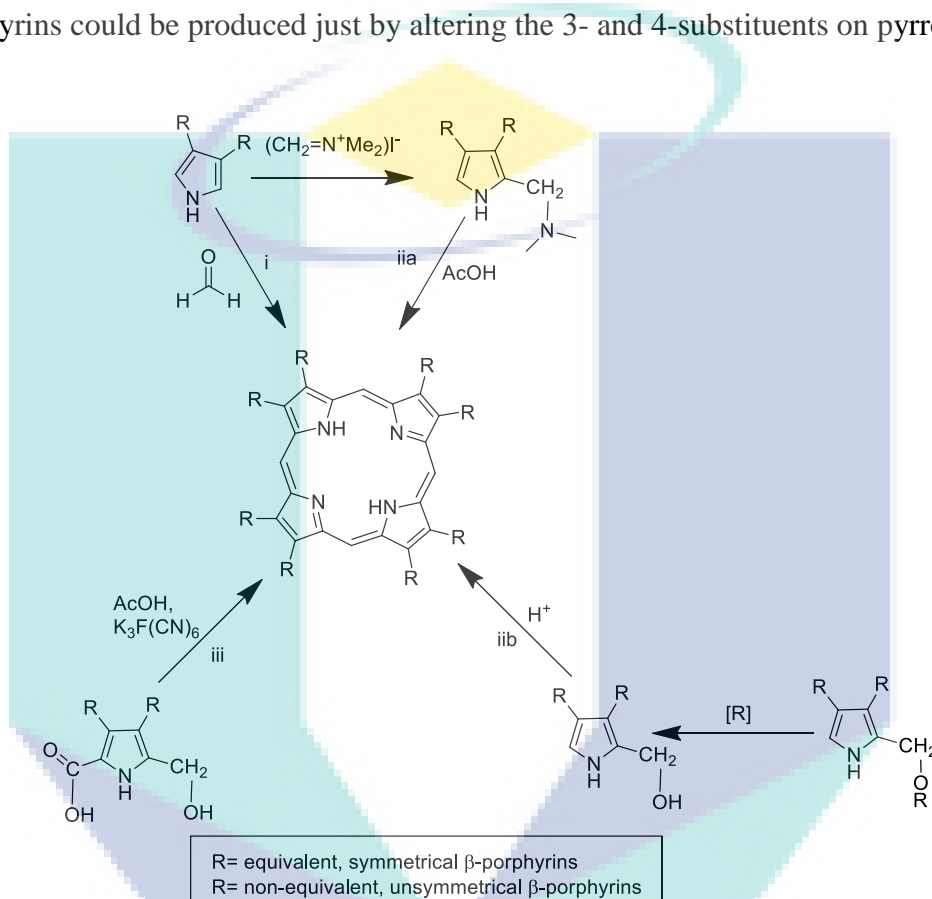


Figure 2.26 Methodologies for β - porphyrin synthesis

If the 3- and 4-substituents on the mono-pyrrole reactants are not alike, a mixture of products is formed because of acid-catalyzed condensation of an aldehyde with unsymmetrically substituted pyrrole rings (Taniguchi & Lindsey, 2012). However, the head-to-tail self-condensation of 2-substituted different pyrroles allow the synthesis of porphyrins with different β -substituents (Figure 2.27) (Kinoshita, Tanaka, Nishimori, Dejima & Inomata, 1992). The reactivity and stability of the carbocation intermediate, created by the exclusion of “L” leaving group, is vital for the efficiency of reaction. Nature utilize this process to produce the uroporphyrinogen.

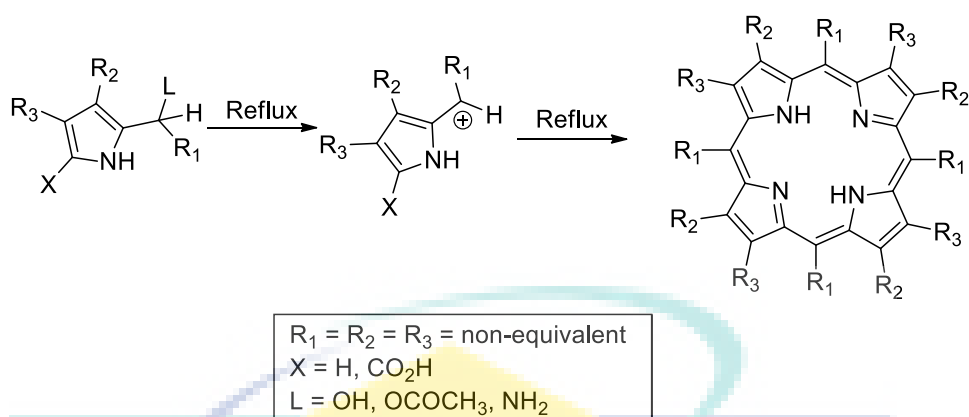


Figure 2.27 Self-condensation of 2- substituted pyrrole for β - & meso-porphyrin synthesis

In short, by tuning the reaction conditions that depend upon the properties of pyrrole and aromatic aldehyde employed, Adler and/or Lindsey process provides a way to the production of porphyrin macrocycles with several substituents on the the β -pyrrolic and/or meso-positions. The flexibility of the mentioned procedures allows the preparation of porphyrin complexes in large number with variety of structural and electronic properties.

2.5.1.2 MacDonald (2+2) Condensation

The MacDonald condensation reaction (MacDonald et al., 1960) has become popular for porphyrin synthesis as it can be used to synthesize both symmetrical and unsymmetrical porphyrin molecules. Dipyrromethanes are the intermediates in the MacDonald method. Symmetrical dipyrromethanes are synthesized via the condensation of two equivalents of unsubstituted pyrrole with either formaldehyde or an aryl aldehyde. This way is termed as the [2+2] way or [2+2] condensation due to the contribution of two dipyrrolic precursors to form the porphyrin. MacDonald work represented that a symmetrical 1,9-formyldipyrromethane reacts with 1,9-di-unsubstituted dipyrromethane or the corresponding acid 1,9-dicarboxylic acid, in the hydroiodic acid (HI) catalyst to form porphyrin, in high yields (Figure 2.28, path i) (MacDonald et al., 1960).

The applications of dipyrrolic intermediates for the unsymmetrical porphyrin synthesis is also well reported (Geier III & Lindsey, 2001; Mamardashvili & Golubchikov, 2000). When two different tetra-substituted dipyrromethanes are used, unsymmetrical porphyrins are formed. Condensation of two unsymmetrical

dipyrromethanes containing bridging carbons (Battersby et al., 1974) (Figure 2.28, path ii, iii, & iv) forms two porphyrin products through 2+2 condensation because the dipyrromethanes can interact with either of two orientations associated by 180° rotation of one of the dipyrromethanes.

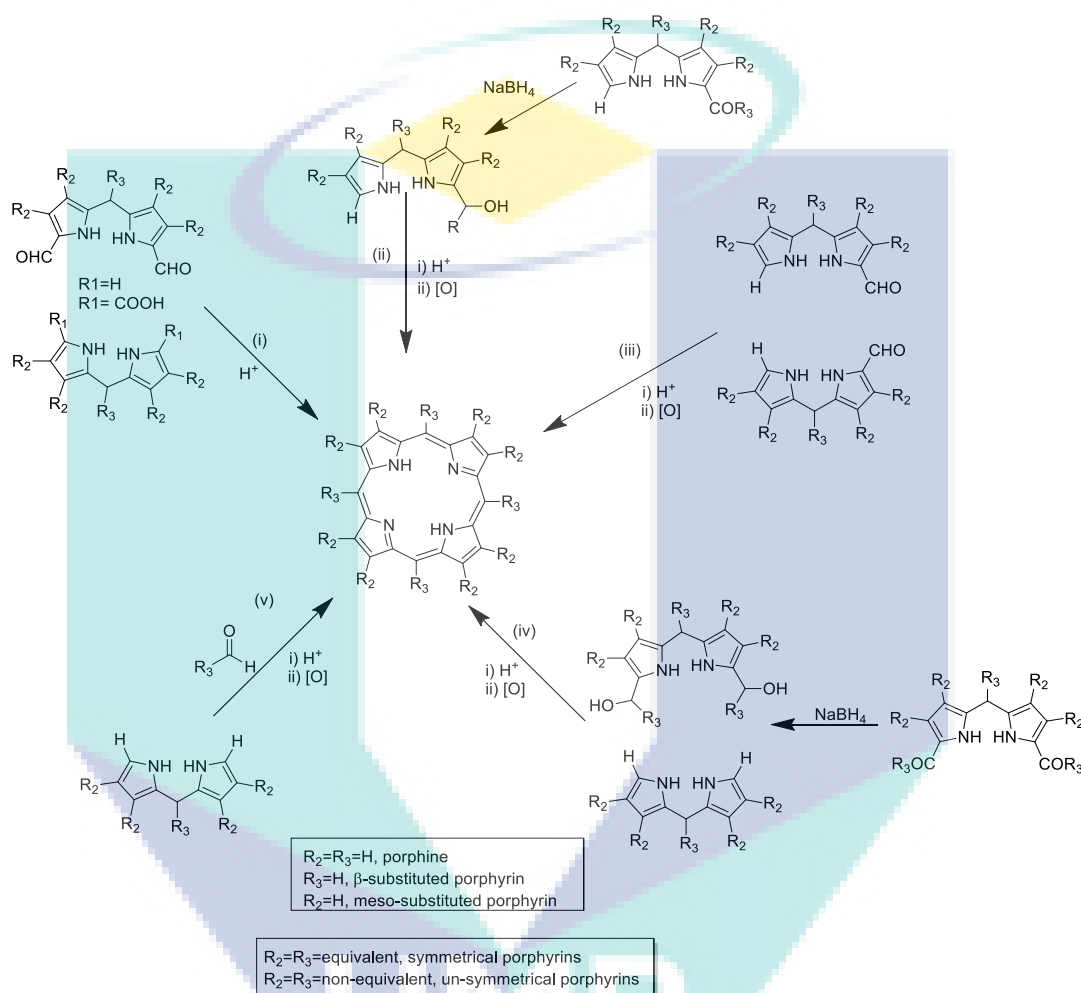


Figure 2.28 MacDonal (2+2) condensation for porphyrin synthesis

MacDonal [2+2] condensation can be modified such that monoformyldipyrromethane is self-condensed to provide symmetrical or un-symmetrical porphyrins as shown in Figure 2.28, path (iii) (Cavaleiro, Gonsalves, Kenner & Smith, 1973; Markovac & MacDonal, 1965). Some other researchers have shown that the *p*-toluenesulfonic acid is a better choice as the catalyst (Cavaleiro, Gonsalves, Kenner & Smith, 1974). Another useful example for MacDonal [2+2] condensation is the reduction of mono- or di-acyldipyrromethanes with NaBH₄ to the corresponding carbinols. Dipyrromethane carbinols in the presence of acid form the symmetrical or un-symmetrical porphyrins (Figure 2.28, path ii & iv) (Geier III, Callinan, Dharma Rao &

Lindsey, 2001; Rao, Dhanalekshmi, Littler & Lindsey, 2000). Moreover, Lindsey presented that condensation of dipyrromethanes with aldehydes can be efficiently utilized for development of *trans*-A₂B₂-porphyrins (Figure 2.28, path v) (Ivanova, Semeikin, Glazunov & Mamardashvili, 2010), but the scrambling processes that leads to a mixture of porphyrins is the main issue for any type of [2+2] synthesis (Geier III, Littler & Lindsey, 2001).

MacDonald also showed schematics for synthesizing *trans*-substituted meso-porphyrins (Figure 2.29). It includes dipyrromethane and another aldehydes despite of the formyl group in TFA and DCM yielding 5,15-diarylporphyrin. This procedure is widely used for synthesis of *trans*-porphyrins (Yella et al., 2011). The [2+2] route using dipyrromethanes is probably the most widely used pathway to synthetic porphyrins.

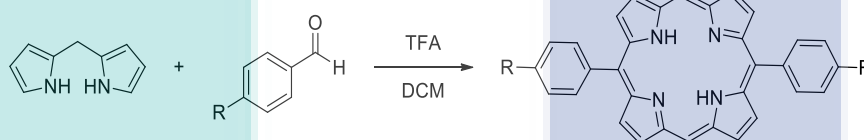


Figure 2.29 MacDonald (2+2) condensation for *trans* substituted meso-porphyrin synthesis

2.5.1.3 Tripyrrolic [3+1] Route

Tripyrrolic [3+1] route (Boudif & Momenteau, 1994; Broadhurst, Grigg & Johnson, 1971) is a variation of the MacDonald (2+2) approach and describes the condensation of mono-pyrrole containing 2- and 5- bridging carbons (e.g., diformylpyrrole) with tripyrranes (Figure 2.30). In some case, the synthesis of a porphyrin is required to conjugate with a functional group bearing unique functionality on porphyrin ring accessing the ring for particular application. Therefore, the [3+1] approach allows the effective porphyrin synthesis in which the desired functional group situated on the mono-pyrrole is to be injected as a last step (Sessler, Johnson & Lynch, 1987). This approach is most commonly used for the synthesis of meso-unsubstituted porphyrins. However, tripyrranes are very unstable species; they can be generated in situ from the corresponding dicarboxylic acids. 2-, 5-dicarboxylic acids on tripyrranes readily decarboxylate upon treatment with an acid. Although the “3+1” route has been ignored for over two decades, it was supported to be the method for the synthesis of several un-symmetrical porphyrin (Lash, 2000).

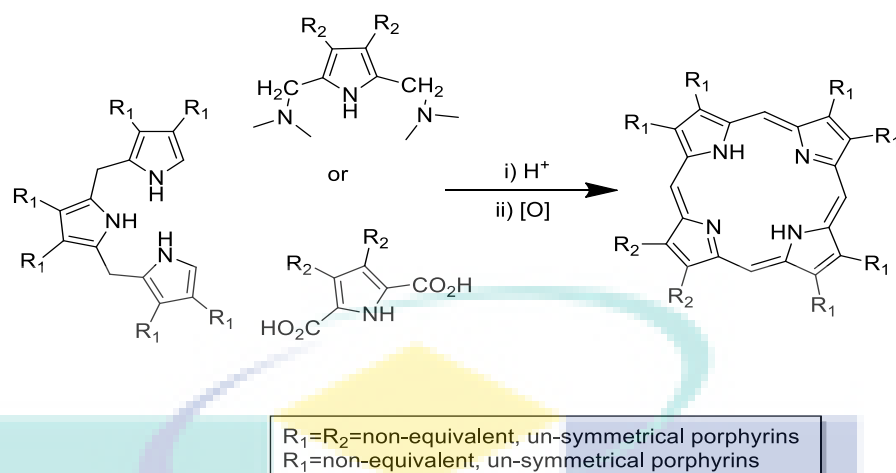


Figure 2.30 Tripyrrolic [3+1] route for β -unsymmetrical porphyrin synthesis

2.5.1.4 Cyclization of Linear Tetrapyrroles

The completely unsymmetrical porphyrin is progressed by cyclization of the linear tetrapyrroles formed by stepwise coupling of individual pyrroles (Johnson, 1978; Johnson & Kay, 1961) (Figure 2.31). Although a variety of linear tetrapyrroles have been investigated (Smith, 2000) over the years, the Bilenes b and Biladienes ac in the presence of Cu(II) salts are the most commonly used precursors forming the copper complexes of porphyrin. Later, demetallation of copper with strong acids forms the metal-free porphyrins.

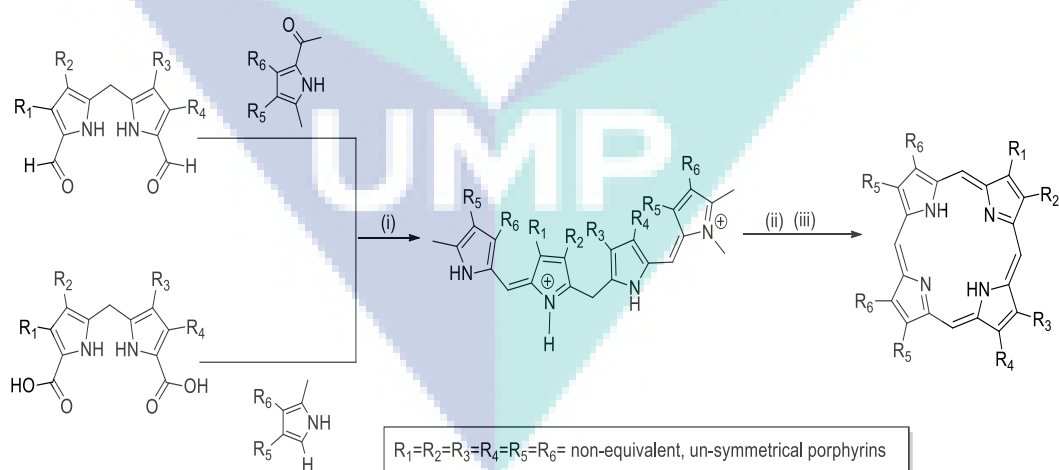


Figure 2.31 Cyclization of linear tetrapyrroles i) MeOH, HCl, RT; ii) MeOH, Cu(OAc)₂, reflux, 48 h; iii) H₂SO₄

2.5.2 Post-Functionalization

Porphyrin synthesis by post-functionalization involves the introduction of functional groups and substituents after the formation of the porphyrin ring (shown in Figure 2.32). This can be further categorized into core-functionalization and the peripheral-functionalization.

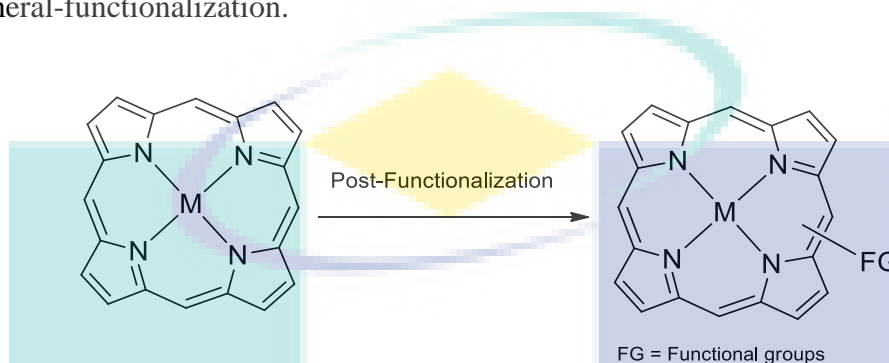


Figure 2.32 General representation of post-functionalization of porphyrins

In core-functionalization, the functional groups and substituents are directly attached at the meso- and/or β - positions of porphyrin core. While in peripheral-functionalization, functional groups or substituents are introduced on the peripheral substituents (Figure 2.33).

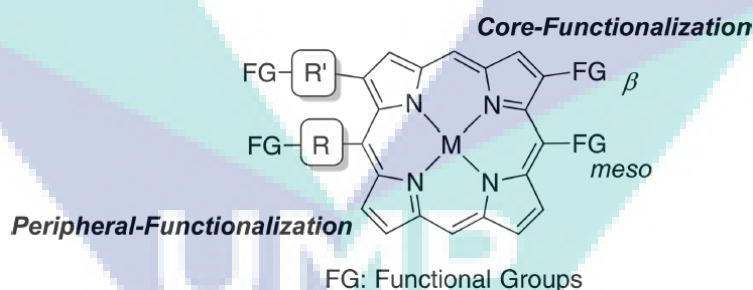


Figure 2.33 Classification of post-functionalization by position

The meso-positions at the porphyrin core are electronically the most reactive sites and are generally favorable for substitutions, additions and radical reactions. On the other hand, the β -positions are sterically the most accessible sites and undergo the same type of reactions. Substitution and cross-couplings reactions are used to produce several functionalization on porphyrin core. Porphyrins can also be coordinated with a variety of metal ions. The metal ions have a significant effect on the π -electron system of porphyrin core; and therefore, strongly influence the reactivity and photo-physical properties porphyrin ring (explain in detail in section 2.6.3). Porphyrin core can undergo

electrophilic, nucleophilic, oxidation, reduction, cyclo-addition and intramolecular cyclization reactions, depending on the nature and surrounding of the reactants (da GH Vicente & M Smith, 2014; Jaquinod, 2000) as showing in Figure 2.34.

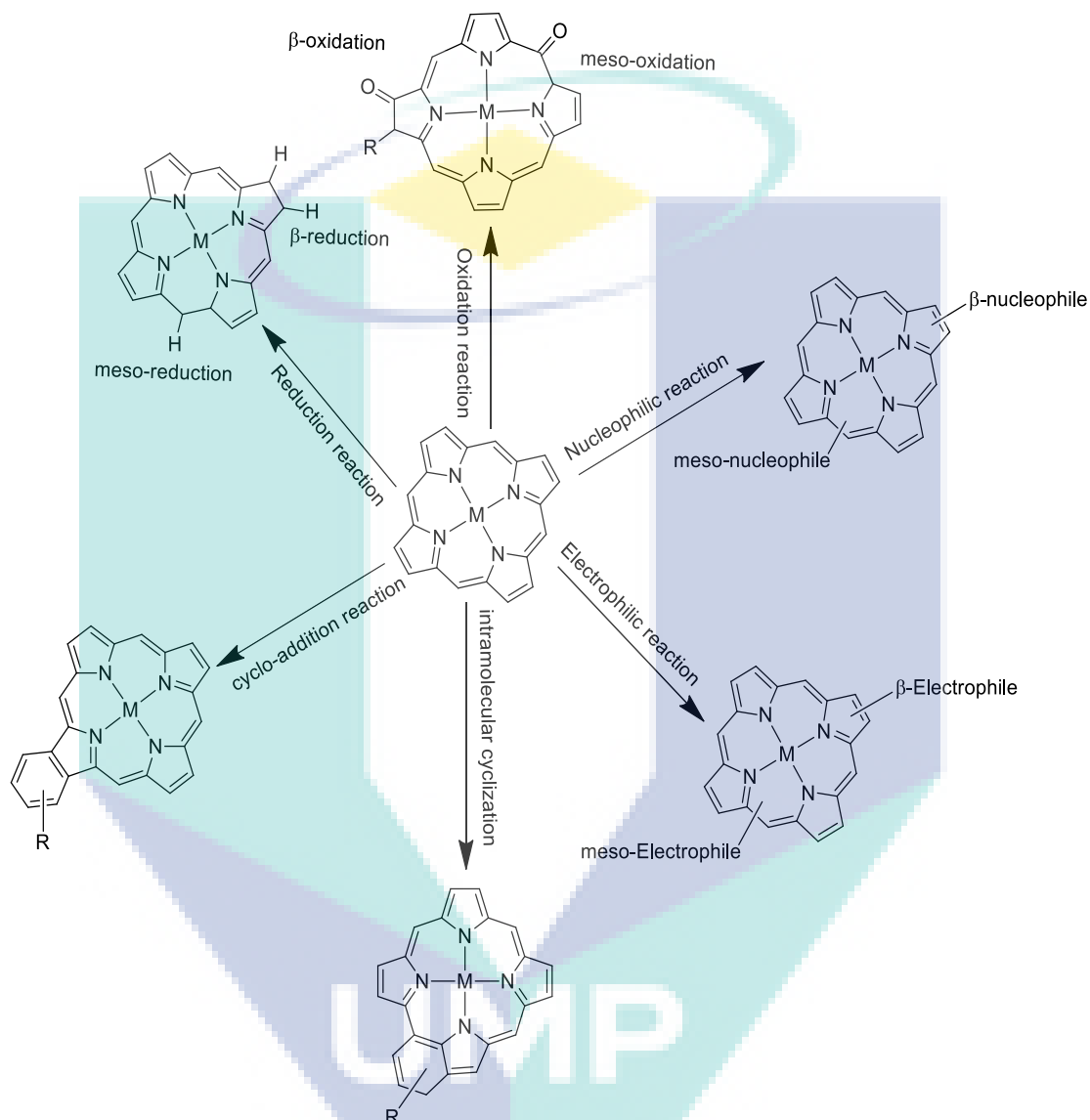


Figure 2.34 Various reaction types of post-functionalization of porphyrins

Mostly, the post-functionalization reactions are performed using porphyrins with reactive substituents such as halogen groups, formyl or acetyl groups, alkyne groups, nitro groups and metal ions on the porphyrin core. Therefore, the porphyrins bearing desirable reactive substituents are formed by the reaction of porphyrin core with corresponding reactants. As shown in Figure 2.35, the addition of halogen, formyl, acetyl, nitro and metallic groups could be carried out by halogenation (Fujimoto, Yorimitsu & Osuka, 2014; Wijesekera, Dupre, Cader & Dolphin, 1996), formylation (Takanami et al.,

2008), acetylation (Jeandon, Bauder & Callot, 1990), nitration (Ostrowski, 2005; Prasath, Butcher & Bhavana, 2012) and organometallic reaction (Atefi & Arnold, 2008), respectively on the porphyrin ring.

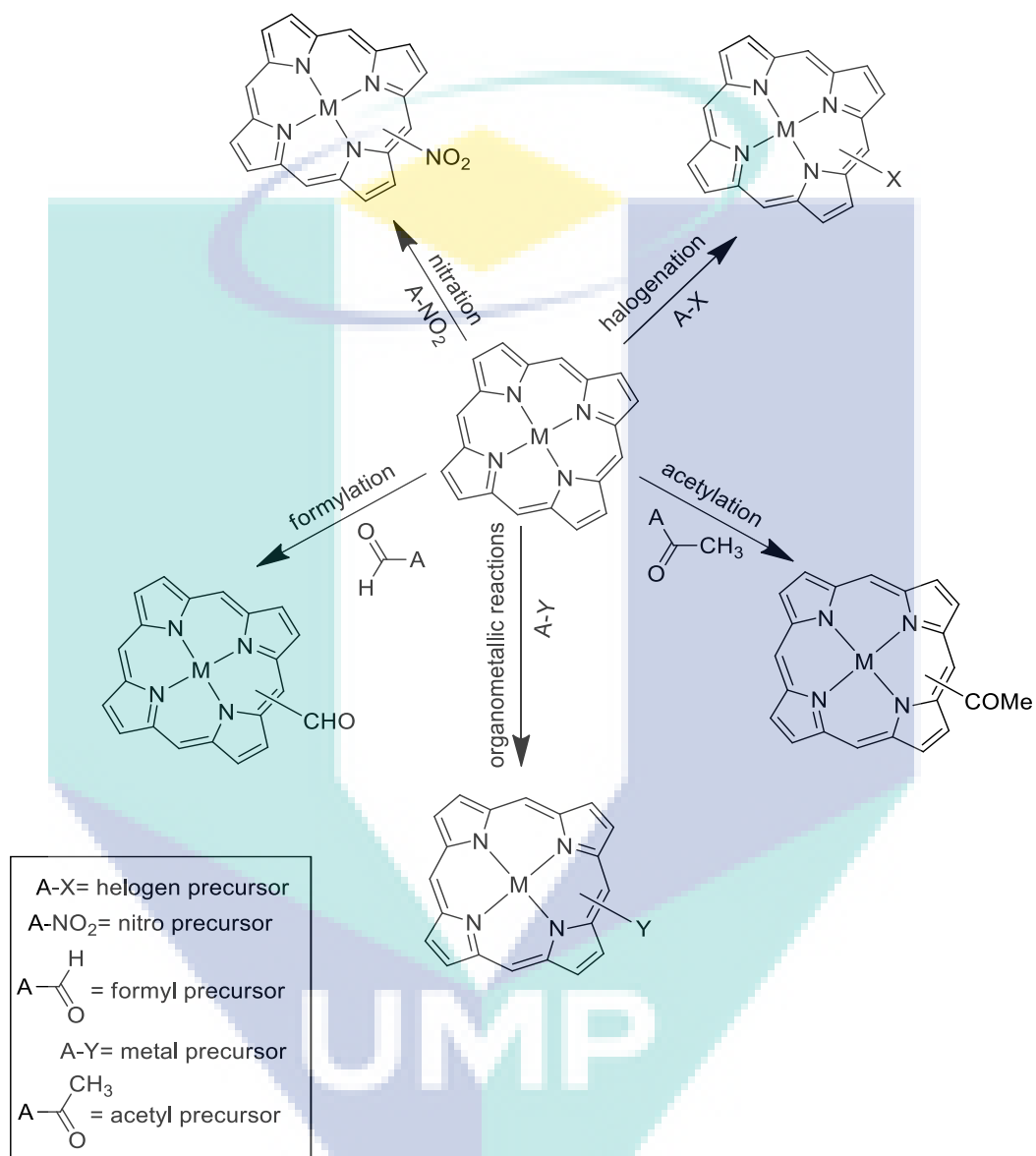


Figure 2.35 Post-functionalization for porphyrins synthesis

The most common reactions of porphyrins and their derivatives are electrophilic substitutions. Porphyrins can undergo halogenation at the un-substituted peripheral β - and meso-positions; fluorination and chlorination are favored at the most reactive meso-positions whereas bromination and iodination occur mainly at the more sterically accessible β -positions. The reagent commonly used for fluorination are N-fluoropyridinium triflates (Naruta, Tani & Maruyama, 1992), cesium fluoroxysulfate

(Andrews, Bonnett, Kozyrev & Appelman, 1988), and fluorides of cobalt or silver (Tsuchiya & Seno, 1989). Chlorination reagents include N-chlorosuccinimide (NCS) (Chorghade et al., 1996; Fujimoto et al., 2014; Wijesekera et al., 1996; Wijesekera, Matsumoto, Dolphin & Lexa, 1990), chlorine (Lin et al., 1997), HCl/H₂O₂ (Bonnett, Gale & Stephenson, 1966), Cl₂/FeCl₃ (Chorghade et al., 1996; Wijesekera et al., 1996) and PhSeCl₃ (Ali & van Lier, 1991). Similarly, for bromination of porphyrin, N-bromosuccinimide (NBS) (Chumakov, Khoroshutin, Anisimov & Kobrakov, 2009; de Almeida, Kenner, Rimmer & Smith, 1976; DiMagno, Lin & Therien, 1993; Fujimoto et al., 2014), HBr/H₂O₂ (Chumakov et al., 2009), Br₂ (Bhyrappa & Krishnan, 1991; Bhyrappa & Purushothaman, 2001; Gonsalves, Johnstone, Pereira, Shaw & Sobral, 1991), copper(II) bromide (Bhyrappa & Krishnan, 1991) and PhSeBr₃ (Chumakov et al., 2009; Jaquinod, 2000) have been used. Iodination can be accomplished with N-iodosuccinimide (NIS) (Fujimoto et al., 2014), I₂ in 1,2-dichlorobenzene (Gonsalves et al., 1991) and bis(trifluoroacetoxy)-iodobenzene-iodine in chloroform/pyridine (Boyle, Johnson & Dolphin, 1995; Shanmugathasan et al., 2000). The halogenation of porphyrins is a regioselective reaction and poly-halogenation can form a mixture of regioisomers when more un-substituted β- and meso-positions are available at the porphyrin core. Nucleophilic substitution of halogens by nitrite (Atkinson, Brady, James & Nolan, 1995; Scheidt, Duval, Neal & Ellison, 2000), cyanide (Monteiro, Pereira, Vicente & Arnaut, 2012; Vicente & Smith, 1990), and thiolate ions (Callot, 1974) has also been reported.

The main use of halogenated porphyrins is to use as starting materials for cross-coupling reactions via palladium-catalyzed cross-coupling reactions. Palladium-catalyzed coupling techniques include Suzuki coupling (Bakar, Sergeeva, Juillard & Senge, 2011; Cunha et al., 2010; Kumar & Sankar, 2014; Shi & Boyle, 2002; ShingáChan & Thomas, 1994; Vaz, Alvarez, Nieto, Paniello & de Lera, 2001), Sonogashira coupling (Ali & van Lier, 1994; Chen, Lee, Peng & Yeh, 2005; Ishida et al., 2013; Ljungdahl, Pettersson, Albinsson & Mårtensson, 2006; Matano et al., 2014; Screen et al., 2002), Stille coupling (Aihara, Jaquinod, Nurco & Smith, 2001; Chandra, Kraft, Huffman & Zaleski, 2003; Frampton et al., 2005; Sergeeva et al., 2009), the Heck reaction (Deshpande et al., 2009; Locos & Arnold, 2006; Pereira, Muller, Ordinas, Azenha & Arnaut, 2002; Risch, Gauler & Keuper, 1999), Negishi coupling (Hayashi, Yotsukura, Noji & Takanami, 2015; Lin, DiMagno & Therien, 1994; Sugita, Hayashi, Ishii & Takanami, 2013), Kumada coupling (Sugita, Hayashi, Hino & Takanami, 2012;

Takanami, 2013) and Buchwald–Hartwig amination (Chen & Zhang, 2003; Pereira et al., 2008). These methodologies have been successfully applied to derivatize halogenated porphyrins at various positions of the porphyrin core and peripheral substituents, as shown in Figure 2.36. The synthesis of porphyrin by palladium-catalyzed cross-coupling reactions is still an active method for their synthesis.

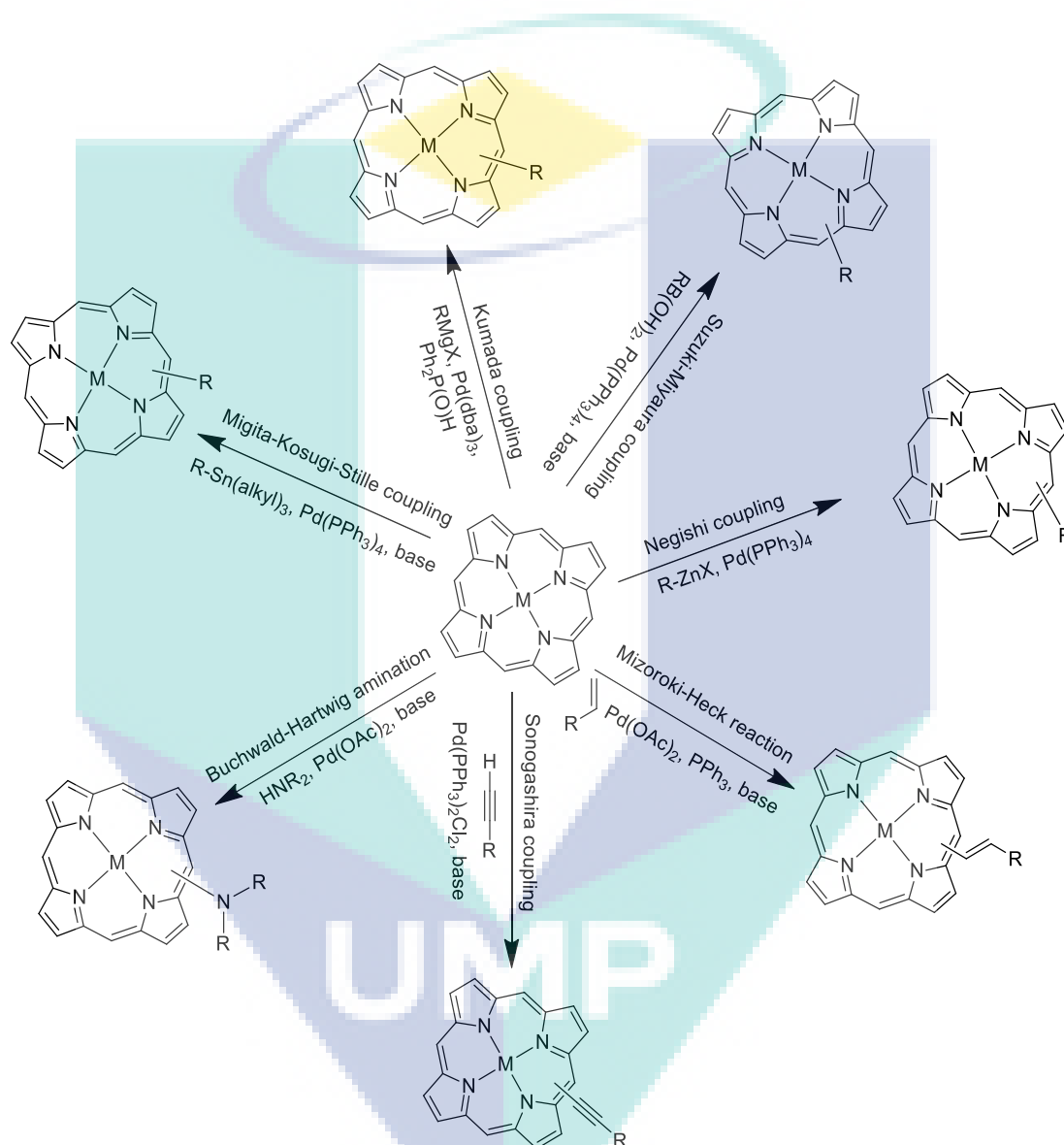


Figure 2.36 palladium-catalyzed cross-coupling reactions for porphyrins synthesis

Copper-catalyzed methodologies including Glaser-type dimerization of terminal alkynes (Anderson, 1994; Youngblood et al., 2002) and the Ullmann coupling reaction (Jiang, Zhang & JIAN, 2006; Weng, Teng, Yue, Zhong & Ye, 2007; Weng, Yue, Zhong & Ye, 2007) are also useful in the synthesis of functionalized porphyrins. However, the most frequently employed copper-catalyzed reaction in porphyrin synthesis is the

Huisgen cycloaddition reaction between organic azides and terminal alkynes, called “click reaction” (Dumoulin & Ahsen, 2011; Ladomenou, Nikolaou, Charalambidis & Coutsolelos, 2016; Shen, Liu & Chen, 2007). This approach is a general mode to connect two units into one molecule. Iridium catalyzed direct C–H borylation reaction (Hata, Shinokubo & Osuka, 2005; Hisaki et al., 2007; Mori, Shinokubo & Osuka, 2008), Rhodium catalyzed reactions (Baba, Chen, Shinokubo & Osuka, 2008; Chen, Aratani, Shinokubo & Osuka, 2009) and Nickel catalyzed reactions (Liu, Shen & Chen, 2007) have also been used for post-functionalization to modify simple and un-functionalized porphyrins.

Nitration of porphyrins occurs preferentially at the meso-positions. Electrophilic nitration is accomplished with HNO₃ in acetic or sulphuric acid (Bonnett & Stephenson, 1965; Ostrowski, 2005), fuming nitric acid (Bartoli, Battioni, De Foor & Mansuy, 1994; Dahal & Krishnan, 1995), NO₂BF₄ (Bonnett & Stephenson, 1965; Smith & Dzyuba, 2010), nitrate salts in acetic anhydride (Prasath et al., 2012), N₂O₄ (Shea, Jaquinod & Smith, 1998; Siri, Jaquinod & Smith, 2000) or nitrite ion (Luguya, Jaquinod, Fronczek, Vicente & Smith, 2004; Osuka & Shimidzu, 1997). The porphyrin core is further deactivated for electrophilic reactions by electron-withdrawing ability of the nitro group. The peripheral nitro substitution on porphyrins can be reduced with SnCl₂/HCl (Lysenko et al., 2006), with NaBH₄ (Devillers et al., 2014; Luguya et al., 2004) or NaN₃ (Devillers et al., 2014) to their corresponding amino derivatives.

The introduction a formyl group at the meso- or the β-position of porphyrin macrocycles can be done by Vilsmeier formylation using DMF/POCl₃ followed by treatment with aqueous base (Smith, Bisset & Tabba, 1982; Takamami et al., 2008; Vicente & Smith, 1991). Formyl groups at the porphyrin periphery undergo a number of reactions, including nucleophilic, reductions, and oxidations etc., which lead to a variety of functionalized porphyrins (Burrell & Officer, 1998; Höper & Montforts, 1995; Ol'shevskaya et al., 2006; Runge & Senge, 1999; Yeh, Miller, Carpenter & Nocera, 2001). Formyl-porphyrins also react with Grignard and Wittig reagents (Gosper & Ali, 1994; Screen et al., 2002) producing a variety of cis- and trans-(2-substituted-vinyl)porphyrins, which can lead to further functionalization.

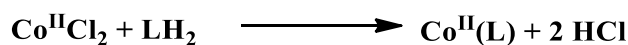
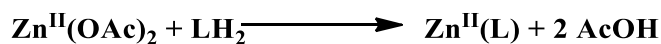
The porphyrins with carbon–metal (Li, Mg, Zn, Pd, Pt, and Hg) and carbon–metalloid (Si and B) bonds at the periphery of porphyrin core have been well reported (Atefi & Arnold, 2008; Hiroto, Miyake & Shinokubo, 2016; Suijkerbuijk & Klein Gebbink, 2008). Porphyrin can react directly with organometallic reagents (nucleophiles) preferentially at the meso-positions forming phlorins and porphodimethenes and less commonly at the β -positions forming chlorins. Porphyrins can also undergo oxidation, reduction, cyclo-addition and intramolecular cyclization reactions forming a variety of porphyrins derivatives all of which possess characteristic chemical and physical properties (da GH Vicente & M Smith, 2014).

2.5.3 Metalloporphyrins Synthesis

Upon metallation, one of the lone pairs present on the nitrogen atom of porphyrin ring is shared with metal ion and thus porphyrin ring is acting as Lewis acid (Falk, 1964; Hambright, 1971). Due to its acidic nature, two protons attached on another two nitrogen atoms of porphyrin ring can easily be deprotonated producing tetradentate anionic porphyrin ligand. Thus, the di-anionic porphyrin ligand having specific size central cavity show an incredible property to form a bond with almost all transition metals, some metalloids, the lanthanides, and some of the actinides (Buchler, 1978). The central metal ions coordinate with porphyrins by σ -coordination with nitrogen atoms containing lone pairs and π -interaction between p_π or d_π orbitals of metal ions with π orbitals of other two nitrogen atoms. σ -coordination always act as an electron donor to the metal ion, while π -coordination can act as either a π -donor or π -acceptor depending on the metal ion and the substituents on the porphyrin ring. Metal ions bonded to porphyrin anionic species exist in a huge variety of available oxidation states (-2 to 6), d electron configurations (d_0 to d_{10}), coordination numbers (from 4 to 8) and spin states ($S=0$ to $S=5/2$), also depending on the substituent at axial position on central metal ion. Due to this great diversity, a great control over the coordination environment of the central metal can be achieved.

The insertion of a metal ion into the porphyrin ring have been employed by different routes showing in Figure 2.37 that mostly depend on the nature of the metal source. Depending on the metal ion oxidation state, the reaction can occur through; 1) coordination, 2) oxidation 3) reduction of the metal (Figure 2.37).

a) Coordination of a metal



b) Reduction of metal



c) Oxidation of metal



Figure 2.37 Routes for inserting metal ions into the porphyrin ring through; a) coordination of metal; b) Reduction of metal; c) Oxidation of metal

i. Coordination of a metal:

For this reaction, the metal salts (MX_2) are generally used for metal insertion (Figure 2.37a). However, the core issue of this reaction is to get soluble both free-base porphyrin and metal salt in same solution simultaneously under reactive condition. The good solvents in their neutral form for porphyrins are poor for metal ions and vice versa. Adler (Adler, Longo, Kampas & Kim, 1970) had reported several solvents as reaction media which give reasonable solubility for both porphyrin and metal ion under same reaction conditions. Many solvents have been tested and amongst all *N,N*-dimethylformamide (DMF) is proved to be of worthy reaction medium providing numerous advantages for synthetic purposes. A number of metal ions (Zn, Fe, Cu, Ni, Mn, Pd, Cd, Co, Cr, Pb, Hg etc.) inserted into the porphyrin ring by this method.

ii. Reduction of metal

In 1984, James and Collman have reported separately the insertion of Ru in porphyrin ring as Ru-CO moiety starting from RuCl_3 salt under carbon monoxide in 2-(2-methoxyethoxy)ethanol solvent (Collman, Barnes, Brothers, et al., 1984; Collman,

Barnes, Swepston & Ibers, 1984). Carbon monoxide acts as a reductant as well as ligand to complete the reaction. A whole and adequate stoichiometry for this reaction has not been observed, due to the fact that competing side reactions may take place during the reaction (Figure 2.37b).

iii. Oxidation of metal

The insertion of metal ion through oxidation can be carried out by two ways; oxidation with external oxidant and spontaneous oxidation (Figure 2.37c). An external oxidant is included into the reaction mixture to stimulate the variation of the central metal oxidation state to have a stable product. In the case of iron, an intermediate Fe(II)(P) initially formed is oxidized to Fe(III) during the work-up runs in air and in the presence of donor ligand. Furthermore, the formation of ruthenium-CO complex (Rillema, Nagle, Barringer Jr & Meyer, 1981; Tsutsui, Ostfeld & Hoffman, 1971), $M^{II}(L)(CO)$, by spontaneous oxidant of the metal (starting from M(0) cluster) involve the reaction between the free-base and the neutral cluster $M_3(CO)_{12}$ in a high boiling point solvent, for example decahydronaphthalene. In this case, the oxidation of the two protons occur from free-base into molecular hydrogen. Different from the above stated reactions, the whole solubility of the two reactants in the reaction media is not a fundamental factor for successful insertion of the metal ion into the porphyrin ring for this synthetic process. However, several solvents have been utilized, based upon the stability of free-base at high temperature and on its conformation in solution (Le Maux, Bahri & Simonneaux, 1991; Le Maux, Bahri & Simonneaux, 1993).

2.6 Density Functional Theory Calculations of Porphyrins

Commonly, in the synthesis of new molecular system, the main focus is to construct and characterize the synthetic system that exhibit a potential application for a particular use and this is often considered as the end goal. A lot of challenges, related to engineering problems and difficulties are to be faced, showing how it could be designed, synthesized and repeated reliably. However, by the theoretical studies of the systems, predictions could be built about which framework are of great worth and promising for studying experimentally. Secondly, experimental results are not always straightforward and easy to interpret, therefore theoretical investigation is one of the important tool to

clarify the fundamentals and to resolve any doubts. There are various Ab-initio quantum chemical methods such as Hartree-Fock (Hartree, 1928), MP2 (Weigend, Köhn & Hättig, 2002), DFT (Gross & Dreizler, 2013) and CCSD (Kowalski, Dean, Hjørth-Jensen, Papenbrock & Piecuch, 2004) are reported in literature adopted to study the properties of a large number of materials. However, DFT methods are the most common method for studying the properties of material. A number of research articles have been published on the porphyrins structural as well as their optoelectronic properties studies either separately or along with synthesis (Baruah & Pederson, 2009; Dong, Hou, Zhao, Fu & Li, 2012; Mathew et al., 2014; Sundholm, 2000; Yasin, Jose & Yusoff, 2015; Zhang, Zhang & Jiang, 2005) because the synthetic approach adopted for porphyrin synthesis are not straightforward and also multistep synthesis is required that are time consuming.

In this doctoral research, DFT methods were the main focus for designing and evaluating the porphyrin molecules and calculating their optical and electronic properties prior to synthetic approaches.

2.6.1 Ab-initio Quantum Chemical Methods

Computational chemistry has established over the last era from a commonly used technique as a specialist field within theoretical calculations for modelling the properties of molecules and materials to a predictive tool for structures, reaction pathways, and ground and excited state properties of molecules, clusters, and crystals (Cramer, 2013; Leach, 2001; Lewars, 2016; Wolfram & Holthausen, 2001). These techniques have mostly been driven through the wide availability of reliable quantum chemical (QC) methods and advance progresses in computational power.

The systems studied by theoretical methods consider materials (irrespective of whether they are molecules, clusters or crystals) as the collections of electrons and the nuclei obeying the quantum mechanical principles governed by the Schrodinger equation shown in the Eq. 2.5 (Schrödinger, 1926).

$$\left\{-\frac{\hbar^2}{2m}\nabla^2 + V\right\}\Psi(r, t) = i\hbar\frac{\partial\Psi(r, t)}{\partial t} \quad 2.5$$

where \hbar is Planck's constant divided by 2π and i denote $\sqrt{-1}$. The position of the particle in space is given by the vector $r = xi + yj + zk$. V represents the external field in which the particle moves and Ψ is the wave function that describes the motion of the particle. ∇^2 is the Laplacian operator,

$$\nabla^2 = \frac{\partial^2}{\partial x^2} + \frac{\partial^2}{\partial y^2} + \frac{\partial^2}{\partial z^2} \quad 2.6$$

However, Schrödinger equation can be used analytically for only a simple system such as hydrogen atom. Complex systems encompassing more than single electron are not able to solve exactly by using this equation because it does not provide any hint how electrons are correlated in a bound system. A large number of approximations are in use such as Hartree-Fock (Hartree, 1928), MP2 (Weigend et al., 2002), DFT (Gross & Dreizler, 2013) and CCSD (Kowalski et al., 2004) to solve many-atom systems like molecules. As the processing abilities of the computer have risen, the scope for utilizing them in theoretical analyses of QC systems has been steadily increasing. Numerous algorithms have been defined that allow the complicated equations to be solved, approximating the QC behavior.

2.6.2 Density Functional Theory Calculations

In order to calculate the electronic structures and properties of atomic systems, different ab-initio method can be utilized. In particular, a number of hierarchical methods, collectively known as quantum chemistry (Szabo & Ostlund, 2012), can generate very accurate information (with an accuracy of 1 in 10^{-27}). Often it all depends upon the size of the studied system that puts limitation on the selection of a method. The more accurate the theory is, the more expensive the calculation will be. Hartree-Fock (HF) (Fock, 1930; Hartree, 1928) method is the simplest approach amongst all. In this approach, electron is counted to exist in all other $n-1$ electrons average potential. However, the HF approach does not involve a correlation term in order to explain the instantaneous interaction between the electrons. This means that HF does not well anticipate the electronic properties that are affected by electron-electron connections. Though HF approach doesn't include association term to account for rapid contact between electrons.

Higher level electron correlation methods, for example; configuration interaction (CI) (Head-Gordon, Rico, Oumi & Lee, 1994) or coupled-cluster (CC) theory (Čížek, 1966) utilize the accurate wave functions to explain e-e repulsion. Such methods are limited to small systems and are computationally expensive.

The most popular method for solving many electron problems is the DFT proposed by Hohenberg, Kohn and Sham (Hohenberg & Kohn, 1964; Kohn & Sham, 1965). It is worthy to utilize it in finding material properties from single molecule to condensed phase system and; therefore, is widely utilized quantum mechanical tool in physics and chemistry since 1970s. DFT approach provides a good equilibrium between cost and accuracy for complex molecular systems where electronic structures for the systems up to hundred atoms needs to be calculated. DFT method is also used to calculate the ground state electronic properties of many atom structures (Hohenberg & Kohn, 1964). Therefore, this method has been used for simulating new porphyrin molecules in this dissertation. Using this method, a series of combinations of hybrid functional with basic sets have been modelled in order to design the desired structures with improved optoelectronic properties.

In DFT, the interacting electrons problem is exchanged by non-interacting electron problem. Mathematically, by using this approach, the functional of electron density is used instead of many electron wave functions and states the total energy of the system as a functional of electron density. Therefore, to make the problem easier, it deals with three variables of density functional instead of $3N$ variable of many-electron wave functions.

As Hohenberg and Kohn stated in their paper published in 1964 that ground state energy and properties of system can be determined through electron density (Hohenberg & Kohn, 1964) indicating the density, ρ , is essential quantity in DFT. According to this, the system energy can be termed as a functional of electron density, $E[\rho(\mathbf{r})]$, where the energy (E) is a function of density (ρ) which in turn is a function of position (\mathbf{r}). The minimum energy of a system corresponds to the precise ground state electron density. System energy is a sum of electronic density functional.

$$E[\rho] = T[\rho] + E_{Ne}[\rho] + J[\rho] + E_{xc}[\rho] \quad 2.7$$

Density of an interacting system is difficult to determine; a usual method is to utilize system of non-interacting electrons termed as Kohn-Sham system (Kohn & Sham, 1965). This system is made exactly the same as the real system with interactive particles. $T[\rho]$ is the kinetic energy of non-interacting electrons. $E_{Ne}[\rho]$ is the attraction between the nuclei and electrons whereas $J[\rho]$ is coulombic electron-electron repulsion energy. $E_{xc}[\rho]$ is exchange-correlation energy to account for interaction between electrons.

Kohn-Sham equation is an iterative method starting by introducing an initial guess of electron density in the equation and generates set of orbitals that are utilized to measure new electron density. The new density is taken as the input to next iteration and method is continued till convergence has been achieved. At this stage of iterative process, the system total energy is calculated (Hohenberg, Kohn & Sham, 1990).

2.6.3 DFT Calculations by Different Functionals

The basic challenge in DFT is to express the exchange-correlation term as accurately as possible. The accuracy thus depends on the approximations used. Commonly an approach in which the exchange-correlation functional is divided into exchange and correlation part, signified by an exchange and a correlation functional.

$$E^{xc}[\rho(r)] = E^x[\rho(r)] + E^c[\rho(r)] \quad 2.8$$

The exchange and correlation terms are related with exchange correlation hole raised from the possibility to find two electrons close to each other due to charge and spin. The exchange part is termed as the Fermi hole that relates to exchange between electrons of same spin, while the correlation part is the Coulomb hole. DFT method includes one exchange and one correlation functional. Hence, these methods are the combinations of various exchange and correlation functionals. Several approaches are available to approximate the two functionals but more precise and accurate method is Becke's gradient-corrected exchange (B) (Becke, 1988) and the gradient-corrected correlation functional by Lee, Yang and Parr(LYP) known as BLYP method (Becke, 1992; Lee, Yang & Parr, 1988b).

Currently the extensively used DFT methods includes the hybrid density functionals, where a part of HF exchange energy is also included in exchange-correlation energy derived from DFT approximation,

$$E_{hybrid}^{XC} = C_{HF}E_{HF}^X + C_{DFT}E_{DFT}^{XC} \quad 2.9$$

where the “c” determines the weight of each functional.

B3LYP (Becke three parameter for exchange, Lee, Yang and Parr for correlation) is most famous and popular hybrid method and are used widely (Becke, 1993). The amount of HF exchange in B3LYP is approximately 20% (Bauschlicher, 1995). B3LYP is believed to be an accurate DFT method which generates minor errors in geometries (Curtiss, Redfern & Raghavachari, 2005) and energies (Tirado-Rives & Jorgensen, 2008). M06 functional (Zhao & Truhlar, 2006; Zhao & Truhlar, 2008) is another hybrid DFT functional that possesses promising long-range properties. These two hybrid functionals are used in this study for calculating the porphyrin molecules.

In order to make more accurate asymptotical behavior, range-separated functionals, comprising an increasing fraction of HF exchange as the interelectronic distance, are added. These functionals are suitable in excited state calculations as non-coulomb part of the exchange functional is not accurate at large distances. The exchange energy is divided into long range and short-range part. In the long range, HF exchange is included, and short range incorporates DFT exchange. The exchange correlation energy can be written as,

$$E_{LC-DFT}^{XC} = E_{LC-HF}^X + E_{SR-DFT}^X + E_{DFT}^C \quad 2.10$$

Long range modified hybrid DFT functionals include CAM-B3LYP (Yanai, Tew & Handy, 2004) (that has been enlisted in this study), LC- ω PBE (Tawada, Tsuneda, Yanagisawa, Yanai & Hirao, 2004; Vydrov, Scuseria & Perdew, 2007) and the ω B97 functional (Chai & Head-Gordon, 2008a; Chai & Head-Gordon, 2008b). In CAM-B3LYP a Coulomb attenuating method is used to include long-range correction on B3LYP. CAM-B3LYP also contains a fraction of short-range HF exchange.

2.6.4 DFT Calculations by Different Basis Sets

Generally, models of a chemical system contain the combination of a theoretical method of DFT such as HF and B3LYP with various basis sets. Each pairing of method characterizes a unique approximation of the Schrödinger equation. Selecting any specific model involves a trade-off between accuracy and computational cost. For more correct methods and larger basis sets make the computational jobs to run longer.

A basis set is defined as mathematical representation of atomic orbitals within specified system and are used for theoretical calculation. By utilizing infinite number of basis sets, will define the exact orbitals. However, computationally it is not possible, and a reasonable solution must be required. For this purpose, predetermined basis sets involve approximations that makes the calculations possible, and the type and number of used functions effect the accuracy. Computational efforts accuracy must be considered while performing tasks. Larger basis sets approximate the orbitals more accurately by imposing some restrictions on the locations of electrons in space (Huzinaga, 1985).

There are two types of atomic orbitals used: Slater Type orbital (STOs) (Slater, 1930), and Gaussian type orbitals (GTOs) (Boys, 1950). Gaussian-type orbitals are mostly used atomic orbitals. STOs are utilized for small systems such as atoms and diatomic molecules when high accuracy is needed. Calculating integrals with STOs is difficult and later revealed that STO is approximated as linear combination of GTOs. Generally, three GTOs are needed to access more accuracy as compare to one STO. However, GTOs are easily integrated in comparison with that of STO and this compensates for large number of functions required. Therefore, atomic orbitals are symbolized as linear combination of Gaussian functions. Lots of Gaussian-type orbitals basis sets are published in literature (Jensen, 2013). Basis sets come in grading of increasing sizes, giving more accurate results but with higher cost.

Minimal basis sets are the sets with smallest basis sets. This set contains only those functions which are required to define all occupied orbitals in an atom. STO-3G (Pietro & Hehre, 1983) is the example of simplest minimal basis set used in ab initio calculations. This basis set consist of a STO characterized as a linear combination of three Gaussian functions. As minimal basis sets are not sufficient to describe chemical systems,

therefore additional functions are needed to include in calculations, such as double Zeta (DZ) basis set that comprises twice number of functions as compared to minimal basis set added to each atomic orbital. Similarly, three and four times the number of functions form triple Zeta (TZ) and quadruple Zeta (QZ) basis sets respectively (Davidson & Feller, 1986). This is common only for valence orbitals while the core orbitals left unaffected. These sets are collectively known as split valence basis sets. The example of these basis sets (DZ) are 6-31G (Frisch, Pople & Binkley, 1984) and 3-21G (Freindorf & Gao, 1996) basis sets. 3-21 G uses a minimal basis set for the core orbitals and a linear combination of three GTOs, each valence orbital is defined by two contractions, one with two primitive GTOs and one with only one GTO. Similarly, 6-31 G uses a minimal basis sets for the core orbitals and a linear combination of six GTOs, each valence orbital is defined by two contractions, one with three primitive GTOs and one with only one GTO. Triple split valence basis sets (TZ) include 6-311 G (Montgomery Jr, Frisch, Ochterski & Petersson, 1999) as an example where each valence orbital is split into three contractions.

Addition of higher angular momentum functions for valence electrons make the description more accurate because these electrons are the most vital participant in the chemistry of an atom. Such functions are called polarization functions and are used to account for charge distribution of an atom. Split valence basis sets allow only a change in orbitals size, but these functions allow orbital to change shape as well. To polarize s-orbitals of hydrogen, the p-orbitals are inserted and to polarize the p-orbitals, d-orbitals are added. In order to extend the 6-31G basis set as an example, the 6-31G(d) basis set includes d-orbitals for heavy atoms, furthermore extended version of 6-31G(d,p) includes d-orbitals for heavy atoms and p-orbitals for hydrogen. Another representations for 6-31G(d) and 6-31G(d,p) are 6-31G* (Rassolov, Pople, Ratner & Windus, 1998) and 6-31G** (Del Bene, Person & Szczepaniak, 1995) respectively. More polarization functions can be used to increase accuracy.

Atoms which are larger than the third-row elements are treated in a different way by using collective basis sets. In these basis sets, the core electrons are considered with effective core potentials (ECPs) and the valence electrons are treated with an appropriate valence basis set. LANL2DZ (Check et al., 2001) is the example of collective basis sets and widely used basis sets for large atoms.

In this study, various combination of basis sets, 3-21G and 6-31G (split-valence basis sets), 6-31G(d) (polarization functions split-valence basis set), and LANL2DZ (combined basis set) have been used to evaluate which basis set gives the theoretical data that are comparable with that of experimental results.

2.6.5 Time Dependent DFT Calculations

The extension of density functional theory (DFT) is TDDFT. In this theory, computational basis is analogous to demonstrate that the wave function which is time dependent is same as the time dependent electronic density, and then to obtain the efficient potential of a non-interacting system which yields the same density as any provided interacting system. TDDFT method is to approximate time dependent Schrödinger equation which defines the system with time (Marques, Maitra, Nogueira, Gross & Rubio, 2012; Ullrich, 2011).

Runge-Gross theorem (Runge & Gross, 1984) is the basis formalism for TDDFT, which is an analogue theorem of Hohenberg-Kohn (HK). The Runge-Gross theorem explains that how a time dependent action, $A[\rho]$ is a distinctive functional of density.

$$A[\rho] = A[\phi(\rho)] \quad 2.11$$

There are many applications of TDDFT in which the most famous is the calculation of excited state energies of isolated systems. This computational calculation can be processed through two different approaches. First approach includes the propagation of Kohn-Sham equations that are time-dependent and the Kohn-Sham orbitals with time (Marques & Gross, 2003). The primary ground state with an exchange-correlation potential is produced with time dependent exchange-correlation potential. Second approach involves the linear response theory, used to compute absorption spectra. The external potential is added to ground state nuclear potential that induce change in system density.

TDDFT calculations are also very useful in forecasting the spectra of several systems (Jacquemin, Perpète, Scuseria, Ciofini & Adamo, 2008; Nazeeruddin et al., 2005; Van Gisbergen, Rosa, Ricciardi & Baerends, 1999), the computation of vibronic

structure of absorption spectra (Dierksen & Grimme, 2004; Neugebauer, Baerends & Nooijen, 2005), calculating nature of electronic transitions and dichroism spectra (Goerigk & Grimme, 2008). TDDFT is valuable to analyse large systems within rational time frame by offering a less computer-demanding method to compute excitation.

Although TDDFT lacks in multi-reference treatment but still can be utilized to predict absorption spectra accurately. However, TDDFT performance is all depends upon density functional used in the method. Several studies have been accomplished to evaluate the accuracy of different functional used for predicting the absorption spectra by TD-DFT methods (Andzelm et al., 2009; Jacquemin, Perpète, Ciofini & Adamo, 2010; Perpète, Wathelet, Preat, Lambert & Jacquemin, 2006; Yasin et al., 2015). Studies also show that this method is effective in the prediction of absorption spectra of porphyrin and its relevant molecules (Dong et al., 2012; Mathew et al., 2014; Van Gisbergen et al., 1999; Yasin et al., 2015).

In this study, TD-DFT calculations are done using B3LYP, CAM-B3LYP and M06 density functionals in combination with 3-21G, 6-31G, 6-31G(d), and LanL2DZ basis sets.

2.7 Applications of Porphyrins

Porphyrins are the most adaptable molecules due to their capability to adopt many metals and substituents, which make them suitable for diverse applications from photovoltaics as a light harvesting molecule to a drug delivery medium in medical treatments, from energy conversion and storage devices as a hole conducting medium to catalysis as a redox agent, from magnetic resonance imaging to boron neutron capture therapy and so on. Figure 2.38 summarizes the application domains of various natural and synthetic porphyrins. As the main objective of this thesis is developing new porphyrins as a contrast agent for photoacoustic imaging (PAI), its principle and progress made in using porphyrins as a contrast agent is briefly reviewed here.

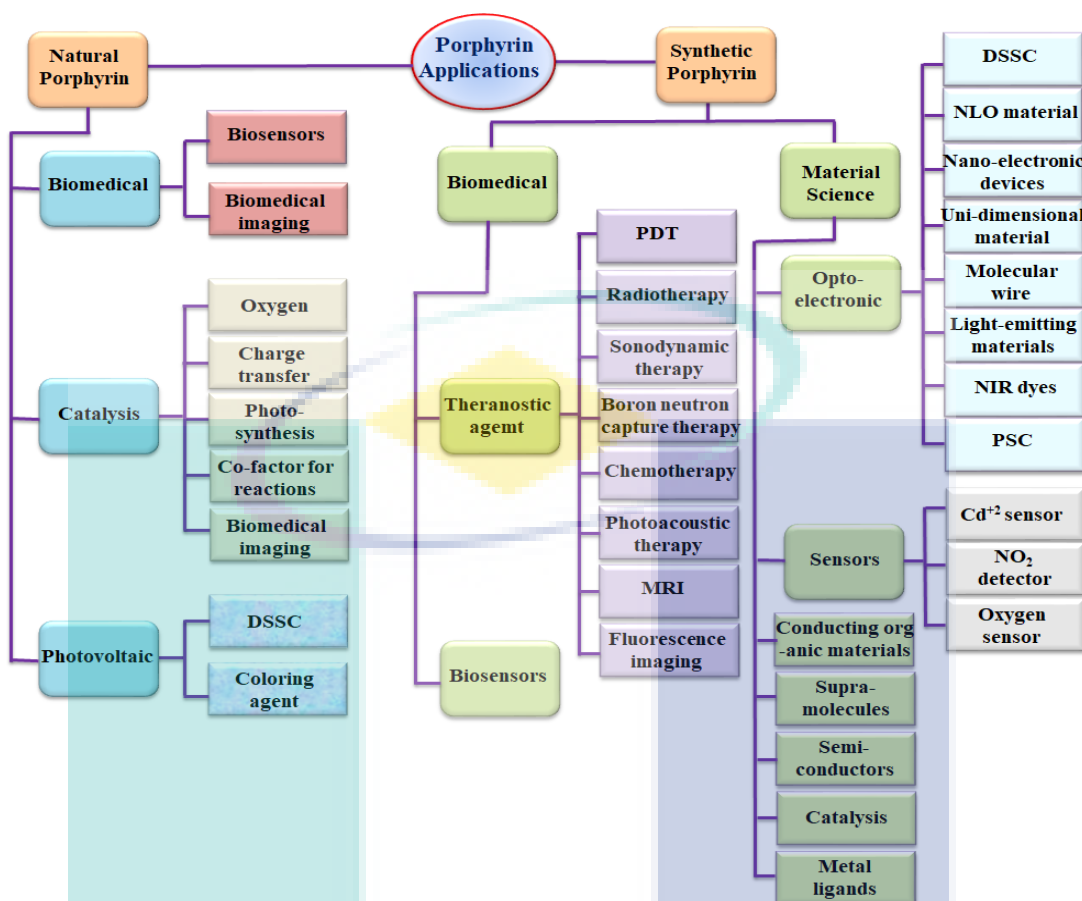


Figure 2.38 Application domains of natural and synthetic porphyrins

2.7.1 Photoacoustic Imaging:

PAI is a non-invasive biomedical imaging modality improved from optical and ultrasound imaging techniques. In general, photoacoustic imaging (PAI) techniques works as ‘light in and sound out’ instead of ‘sound in and sound out’ as in ultrasound imaging and ‘light in and light out’ as in optical imaging (Zackrisson, van de Ven & Gambhir, 2014). In PAI, lasers pulses are utilized as source of light to penetrate in tissues, which is absorbed either by endogenous biomolecules or exogenous contrast agents and converted to heat. The released heat leads to thermal expansion, which generates acoustic waves that are detected with an ultrasound transducer (de la Zerda et al., 2012; Yuan, Wu, Zhao & Jiang, 2005). The image formation in PAI is by detecting thermoelastically induced acoustic waves on light absorption by biomolecules or contrast agents. Photoacoustic signals are optically generated and ultrasonically detected; PAI thereby combines advantages of large optical window usable for imaging tissues and deep penetrating depth and spatial resolution of ultrasound. Variations of PAI are photoacoustic microscopy (PAM) (Wang, Nandy, Salehi, Kumavor & Zhu, 2014; Yao et

al., 2015) utilized for small scale and photoacoustic tomography (PAT) (Wang & Hu, 2012; Xiang, Wang, Ji & Jiang, 2013) used for large-scale high-resolution image production (Luciano et al., 2016).

PAI makes the use of linear and non-linear photoacoustic effects. In linear PAI, light irradiation is generally absorbed by the contrast agents and then converted into heat. The transient temperature rise leads to thermoelastic expansion (Hoelen, De Mul, Pongers & Dekker, 1998) and acoustic emission that could be probed by the ultrasound transducer to construct the PA image (de la Zerda et al., 2012; Sreejith, Joseph, et al., 2015). Overall, the contrast in PA imaging depends on the light absorbance and the optical to acoustic conversion efficiency because the amplitude of the generated PA signal is linearly proportional to the optical absorption and the thermoelastic properties of the absorbing medium (Feng, Gao, Xu, Gaoming & Zheng, 2015; Gao, Feng & Zheng, 2016). On the other hand, the utilization of multiple laser pulse irradiation to realize the nonlinear signal amplification has also attracted a lot of attention (Gao, Bai, et al., 2016). Nonlinear PA imaging is mainly based on the increased Gruneisen coefficient on account of the heat accumulation and temperature increase of an object in the process of laser irradiation and heating. Thus, optical absorption and photothermal conversion efficiency of the contrast agents play an important role in both linear and nonlinear PA imaging (Gao et al., 2017).

The endogenous biomolecules used commonly for PAI are haemoglobin (Hu, Maslov & Wang, 2011), deoxyhaemoglobin (Bayer, Wlodarczyk, Finnell & Emelianov, 2017), melanin (Schwarz, Buehler, Aguirre & Ntziachristos, 2016), and other biological molecules (Guggenheim et al., 2015; Wang et al., 2010) found in normal tissues. These allowed the imaging of the blood content of the vascular network in rodent brains (Yao et al., 2015) ovary tissues (Wang et al., 2013), and cancer in breast (Heijblom et al., 2012). However, the cancers in early stages mostly, are not detected by endogenous biomolecules. Therefore, the exogenous contrast agents have been used in order to enhance the sensitivity because of their capability of absorbing more incident light energy significantly as compared to that of endogenous biomolecules, achieve deep penetration, outstanding temporal resolution and high spatial resolution of ultrasound with the superior contrast and spectral features of optical imaging (Gao et al., 2017; Huynh et al., 2012). However, achieving sufficient contrast between the target and the background cannot be straightforward because endogenous biomolecules in normal tissues can also

produce photoacoustic signals by absorbing light (Jokerst, 2014). Therefore, exogenous contrast agents must be designed such that they absorb incident photons efficiently and undergo thermal expansion.

Similarly, PAI applicability in early stage cancer detection depends on the properties of contrast agents accumulated in the target tissue or organ, are photo-stable and biocompatible, have selective absorption in the spectral regions where the endogenous molecules are not absorbed (the phototherapeutic window: 700–1000 nm), and also have high efficiency liberating the absorbed pulse energy in the form of heat (Schaberle et al., 2010; Schaberle et al., 2011). Hence, it follows that a good exogenous contrast agent should have a strong absorption in the NIR, particularly in the region between ~700 and 800 nm (Braslavsky & Heibel, 1992) (Abuteen et al., 2013; Wang & Hu, 2012; Xu & Wang, 2006).

In recent years, various kind of inorganic and/or organic based micro- or nano-material such as nanoparticles (Maji et al., 2014; Mallidi et al., 2009), nanofibers (Zhang et al., 2015), nanorods (Chen et al., 2011; Gao et al., 2017), nanocages (Kim et al., 2010), nanodroplets (Paproski et al., 2016) and nanotubes (de la Zerda et al., 2012), have been introduced as PAI and/or multimodal contrast agents and few of them showed good in-vivo imaging characteristics (Ho et al., 2014; Huynh, Jin, Wilson & Zheng, 2014; Huynh et al., 2012; Paproski et al., 2016). The inorganic nanostructures such as gold nanoparticles and carbon nanotubes have attracted great interest because of their thermal effect and high level of light absorption (de la Zerda et al., 2012; Kim et al., 2010; Mallidi et al., 2009). However, there is a constant argument on the safety and usage of inorganic contrast agents for clinical proposes (Browning et al., 2009; Poland et al., 2008). Also, the use of inorganic nanoparticles is still concern with problems regarding their bio-distribution, toxicity, or homogeneity (Gnach, Lipinski, Bednarkiewicz, Rybka & Capobianco, 2015; Lewinski, Colvin & Drezek, 2008; Srivastava, Gusain & Sharma, 2015). Therefore, alternative approaches have been adopted to use the organic dyes either assembled into vesicles such as porphyrinsomes (Lovell et al., 2011; Wang, Yang, Zhao & Wang, 2016), micelles (Liu et al., 2016), microbubbles (Huynh et al., 2014; Huynh et al., 2012) or nanodroplets (Paproski et al., 2016) and also photoacoustic probes generated in tissue (Filonov et al., 2012; Zhang et al., 2011) or as molecular photoacoustic contrast agents (Abuteen et al., 2013; Frenette et al., 2014). Generally, organic or metallorganic

NIR dye molecules are either covalently attached on the external surface, noncovalently encapsulated inside the core/shell structure, or doped within suitable matrixes which are optically transparent to excitation or emission light. Among these approaches, the use of NIR organic dyes as molecular photoacoustic contrast agents have aroused tremendous attention recently because of their high optical absorption, biocompatibility and stability. However, very rare literature is reported on small molecular photoacoustic contrast agents. The examples for molecular photoacoustic contrast agents include cyanine (Licha et al., 2000; Luo, Zhang, Su, Cheng & Shi, 2011; Wang et al., 2012) porphyrin (Abuteen et al., 2013) and BODIPY derivatives (Frenette et al., 2014). Among them, porphyrins are particularly interesting due to their tunable optical wavelength windows toward NIR region, stability, and biocompatibility, long lifetimes and can be used for lifetime-base PA imaging to probe the molecular environment surrounding a sample (Forbrich, Shao, Shi & Zemp, 2016; Zhou et al., 2016).

Recently, there has been increasing interest in developing the multifunctional contrast agents for their use in multimodal imaging techniques for simultaneous studies of self-assembly status of the particles, deepest imaging capabilities, penetration depth and spatial resolution, morphological and physiological information that may be useful for the development of hyper-integrated imaging systems (Liu et al., 2016; Rieffel et al., 2015). By combining the contrast of imaging techniques, a contrast agent has the potential to detect, diagnose and treat the early stage tumor. Most recent interest is in ultrasound and photoacoustic bifunctional imaging to enhance photoacoustic and ultrasound imaging simultaneously (Huynh et al., 2012).

2.7.2 Porphyrin as Photoacoustic Contrast Agent

Porphyrin and its derivatives have attracted a great interest not only because of their well-defined optoelectronic properties, biocompatibility, photosensitizing properties and stability but also because of their ability to accumulate selectively in tumour tissues, and persist inside the cell for long time (Vicente, 2001). Because of these unique features, porphyrin is attracting the researcher attention to its potential use as molecular photoacoustic contrast agent in biomedical imaging, although the literature is rare so far. The heavy metal insertion in a porphyrin core also affects the optoelectronic properties significantly, causing the increase in non-radiative decay that allow the

molecule to act as potential molecular photoacoustic contrast agent (Chaves, Jesus, Henriques, Brito & Serpa, 2016; Ho et al., 2014; Serpa et al., 2008). In the following, efforts in utilizing porphyrin as a contrast agent for PAI is briefly described and a Table summarizing these are given in the Appendix B.

In 2014, Hui Huo et al., compared the PA activity of 5 photosensitizers: zinc phthalocyanine, protoporphyrin IX (shown in Figure 2.39), 2,4-bis[4-(N,N-dibenzylamino)-2,6-dihydroxyphenyl] squaraine, chlorin e6 and methylene blue in phantoms and observed that zinc phthalocyanine showed the highest photoacoustic activity (Ho et al., 2014).

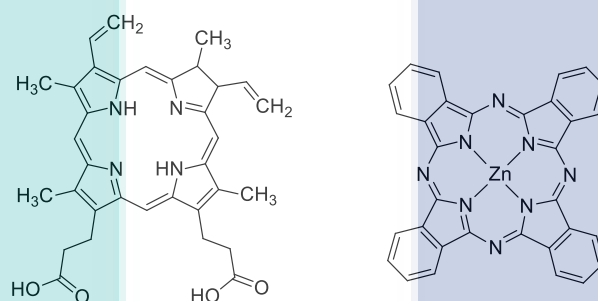


Figure 2.39 Structures of zinc phthalocyanine, protoporphyrin IX employed as PAI contrast agents

In 2015, Ho et al., used uranium containing porphyrinoid conjugates (Figure 2.40) with PLGA nanoparticles and employed PAI to detect the active concentration (Ho, Sessler, Gambhir & Jokerst, 2015).

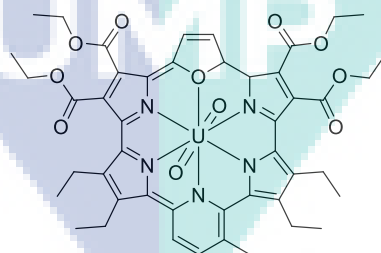


Figure 2.40 Structures of uranium porphyrinoid complex employed PAI contrast agents

In 2013, Abuteen et al., modified the free-base porphyrin core structure to porphyrinoids containing quinoline-annulated porphyrins and bacteriochlorins (Figure 2.41) and observed that PA signal from the above molecules are 2.5 times than that of the standard ICG dye used (Abuteen et al., 2013).

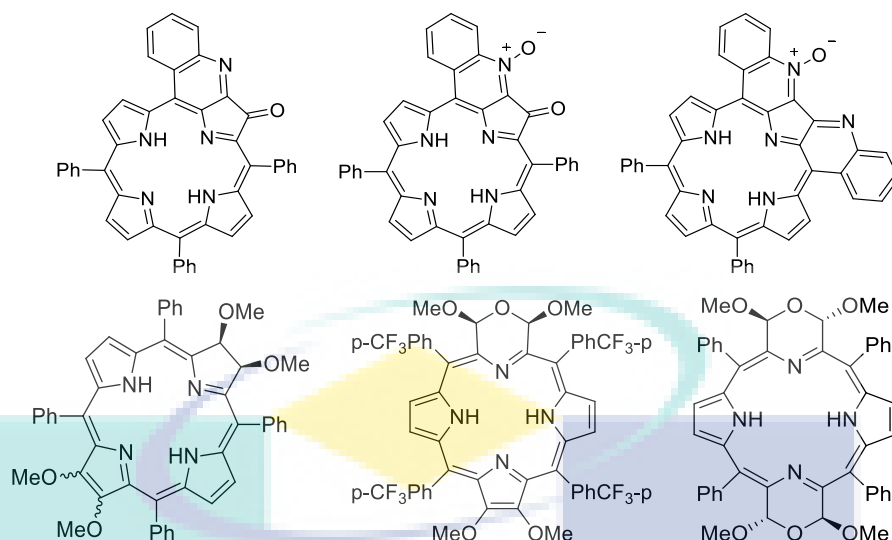


Figure 2.41 Structures of quinoline-annulated porphyrins and bacteriochlorins employed as PAI contrast agents

A similar strategy was adopted by Michael et al., in 2016 by using tetra-PEG modified and freely water soluble quinoline-annulated porphyrin derivative in PAI (Figure 2.42). However, the principle focus on this work is on solubility issue rather than the strength of PA signals (Luciano et al., 2016).

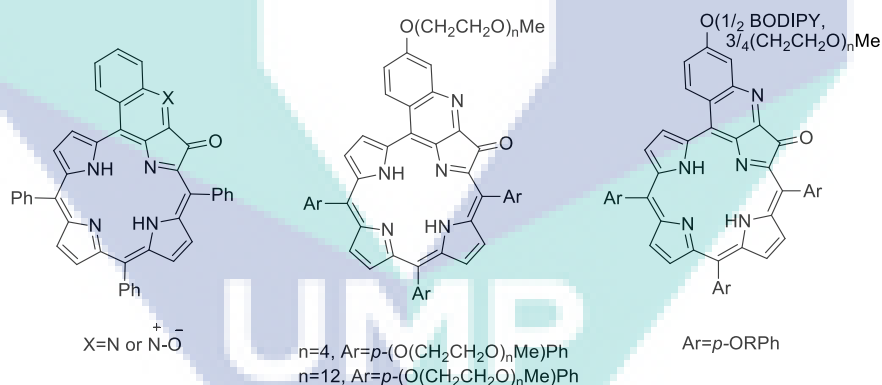


Figure 2.42 Structures of quinoline-annulated porphyrin derivatives employed as PAI contrast agents

So far, dedicated efforts to develop common metalloporphyrins such as Zn(II)porphyrins as a contrast agent by tailoring their absorption spectra have not been undertaken. Besides, correlation between structure and optoelectronic properties to PA signal has also not been undertaken. Although, only few of the literature maps the optical properties of porphyrins as NIR molecular photoacoustic contrast agent, the studies on vibrational IR absorption of porphyrins in combination with optical absorption has not been reported yet to the best of our knowledge.

2.8 Conclusions

Porphyrins represent a molecular system offering diverse properties which could be modified by appropriate molecular engineering. Intense research on porphyrins spanning over a century have developed many viable synthetic methodologies to produce them such that attempts can be made to develop a specially designed porphyrin for a potential new application. Such is the case of photoacoustic imaging – which is an emerging biomolecule imaging technique adopting a “light-in” and “sound-out” strategy. Successful photoacoustic imaging requires a contrast agent having high absorption cross-section and low light emission characteristics. Many micro- or nano- scale materials and organic molecules, have been examined as contrast agents; however, the micro- and nano-scale material systems impose severe restrictions on clinical use due to toxicity and metabolism and the organic molecules suffers from poor photoacoustic coefficients. Among the tested organic molecules, porphyrins are particularly interesting due to their high optical absorption, stability, and biocompatibility, long lifetimes and can be used for lifetime-based photoacoustic imaging to probe the molecular environment surrounding a sample. This survey of literature shows that there is no dedicated effort to develop metalloporphyrins, such as Zn(II)porphyrins, as contrast agents; it is hypothesized that they would be better contrast agents than pure porphyrins as they could additionally contribute to optical nonlinearity and widen absorption wavelength window. In addition, the development of new photoacoustic molecules is limited because the factors influencing the photoacoustic effect have rarely been systematically studied, resulting in a lack of guidance for the design of molecular photoacoustic contrast agents. Besides, a correlation between structure and optoelectronic properties to photoacoustic signal has also not been established. Therefore, there is a dire need for a general design criterion for an organic molecule to show photoacoustic characteristics; porphyrin molecules would provide one of the ideal model systems to test the corresponding properties.

CHAPTER 3

MATERIALS AND METHODS

3.1 Introduction

This chapter explains the methodology adopted in this course of research and structural characteristics of the materials thereby developed. The methodology has three parts: the first part is the design of new porphyrin molecules by using DFT calculations such that they have broader absorption spectra as well as high vibrational absorption of C-H bonds; the second part is the synthesis of four representative molecules identified from the calculations; the third part is the application of the new molecules in photoacoustic imaging. The criteria of molecular design by the quantum chemical calculations, synthetic details of the four representative molecules, and the structural characteristics of the synthesized molecules are also described in detail in this chapter.

3.2 Research Methodology

The flow chart of the research methodology adopted in this dissertation is shown in the Figure 3.1. Initially, porphyrins were modelled by modification of basic porphine core using various π -conjugated functional groups through DFT methods and calculated their absorption spectra and vibrational IR spectra. Gaussian 9W program package (Gaussian09, 2009) were used for designing new porphyrin molecules in this work. Details of the design criteria is in the next sections. More than fifty porphyrin molecules were simulated. However, only four representative molecules belong to a series named as RJ-C_n-MY_m, where $n = 12$ or 8 and $m = 1 - 4$, showing broader spectra were selected to be synthesized and were then characterized by NMR (¹HNMR and ¹³CNMR), HRMS, FTIR, UV-Vis and TGA. These

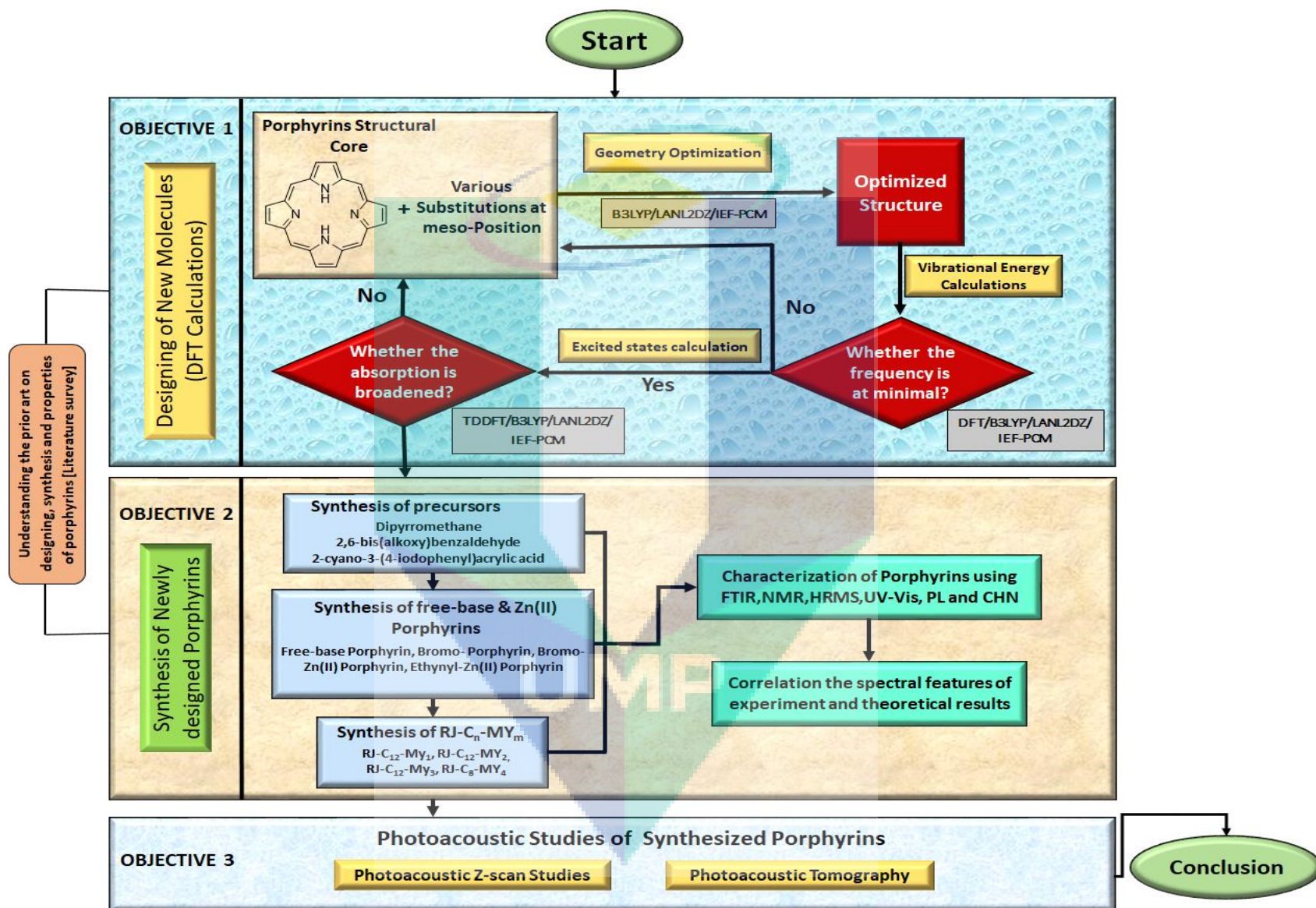


Figure 3.1 The flow chart of general research methodology

four molecules were selected on the basis of their systematic increase in π -conjugation and the electron withdrawing abilities of the substituents on porphyrin core. The Zn(II)porphyrin molecules were chosen in this work because the Zn metal have the closed-shell valence electrons (d^{10}) orbital, therefore, does not affect the geometry of porphyrin core more. The phenyl groups in the 10, 20-meso- positions were linked through ethynyl group to increase π -conjugation and the ones at the 5, 15-meso-positions were anchored with a long alkyl chain to avoid aggregation as well as to improve the stability of the molecule. However, two electron withdrawing functional groups, one carboxylic and the other 2-carboxy-2-cyanoethenyl group, were then attached at the *meta*- and *para*- positions of the meso-substituted phenyl groups symmetrically and unsymmetrically in order to observed the electronegativity effect on their properties. Finally, the application of the newly synthesized porphyrin molecules in photoacoustic imaging were explored.

3.3 Materials and Chemicals

All the quantum chemical simulations were done by using Gaussian 9W software installed in the windows computers having 64-bit version with intel core i5 CPU processor and 4GB RAM capacity for small molecules calculations. However, Linux operating system of supercomputer (HPC) was used for complex molecules calculations. The structural models were designed by either using Z-matrix or Gauss view software (Frisch, Keith & Dennington, 2003).

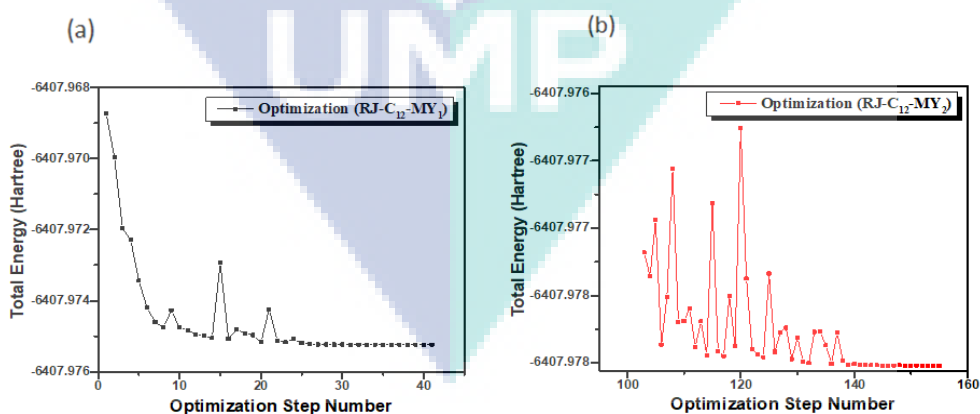
For synthesis, all the reactions were carried out under a nitrogen atmosphere by using Schlenk-tube apparatus. All glass wares were oven-dried at about 100°C prior to use. All the solvents were analytical grades and were purchased from commercial sources. All the solvents were dried and double distilled from appropriate drying agents. All reagents and chemicals were purchased from commercial sources and used without further purification, unless otherwise stated. Pyrrole was fractional distilled prior to use. Tetra-n-butylammonium fluoride (TBAF) was recrystallized twice from absolute ethanol and further dried for two days under vacuum. Thin-Layer Chromatograph (TLC) was performed with Merck pre-coated TLC silica gel 60 F254 aluminum sheets, visualizing with UV light where required. Flash column chromatography and preparative TLC were performed using Silica gel 60 from Merck (0.02-0.06 mm).

3.4 Design of Porphyrins by DFT Calculation

The initial requirement for quantum chemical simulation of a material is a knowledge on the atomic arrangement in it. i.e., developing a structural model is the first step, which can be done either using Z-matrix or simulation using a graphical user interface (GUI). In the Z-matrix, the atoms are specified according to their bond length, bond angle, and dihedral angle with reference to a reference atom(s). The GUI used in this work is Gauss view (Frisch et al., 2003).

3.4.1 Molecular Geometry Optimization

The properties of a molecule are calculated from its stable minimum energy structure, but a molecular structure produced from computational software may have higher energy than its stable structure. Therefore, geometry optimization is applied for energy minimization and to generate a stable minimum energy structure. Geometry optimization is a numerical approach to obtain minimum potential energy surface starting with high energy structure – which is an iterative minimization technique where the program modifies the atomic coordinates of a predefined structure and again calculate the energy. The iterative minimization process is repeated until the final step where the global minimum potential energy surface is reached. Figure 3.2 shows the representative graphs of four compounds (RJ-C₁₂-MY₁, RJ-C₁₂-MY₂, RJ-C₁₂-MY₃ and RJ-C₈-MY₄) showing the variation of energy with number of iterations.



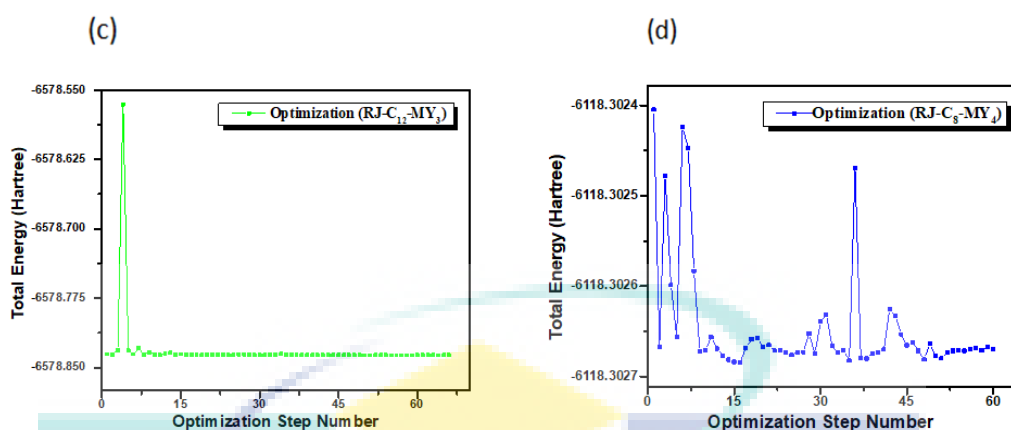


Figure 3.2 Geometry optimization steps for the global minimum energies a) compound RJ-C₁₂-MY₁; b) compound RJ-C₁₂-MY₂; c) compound RJ-C₁₂-MY₃; d) compound RJ-C₈-MY₄

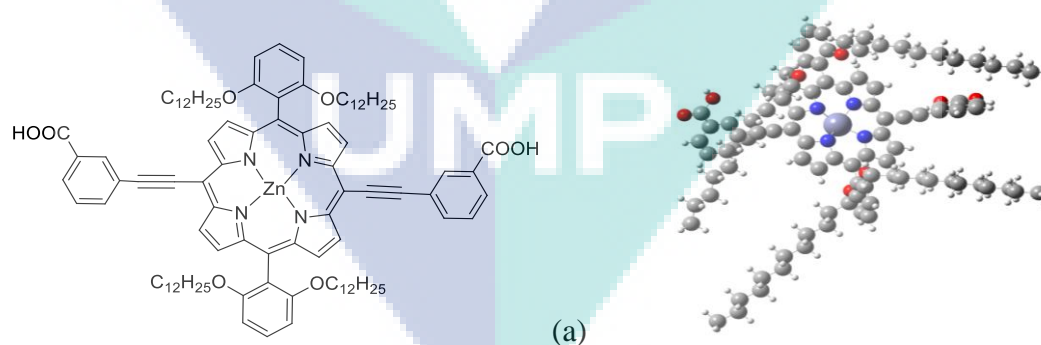
The parameters that were used in geometry optimization calculations are listed in Table 3.1. Geometry optimizations were accomplished using density functional theory employing two choices of hybrid functional, viz. B3LYP (Lee, Yang & Parr, 1988a) and CAM-B3LYP (Yanai et al., 2004), and basic sets 3-21G (Pietro et al., 1982), 6-31G(d) (Hariharan & Pople, 1973; Hehre, Ditchfield & Pople, 1972) and LANL2DZ (Hay & Wadt, 1985a; Hay & Wadt, 1985b). Representative screen shot of a calculation is given in the Appendix C. Typically, the molecules are optimized at the B3LYP/3-21G, B3LYP/6-31G, B3LYP/6-31G(d), B3LYP/LANL2DZ, CAMB3LYP/3-21G, CAMB3LYP/6-31G, and CAMB3LYP/LANL2DZ levels of the DFT. In the above notation, the parameter before the “/” is the method, which define mathematical function explaining the electron correlation and exchange and the one after the “/” is the basis set, which is a file containing electronic and nuclear wave functions of an atom under consideration. It is notable that the theoretical and experimental data are well fitted by using B3LYP/LANL2DZ level of theory. All the molecules were optimized in two solvents, viz., methanol (CH₃OH) and dichloromethane (DCM) to best fit with absorption spectroscopic experiments. These effects were taken into account using a self-consistent reaction field (SCRF) model (Marten et al., 1996; Tapia & Goscinski, 1975). Within the different approaches used, the integral equation formalism of the polarizable continuum model (IEF-PCM) (Tomasi, Mennucci & Cammi, 2005) have been employed in which the solvent used as a polarizable continuum rather than an individual molecule.

Table 3.1 Approaches used to optimize the porphyrin molecules

Optimization	
Calculation Type	Geometrical optimization
Method	B3LYP, CAM-B3LYP
Basis sets	3-21G, 6-31G, 6-31G(d), LanL2dz
Spin	Singlet
Charge	Zero
SCRF	IEF-PCM= THF, CH ₃ OH, DCM

3.4.2 Molecular Structures and Nomenclatures

Porphine (parent molecule) is the preliminary porphyrins core to study several porphyrins molecules. To compute the effect of substituent on optical properties, various substituents at meso-position are added. The molecules considered in this study are classified into three sets, viz. mono, di, and tetra meso-substituted porphyrins. Structure and nomenclature of the porphyrins studied in this research are in Appendix D. Among them, four molecules were chosen to be synthesized because of their broader absorption wavelength window and high vibrational IR absorption at C-H bonds region, which are shown in Figure 3.3 along with their IUPAC names.



[5,15-bis(3,5-di-dodecyloxyphenyl)-10,20-bis[(3-carboxylphenyl)ethynyl]porphyrinato] Zn(II)

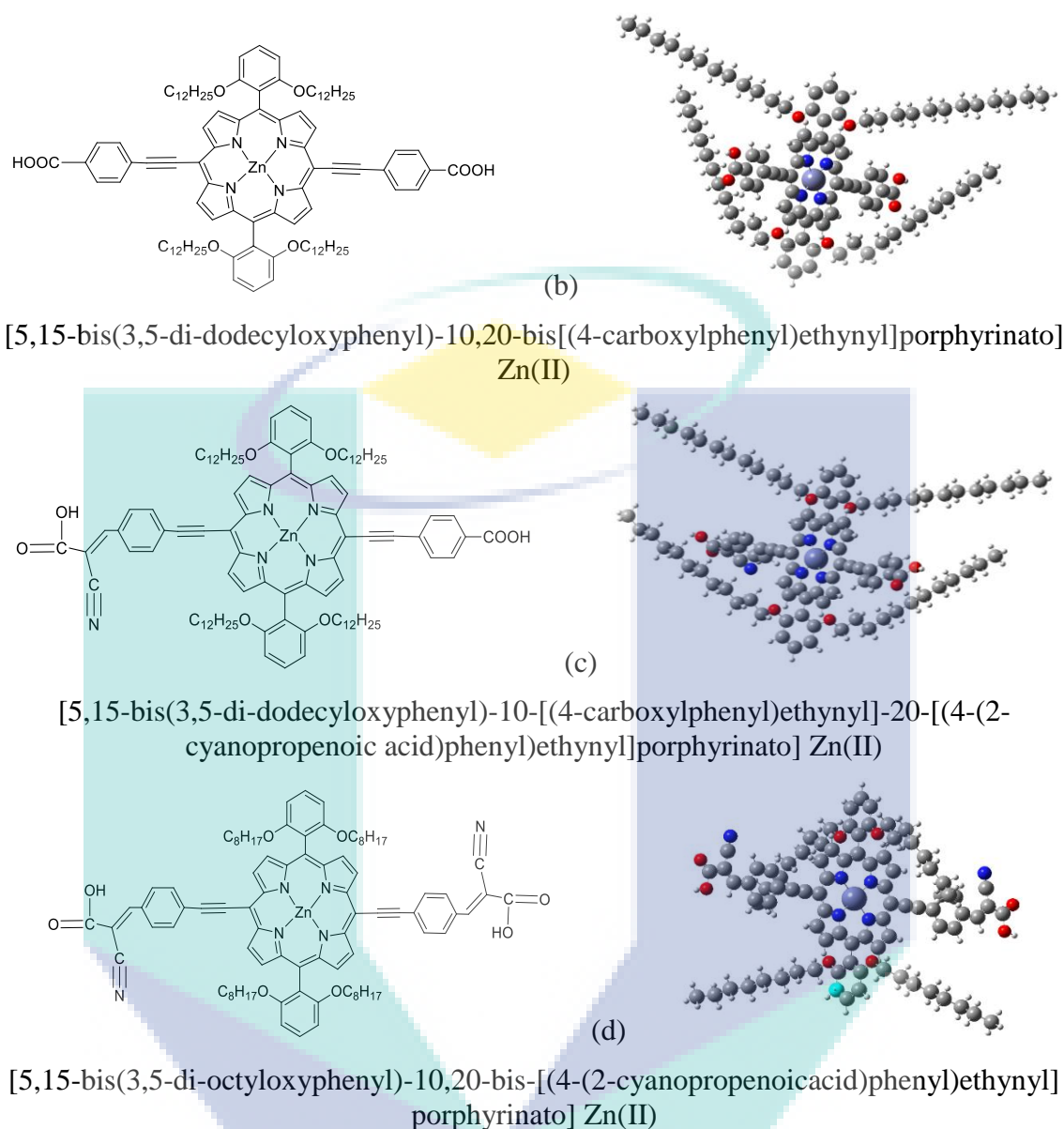
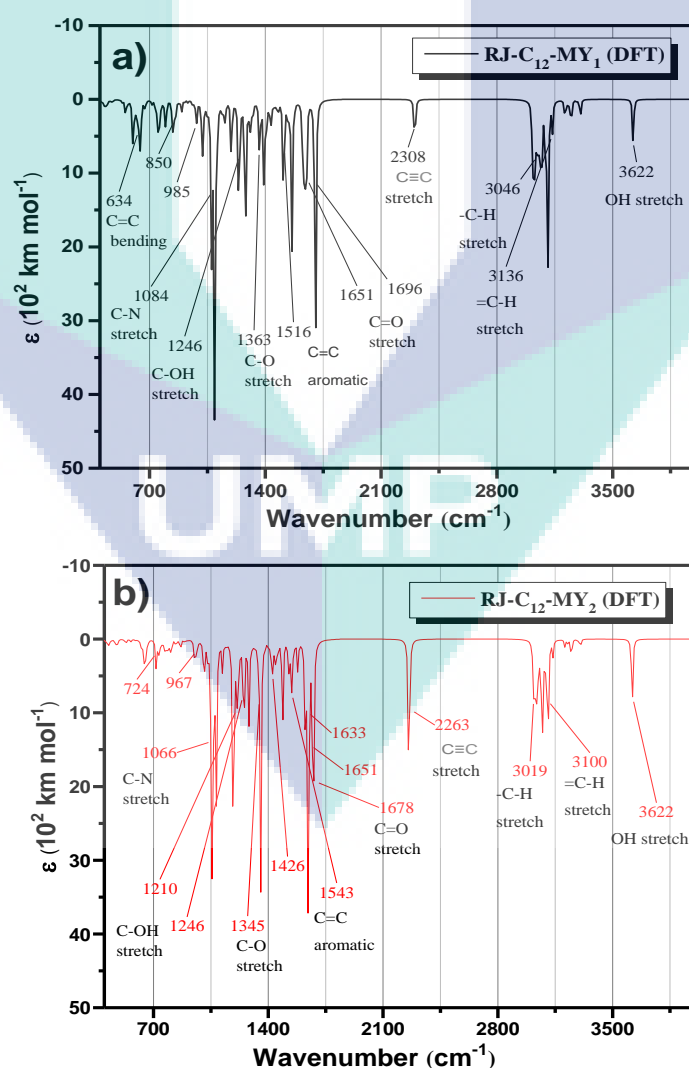


Figure 3.3 Structures and IUPAC naming of porphyrin molecules. The left panel shows planer ChemDraw sketch and right panel are the computed geometry developed using Gauss View. a) compound RJ-C₁₂-MY₁; b) compound RJ-C₁₂-MY₂; c) compound RJ-C₁₂-MY₃; d) compound RJ-C₈-MY₄

3.4.3 Frequency and Vibrational Energy Calculations

Upon completion of geometry optimization, it is vital to examine whether or not the optimized geometry is with a global minimum energy structure. This is because the iterative minimization technique can lead to a “false” minimum energy point (synonymously “local” minimum) where the optimization program accidentally falls into the convergence criteria – that the forces on the atoms are at a certain minimum value such that its first derivative is zero (Scales, 1985; Schlegel, 1989). Computational

chemistry routinely employs harmonic frequency calculations to determine whether or not the optimized geometry is at a global minimum energy structure – the frequencies are real (positive) for a global minimum energy; and observe imaginary frequencies (negative) in the case of fall minimum. Therefore, the acceptability of the geometry of all studied porphyrin molecules were verified by determining vibrational frequencies by calculating their IR spectra at the same levels of the theory as displayed in Table 3.1. However, the primary purpose for vibrational energy calculations was to study the effect of various vibrational modes on photoacoustic properties of porphyrin molecules by substituting the meso-position with various π -conjugated functional groups. As per consideration, the high frequency vibrational modes could be the source of non-radiative decays through thermalization by absorption of high energy quanta (photons) causing the excitation of electrons from $v=0$ to $v=n$ vibrational energy levels (where $n=2,3,4,\dots$). Representative IR spectra and source of the vibrations are shown in Figure 3.4.



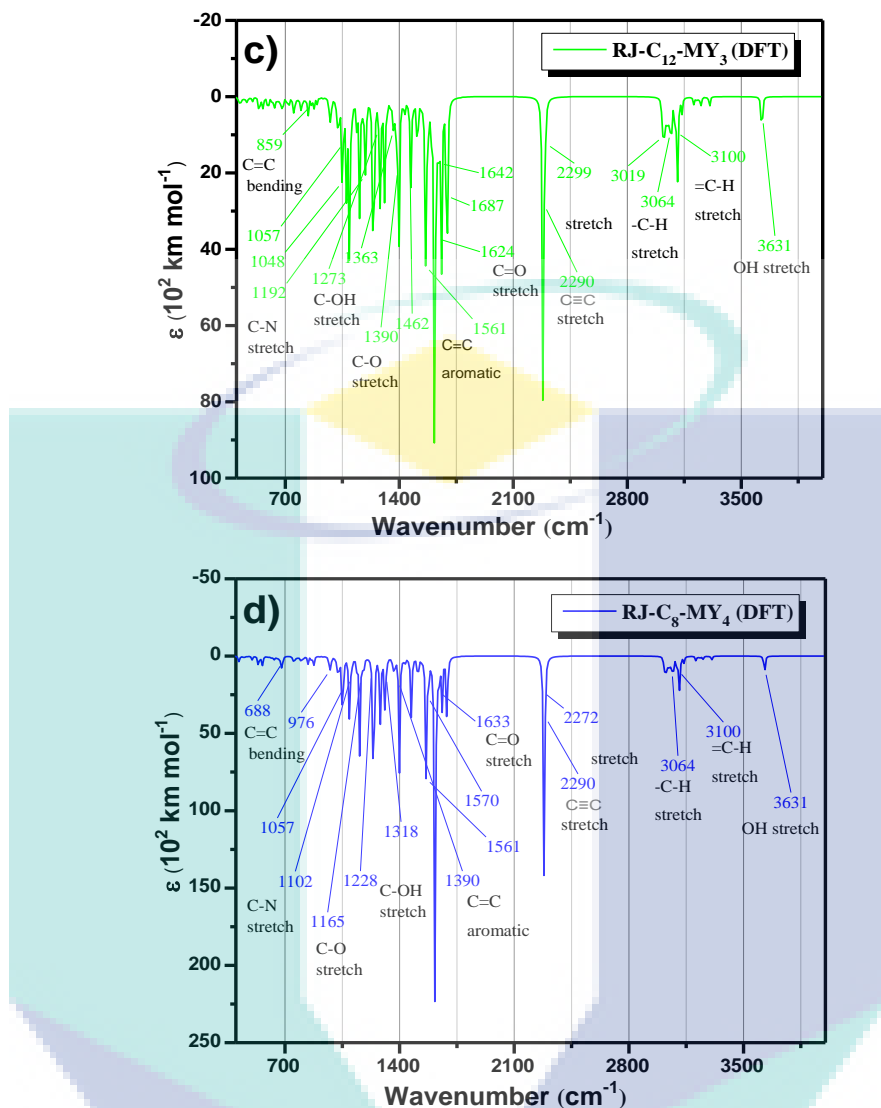


Figure 3.4 IR spectra for a) compound RJ-C₁₂-MY₁; b) compound RJ-C₁₂-MY₂; c) compound RJ-C₁₂-MY₃; d) compound RJ-C₈-MY₄

3.4.4 Excitation Energy Calculations

The absorption spectra of the four newly designed representative molecules were developed from the energy calculation carried out at linear response time-dependent DFT (LR-TDDFT) theory (Marques et al., 2012; Ullrich, 2011). This method calculates the discrete singlet excitation energies from the optimized geometries from where continuous absorption spectra of the molecules could be developed. All the energy calculations were done from ground state to singlet state excitation using IEF-PCM model (Tomasi et al., 2005) to study the effect of various solvents (THF, CH₃OH and DCM) on absorption spectra. It is notable that there is a slight change in absorption spectra of all studied molecules (See Appendix E) by changing the solvent. The bathochromic shift of almost

all absorption spectra are in order of DCM > CH₃OH > THF. However, the experimental absorption spectra of all synthesized compounds were measured in CH₃OH, therefore; the absorption spectra calculated in CH₃OH are more preferable for comparison with experimental data. At each singlet geometry, LR-TDDFT/IEF-PCM calculations were performed for the first 50 excited singlet states by using the same basis sets and functional those were used for geometry optimizations. The oscillator strengths of the singlet transition thereby obtained were used for simulating the absorption spectra. Singlet transitions and their oscillator strength of the four representative molecules are in the Figure 3.5. Since the computed absorption for light polarized perpendicular to the central ring found to be negligible, only the in-plane (x and y) components are considered. Note that vibrational coupling effects are not included in the present calculation and hence the Q_x(0,1) and Q_y(0,1) replicas, present in the experimental spectra, are always absent in the theoretical spectra.

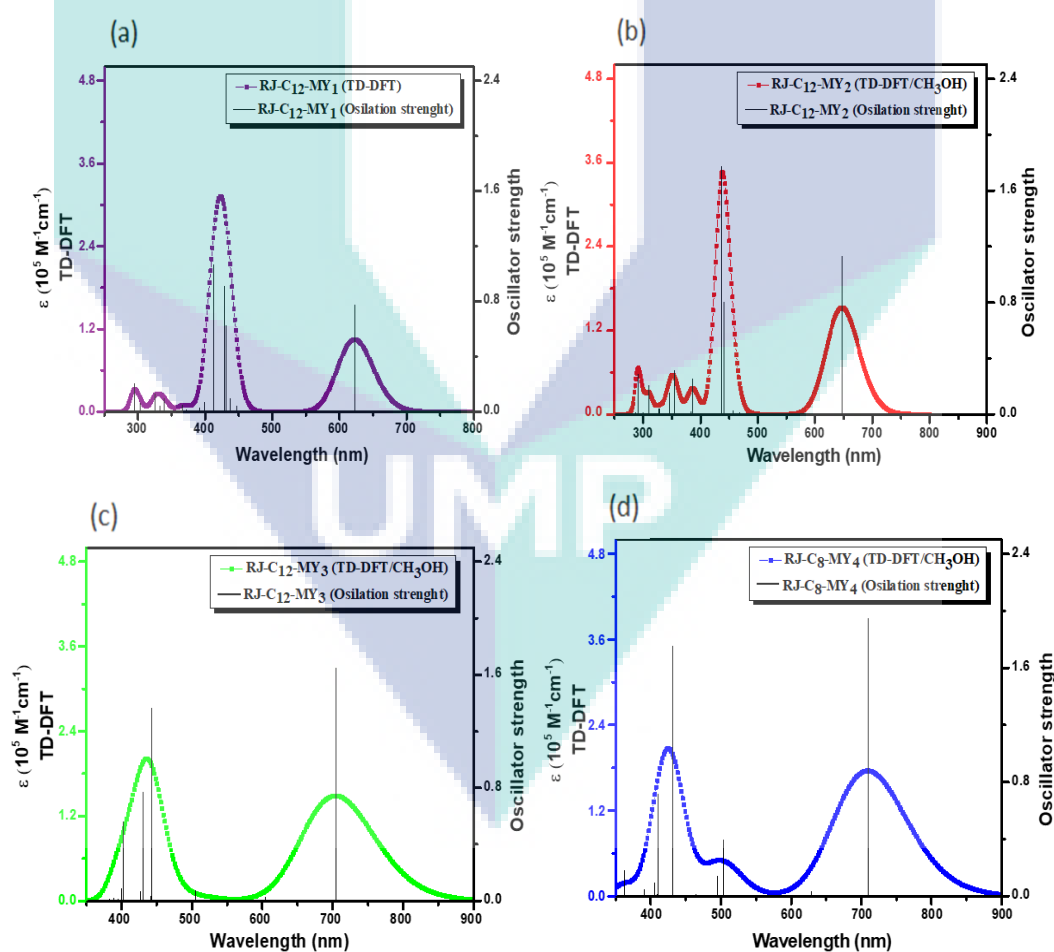


Figure 3.5 UV-Vis spectra for a) compound RJ-C₁₂-MY₁; b) compound RJ-C₁₂-MY₂; c) compound RJ-C₁₂-MY₃; d) compound RJ-C₈-MY₄

3.5 Synthesis of Newly Designed Zn(II)Porphyrins

The methodologies adopted for the synthesis of four representative porphyrin molecules are explained in Schemes 1-5.

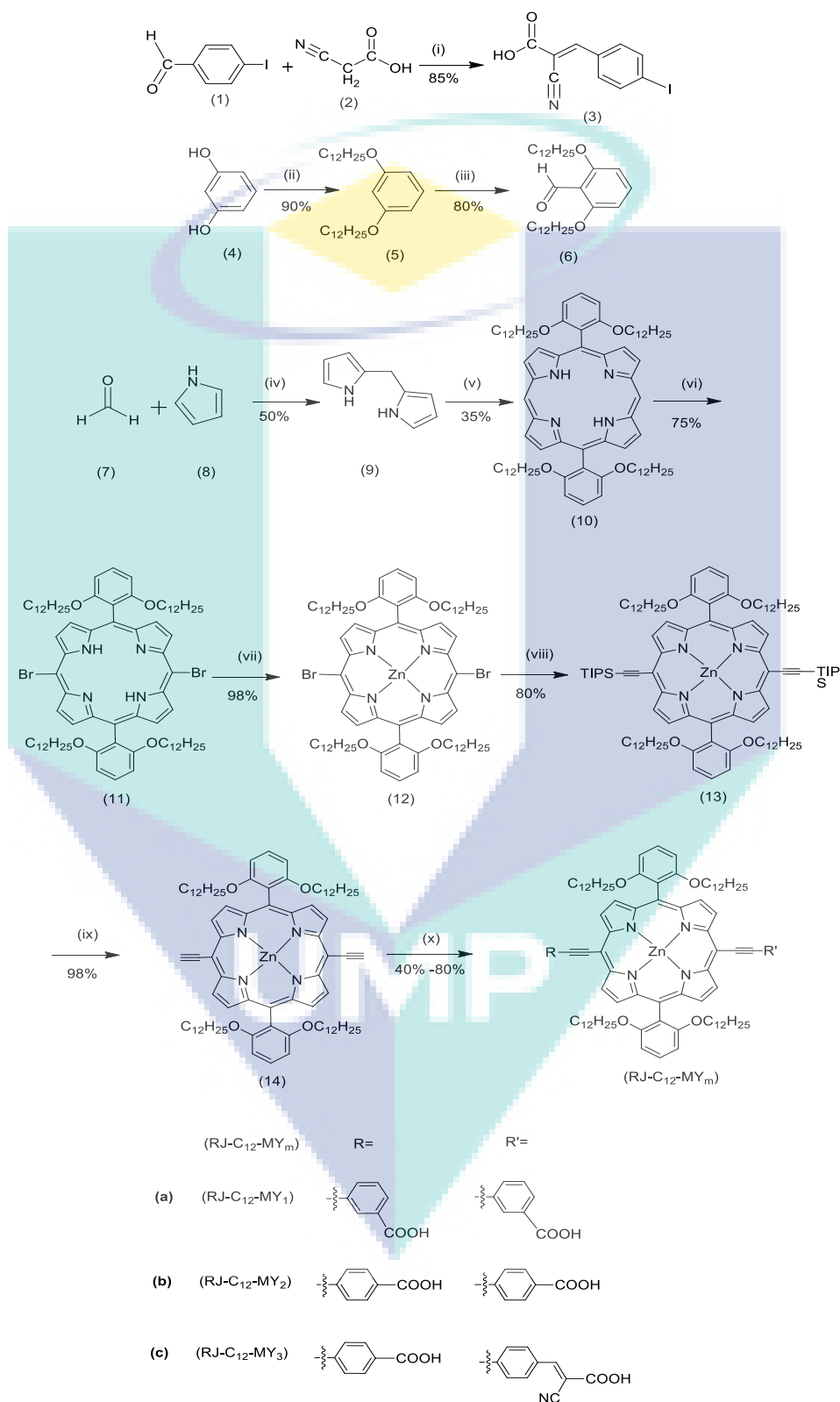
3.5.1 Instrumentation

NMR spectra (^1H & ^{13}C NMR) were recorded on a Bruker ultra-shield plus 500 (500 MHz) using tetramethylsilane as an internal standard. The coupling constants are calculated in Hz and chemical shifts (δ) in ppm. Multiplicities of peaks are denoted as: s= singlet, d= doublet, dd= double doublet, t= triplet and m= multiplet. IPC-TOF mass spectra were recorded on a Bruker BIFLEX III TOF mass spectrometer (Bruker Daltonics, Billerica, MA, USA). The absorption spectra in solution were obtained by UV-Vis NIR spectrophotometer UV-2600 SHIMADZU, Japan. All the spectra were measured by preparing fresh samples from 200 nm to 900 nm range. The steady state fluorescence and the corresponding excitation spectra were recorded on an Edinburgh Instruments FLS920 phosphorimeter equipped with single monochromators. Fluorescence lifetime measurements were made on a mode-locked Ti:sapphire laser (Coherent Mira 900) having a laser power output of 1.90W at 800 nm. Thermogravimetric analysis (TGA) measurements were performed on Mettler Toledo thermogravimetric analyzer, model Perkin-Elmer TGA/DSC 1, at $10^\circ\text{C min}^{-1}$ heating rate. FTIR data were measured on a PerkinElmer Spectrum using thin films KBr method. The photoacoustic measurements were conducted using the Nd:YAG laser (3 ns pulse width) at 532 nm and using OPO laser (3 ns pulse width) at 680 nm. For all the experiments performed at 532 nm, the porphyrin dyes were compared to ZnTPP as a reference. The PAZ-Scan experiments were conducted at 100 μJ laser energy and at 130 μJ laser energy on all the samples prepared in DMF absorbing 0.1 OD at 532 nm and at 680 nm in 2 mm quartz cuvettes. PAT experiments were carried out by using a doubled Nd:YAG laser, a transducer (Olympus V311-SU) and a pulse amplifier that is fed to a Lecroy Wavepro oscilloscope for display and data collection.

3.5.2 Synthesis of π -Conjugated Meso-Ethynyl-Zn(II)Porphyrins

The route for π -conjugated meso-ethynyl-Zn(II)porphyrins synthesis (RJ-C₁₂-MY_m, where m = 1 – 3) is shown in Figure 3.6. The scheme adopted for the synthesis

limits the ten step reactions. The method adopted for each step is explained below in detail.

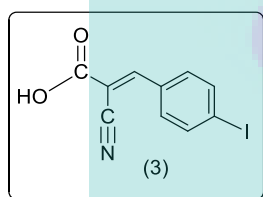


Reagents: (i) CH₃COOH, NH₄Ac reflux, overnight; (ii) C₁₂H₂₅Br, K₂CO₃, (CH₃)₂CO, reflux, 3 days; (iii) a) TMEDA, (C₂H₅)₂O, n-BuLi, N₂, 0 °C, 4 h; b) DMF, (C₂H₅)₂O, N₂, 2 h; (iv) a) TFA, N₂, 70 °C, 2 h; b)

0.4M NaOH, stirring, 30 min; (v) a) 6, TFA, DCM, N₂, 23 °C, 4 h; b) DDQ, stirring, 1 h; (vi) NBS, DCM, N₂, stirring, 6 h; (vii) Zn(OAc)₂·2H₂O, DCM, CH₃OH, 23 °C, 24 h; (viii) TIPS-acetylene, THF, CuI, Pd(PPh₃)₂Cl₂, NEt₃, N₂, 85 °C, 8 h; (ix) TBAF, THF, N₂, stirring, 2 h; (x) various substituted benzyl iodide, THF, NEt₃, Pd₂(dba)₃, AsPh₃, N₂, 85 °C, 6-8 h.

Figure 3.6 Synthetic schemes for a) compound RJ-C₁₂-MY₁; b) compound RJ-C₁₂-MY₂; c) compound RJ-C₁₂-MY₃

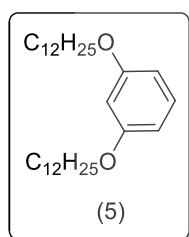
3.5.2.1 Synthesis of 2-cyano-3-(4-iodophenyl)acrylic Acid (3)



To a solution of ammonium acetate (22.00 mg, 0.28 mmol) in acetic acid (3.00 ml), 4-iodobenzaldehyde (200.00 mg, 0.86 mmol) and cyanoacetic acid (88.00 mg, 1.04 mmol) were added and the solution was refluxed overnight. The reaction mixture was allowed to cool at room temperature; the product was crystallized as off-white precipitate from the solution. The precipitate was washed with distilled water and then recrystallized from Hexane and DCM (1:1 v/v) to yield compound 3 as off-white solid (219.1 mg, 85% yield).

¹H NMR (CD₃OH, 500 MHz): δ 8.25 (s, 1H), 7.93 (d, J = 8.55 Hz, 2H), 7.76 (d, J = 8.55 Hz, 2H). ¹³C NMR (CD₃OH, 160 MHz): δ 164.66, 154.69, 139.76, 138.97, 133.08, 132.57, 132.26, 116.56, 105.66, 101.19.

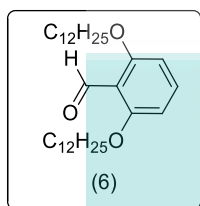
3.5.2.2 Synthesis of 1,3-di(dodecyloxy)benzene (5)



Compound 5 was synthesized by modified method of literature procedure (Mohr, Enkelmann & Wegner, 1994). In a mixture of resorcinol (5.00 g, 0.045 mol) and potassium carbonate (K₂CO₃) (31.10 g, 0.22 mol), 1-bromododecane (43.20 mL, 0.18 mol) was added and refluxed for 3 days in dry acetone (300 mL). The reaction was monitored by TLC. When all the reactants were consumed, the solvent was removed under reduced pressure. The residue was extracted with EtOAc (3 × 100 mL), washed with water and dried over anhydrous MgSO₄. The solvent was removed under reduced pressure and the product was purified by column chromatography eluting with pure n-Hexane giving the white colored product (18.27 g, 90% yield).

^1H NMR (CDCl_3 , 500 MHz): δ 7.15 (t, $J=8.15$ Hz, 1H), 6.48 (d, $J=2.35$ Hz, 1H), 6.46 (m, 2H), 3.92 (t, $J=6.65$ Hz, 4H), 1.78-1.72 (m, 4H), 1.43-1.42 (m, 4H), 1.33-1.26 (m, 32H), 0.89 (t, $J=7.1$ Hz, 6H). ^{13}C NMR (CDCl_3 , 160 MHz): δ 160.39, 129.72, 106.62, 101.44, 67.96, 31.97, 29.71, 29.68, 29.65, 29.63, 29.44, 29.40, 29.32, 26.10, 22.73, 14.15.

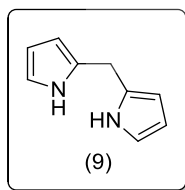
3.5.2.3 Synthesis of 2,6-bis(dodecyloxy)benzaldehyde (6)



Compound 6 was synthesized by modified method of literature procedure (Katritzky, He, Long & Wilcox, 2001). A solution of compound 5 (5.00 g, 11.21 mmol) and tetramethylethylenediamine (TMEDA) (0.33 mL, 2.24 mmol) in 100 mL of anhydrous ether was degassed with N_2 gas for 25 min using Schlenk-tube apparatus and cooled to 0 °C. A solution of *n*-butyllithium (8.4 mL, 2 M solution in hexanes, 16.80 mmol) was then added drop-wise over 2 h and allowed the mixture to stir for additional 2 h. The reaction mixture was warmed to room temperature for 30 min and then anhydrous dimethylformamide (DMF) (1.72 mL, 22.40 mmol) was added drop-wise. The reaction mixture was again stirred for an additional 2 h. After 2 h, the reaction mixture was quenched with water, and extracted with ether (3×80 mL), dried over anhydrous MgSO_4 . The solvent was removed under reduced pressure. The product was recrystallized from *n*-Hexane to yield a white solid (4.25 g, 80% yield).

^1H NMR (CDCl_3 , 500 MHz): δ 10.53 (s, 1H), 7.38 (t, $J=8.45$ Hz, 1H), 6.53 (d, $J=8.55$ Hz 2H), 4.03 (t, $J=6.5$ Hz, 4H), 1.84-1.79 (m, 4H), 1.49-1.43 (m, 4H), 1.34-1.26 (m, 32H), 0.89 (t, $J=7.1$ Hz, 6H). ^{13}C NMR (CDCl_3 , 160 MHz): δ 189.51, 161.85, 135.69, 114.93, 104.67, 69.11, 32.10, 29.84, 29.81, 29.78, 29.74, 29.53, 29.23, 26.16, 22.87, 14.30.

3.5.2.4 Synthesis of di(1H-pyrrol-2-yl)methane (9)



Method 1: Compound 9 was synthesized by previously reported procedure with modification (Littler et al., 1999). To the freshly distilled pyrrole (104.50 mL, 1.5 mol) in 500 mL flask shielded from light, was added paraformaldehyde (1.80 g, 0.06 mol by formaldehyde) and the solution was degassed for 15 minutes under N_2 . The solution was then heated at 70 °C to dissolve most of the solid. At this temperature, trifluoroacetic acid (TFA) (1.30

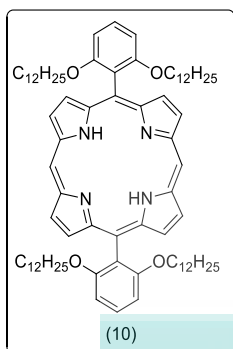
mL, 17.14 mmol) was added in one portion. The reaction mixture was stirred for 2 h until it became clear and dark. After cooling at room temperature, the mixture was quenched by addition of 10% NaOH (40 mL) solution and was stirred for additional 30 minutes. The reaction mixture was then extracted with DCM (3 × 30 mL). The combined organic layer was washed with water twice and dried over anhydrous MgSO₄. The solvent was removed under reduced pressure. Excess of pyrrole was distilled off by vacuum distillation. The remaining crude product was purified by silica gel column chromatography with DCM: Hexane (2:1 v/v) as eluent to afford the off-white product (4.38 g, 50% yield).

¹H NMR (CDCl₃, 500 MHz): δ=7.69 (s, 2H), 6.59 (q, 2.7 Hz, 2H), 6.14 (q, 2.75 Hz, 2H), 6.02 (br s, 2H), 3.91 (s, 2H). ¹³C NMR (CDCl₃, 160 MHz): δ = 129.14, 117.37, 108.33, 106.47, 26.36.

Method 2: TFA (1.30 mL, 0.017 mol) was added in a mixture of freshly distilled pyrrole (20.80 mL, 0.3 mol) and paraformaldehyde (1.74 g, 0.06 mol by formaldehyde) dissolved in dry methanol (100 mL). The reaction mixture was stirred for 5 h at 70 °C under inert environment. After cooling at room temperature, the mixture was quenched by addition of 10% NaOH (40 mL) solution and was stirred for additional 30 minutes. The reaction mixture was then extracted with DCM (3 × 30 mL). The combined organic layer was washed with water twice and dried over anhydrous MgSO₄. The solvent was removed under reduced pressure. The crude product was purified by silica gel column chromatography with DCM: Hexane (2:1 v/v) as eluent to afford the off-white product. Yield: (2.5 g, 28.5% yield).

¹H NMR (CDCl₃, 500 MHz): δ=7.69 (s, 2H), 6.59 (q, 2.7 Hz, 2H), 6.14 (q, 2.75 Hz, 2H), 6.02 (br s, 2H), 3.91 (s, 2H). ¹³C NMR (CDCl₃, 160 MHz): δ = 129.14, 117.37, 108.33, 106.47, 26.36.

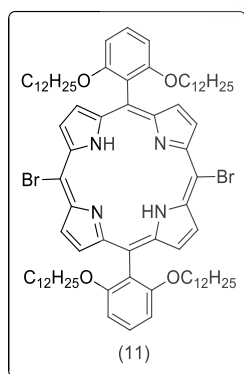
3.5.2.5 Synthesis of 5,15-bis(2,6-di(dodecyloxy)phenyl)porphyrin (10)



A solution of compound 9 (5 g, 34.24 mmol) and compound 6 (16.23 g, 34.24 mmol) in anhydrous DCM (1 L) was degassed with N₂ for 15 minutes and was added TFA (2.38 mL, 31.13 mmol). The reaction mixture was stirred under N₂ for 4 h. DDQ (11.66 g, 51.36 mmol) was added in the reaction mixture and was stirred for additional 1 h. The reaction mixture was then basified with triethylamine (NEt₃) (7 mL) and filtered through silica. The solvent was removed under reduced pressure. The remaining crude product was purified by column chromatography (silica gel) using DCM: Hexane (1:2 v/v) as an eluent. The product was recrystallized from MeOH/DCM to give the purple colored product (14.36 g, 35% yield).

¹HNMR (CDCl₃, 500 MHz): δ 10.13 (s, 2H), 9.25 (d, J=4.5 Hz, 4H), 8.97 (d, J=4.55 Hz, 4H), 7.71 (t, J=8.45 Hz, 2H), 7.02 (d, J=8.5 Hz, 4H), 3.83 (t, J=6.6 Hz, 8H), 1.27-1.21 (m, 8H), 1.17-1.09 (m, 16H), 1.01-0.98 (m, 8H), 0.92-0.83 (m, 28H), 0.72-0.69 (m, 8H), 0.56-0.53 (m, 16H), 0.45-0.42 (m, 8H), -3.02(s, 2H). ¹³CNMR (CDCl₃, 160 MHz): δ 160.12, 157.69, 130.77, 130.40, 129.96, 119.95, 111.50, 105.28, 103.89, 68.66, 31.90, 29.49, 29.42, 29.30, 29.19, 29.05, 28.68, 28.58, 25.27, 22.69, 14.13.

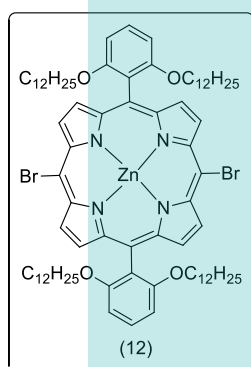
3.5.2.6 Synthesis of 5,15-bisbromo-10,20-bis(2,6-di(dodecyloxy)phenyl)porphyrin (11)



A solution of NBS (1.48 g, 8.35 mmol) in anhydrous DCM (200 mL) was slowly added to a stirred solution of compound 10 (5.00 g, 4.17 mmol) in anhydrous DCM (1000 mL) for 4 h at 0 °C under N₂ gas. The reaction mixture was further stirred for 2 h more at room temperature. After that, the reaction mixture was quenched with acetone (30 mL) and the solvent was removed under reduced pressure. The crude product was purified by column chromatography (silica gel) using DCM: Hexane (0.5:2 v/v) as an eluent. Recrystallization by MeOH/DCM gave the final product as a purple solid. (4.25 g, 75% yield).

^1H NMR (CDCl_3 , 500 MHz): δ 9.50 (d, $J=4.75$ Hz, 4H), 8.78 (d, $J=4.9$ Hz, 4H), 7.69 (t, $J=8.55$ Hz, 2H), 6.98 (d, $J=8.5$ Hz, 4H), 3.84 (t, $J=6.5$ Hz, 8H), 1.23-1.19 (m, 8H), 1.14-1.05 (m, 16H), 0.97-0.91 (m, 12H), 0.86-0.80 (m, 24H), 0.67-0.64 (m, 8H), 0.54-0.48 (m, 16H), 0.42-0.39 (m, 8H), -2.59(s, 2H). ^{13}C NMR (CDCl_3 , 160 MHz): δ 159.94, 153.07, 139.33, 137.79, 130.24, 123.60, 119.90, 105.03, 102.24, 68.60, 31.87, 29.72, 29.46, 29.37, 29.29, 29.20, 29.04, 28.70, 28.57, 25.31, 22.69, 14.14.

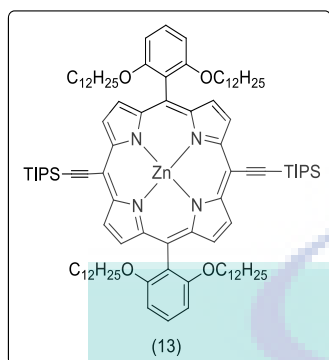
3.5.2.7 Synthesis of [5,15-bisbromo-10,20-bis(2,6-di(dodecyloxy)phenyl)porphyrinato]zinc(II) (12)



A solution of compound 11 (4.00 g, 2.95 mmol) and $\text{Zn}(\text{OAc})_2 \cdot 2\text{H}_2\text{O}$ (3.88 g, 17.70 mmol) in anhydrous DCM (400 mL) and anhydrous MeOH (200 mL) was stirred at room temperature for 24 h. The reaction mixture was quenched with water (100 mL) and was extracted with DCM (2×100 mL). The combined organic layers were washed with water and dried over anhydrous MgSO_4 . The solvent was removed under reduce pressure. The crude product was purified by column chromatography (silica gel) using DCM: Hexane (1:2 v/v) as an eluent. Recrystallization by MeOH/DCM gave the final product as a purple solid (4.11 g, 98% yield).

^1H NMR (CDCl_3 , 500 MHz): δ 9.62 (d, $J=4.65$ Hz, 4H), 8.88 (d, $J=4.65$ Hz, 4H), 7.69 (t, $J=8.55$ Hz, 2H), 6.99 (d, $J=8.7$ Hz, 4H), 3.84 (t, $J=6.5$ Hz, 8H), 1.22-1.19 (m, 8H), 1.13-1.04 (m, 10H), 0.95-0.90 (m, 20H), 0.84-0.78 (m, 22H), 0.62-0.59 (m, 8H), 0.51-0.42 (m, 16H), 0.35-0.32 (m, 8H). ^{13}C NMR (CDCl_3 , 160 MHz): δ 159.90, 151.36, 149.67, 132.79, 132.76, 129.99, 120.67, 114.89, 105.15, 103.91, 68.58, 31.87, 29.45, 29.34, 29.28, 29.20, 29.04, 28.67, 28.57, 25.23, 22.69, 14.14.

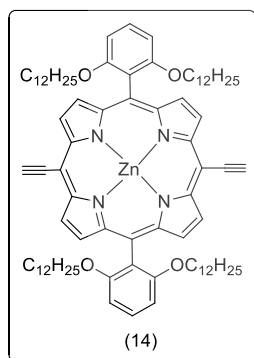
3.5.2.8 Synthesis of [5,15-bis(2,6-di(dodecyloxy)phenyl)-10,20-bis(triisopropylsilyl)ethynyl]porphinato]zinc(II) (13)



To a degassed solution of compound 12 (1.50 g, 1.06 mmol), triisopropylsilyl-acetylene (0.60 mL, 2.65 mmol) and copper iodide (CuI) (0.057 g, 0.30 mmol) in anhydrous THF (20 mL) was added NEt₃ (9 mL) under N₂ gas flow. Bis(triphenylphosphine)palladium(II)chloride (Pd(PPh₃)₂Cl₂) (0.15 g, 0.21 mmol) was added to the solution and was stirred at 85 °C for 8 h under N₂. The reaction mixture was cooled at room temperature and the solvent was removed under vacuum. The crude product was purified by column chromatography (silica gel) using DCM: Hexane (1:2 v/v) as an eluent to give the product as a purple solid (1.37 g, 80% yield).

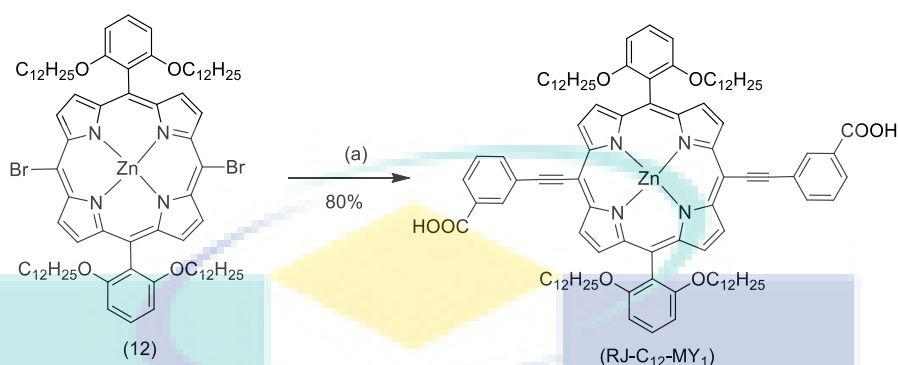
¹HNMR (CDCl₃, 500 MHz): δ 9.66 (d, J=4.55 Hz, 4H), 8.86 (d, J=4.45 Hz, 4H), 7.67 (t, J=8.55 Hz, 2H), 6.98 (d, J=8.5 Hz, 4H), 3.82 (t, J=6.4 Hz, 8H), 1.46-1.39 (m, 42H), 1.18-1.13 (m, 8H), 1.08-0.97 (m, 16H), 0.95-0.90 (m, 10H), 0.88-0.82 (m, 8H), 0.81-0.70 (m, 26H), 0.57-0.46 (m, 16H), 0.41-0.34 (m, 8H). ¹³CNMR (CDCl₃, 160 MHz): δ 159.93, 152.06, 150.68, 131.94, 130.90, 129.82, 120.94, 115.25, 109.85, 105.34, 100.49, 96.82, 68.76, 31.86, 29.46, 29.26, 29.25, 29.16, 28.96, 28.63, 28.59, 25.21, 22.68, 19.14, 14.13, 11.95.

3.5.2.9 Synthesis of [5,15-bis(2,6-di(dodecyloxy)phenyl)-10,20-bis(ethynyl)porphinato]zinc (II) (14)



To a degassed solution of compound 13 (200.00 mg, 0.12 mmol) in anhydrous THF (30 mL) was added TBAF (1.23 mL, 1M in THF, 1.23 mmol). The solution was stirred at room temperature for 2 h and was quenched with H₂O. The mixture was then extracted with DCM (3 × 30 mL) and combined organic layer was dried over anhydrous MgSO₄. The solvent was removed under reduced pressure. The residue of compound 13 was used as such without further purification for the synthesis of RJ-C₁₂-MY₂ and RJ-C₁₂-MY₃ complexes (158.2 mg, 98% yield).

3.5.2.10 Synthesis of [5,15-bis(2,6-di(dodecyloxy)phenyl)-10,20-bis(3-carboxyl-phenyl)ethynyl]porphinato]zinc(II) (RJ-C₁₂-MY₁)

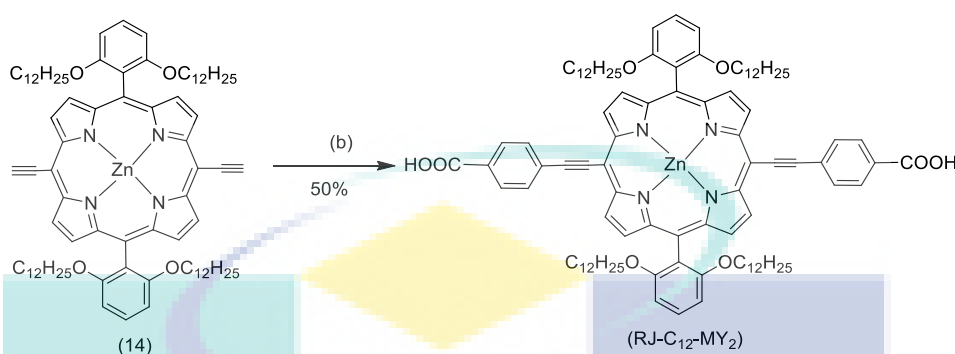


Scheme 3.2 Reagents: (a) 3-ethynyl benzoic acid, THF, CuI, Pd(PPh₃)₂Cl₂, NEt₃, N₂, 85 °C, 8 h

To a degassed solution of compound 12 (100.00 mg, 0.071 mmol), 3-ethynyl benzoic acid (41.50 mg, 0.284 mmol) and CuI (3.86 mg, 0.020 mmol) in anhydrous THF (10 mL) was added NEt₃ (1 mL) under N₂ gas flow. Pd(PPh₃)₂Cl₂ (9.96 mg, 0.014 mmol) was added to the solution and was stirred at 85 °C for 8 h under N₂. The reaction mixture was cooled at room temperature and the solvent was removed under vacuum. The crude product was purified by column chromatography (silica gel) using DCM: MeOH (1:5 v/v) as an eluent. Further purification was done by pre-TLC method to get the pure compound. Recrystallization from MeOH to give final product (87.3 mg, 80%) as a green solid.

¹HNMR (CD₃OH, 500 MHz): δ 9.42 (d, J=4.4 Hz, 4H), 8.52 (d, J=4.5 Hz, 4H), 8.44 (s, 2H), 7.85 (q, J=7.6 Hz, 4H), 7.52 (t, J=8.55 Hz, 2H), 7.35 (t, J=7.5 Hz, 2H), 6.86 (d, J=8.55 Hz, 4H), 3.67 (t, J=5.9 Hz, 8H), 1.10-1.04 (m, 16H), 0.95-0.87 (m, 8H), 0.83-0.77 (m, 8H), 0.73-0.65 (m, 24H), 0.60-0.56 (m, 20H), 0.52-.049 (m, 8H), 0.38-0.32 (m, 8H). ¹³CNMR (CD₃OH, 160 MHz): δ 173.16, 159.94, 151.53, 150.55, 132.49, 131.23, 129.92, 128.62, 127.78, 114.83, 105.22, 99.59, 93.40, 68.42, 31.61, 30.60, 29.38, 29.13, 29.05, 29.03, 28.83, 28.69, 28.56, 28.47, 25.19, 22.35, 20.24, 13.12, 9.91

3.5.2.11 Synthesis of [5,15-bis(2,6-di(dodecyloxy)phenyl)-10,20-bis(4-carboxyl phenyl)ethynyl]porphyrinato]zinc(II) (RJ-C₁₂-MY₂)

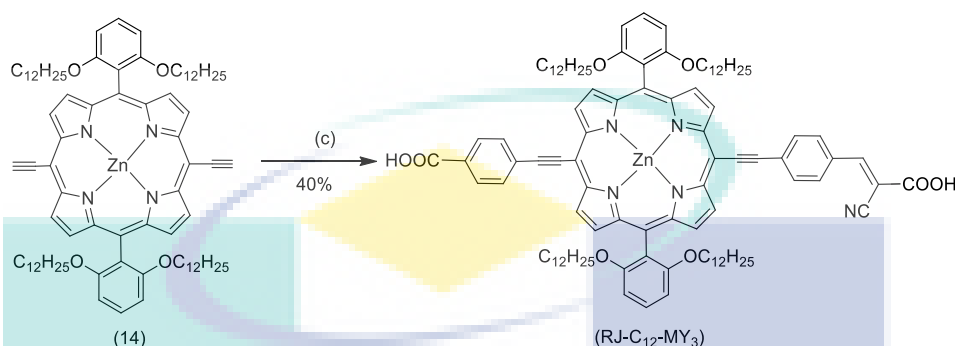


Scheme 3.3 Reagents: (b) 4-iodobenzoic acid, THF, NEt₃, Pd₂(dba)₃, AsPh₃, N₂, 85 °C, 6 h

To a degassed solution of compound 14 (100.00 mg, 0.076 mmol) and 4-iodobenzoic acid (56.54 mg, 0.23 mmol) in anhydrous THF (10 mL) was added NEt₃ (1 mL) under N₂ gas flow. Tris(dibenzylideneacetone)dipalladium(0) (Pd₂(dba)₃) (17.39 mg, 0.019 mmol) and triphenylarsine (AsPh₃) (46.54 mg, 0.15 mmol) were added to the mixture and was stirred at 85 °C for 6 h under N₂. The reaction mixture was cooled at room temperature and the solvent was removed under vacuum. The crude product was purified by column chromatography (silica gel) using DCM: MeOH (1:5 v/v) as an eluent. Further purification was done by pre-TLC method to get the pure compound. Recrystallization from MeOH to give final product (59.16 mg, 50%) as a green solid.

¹HNMR (CD₃OH, 500 MHz): δ 9.51 (d, J=4.5 Hz, 4H), 8.63 (d, J=4.5 Hz, 4H), 8.08 (d, J=8.45 Hz, 4H), 7.90 (d, J=8.45 Hz, 4H), 7.60 (t, J=8.55 Hz, 2H), 6.94 (d, J=8.6 Hz, 4H), 3.73 (t, J=6.1 Hz, 8H), 1.10-1.04 (m, 8H), 1.02-0.94 (m, 8H), 0.92-0.79 (m, 12H), 0.74-0.63 (m, 48H), 0.52-0.049 (m, 8H), 0.22-0.17 (m, 8H). ¹³CNMR (CD₃OH, 160 MHz): δ 174.61, 159.90, 151.51, 150.60, 132.70, 131.03, 129.55, 129.31, 123.36, 115.02, 114.56, 105.16, 100.66, 97.66, 83.35, 68.35, 31.62, 29.38, 29.35, 29.15, 29.04, 28.85, 28.53, 28.45, 25.17, 22.37, 13.15.

3.5.2.12 Synthesis of [5,15-bis(2,6-di(dodecyloxy)phenyl)-10-[(4-carboxylphenyl)ethynyl]-20-[(4-(2-cyanopropenoic acid)phenyl)ethynyl]porphyrinato] zinc(II) (RJ-C₁₂-MY₃)

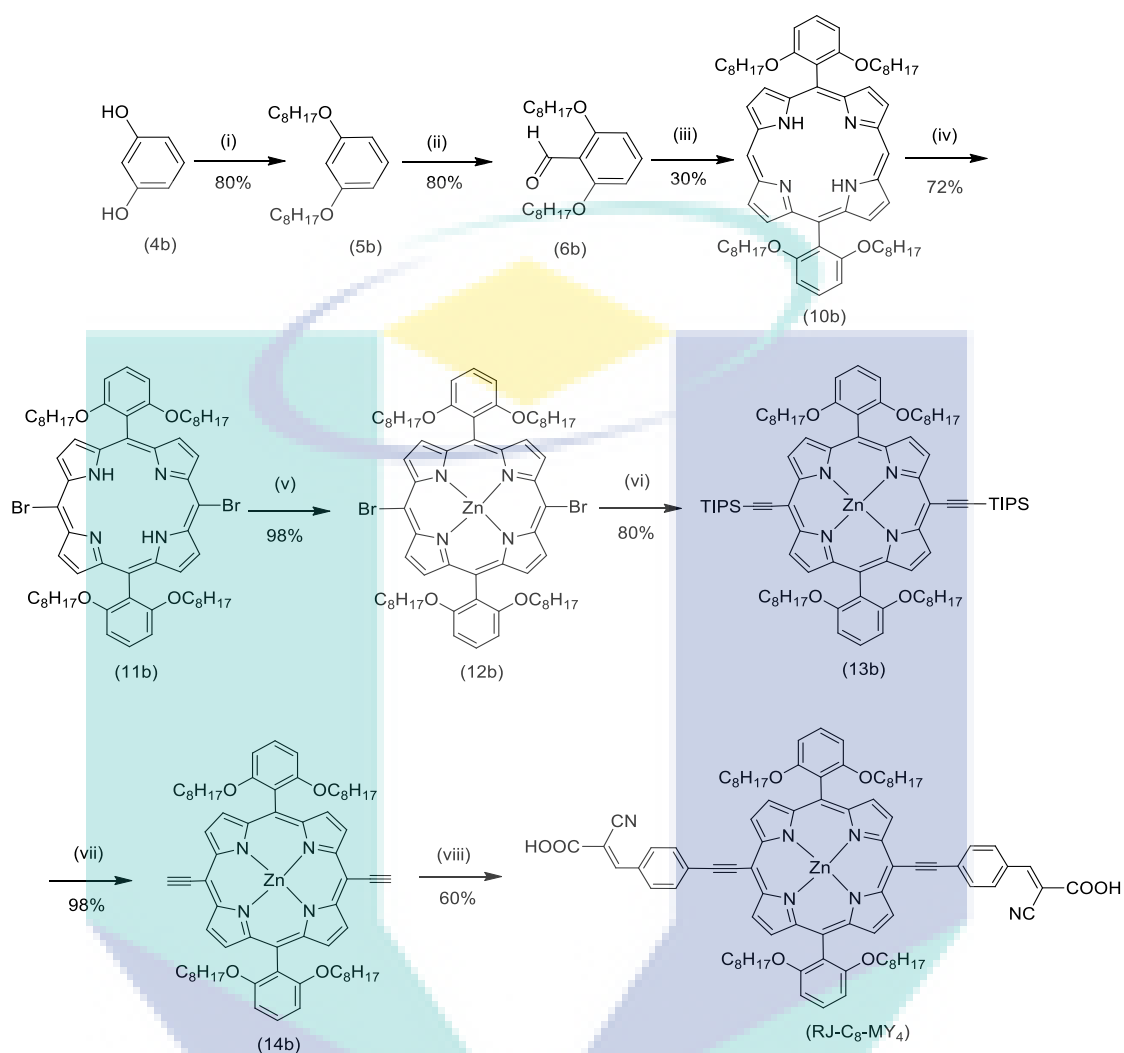


Scheme 3.4 Reagents: (c) 4-iodobenzoic acid, 2-cyano-3-(4-iodophenyl)acrylic acid, THF, NEt₃, Pd₂(dba)₃, AsPh₃, N₂, 85 °C, 6 h

To a degassed solution of compound 14 (100.00 mg, 0.076 mmol), compound 3 (34.08 mg, 0.114 mmol) and 4-iodobenzoic acid (28.27 mg, 0.114 mmol) in anhydrous THF (10 mL) was added NEt₃ (1 mL) under N₂ gas flow. Pd₂(dba)₃ (17.39 mg, 0.019 mmol) and AsPh₃ (46.54 mg, 0.15 mmol) were added to the mixture and was stirred at 85 °C for 6 h under N₂. The reaction mixture was cooled at room temperature and the solvent was removed under vacuum. The crude product was purified by column chromatography (silica gel) using DCM: MeOH (1:7 v/v) as an eluent. Further purification was done by pre-TLC method to get the pure compound. Recrystallization from MeOH to give final product (48.88 mg, 40%) as a green solid.

¹HNMR (CD₃OH, 500 MHz): δ 9.46 (d, J=4.5 Hz, 4H), 8.60 (d, J=4.5 Hz, 2H), 8.58 (d, J=4.5 Hz, 2H), 8.02 (s, 1H), 8.01 (d, J=8.2 Hz, 4H), 7.95 (d, J=8.1 Hz, 2H), 7.84 (d, J=8.15 Hz, 2H), 7.59 (t, J=8.5 Hz, 2H), 6.93 (d, J=8.55 Hz, 4H), 3.74 (t, J=6.0 Hz, 8H), 1.03-0.97 (m, 8H), 0.93-0.85 (m, 8H), 0.81-0.72 (m, 8H), 0.67-0.58 (m, 52H), 0.48-0.42 (m, 8H), 0.19-0.13 (m, 8H). ¹³CNMR (CD₃OH, 160 MHz): δ 174.63, 159835, 151.61, 151.45, 148.80, 131.33, 130.36, 130.14, 129.75, 129.31, 115.26, 105.05, 99.86, 88.89, 68.25, 31.65, 29.21, 29.15, 29.08, 28.92, 28.77, 28.46, 25.16, 22.39, 13.16.

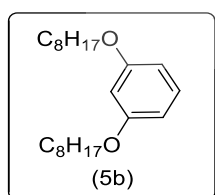
3.5.3 Synthesis of Porphyrins RJ-C₈-MY₄:



Reagents: (i) C₈H₁₇-Br, K₂CO₃, (CH₃)₂CO, reflux, 3 days; (ii) a) TMEDA, (C₂H₅)₂O, n-BuLi, N₂, 0 °C, 4 h; b) DMF, (C₂H₅)₂O, N₂, 2 h; (iii) a) 9, TFA, DCM, N₂, 23 °C, 4 h; b) DDQ, stirring, 1 h; (iv) NBS, DCM, N₂, stirring, 6 h; (v) Zn(OAc)₂·2H₂O, DCM, CH₃OH, 23 °C, 24 h; (vi) TIPS-acetylene, THF, CuI, Pd(PPh₃)₂Cl₂, NEt₃, N₂, 85 °C, 6 h; (vii) TBAF, THF, N₂, stirring, 1 h; (viii) 3, THF, NEt₃, Pd₂(dba)₃, AsPh₃, N₂, 85 °C, 6 h

Figure 3.7 Synthesis of RJ-C₈-MY₄

3.5.3.1 Synthesis of 1,3-di(octyloxy)benzene (5b)

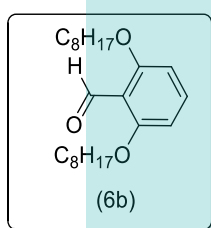


Compound 5b was synthesized by modified method of literature procedure (Mohr et al., 1994). In a mixture of resorcinol (5.00 g, 0.045 mol) and K₂CO₃ (31.10 g, 0.22 mol), 1-bromooctane (34.76 mL, 0.18 mol) was added and refluxed for 3 days in dry acetone (500 mL). The reaction was monitored by TLC. When all the reactants were consumed, the

solvent was removed under reduced pressure. The residue was extracted with EtOAc (3 × 100 mL), washed with water and dried over anhydrous MgSO₄. The solvent was removed under reduced pressure and the product was purified by column chromatography eluting with pure n-Hexane giving 1,3-di(octyloxy)benzene (12.50 g, 80%).

¹H NMR (CDCl₃, 500 MHz): δ 7.15 (t, J=8.3 Hz, 1H), 6.48 (d, J=2.35 Hz, 1H), 6.46 (m, 2H), 3.93 (t, J=6.5 Hz, 4H), 1.78-1.73 (m, 4H), 1.46-1.40 (m, 4H), 1.35-1.26 (m, 16H), 0.89 (t, J=6.95 Hz, 6H). ¹³C NMR (CDCl₃, 160 MHz): δ 160.40, 129.73, 106.63, 101.44, 67.97, 31.86, 29.41, 29.32, 29.29, 26.10, 22.70, 14.12.

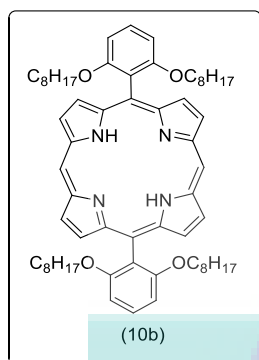
3.5.3.2 Synthesis of 2,6-bis(octyloxy)benzaldehyde (6b)



Compound 6b was synthesized by modified method of literature procedure (Katritzky et al., 2001). A solution of compound 5b (5.00 g, 0.015 mol) and TMEDA (0.45 mL, 3.00 mmol) in 84 mL of anhydrous ether was degassed with dinitrogen for 25 min using Schlenk-tube apparatus and cooled to 0 °C. A solution of n-butyllithium butyllithium (11.25 mL, 2 M solution in hexanes, 22.50 mmol) was then added drop-wise over 2 h and allowed the mixture to stir for additional 2 h. The reaction mixture was warmed to room temperature for 30 min and then anhydrous DMF (2.31 mL, 30.00 mmol) was added drop-wise. The reaction mixture was again stirred for an additional 2 h. After 2 h, the reaction mixture was quenched with water, and extracted with ether (3 × 80 mL), dried over anhydrous MgSO₄. The solvent was removed under reduced pressure. The product was recrystallized from hexane to yield a white solid (4.35 g, 80% yield).

¹H NMR (CDCl₃, 500 MHz): δ 10.26 (s, 1H), 7.10 (t, J=8.4 Hz, 1H), 6.25 (d, J=8.4 Hz 2H), 3.74 (t, J=6.5 Hz, 4H), 1.56-1.50 (m, 4H), 1.21-1.15 (m, 4H), 1.07-1.03 (m, 16H), 0.63 (t, J=6.95 Hz, 6H). ¹³C NMR (CDCl₃, 160 MHz): δ 189.10, 161.61, 135.52, 114.68, 104.45, 68.85, 31.79, 29.29, 29.24, 29.20, 29.16, 29.04, 25.97, 22.63, 14.05

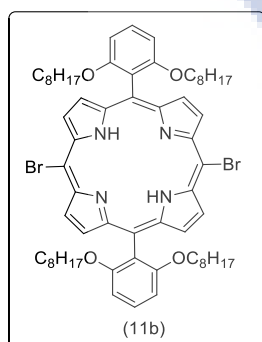
3.5.3.3 Synthesis of 5,15-bis(2,6-di(octyloxy)phenyl)porphyrin (10b)



A solution of compound 9 (5.00 g, 34.24 mmol) and compound 6b (12.40 g, 34.24 mmol) in anhydrous DCM (1 L) was degassed with N₂ for 15 minutes and was added trifluoroacetic (2.38 mL, 31.13 mmol). The reaction mixture was stirred under N₂ for 4 h. DDQ (11.66 g, 51.36 mmol) was added in the reaction mixture and was stirred for additional 1 h. The reaction mixture was then basified with NEt₃ (7 mL) and filtered through silica. The solvent was removed under reduced pressure. The remaining crude product was purified by column chromatography (silica gel) using DCM: Hexane (1:2 v/v) as an eluent. The product was recrystallized from MeOH/DCM to give the purple colored product (10.1 g, 30%).

¹HNMR (CDCl₃, 500 MHz): δ 10.13 (s, 2H), 9.25 (d, J=4.4 Hz, 4H), 8.97 (d, J=4.6 Hz, 4H), 7.71 (t, J=8.5 Hz, 2H), 7.01 (d, J=8.55 Hz, 4H), 3.83 (t, J=6.4 Hz, 8H), 0.93-0.88 (m, 8H), 0.85-0.79 (m, 8H), 0.66-0.60 (m, 8H), 0.57-0.51 (m, 28H), 0.45-0.40 (m, 8H), -3.01 (s, 2H). ¹³CNMR (CDCl₃, 160 MHz): δ 160.15, 130.79, 130.40, 129.99, 119.99, 111.51, 105.31, 103.91, 68.70, 31.31, 28.66, 28.62, 28.60, 25.30, 22.31, 13.85.

3.5.3.4 Synthesis of 5,15-bisbromo-10,20-bis(2,6-di(octyloxy)phenyl)porphyrin (11b)

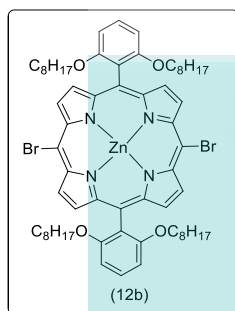


A solution of NBS (1.83 g, 10.26 mmol) in anhydrous DCM (200 mL) was slowly added to a stirred solution of compound 10b (5.00 g, 5.13 mmol) in anhydrous DCM (1 L) for 4 h at 0 °C under N₂ gas. The reaction mixture was further stirred for 2 h more at room temperature. After that, the reaction mixture was quenched with acetone (30 mL) and the solvent was removed under reduced pressure. The crude product was purified by column chromatography (silica gel) using DCM: Hexane (0.5:2 v/v) as an eluent. Recrystallization by MeOH/DCM gave the final product as a purple solid. (4.20 g, 72%).

¹HNMR (CDCl₃, 500 MHz): δ 9.50 (d, J=4.9 Hz, 4H), 8.78 (br s, 4H), 7.70 (t, J=8.55 Hz, 2H), 6.98 (d, J=8.5 Hz, 4H), 3.84 (t, J=6.4 Hz, 8H), 0.97-0.91 (m, 8H), 0.85-

0.78 (m, 8H), 0.64-0.58 (m, 8H), 0.55-0.47 (m, 28H), 0.43-0.37 (m, 8H), -2.59 (s, 2H).
 ^{13}C NMR (CDCl_3 , 160 MHz): δ 159.95, 130.26, 119.93, 114.16, 109.88, 105.05, 102.26, 68.63, 31.33, 28.66, 28.64, 28.58, 25.33, 22.27, 13.84.

3.5.3.5 Synthesis of [5,15-bisbromo-10,20-bis(2,6-di(octyloxy)phenyl)porphina - to]zinc(II) (12b)

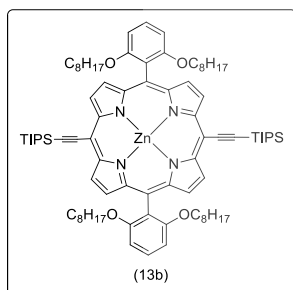


A solution of compound 11b (4.00 g, 3.53 mmol) and $\text{Zn}(\text{OAc})_2 \cdot 2\text{H}_2\text{O}$ (4.65 g, 21.20 mmol) in anhydrous DCM (400 mL) and anhydrous MeOH (200 mL) was stirred at room temperature for 24 h. The reaction mixture was quenched with water (100 mL) and was extracted with DCM (2×100 mL). The combined organic layers were washed with water and dried over anhydrous MgSO_4 .

The solvent was removed under reduce pressure. The crude product was purified by column chromatography (silica gel) using DCM: Hexane (1:2 v/v) as an eluent. Recrystallization by MeOH/DCM gave the final product as a purple solid (4.14 g, 98%).

^1H NMR (CDCl_3 , 500 MHz): δ 9.62 (d, $J=4.6$ Hz, 4H), 8.88 (d, $J=4.6$ Hz, 4H), 7.71 (t, $J=8.55$ Hz, 2H), 7.00 (d, $J=8.55$ Hz, 4H), 3.84 (t, $J=6.4$ Hz, 8H), 0.97-0.91 (m, 8H), 0.83-0.76 (m, 8H), 0.61-0.55 (m, 8H), 0.52-0.43 (m, 28H), 0.37-0.31 (m, 8H).
 ^{13}C NMR (CDCl_3 , 160 MHz): δ 159.89, 151.34, 149.67, 132.77, 132.72, 129.99, 120.70, 114.80, 105.17, 103.90, 68.60, 31.33, 28.66, 28.61, 28.56, 25.23, 22.26, and 13.82.

3.5.3.6 Synthesis of [5,15-bis(2,6-di(octyloxy)phenyl)-10,20-bis(triisopropylsilyl) ethynyl]porphinato]zinc(II) (13b)

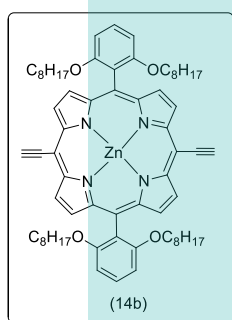


To a degassed solution of compound 12b (1.50 g, 1.25 mmol), triisopropylsilyl-acetylene (0.70 mL, 3.13 mmol) and CuI (0.068 g, 0.35 mmol) in anhydrous THF (20 mL) was added NEt_3 (9 mL) under N_2 gas flow. $\text{Pd}(\text{PPh}_3)_2\text{Cl}_2$ (0.17 g, 0.25 mmol) was added to the solution and was stirred at 85°C for 6 h under N_2 . The reaction mixture was cooled at room temperature and the solvent was

removed under vacuum. The crude product was purified by column chromatography (silica gel) using DCM: Hexane (1:2 v/v) as an eluent to give the product as a purple solid (1.41 g, 78%).

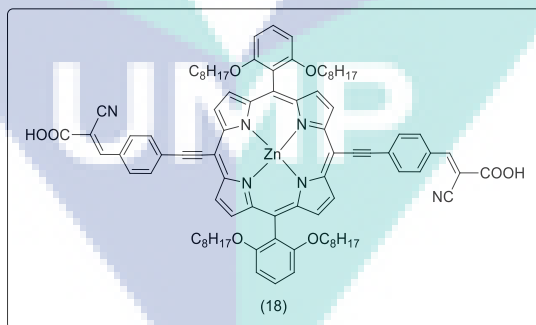
^1H NMR (CDCl_3 , 500 MHz): δ 9.58 (d, $J=4.5$ Hz, 4H), 8.78 (d, $J=4.5$ Hz, 4H), 7.60 (t, $J=8.4$ Hz, 2H), 6.91 (d, $J=8.55$ Hz, 4H), 3.73 (t, $J=6.5$ Hz, 8H), 1.39-1.33 (m, 42H), 1.02-0.84 (m, 26H), 0.83-0.65 (m, 22H), 0.53-0.41 (m, 12H). ^{13}C NMR (CDCl_3 , 160 MHz): δ 159.91, 152.05, 150.64, 131.86, 130.85, 129.80, 121.03, 115.11, 109.93, 105.40, 100.42, 96.75, 68.78, 31.24, 29.73, 28.56, 28.54, 28.53, 25.19, 22.16, 19.10, 13.78, 11.94.

3.5.3.7 Synthesis of [5,15-bis(2,6-di(octyloxy)phenyl)-10,20bis(ethynyl)porphinato]zinc(II) (14b)



To a degassed solution of compound 13b (200.00 mg, 0.143 mmol) in anhydrous THF (30 mL) was added TBAF (1.43 mL, 1M in THF, 1.43 mmol). The solution was stirred at room temperature for 1 h and was quenched with H_2O . The mixture was then extracted with DCM (3×30 mL) and combined organic layer was dried over anhydrous MgSO_4 . The solvent was removed under reduced pressure. The residue of compound 13b was used as such without further purification for the synthesis of RJ-C₈-MY₄ complex (152.22 mg, 98% yield).

3.5.3.8 Synthesis of [5,15-bis(2,6-di(octyloxy)phenyl)-10,20-[(4-(2cyanopropenoic acid)phenyl)ethynyl]porphyrinato]zinc(II) (RJ-C₈-MY₄)



To a degassed solution of compound 14b (100.00 mg, 0.092 mmol) and Compound 3 (82.64 mg, 0.27 mmol) in anhydrous THF (10 mL) was added NEt_3 (1 mL) under N_2 gas flow. $\text{Pd}_2(\text{dba})_3$ (21.06 mg, 0.023 mmol) and AsPh_3 (56.35 mg, 0.18 mmol) were added to the mixture and was stirred at 85°C for 6 h under N_2 . The reaction mixture was cooled at room temperature and the solvent was removed under vacuum. The crude product was purified by column chromatography (silica gel) using DCM: MeOH (1:8

v/v) as an eluent. Further purification was done by pre-TLC method to get the pure compound. Recrystallization from MeOH to give final product (78.90 mg, 60%) as a green solid.

^1H NMR (CD_3OH , 500 MHz): δ 9.49 (d, $J=4.4$ Hz, 4H), 8.61 (d, $J=4.45$ Hz, 4H), 8.07 (s, 2H), 8.06 (d, $J=8.35$ Hz, 4H), 7.98 (d, $J=8.1$ Hz, 4H), 7.55 (t, $J=8.45$ Hz, 2H), 6.88 (d, $J=8.6$ Hz, 4H), 3.67 (t, $J=5.25$ Hz, 8H), 1.22-1.13 (m, 8H), 1.07-1.02 (m, 8H), 0.95-0.89 (m, 8H), 0.86-0.80 (m, 8H), 0.73-0.64 (m, 12H), 0.55-0.52 (m, 8H), 0.26-0.21 (m, 8H). ^{13}C NMR (CD_3OH , 160 MHz): δ 179.47, 178.04, 162.08, 155.85, 154.75, 147.54, 143.80, 133.00, 131.99, 128.41, 124.16, 123.08, 123.02, 117.09, 112.45, 109.36, 103.07, 101.67, 87.97, 85.70, 83.32, 62.15, 52.21, 30.93, 30.61, 29.35, 29.03, 22.32, 22.06, 20.70, 18.92, 17.44, 15.45, 13.07.

3.6 Photoacoustic Measurements

A frequency doubled Nd:YAG laser (Minilite II, Continuum) producing 532 nm laser pulses of 3 ns pulse width was focused with a 20 cm focal length lens. The sample was placed in a 2 mm quartz cuvette and mounted in a custom made cell containing water for ultrasound coupling. The sample cell was placed at 45° with respect to the incident laser beam and the effective optical path length equals to 2.83 mm. The whole system was mounted on a XYZ translation stage (Thorlabs NRT 150) and was moved such that the focal point of the beam was scanned by the sample along the beam direction (Z direction). As the sample moved through the focal region of the nanosecond laser, the transmitted and generated photoacoustic signals were recorded simultaneously. Concurrently the absorbed energy was converted into heat. This produced pressure transients and thus wideband ultrasonic emission. The ultrasonic waves were then detected using the photoacoustic transducer. Water acted as the medium to transmit the generated acoustic waves. The PA signal was recorded using a 10 MHz focused water immersion transducer (Olympus NDT Inc.) which was 1.27 cm in diameter and had a focal length of 2.54 cm. Schematic of experimental setup used to obtain nonlinear optical transmission and scattering, and photoacoustic data are shown in Figure 3.8.

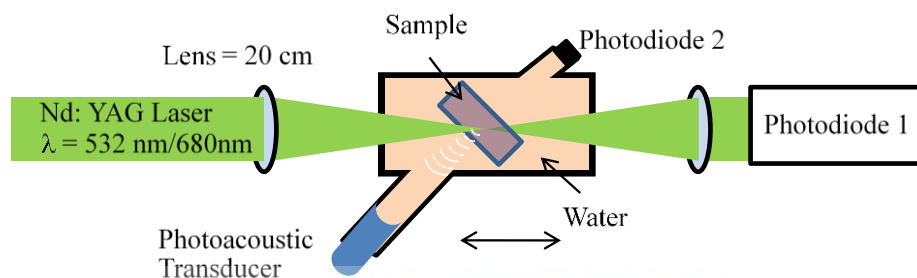


Figure 3.8 Schematic of experimental setup used to obtain nonlinear optical transmission and scattering, and photoacoustic data

3.7 Summary

In chapter 3, the first part includes the details of DFT methods adopted to design and to study the optical properties of the meso-substituted porphyrin molecules using Gaussian 09W software. Geometry optimisations were carried out using DFT/B3LYP/3-21G, DFT/B3LYP/6-31G, DFT/B3LYP/6-31G(d), DFT/B3LYP/LANL2DZ, DFT/CAMB3LYP/3-21G, DFT/CAMB3LYP/6-31G, and DFT/CAMB3LYP/LANL2DZ levels of the theory to verify the lowest energy structures, from which frequency calculations (IR vibrational) were performed at the same levels of theory. None of the frequency calculations produced negative frequencies, being consistent with energy minima for all the optimized geometries. The optimized structures were then employed for studying the absorption spectra using LR TD-DFT method. All the calculations were done under the solvent effect using IEF-PCM model. The calculated vibrational IR and absorption spectra were compared in order to determine the porphyrin of interest for their synthesis. In second part, the methodology adopted for synthesis are described in detail, dipyrromethane (9) synthesized from pyrrole and formaldehyde, was condensed with aldehyde derivatives to give the free-base porphyrins 10 and 10b, respectively. The free-base porphyrins were then brominated using N-bromosuccinimide to get porphyrins 11 and 11b, followed by metalation with zinc acetate to afford 12 and 12b. Finally, Sonagashira coupling with triisopropylsilyl (TIPS) acetylenes gave the porphyrins 13 and 13b respectively, which were in turn coupled with various carboxyl phenyl iodides under mild conditions via a Sonogoshira coupling reaction that included an in situ deprotection step (14 and 14b) with TBAF, to afford good yields of desired Zn(II)porphyrins. The synthesized Zn(II)porphyrins were then characterized by FTR, UV-Vis, NMR, MS, PL and TGA. In third part, the method adopted for photoacoustic studies are explained.

CHAPTER 4

RESULTS AND DISCUSSION: SYNTHESIS AND OPTOELECTRONIC PROPERTIES OF π -CONJUGATED MESO-ETHYNYL-Zn(II)PORPHYRINS

4.1 Introduction

This chapter explains the synthetic protocols adopted for the synthesis of four novel meso-ethynyl-Zn(II)porphyrins designed using DFT along with their detailed reaction mechanism. The structure and properties of these porphyrins are also explained here; a comparative approach between experimental results and theoretical data has been adopted. Moreover, the optoelectronic studies of these macromolecules for their application in photoacoustic imagining are also explored deeply in this chapter.

4.2 Synthesis of Meso-Ethynyl-Zn(II)porphyrins

The meso-ethynyl-Zn(II)porphyrins – they are termed RJ-C_n-MY_m, where n = 12 or 8 and m = 1 – 4, were synthesized according to MacDonald (2+2) condensation followed by bromination and Sonogashira cross-coupling reactions using the precursors dipyrromethane (9) and 2,6-bis(alkoxy)benzaldehyde (6 & 6b). Briefly, as shown in Figure 4.1, dipyrromethane (9) was synthesized by acid catalyzed oxidation reaction from pyrrole and formaldehyde and was then condensed with 2,6-bis(alkoxy)benzaldehyde (6 & 6b), which were synthesized from 1,3-di(alkoxy)benzene (5 & 5b), to give the free-base porphyrins 10 and 10b, respectively. The free-base porphyrins were then brominated using N-bromosuccinimide to obtain dibromo-porphyrins 11 and 11b followed by metalation with zinc acetate to afford 12 and 12b with 98% yields. Finally, Sonogashira coupling with TIPS-acetylene gave the porphyrins 13 and 13b with 80% and 78% yields, respectively, which

were in turn coupled with various carboxylic acid benzyl iodides under mild conditions via a Sonogashira coupling reaction that included an in situ deprotection step with TBAF to afford good yields of novel RJ-C_n-MY_m series of Zn(II)porphyrins. The detailed mechanism for each step is explained in the following section.

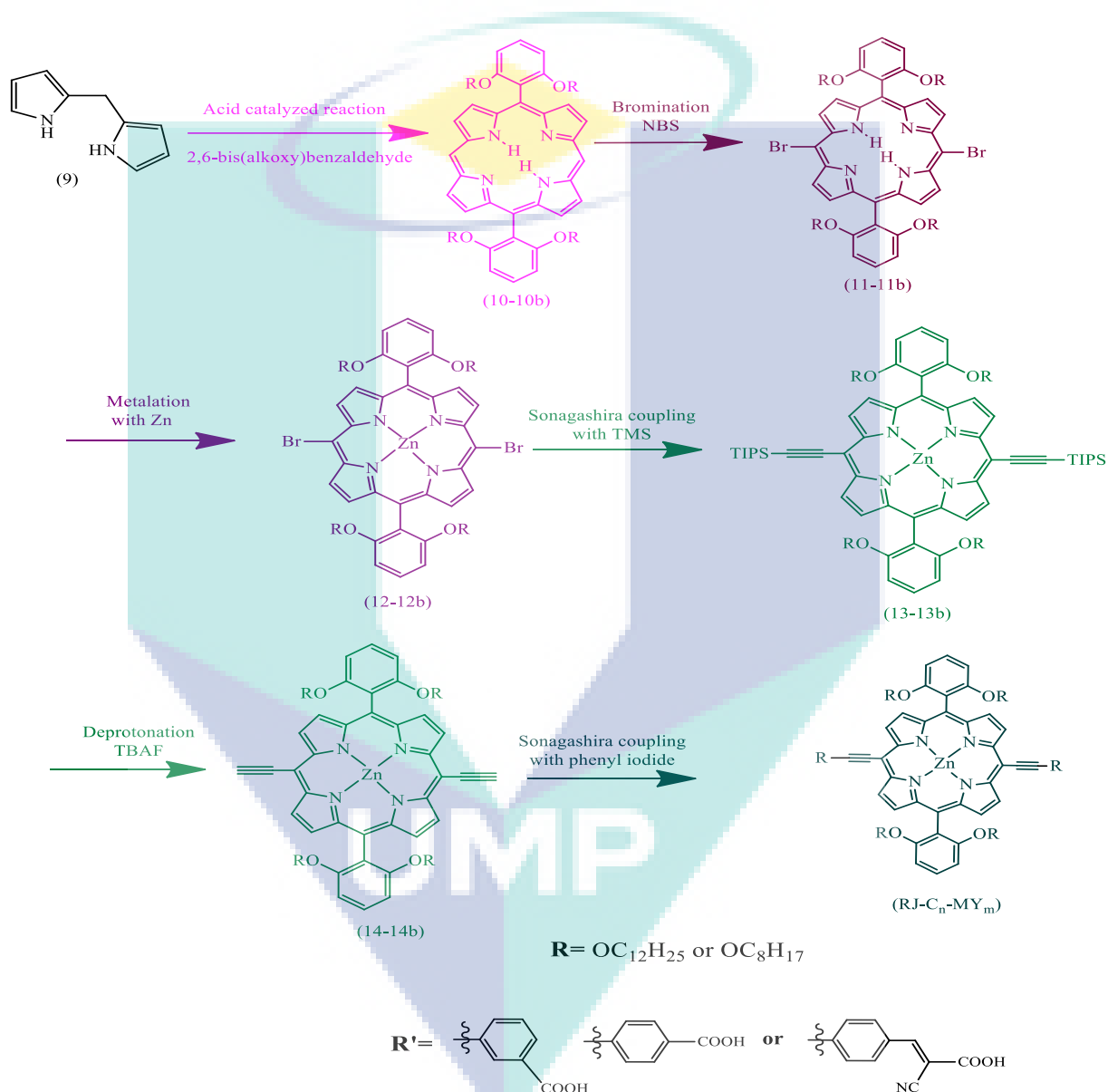


Figure 4.1 Synthesis of meso-ethynyl-Zn(II)porphyrins

Various types of precursors synthesized for the synthesis of meso-ethynyl-Zn(II)porphyrins and four novel RJ-C_n-MY_m porphyrins are shown Table 4.1.

Table 4.1 Starting materials and the yields of porphyrin precursors and the meso-ethynyl-Zn(II)porphyrins

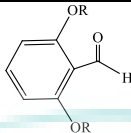
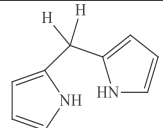
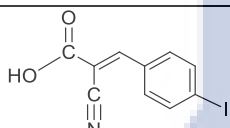
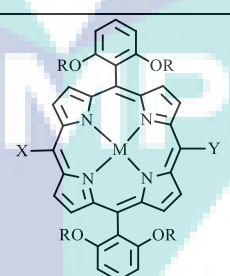
					
Comp	Starting material	1,3-di(alkoxy)benzene precursor "R"	Yield	2,6-bis(alkoxy)benzaldehyde precursor "R"	Yield
5 & 6	benzene-1,3-diol & C ₁₂ H ₂₅ Br	-C ₁₂ H ₂₅	90%	-C ₁₂ H ₂₅	80%
5b & 6b	benzene-1,3-diol & C ₈ H ₁₇ Br	-C ₈ H ₁₇	80%	-C ₈ H ₁₇	80%
					
Comp	Starting material				Yield
9	Pyrrole & formaldehyde				50%
					
Comp	Starting material				Yield
3	4-Iodo-benzaldehyde & cyanoacetic acid				85%
					
Comp	R	M	X	Y	Yield
10	-C ₁₂ H ₂₅	H ₂	-	-	35%
10b	-C ₈ H ₁₇	H ₂	-	-	30%
11	-C ₁₂ H ₂₅	H ₂	Br	Br	75%
11b	-C ₈ H ₁₇	H ₂	Br	Br	72%
12	-C ₁₂ H ₂₅	Zn	Br	Br	98%

Table 4.2 Continued

Comp	R	M	X	Y	Yield
12b	-C ₈ H ₁₇	Zn	Br	Br	98%
13	-C ₁₂ H ₂₅	Zn	≡TIPS	≡TIPS	80%
13b	-C ₈ H ₁₇	Zn	≡TIPS	≡TIPS	78%
14	-C ₁₂ H ₂₅	Zn	≡	≡	98%
14b	-C ₈ H ₁₇	Zn	≡	≡	98%
RJ-C₁₂-MY₁	-C ₁₂ H ₂₅	Zn			80%
RJ-C₁₂-MY₂	-C ₁₂ H ₂₅	Zn			50%
RJ-C₁₂-MY₃	-C ₁₂ H ₂₅	Zn			40%
RJ-C₈-MY₄	-C ₈ H ₁₇	Zn			60%

The synthesis of starting precursors, 2,6-bis(alkoxy)benzaldehyde (6-6b) for porphyrin synthesis were further carried out by two steps, i.e., the synthesis of 1,3-di(alkoxy)benzene (5-5b) and the synthesis of 2,6-bis(alkoxy)benzaldehyde (6-6b). Generally, bis(alkoxy)benzaldehydes are useful and important precursors for many organic syntheses. O-Alkylation of benzene-1,3-diol (4) with an excess alkyl bromide i.e., 1-bromododecane and 1-bromooctane, in the presence of potassium carbonate formed the 1,3-di(alkoxy)benzene (5-5b), shown in Figure 4.2, which were confirmed by ¹HNMR, ¹³CNMR and FTIR, shown in Appendix F (Figures S1-S5). This was a simple and straightforward reaction. The absence of O–H peak in 300–3500 region and the presence of C–O stretching at 1184 cm⁻¹ and 1154 cm⁻¹ indicate the formation of 1,3-di(dodecyloxy)benzene (5) and 1,3-di(octyloxy)benzene (5b) respectively. Moreover, the ¹HNMR spectra show the triplet at 3.92 ppm for (H₂C-O-) hydrogen and multiplet at 1.78-0.87 ppm for long alkyl chain confirming the desired product. The lithiation of 1,3-di(alkoxy)benzene (5 & 5b) with nBuLi in the presence of TMEDA and subsequent formylation of the corresponding intermediate with DMF to give symmetrical 2,6-bis(alkoxy)benzaldehyde 6 and 6b (Figure 4.2) with the yield of up to 80%. However, the reaction condition was quite harsh, involved safety problems at a large scale and employed environmentally harmful reagents such as nBuLi. The reaction was carried out under completely inert atmosphere and low temperature (0 °C). The ¹HNMR

spectra show there is no singlet proton peak in the aromatic region and a sharp singlet peak for aldehyde hydrogen is at 10.55 ppm indicating introduction of formyl group (shown in Appendix F, Figures S7 & S9). Similarly, in ^{13}C NMR spectra (shown in Appendix F, Figures S8 & S10), aldehydic carbon peak at 189.53 ppm clearly indicate that the formyl group is introduced into the desired position with high regioselectivity between the two ortho directing alkoxy groups. No regioisomers with the formyl group at other positions of the benzene ring were detected. In FTIR, the presence of sharp aldehyde $\text{C}=\text{O}$ stretching at 1661 cm^{-1} and 1690 cm^{-1} indicate the formation of **6** and **6b** respectively, as shown in Appendix F, Figure S6.

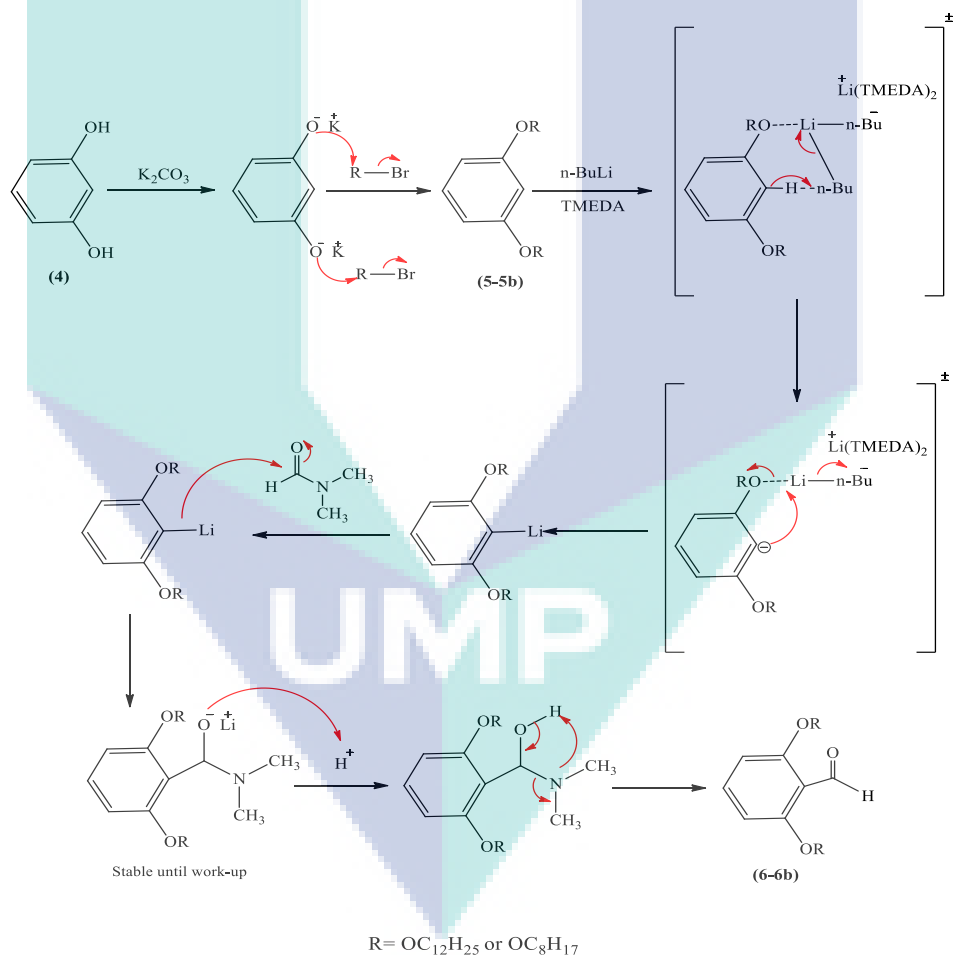


Figure 4.2 Reaction mechanism for 1,3-di(alkoxy)benzene (**5-5a**) and 2,6-bis(alkoxy)benzaldehyde (**6-6a**)

4.2.1 Knoevenagel Condensation Reaction

Knoevenagel condensation reaction is the reaction between the carbonyl compound and any compound containing the active methylene group to afford the α - β unsaturated compounds. The reaction occurs in neutral or mild basic medium in the presence of salts as ammonium acetate or piperidine acetate. The catalytic activity of salts furnishes both the conjugate base, mostly acetate ion, which catalyzes the enolization of active methylene compound and the conjugate acid, the ammonium ion which catalyzes the elimination of water. The general mechanism of the Knoevenagel condensation reaction is shown in Figure 4.3.

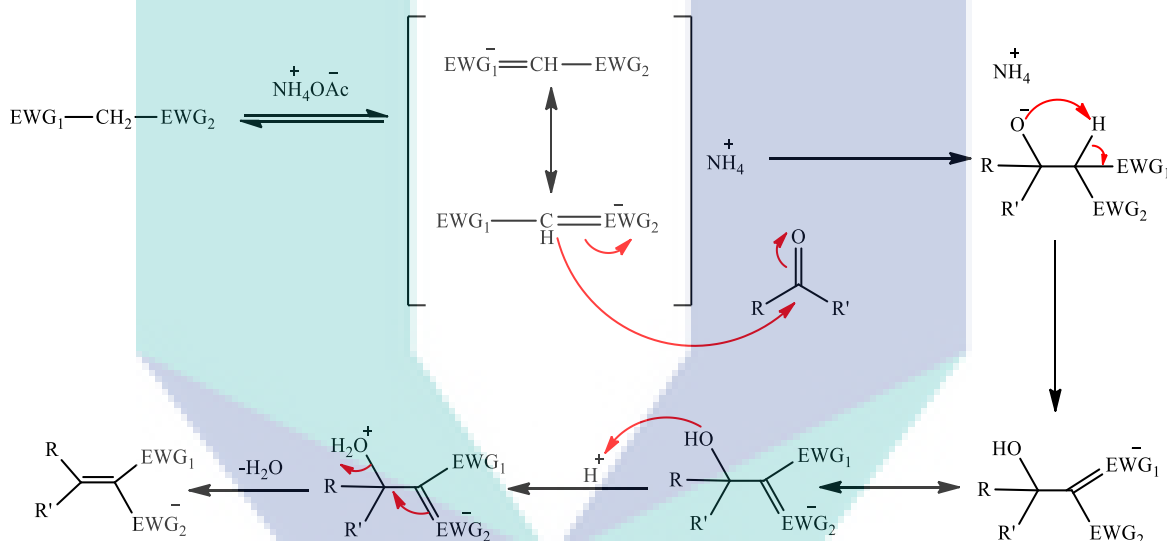


Figure 4.3 General mechanism of Knoevenagel condensation reaction

The 2-cyano-3-(4-iodophenyl)acrylic acid (3), a precursor for the synthesis of meso-ethynyl-Zn(II)porphyrins 17 and 18, was synthesized by Knoevenagel condensation reaction between cyano-acetic acid and 4-iodobenzaldehyde using ammonium acetate as a catalyst in the presence of glacial acetic acid with 85% yield and was characterized by ^1H NMR, ^{13}C NMR and FTIR (shown in Appendix F, Figures S11-S13). The ^1H NMR spectrum shows the signals at 8.25 ppm as a singlet for alkenyl proton, 7.93 ppm as doublet and 7.76 ppm as doublet for benzene protons indicating the formation of desired compound (3). In ^{13}C NMR spectrum, the signal at 164.65 ppm corresponds to the carboxylic acid carbon, signals at 154.69 ppm and 105.67 ppm are for two carbons of the double bond and signal for $\text{C}\equiv\text{N}$

carbon is at 116.56 ppm which confirm the structure of compound (3). Moreover, the FTIR spectrum shows the characteristic stretching frequencies of the O–H bond at 3438 cm^{-1} , C≡N group at around 2226 cm^{-1} and carboxylic acid at around 1690 cm^{-1} indicating the formation of the desired compound. The detailed mechanism for the reaction is shown in Figure 4.4.

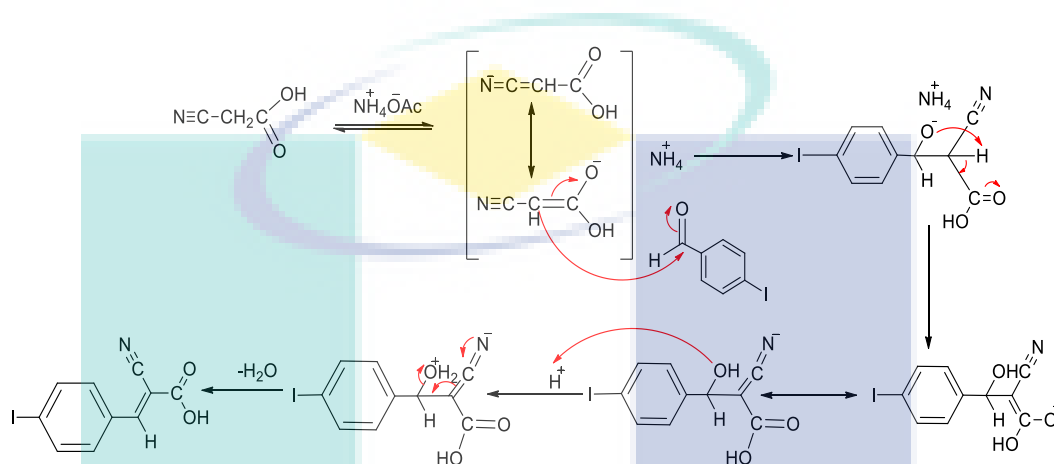


Figure 4.4 Reaction mechanism for 2-cyano-3-(4-iodophenyl)acrylic acid (3)

The synthesis of second precursor di(1H-pyrrol-2-yl)methane (9), as shown in Figure 4.5, is well described in literature (Littler et al., 1999). Acid catalyzed condensation of formaldehyde with pyrrole is an important method for the synthesis of di(1H-pyrrol-2-yl)methane (dipyrrometane). Dipyrromethane consist of two pyrrole rings linked through the pyrrole 2 and 5 positions by meso-carbon atom. The dipyrrometane was formed by dissolving the formaldehyde in excess pyrrole in the presence of strong acid i.e., TFA and was characterized by ^1H NMR, ^{13}C NMR and FTIR (shown in Appendix F, Figures S14-S16). The appearance of N–H protons at 7.69 ppm with twice integration in ^1H NMR spectrum (Appendix F, Figure S15) indicate the presence of two equivalent N–H protons and appearance of C–H protons at 3.9 ppm indicate the deshielding due to electron withdrawing effect of nitrogen atom. Generally, meso-CH protons of dipyrrometane moiety are the most deshielded, followed by α -pyrrolic protons. The β -pyrrolic protons adjacent to α -substituted pyrrolic unit are the most shielded protons. The α -pyrrolic protons appear at 6.59 ppm as a doublet of doublet, β -pyrrolic protons adjacent to α -unsubstituted pyrrolic unit at 6.14 ppm as a doublet of doublet and β -pyrrolic adjacent to α -substituted pyrrolic unit as most shielded protons at 6.02 ppm as a broad singlet. Furthermore, in FTIR, the stretching frequency at

3366 cm^{-1} indicates the presence of N–H bonds. The detailed mechanism for the reaction is shown in Figure 4.5. Excess pyrrole was used in order to maximize the formation of dipyrromethane. Lowering the pyrrole favoured the formation of higher polymers. Unreacted pyrrole was recovered by distillation after reaction completion and can be recycled. The slow heating and application of vacuum were the crucial step to avoid bumping of the crude oil. The dipyrromethane was chromatographed under neutral or slightly basic conditions from the crude oil giving the 50% yield.

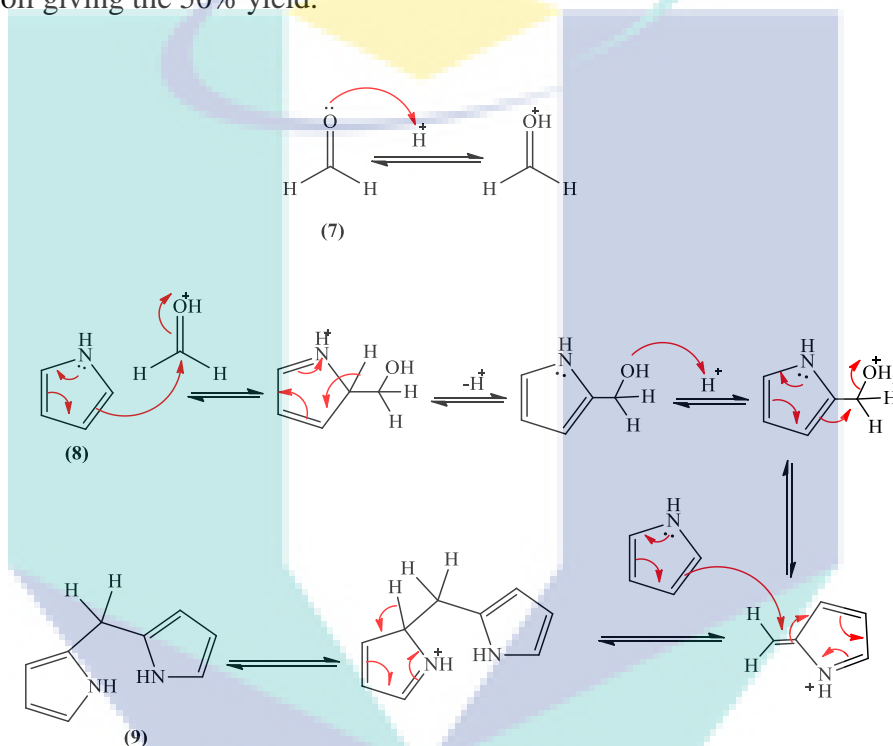


Figure 4.5 Reaction mechanism for di(1H-pyrrol-2-yl)methane (9)

The synthesis of free-base porphyrins (10-10b) were carried out by modification of MacDonald (2+2) condensation. Acid catalyzed condensations of equivalent molar ratio of aldehydes 6 and 6b with di(1H-pyrrol-2-yl)methane (9) under optimized Lindsey et al., conditions (Lindsey et al., 1987) formed the porphyrinogen intermediates which were oxidized by using 2,3-dichloro-5,6-dicyano-1,4-benzoquinone (DDQ) to form free-base porphyrins 10 and 10b with the yield of 35% and 30% respectively. A series of column chromatographic techniques were used to get the target porphyrins as purple solids. The complete mechanism for the synthesis of free-base porphyrins are shown in Figure 4.6.

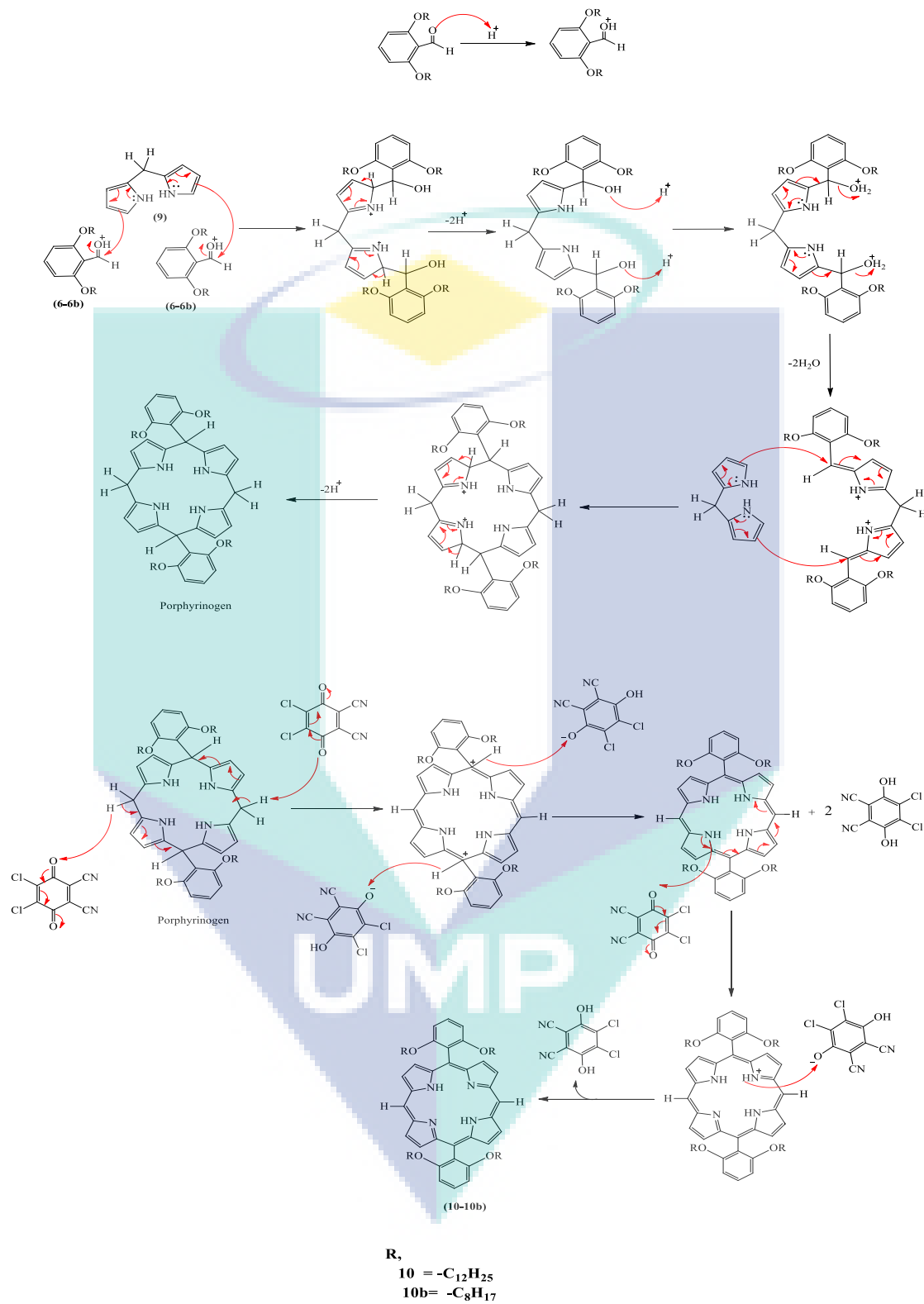


Figure 4.6 Reaction mechanism for Free-base porphyrins (10-10b)

The formation of free-base porphyrins 10 and 10b were confirmed by ^1H NMR, ^{13}C NMR, FTIR and UV-Vis spectra (shown in Appendix F, Figures S17-S19 & S20- S22 respectively). UV-Vis spectra were used to identify the formation of free-base porphyrins for their characteristic four Q-bands in the region 500-650 nm. The ^1H NMR spectra of porphyrins 10 and 10b also exhibit characteristics of porphyrin. The inner N-H protons of porphyrin macrocycle are the most shielded protons and are observed at around -3.02 ppm. The β protons are of two different environments, β_1 protons and β_2 protons, and are identified by the peaks at around 9.25 ppm and 8.96 ppm respectively. The ^1H NMR spectra also show the expected signals at around 10.2 ppm corresponding to two meso-protons (Appendix F, Figures S17 & S21). In addition, the triplet peak at around 3.82 ppm corresponds to -OCH₂- protons and multiplet at around 1.34-0.5 corresponds to alkyl chain. Moreover, in FTIR, the stretching frequencies at around 3450 cm⁻¹ indicate the presence of N-H bonds and at around 1270 cm⁻¹ are for C-O bonds (Appendix F, Figures S19 & S20).

The synthesis of bromo-porphyrins (11-11b) were accomplished by ionic bromination using NBS as a brominating agent. NBS is used as source for bromine in organic synthesis. Adopting a method from Therien et al., (Hartnell, Edwards & Arnold, 2002), selective bromination of free-base porphyrin 10 and 10b produced the meso bromo-porphyrins 11 and 11b by using 2.1 equivalent of NBS with yield of 75% and 72% respectively. Bromination of porphyrins take place preferentially at meso-position if both meso- and β -position are free because of less hindrance. The formation of bromo-porphyrins 11 and 11b were confirmed by ^1H NMR, ^{13}C NMR and FTIR (shown in Appendix F, Figures S23-S25 & S26-S28 respectively). The ^1H NMR spectra of bromo-porphyrins 11 and 11b are like that of porphyrins 10 and 10b with the exception of the absence of the signal at 10.2 ppm that correspond to two meso-protons indicating the bromination of the porphyrins 10 and 10b at meso-position (Appendix F, Figures S23 & S27). The detailed mechanism for the synthesis of free-base bromo-porphyrins are shown in Figure 4.7. The resulting bromo-porphyrins are the important building block for easy addition of a variety of functionalities in porphyrins especially via palladium catalyzed coupling reaction, including Suzuki, Stille, Sonogashira and Heck reactions. In this work, bromo-porphyrins were used for the addition of ethynyl substituted groups via Sonogashira cross coupling reactions.

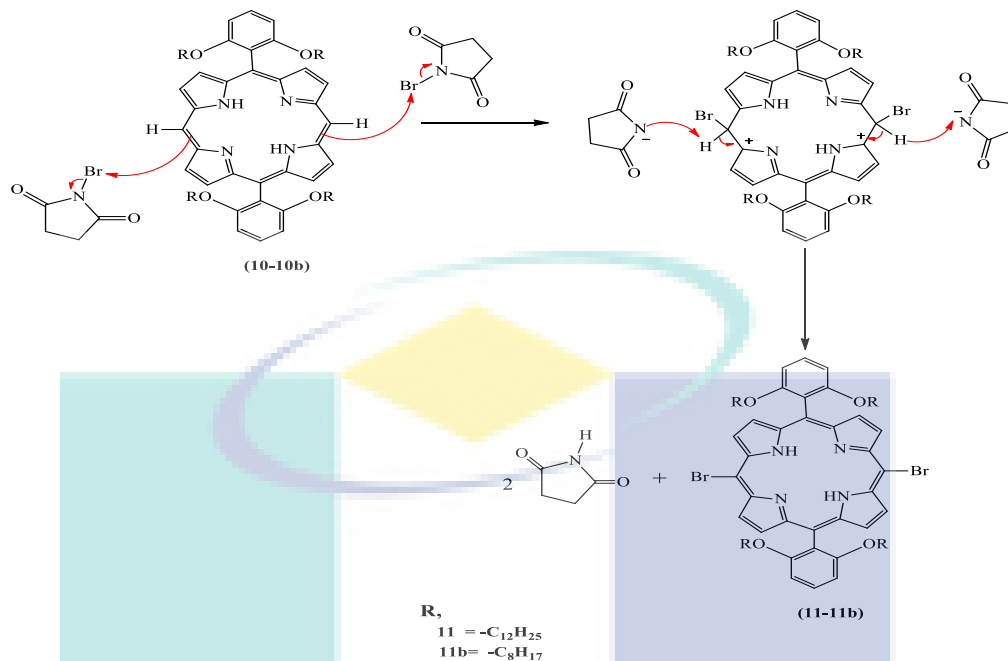


Figure 4.7 Reaction mechanism for Free-base bromo-porphyrins (11-11b)

The synthesis of metalloporphyrins (12-12b) were carried out by metallation of bromo-porphyrins (11-11b) with zinc acetate dihydrate ($Zn(OAc)_2 \cdot 2H_2O$), according to Buchler et al., (Buchler, 1978). Zn complexes were chosen because of the easy Zn insertion and their good stabilities under neutral and basic conditions. The porphyrins 11-11b were treated with ($Zn(OAc)_2 \cdot 2H_2O$) at room temperature in CH_2Cl_2/CH_3OH mixture. The metal carrier dissociated into an unsaturated species that combined with the dianion porphyrins produced by the deprotonation of the free-base porphyrin. Zn(II)porphyrins 12 and 12b were obtained with quantitative yields of 98%. The detailed mechanism for the synthesis of Zn(II)porphyrins are shown in Figure 4.8. The Zn(II)porphyrins 12 and 12b were characterized by 1H NMR, ^{13}C NMR, FTIR and UV-Vis spectra (shown in Appendix F, Figures S29-S31 & S32- S34 respectively). UV-Vis spectra show the reduction of four Q bands into two Q-bands in the region 500-650 nm due to increase symmetry in Zn(II)porphyrins 12 and 12b as compared to free-base porphyrins 10 and 10b, indicating the formation of Zn(II)porphyrins (Appendix F, Figures S31b & S32b). The 1H NMR spectra of Zn(II)porphyrins 12 and 12b do not show the signals in -3.04 ppm, corresponding to two protons (N-H) linked with the nitrogen rings of the free-base porphyrins, which prove the complete conversion of bromo-porphyrins (11-11b) into Zn(II)porphyrins (12-12b)

(Appendix F, Figures S29 & S33). Moreover, in FTIR, the absence of stretching frequencies at around 3450 cm^{-1} indicates the formation of Zn complexes.

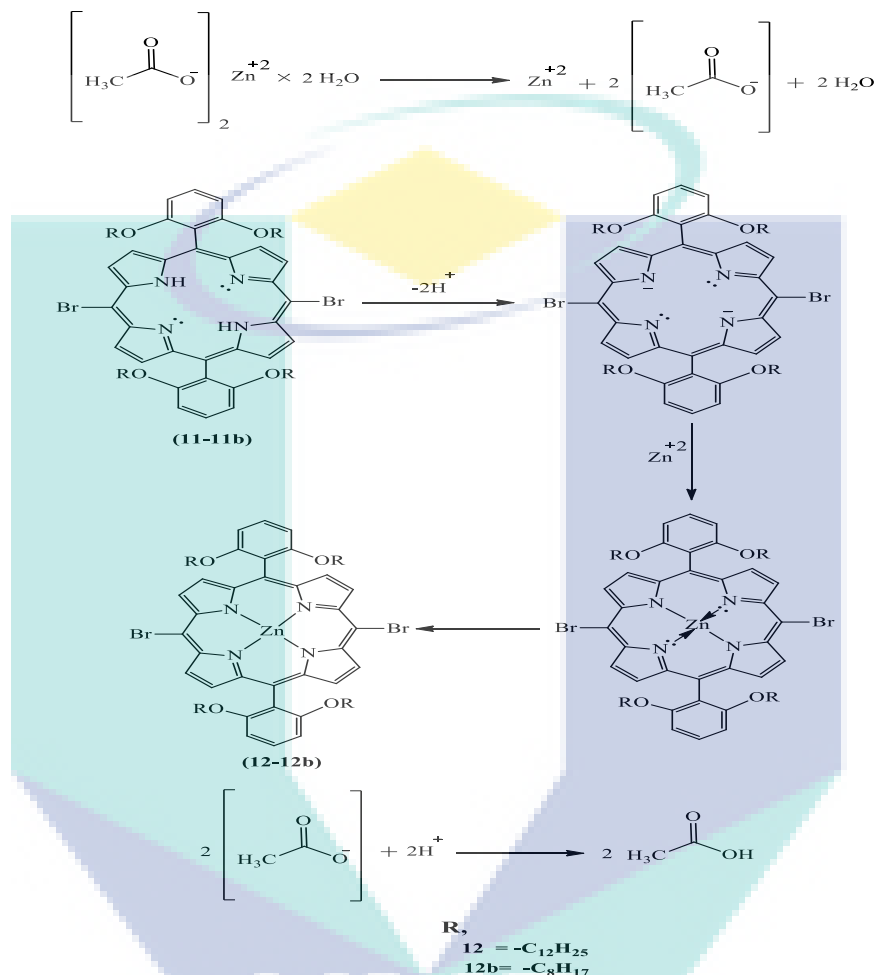


Figure 4.8 Reaction mechanism for Zn(II) porphyrins (12-12b)

The synthesis of Zn(II)porphyrins 13-13b were carried out by Sonogashira cross-coupling reaction of bromo-Zn(II)porphyrins 12-12b with TIPS-acetylene. The detailed mechanism of Sonogashira cross-coupling reaction is explained below.

4.2.2 Sonogashira Cross-Coupling Reaction

Sonogashira cross-coupling reaction is generally used to form carbon-carbon bond in organic synthesis. It is a cross-coupling reaction between a terminal alkyne and an organohalide using a palladium catalyst, a copper co-catalyst, and a base. Generally, the

reaction mechanism occurs through two independent catalytic cycles, as shown in Figure 4.9. The palladium cycle begins with catalytically active species Pd^0L_2 . The first step is initiated by oxidative addition of the organohalide to the Pd(0) to form a Pd(II) complex. The Pd(II) complex undergoes transmetalation with a copper acetylide that is generated in the copper cycle to form palladium acetylide complex eliminating the copper halide. In palladium acetylide complex, both organic ligands are in trans orientation and convert to cis by trans-cis isomerization. In the final step, the trans palladium acetylide complex undergoes reductive elimination to produce the final alkyne, regenerating the Pd^0L_2 catalyst. The copper cycle is poorly understood. However, the base is assumed to enhance the copper acetylide formation with the help of a π -alkyne copper complex, which makes the alkyne terminal proton more acidic (Chinchilla & Nájera, 2007; Elschenbroich, 2006).

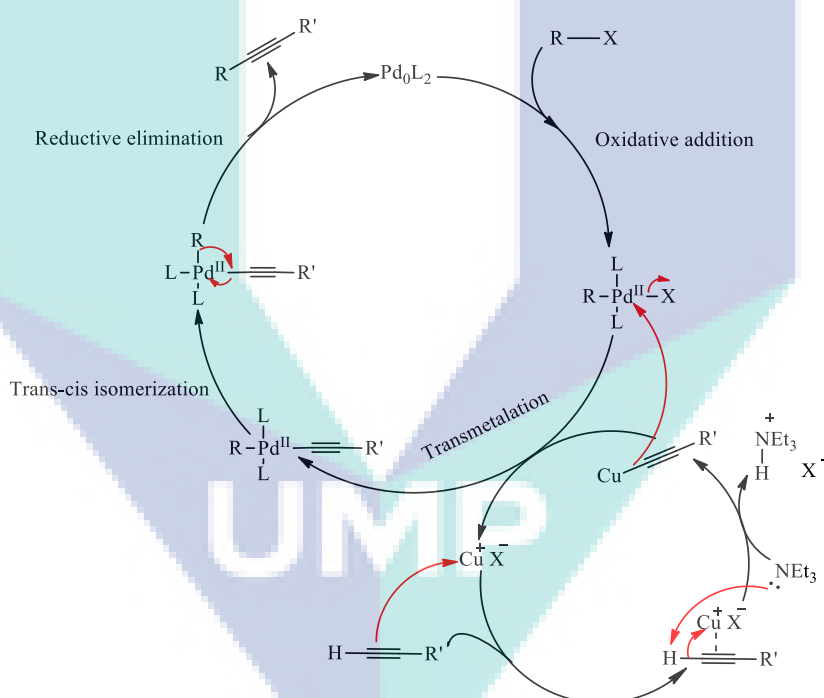


Figure 4.9 General mechanism of Sonogashira cross coupling reaction

The addition of copper salt into the reaction is important for increasing the rate of the reaction, however, the presence of copper causes the undesirable alkyne homo-coupling. Therefore, Sonogashira reaction was modified by performing the reaction in the absence of copper salt known as copper-free Sonogashira coupling reaction. The mechanism of the copper-free Sonogashira coupling reaction is not clear understood, however the proposed

mechanism is shown in Figure 4.10. The catalytic cycle is initiated as usual by the oxidative addition of the organohalide to the catalytic active species $[\text{Pd}^0\text{L}_2]$ forming Pd(II) complex. The Pd(II) complex undergoes a reversible π -coordination of the alkyne by displacing of one ligand to generate an alkyne–Pd(II) intermediate complex. This intermediate complex facilitates the elimination of acetylenic proton by the base subsequent ligand exchange with the leaving group, forming the palladium acetylide complex. Finally, the palladium acetylide complex undergoes reductive elimination to produce the desired cross-coupled product by regenerating the Pd^0L_2 catalyst (Chinchilla & Nájera, 2011).

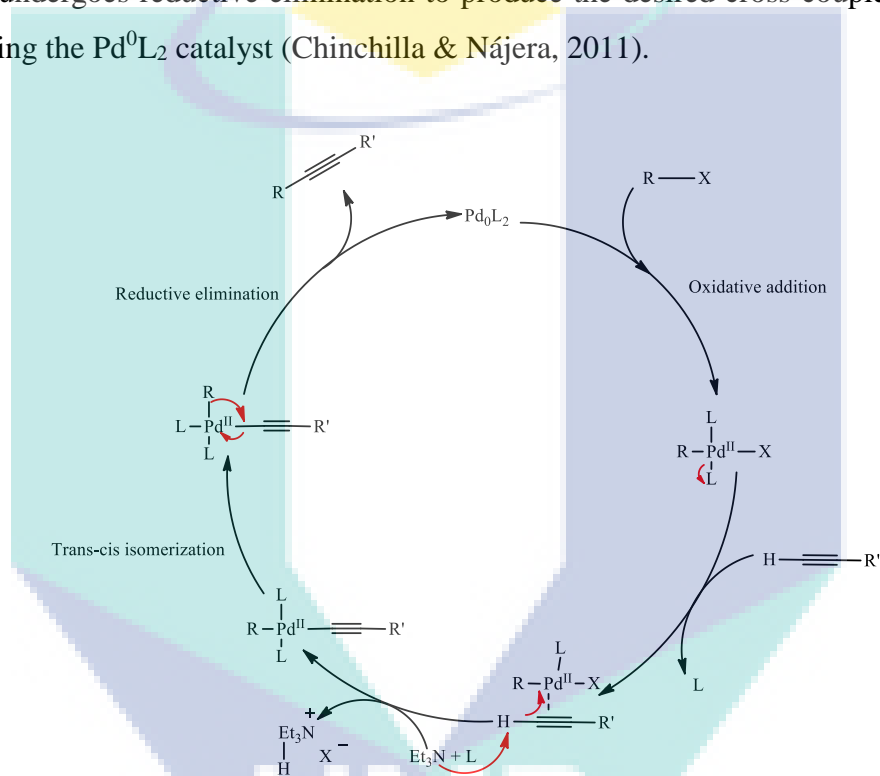


Figure 4.10 General mechanism of copper-free Sonogashira cross coupling reaction

Sonogashira cross coupling reaction is the most commonly used reaction in this work for achieving the desired meso-ethynyl-Zn(II)porphyrins. The Zn(II)porphyrins (13-13b) were synthesized by Sonogashira cross-coupling reaction between bromo-Zn(II)porphyrins 12 and 12b and TIPS-acetylene using $\text{Pd}(\text{PPh}_3)_2\text{Cl}_2$ as a catalyst, CuI as a co-catalyst and amine base (NEt_3) to produce a carbon-carbon bond between the terminal alkyne of the TIPS-acetylene and the Zn(II)porphyrins 12 and 12b. These reactions require inert atmosphere conditions to obtain Zn(II)porphyrins 13 and 13b with 80% and 78% yields respectively. The complete mechanism for the synthesis of Zn(II)porphyrins 13 and 13b are shown in Figure 4.11. The Zn(II)porphyrins 13 and 13b were characterized by ^1H NMR, ^{13}C NMR and FTIR

spectra (shown in Appendix F, Figures S35-S37 & S38-S40 respectively). The ^1H NMR spectra show the presence of the multiplet at 1.46-1.39 ppm representing the protons of two TIPS groups (Appendix F, Figures S35 & S39). The FTIR spectra show the characteristic band of the $\text{C}\equiv\text{N}$ group at around 2144 cm^{-1} indicating the formation of desired porphyrins (Appendix F, Figures S37 & S38). In ^{13}C NMR spectra, the signals at 100.63 and 101.50 ppm correspond to the two carbons of the triple bond.

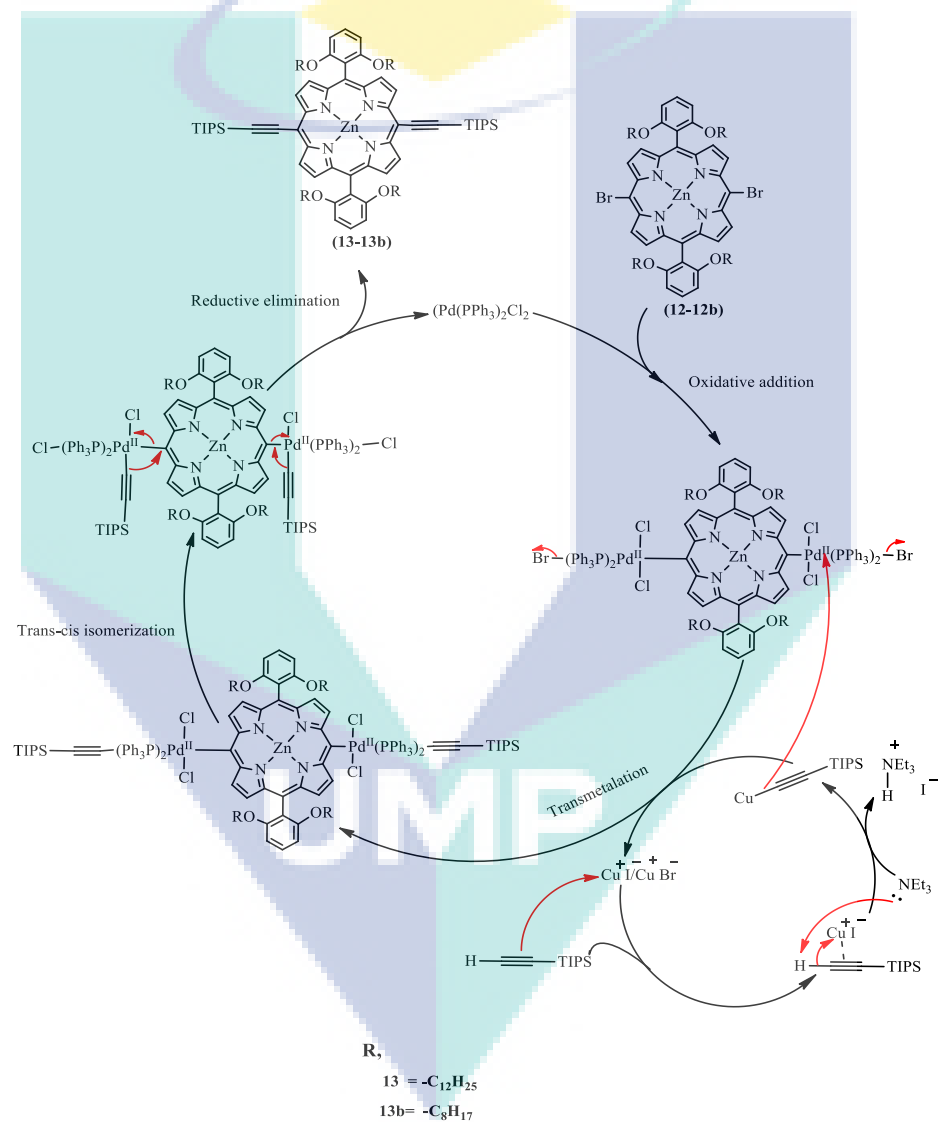


Figure 4.11 Reaction mechanism for Zn(II) porphyrins (13-13b)

The synthesis of porphyrin 14-14b were done by deprotection of TIPS group with TBAF to afford Zn(II)porphyrins 14 and 14b. The TIPS groups from the porphyrins 13-13b were removed quantitatively by hydrolysis with TBAF. The reactions were quenched by water and liquid-liquid extractions with CHCl_3 afforded the porphyrins 14 and 14b with 98% yields. The deprotection reaction is straightforward and formation of products were confirmed by only TLC. The crude products were used for final reaction without further purification. The complete mechanism for the deprotection of Zn(II)porphyrins 13 and 13b are shown in Figure 4.12.

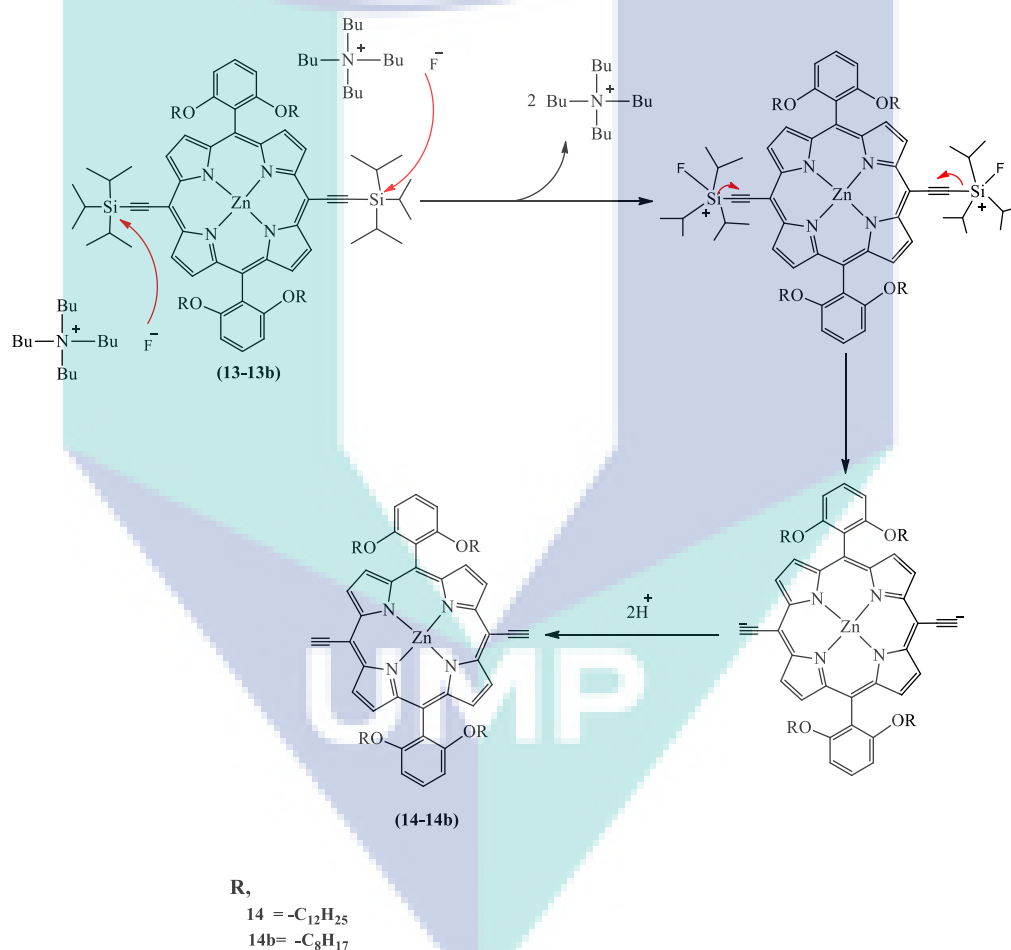


Figure 4.12 Reaction mechanism for Zn(II) porphyrins (14-14b).

The synthesis of meso-ethynyl-Zn(II)porphyrin coded as RJ-C₁₂-MY₁ was synthesized by Sonogashira cross-coupling reaction of bromo-Zn(II)porphyrin (12) with 3-ethynyl-benzoic acid using $\text{Pd}(\text{PPh}_3)_2\text{Cl}_2$ as a catalyst, CuI as a co-catalyst and amine base

(NEt₃) to produce a carbon-carbon bond between the terminal alkyne of the 3-ethynylbenzoic acid and the Zn(II)porphyrin (12) with 80% yield. The detailed mechanism for the synthesis of RJ-C₁₂-MY₁ is shown in Figure 4.13.

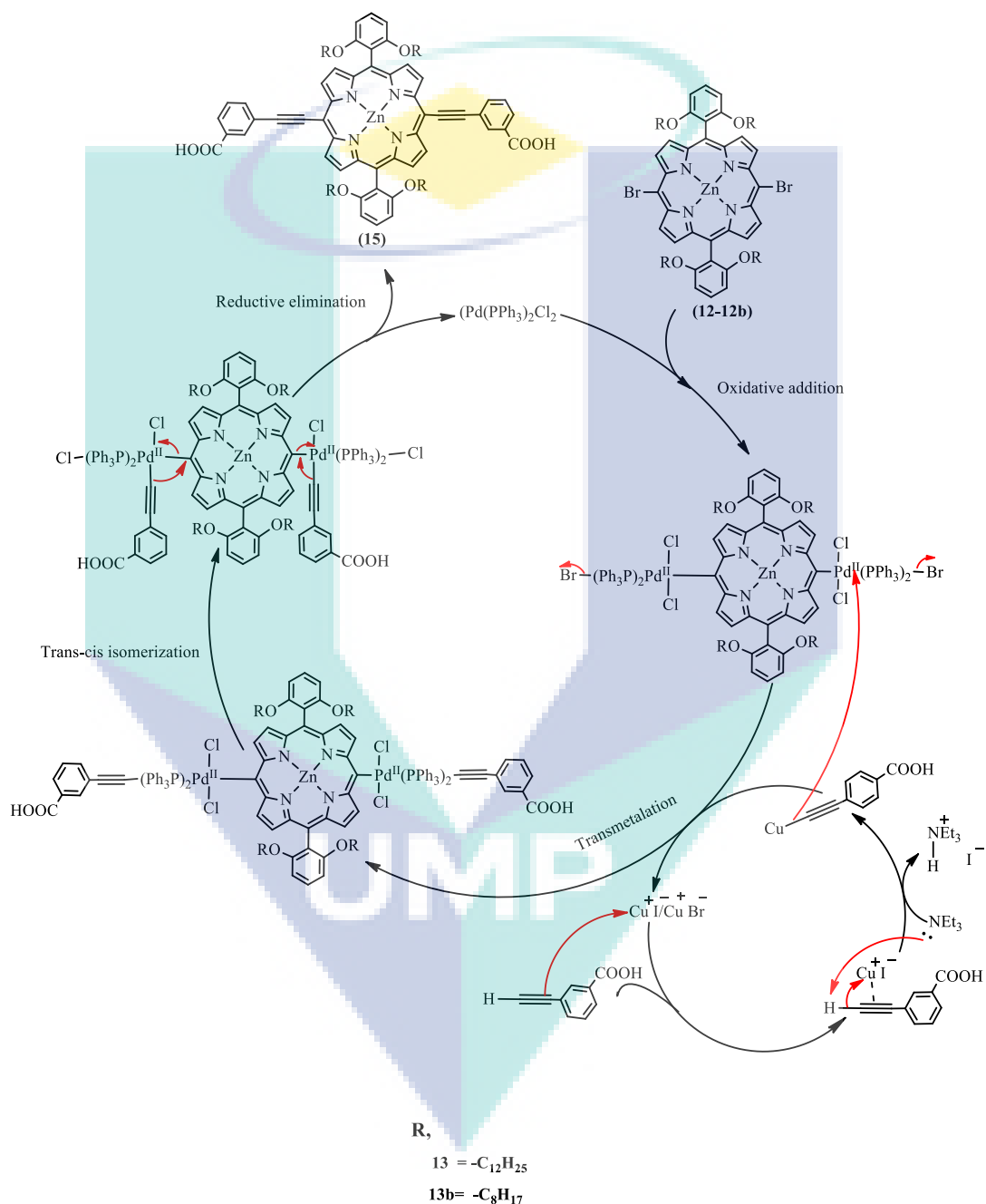


Figure 4.13 Reaction mechanism for RJ-C₁₂-MY₁

The RJ-C₁₂-MY₁ was characterized by ¹HNMR, ¹³CNMR and FTIR spectra (shown in Appendix F, Figures S41-S43). The ¹HNMR spectrum shows the additional signals at 8.44 ppm as singlet, 7.85 ppm as double doublet and 7.52 ppm as triplet indicating the presence of 3-carboxylphenyl group (Appendix F, Figure S41). The FTIR spectrum shows the characteristic band of the C≡C bond at around 2187 cm⁻¹ and carboxylic acid C–O band at around 1690 cm⁻¹ and O–H band at 3448 indicating the formation of the desired porphyrin (Appendix F, Figure S43). In ¹³CNMR spectra, the signal at 173.16 ppm corresponds to carboxylic acid groups and the signals at 99.59 ppm and 93.40 ppm correspond to the two carbons of the triple bond (Appendix F, Figure S42).

The synthesis of the meso-ethynyl-Zn(II)porphyrin coded as RJ-C₁₂-MY₂ was achieved by copper-free Sonogashira coupling reaction of Zn(II)porphyrin (14) with 2.5 equivalent of 4-iodobenzoic acid using Pd₂(dba)₃ as a catalyst, AsPh₃ and amine base (NEt₃) to form the desired RJ-C₁₂-MY₂ with 50% yield. The RJ-C₁₂-MY₂ was characterized by ¹HNMR, ¹³CNMR and FTIR spectra (shown in Appendix F, Figures S44-S46). The ¹HNMR spectrum shows the additional signals at 8.08 ppm as doublet and 7.90 ppm as doublet indicating the presence of 4-carboxylphenyl group (Appendix F, Figure S45). The FTIR spectrum shows the characteristic band of C≡C stretching at around 2192 cm⁻¹ and carboxylic acid C–O band stretching at 1725 cm⁻¹ and O–H stretching at 3422 cm⁻¹ indicating the formation of the desired porphyrin (Appendix F, Figure S44). In ¹³CNMR spectra, the signal at 174.61 ppm corresponds to the carboxylic acid groups (shown in Appendix F, Figure S46).

The synthesis of the meso-ethynyl-Zn(II)porphyrin coded as RJ-C₁₂-MY₃ was achieved by copper-free Sonogashira coupling reaction of Zn(II)porphyrin (14) with 1.5 equivalent of 4-iodobenzoic acid and 1.8 equivalent 2-cyano-3-(4-iodophenyl)acrylic acid (3) using Pd₂(dba)₃ as a catalyst, AsPh₃ and amine base (NEt₃) to afford the desired RJ-C₁₂-MY₃ with 40% yield. The RJ-C₁₂-MY₃ was characterized by ¹HNMR, ¹³CNMR and FTIR spectra (shown in Appendix F, Figures S47-S49). The ¹HNMR spectrum shows the additional signals at 8.20 ppm as singlet with unity integration, at 8.18 ppm as a doublet with four times integration, at 8.13 as doublet with two times integration and at 8.03 ppm as a doublet with two times integration confirming the presence of 4-carboxylphenyl and 2-

cyano-propenoic acid)phenyl groups. The splitting of doublet at 8.80 ppm into quartet signals indicate the presence of two non-equivalent pyrrolic β -CH protons (Appendix F, Figure S47). The FTIR spectrum shows the characteristic stretching of the $C\equiv N$ at around 2214 cm^{-1} , $C\equiv C$ stretching at around 2191 cm^{-1} and carboxylic acid $C-O$ and $O-H$ bands stretching at around 1625 cm^{-1} and 3453 cm^{-1} respectively, indicating the formation of the desired porphyrin (Appendix F, Figure S49). In ^{13}C NMR spectra, the signal at 174.63 ppm corresponds to the carboxylic acid carbons, signal at 148.80 ppm corresponds to $N\equiv C$ carbon and the signals at 99.86 ppm correspond to $C\equiv C$ carbons (shown in Appendix F, Figure S48).

The meso-ethynyl-Zn(II)porphyrin coded as RJ-C₈-MY₄ was synthesized by copper-free Sonogashira coupling reaction of Zn(II)porphyrin (14b) with 2-cyano-3-(4-iodophenyl)acrylic acid (3) using $\text{Pd}_2(\text{dba})_3$ as a catalyst, AsPh_3 and amine base (NEt_3) to afford the desired RJ-C₈-MY₄ with 40% yield. The RJ-C₈-MY₄ was characterized by ^1H NMR, ^{13}C NMR and FTIR spectra (shown Appendix F, Figures S50-S52). The ^1H NMR spectrum shows the additional signals at 8.07 ppm as singlet, 8.06 as doublet and 7.98 ppm as doublet indicating the presence of 2-cyano-propenoic acid)phenyl group (Appendix F, Figure S51). The FTIR spectrum shows the characteristic stretching of the $C\equiv N$ at around 2217 cm^{-1} , $C\equiv C$ stretching at around 2190 cm^{-1} and carboxylic acid $C-O$ and $O-H$ bands stretching at around 1635 cm^{-1} and 3446 cm^{-1} respectively, indicating the formation of desired porphyrin (Appendix F, Figure S50). In ^{13}C NMR spectra, the signal at 178.04 ppm corresponds to the carboxylic acid carbons, signal at 147.54 ppm corresponds to $N\equiv C$ carbons and the signals at 101.67 ppm correspond to $C\equiv C$ carbons (Appendix F, Figure S52). The detailed reaction mechanism for the meso-ethynyl-Zn(II)porphyrins (16-18) are shown in Figure 4.14.

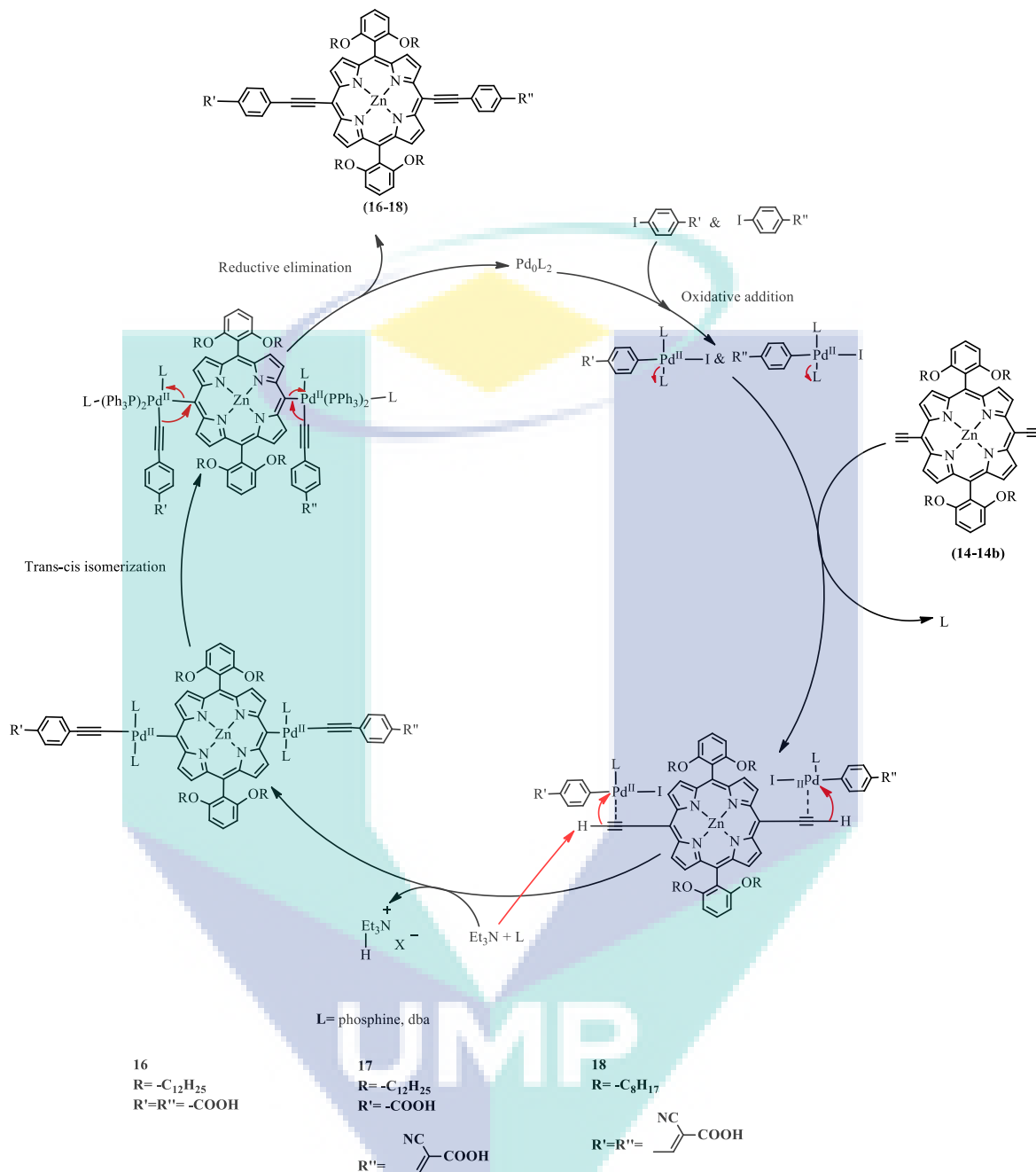


Figure 4.14 Reaction mechanism for RJ-C₁₂-MY₂, RJ-C₁₂-MY₃ and RJ-C₈-MY₄

4.3 Steady State Absorption Spectral Studies

The UV-Vis absorption spectroscopy of porphyrin compounds described in this dissertation is performed as a tool for characterization as well as for detailed studies of excitation states of the porphyrin complexes in order to understand their effect in photoacoustic signals. UV-Vis absorption spectroscopy is considered to be one of the long-

standing physical methods used for structure elucidation and quantitative analysis of compounds. The absorption spectra of porphyrins are characterized by their bands position variability and their intensity as a function of structure. As described previously, it is possible to tune up the properties of porphyrins by modification of peripheral substitutions/functional groups on their different reaction sites (meso and β -positions) and by various metal coordination, that makes the porphyrins ideal for their photo-physical studies. Typically, porphyrins contain one intense Soret band with $\epsilon > 1 \times 10^5 \text{ M}^{-1} \text{ cm}^{-1}$ in near-ultraviolet region at around 400 nm or above depending on peripheral substitution on porphyrin core, followed by four low-intensity Q-bands at higher wavelengths (600 nm or above) with $\epsilon > 1 \times 10^4 \text{ M}^{-1} \text{ cm}^{-1}$ in the visible region i.e., $Q_y(1,0)$, $Q_y(0,0)$, $Q_x(1,0)$ and $Q_x(0,0)$. Although possessing numerous common features, the absorption spectra of porphyrins show considerable variations that can reflect the changes in the molecular structure. The number and intensity of their absorption bands can provide strong clues to the substitution pattern on porphyrin core and whether they are metallated or not. Therefore, the electronic absorption spectra are important spectral tool to distinguish between the free-base porphyrins and their metallo-derivatives. The electronic transitions and the absorption bands are strongly influence by the nature of peripheral substitution pattern on a porphyrin core, the conjugating systems, the central metal ions, and their axially bound ligands (Binstead, Crossley & Hush, 1991; Seybold & Gouterman, 1969; Shelnett & Ortiz, 1985). Generally, metalloporphyrins exhibit more symmetrical structures (D_{4h}) than free-base porphyrins (D_{2h}) that causes the four Q-bands to collapse into two Q-bands spectra. Due to the presence of two imino-protons, the $Q_x(0,0)$ and $Q_y(0,0)$ bands in the free-base porphyrins are no longer degenerate. It has been observed in most of the case that the presence of peripheral substituents, conjugating groups on porphyrin core, central metal ions and their axially linked ligands induce a bathochromic shift in electronic absorption spectra compare to that of parent porphine. In order to demonstrate the effect of conjugating system with various electron donating and withdrawing groups on optoelectronic properties of free-base porphyrins and their metallo derivatives, mainly Zn(II)porphyrins, the optical properties of two series of meso-substituted porphyrins are well studied in this dissertation. The absorption spectra of first series of porphyrin complexes are displayed in Figure 4.15.

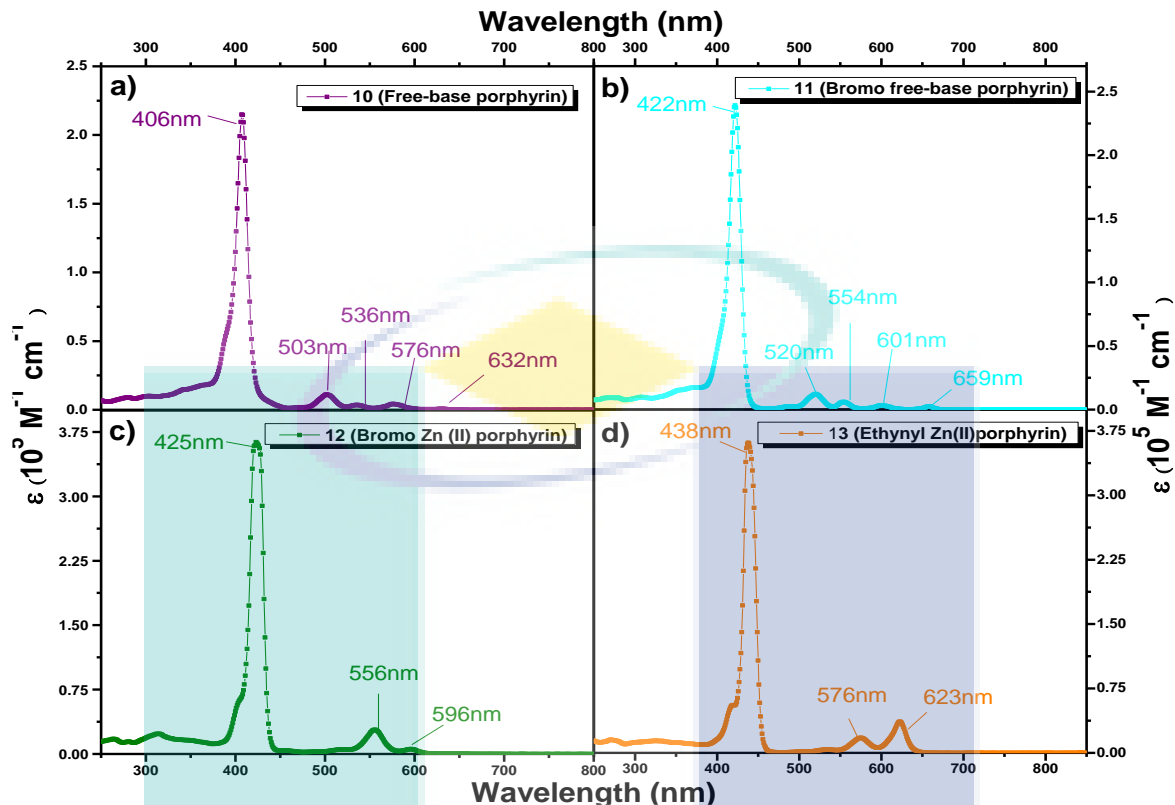


Figure 4.15 Absorption spectra of a) free-base porphyrin (10); b) bromo free-base porphyrin (11); c) bromo Zn(II)porphyrin (12); d) ethynyl-Zn(II)porphyrin (13)

From Figure 4.15, it is clearly notable that all the meso-substituted porphyrins (10-13) are shown the typical absorption spectra consisting of both Soret band and Q-bands absorption that indicate the presence of porphyrin macrocycles. Both Soret and Q bands absorption lead to singlet excited states and all bands are of $\pi \rightarrow \pi^*$ origin. Generally, the electronic absorption spectra of porphyrins do not exhibit $n \rightarrow \pi^*$ transitions because of the symmetry of the n-orbitals and anti-symmetry of the π -orbitals with respect to the plane of the porphyrin molecule. The Soret band arises because of an electronic ${}^1A_{1g} \rightarrow {}^1E'_u$ transition. In the case of substituted porphyrins, the splitting of E'_u into two closely energy states B'_{2u} and B'_{3u} is happened, resulting the reduce symmetry of the π -electron cloud. The electronic transitions to state E'_u (or B'_{2u} and B'_{3u}) are allowed, therefore the intensity of the Soret band is always high ($\epsilon \geq 10^5$). While the different types of Q-bands in the visible region of spectra represent the various vibrational energy states and are classified as I, II, III and IV based on their relative intensities. Bands I and III are due to quasi-forbidden electronic transitions and bands II and IV are of vibrational origin, that is they are vibronic overtone of bands II and

III, respectively. As clearly noted from Figure 4.16, the Q-band spectra of free-base porphyrins **10-11** are belong to etio-type porphyrins. The number of Q-bands depend on the symmetry of porphyrin complexes, i.e; free-base porphyrins **10-11** show four Q-bands while the Zn(II)porphyrins **12-13** show only two Q-bands because of degeneration of orbitals, causing to increase the symmetry (D_{2h} - D_{4h}). The observations of these transitions were interpreted in terms of Gouterman's four orbital models (as explained in detailed in section 2.4.1.2).

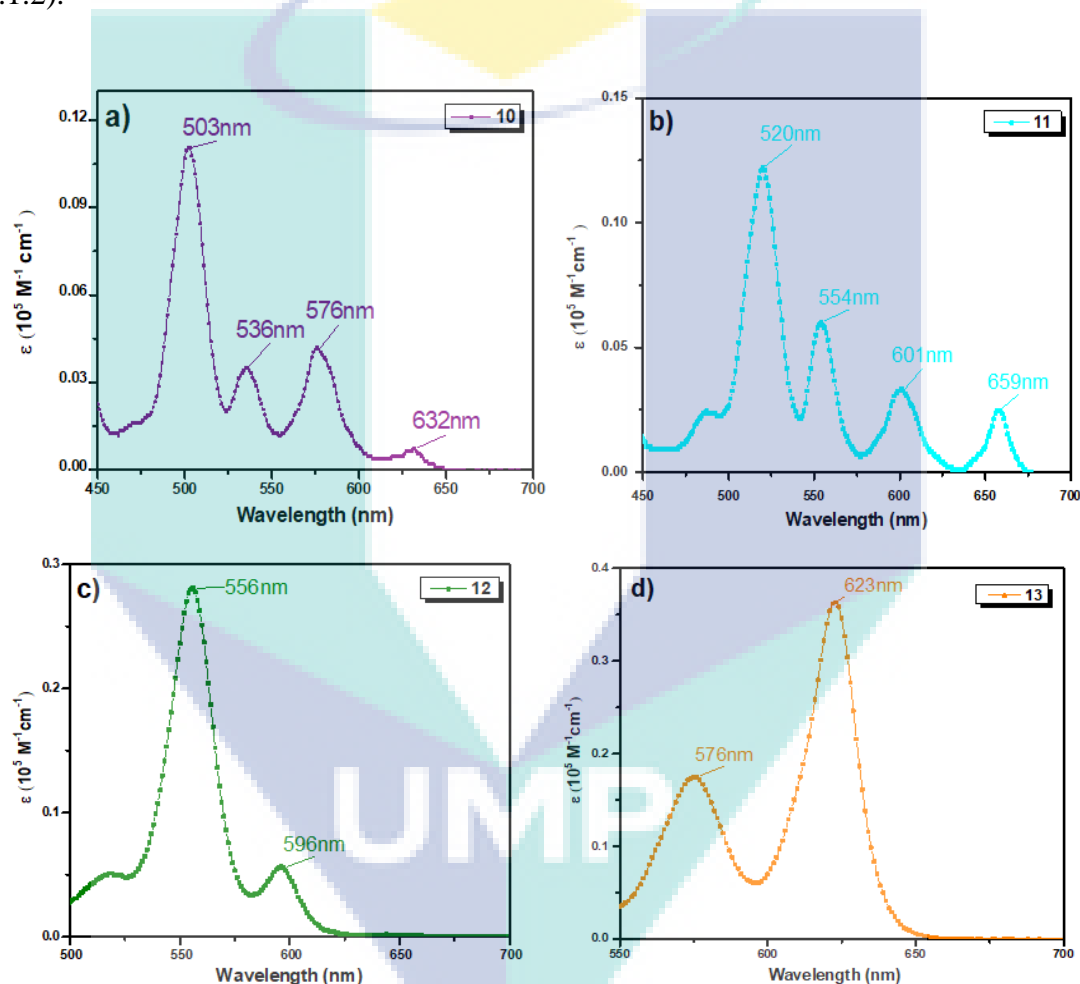


Figure 4.16 Q-band absorption spectra of a) free-base porphyrin (10); b) bromo free-base porphyrin (11); c) bromo Zn(II)porphyrin (12); d) ethynyl-Zn(II)porphyrin (13)

However, as observed from Figure 4.17 and Table 4.3, the position and intensities of absorption bands varied with various meso-substituted groups. Some trends can be distinguished, even with this limited number of examples. Different substitutions and metalation of porphyrin core have influence on the absorption, causing band shifts and minor

bands shape change. Although, all the groups in the meso- positions cause a red-shift as compared to parent porphine, which is usual for these and related porphyrinic systems (Aratani, Kim & Osuka, 2009; Holten, Bocian & Lindsey, 2002), the electron withdrawing groups have more influence on band shift compared to that of electron donating groups and similarly, metalation of porphyrin ring causes the more intense bands as compared to free-base porphyrins.

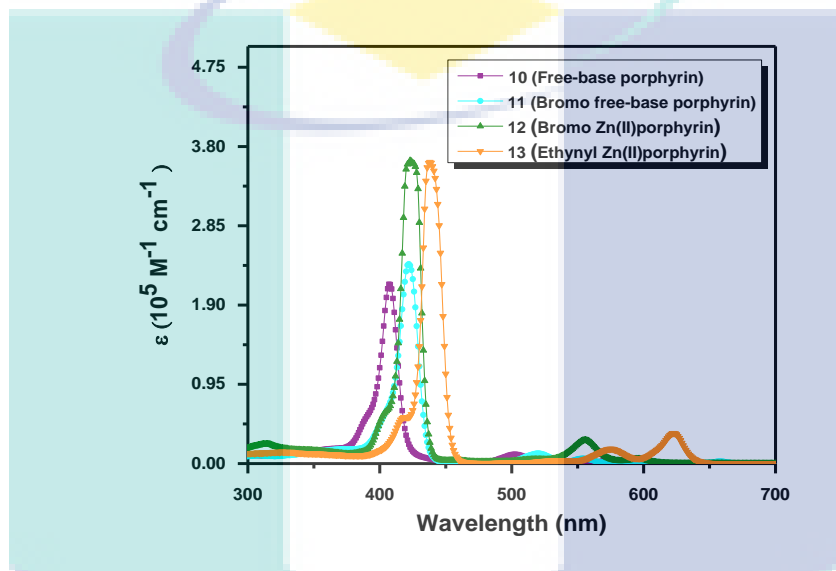


Figure 4.17 Comparison absorption spectra of free-base porphyrin (**10**), bromo free-base porphyrin (**11**), bromo Zn(II)porphyrin (**12**) and ethynyl-Zn(II)porphyrin (**13**)

It is apparent clearly from the absorption bands (shown in Table 4.2) that small band shifts in the absorption maxima of compound **10** occur as the result of electron donating alkoxy-phenyl groups, while the presence of highly polar halogen groups in complex **11** causes the redder shifted absorption bands. However, the values of ϵ_{\max} for complex **10** and **11** are influenced equally by both alkoxy-phenyl and halogen groups. For instant, the B-band of free-base porphyrin **10** occurs at 407 nm whereas for bromo free-base porphyrin, it appears at 422 nm in DCM. On the other hand, the four Q bands of **10** appear at 503 nm, 536 nm, 576 nm and 632 nm (Figure 4.16a), whereas for complex **11**, they appear at 520 nm, 554 nm, 601 nm and 659 nm. This shows that the meso-substituents on porphyrin core reflect in proportional increase in ϵ_{\max} and bathochromic shifts of absorption spectra.

Table 4.3 The absorbance spectral data for free-base and Zn(II)porphyrins

	SORET BAND				Q-BANDS					
	λ_{\max} (nm)	ϵ ($10^5 M^{-1} cm^{-1}$)	$Q_y(1,0)$ (nm)	ϵ ($10^5 M^{-1} cm^{-1}$)	$Q_y(0,0)$ (nm)	ϵ ($10^5 M^{-1} cm^{-1}$)	$Q_x(1,0)$ (nm)	ϵ ($10^5 M^{-1} cm^{-1}$)	$Q_x(0,0)$ (nm)	ϵ ($10^5 M^{-1} cm^{-1}$)
Porphine	396		490		521		563		634	
10 (free-base porphyrin)	407	2.1492	503	0.1105	536	0.0350	576	0.0422	632	0.0071
11 (bromo free-base porphyrin)	422	2.3916	520	0.1220	554	0.0599	601	0.0335	657	0.0244
12 (bromo Zn(II)porphyrin)	423	3.6309	556	0.2810	596	0.0564	-	-	-	-
13 (ethynyl- Zn(II)porphyrin)	438	3.6118	576	0.1748	623	0.3633	-	-	-	-
10b (free-base porphyrin)	408	2.0409	502	0.1236	535	0.0367	575	0.0442	632	0.0074
11b (bromo free-base porphyrin)	422	2.3064	520	0.1244	556	0.0598	600	0.0371	656	0.0266
12b (bromo Zn(II)porphyrin)	424	3.3800	556	0.1517	597	0.0298	-	-	-	-
13b (ethynyl- Zn(II)porphyrin)	438	3.6744	575	0.1346	623	0.2668	-	-	-	-

Generally, the absorption spectra of Zn(II)porphyrins show “normal” spectra because of Zn having closed-shell valence electrons orbital. The electronic absorption spectral data of Zn(II)porphyrin derivatives **12-13** in DCM are shown in the Table 4.2 and comparative spectra are displayed in Figure 4.17. When a comparative study of absorption spectral data of the bromo Zn(II)porphyrin **12** is done with respect to its respective free-base porphyrin, only a slight bathochromic shift in Q-bands region is observed, however; the variation in intensities of absorption bands are more pronounced due to incorporation of the metal ion in the porphyrin core. In order to investigate the influence of ethynyl groups on absorption spectra of porphyrin, it is more appropriate to compare the absorption bands shifts relative to their parent molecule, shown in Figure 4.17. Ethynyl groups are the known to have best surroundings for carbon-carbon bridging, which causes to overlap the π -orbitals of porphyrins core and the substituents (Screen et al., 2002). The addition of ethynyl groups causes the bathochromic shift of absorption i.e.; ethynyl-Zn(II)porphyrin **13** exhibits Soret band at 438 nm and Q-bands at 576 nm and 623 nm compared to that of Soret band at 423 nm and Q-bands 556 nm and 596 nm for complex **12**. This shift attribute to raising the a_{2u} orbital and lowering the e_g orbital, that causes a decrease in HOMO-LUMO gap (energy gap). The further the bathochromic shift of absorption bands, the greater the contraction of energy gap. This decrease in energy gap is the result of the change in electron density distribution on porphyrin core due to the extension of conjugation of porphyrin macrocycle. The extension of conjugation also influences the intensities of absorption especially on Q-bands. As observed from Figure 4.2, the Q(0,0) band in complex **13** has more intensified (ϵ value is higher), while the Q(1,0) band has relative less intensity due to increasing of conjugation compared to that of complex **12**. However, in the case of complex **12** and other porphyrins, the situation is on other way around i.e; the effect of substituents are more on the intensities (ϵ) of Q(1,0) bands as compared to Q(0,0) band.

The electronic absorption spectra of second series of synthesized porphyrin complexes included in this dissertation are shown in Figure 4.18. All the porphyrins complexes show the characteristic of typical porphyrin spectrum with red shifted absorption bands. Like that of first series porphyrin complexes, the free-base porphyrins **10b-11b** show the etio-type spectra and similarly, the Zn(II)porphyrins **12b-13b** show the reduction of Q-bands indicating the insertion of zinc ions into the porphyrin inner core,

as shown in Figure 4.19. Moreover, it is notable from the Figure 4.20 and Table 4.2 that a similar trend is found in comparison between electronic absorption properties of these second series of complexes as that of first series.

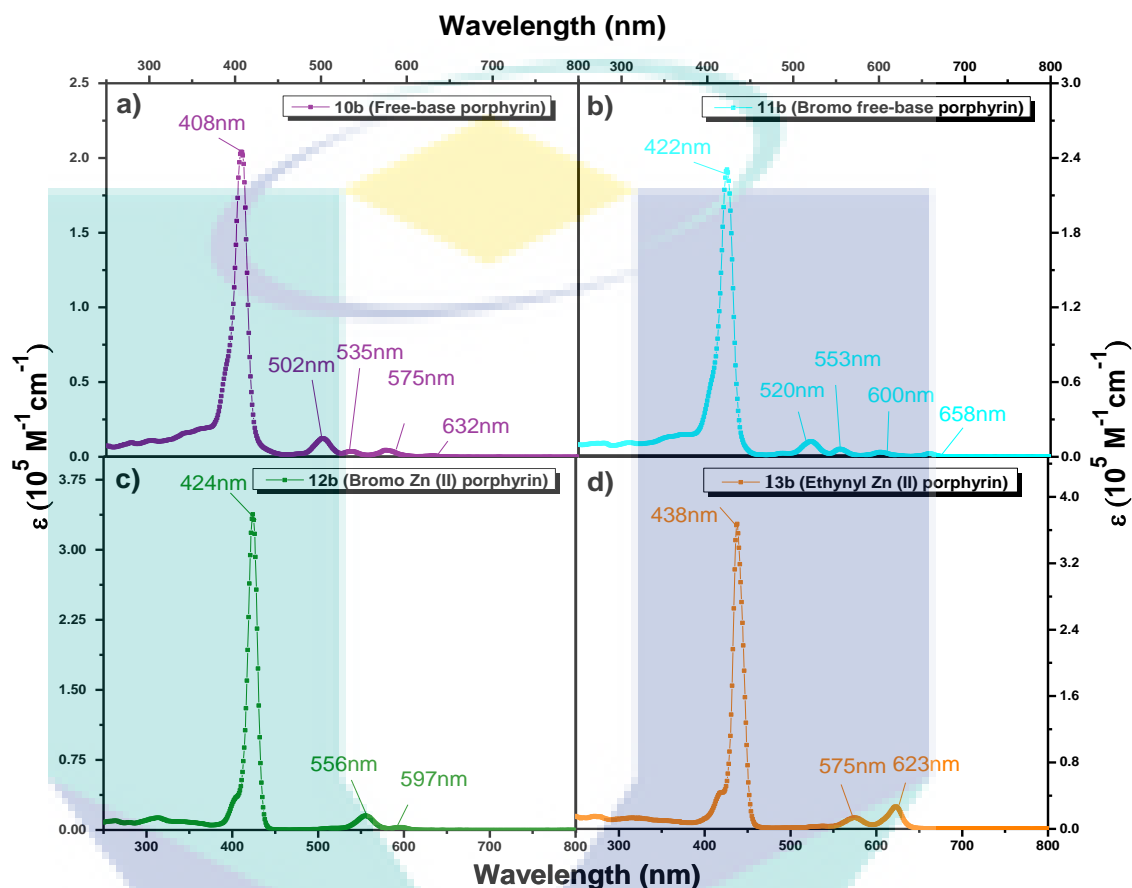
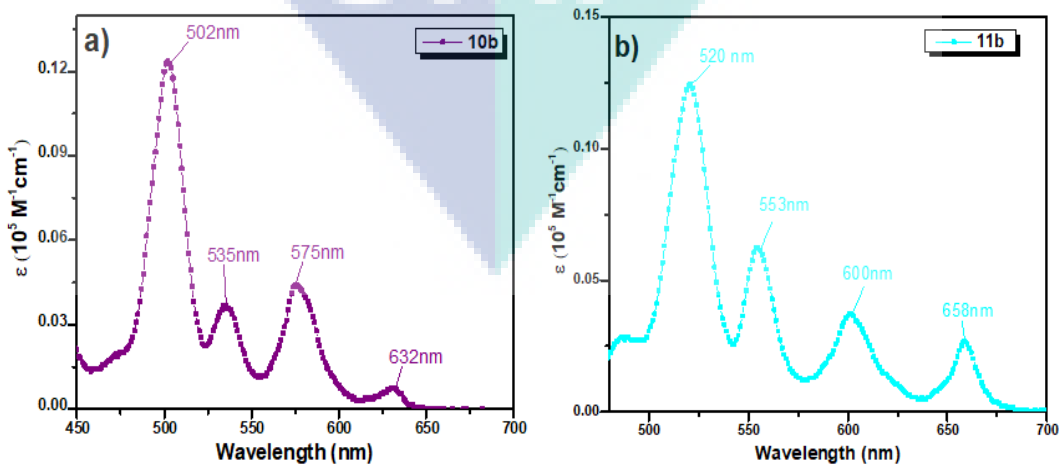


Figure 4.18 Absorption spectra of a) free-base porphyrin (10b); b) bromo free-base porphyrin (11b); c) bromo Zn(II)porphyrin (12b); d) ethynyl-Zn(II)porphyrin (13b)



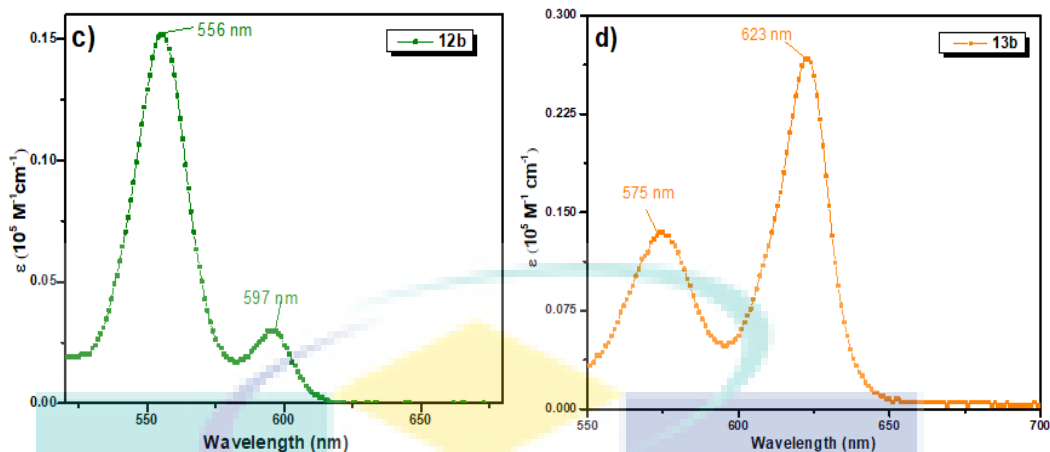


Figure 4.19 Q-band absorption spectra of a) free-base porphyrin (10b); b) bromo free-base porphyrin (11b); c) bromo Zn(II)porphyrin (12b); d) ethynyl-Zn(II)porphyrin (13b)

However, it is apparent from comparative study of first and second series of porphyrin complexes that the electronic absorption band shifts are not influenced by increasing the long chain of alkoxy groups on meso-substituted phenyl groups, as shown in Figure 4.21 and Table 4.2. Only slight change in intensities of absorption bands can be observed by changing the length of long chain alkoxy groups when compared with their respective porphyrins.

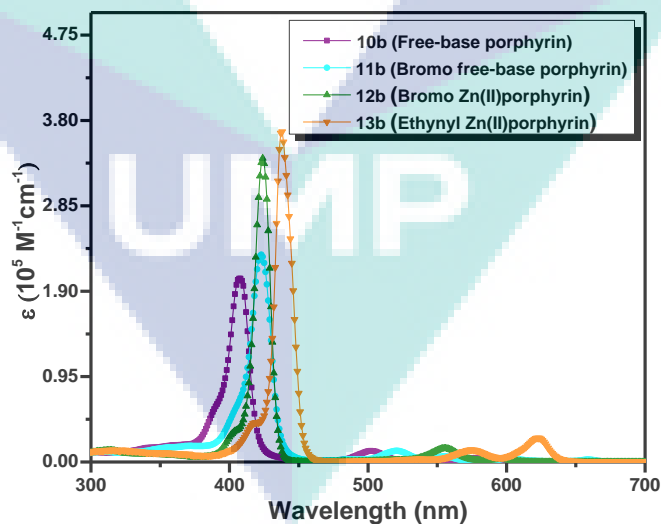


Figure 4.20 Comparison absorption spectra of free-base porphyrin (10b), bromo free-base porphyrin (11b), bromo Zn(II)porphyrin (12b) and ethynyl-Zn(II)porphyrin (13b)

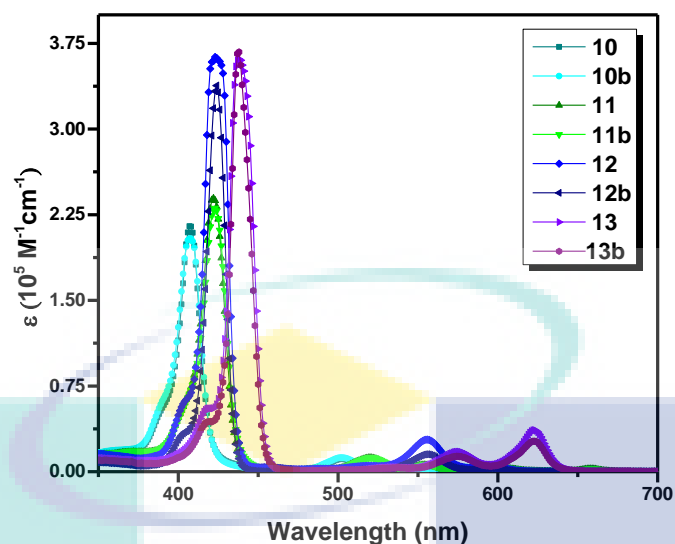


Figure 4.21 Comparison of absorption spectra between first & second series of porphyrins

The absorption spectra of four representative RJ-C_n-MY_m series of molecules in CH₃OH are shown in Figure 4.22. As observed from Figure 4.22, the absorption spectra of these newly synthesized meso-ethynyl-Zn(II)porphyrins (RJ-C₁₂-MY₁, RJ-C₁₂-MY₂, RJ-C₁₂-MY₃, & RJ-C₈-MY₄) are similar to that of typical porphyrin absorption spectrum, indicating the presence of porphyrin ring. The porphyrins of same kind have quite similar absorbance having characteristic π - π^* transition of delocalized core electrons. However, some information can be collected from these spectra to understand the optical properties of complexes for their photoacoustic applications. From the absorption spectra, the Soret bands are observed in the range 450-465 nm (at 453 nm for RJ-C₁₂-MY₁, 458 nm for RJ-C₁₂-MY₂, 461 nm for RJ-C₁₂-MY₃ & 464 nm for RJ-C₈-MY₄) assigned to the S₀-S₂ (LUMO+1) transitions. Similarly, the two Q-bands, designed as Q(0,0) having lower energy and their vibronic overtones Q(1,0) as explained in detailed in Chapter 2, are in the range 590-670 nm (at 605 & 660 nm for RJ-C₁₂-MY₁, 606 & 661 nm for RJ-C₁₂-MY₂, 617 & 667 nm for RJ-C₁₂-MY₃ & 593 & 670 nm for RJ-C₈-MY₄) assigned to the S₀-S₁ (LUMO) transitions. The Soret and Q bands however are significantly broadened as compared to relative parent porphyrin. It is notable that band shifting and band boarding are attributed to the extension of conjugation of porphyrin ring (more resonance) by ethynyl group linker as it is often observed with porphyrin of this kind (Aratani et al., 2009; Screen et al., 2002).

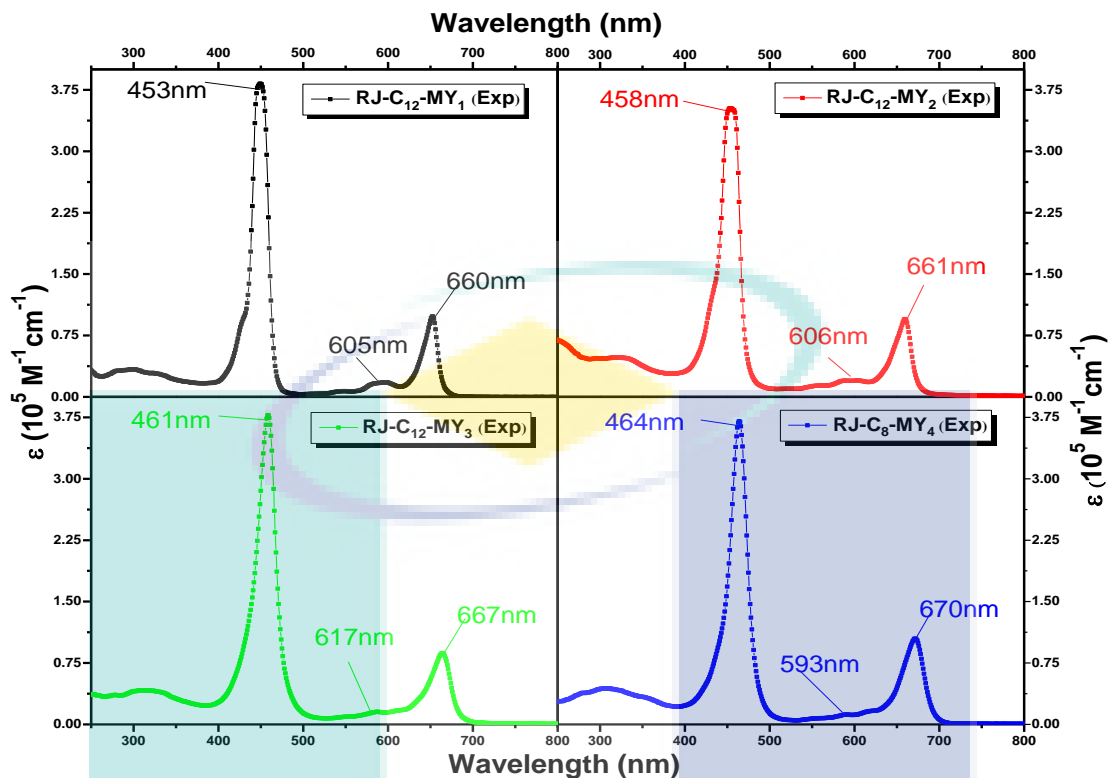


Figure 4.22 Absorption spectra of RJ-C₁₂-MY₁, RJ-C₁₂-MY₂, RJ-C₁₂-MY₃ and RJ-C₈-MY₄

A comparison of absorption spectra for RJ-C_n-MY_m series porphyrins is shown in Figure 4.23. It is notable that the RJ-C₁₂-MY₁ functionalized with (3-carboxylphenyl)ethynyl group at two meso-positions features an absorption spectrum with least absorption at 453 nm for Soret band and at 605 nm and 660 nm for Q(0,0) and Q(1,0) bands respectively relevant to that of other molecules of same series. The replacement of (4-carboxylphenyl)ethynyl groups in RJ-C₁₂-MY₂ compared to (3-carboxylphenyl)ethynyl group in RJ-C₁₂-MY₁ causes a significant impact on the absorption spectrum of RJ-C₁₂-MY₂ due to inductive effect, the carboxyl group at para position of meso-substituted phenyl groups contributes more π -electrons in conjugation, leading to the bathochromic shift of Soret band at 458 nm. There is a slight change in Q-bands (606 nm & 661 nm) compared to that of RJ-C₁₂-MY₁ are also observable. Similarly, in the case of RJ-C₁₂-MY₃ where one of the (4-carboxylphenyl)ethynyl groups are substituted with (4-(2-cyanopropenoic acid)phenyl)ethynyl unit at meso-position of porphyrin ring causes the more red-shifted absorption bands i.e.; Soret at 461 and Q-bands at 617 and 667 nm compared to that of RJ-C₁₂-MY₁ and RJ-C₁₂-MY₂. Moreover, the RJ-C₈-MY₄ functionalized with (4-(2-cyanopropenoic acid)phenyl)ethynyl units on

both meso-positions attributes the most red shifted absorption spectrum i.e.; Soret band at 464 nm and Q-bands at 593 and 672 nm. This indicate that the more effective electronic interaction between the porphyrin core and meso-substituents are happened if move from RJ-C₈-MY₄ to RJ-C₁₂-MY₁ due to extension of π -conjugation from RJ-C₁₂-MY₁ having (3-carboxylphenyl)ethynyl substituents on its meso-positions phenyl groups to RJ-C₈-MY₄ having (4-(2-cyanopropenoic acid)phenyl)ethynyl substituents on meso-phenyl groups.

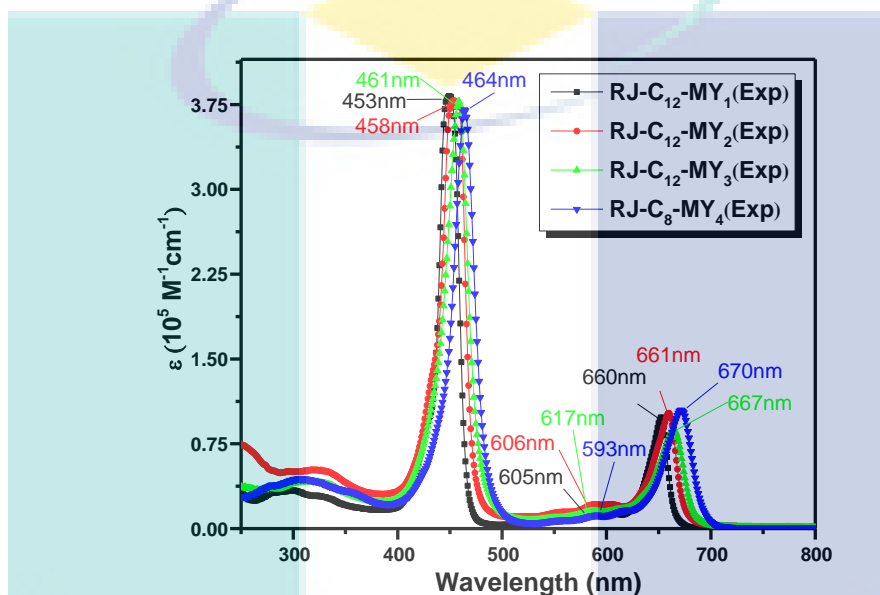


Figure 4.23 Comparison between absorption spectra of RJ-C₁₂-MY₁, RJ-C₁₂-MY₂, RJ-C₁₂-MY₃ and RJ-C₈-MY₄

Figure 4.24 shows the comparisons between RJ-C_n-MY_m series complexes with that of their respective parent compounds, which have been involved for their synthesis. It is clearly noticed from the Figure 4.24 that the bathochromic shifts of absorptions bands are correlated to the electron withdrawing ability of meso-substituents. As the electron withdrawing ability of meso-substituents increases, the absorption bands shift toward longer wavelength also increases. Similarly, more the extension of π -conjugation in the system, more the bathochromic shift of absorption bands. The absorption band shifts in RJ-C₁₂-MY₁ compound with respect to its parent compounds are in the order of RJ-C₁₂-MY₁ > 13 > 12 > 11 > 10. The similar behaviours have also been observed in case of RJ-C₁₂-MY₂ and RJ-C₁₂-MY₃. While, the absorption band shifts in RJ-C₈-MY₄ compound with respect to its parent compounds are in the order of RJ-C₈-MY₄ > 13b > 12b > 11b > 10b.

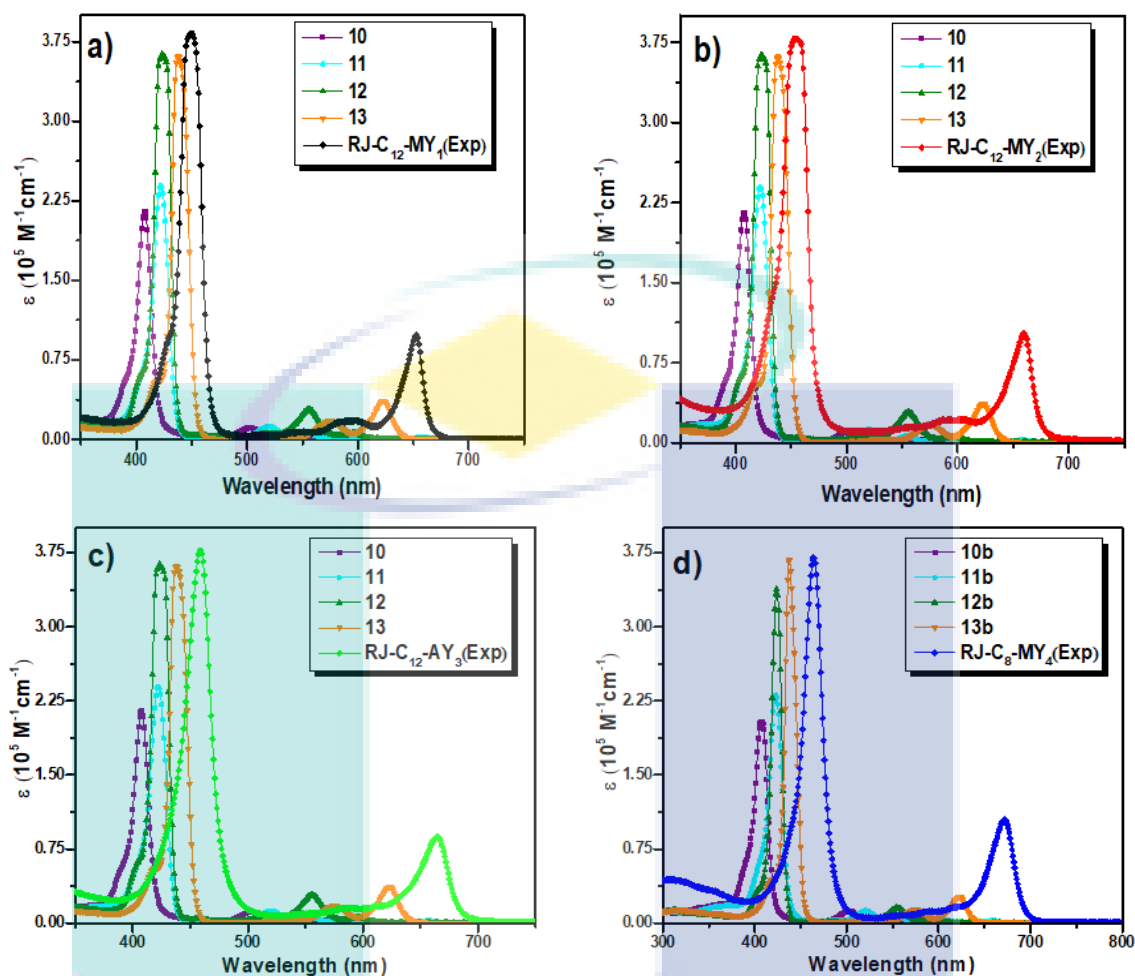


Figure 4.24 Comparison between absorption spectra of a) RJ-C₁₂-MY₁; b) RJ-C₁₂-MY₂; c) RJ-C₁₂-MY₃ and d) RJ-C₈-MY₄ with their respective parent compounds

4.3.1 Absorption Spectral Studies Relates to PAI Signals

The detailed optoelectronic properties for RJ-C_n-MY_m series complexes are important in order to investigate their influence on photoacoustic imaging. A most common assumption is that a molecular dye showing more absorption in NIR region must act as a suitable PA contrast agent because of deep penetration in tissue and having the same wavelength window as that of tissue (700 nm-1000 nm) (Xu & Wang, 2006). According to this respect, RJ-C₈-MY₄ could have more promising molecular photoacoustic properties among all the studied complexes. Contrary to this assumption, this study aims to demonstrate how a dye with less absorption in NIR region can display enhanced PA signals. As shown in Figure 4.23 and Table 4.3, it is noticed from the absorption spectra of RJ-C_n-MY_m series complexes that the molar absorption coefficients (ϵ) of the Soret band increases in the order of RJ-C₁₂-MY₁ > RJ-C₁₂-MY₂ > RJ-C₁₂-MY₃

> RJ-C₈-MY₄ and the lowest-energy Q-band increases in the order of RJ-C₈-MY₄ > RJ-C₁₂-MY₂ > RJ-C₁₂-MY₁ > RJ-C₁₂-MY₃. As observed the ϵ value of Soret band is higher for RJ-C₁₂-MY₁ as compared to that of other dyes indicating that the more electrons are excited from S₀-S₂ (HOMO to LUMO+2) in RJ-C₁₂-MY₁ dye, that may cause the rapid non-radiative decay of S₂ excited electrons to S₁ excited state by thermal expansion and thereby causing the higher photoacoustic signals. Hence the decreases of ϵ values of Soret band from RJ-C₁₂-MY₁ to RJ-C₈-MY₄ also decrease the photoacoustic signal in similar order of RJ-C₁₂-MY₁ > RJ-C₁₂-MY₂ > RJ-C₁₂-MY₃ > RJ-C₈-MY₄. A similar manner is also observed in Q-bands region with a little variation where the molar absorption coefficients decreases in order of RJ-C₈-MY₄ > RJ-C₁₂-MY₂ > RJ-C₁₂-MY₁ > RJ-C₁₂-MY₃ i.e; opposite to that of ϵ of the Soret bands, showing the more S₀-S₁ (HOMO to LUMO) electron transitions with less photoacoustic effect in RJ-C₈-MY₄ complex.

This can be further proved by calculating the discrete transition energies (oscillation strengths) of RJ-C_n-MY_m series complexes using DFT to time dependent domain (TD-DFT). Before calculating the transition energies states of these complexes, full geometry optimizations of RJ-C_n-MY_m series complexes in their singlet ground state were performed with DFT using the functionals B3LYP (Lee et al., 1988a) with the effective core potential and basis sets LANL2DZ (Hay & Wadt, 1985a; Hay & Wadt, 1985b) and 6-31G* (Hariharan & Pople, 1973) with the Gaussian 09 package. Upon completion of geometry optimization, it is vital to examine the global minimum energy structures by frequency calculations. The details of all these calculations have been explained in Chapter 3. More than 50 compounds have been studied in this dissertation using DFT, however the optimized structure of these four RJ-C_n-MY_m complexes are included in Chapter 3. The remaining other structures are included in Appendix D. All the calculations were done in the presence of implicit solvent effects using a self-consistent reaction-field (SCRF) model (Marten et al., 1996). The discrete transition energies calculations were carried out at linear response time-dependent DFT (LR-TD-DFT) theory for the first 50 excited singlet states by using the B3LYP functional (Lee et al., 1988a) with LANL2DZ and 6-31G* basis sets. However, the excitation energies obtained from B3LYP/LanL2DZ agreed well with experimental data compared to that of B3LYP/6-31G*, for example; the first transition of RJ-C₁₂-MY₂ measured experimentally is at 661 nm and is calculated at 647 nm (1.916 eV) by LanL2DZ. Based

on same computational protocol, the 6-31G* basic set gives this first transition at 631 nm (1.964 eV). All the energy calculations were done from ground state to singlet state excitation using IEF-PCM model (Tomasi et al., 2005) to study the effect of methanol as a solvent on absorption spectra because the experimental absorption spectra of all the RJ-C_n-MY_m series complexes were measured in methanol. The comparisons between experimentally measured absorption spectra in term of ϵ for RJ-C_n-MY_m series complexes with their calculated absorption spectra in term of oscillation strengths are shown in Figure 4.25. The wavelength of absorption bands along with their molar extinction coefficients and oscillation strengths for all the RJ-C_n-MY_m series complexes are displayed in Table 4.3. A noticeable difference in the oscillation strengths of RJ-C_n-MY_m series complexes can be observed. The oscillation strength in Soret region is higher as compare to Q bands region in RJ-C₁₂-MY₁ indicating the probability of electrons to excite from S₀-S₂ in Soret band region is more as compare to Q bands region. While the probability of electrons to excite from S₀-S₁ in Q bands region (oscillation strengths) is increasing in order of RJ-C₈-MY₄ > RJ-C₁₂-MY₃ > RJ-C₁₂-MY₂ > RJ-C₁₂-MY₁ showing that the complexes with more population of electrons in Soret band region compared to that of Q bands region have more strong PA signals. Moreover, HOMO-LUMO energy gaps for RJ-C_n-MY_m series complexes calculated by their optimized structures show the similar trend as explained previously i.e; by extending the π -conjugation of a system causes the decrease in energy gaps (E_g). It is worth noting that HOMO-LUMO gaps are decrease in order of RJ-C₁₂-MY₁ > RJ-C₁₂-MY₂ > RJ-C₁₂-MY₃ > RJ-C₈-MY₄ suggesting the higher energy gap causes the more non-radiative decay in RJ-C₁₂-MY₁ due to relatively long S₁ excitation state. Similarly, stability of LUMO may affect the photoacoustic properties of a molecule. As observed, more stable the LUMO on porphyrin core cause more high PA signals. In this regard, the LUMO for RJ-C₁₂-MY₁ are more stabilized on porphyrins core as shown in Figure 4.26. While the LUMO for RJ-C₁₂-MY₂ is comparatively destabilized by (4-carboxylphenyl)ethynyl groups causing the HOMO-LUMO gap reduction and red shifting of absorption spectra, however the PA signal intensity reduces due to the destabilization of LUMO. Similarly, in case of RJ-C₁₂-MY₃, (4-(2-cyanopropenoicacid)phenyl)ethynyl group causes the more destabilization of LUMO level producing less intensive PA signals. Like wisely in the case of RJ-C₈-MY₄ where two (4-(2-cyanopropenoicacid)phenyl)ethynyl groups are responsible for lowering the PA signals due to more destabilized LUMO level.

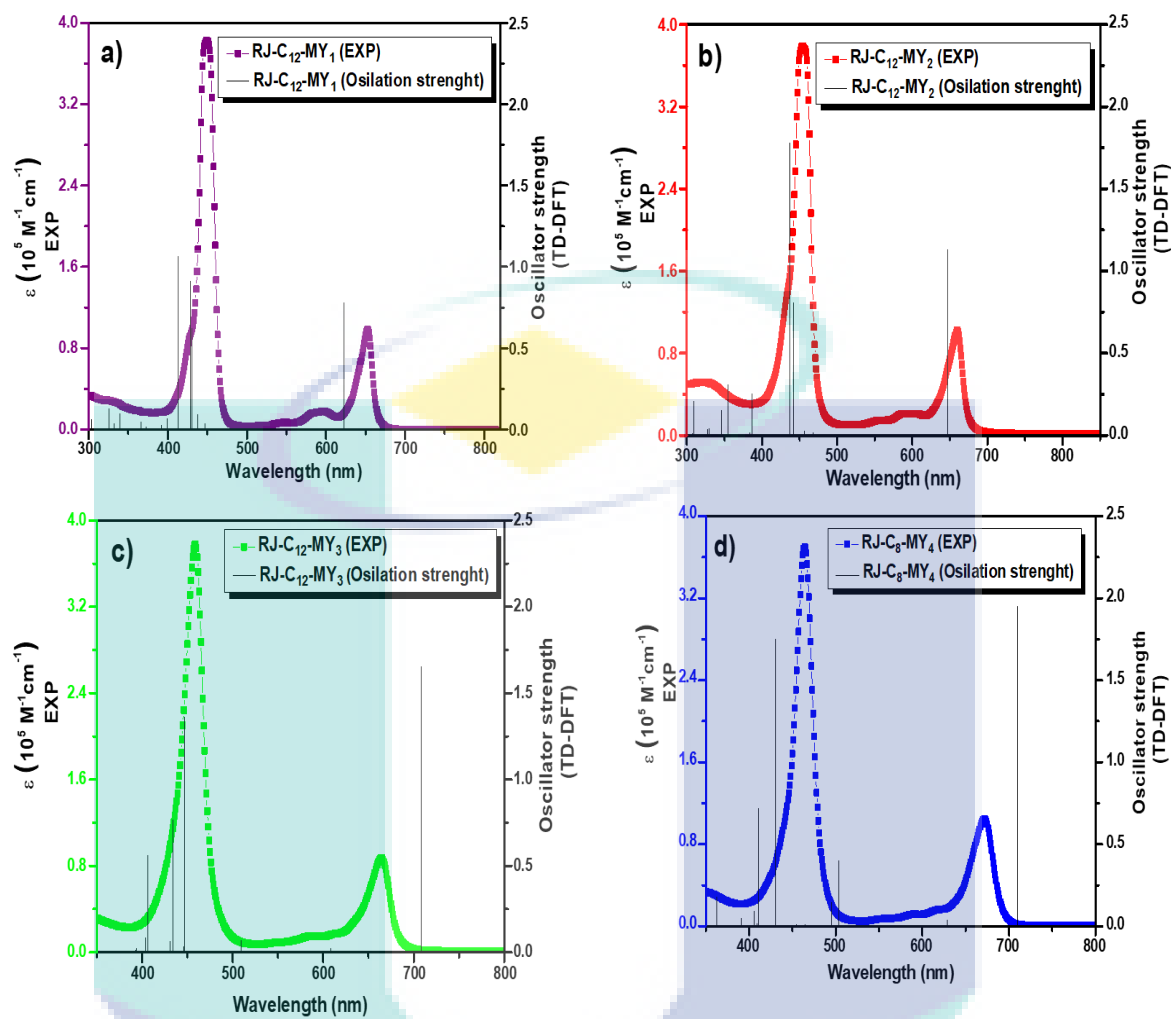


Figure 4.25 Comparison between experimental and calculated absorption spectra of a) RJ-C₁₂-MY₁; b) RJ-C₁₂-MY₂; c) RJ-C₁₂-MY₃ and d) RJ-C₈-MY₄

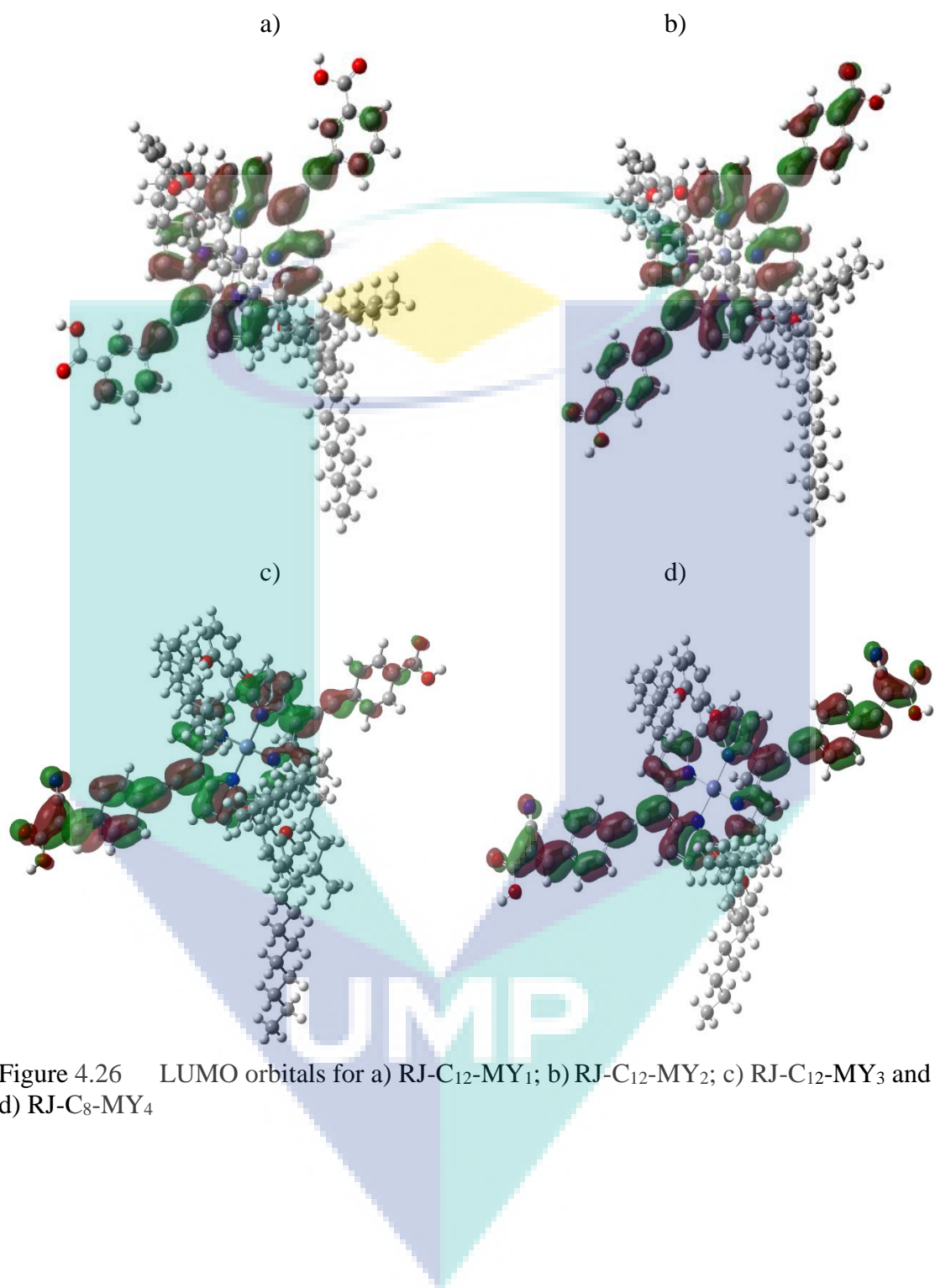


Figure 4.26 LUMO orbitals for a) RJ-C₁₂-MY₁; b) RJ-C₁₂-MY₂; c) RJ-C₁₂-MY₃ and d) RJ-C₈-MY₄

Table 4.4 Experimental and calculated absorption bands (λ) alone with their molar extinction coefficients (ϵ) for RJ-C_n-MY_m series complexes

	RJ-C ₁₂ -MY ₁	RJ-C ₁₂ -MY ₂	RJ-C ₁₂ -MY ₃	RJ-C ₈ -MY ₄	
Experimental	$\lambda\{B(0,0)\}/nm$	453	458	461	464
	$\epsilon\{B(0,0)\}/10^5 M^{-1} cm^{-1}$	382635.7	378299.99	377540.10	370355.00
	$\lambda\{Q(0,0)\}/nm$	660	661	667	670
	$\epsilon\{Q(0,0)\}/10^4 M^{-1} cm^{-1}$	98139.53	101999.98	87108.97	11775.39
	$\lambda\{Q(1,0)\}/nm$	605	606	617	593
	$\epsilon\{Q(1,0)\}/10^4 M^{-1} cm^{-1}$	17829.46	4409.93	15060.89	104649.05
	Optical Energy gap (E_g)	1.88	1.87	1.86	1.85
Calculated	$\lambda_{gau}\{B(0,0)\}/nm$	423.4	438.8	442.98	432.49
	$\epsilon_{gau}\{B(0,0)\}/10^5 M^{-1} cm^{-1}$	312599.37	346763.82	195339.31	199258.21
	$f\{B(0,0)\}$	1.0656	1.7789	1.3645	1.7521
	$\lambda_{gau}\{Q(0,0)\}/nm$	622.62	647.4	704.14	708.58
	$\epsilon_{gau}\{Q(0,0)\}/10^4 M^{-1} cm^{-1}$	104814.55	152678.85	148666.24	175875.20
	$f\{Q(0,0)\}$	0.7772	1.132	1.6518	1.9488
	$\lambda_{gau}\{Q(1,0)\}/nm$	578.95	585.8	604.3	628.6
	$\epsilon_{gau}\{Q(1,0)\}/10^4 M^{-1} cm^{-1}$	21700.69	10050.65	14448.64	44053.10
	$f\{Q(1,0)\}$	0.0003	0.0037	0.0215	0.0355
	$E_{g(gau)}$	2.32	2.22	2.00	1.98

4.4 Steady State Emission Spectral Studies

An important characteristic of porphyrins and their metallo-derivatives is their emission spectra. Although, the emission properties of porphyrin complexes are not as uniform as that of their absorption properties, they show some regularity. One of the primary purpose of emission spectra measurements for synthesized porphyrin complexes is to investigate their structural behaviors, the changes in their systems during transitions and to measure the fluorescence quantum yields (Φ_f). By measuring the emission spectra of the complexes at particular excitation wavelengths, it is possible to observe the ability of the complexes to upconvert light and the quenching properties that the system displayed. Fluorescence assumes in the molecules having aromaticity or containing multiple conjugated double bonds that show high degree of resonance stability. The porphyrin compounds fit well in these definitions. They contain the delocalised π -electrons that can place in low-lying excited singlet states. Substituents on porphyrin core strongly influence the fluorescence spectra which involve the delocalization of the π -electrons by increasing the probability of transitions between the low-lying singlet excited states and the ground state, however; mostly electron withdrawing groups cause to quench the fluorescence. Similarly, the addition of bulky substituents on porphyrin core that cause planar symmetry to become non-planar also quench the fluorescence (Willard, Merritt Jr, Dean & Settle Jr, 1988). The emission spectra of porphyrins provide an important information regarding the excited singlet state properties. The Φ_f and lifetime calculation of metalloporphyrins found to quench by increasing spin-orbital coupling constant of the metal ions. This heavy atoms effects cause to decrease the Φ_f and increase the intersystem crossing rate constant (Harriman, 1981; Seybold & Gouterman, 1969).

Generally, the steady-state emission spectra of the porphyrin complexes exhibit two types of bands. One band is observed at 400–460 nm corresponding to the Soret band emission (S_2-S_0), and the other type is at 550–700 nm corresponding to Q band emission (S_1-S_0). When observing the S_2 emission the porphyrin dyes are excited directly to the S_2 state using a wavelength of ~406 nm and for S_1 emission they are excited at or above 550 nm depending on their absorbed wavelength regions. However, in this dissertation, the focus is to investigate Q-bands emission spectra only because usually very low

fluorescence from the S_2 state is observed, although the Soret band exhibit the strongest absorption corresponding to S_0 to S_2 excitation. The non-radiative decay from S_2 to the S_1 state is more favorable pathway and takes place in approximately 10^{-3} - 10^{-4} nanoseconds. However, if S_2 - S_0 fluorescence appears as a weak emission band. The fluorescence from the S_2 state can happen only when the S_2 and S_1 excited singlet states energy gap is large enough as explained by energy gap law (Appendix G), the energy surfaces of two excited singlet states are parallel to each other and the intersystem crossing to triplet states are slow. The parallel nature of the energy surfaces of S_1 and S_2 excited singlet state is particularly important as it delay the rapid non-radiative decay of the S_2 state due to conical intersection of the S_2 and S_1 surfaces (Gouterman, Rentzepis & Straub, 1986).

In the current investigation, steady state fluorescence spectra for first series porphyrin complexes are shown in Figure 4.27. The free-base porphyrin complexes **10** excited at 600 nm, exhibits two emission bands at 645 nm and 697 nm that correspond to $Q(0,0)$ and $Q(1,0)$ transitions respectively. The intensity of the $Q(0,0)$ higher than the $Q(1,0)$ transition. However, the relative intensities of these bands significantly depend on the nature of the meso-substituents on porphyrin core and that of central metal ion. In general, electron-donating substitution in meso-position leads to red shift of emission spectra and blue shift if the meso-substituents are electron withdrawing groups. As it is noticed from the Figure 4.27, the presence of bromo groups in bromo free-base porphyrin **11** cause the blue shift and broadening of emission spectra as compared to that of its respective parent compound **10**. This blue shift in emission spectra may due to the presence of heavy atoms on external substituents (particularly halogens) creating a similar heavy atom effect. It is also observable that the external heavy atom substituent also causes the splitting of $Q(0,0)$ band. The presence of additional peaks in complex **11** could be a verification of increased aggregation (Scolaro, Romeo, Castriciano & Micali, 2005) making it possible for the population of other vibrational states to occur causing the presence of the additional peaks. The further blue emission spectra are observed in bromo Zn(II)porphyrin **12** upon complexation of porphyrin core with Zn(II) ions due to the interaction of the metal and the aromatic system of the porphyrin core. Furthermore, the replacement of bromo groups with conjugating ethynyl systems in ethynyl-Zn(II)porphyrin **13** shows the prominent red shifts in both $Q(0,0)$ and $Q(1,0)$ emission bands. This red shift bands could be due to the presence of conjugating system.

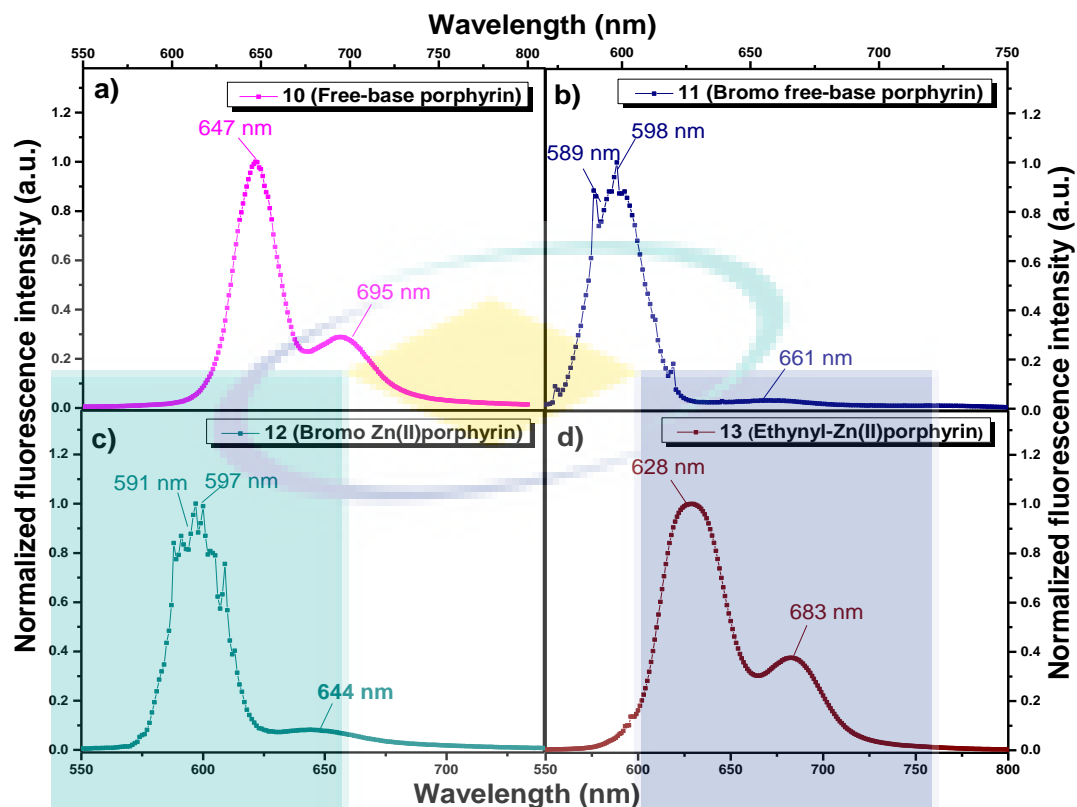


Figure 4.27 Emission spectra of a) free-base porphyrin (10); b) bromo free-base porphyrin (11); c) bromo Zn(II)porphyrin (12); d) ethynyl-Zn(II)porphyrin (13)

As shown in Figure 4.28, the fluorescence emission spectra of first series complexes are in agreement with their absorption spectra and are reverse mirror images of their respective absorption spectra. This implies that the fluorescence of first series porphyrin do not originate from some impurities. Stokes shift for first series of complexes are calculated using an equation 2.2 shown in section 2.4.1.3 in chapter 2 and their values are shown in Table 4.4. The stokes shift of porphyrin complexes is the energy gap between the emission $Q(0,0)$ band and the absorbance $Q_x(0,0)$ band providing the information on their excited states. The small values of stokes shift provide the evidence for minor differences in the geometry of porphyrin macrocycle in the ground and excited states. While, large stokes shift values are expected in the case of the reverse mirror image spectra (Wu, Gan & Leung, 1991). As show in

Table 4.5, stokes shift values are in the range of $69\text{-}1051\text{ cm}^{-1}$, indicating the reverse mirror image spectra of the first series porphyrins. The stokes shift for first series of porphyrins decrease in the order of $11 < 12 < 13 < 10$. The lower stoke shift of **11** is in

agreement with effect of electron withdrawing substituents (bromo) on porphyrin core. The higher value of stoke shift for **12** in comparison with that of **11** is expected due to the interaction of the metal and the porphyrin aromatic system. Moreover, complex **10** exhibits higher stoke shift value as compare to other complex of same series because of the electron donating ability of alkoxy-groups.

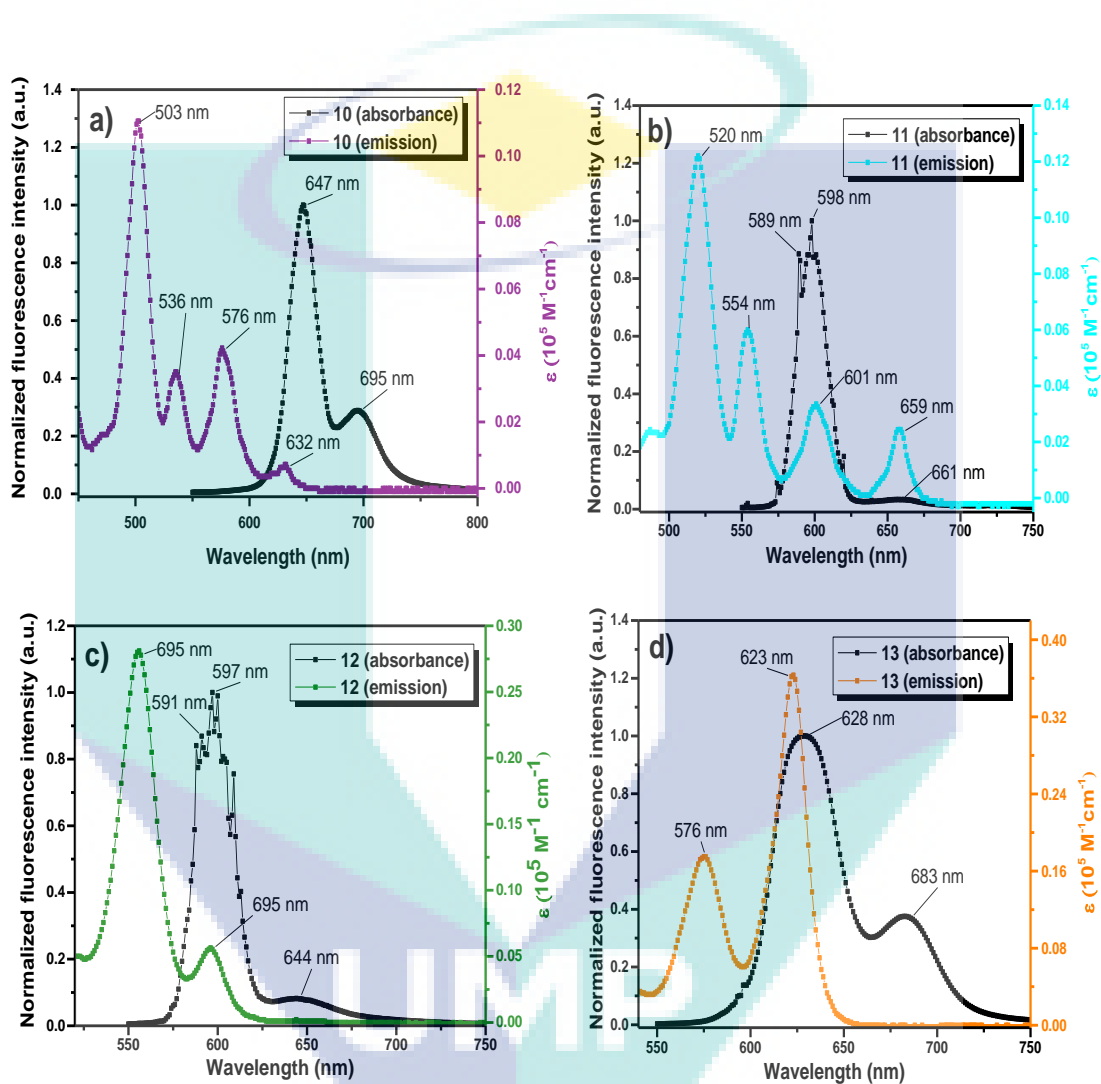


Figure 4.28 Comparison between absorption and emission spectra of a) free-base porphyrin (**10**); b) bromo free-base porphyrin (**11**); c) bromo Zn(II)porphyrin (**12**); and d) ethynyl-Zn(II)porphyrin (**13**)

From the Figure 4.29, it is noteworthy that the intensities of emission spectra are largely influenced by electron donating groups and withdrawing groups that directly linked to meso-position of porphyrin core. As shown from the Figure 4.29, the insertion of heavy atoms on meso-position cause the quenching of fluorescence emission spectra. This quenching may attribute by increasing the intersystem crossing rate from the S_1 excited state to the T_1 excited state and thereby increasing the phosphorescence emission.

However, the heavy atom effect can also increase the rate of non-radiative decay from T₁ excited state to S₀ ground state. As show in Figure 4.29 onset, the complexes **11** and **12** are quenched by bromo-substituents and Zn central metal ion respectively. On the other hand, the presence of ethynyl substituents on meso-positions on porphyrin core causes to increase the intensity of emission spectrum dramatically, indicating the increase in fluorescence of complex **13** by the addition of conjugating ethynyl system.

Table 4.5 The fluorescence spectral data for first series porphyrin complexes

		10	11	12	13
Absorbance	Q(0,0) (λ/nm)	632	657	596	623
	Q(1,0) (λ/nm)	576	601	556	576
	Splitting (Δv ₁ /cm ⁻¹) ^a	1538.33	1418.24	1207.09	1309.75
Emission	Q(0,0) (λ/nm)	677	660	625	658
	Q(1,0) (λ/nm)	725	681	674	613
	Splitting (Δv ₂ /cm ⁻¹) ^b	977.95	467.23	1163.2	1172.32
	Δv ₃ = Δv ₁ -Δv ₂ (cm ⁻¹)	540.38	1885.47	43.89	137.43
Stokes shift (Δv/cm ⁻¹)		1051.73	69.18	778.52	853.79

^aEnergy difference between the absorbance Q(1,0) and Q(0,0) bands. ^bEnergy differences between the emission Q(0,0) and Q(1,0) bands.

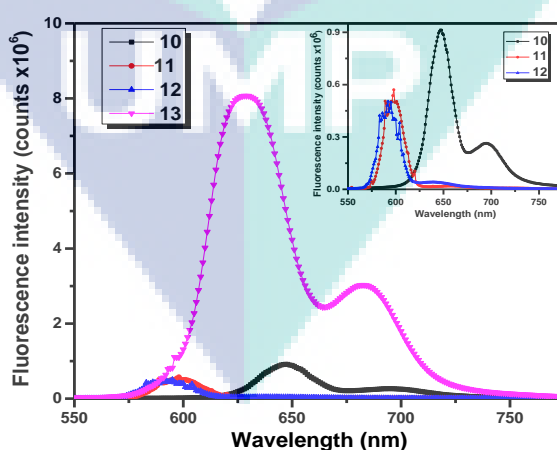


Figure 4.29 Comparison of emission spectra of free-base porphyrin (10), bromo free-base porphyrin (11), bromo Zn(II)porphyrin (12) and ethynyl-Zn(II)porphyrin (13)

The emission spectra of second series of porphyrin complexes are shown in Figure 4.30. All the complexes show the same characteristics as observed in first series complexes. Like that of first series porphyrins, the Q bands exhibited two fluorescence bands, Q(0,0) band (located at the shorter wavelength) with emission ranging from 628 nm–647 nm and Q(1,0) band (located at longer wavelength) with emission ranging from 664 nm – 695 nm, with each porphyrin revealing different emission intensities. Usually, the Q(0,0) band has larger relative intensity than the Q(1-0) band. The occurrence of Q(1,0) band is expected due to the “forbidden 0–0 dipole transition” as stated by Franck-Condon principle (Valeur & Berberan-Santos, 2012).

Figure 4.31 shows the fluorescence emission spectra of second series complexes along with their absorption spectra. It is noticeable that as like that of first series of porphyrin complexes, the second series complexes are also in well agreement and are reserve mirror images of their respective absorption spectra. The stokes shift values for second series of complexes are shown in Table 4.5. Same trend in stokes shift values of second series of complexes are observed as in first series complexes, i.e., stokes shift values decrease in the order of **11b<12b<13b<10b**.

Table 4.6 The fluorescence spectral data for second series porphyrin complexes

		10b	11b	12b	13b
Absorbance	Q(0,0) (λ/nm)	632	657	596	623
	Q(1,0) (λ/nm)	576	601	556	576
	Splitting (Δv ₁ /cm ⁻¹) ^a	1538.33	1418.24	1207.09	1309.75
Emission	Q(0,0) (λ/nm)	677	660	625	658
	Q(1,0) (λ/nm)	725	681	674	613
	Splitting (Δv ₂ /cm ⁻¹) ^b	977.95	467.23	1163.2	1172.32
	Δv ₃ = Δv ₁ -Δv ₂ (cm ⁻¹)	540.38	1885.47	43.89	137.43
	Stokes shift (Δv/cm ⁻¹)	1051.73	69.18	778.52	853.79

^aEnergy difference between the absorbance Q(1,0) and Q(0,0) bands. ^bEnergy differences between the emission Q(0,0) and Q(1,0) bands.

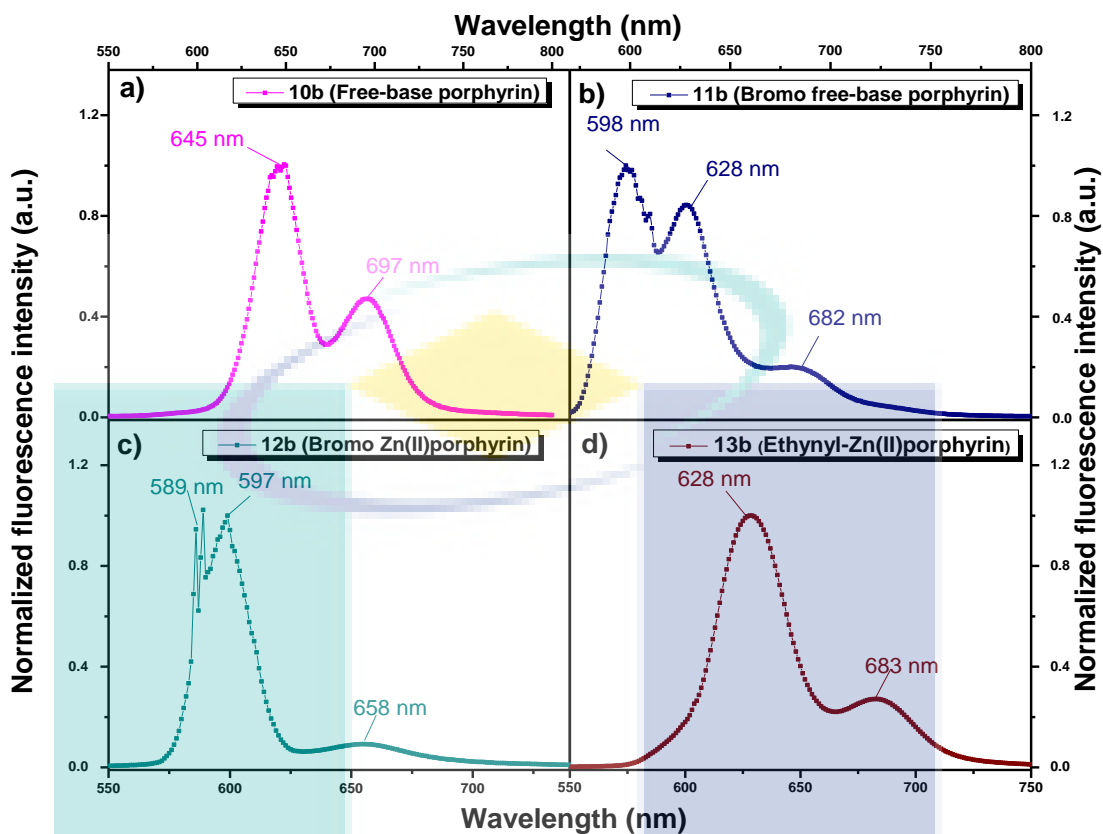
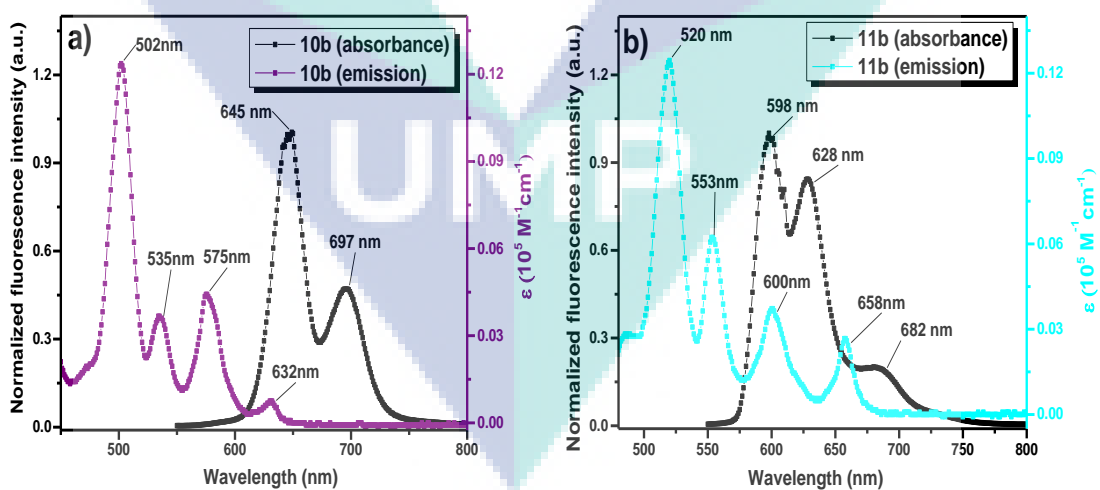


Figure 4.30 Emission spectra of a) free-base porphyrin (10b); b) bromo free-base porphyrin (11b); c) bromo Zn(II)porphyrin (12b); d) ethynyl-Zn(II)porphyrin (13b)



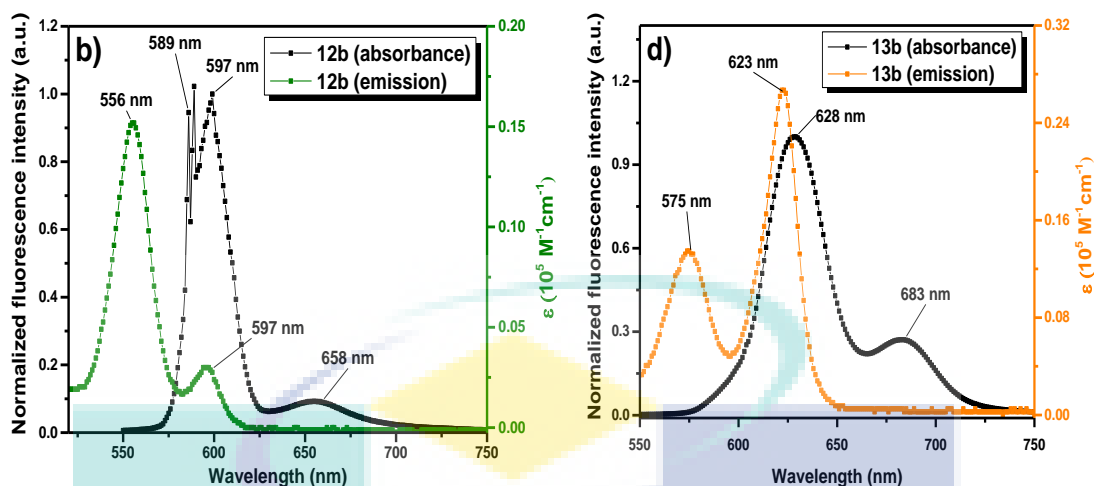


Figure 4.31 Comparison absorption and emission spectra of a) free-base porphyrin (10b); b) bromo free-base porphyrin (11b); c) bromo Zn(II)porphyrin (12b); and d) ethynyl-Zn(II)porphyrin (13b)

Figure 4.32 shows a comparison between emission spectra for all the complexes that belong to second series. A similar trend on intensities of emission spectra by various electron donating groups and withdrawing groups are noticeable as that of first series complexes. It is noteworthy that there is not much influence on the emission properties of porphyrin complexes by changing the length of alkoxy group chain.

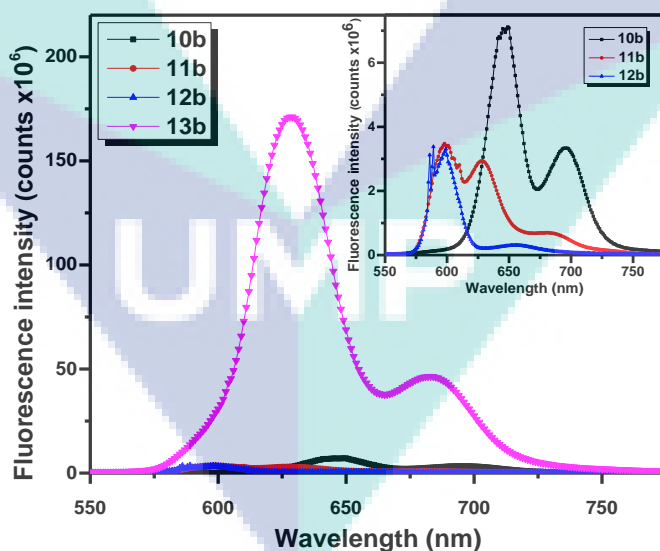


Figure 4.32 Comparison of emission spectra of free-base porphyrin (10b), bromo free-base porphyrin (11b), bromo Zn(II)porphyrin (12b) and ethynyl-Zn(II)porphyrin (13b)

The fluorescence emission spectra for RJ-C_n-MY_m series complexes are displayed in Figure 4.33 and data are tabulated in Table 4.6. All the metalloporphyrins exhibited

two fluorescence bands (Q(0,0) and Q(1,0)) with emission ranging from 675 nm–755 nm. However, the relative intensities for Q(1,0) bands are decreased for all the complexes, indicating the differences in electrons population of excited states, as shown in Figure 4.33. This decrease in Q(1,0) band could also be correlated with the increase in conjugation of the system. The increase in conjugation results in broadening of Q(0,0) emission band to the point where there is no longer identification Q(1,0) band. As noticed from the Figure 4.33, all the RJ-C_n-MY_m series complexes have red shifted broad emission spectra with low intensity of Q(1,0) bands relative to that of Q(0,0) bands.

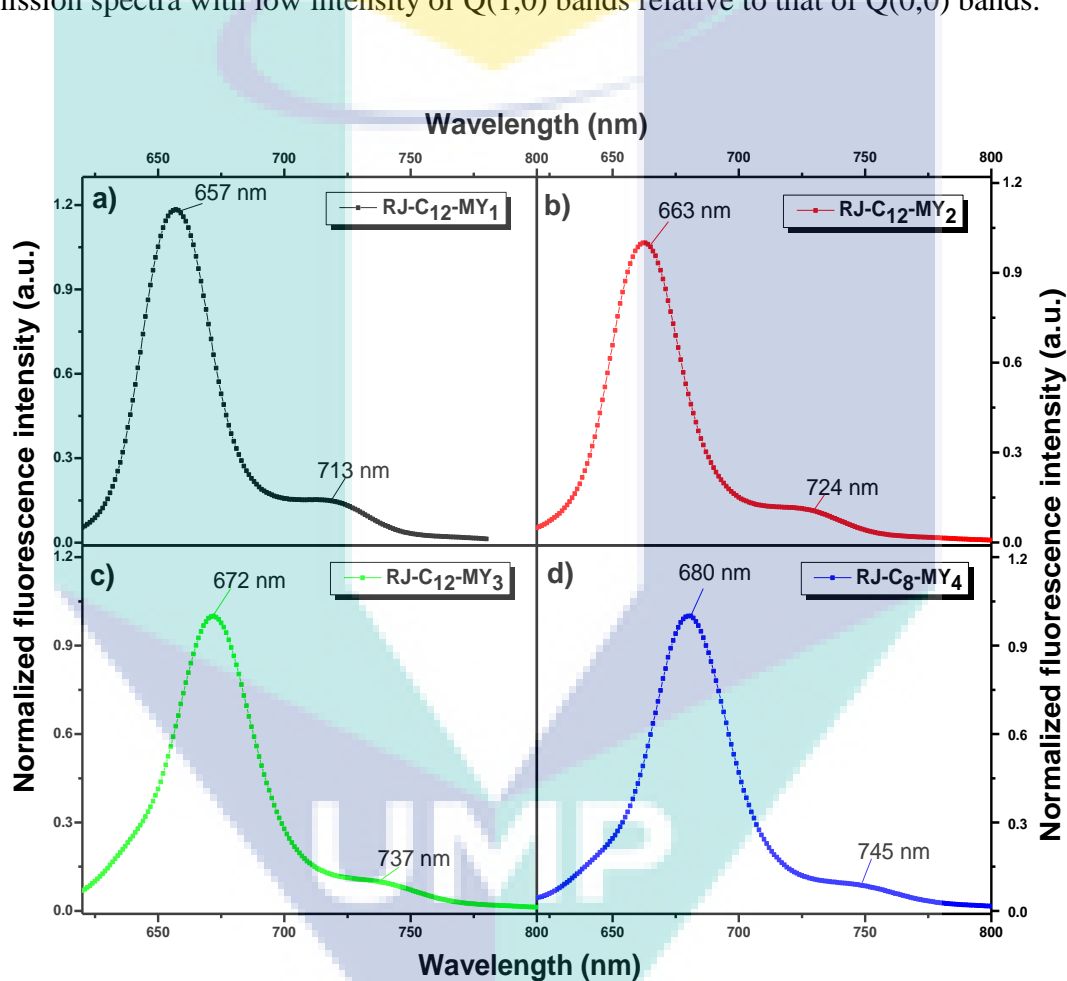


Figure 4.33 Emission spectra of RJ-C_n-MY_m series complexes a) RJ-C₁₂-MY₁; b) RJ-C₁₂-MY₂; c) RJ-C₁₂-MY₃; d) RJ-C₈-MY₄

The comparison between absorbance and emission bands for RJ-C_n-MY_m series complexes are shown Figure 4.34. It is noticed that all the emission spectra are mirror images of their respective absorption spectra, confirming the same geometries of complexes in excited and ground states and also showing that the fluorescence do not originate from some impurities. The stokes shift values for the RJ-C_n-MY_m series

complexes are calculated by energy difference between the emission Q(0,0) band and the absorbance Q(0,0) band and are tabulated in Table 4.7. As observed, the stokes shift decrease in the order of RJ-C₁₂-MY₂>RJ-C₁₂-MY₃>RJ-C₁₂-MY₁>RJ-C₈-MY₄. This decrease in stokes shift order could be explained on the basis of increasing the conjugation in the system. For instance, RJ-C₁₂-MY₂ complex showing the highest stokes shift value i.e; 658.77 cm⁻¹ due to the presence of para-carboxylphenyl groups that contribute in increasing the conjugation in RJ-C₁₂-MY₂ complex. While in the case of RJ-C₁₂-MY₁, the stokes shift value is lowered (429.09 cm⁻¹) as compared to that of RJ-C₁₂-MY₂ due to the decrease in conjugation of the system by moving the carboxyl groups from para to meta position of phenyl unit. On the other hand, the complexes RJ-C₁₂-MY₃ and RJ-C₈-MY₄ exhibiting the high conjugating systems compared to that of RJ-C₁₂-MY₁ and RJ-C₁₂-MY₂ complexes, are shown the low values of stokes shift. This lowering of stokes shift could be the cause of the presence of electron withdrawing groups (nitrile groups) in the system. The effect of electron withdrawing group is more prominent than that of the extension of conjugation. Therefore, RJ-C₈-MY₄ shows the lowest stokes shift value (411.58 cm⁻¹) in RJ-C_n-MY_m series.

Table 4.7 The fluorescence spectral data for RJ-C_n-MY_m series porphyrin complexes

	RJ-C ₁₂ -MY ₁	RJ-C ₁₂ -MY ₂	RJ-C ₁₂ -MY ₃	RJ-C ₈ -MY ₄
Absorbance	Q(0,0) (λ/nm)	656	660	668
	Q(1,0) (λ/nm)	600	606	617
	Splitting (Δv ₁ /cm ⁻¹) ^a	1422.77	1350.13	1237.4
Emission	Q(0,0) (λ/nm)	675	690	693
	Q(1,0) (λ/nm)	731	754	763
	Splitting (Δv ₂ /cm ⁻¹) ^b	1134.92	1230.15	1323.85
Stokes shift (Δv/cm ⁻¹)	429.09	658.77	540.05	411.58
Φ_f	0.52	0.53	0.52	0.22
¹τ (ps)	41.79	21.94	23.87	31.27
k_{nr} (s ⁻¹)	1.26×10 ¹⁰	2.14×10 ¹⁰	2.01×10 ¹⁰	2.49×10 ¹⁰
k_r (s ⁻¹)	1.12×10 ¹⁰	2.41×10 ¹⁰	2.17×10 ¹⁰	7.03×10 ⁹

^aEnergy difference between the absorbance Q(1,0) and Q(0,0) bands. ^bEnergy differences between the emission Q(0,0) and Q(1,0) bands.

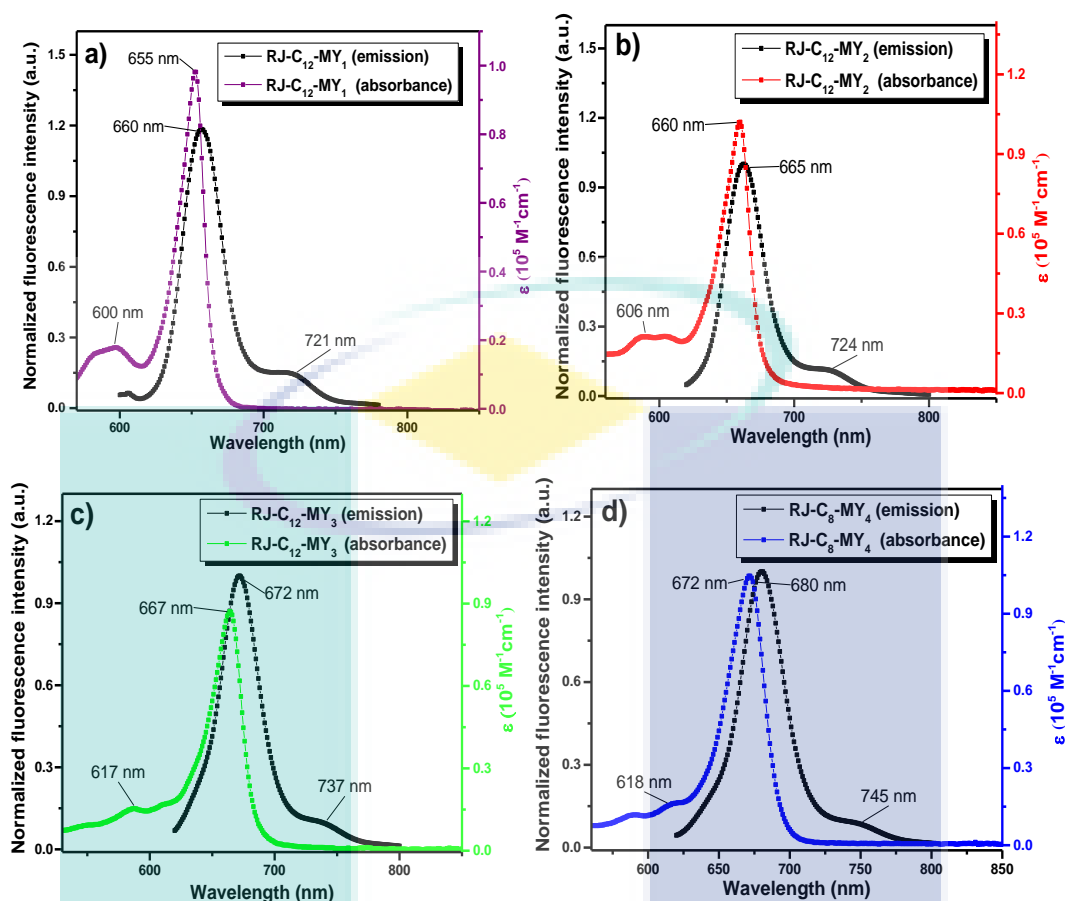


Figure 4.34 Comparison between absorption and emission spectra of RJ-C_n-MY_m series complexes a) RJ-C₁₂-MY₁; b) RJ-C₁₂-MY₂; c) RJ-C₁₂-MY₃; d) RJ-C₈-MY₄

In order to compare the intensities of fluorescence emission spectra for RJ-C_n-MY_m series complexes, photoluminescence measurements were done using wavelength-integrated time-resolved photoluminescence (TRPL) down to the sub-nanosecond regime. PL spectra of all the complexes excited by femtosecond laser at 400 nm wavelength and having 1.4 mW power, are shown in Figure 4.35. It is clearly noticeable that the RJ-C₁₂-MY₁ complex exhibits the hypochromic shift of emission band at 675 nm relative to other RJ-C_n-MY_m series complexes, while RJ-C₁₂-MY₃ complex exhibits the bathochromic shift in emission band at 693 nm. This characteristic could be attributed by extended conjugation in the macrocycle. Further extending of conjugation in RJ-C₈-MY₄ has not bathochromic effect on band rather than causing the blue shift of emission band (689 nm). This blue shifted band could be well explained by the effect of electron withdrawing groups. Similarly, if considering the curve area under the spectra, the RJ-C₁₂-MY₁ complex shows the less broaden emission spectrum, however, the RJ-C₈-MY₄ displays more broadening in emission spectrum, indicating that the extension of conjugation also causes the spectral broadening.

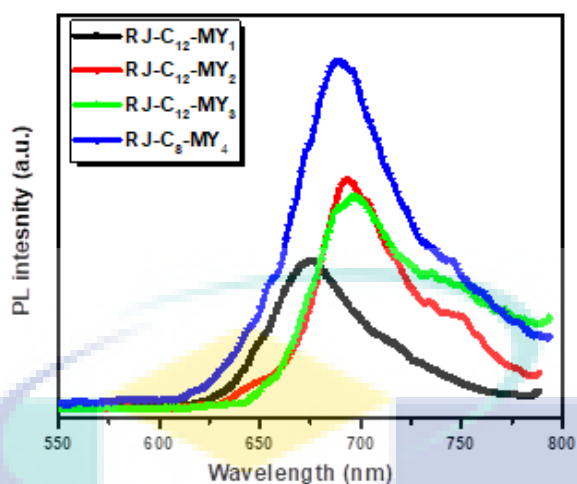
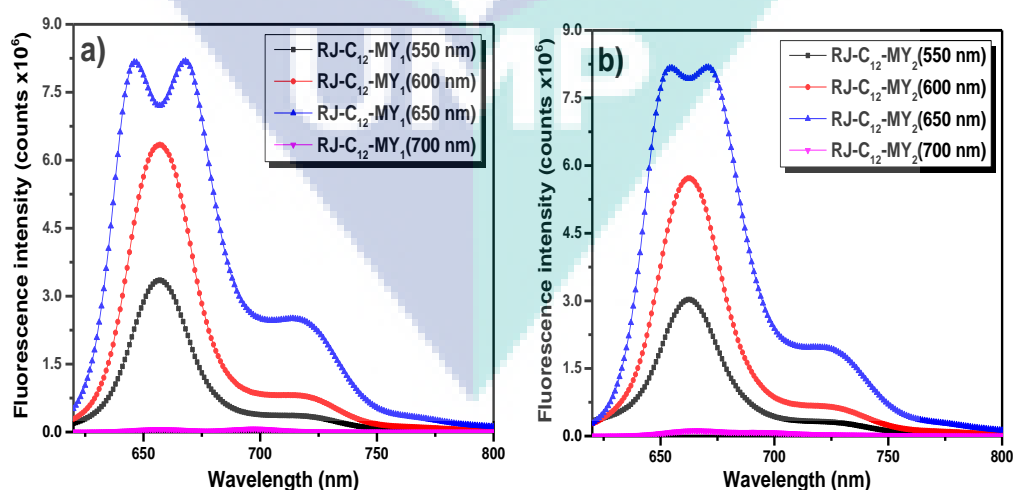


Figure 4.35 PL spectra of RJ-C_n-MY_m series complexes excited by femtosecond laser at 400 nm wavelength and having 1.4 mW power

Moreover, the emission spectra obtained at different wavelengths for RJ-C_n-MY_m series complexes are displayed in Figure 4.36. It is clearly shown that the relative intensity of the Q bands depends on the emission-monitoring wavelength. The maximum intensity for the Q(0,0) emission band occurs when monitoring at $\lambda=650$ nm, indicating an increased probability of radiative decay for the excited electrons at 650 nm wavelength. On the other hand, it can also be observed that the number of energy bands are same at each excitation wavelength, however only difference is in their relative intensities that may be supported by the possibilities of various confirmations exciting in excited states which lead to fluorescence of these complexes.



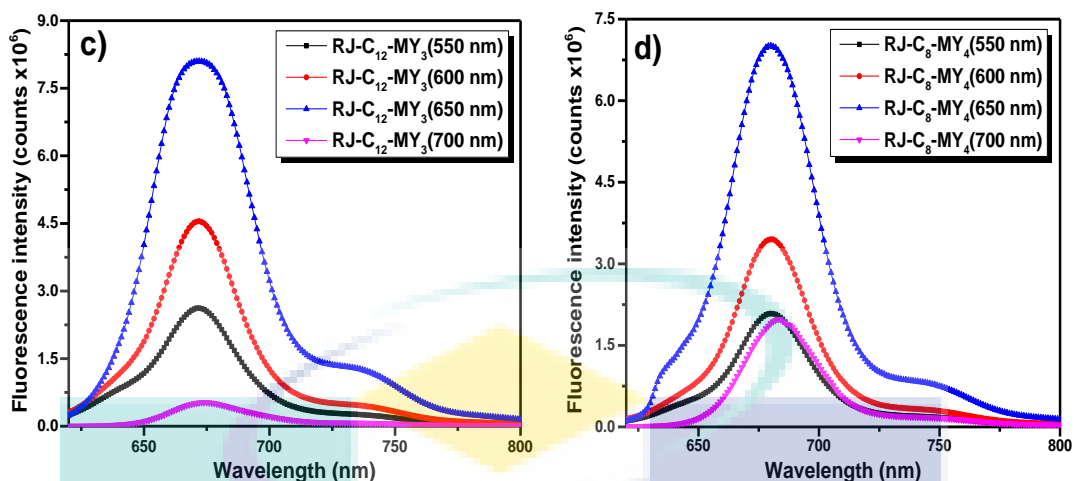


Figure 4.36 Emission spectra of RJ-C_n-MY_m series complexes at different excitation wavelength a) RJ-C₁₂-MY₁; b) RJ-C₁₂-MY₂; c) RJ-C₁₂-MY₃; d) RJ-C₈-MY₄

4.4.1 Quantum Yield Studies

The quantum yield (Φ_f) calculations for RJ-C_n-MY_m series complexes were done by comparing with Rhodamine B as a reference using the comparative method ($\lambda_{\text{exc}} = 450$ nm in ethanol). Two different methods are used to measure the relative quantum yield; (i) a single-point method and (ii) a comparative method (Lakowicz, 1999b). In single-point method, the Φ_f is measured by integrating the emission intensities from a single sample and a reference at identical concentration. However, in the comparative method, the Φ_f is measured by calculating the slope of the line obtained from plotting the absorbance against the integrated emission intensities for multiple concentration of a dye. In this case, the Φ_f is calculated by using the equation 4.1:

$$\Phi_f = \Phi_R \left(\frac{s}{s_R} \right) \left(\frac{n^2}{n_R^2} \right) \quad 4.1$$

where “s” is the slope of the line generated from plotting the integrated fluorescence intensity vs. absorbance. “n” is the refractive index of solvent, while the subscript “R” refers to the reference of known quantum yield (Williams, Winfield & Miller, 1983). If the ethanol is the solvent system for both reference and sample, the n^2/n_R^2 ratio will be 1. Figure 4.37 shows the absorbance profile at 600 nm for RJ-C_m-MY_m series of porphyrin complexes served as a reference for Φ_f calculation of RJ-C_m-MY_m series and Figure 4.38 shows the fluorescence profile at 600 nm for RJ-C_m-MY_m

series of porphyrin complexes served as a reference for Φ_f calculation of RJ-C_m-MY_m series.

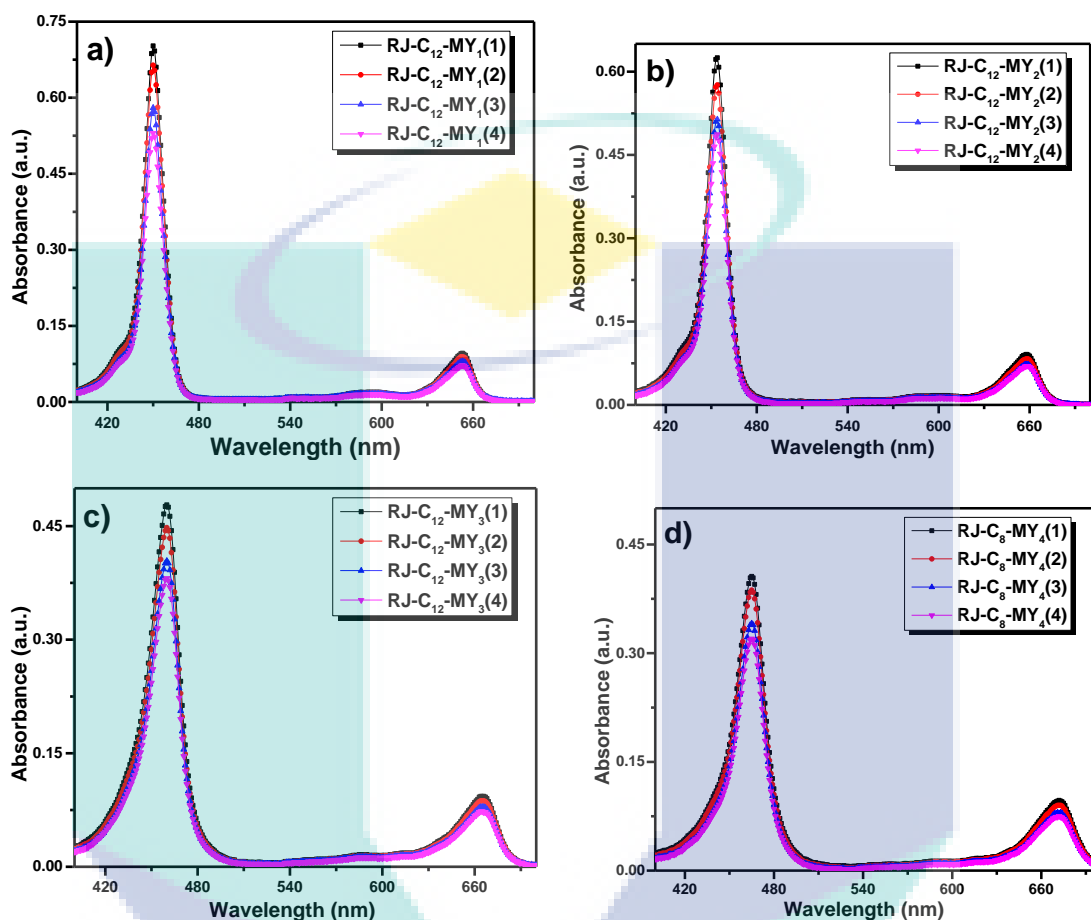
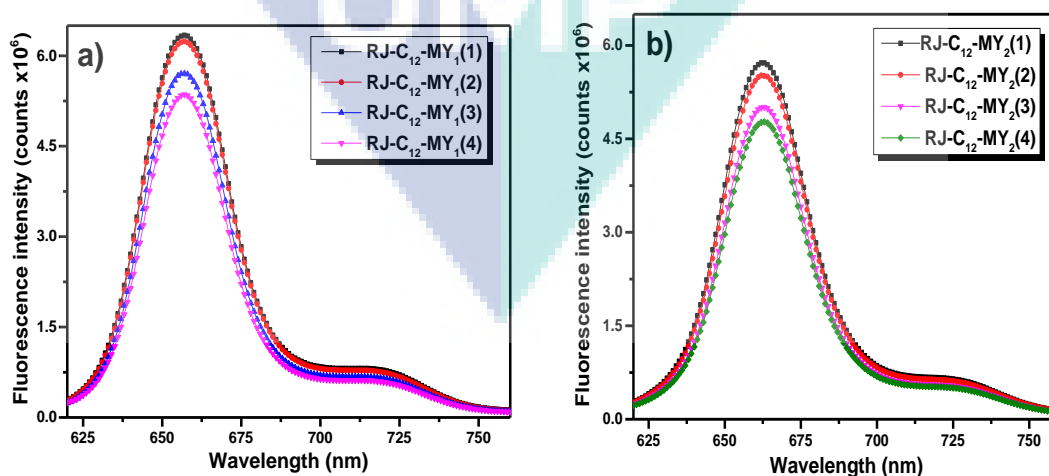


Figure 4.37 Absorbance profile for Φ_f calculation of RJ-C_n-MY_m series of porphyrin complexes at different concentrations a) RJ-C₁₂-MY₁; b) RJ-C₁₂-MY₂; c) RJ-C₁₂-MY₃; d) RJ-C₈-MY₄



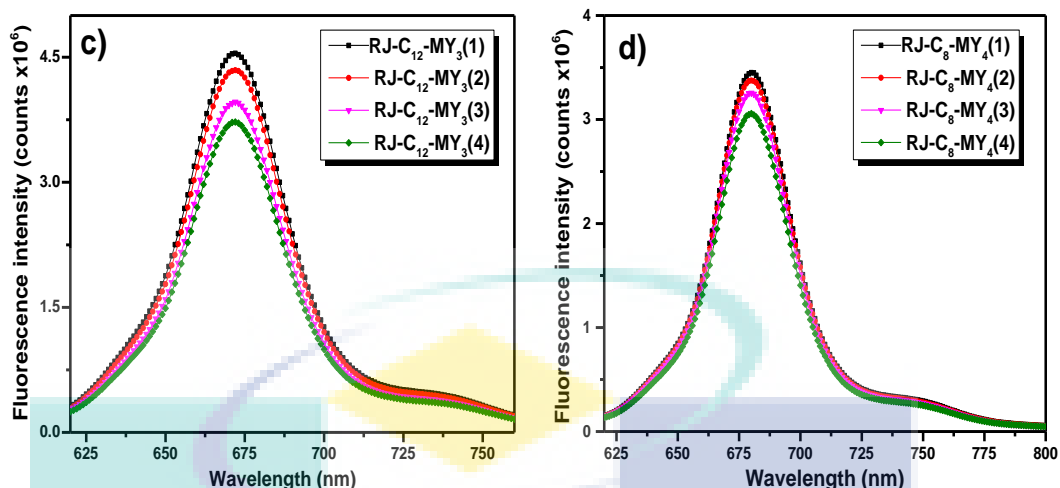


Figure 4.38 Emission profile for Φ_f calculation of RJ- C_n -MY $_m$ series of porphyrin complexes at different concentrations a) RJ- C_{12} -MY $_1$; b) RJ- C_{12} -MY $_2$; c) RJ- C_{12} -MY $_3$; d) RJ- C_8 -MY $_4$

The more common fluorescence (radiative decay) from the S_1 state is highly depend on the porphyrin structure and particularly the nature of its peripheral substituents and central atom. As the central metal ion and substituents become heavier, the rate of non-radiative intersystem crossing to the T_1 state increases which, in turn, lowers the Φ_f . This increase in the population of the triplet state generally increases the quantum yield of phosphorescence but the heavy atom effect can also increase the non-radiative decay from T_1 to S_0 thus opposing the increased rate of population of the triplet state. As explained previously, it is also possible for heavy atoms on peripheral position to create a similar heavy atom effect (Dolphin, 1978). As shown in Table 4.8, in the case of RJ- C_n -MY $_m$ series complexes, the Φ_f measured at 600 nm (excitation wavelength) decrease in the order of RJ- C_{12} -MY $_2 > RJ-C_{12}$ -MY $_3 \approx RJ-C_{12}$ -MY $_1 > RJ-C_8$ -MY $_4$. In RJ- C_8 -MY $_4$, the relative decrease in Φ_f may be attributed to the effect of electron withdrawing substituents compared to that of other complexes of same series. Here the Φ_f for RJ- C_n -MY $_m$ series complexes are also calculated at different excitation wavelengths (550 nm, 600 nm and 650 nm), showing the different Φ_f values that indicate the fluctuating radiative probability for excited electrons. The relative Φ_f for excitation at 650 nm higher than that at 550 nm. Therefore there is an increased radiative probability for the excited electron when the excitation wavelength 650 nm falls on the Q(0,0) band.

Table 4.8 The quantum yield data for RJ-C_n-MY_m series complexes

	QUANTUM YIELD (Φ_f)		
	550 nm	600 nm	650 nm
RJ-C ₁₂ -MY ₁	0.28	0.47	0.52
RJ-C ₁₂ -MY ₂	0.31	0.53	0.58
RJ-C ₁₂ -MY ₃	0.31	0.52	0.73
RJ-C ₈ -MY ₄	0.14	0.22	0.43

Figure 4.39, Figure 4.40, Figure 4.41 and Figure 4.42 represent the slope of the lines obtained from plotting the absorbance against the integrated emission intensities at various concentrations for complex RJ-C₁₂-MY₁, RJ-C₁₂-MY₂, RJ-C₁₂-MY₃, and RJ-C₈-MY₄ respectively.

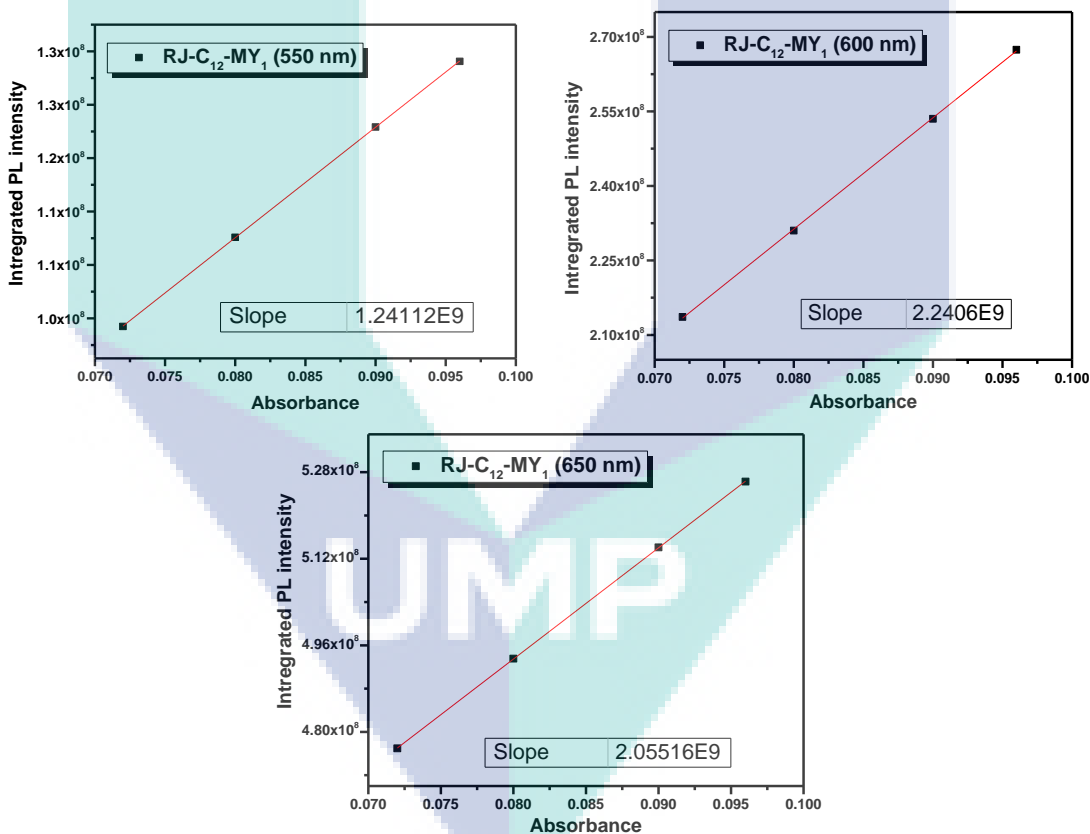


Figure 4.39 Slopes of the line generated from plotting the absorbance against the integrated emission intensity at various wavelengths for RJ-C₁₂-MY₁ complex

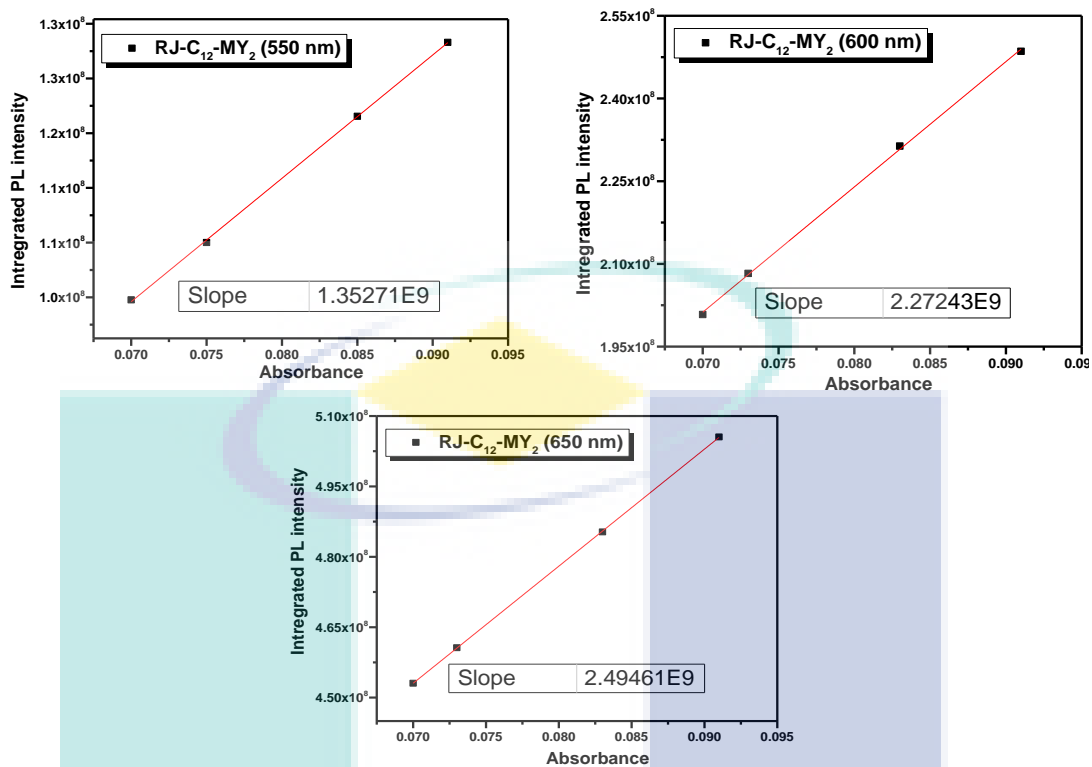


Figure 4.40 Slopes of the line generated from plotting the absorbance against the integrated emission intensity at various wavelengths for RJ-C₁₂-MY₂ complex

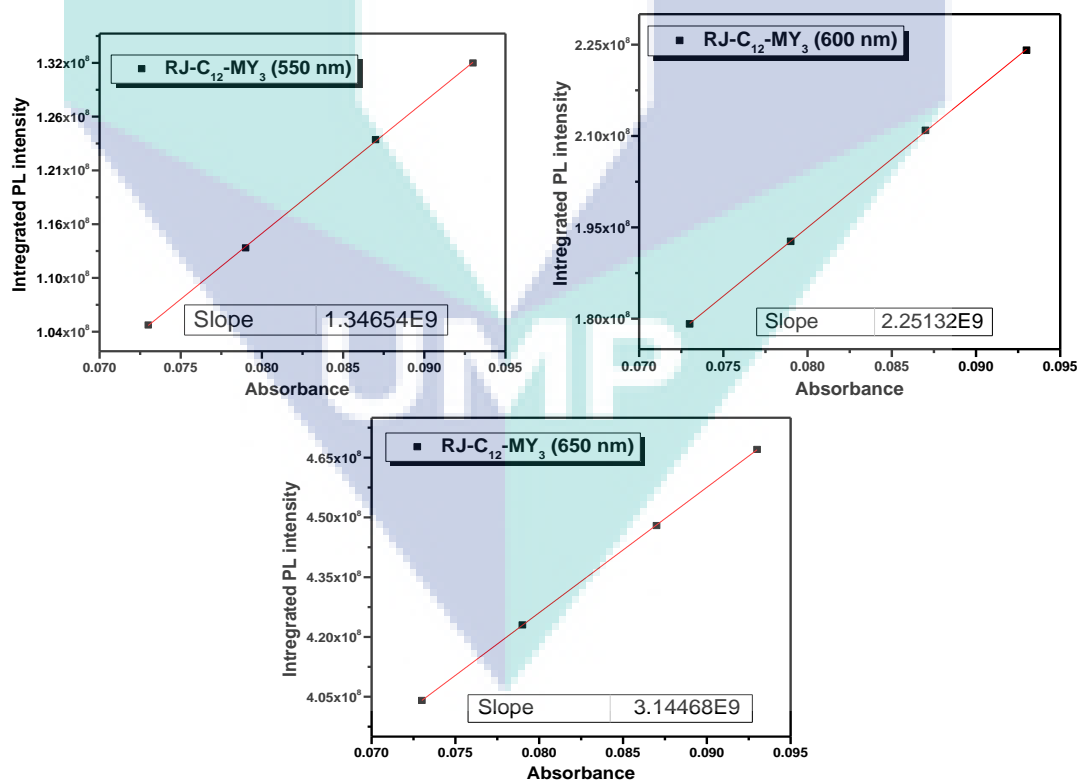


Figure 4.41 Slopes of the line generated from plotting the absorbance against the integrated emission intensity at various wavelengths for RJ-C₁₂-MY₃ complex

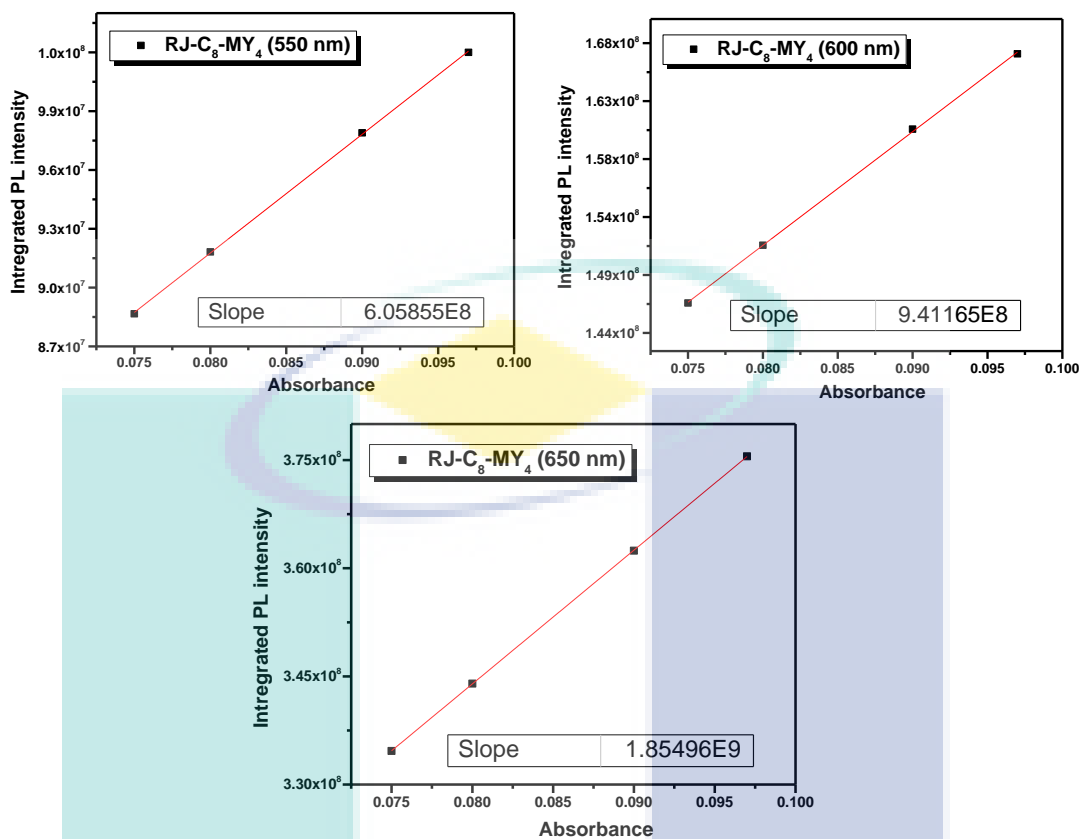


Figure 4.42 Slopes of the line generated from plotting the absorbance against the integrated emission intensity at various wavelengths for RJ-C₈-MY₄ complex

4.4.2 Time Resolved Photoluminescence Studies

In this work, the ultrafast dynamics of photocarriers were studied using wavelength-integrated time-resolved photoluminescence (TRPL) down to the sub-nanosecond regime. TRPL measurements were performed with a mode-locked Ti:sapphire laser (Coherent Mira 900) having a laser power output of 1.90 W at 800 nm, and the measurements were used to study the carrier lifetimes of RJ-C_n-MY_m series complexes. A second harmonic generator (APE-SHG /THG) was used to excite the sample by an output wavelength of 400 nm (pulse width 150 fs, pulse repetition rate of 76 MHz). Emission of the sample was detected by the monochromator attached to a Hamamatsu C6860 streak camera with a temporal resolution of 2 ps. The integration time was kept 100 ms for 500 integrations. All the TRPL measurements of the RJ-C_n-MY_m samples were carried out keeping all the measurement parameters constant.

The TRPL decay curves were analyzed using a double exponential decay model. TRPL decay curves were chosen to fit by using a two-term exponential decay model

because it better depicts the multiple recombination characteristics exemplified by TRPL curves. Put differently, the two-term exponential model best fits the fast decay process that involves the thermalization carrier dynamics and the slow decay involves slow cooling process as shown in Figure 4.43.

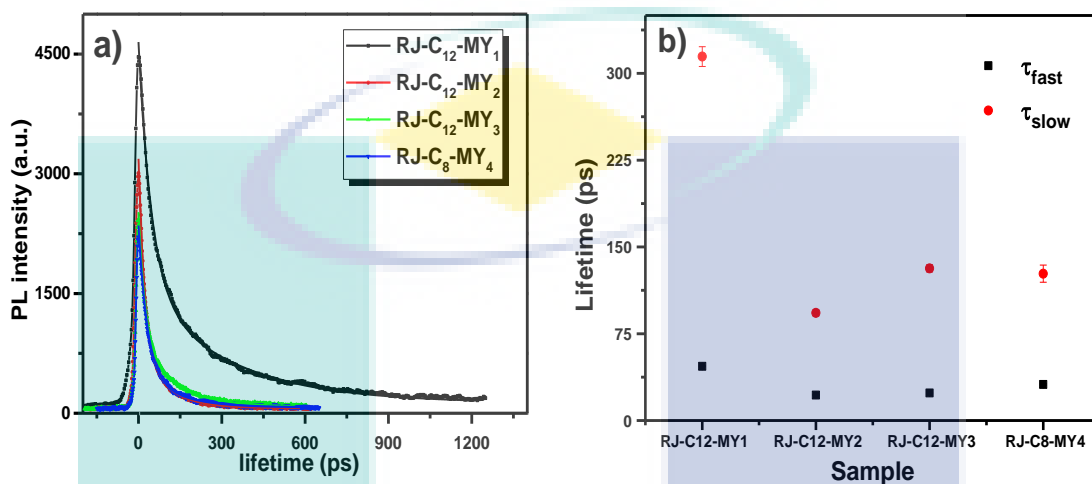
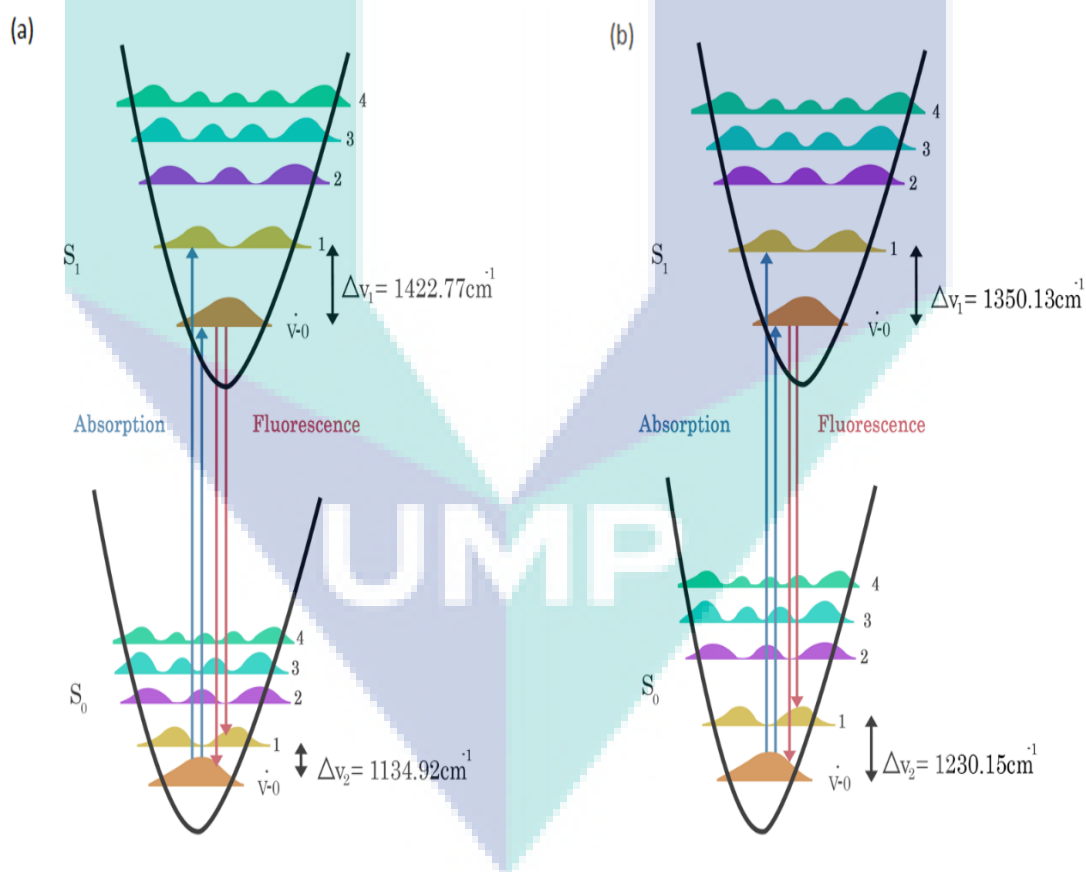


Figure 4.43 a) Time-resolved photoluminescence spectra (TRPL) of RJ-C_n-MY_m series complexes b) the fast and slow time components for RJ-C_n-MY_m series complexes

4.4.3 PAI Signals Correlation with Emitting Excited States

In order to understand the photo-physical pathway responsible for enhanced PA signal, deep studies of fluorescence emission spectra for RJ-C_n-MY_m series complexes are needed. A most common assumption is that a molecular dye showing a low fluorescence quantum yield would make suitable PA contrast agent (Wang et al., 2012). According to this respect, RJ-C₈-MY₄ having the low Φ_f could act as promising molecular photoacoustic contrast agent among all the studied complexes. Contrary to this assumption, the study is demonstrating how a dye with low Φ_f can display enhanced PA signal. More importantly, it was reported that a dye having long-lived S₁ excited state along with a high Φ_f facilitates a strong PA emission because of an excited-state sequential absorption mechanism responsible for this PA enhancement (Frenette et al., 2014). However, as shown in Table 4.7 and Figure 4.44, the life-time of S₁ excited state for RJ-C_n-MY_m series complexes decrease in the order of RJ-C₁₂-MY₁ > RJ-C₈-MY₄ > RJ-C₁₂-MY₃ > RJ-C₁₂-MY₂ and PA signals increase in the order of RJ-C₁₂-MY₁ > RJ-C₁₂-MY₂ > RJ-C₁₂-MY₃ > RJ-C₈-MY₄ (explain in detail in chapter 5). According to above assumption, the RJ-C₁₂-MY₁ showing relatively long-lived S₁ excited state (41.79 ps)

may generate the high PA signals due to excited-state sequential absorption mechanism. While, the RJ-C₁₂-MY₂ having the low S₁ excited state lifetime (21.94 ps) produced the enhanced PA signals relatively to that of RJ-C₈-MY₄ and RJ-C₁₂-MY₃ complexes with S₁ lifetimes 23.87 ps and 31.27 ps respectively. Therefore, the above assumption may not be fit for all the dyes. On the other hand, if considering the splitting of vibrational levels of S₁ excited state, it is clear that the distance between the vibration states may contribute in PA enhancement. As shown from the Table 4.6 and Figure 4.44, the splitting between v=1 vibration level contributing for Q(1,0) emission and v=0 vibration level contributing for Q(0,0) emission in S₁ excited state decreases in the order of RJ-C₈-MY₄ > RJ-C₁₂-MY₃ > RJ-C₁₂-MY₂ > RJ-C₁₂-MY₁. This indicates that lower the distance between v=1 and v=0 vibrational levels of S₁ excited state favors the non-radiative decay and thereby enhancement PA signals.



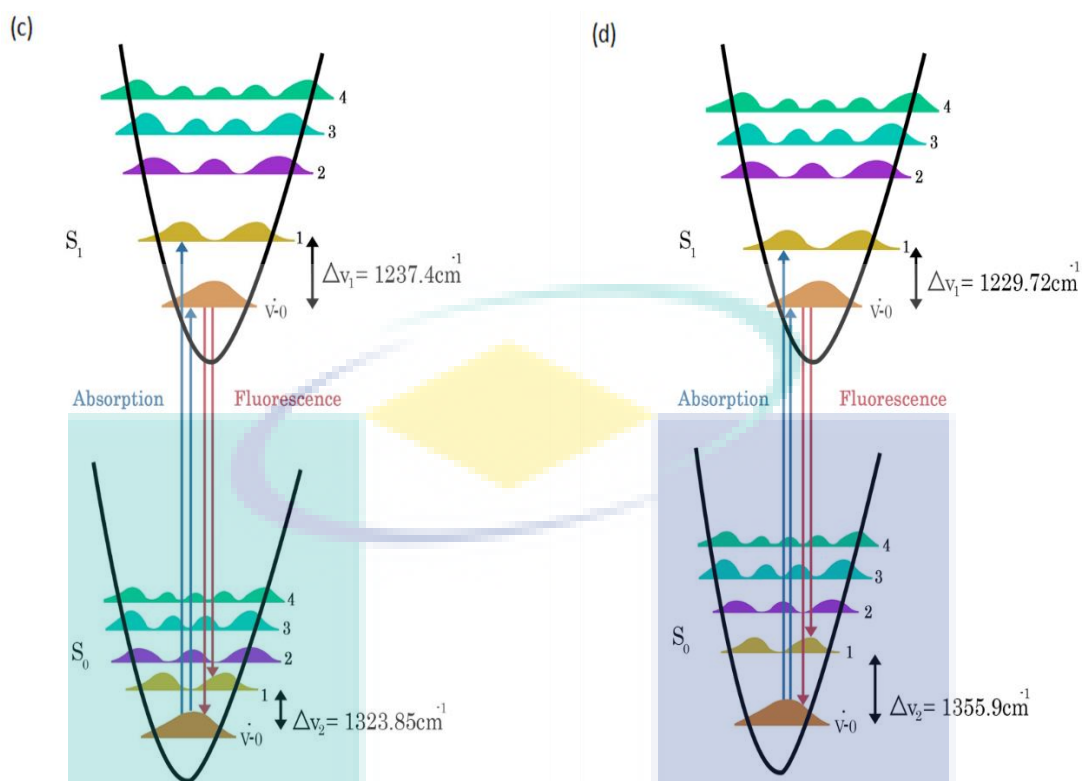


Figure 4.44 The contribution from vibrational states in the absorption and emission spectra of a) RJ-C₁₂-MY₁; b) RJ-C₁₂-MY₂; c) RJ-C₁₂-MY₃; d) RJ-C₈-MY₄

4.5 IR-Vibrational Modes Studies

The optimized structures of the RJ-C_n-MY_m series of molecules are shown in Chapter 3. Harmonic frequency calculations indicated that all the structures optimized are real. The calculated IR spectra of the molecules are in well agreement with the experimental spectra as show in Figure 4.45. Dynamics of the molecules generated from the Graphical User Interface (GUI, Gauss View) ((Frisch et al., 2003; Nielsen & Holder, 1998) of the Gaussian program package (Gaussian09, 2009) is in the PowerPoint file uploaded, where visuals of all vibrations are provided (Appendix H). Figure 4.47 and Figure 4.46 represent the experimental FTIR data and theoretical DFT results for most of the finger print (low-frequency) spectral region (600–1650 cm⁻¹ or 0.074–0.204 eV) as well as high-frequency (4000–2900 cm⁻¹ or 0.49–0.36 eV) spectral region. A number of experimental as well as DFT studies have been published in detail about IR and Raman spectra of substituted di-phenyl and tetraphenyl porphyrins (Minaev & Lindgren, 2009; Şen et al., 2010) at finger print spectral region (0.074–0.204 eV) and the assignment of several IR bands has been proposed. However, there is a very limited literature focused on the IR vibrational bands at high-frequency spectral region of porphyrin molecules,

thus ignoring the effect of high frequency vibrational modes on photoacoustic signals. As observed, the vibrational bands at high-frequency region are of more important to interpret because of their direct effect on photoacoustic properties of a porphyrin molecule.

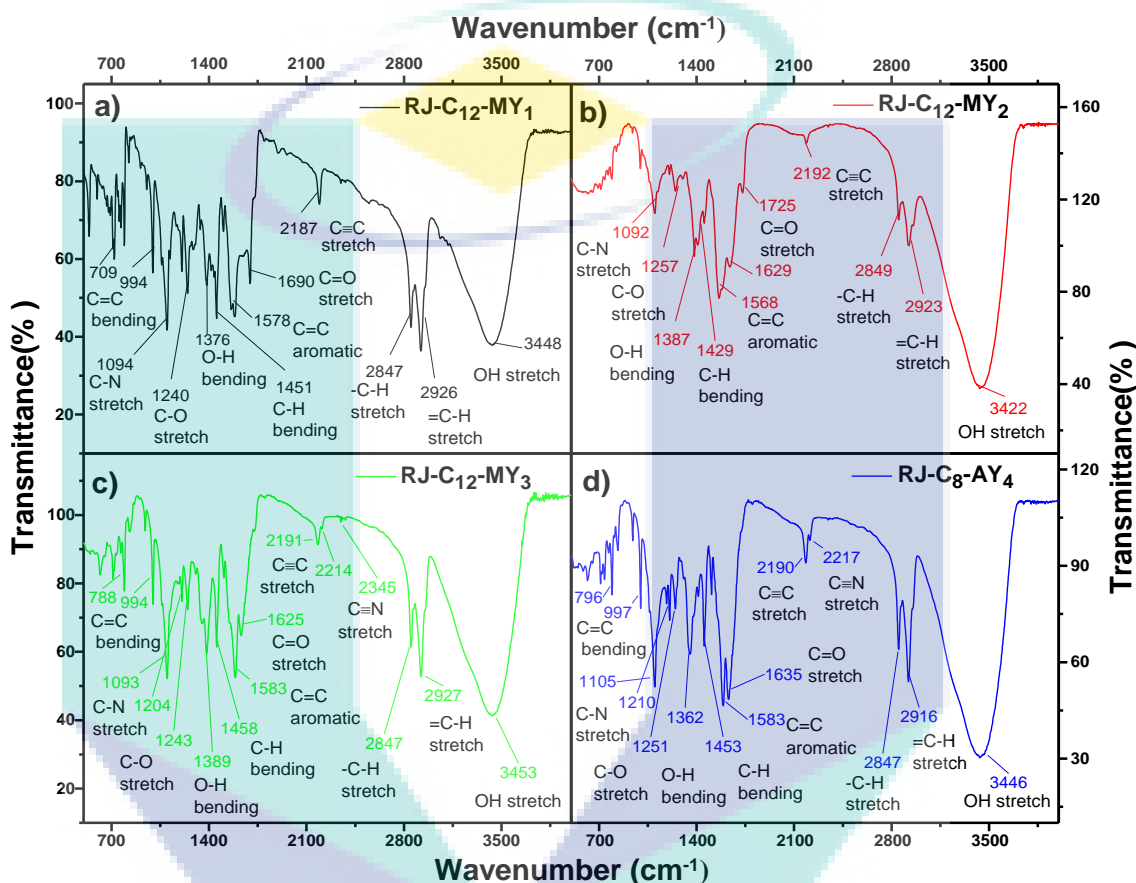


Figure 4.45 Experimental FTIR spectra for RJ-C_n-MY_m series complexes; a) RJ-C₁₂-MY₁; b) RJ-C₁₂-MY₂; c) RJ-C₁₂-MY₃; d) RJ-C₈-MY₄

To characterize the difference in thermalization pathways of the porphyrin molecules, calculated absorption coefficients of the vibrational energies (normalized for comparison) of the RJ-C_n-MY_m series of molecules are presented in Figure 4.47.

As noted from calculated vibrational energy spectra, in total there are 483, 483, 489 and 513 modes of vibrations in compounds RJ-C₁₂-MY₁, RJ-C₁₂-MY₂, RJ-C₁₂-MY₃, and RJ-C₈-MY₄ respectively, and the vibrational spectra of each molecule are similar to each other (Figures 4.33). However, some obvious differences could be very informative in high-frequency region of C-H bands providing evidence for non-radiative decay. In calculated IR spectrum of RJ-C₁₂-MY₁, out of 483 there are 73 stretching vibration modes

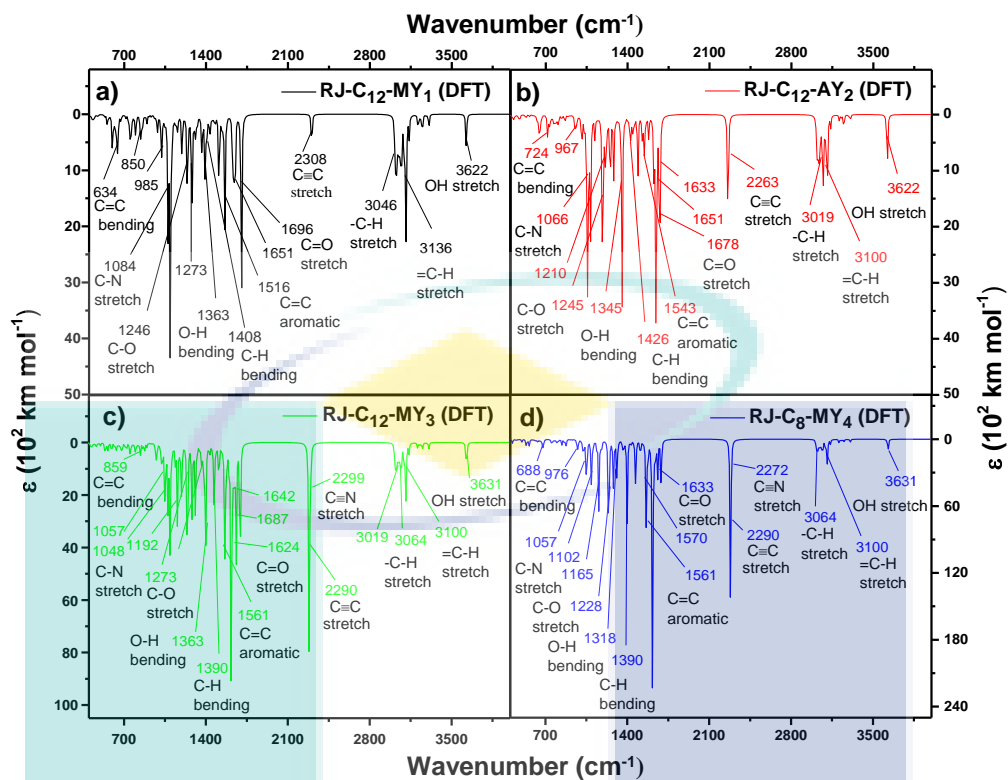


Figure 4.46 Computed FTIR spectra for RJ-C_n-MY_m series complexes; a) RJ-C₁₂-MY₁; b) RJ-C₁₂-MY₂; c) RJ-C₁₂-MY₃; d) RJ-C₈-MY₄

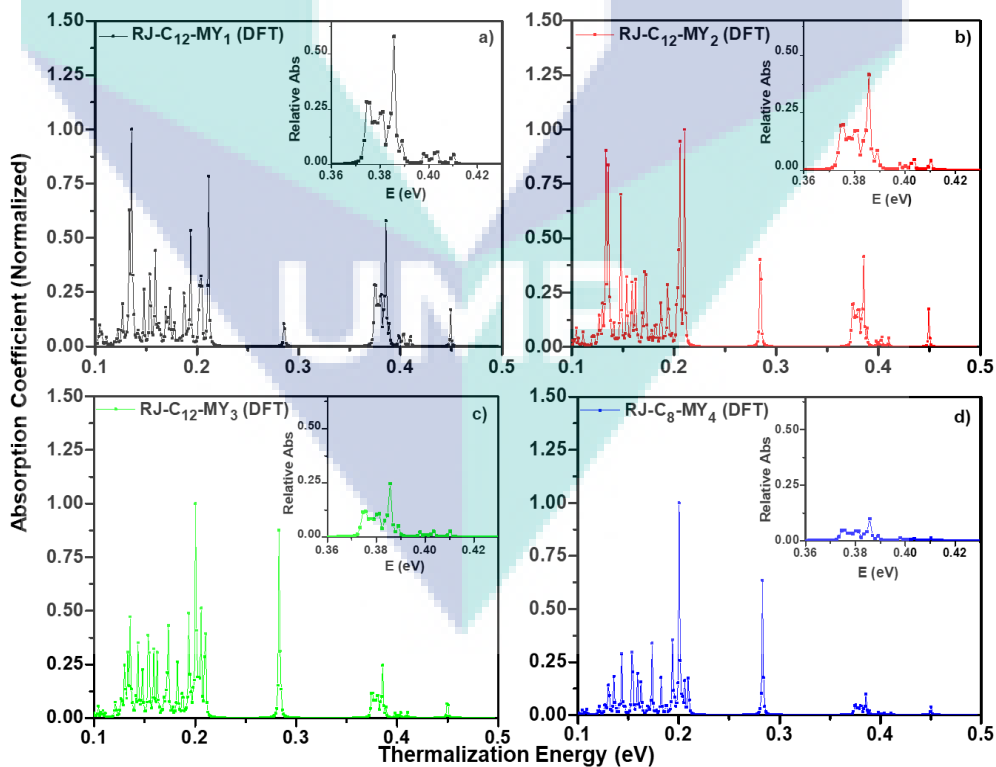


Figure 4.47 Vibrational spectra of a) RJ-C₁₂-MY₁; b) RJ-C₁₂-MY₂; c) RJ-C₁₂-MY₃ and d) RJ-C₈-MY₄

belong to C–H groups in the region 0.409–0.373 eV. The highest frequencies at ~0.409–0.407 eV correspond to C_β–H stretching vibrations of the pyrrole rings. The calculated C–H stretching vibrations in benzene rings substituted with porphyrin core either directly or through ethynyl groups are observed in the region of ~0.403–0.398 eV. The absorption coefficients of the C_β–H vibrations are higher than that of C–H stretching in benzene rings. The C–H stretching vibration modes of the long alkoxy groups are observed in the interval ~0.389–0.373 eV. As clearly observable, the absorption coefficients of the C–H stretching vibration modes for long alkoxy chain are much higher in intensity than that of C–H stretching in benzene rings and C_β–H vibrations of pyrrole rings. Similar trends were observed in the calculated vibrational energy spectra of RJ-C₁₂-MY₂, RJ-C₁₂-MY₃ and RJ-C₈-MY₄, as shown in Figure 4.47.

A comparison of relative changes in the vibrational absorption spectra of the RJ-C_n-MY_m series of molecules are presented in Figure 4.48. It is clear from the figure that the absorption coefficients of RJ-C₁₂-MY₁ in C-H vibrational bands are higher compared to other complexes, thus indicating the higher density of phonons on RJ-C₁₂-MY₁, thereby expecting high intense photoacoustic signal as compared to other complexes. As the absorption coefficients of C-H vibrational modes decrease in the order of RJ-C₁₂-MY₁ > RJ-C₁₂-MY₂ > RJ-C₁₂-MY₃ > RJ-C₈-MY₄, it is predicted that the photoacoustic signals also follow the same order.

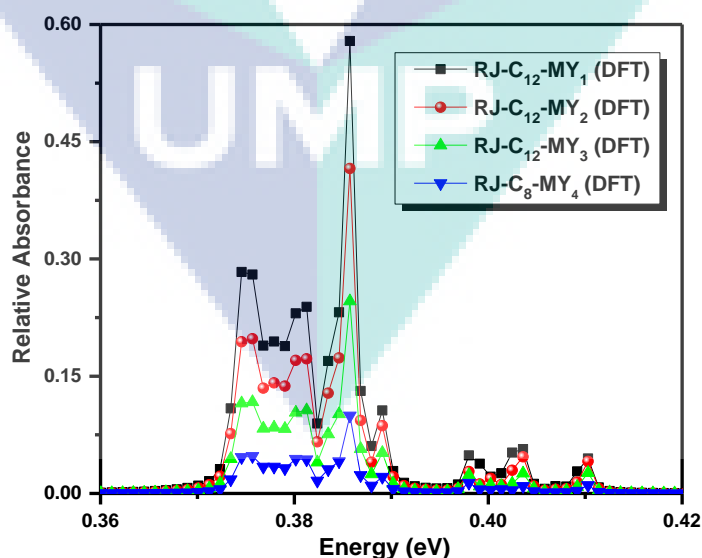


Figure 4.48 Comparison between vibrational modes of RJ-C₁₂-MY₁, RJ-C₁₂-MY₂, RJ-C₁₂-MY₃ and RJ-C₈-MY₄

4.5.1 Phonon Emission Correlation with Extended-Conjugation

The molecular orbital diagrams of the RJ-C_n-MY_m series of molecules are shown in Appendix I. To our best knowledge the effect of resonating structures on phonon emission (non-radiative decay) through vibrational IR absorption of porphyrin molecules are studied here for first time, however the resonance effect of typical molecules are well documented phenomena. As clearly observed, the compound RJ-C₈-MY₄ have the more resonating structure due to the presence of 2-carboxy-2-cyanoethenyl groups, thereby having the more electron density compared to that of other complexes. However, the electron withdrawing abilities of nitrile and carboxylic acid groups reduce the electron density on the porphyrin core and therefore on the most electron positive C-H bonds. This influences the C-H bonds to act as less IR energy absorber in the region 2900-3100 cm⁻¹ and thus causing the phonon emission of lower number, thereby reducing the non-radiative decay and PA signals strength. While in the compound RJ-C₁₂-MY₃, one of the 2-carboxy-2-cyanoethenyl group on meso ethynyl substituted phenyl ring is replaced by carboxylic acid group that causes the lowering of π -conjugation on the RJ-C₁₂-MY₃ molecule and the electron withdrawing ability towards the carboxylic acid is also reduced compared to that of 2-carboxy-2-cyanoethenyl group. This increases the electron density on the porphyrin core and thereby on C-H bond regions. As a result of this, RJ-C₁₂-MY₃ has shown the enhanced PA signal due to the high energy quanta absorption. Compared to RJ-C₁₂-MY₃, compound RJ-C₁₂-MY₂ has shown more intense PA signals due to the presence of less electron withdrawing carboxylic acid groups compared to that of 2-carboxy-2-cyanoethenyl groups, therefore possessing more electron density on porphyrin core and C-H bond region. On the other hand, the compound RJ-C₁₂-MY₁ comprises of two carboxyl groups as that of compound RJ-C₁₂-MY₂, however at 3-position of meso-ethynyl substituted phenyl rings and showing the strong PA signals. This could be explained by inductive effect on RJ-C₁₂-MY₁, the carboxyl groups on 3-position of phenyl group have less ability to attract the electronic cloud and therefore having more electron density on porphyrin core and C-H bond region that causes the strong PA signal relative to that of RJ-C₁₂-MY₂ and with other studied compounds.

4.6 Thermogravimetric Thermal Analysis (TGA)

Thermogravimetric analysis (TGA) is commonly used technique for evaluating the thermal stability of samples. Porphyrins has received considerable attention for the study of their thermal stability because of their well-known technological applications concerning the field in which the stability is one of the essential parameters to be considered. Simultaneous TG-DTA measures both the weight changes and the heat flow as a function of temperature or time in a controlled atmosphere.

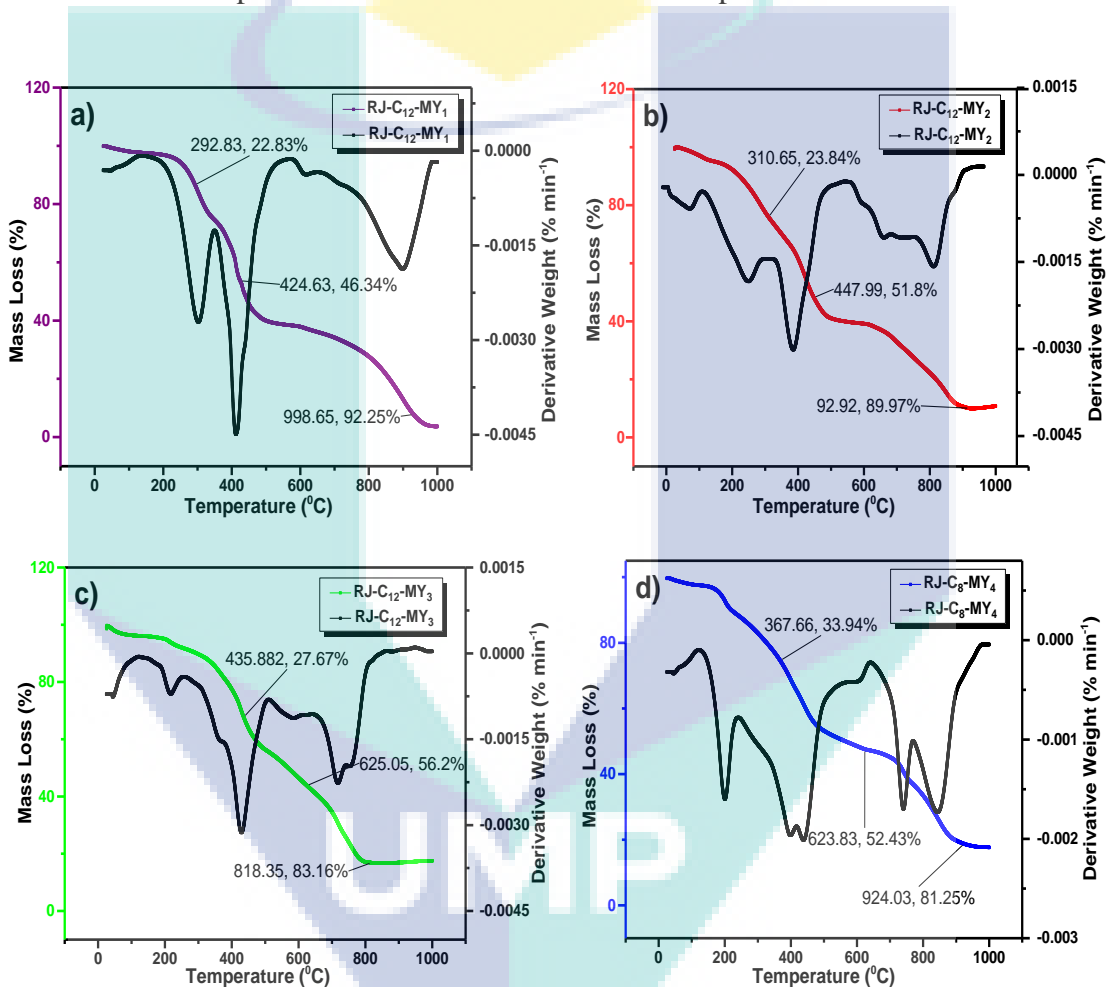


Figure 4.49 TGA curve of a) RJ-C₁₂-MY₁; b) RJ-C₁₂-MY₂; c) RJ-C₁₂-MY₃ and d) RJ-C₈-MY₄

The TGA of RJ-C_n-MY_m series of porphyrin complexes were explored in order to know their thermal stability. Figure 4.49 shows the TGA curves for all the samples. It is revealed that the TG curves of all the complexes show a continuous weight loss starting from 150 °C to 990 °C, until stable ZnO oxides are formed at around 950 °C or above. The initial weight loss of about 22.83%, 23.84%, 27.67% and 33.94% observed between 200 °C and 450 °C for RJ-C₁₂-MY₁, RJ-C₁₂-MY₂, RJ-C₁₂-MY₃ and RJ-C₈-MY₄

respectively, are attributed to the removal of ethynyl-phenyl rings. At 450 °C- 550 °C, up to 50% of the total weights had been lost which correspond to the loss of alkoxy-phenyl groups. The organic moiety decomposes further with increasing temperature. At around 410 °C-4450 °C, up to 70% of the total mass had been lost; correspondingly there is a large peak in DTA curves attributed to the collapse of macrocyclic ligand. Further in the range of 500 °C – 950 °C, the weight losses reach up to 97% which are attributed to the removal of pyrrole groups and complete decomposition of macrocyclic rings finally leaving behind zinc oxide. Simultaneously, there are some peaks in 200 °C–950 °C region in the DTA curves indicating the major loss in this region. The small peaks correspond to the loss of substituents on porphyrin ring and the large peaks correspond to the collapse of the porphyrin skeleton.

4.7 Conclusions

In conclusion, to assess the photoacoustic properties of porphyrins dyes, the optoelectronic investigations of a new series of meso-ethynyl-Zn(II)porphyrins (RJ-C_n-MY_m) were undertaken. Firstly, mechanistic studies for all the synthesized molecules were performed in order to elucidate the mechanism pathway to the arrangement of the atoms from their starting precursors to desired products.

In all cases, the introduction of π -conjugating meso-substituents caused the bathochromic shift of absorption and emission bands. It is also noticeable that the shifts of absorptions and emission bands are correlated to the electron withdrawing ability of meso-substituents. In case of absorption, the electron withdrawing ability of meso-substituents result the red shift of the absorption bands. While in emission spectra, the band shifts are other way around – by increasing the electron withdrawing ability of meso-substituents cause the hypochromic shift of emission bands. It is also observable that the effect of electron withdrawing group is more prominent than that of the extension of π -conjugation. Similar trends are observed in stokes shift and Φ_f of the RJ-C_n-MY_m series complexes. A most common assumption is that a dye showing more absorption in NIR region, a low fluorescence quantum yield and long-lived S₁ excited state could act as a promising PA contrast agent. Contrary to this assumption, a porphyrin dye with less absorption in NIR region, high Φ_f and short-lived S₁ excited state has been established in order to display enhanced PA signals. The enhancement of PA signals correlates to molar

absorption coefficients (ϵ) of S_0 - S_2 transition, energy gap, stability of LUMO orbitals and splitting of vibrational levels of S_1 excited state. Higher the ϵ of S_0 - S_2 transition could increase the possibility of strong PA signals due to the rapid non-radiative decay of S_2 excited electrons to S_1 excited state by thermal expansion. Higher the band gaps cause the more rapid non-radiative thermalization due to long-lived S_1 excited state. More stable the LUMO on porphyrin core causes more high PA signals because more electron density on porphyrin core enhance the non-radiative decay. Lower the distance between $v=1$ and $v=0$ vibrational levels of S_1 excited state favors the non-radiative decay and thereby enhancement of PA signals. The interpretation of vibrational spectra of RJ- C_n - MY_m series of complexes are also important to investigate their effect on PA signal. The highest absorption coefficients of RJ- C_{12} - MY_1 in C-H vibrational bands indicate the removal of higher density of phonons, thereby expecting high intense photoacoustic signal as compared to other complexes. Moreover, the strength of PA signal also depends on the resonating structures of porphyrin molecules. Higher the resonance effect reduces the PA properties of porphyrin molecules due to the delocalization of electron density on porphyrin core. The effect of resonating structures on PA signal strength by phonon emission (non-radiative decay) were studied here for the first time.

The logo for UIMP (University of Malaya Physics) is a large, stylized letter 'M' shape. It is composed of several overlapping geometric shapes in shades of teal, light blue, and yellow. The letters 'UIMP' are written in a bold, white, sans-serif font across the center of the 'M' shape.

UIMP

CHAPTER 5

RESULTS AND DISCUSSION: PHOTOACOUSTIC STUDIES OF π -CONJUGATED MESO-ETHYNYL-Zn(II)PORPHYRINS

5.1 Introduction

This chapter explains the photoacoustic studies of four newly synthesized RJ-C_n-MY_m series of complexes. The optical and photoacoustic Z-scan studies as well as photoacoustic tomography studies are deeply explored in this chapter. Moreover, the setups adopted for photoacoustic Z-scan and photoacoustic tomography studies are also enlightened here in detail.

5.2 Photoacoustic Studies

A photoacoustic signal is produced through the conversion of light energy to sound energy by an absorbing material. The PA signal generated due to the irradiation of the laser pulse can be expressed as

$$PA = \varepsilon_g C_g \Gamma I \Phi_{nr} \quad 5.1$$

where “ ε_g ” is the ground state molar extinction coefficient at the incident wavelength, “ C_g ” is the ground state concentration of dye molecules, “ Γ ” is the Grüneisen coefficient, “ I ” is the incident photon fluence, and “ Φ_{nr} ” is the quantum yield for non-radiative decay. The Grüneisen coefficient, Γ , is a constant that quantifies a medium ability to conduct sound efficiently that is defined as

$$\Gamma = \frac{V_s^2 \alpha}{C_p} \quad 5.2$$

where “ V_s ” is the velocity of sound, “ α ” is the thermal expansion coefficient of the medium, and “ C_p ” is the specific heat of the medium at constant pressure, “ C_v ” is the specific heat of the medium at constant volume, “ K_s ” and “ K_T ” are adiabatic and isothermal bulk moduli, respectively (Knopoff & Shapiro, 1970). While Eq. 5.1 holds true in a linear optical absorption regime, as recently demonstrated (Frenette et al., 2014) that photoacoustic transients are produced due to the interaction between the incident laser fluence and the nonlinear absorbing medium

$$PA = \varepsilon_g C_g \Gamma I \Phi_{nr} + \varepsilon_e C_e \Gamma I^2 \dots + \varepsilon_n C_n \Gamma I^{n+1} \quad 5.3$$

where “ ε_e ” is the first excited state molar extinction coefficient at the incident wavelength and “ C_e ” is the concentration of excited state dye molecules (Christodoulides, Khoo, Salamo, Stegeman & Van Stryland, 2010; Frenette et al., 2014). In this case, consistent with Kasha’s rule, “ Φ_{nr} ” should equal unity for any excited state relaxation process equivalent to $S_n \rightarrow S_1$ or $T_n \rightarrow T_1$, hence “ Φ_{nr} ” is only relevant for the initial linear term in Eq. 3. Thus nonlinear absorption processes contribute quantitatively to the PA response resulting in a nonlinear PA amplification for a fluorescent dye even with a significantly large fluorescence (Φ_{fl}), or indeed phosphorescence (Φ_{ph}), quantum yield, pending that the excited state absorption cross section is non-negligible. It is also important to note that the concentration of excited state dye molecules will vary with time and thus the laser pulse width is also an important consideration when optimizing such a nonlinear PA amplification with respect to the lifetime of the excited state chromophore.

5.3 Optical and Photoacoustic Z-Scan Studies

For effective correlation of the PA emission to its corresponding photophysical properties, optical and PA Z-scan (OPAZ) experiments (Yelleswarapu & Kothapalli, 2010) were performed for the RJ- C_n -MY $_m$ series of porphyrin samples. All the samples were dissolved in DMF solvent and by using a 2.0 mm path length quartz cuvette, their optical density were adjusted to 0.1 at 532 nm excitation wavelength. Same sample cuvette was used for all the measurements to avoid ambiguity. Sample preparation and PAZ-scan arrangement are explained in detail in the section 5.5. Figure 5.1 depicts the variation of optical absorbance with respect to the incident laser fluence for all RJ- C_n -

MY_m porphyrin samples as well as ZnTPP which was used as reference material. The corresponding PA response of all samples are presented in Figure 5.2.

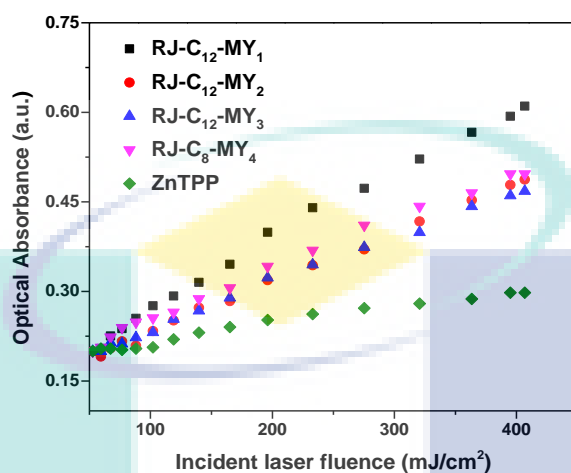


Figure 5.1 Optical absorbance as a function of laser fluence for the RJ-C_n-MY_m series of porphyrins absorbing 0.1 OD in a 2 mm quartz cuvette at 532 nm

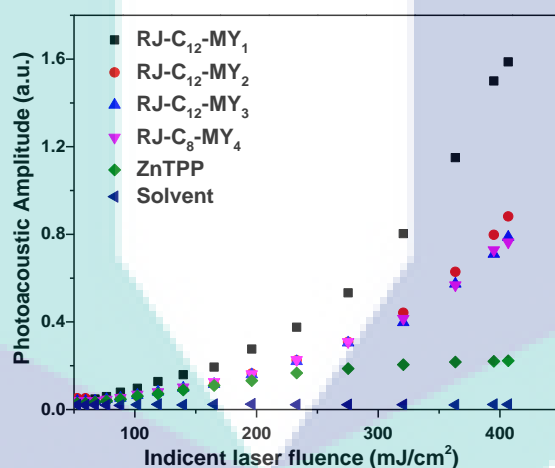


Figure 5.2 Photoacoustic response plotted with laser fluence. All the porphyrin samples were recorded at 0.1 OD in a 2 mm quartz cuvette at 532 nm

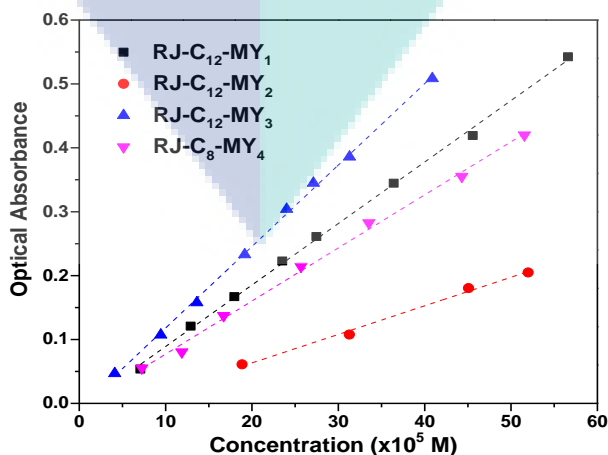
In a recent article, the correlation of photophysical properties with the PA emission of various commercial dyes have been studied (Hatamimoslehabadi et al., 2017). The dyes were categorized into linear, saturable, and reverse saturable absorbers. It was shown that crystal violet displays a characteristic linear absorber optical response where the optical absorbance is constant with the increase of incident laser fluence. However, saturable absorber's optical absorbance signals falls below that of crystal violet due to negligible excited state absorption. In contrast, reverse saturable absorber's optical absorbance is above the crystal violet and increased with laser fluence due to excited state absorption. As seen in Figure 5.1, ZnTPP and all the four newly synthesized porphyrin

molecules show typical reverse saturable absorption (RSA) behavior. Since the generated PA signal is linearly proportional to optical absorbance, the corresponding PA signal for ZnTPP and all the newly synthesized molecules (Figure 5.2) shows increase of PA signal with the incident laser fluence. Relative to the well-recognized ZnTPP, a ~7-fold enhancement is observed for the PA emission of compound RJ-C₁₂-MY₁ at the highest laser fluence of 410 mJ/cm². Similarly, compounds RJ-C₁₂-MY₂, RJ-C₁₂-MY₃, and RJ-C₈-MY₄ also exhibit a ~ 4-fold PA enhancement.

5.3.1 Dye Concentration Dependence – Low Laser Fluence

To effectively estimate the photoacoustic emission strength of each porphyrin sample, PA signal generation as a function of optical density/molar concentration at fixed low and high laser fluences have been examined. This study informs the potential of each sample as a PA contrast agent with respect to both the high and light dosage. The optical Z-scan absorption and corresponding PA emission at low laser fluence (20 mJ/cm², which is below the maximum permissible exposure limit at 532 nm) is presented in Figure 5.3.

At low incident laser fluence, RJ-C_n-MY_m series of porphyrins behave as linear absorbers, a stark contrast to that of at high laser fluence. The expected linear correlation with the observed slopes is proportional to the corresponding molar absorption coefficients (ϵ) at 532 nm (Table 5.1) – increase of slope with ϵ . The corresponding PA emission is also linear in accordance with linear relationship between the optical absorption and the PA signal generation. Results effectively illustrate the dosage vs PA response profile for each sample.



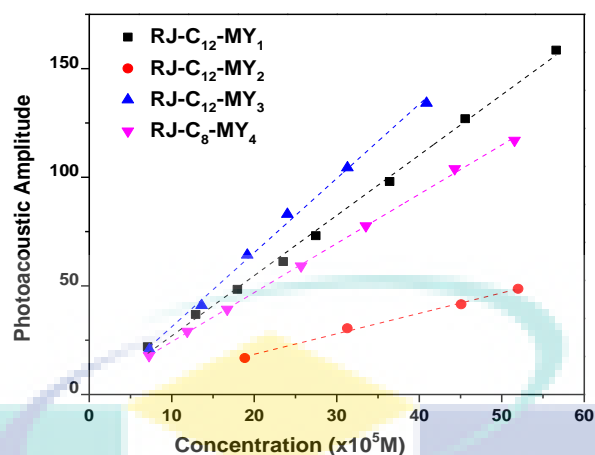


Figure 5.3 Optical Z-scan absorption (top) and photoacoustic emission (bottom) of all dyes as a function of optical density and concentration, respectively, measured at 20 mJ/cm² fluence

5.3.2 Dye Concentration Dependence – High Laser Fluence

Studies at high laser fluence could be useful for ex vivo applications such as photoacoustic microscopy (Strohm, Berndl & Kolios, 2013). The nonlinear PAM technique will also allow for high resolution optical imaging (Shelton & Applegate, 2010). Plots of optical absorption and PA amplitude vs concentration at a high laser fluence of 400 mJ/cm² are presented in Figure 5.4. Although the plots of optical absorbance vs sample concentration appear to be linear, a close observation shows slight nonlinearity. In spite of having excited state absorption, albeit low, at a fixed laser fluence and upon increasing of sample concentration, more number of molecules are competing for the same number density of photons in the ground state. Hence, there is less probability for excited state absorption. Thus reduced nonlinear absorption contribution at increased sample concentration.

The amplitude of PA emission vs sample concentrations recorded at high laser fluence is plotted in Figure 5.4. A linear enhancement of PA signal amplitude is observed with the increase in concentration for all the studied samples. The PA amplitude soars sharply with concentration for compounds RJ-C₁₂-MY₁ and RJ-C₁₂-MY₃, closely followed by compound RJ-C₁₂-MY₂, and compound RJ-C₈-MY₄ exhibiting a weak dependence of PA emission on concentration. The substantial growth of PA signal in these sample is conforming to their extinction coefficients. This confirms that the nonlinear contribution is negligible under the experimental conditions. At high laser

fluence, compound RJ-C₁₂-MY₁ featuring strong RSA behavior shows superior characteristics in the conversion of absorbed photons into acoustic signal.

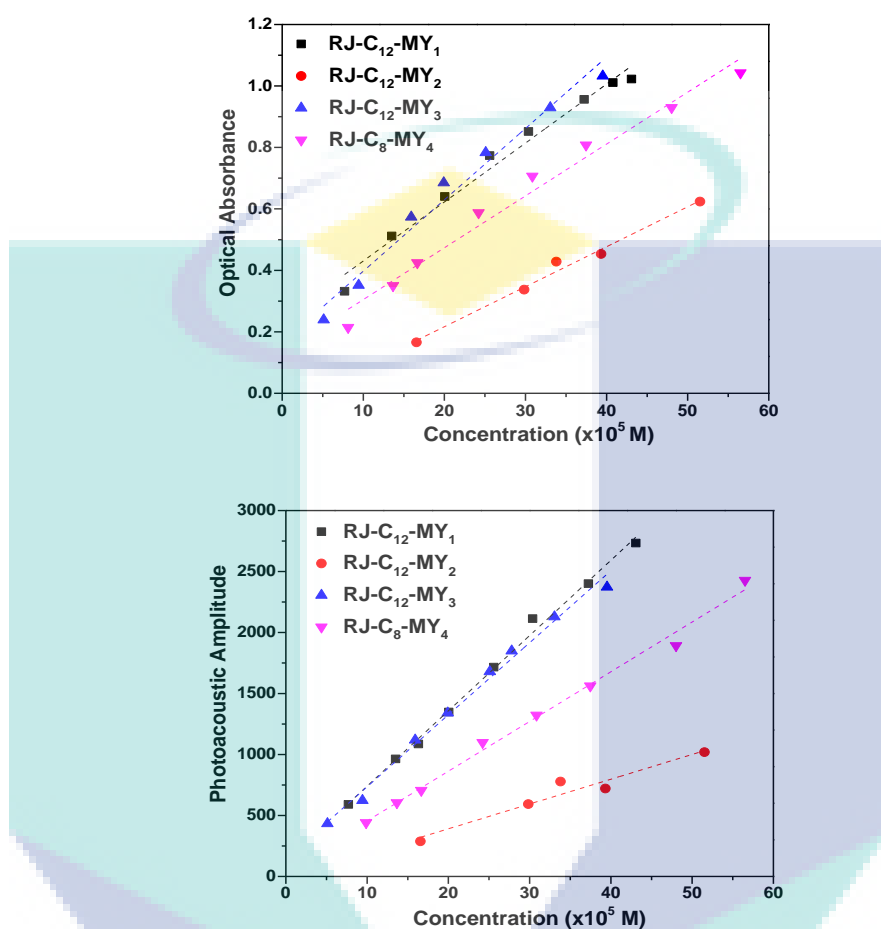


Figure 5.4 Plots of optical Z-scan absorption and PA emission vs concentration recorded 400 mJ/cm² laser fluence

Table 5.1 Molar absorption coefficients (ϵ) of RJ-C_n-MY_m series of porphyrins at 532 nm & 680 nm

Extinction Coefficient	532 nm	680 nm
RJ-C ₁₂ -MY ₁	0.48 x 10 ⁴	0.12 x 10 ⁴
RJ-C ₁₂ -MY ₂	1.05 x 10 ⁴	1.02 x 10 ⁴
RJ-C ₁₂ -MY ₃	0.75 x 10 ⁴	2.36 x 10 ⁴
RJ-C ₈ -MY ₄	0.5 x 10 ⁴	7.43 x 10 ⁴
ZnTPP	4200	0

A major requirement for contrast agents to be able to utilize for photoacoustic tomography is to have absorption in the biological window – 680 nm to 980 nm. By the

modification discussed above, the absorption of Q-bands for newly synthesized porphyrin molecules are extended into the biological window. In fact the extinction coefficient for these molecules is higher at 680 nm compared to 532 nm (Table 5.1). The photoacoustic emission behaviour as the function of input laser fluence as well as the concentration were studied. To be consistent with the studies at 532 nm, the samples were prepared in DMF solution and have an OD of 0.1 at 680 nm. Figure 5.5 shows the photoacoustic emission as the laser fluence is varied. Similar to 532 nm results, dyes display reverse saturable absorption property. Strongest PA signal emission is observed from compound RJ-C₁₂-MY₁, which is a 7-fold enhancement over the weakest PA emitter (compound RJ-C₈-MY₄). As ZnTPP do not absorb at 680 nm, it is not included for this part of the study.

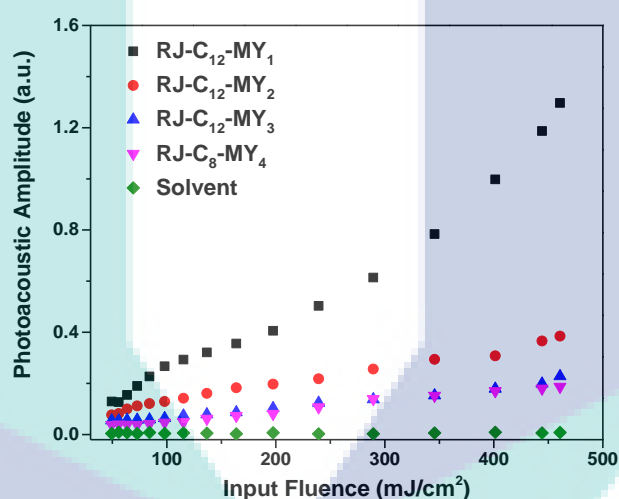


Figure 5.5 Photoacoustic response plotted with laser fluence. All the porphyrin samples were recorded at 0.3 OD in a 2 mm quartz cuvette at 680 nm

PA emission at high laser fluence is not warranted for photoacoustic tomography. Thus the photoacoustic emission strength studies have been limited to fixed low laser fluence only. Figure 5.6 denotes the variation of PA signal strength with molar concentration of all the samples. While the slopes for compounds RJ-C₁₂-MY₃ and RJ-C₈-MY₄ have increased, in comparison to 532 nm studies, and compound RJ-C₈-MY₄ shows a drastic change.

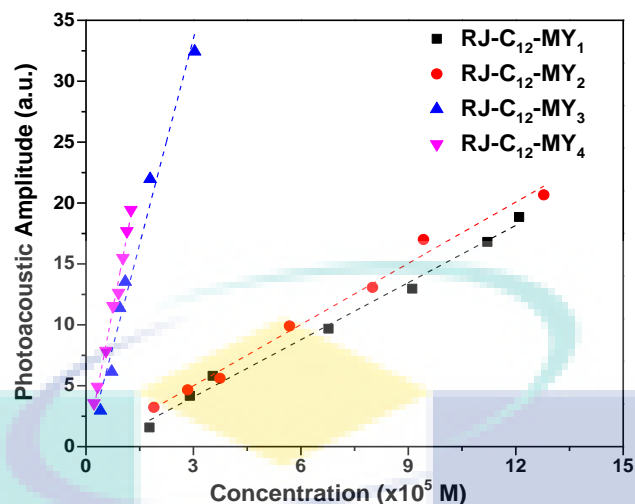


Figure 5.6 Photoacoustic emission of all the RJ-C_n-MY_m series of porphyrin as a function of concentration, respectively, measured at 20 mJ/cm² fluence

5.4 Photoacoustic Tomography

Even though all the necessary precaution to avoid any ambiguity have been taken when performing the above studies to demonstrate the strength of PA emission with the variation of incident laser fluence and/or molar concentration, a side by side comparison of each RJ-C_n-MY_m sample as PA imaging contrast agents is also necessary. Figure 5.7 displays the photoacoustic tomography reconstructed images of all the RJ-C_n-MY_m samples along with DMF solvent blank that were recorded side by side using the apparatus detailed in the section 5.6. To correlate the Z-scan results with the tomography data, imaging was conducted at 20 mJ/cm² and 400 mJ/cm². After the reconstruction of images, entire data set was normalized with respect to the optimum signal i.e., with the signal of RJ-C₁₂-MY₁ at high fluence. Both for the low and high fluence PAT, RJ-C₁₂-MY₁ displays superior PA contrast agent, agreeing with the Z-scan data.

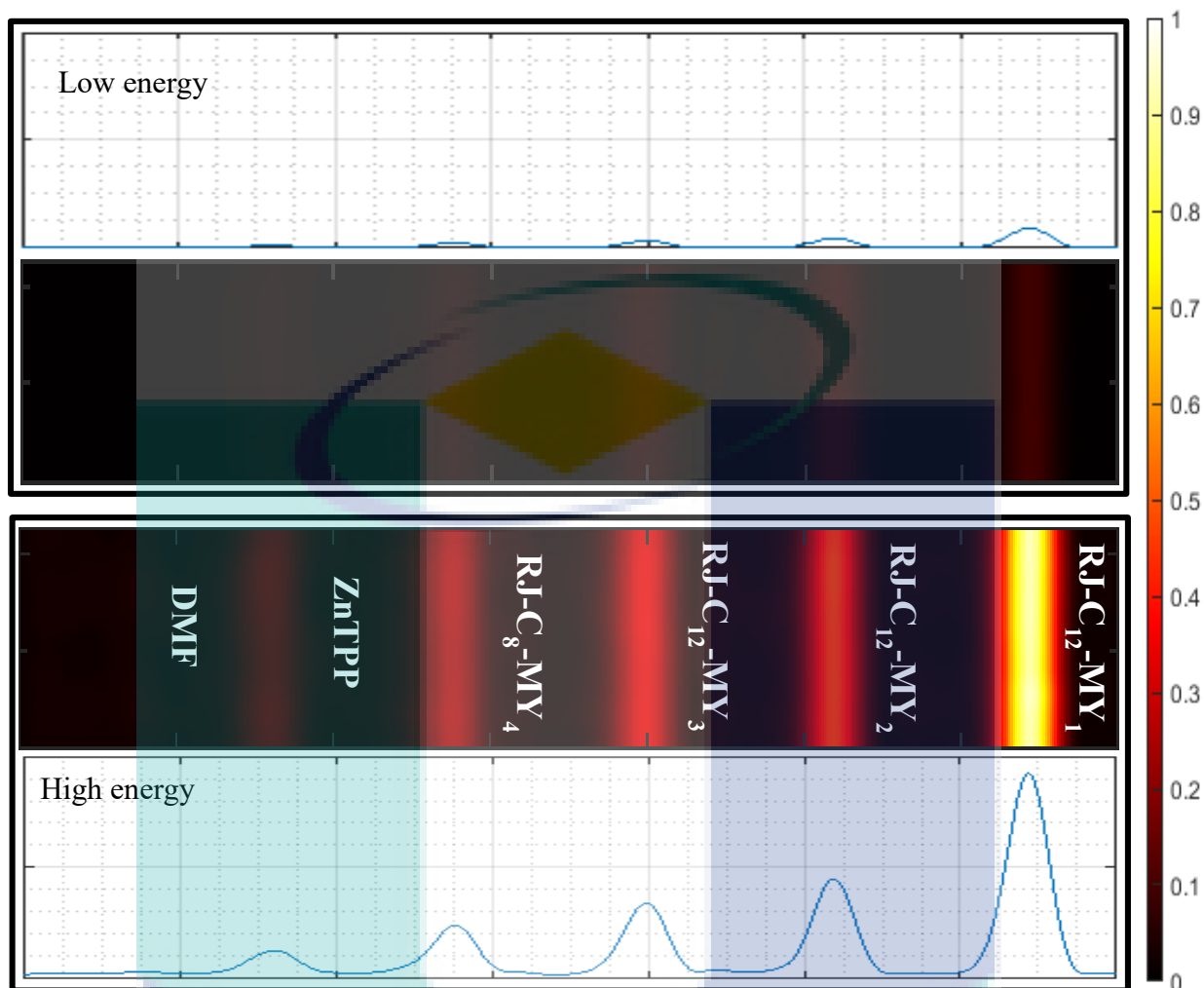


Figure 5.7 PAT image recorded at the low laser fluence of 20 mJ/cm^2 and high laser fluence of 400 mJ/cm^2 at $\lambda_{\text{exc}} = 532 \text{ nm}$. All the RJ-C_n-MY_m samples had 0.1 O.D. at 532 nm in the 1 mm path length borosilicate capillary tubes. (top) Reconstructed WORD FOR WORD image at low laser fluence, normalized with the maximum PA signal strength of high laser fluence. The line plot is the PA signal strength for each sample. (bottom) Reconstructed PAT image obtained at high laser fluence and the corresponding line profile

Once again PAT was performed using 680 nm laser with fixed low laser intensity fluence. Consistent with the molar extinction coefficient values, both within the samples at 680 nm as well as when compared to 532 nm, the PA emission is much stronger as shown in Figure 5.8.

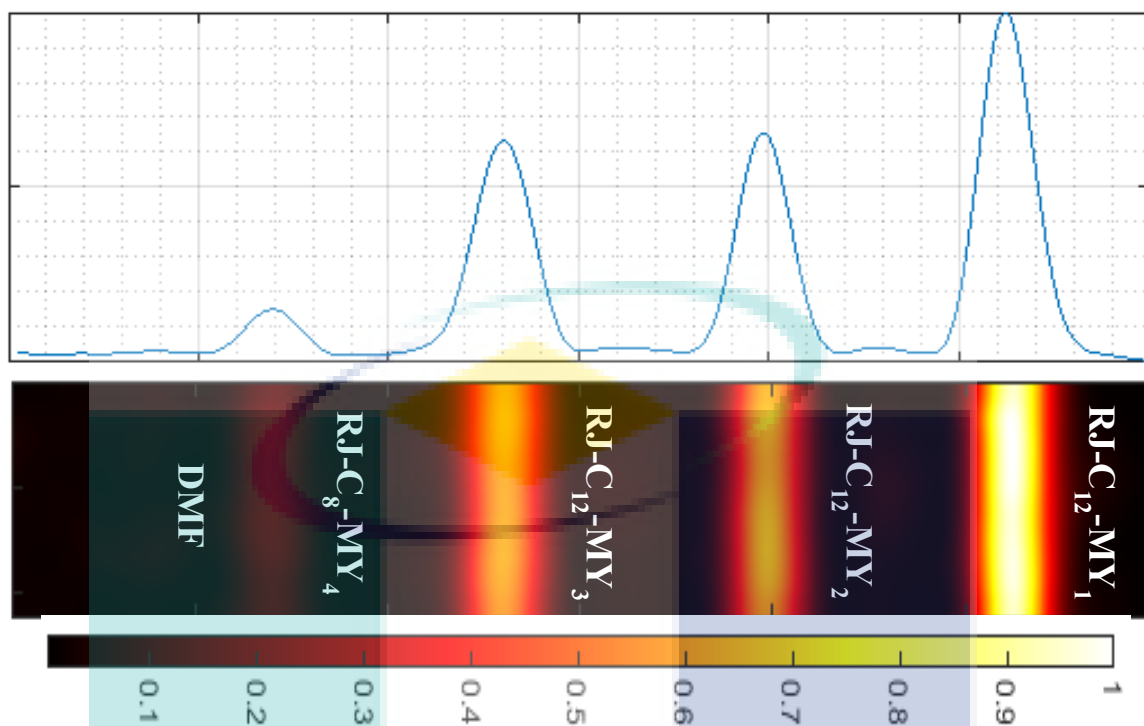


Figure 5.8 PAT image recorded at $\lambda_{\text{exc}} = 680$ nm. All the RJ-C_n-MY_m samples had 0.1 O.D. at 680 nm in the 1 mm path length borosilicate capillary tubes

5.5 Optical Photoacoustic Z-Scan Arrangement Details

All the porphyrin samples were dissolved in DMF utilizing a 2.0 mm path length quartz cuvette for preparing the solutions of 0.3 optical density (50% transmission) at excitation wavelength 532 nm. An incident angle of 45° that give an effective path length of 2.83 mm, is equivalent to a linear absorption coefficient (α) of 345 m^{-1} at 532 nm for each porphyrin sample. The UV-Vis absorption spectra of all the porphyrin samples over the range of 200 nm-800 nm wavelength were measured before and after OPAZ-scan experiments in order to confirm the stability of samples by using an Agilent Cary 60 UV-Vis Spectrophotometer. Utilizing a lens of 20 cm focal length, light from a Q-switched, doubled Nd:YAG laser (Minilite II, Continuum) with 10 Hz repetition rate of pulses, produced by 532 nm laser of 3 ns pulse width, was focused on the each porphyrin sample in order to achieve the OPAZ-scan on each sample. The 2 mm path length quartz cell containing the solution of porphyrin sample was positioned in a sample holder at 45° of incident laser light and surrounded by deionized water to get ultrasound coupling. The sample holder was then attached on an automatic XYZ translation stage (Thorlabs NRT 150) that help to move the sample holder gently in very small steps. As the porphyrin sample interpreted along the beam direction of laser through the focal plane of the lens,

the sample opposed a moderate increasing laser intensity that reached its maximum at focus and then moving the sample forward, therefore, the sample experienced a gradual drop in laser energy. Depending on the absorption properties of each porphyrin dye, the optical light transmittance and the generated PA signals have been changed by moving the sample along the direction of laser beam due to changes in the energy of laser transmitted through the sample. The PA response of each porphyrin sample was then detected by a 10 MHz focused transducer in water immersion and the light transmitted through the sample was collected by a photodiode. The beam of the laser light was measured that is 70 μm at focal point of the lens where the porphyrin sample experiences the highest laser intensity. The energy of the laser pulses was observed to be 60 μJ before it reaches the focusing lens. A neutral density filter of 1.00 OD was located in front of the detector in order to ensure the linearity of the optical detector.

For experiments with variable sample concentration accompanied at a low laser fluence of 20 mJ/cm^2 , PA data was obtained by placing the porphyrin samples at a far distance from the focal plane. For experiment with variable sample concentration done at high laser fluence (400 mJ/cm^2) PA data was obtained by placing the porphyrin samples at the focal plane.

5.6 Photoacoustic Tomography Experimental Details

All the sample solutions for PAT images were prepared similar to PAZ-scan studies, i.e. 0.3 optical density (50% transmission) at excitation wavelength of 532 nm in 2.0 mm path length quartz cuvette, and then transferred to 1 mm diameter borosilicate glass tubes that give the final optical density of 0.15. To perform PAT, all borosilicate tubes were positioned parallel inside a sample-housing unit filled with water. An arrangement of two linear translation stages (Thorlabs NRT 150) with increase movement size of 0.2 mm in longitudinal trend and 0.5 mm in the direction beside the length of capillary tube was used to move the sample holder along a planar 2D trajectory. A transducer of 10 MHz with the focal length of 25.5 mm (Olympus V311-SU) was placed at 2.54 cm vertical translation from the borosilicate tubes. A right angle prism was positioned in the setup in order to direct the beam of the Nd: YAG laser onto the borosilicate tubes. The PA signals were enhanced by using the 30 dB gain on a pulser-receiver (Olympus 5072PR) and then digitized with an oscilloscope (WaveRunner 625Zi,

Lecroy). At each step of scanning, the signals were around over 20 laser pulses. A LabVIEW interface was used to obtain the signal data while communicating with stage controllers that control the scanning movements. The PA images were then reconstructed by using MATLAB in order to calculate the absolute values of the Hilbert envelope of the developed signals at each position.

5.7 Conclusions

In conclusion, the PA studies of RJ-C_n-MY_m series of complexes were performed by OPAZ-scan and PAT in order to correlate the PA emission to its corresponding photophysical properties. The PAI properties of the complexes were analysed by using them as contrast agents using 532 and 680 nm lasers at various fluence. For PA studies at the laser of 532 nm, ZnTPP was used as reference. All the porphyrin complexes show typical reverse saturable absorption behavior. It is observed that the generated PA signal is linearly proportional to optical absorbance, therefore the corresponding PA signal for all the porphyrin complexes show increase of PA signal with the incident laser fluence. Relative to the well-recognized ZnTPP, ~7-fold PA emission enhancement is observed for the compound RJ-C₁₂-MY₁ and ~4-fold enhancement for compounds RJ-C₁₂-MY₂, RJ-C₁₂-MY₃, and RJ-C₈-MY₄ at the highest laser fluence of 410 mJ/cm². The PA signal generation as a function of optical density/molar concentration at fixed low and high laser fluences were studied to estimate the photoacoustic emission strength of each sample effectively. At low incident laser fluence, RJ-C_n-MY_m samples behave as linear absorbers and the corresponding PA emission is linear in accordance with linear relationship between the optical absorption and the PA signal generation. At a high laser fluence, a linear enhancement of PA signal with the increase in concentration is observed for all porphyrin complexes. At 680 nm laser, similar to that of 532 nm results, porphyrin molecules displayed reverse saturable absorption property and a ~7-fold PA emission enhancement was observed for compound RJ-C₁₂-MY₁ relative to that of RJ-C₈-MY₄. Beside these studies, comparison of each sample as PA imaging contrast agents was carried out by PAT studies to correlate the results with that Z-scan data. All the studies show that RJ-C₁₂-MY₁ exhibited the superior characteristics in the conversion of absorbed photons into acoustic signal, thereby displaying the superior PA contrast agent. The experimental setup used for OPAZ-scan and PAT studies are also explained in detail.

CHAPTER 6

CONCLUSIONS AND RECOMMENDATIONS

6.1 Conclusions

Broad aim of this thesis was to design, synthesize and investigate the optoelectronic properties of a series of π -conjugated meso-ethynyl-Zn(II)porphyrins for their application as contrast agents in PAI. Experimental results described in Chapters 4 and 5 show that the specific objectives outlined in Chapter 1 have been achieved. A number of meso π -conjugated porphyrins have been designed by chemical modification of basic porphine core using DFT calculations. The desired structures were investigated by their vibrational energies states as well as excited and emitting states deeply. Among them, four representative molecules (RJ-C_n-MY_m) were synthesized by adopting various synthetic protocols, characterized them and then their optoelectronic and PA properties were systematically studied. Structure of the molecules were studied by NMR spectroscopy, Mass spectrometry, and FTIR spectroscopy; optical properties were studied by UV-Vis absorption spectroscopy, photoluminescence spectroscopy, and TRPL spectroscopy; and PA properties were studied by photoacoustic spectroscopy, photoacoustic Z-scan studies and PAT. The PAI properties of the synthesized porphyrins were analyzed by using them as contrast agents using 532 and 680 nm lasers. The theoretical predictions are proven to be well established experimentally.

It is hypothesized that high PA signals could be achieved if a molecular structure is manipulated in such a way that the oscillation strength of vibrations of functional groups lying above the atoms composing the lowest unoccupied molecular orbitals are enhanced upon suitable chemical modification. Based on this assumption, a number of porphyrins molecules have been modelled. The DFT methods adopted for designing the meso-substituted porphyrin molecules included DFT/B3LYP/3-21G, DFT/B3LYP/6-

31G, DFT/B3LYP/6-31G(d), DFT/B3LYP/LANL2DZ, DFT/CAMB3LYP/3-21G, DFT/CAMB3LYP/6-31G, and DFT/CAMB3LYP/LANL2DZ levels of the theory. In order to verify the lowest energy structures, frequency calculations (IR vibrations) were performed at the same levels of theory. None of the frequency calculations produced negative frequencies, being consistent with energy minima for all the optimized geometries. The absorption spectra were calculated using LR-TDDFT method. It is notable that the theoretical and experimental data are well fitted by using B3LYP/LANL2DZ level of theory. All the calculations were done under the solvent effect using IEF-PCM model. The calculated vibrational energy levels and excited energy states were compared in order to determine the porphyrin of interest for their synthesis. It is observed that less resonating functional groups in a phenyl group attached to the porphyrin core amplify the oscillation strengths of the alkoxy groups – a systematic variation in the molecular vibrations was observed with relative change in the resonance of the molecular groups anchored.

Based on above results, four representative porphyrin molecules (RJ-C_n-MY_m) were synthesized in good yields by acid catalyzed oxidation, Knoevenagel condensation, MacDonald (2+2) condensation, bromination, metalation, deprotection, and Sonogashira coupling reactions. Utilizing the bromo Zn(II)porphyrin as reagent, RJ-C₁₂-MY₁ was synthesized with 80% yield by using Palladium-Catalyzed Sonogashira coupling reaction. Like wisely, by utilizing ethynyl-Zn(II)porphyrins and various benzyl iodides as Sonogashira reagents, RJ-C₁₂-MY₂, RJ-C₁₂-MY₃, and RJ-C₈-MY₄ were synthesized with 50%, 40% and 60% respectively by copper-free Sonogashira coupling reactions. Interestingly, RJ-C₁₂-MY₃ was synthesized by using 4-iodobenzoic acid (1.5 molar ratio) and 2-cyano-3-(4-iodophenyl)acrylic acid (1.8 molar ratio), however, mixture of products was formed. The desired RJ-C₁₂-MY₃ was separated by pre-TLC and structural confirmation was done by NMR and FTIR. Structures of the RJ-C_n-MY_m series of porphyrins were studied by NMR spectroscopy, Mass spectrometry, and FTIR spectroscopy; optical properties were studied by UV-Vis absorption spectroscopy, PL spectroscopy, and TRPL spectroscopy.

The absorption spectra of RJ-C_n-MY_m complexes, nature of their electronic transitions and their effects on PA signal were studied in detail. All the porphyrins possess typical spectrum; one intense Soret band with $\epsilon > 1 \times 10^5 \text{ M}^{-1}\text{cm}^{-1}$ at around 400 nm

followed by various low-intensity Q-bands at higher wavelengths (600 nm or above) with $\epsilon > 1 \times 10^4 \text{ M}^{-1}\text{cm}^{-1}$. The electronic transitions and the absorption bands are strongly influenced by the nature of peripheral substituents on a porphyrin core, the π -conjugating systems, the central metal ions, and their axially bound ligands. It is notable that band shifts and band broadening are attributed to the extension of π -conjugation of porphyrin ring (more resonance) by ethynyl group linker. It is also noticed that the bathochromic shifts of absorption bands are correlated to the electron withdrawing ability of meso-substituents. As the electron withdrawing ability of meso-substituents increases, the absorption bands shift toward longer wavelength also increased. The absorption band shift in RJ-C_n-MY_m series of complexes are in the order of RJ-C₈-MY₄ > RJ-C₁₂-MY₃ > RJ-C₁₂-MY₂ > RJ-C₁₂-MY₁. A most common assumption is that a molecular dye showing more absorption in NIR region could act as a strong PA contrast agent because of having the same biological transmission wavelength window (700 nm-1000 nm), thereby causing the deep penetration inside the tissue. Therefore, RJ-C₈-MY₄ could have more promising molecular PA properties among all the studied complexes. However, contrary to this assumption, the studies have demonstrated a dye with less absorption in NIR region displays enhanced PA signal because the intensity of PA signal depends on the molar absorption coefficients (ϵ) of S₀-S₂ transition. Higher the ϵ of S₀-S₂ transition could increase the possibility of strong PA signals due to the rapid non-radiative decay of S₂ excited electrons to S₁ excited state by thermal expansion. This prediction is further proved by calculating the discrete transition energies of RJ-C_n-MY_m series complexes using TDDFT calculations. In RJ-C_n-MY_m series of complexes, the ϵ values of S₀-S₂ transition decrease from RJ-C₁₂-MY₁ to RJ-C₈-MY₄ causing to decrease the PA signal in a manner of RJ-C₁₂-MY₁ > RJ-C₁₂-MY₂ > RJ-C₁₂-MY₃ > RJ-C₈-MY₄. Similarly, the strength of PA signal also depends on the energy gap. Higher the band gaps cause more rapid non-radiative decay.

The fluorescence profiles of RJ-C_n-MY_m porphyrin series changed dramatically depending upon the nature of meso-substituents as well as the wavelength used for irradiation. It is important to study the fluorescence emission spectra deeply for understanding the photophysical pathway responsible to enhance the PA signal. It is noteworthy that the intensities as well as band shifting of emission spectra depend upon the extended π -conjugation and electron donating and withdrawing groups linked to

meso-position of porphyrin core. The presence of electron donating groups and extension of π -conjugation cause the bathochromic shift of emission spectra. Whereas, hypochromic shift is occurred if there is the presence of withdrawing groups on porphyrin core. It is also observable that the effect of electron withdrawing group is more prominent than that of the extension of π -conjugation. Similarly, the Stokes shift and Φ_f of the RJ-C_n-MY_m series complexes increase as the π -conjugation increases and decrease by addition of electron withdrawing groups. A most common assumption is that a molecular dye showing a low fluorescence quantum yield would make suitable PA contrast agent. According to this respect, RJ-C₈-MY₄ having the low Φ_f could act as promising molecular PA contrast agent among all the studied complexes. However, contrary to this assumption, a dye with high Φ_f (RJ-C₁₂-MY₁) displayed the enhanced PA signal. Similarly, it is reported that a dye having long-lived S₁ excited state along with a high Φ_f facilitate a strong PA emission. However, in this study the above assumption is not corrected for all the dyes. The RJ-C₁₂-MY₂ having the low S₁ excited state lifetime (21.94 ps) produces the higher PA signal compared to that of RJ-C₈-MY₄ and RJ-C₁₂-MY₃ complexes with S₁ lifetimes 23.87 ps and 31.27 ps respectively. Instead, if considering the splitting of vibrational levels of S₁ excited state, the distance between the vibrational states may contribute in PA enhancement. Lower the distance between $v=1$ and $v=0$ vibrational levels of S₁ excited state favors the non-radiative decay and thereby enhance the PA signal.

The vibrational spectra of RJ-C_n-MY_m series of complexes are important to interpret for studying their effect on PA applications. As observed, the vibrational bands at high-frequency region are of more important for providing evidence for non-radiative decay. It is observed that the absorption coefficients of RJ-C₁₂-MY₁ in C-H vibrational bands are higher compared to other complexes indicating the removal of higher density of phonons, thereby expecting high intense photoacoustic signal as compared to other studied complexes. As the absorption coefficients of C-H vibrational modes decrease from RJ-C₁₂-MY₁ to RJ-C₈-MY₄ cause the decrease in PA signals.

Optical and PA Z-scan (OPAZ) and PAT have been performed for RJ-C_n-MY_m series of complexes to effectively correlate of the PA emission to its corresponding photophysical properties. At the laser of 532 nm, ZnTPP and all the porphyrin dyes have shown typical reverse saturable absorption behavior. Since the generated PA signal is

linearly proportional to optical absorbance, the corresponding PA signal for ZnTPP and all the porphyrin dyes show increase of PA signal with the incident laser fluence. Relative to the well-recognized ZnTPP, ~7-fold enhancement is observed for the PA emission of compound RJ-C₁₂-MY₁. The PA signal generation as a function of optical density/molar concentration at fixed low and high laser fluences have also been examined in order to estimate the PA emission strength of each RJ-C_n-MY_m porphyrin effectively. At low incident laser fluence, porphyrin dyes behave as linear absorbers. At a high laser fluence, compound RJ-C₁₂-MY₁ has shown the superior characteristics in the conversion of absorbed photons into acoustic signal. Similar to 532 nm results, porphyrin molecules display reverse saturable absorption property at 680 nm laser. Enhanced PA signal emission is observed in compound RJ-C₁₂-MY₁, which is ~4-fold enhancement over the RJ-C₈-MY₄. Moreover, PAT images show that the RJ-C₁₂-MY₁ displayed the superior PA contrast agent relative to other studies complexes.

More importantly, the effect of resonating structures on PA signal strength by phonon emission (non-radiative decay) through vibrational IR absorption were studied here for the first time. It is observable that the electron withdrawing abilities of nitrile and carboxylic acid groups linked to RJ-C₈-MY₄ cause the reduction of electron density on the porphyrin core, thus influencing the C-H bonds to act as less intense IR absorber. This causes the phonon emission of lower energy and thereby reducing the PA signal strength. While in case of RJ-C₁₂-MY₁, the two carboxyl groups on 3-position of phenyl groups have less ability to attract the electronic density, therefore having more electron density on porphyrin core and that of C-H bonds region which causes the generation of strong PA signal.

6.2 Future Recommendations

Because of time constraints for this doctoral research, there are still number of experiments which could be done to further characterize the optoelectronic properties of porphyrins dyes for their PA applications. As the development of molecular photoacoustic contrast agent is newly emerging field of research, there is rare literature on designing the small molecular porphyrin contrast agent for PAI. Moreover, the development of new PA molecule is limited because the factors influencing the PA effect have rarely been systematically studied, thus lacking the guidance for designing the

molecular PA contrast agent. Therefore, a number of opportunities to explore this area of research is still waiting. So far, dedicated efforts to develop Zn(II)porphyrins as a molecular contrast agent by tailoring their optoelectronic properties have not been undertaken and a first attempt has been made in this dissertation. The questions that need to be answered at the end of the study are: *(i) how to synthesize the water-soluble porphyrin dyes that could be suitable for PAI? (ii) what strategies are required to design porphyrin dyes suitable for in-vivo studies? And (iii) what are the porphyrins that could be clinical used as PAI contrast agents?*

There are only few PAI contrast agents that are clinical used. The best studied PAI contrast agent is the FDA-approved ocular angiographic dye indocyanine green (ICG) and their derivatives possessing NIR absorption at $\lambda_{\text{max}} \sim 800$ nm, although the significant fluorescence of ICG derivatives do not make them ideal contrast agents. A part of the absorbed light is not translated as a PA signal, reducing their usefulness as a PAI contrast agent. Moreover, ICG derivatives are limited to the vasculature space and clear rapidly ($t_{1/2} \leq 3$ min), thus complicating the longitudinal in-vivo studies. Regardless of these shortcomings, the ICG derivatives are suggested as benchmark dyes. The limitation for the development of molecular PA contrast agent highlights the rational development of PA dyes that could be suitable for biological PA applications. Porphyrins are particularly interesting due to their high optical absorption, stability, and biocompatibility, long lifetimes and tunable optoelectronic properties. By continuing the current work, the structure of studied porphyrins could be modified by two different approaches i.e.; i) by replacing the long alkoxy-chain groups with water-soluble functional groups such as polyethylene glycol that could synthesize the suitable water-soluble porphyrin PAI contrast agents and ii) by replacing the acid groups with their corresponding salts that could make them water soluble.

REFERENCES

- Abedian, N. and Dehghani, H. (2013). Novel molecular complexation between meso-tetraarylporphyrinato magnesium(II) and phosphorus(III) chloride. *Inorganic Chemistry Communications*, 36, 77-80.
- Abraham, R. J., Hawkes, G. E., Hudson, M. F. and Smith, K. M. (1975). The nuclear magnetic resonance spectra of porphyrins. Part X. Carbon-13 nuclear magnetic resonance spectra of some meso-tetraarylporphyrins and their metal chelates. *Journal of the Chemical Society, Perkin Transactions*, 2(3), 204-211.
- Abrahamse, H. and Hamblin, M. R. (2016). New photosensitizers for photodynamic therapy. *Biochemical Journal*, 473(4), 347-364.
- Abuteen, A., Zanganeh, S., Akhigbe, J., Samankumara, L. P., Aguirre, A., Biswal, N. . . Brückner, C. (2013). The evaluation of NIR-absorbing porphyrin derivatives as contrast agents in photoacoustic imaging. *Physical Chemistry Chemical Physics*, 15(42), 18502-18509.
- Adar, F. (1978). Electronic absorption spectra of hemes and hemoproteins. In D. Dolphin (Ed.), *The Porphyrins* (Vol 3, pp 167-209). New York: Academic Press.
- Adler, A. D. and Gouterman, M. (1985). *An historical survey of porphyrins, their related spectra and their interpretation*. Paper presented at the Optical properties and structure of tetrapyrroles: proceedings of a symposium held at the University of Konstanz, West Germany, August 12-17, 1984.
- Adler, A. D., Longo, F. R., Finarelli, J. D., Goldmacher, J., Assour, J. and Korsakoff, L. (1967). A simplified synthesis for meso-tetraphenylporphine. *The Journal of Organic Chemistry*, 32(2), 476-476.
- Adler, A. D., Longo, F. R., Kampas, F. and Kim, J. (1970). On the preparation of metalloporphyrins. *Journal of Inorganic and Nuclear Chemistry*, 32(7), 2443-2445.
- Aihara, H., Jaquinod, L., Nurco, D. J. and Smith, K. M. (2001). Multicarbocycle Formation Mediated by Arenoporphyrin 1, 4-Diradicals: Synthesis of Picenoporphyrins. *Angewandte Chemie International Edition*, 40(18), 3439-3441.
- Aizawa, K., Okunaka, T., Ohtani, T., Kawabe, H., Yasunaka, Y., O'Hata, S. . . . Kato, H. (1987). Localization of mono-l-aspartyl chlorin e6 (npe6) in mouse tissues. *Photochemistry and Photobiology*, 46(5), 789-793.

- Akins, D., Zhu, H.-R. and Guo, C. (1994). Absorption and Raman scattering by aggregated meso-tetrakis (p-sulfonatophenyl) porphine. *The Journal of Physical Chemistry*, 98(14), 3612-3618.
- Akins, D. L., Özçelik, S., Zhu, H.-R. and Guo, C. (1996). Fluorescence decay kinetics and structure of aggregated tetrakis (p-sulfonatophenyl) porphyrin. *The Journal of Physical Chemistry*, 100(34), 14390-14396.
- Al-Karadaghi, S., Franco, R., Hansson, M., Shelnut, J. A., Isaya, G. and Ferreira, G. C. (2006). Chelataes: distort to select? *Trends in Biochemical Sciences*, 31(3), 135-142.
- Ali, H. and van Lier, J. E. (1991). Phenylselenenyl halides: Efficient reagents for the selective halogenation and nitration of porphyrins. *Tetrahedron Letters*, 32(38), 5015-5018.
- Ali, H. and van Lier, J. E. (1994). Synthesis of β -substituted porphyrins using palladium catalysed reactions. *Tetrahedron*, 50(41), 11933-11944.
- Amao, Y., Asai, K., Miyakawa, K. and Okura, I. (2000). Oxygen sensing using palladium porphyrin with long alkyl chain self-assembled film. *Journal of Porphyrins and Phthalocyanines*, 4(1), 19-22.
- Ambroise, A., Wagner, R. W., Rao, P. D., Riggs, J. A., Hascoat, P., Diers, J. R. . . . Holten, D. (2001). Design and synthesis of porphyrin-based optoelectronic gates. *Chemistry of Materials*, 13(3), 1023-1034.
- Anderson, H. L. (1994). Conjugated porphyrin ladders. *Inorganic Chemistry*, 33(5), 972-981.
- Andrews, L. E., Bonnett, R., Kozyrev, A. N. and Appelman, E. H. (1988). meso-Reactivity of porphyrins and related compounds. Part 10. Direct fluorination of octaethylporphyrin with caesium fluoroxysulphate. *Journal of the Chemical Society, Perkin Transactions*, 1(7), 1735-1738.
- Andzelm, J., Rinderspacher, B. C., Rawlett, A., Dougherty, J., Baer, R. and Govind, N. (2009). Performance of DFT methods in the calculation of optical spectra of TCF-chromophores. *Journal of Chemical Theory and Computation*, 5(10), 2835-2846.
- Aoyagi, K., Haga, T., Toi, H., Aoyama, Y., Mizutani, T. and Ogoshi, H. (1997). Electron Deficient Porphyrins III. Facile Syntheses of Perfluoroalkylporphyrins Including Water Soluble Porphyrin. *Bulletin of the Chemical Society of Japan*, 70(4), 937-943.
- Aratani, N., Kim, D. and Osuka, A. (2009). π -Conjugation Enlargement Toward the Creation of Multi-Porphyrinic Systems with Large Two-Photon Absorption Properties. *Chemistry—An Asian Journal*, 4(8), 1172-1182.

- Atefi, F. and Arnold, D. P. (2008). Porphyrins with metal, metalloid or phosphorus atoms directly bonded to the carbon periphery. *Journal of Porphyrins and Phthalocyanines*, 12(07), 801-831.
- Atkinson, S., Brady, S., James, J. and Nolan, K. (1995). Synthetic haems as mimics for high valent intermediates in haemoprotein catalysed oxidations. Synthesis and oxidation of chloro-7, 8, 17, 18-tetracyano-5, 10, 15, 20-tetraphenylporphyrinatoiron (III), a haem which contains strongly electron-withdrawing groups in the β -pyrrole positions. *Pure and Applied Chemistry*, 67(7), 1109-1116.
- Baba, H., Chen, J., Shinokubo, H. and Osuka, A. (2008). Efficient Rhodium-Catalyzed Installation of Unsaturated Ester Functions onto Porphyrins: Site-Specific Heck-Type Addition versus Conjugate Addition. *Chemistry-A European Journal*, 14(14), 4256-4262.
- Bakar, M. A., Sergeeva, N. N., Juillard, T. and Senge, M. O. (2011). Synthesis of ferrocenyl porphyrins via suzuki coupling and their photophysical properties. *Organometallics*, 30(11), 3225-3228.
- Barkigia, K., Fajer, J., Adler, A. and Williams, G. (1980). Crystal and molecular structure of (5, 10, 15, 20-tetra-N-propylporphinato) lead (II): a "roof" porphyrin. *Inorganic Chemistry*, 19(7), 2057-2061.
- Barkigia, K. M., Berber, M. D., Fajer, J., Medforth, C. J., Renner, M. W. and Smith, K. M. (1990). Nonplanar porphyrins. X-ray structures of (2, 3, 7, 8, 12, 13, 17, 18-octaethyl-and-octamethyl-5, 10, 15, 20-tetraphenylporphinato) zinc (II). *Journal of the American Chemical Society*, 112(24), 8851-8857.
- Barnes, J. and Dorough, G. (1950). Exchange and Replacement Reactions of α , β , γ , δ -Tetraphenyl-metalloporphyrins. *Journal of the American Chemical Society*, 72(9), 4045-4050.
- Barnett, G. H., Hudson, M. F. and Smith, K. M. (1975). Concerning meso-tetraphenylporphyrin purification. *Journal of the Chemical Society, Perkin Transactions*, 1(14), 1401-1403.
- Bartoli, J., Battioni, P., De Foor, W. and Mansuy, D. (1994). Synthesis and remarkable properties of iron β -polynitroporphyrins as catalysts for monooxygenation reactions. *Journal of the Chemical Society. Chemical Communications*, (1), 23-24.
- Baruah, T. and Pederson, M. R. (2009). DFT calculations on charge-transfer states of a Carotenoid-Porphyrin-C60 molecular triad. *Journal of Chemical Theory and Computation*, 5(4), 834-843.

- Battersby, A. R., Hunt, E., Ihara, M., McDonald, E., Paine, J. B., Satoh, F. and Saunders, J. (1974). Structure of a heptacarboxylic porphyrin enzymically derived from porphobilinogen. *Journal of the Chemical Society, Chemical Communications*, (23), 994-995.
- Bauschlicher, C. W. (1995). A comparison of the accuracy of different functionals. *Chemical Physics Letters*, 246(1), 40-44.
- Bayer, C. L., Wlodarczyk, B. J., Finnell, R. H. and Emelianov, S. Y. (2017). Ultrasound-guided spectral photoacoustic imaging of hemoglobin oxygenation during development. *Biomedical Optics Express*, 8(2), 757-763.
- Becke, A. D. (1988). Density-functional exchange-energy approximation with correct asymptotic behavior. *Physical Review A*, 38(6), 3098-3100.
- Becke, A. D. (1992). Density-functional thermochemistry. I. The effect of the exchange-only gradient correction. *The Journal of Chemical Physics*, 96(3), 2155-2160.
- Becke, A. D. (1993). Becke's three parameter hybrid method using the LYP correlation functional. *Journal of Chemical Physics*, 98, 5648-5652.
- Beyzavi, M. H., Lentz, D., Reissig, H. U. and Wiehe, A. (2013). Synthesis of Functionalized, Sterically Congested Calix [4] phyrin Macrocycles Using Donor–Acceptor-Substituted Cyclopropanes—First Example of a Mono-meso-spirolactone Incorporated into a Calix [4] phyrin. *European Journal of Organic Chemistry*, 2013(2), 269-282.
- Bhyrappa, P. and Krishnan, V. (1991). Octabromotetraphenylporphyrin and its metal derivatives: Electronic structure and electrochemical properties. *Inorganic Chemistry*, 30(2), 239-245.
- Bhyrappa, P. and Purushothaman, B. (2001). Perbrominated 2-nitrotetraphenylporphyrins: electrochemical and axial ligation properties. *Journal of the Chemical Society, Perkin Transactions*, 2(2), 238-242.
- Binstead, R. A., Crossley, M. J. and Hush, N. S. (1991). Modulation of valence orbital levels of metalloporphyrins by beta.-substitution: evidence from spectroscopic and electrochemical studies of 2-substituted metallo-5, 10, 15, 20-tetraphenylporphyrins. *Inorganic Chemistry*, 30(6), 1259-1264.
- Böhm, P. and Gröger, H. (2015). Iron (III)-porphyrin Complex FeTSP: A Versatile Water-soluble Catalyst for Oxidations in Organic Syntheses, Biorenewables Degradation and Environmental Applications. *ChemCatChem*, 7(1), 22-28.
- Bonnett, R., Gale, I. and Stephenson, G. (1966). The meso-reactivity of porphyrins and related compounds. Part II. Halogenation. *Journal of the Chemical Society C: Organic*, 1600-1604.

- Bonnett, R. and Stephenson, G. (1965). The meso reactivity of porphyrins and related compounds. I. Nitration. *The Journal of Organic Chemistry*, 30(8), 2791-2798.
- Borah, K. D. and Bhuyan, J. (2017). Magnesium porphyrins with relevance to chlorophylls. *Dalton Transactions*, 46(20), 6497-6509.
- Boudif, A. and Momenteau, M. (1994). Synthesis of a porphyrin-2, 3-diacrylic acid using a new '3+ 1' type procedure. *Journal of the Chemical Society, Chemical Communications*, (18), 2069-2070.
- Boudif, A. and Momenteau, M. (1996). A new convergent method for porphyrin synthesis based on a '3+ 1' condensation. *Journal of the Chemical Society, Perkin Transactions*, 1(11), 1235-1242.
- Boyle, R. W., Johnson, C. K. and Dolphin, D. (1995). Iodination and Heck alkynylation of 5, 15-diphenylporphyrin. A convenient entry to asymmetrically meso-substituted porphyrins. *Journal of the Chemical Society, Chemical Communications*, (5), 527-528.
- Boys, S. F. (1950). *Electronic wave functions. I. A general method of calculation for the stationary states of any molecular system*. Paper presented at the Proceedings of the Royal Society of London A: Mathematical, Physical and Engineering Sciences.
- Braslavsky, S. E. and Heibel, G. E. (1992). Time-resolved photothermal and photoacoustic methods applied to photoinduced processes in solution. *Chemical Reviews*, 92(6), 1381-1410.
- Broadhurst, M., Grigg, R. and Johnson, A. (1971). Synthesis of porphin analogues containing furan and/or thiophen rings. *Journal of the Chemical Society C: Organic*, 3681-3690.
- Browning, L. M., Lee, K. J., Huang, T., Nallathamby, P. D., Lowman, J. E. and Nancy Xu, X.-H. (2009). Random walk of single gold nanoparticles in zebrafish embryos leading to stochastic toxic effects on embryonic developments. *Nanoscale*, 1(1), 138-152.
- Brückner, C., Hyland, M. A., Sternberg, E. D., MacAlpine, J. K., Rettig, S. J., Patrick, B. O. and Dolphin, D. (2005). Preparation of [meso-tetraphenylchlorophinato] nickel (II) by stepwise deformylation of [meso-tetraphenyl-2, 3-diformyl-secochlorinato] nickel (II): conformational consequences of breaking the structural integrity of nickel porphyrins. *Inorganica Chimica Acta*, 358(10), 2943-2953.
- Buchler, J. (1978). Synthesis and properties of metalloporphyrins. In D. Dolphin (ed.), *The porphyrins* (Vol. 1, pp. 389). New York: Academic Press.

- Burrell, A. K. and Officer, D. L. (1998). Functionalizing porphyrins via Wittig reactions: a building block approach. *Synlett*, 1998(12), 1297-1307.
- Callot, H. (1974). Bromination of meta-tetraphenylporphine-preparation of alkyl derivatives and polycyanoporphines. *Bulletin De La Societe Chimique De France Partie Ii-Chimie Moleculaire Organique Et Biologique* (7-8), 1492-1496.
- Calvin, M., Ball, R. and Aronoff, S. (1943). α , β , γ , δ -Tetraphenylchlorin. *Journal of the American Chemical Society*, 65(11), 2259-2259.
- Caspar, J. V. and Meyer, T. J. (1983). Application of the energy gap law to nonradiative, excited-state decay. *The Journal of Physical Chemistry*, 87(6), 952-957.
- Cavaleiro, J. A., Gonsalves, A. M. d. A. R., Kenner, G. W. and Smith, K. M. (1973). Pyrroles and related compounds. Part XXII. Syntheses of pyrromethanes and a tripyrrane. *Journal of the Chemical Society, Perkin Transactions, 1*, 2471-2478.
- Cavaleiro, J. A., Gonsalves, A. M. d. A. R., Kenner, G. W. and Smith, K. M. (1974). Pyrroles and related compounds. Part XXXIII. Total synthesis of deuteriated derivatives of protoporphyrin-IX for nuclear magnetic resonance studies of haemoproteins. *Journal of the Chemical Society, Perkin Transactions, 1*, 1771-1781.
- Chai, J.-D. and Head-Gordon, M. (2008a). Long-range corrected hybrid density functionals with damped atom-atom dispersion corrections. *Physical Chemistry Chemical Physics*, 10(44), 6615-6620.
- Chai, J.-D. and Head-Gordon, M. (2008b). Systematic optimization of long-range corrected hybrid density functionals. *The Journal of Chemical Physics*, 128(8), 084106 (1-15).
- Chandra, T., Kraft, B. J., Huffman, J. C. and Zaleski, J. M. (2003). Synthesis and structural characterization of porphyrinic enediynes: Geometric and electronic effects on thermal and photochemical reactivity. *Inorganic Chemistry*, 42(17), 5158-5172.
- Chaves, O. A., Jesus, C. S., Henriques, E. S., Brito, R. M. and Serpa, C. (2016). In situ ultra-fast heat deposition does not perturb the structure of serum albumin. *Photochemical & Photobiological Sciences*, 15(12), 1524-1535.
- Check, C. E., Faust, T. O., Bailey, J. M., Wright, B. J., Gilbert, T. M. and Sunderlin, L. S. (2001). Addition of polarization and diffuse functions to the LANL2DZ basis set for p-block elements. *The Journal of Physical Chemistry A*, 105(34), 8111-8116.

- Chen, D.-M., Zhang, Y.-H., He, T.-J. and Liu, F.-C. (2002). Raman and UV–visible absorption spectra of ion-paired aggregates of copper porphyrins. *Spectrochimica Acta Part A: Molecular and Biomolecular Spectroscopy*, 58(10), 2291-2297.
- Chen, J., Aratani, N., Shinokubo, H. and Osuka, A. (2009). Post-Modification of meso–meso-Linked Porphyrin Arrays by Iridium and Rhodium Catalyses for Tuning of Energy Gap. *Chemistry–An Asian Journal*, 4(7), 1126-1133.
- Chen, Y.-J., Lee, G.-H., Peng, S.-M. and Yeh, C.-Y. (2005). Unexpected formation of porphyrinic enyne under Sonogashira conditions. *Tetrahedron Letters*, 46(9), 1541-1544.
- Chen, Y.-S., Frey, W., Kim, S., Kruizinga, P., Homan, K. and Emelianov, S. (2011). Silica-coated gold nanorods as photoacoustic signal nanoamplifiers. *Nano Letters*, 11(2), 348-354.
- Chen, Y. and Zhang, X. P. (2003). Facile and Efficient Synthesis of meso-Arylamino- and Alkylamino-Substituted Porphyrins via Palladium-Catalyzed Amination. *The Journal of Organic Chemistry*, 68(11), 4432-4438.
- Chinchilla, R. and Nájera, C. (2007). The Sonogashira reaction: a booming methodology in synthetic organic chemistry. *Chemical Reviews*, 107(3), 874-922.
- Chinchilla, R. and Nájera, C. (2011). Recent advances in Sonogashira reactions. *Chemical Society Reviews*, 40(10), 5084-5121.
- Chizhova, N., Kumeev, R. and Mamardashvili, N. Z. (2013). Synthesis and spectral properties of cobalt (II) and cobalt (III) tetraarylporphyrinates. *Russian Journal of Inorganic Chemistry*, 58(6), 740-743.
- Chorghade, M., Dolphin, D., Dupre, D., Hill, D., Lee, E. and Wijesekera, T. (1996). Improved protocols for the synthesis and halogenation of sterically hindered metalloporphyrins. *Synthesis*, 1996(11), 1320-1324.
- Christodoulides, D. N., Khoo, I. C., Salamo, G. J., Stegeman, G. I. and Van Stryland, E. W. (2010). Nonlinear refraction and absorption: mechanisms and magnitudes. *Advances in Optics and Photonics*, 2(1), 60-200.
- Chumakov, D., Khoroshutin, A., Anisimov, A. and Kobrakov, K. (2009). Bromination of porphyrins. *Chemistry of Heterocyclic Compounds*, 45(3), 259-283.
- Čížek, J. (1966). On the correlation problem in atomic and molecular systems. Calculation of wavefunction components in Ursell-type expansion using quantum-field theoretical methods. *The Journal of Chemical Physics*, 45(11), 4256-4266.

- Collman, J., Barnes, C., Brothers, P., Collins, T., Ozawa, T., Gallucci, J. and Ibers, J. A. (1984). Oxidation of ruthenium (II) and ruthenium (III) porphyrins. Crystal structures of μ -oxo-bis [(p-methylphenoxy)(meso-tetraphenylporphyrinato)ruthenium (IV)] and ethoxo (meso-tetraphenylporphyrinato)(ethanol) ruthenium (III)-bisethanol. *Journal of the American Chemical Society*, 106(18), 5151-5163.
- Collman, J. P., Barnes, C. E., Swepston, P. N. and Ibers, J. A. (1984). Synthesis, proton NMR, and structural characterization of binuclear ruthenium porphyrin dimers. *Journal of the American Chemical Society*, 106(12), 3500-3510.
- Cook, L., Brewer, G. and Wong-Ng, W. (2017). Structural aspects of porphyrins for functional materials applications. *Crystals*, 7(7), 223(1-22).
- Cramer, C. J. (2013). *Essentials of computational chemistry: theories and models*. USA: John Wiley & Sons.
- Cunha, A. C., Gomes, A. T., Ferreira, V. F., de Souza, M. C., Neves, M. G., Tomé, A. C., . . . Cavaleiro, J. A. (2010). Synthesis of β -Arylporphyrins and Oligophenylenediporphyrins by the Suzuki-Miyaura Reaction. *Synthesis*, 2010(03), 510-514.
- Curtiss, L. A., Redfern, P. C. and Raghavachari, K. (2005). Assessment of Gaussian-3 and density-functional theories on the G3/05 test set of experimental energies. *The Journal of Chemical Physics*, 123(12), 124107(1-12).
- D'Souza, F. and Ito, O. (2005). Photoinduced electron transfer in supramolecular systems of fullerenes functionalized with ligands capable of binding to zinc porphyrins and zinc phthalocyanines. *Coordination Chemistry Reviews*, 249(13), 1410-1422.
- da GH Vicente, M. and M Smith, K. (2014). Syntheses and functionalizations of porphyrin macrocycles. *Current Organic Synthesis*, 11(1), 3-28.
- Dahal, S. and Krishnan, V. (1995). Charge transfer excited states of zinc (II) derivatives of β -substituted dinitrotetraphenylporphyrin. *Journal of Photochemistry and Photobiology A: Chemistry*, 89(2), 105-112.
- Danquah, M. (2017). Review of Handbook of Porphyrin Science with Application to Chemistry, Physics, Materials Science, Engineering, Biology and Medicine. Volume 40: Nanoorganization of Porphyrinoids. *Journal Of Natural Products*, 80(4), 1232-1232.
- Davidson, E. R. and Feller, D. (1986). Basis set selection for molecular calculations. *Chemical Reviews*, 86(4), 681-696.
- de Almeida, J. B., Kenner, G., Rimmer, J. and Smith, K. (1976). Pyrroles and related compounds—XXXV: A stepwise, general synthesis of unsymmetrically substituted porphyrins. *Tetrahedron*, 32(14), 1793-1799.

- de la Zerda, A., Bodapati, S., Teed, R., May, S. Y., Tabakman, S. M., Liu, Z. . . . Gambhir, S. S. (2012). Family of enhanced photoacoustic imaging agents for high-sensitivity and multiplexing studies in living mice. *ACS Nano*, 6(6), 4694-4701.
- Del Bene, J. E., Person, W. B. and Szczepaniak, K. (1995). Properties of Hydrogen-Bonded Complexes Obtained from the B3LYP Functional with 6-31G (d, p) and 6-31+ G (d, p) Basis Sets: Comparison with MP2/6-31+ G (d, p) Results and Experimental Data. *The Journal of Physical Chemistry*, 99(27), 10705-10707.
- Deshpande, R., Jiang, L., Schmidt, G., Rakovan, J., Wang, X., Wheeler, K. and Wang, H. (2009). A Concise Approach to the Synthesis of opp-Dibenzoporphyrins through the Heck Reaction. *Organic Letters*, 11(19), 4251-4253.
- Devillers, C. H., Hebié, S., Lucas, D., Cattey, H., Clément, S. and Richeter, S. (2014). Aromatic Nucleophilic Substitution (S_NAr) of meso-Nitroporphyrin with Azide and Amines as an Alternative Metal Catalyst Free Synthetic Approach To Obtain meso-N-Substituted Porphyrins. *The Journal of Organic Chemistry*, 79(14), 6424-6434.
- Dierksen, M. and Grimme, S. (2004). Density functional calculations of the vibronic structure of electronic absorption spectra. *The Journal of Chemical Physics*, 120(8), 3544-3554.
- DiMagno, S. G., Lin, V. S. and Therien, M. J. (1993). Facile elaboration of porphyrins via metal-mediated cross-coupling. *The Journal of Organic Chemistry*, 58(22), 5983-5993.
- Djelal, B. and George Truscott, T. (1999). Photophysical properties of 5, 10, 15, 20-tetrakis (m-hydroxyphenyl) porphyrin (m-THPP), 5, 10, 15, 20-tetrakis (m-hydroxyphenyl) chlorin (m-THPC) and 5, 10, 15, 20-tetrakis (m-hydroxyphenyl) bacteriochlorin (m-THPBC): a comparative study. *Journal of the Chemical Society, Perkin Transactions*, 2(2), 325-328.
- Dogutan, D. K., Ptaszek, M. and Lindsey, J. S. (2007). Direct synthesis of magnesium porphine via 1-formyldipyromethane. *The Journal of Organic Chemistry*, 72(13), 5008-5011.
- Dogutan, D. K., Ptaszek, M. and Lindsey, J. S. (2008). Rational or statistical routes from 1-acyldipyromethanes to meso-substituted porphyrins. Distinct patterns, multiple pyridyl substituents, and amphipathic architectures. *The Journal of Organic Chemistry*, 73(16), 6187-6201.
- Dolphin, D. (Ed.). (1978). *The Porphyrins: Structure and Synthesis, Part A* (Vol. 1). London: Academic Press.

- Dong, H., Hou, T., Zhao, Y., Fu, X. and Li, Y. (2012). DFT study of cobalt porphyrin complex for living radical polymerization of olefins. *Computational and Theoretical Chemistry*, 1001, 51-59.
- Drabkin, D. L. (2012). Selected landmarks in the history of porphyrins and their biologically functional derivatives. In D. Dolphin (ed.), *The porphyrins, Structure and Synthesis, Part 1* (Vol. 1, pp. 29-71) New York: Academic Press.
- Drain, C. M., Kirmaier, C., Medforth, C. J., Nurco, D. J., Smith, K. M. and Holten, D. (1996). Dynamic photophysical properties of conformationally distorted nickel porphyrins. 1. Nickel (II) dodecaphenylporphyrin. *The Journal of Physical Chemistry*, 100(29), 11984-11993.
- Dumoulin, F. and Ahsen, V. (2011). Click chemistry: the emerging role of the azide-alkyne Huisgen dipolar addition in the preparation of substituted tetrapyrrolic derivatives. *Journal of Porphyrins and Phthalocyanines*, 15(07), 481-504.
- Duncan, M. A. (2001). *Advances in Metal and Semiconductor Clusters: Metal Ion Solvation and Metal-Ligand Interactions*. Amsterdam: Elsevier.
- Dwyer, P. N., Puppe, L., Buchler, J. and Scheidt, W. R. (1975). Molecular stereochemistry of (alpha., gamma.-dimethyl-, alpha., gamma.-dihydrooctaethylporphinato) oxotitanium (IV). *Inorganic Chemistry*, 14(8), 1782-1785.
- Éll, A. H., Csjernyk, G., Slagt, V. F., Bäckvall, J. E., Berner, S., Puglia, C. . . . Oscarsson, S. (2006). Synthesis of Thioacetate-Functionalized Cobalt (II) Porphyrins and Their Immobilization on Gold Surface—Characterization by X-ray Photoelectron Spectroscopy. *European Journal of Organic Chemistry*, 2006(5), 1193-1199.
- Elschenbroich, C. (2006). Organometallics, Third Completely Revised and Extended Edition: Wiley-VCH, Weinheim. *Journal Of the American Chemical Society*, 128(46), 12029–12030.
- Falk, J. E. (1964). *Porphyrins and metalloporphyrins: their general, physical and coordination chemistry, and laboratory methods*. Amsterdam, New York: Elsevier Publishing Company.
- Feng, X., Gao, F., Xu, C., Gaoming, L. and Zheng, Y. (2015). Self temperature regulation of photothermal therapy by laser-shared photoacoustic feedback. *Optics Letters*, 40(19), 4492-4495.
- Filonov, G. S., Krumholz, A., Xia, J., Yao, J., Wang, L. V. and Verkhusha, V. V. (2012). Deep-Tissue Photoacoustic Tomography of a Genetically Encoded Near-Infrared Fluorescent Probe. *Angewandte Chemie International Edition*, 51(6), 1448-1451.

- Fischer, H. and Zeile, K. (1929). Synthese des haematoporphyrins, protoporphyrins und haemins. *European Journal of Organic Chemistry*, 468(1), 98-116.
- Fock, V. (1930). Approximation method for the solution of the quantum mechanical multibody problems. *Zeitschrift fur Physik*, 61, 126-148.
- Forbrich, A., Shao, P., Shi, W. and Zemp, R. J. (2016). Lifetime-weighted photoacoustic imaging. *Journal of Optics*, 18(12), 124001(1- 6).
- Frampton, M. J., Akdas, H., Cowley, A. R., Rogers, J. E., Slagle, J. E., Fleitz, P. A. . . . Anderson, H. L. (2005). Synthesis, Crystal Structure, and Nonlinear Optical Behavior of β -Unsubstituted *meso-meso* E-Vinylene-Linked Porphyrin Dimers. *Organic Letters*, 7(24), 5365-5368.
- Freindorf, M. and Gao, J. (1996). Optimization of the Lennard-Jones parameters for a combined ab initio quantum mechanical and molecular mechanical potential using the 3-21G basis set. *Journal of Computational Chemistry*, 17(4), 386-395.
- Frenette, M., Hatamimoslehabadi, M., Bellinger-Buckley, S., Laoui, S., La, J., Bag, S. . . . Yelleswarapu, C. (2014). Shining light on the dark side of imaging: excited state absorption enhancement of a bis-styryl BODIPY photoacoustic contrast agent. *Journal of the American Chemical Society*, 136(45), 15853-15856.
- Frisch, M. J., Keith, T. A. and Dennington, R. D. (2003). *GaussView reference*. Gaussian.
- Frisch, M. J., Pople, J. A. and Binkley, J. S. (1984). Self-consistent molecular orbital methods 25. Supplementary functions for Gaussian basis sets. *The Journal of Chemical Physics*, 80(7), 3265-3269.
- Fujii, H. (2002). Electronic structure and reactivity of high-valent oxo iron porphyrins. *Coordination Chemistry Reviews*, 226(1), 51-60.
- Fujimoto, K., Yorimitsu, H. and Osuka, A. (2014). Facile Preparation of β -Haloporphyrins as Useful Precursors of β -Substituted Porphyrins. *Organic Letters*, 16(3), 972-975.
- Fungo, F., Otero, L. A., Sereno, L., Silber, J. J. and Durantini, E. N. (2000). Synthesis of porphyrin dyads with potential use in solar energy conversion. *Journal of Materials Chemistry*, 10(3), 645-650.
- Galich, L., Hückstädt, H. and Homborg, H. (1998). Tetra (n-butyl) ammonium dicyanotetraphenylporphyrinatomanganate (III); crystal structure and electronic resonance Raman and absorption spectra. *Journal of Porphyrins and Phthalocyanines*, 2(1), 79-87.

- Gao, F., Bai, L., Feng, X., Tham, H. P., Zhang, R., Zhang, Y. . . . Zhao, Y. (2016). Remarkable In Vivo Nonlinear Photoacoustic Imaging Based on Near-Infrared Organic Dyes. *Small*, 12(38), 5239-5244.
- Gao, F., Bai, L., Liu, S., Zhang, R., Zhang, J., Feng, X. . . . Zhao, Y. (2017). Rationally encapsulated gold nanorods improving both linear and nonlinear photoacoustic imaging contrast in vivo. *Nanoscale*, 9(1), 79-86.
- Gao, F., Feng, X. and Zheng, Y. (2016). Advanced photoacoustic and thermoacoustic sensing and imaging beyond pulsed absorption contrast. *Journal of Optics*, 18(7), 74006-74025.
- Gaussian09, R. A. (2009). 1, MJ Frisch, GW Trucks, HB Schlegel, GE Scuseria, MA Robb, JR Cheeseman, G. Scalmani, V. Barone, B. Mennucci, GA Petersson et al., Gaussian. Inc., Wallingford CT.
- Geier III, G. R., Callinan, J. B., Dharma Rao, P. and Lindsey, J. S. (2001). A survey of acid catalysts in dipyrromethanecarbinol condensations leading to meso-substituted porphyrins. *Journal of Porphyrins and Phthalocyanines*, 5(12), 810-823.
- Geier III, G. R. and Lindsey, J. S. (2001). Investigation of porphyrin-forming reactions. Part 2. 1 Examination of the reaction course in two-step, one-flask syntheses of meso-substituted porphyrins. *Journal of the Chemical Society, Perkin Transactions*, 2(5), 687-700.
- Geier III, G. R., Littler, B. J. and Lindsey, J. S. (2001). Investigation of porphyrin-forming reactions. Part 3. 1 The origin of scrambling in dipyrromethane+ aldehyde condensations yielding trans-A 2 B 2-tetraarylporphyrins. *Journal of the Chemical Society, Perkin Transactions*, 2(5), 701-711.
- Giovannetti, R. (2012). The use of Spectrophotometry UV-Vis for the Study of Porphyrins. In Dr. Jamal Uddin (Ed.), *Macro to nano spectroscopy* (pp. 87-108). Rijeka, Croatia: InTech.
- Gnach, A., Lipinski, T., Bednarkiewicz, A., Rybka, J. and Capobianco, J. A. (2015). Upconverting nanoparticles: assessing the toxicity. *Chemical Society Reviews*, 44(6), 1561-1584.
- Goerigk, L. and Grimme, S. (2008). Calculation of electronic circular dichroism spectra with time-dependent double-hybrid density functional theory. *The Journal of Physical Chemistry A*, 113(4), 767-776.
- Gonsalves, A. M. d. A. R., Johnstone, R. A., Pereira, M. M., Shaw, J. and Sobral, A. J. d. N. (1991). Metal-assisted reactions. Part 22. Synthesis of perhalogenated porphyrins and their use as oxidation catalysts. *Tetrahedron Letters*, 32(10), 1355-1358.

- Gosper, J. J. and Ali, M. (1994). A conformationally constrained conjugated porphyrin dimer. *Journal of the Chemical Society, Chemical Communications*, (14), 1707-1708.
- Gouterman, M. (1959). Study of the effects of substitution on the absorption spectra of porphin. *The Journal of Chemical Physics*, 30(5), 1139-1161.
- Gouterman, M. (1961). Spectra of porphyrins. *Journal of Molecular Spectroscopy*, 6, 138-163.
- Gouterman, M. (1978). Optical Spectra and Electronic Structure of Porphyrins and Related Rings. In D. Dolphin (ed.), *The Porphyrins. Physical Chemistry Part 1 (Vol. 3 pp. 1-165)*. New York: Academic Press.
- Gouterman, M., Rentzepis, P. M. and Straub, K. D. (1986). Porphyrins: excited states and dynamics. *Analytical Chemistry*, 58 (14), 1438A-1438A.
- Grinstaff, M. W., Hill, M. G., Labinger, J. A. and Gray, H. B. (1994). Mechanism of catalytic oxygenation of alkanes by halogenated iron porphyrins. *Science*, 264(5163), 1311-1314.
- Gross, E. K. and Dreizler, R. M. (2013). *Density functional theory*. New York: Springer Science & Business Media.
- Guggenheim, J. A., Allen, T. J., Plumb, A., Zhang, E. Z., Rodriguez-Justo, M., Punwani, S. and Beard, P. C. (2015). Photoacoustic imaging of human lymph nodes with endogenous lipid and hemoglobin contrast. *Journal of Biomedical Optics*, 20(5), 050504-050504.
- Guilbault, G. G. (1990). *Practical fluorescence*. Second Edition, revised and expanded. New York: Marcel Dekker Inc.
- Ham, N. S. and Ruedenberg, K. (1956a). Electronic Interaction in the Free-Electron Network Model for Conjugated Systems. I. Theory. *The Journal of Chemical Physics*, 25(1), 1-13.
- Ham, N. S. and Ruedenberg, K. (1956b). Electronic Interaction in the Free-Electron Network Model for Conjugated Systems. II. Spectra of Aromatic Hydrocarbons. *The Journal of Chemical Physics*, 25(1), 13-26.
- Hambricht, P. (1970). Kinetics of incorporation of Cu (II) and Zn (II) into meso-tetrapyridylporphin in the presence of Li (I). *Journal of Inorganic and Nuclear Chemistry*, 32(7), 2449-2452.
- Hambricht, P. (1971). The coordination chemistry of metalloporphyrins. *Coordination Chemistry Reviews*, 6(2-3), 247-268.

- Han, Y., Fang, H., Jing, H., Sun, H., Lei, H., Lai, W. and Cao, R. (2016). Singly versus Doubly Reduced Nickel Porphyrins for Proton Reduction: Experimental and Theoretical Evidence for a Homolytic Hydrogen-Evolution Reaction. *Angewandte Chemie International Edition*, 55(18), 5457-5462.
- Harada, R., Matsuda, Y., Ōkawa, H., Miyamoto, R., Yamauchi, S. and Kojima, T. (2005). Synthesis and characterization of chromium (III) octaphenylporphyrin complexes with various axial ligands: An insight into porphyrin distortion. *Inorganica Chimica Acta*, 358(8), 2489-2500.
- Hariharan, P. C. and Pople, J. A. (1973). The influence of polarization functions on molecular orbital hydrogenation energies. *Theoretical Chemistry Accounts: Theory, Computation, and Modeling (Theoretica Chimica Acta)*, 28(3), 213-222.
- Harrach, G., Valicsek, Z. and Horváth, O. (2011). Water-soluble silver (II) and gold (III) porphyrins: The effect of structural distortion on the photophysical and photochemical behavior. *Inorganic Chemistry Communications*, 14(11), 1756-1761.
- Harriman, A. (1981). Luminescence of porphyrins and metalloporphyrins. Part 3.— Heavy-atom effects. *Journal of the Chemical Society, Faraday Transactions 2: Molecular and Chemical Physics*, 77(7), 1281-1291.
- Hartnell, R. D., Edwards, A. J. and Arnold, D. P. (2002). Peripherally-metallated porphyrins: meso- η^1 -porphyrinyl-platinum (II) complexes of 5, 15-diaryl- and 5, 10, 15-triarylporphyrins. *Journal of Porphyrins and Phthalocyanines*, 6(11), 695-707.
- Hartree, D. R. (1928). *The wave mechanics of an atom with a non-Coulomb central field. Part I. Theory and methods*. Paper presented at the Mathematical Proceedings of the Cambridge Philosophical Society.
- Hashimoto, T., Choe, Y.-K., Nakano, H. and Hirao, K. (1999). Theoretical study of the Q and B bands of free-base, magnesium, and zinc porphyrins, and their derivatives. *The Journal of Physical Chemistry A*, 103(12), 1894-1904.
- Hata, H., Shinokubo, H. and Osuka, A. (2005). Highly Regioselective Ir-Catalyzed β -Borylation of Porphyrins via C–H Bond Activation and Construction of β – β -Linked Diporphyrin. *Journal of the American Chemical Society*, 127(23), 8264-8265.
- Hatamimoslehabadi, M., Bellinger, S., La, J., Ahmad, E., Frenette, M., Yelleswarapu, C. and Rochford, J. (2017). Correlation of Photophysical Properties with the Photoacoustic Emission for a Selection of Established Chromophores. *The Journal of Physical Chemistry C*, 121(43), 24168-24178.

- Hay, P. J. and Wadt, W. R. (1985a). Ab initio effective core potentials for molecular calculations. Potentials for K to Au including the outermost core orbitals. *The Journal of Chemical Physics*, 82(1), 299-310.
- Hay, P. J. and Wadt, W. R. (1985b). Ab initio effective core potentials for molecular calculations. Potentials for the transition metal atoms Sc to Hg. *The Journal of Chemical Physics*, 82(1), 270-283.
- Hayashi, S., Yotsukura, M., Noji, M. and Takanami, T. (2015). Bis (zinc porphyrin) as a CD-sensitive bidentate host molecule: Direct determination of absolute configuration of mono-alcohols. *Chemical Communications*, 51(55), 11068-11071.
- Head-Gordon, M., Rico, R. J., Oumi, M. and Lee, T. J. (1994). A doubles correction to electronic excited states from configuration interaction in the space of single substitutions. *Chemical Physics Letters*, 219(1-2), 21-29.
- Hehre, W. J., Ditchfield, R. and Pople, J. A. (1972). Self-consistent molecular orbital methods. XII. Further extensions of gaussian-type basis sets for use in molecular orbital studies of organic molecules. *The Journal of Chemical Physics*, 56(5), 2257-2261.
- Heijblom, M., Piras, D., Xia, W., van Hespden, J. C., Klaase, J., Van den Engh, F. . . . Manohar, S. (2012). Visualizing breast cancer using the Twente photoacoustic mammoscope: what do we learn from twelve new patient measurements? *Optics Express*, 20(11), 11582-11597.
- Hiroto, S., Miyake, Y. and Shinokubo, H. (2016). Synthesis and functionalization of porphyrins through organometallic methodologies. *Chemical Reviews*, 117(4), 2910-3043.
- Hisaki, I., Hiroto, S., Kim, K. S., Noh, S. B., Kim, D., Shinokubo, H. and Osuka, A. (2007). Synthesis of Doubly β -to- β 1, 3-Butadiyne-Bridged Diporphyrins: Enforced Planar Structures and Large Two-Photon Absorption Cross Sections. *Angewandte Chemie International Edition*, 46(27), 5125-5128.
- Ho, C. J. H., Balasundaram, G., Driessen, W., McLaren, R., Wong, C. L., Dinish, U. . . . Olivo, M. (2014). Multifunctional photosensitizer-based contrast agents for photoacoustic imaging. *Scientific Reports*, 4, 5342(1-6).
- Ho, I.-T., Sessler, J. L., Gambhir, S. S. and Jokerst, J. V. (2015). Parts per billion detection of uranium with a porphyrinoid-containing nanoparticle and in vivo photoacoustic imaging. *Analyst*, 140(11), 3731-3737.
- Hoard, J. (1971). Stereochemistry of hemes and other metalloporphyrins. *Science*, 174(4016), 1295-1302.

- Hoard, J. and Smith, K. (1975). *Porphyryns and metalloporphyryns*. Amsterdam: Elsevier.
- Hoelen, C., De Mul, F., Pongers, R. and Dekker, A. (1998). Three-dimensional photoacoustic imaging of blood vessels in tissue. *Optics Letters*, 23(8), 648-650.
- Hohenberg, P. and Kohn, W. (1964). Inhomogeneous electron gas. *Physical Review*, 136(3B), 864-871.
- Hohenberg, P., Kohn, W. and Sham, L. (1990). The beginnings and some thoughts on the future. *Advances in Quantum Chemistry*, 21, 7-26.
- Holten, D., Bocian, D. F. and Lindsey, J. S. (2002). Probing electronic communication in covalently linked multiporphyrin arrays. A guide to the rational design of molecular photonic devices. *Accounts of Chemical Research*, 35(1), 57-69.
- Höper, F. and Montforts, F. P. (1995). A simple synthesis of functionalized rac-chlorins via allylboration of porphyrin aldehydes. *European Journal of Organic Chemistry*, 1995(6), 1033-1038.
- Horning, T. L., Fujita, E. and Fajer, J. (1986). ESR and ENDOR of bacteriopheophytin a radicals. Implications for bacteriochlorophylls in vivo. *Journal of the American Chemical Society*, 108(2), 323-325.
- Horrocks Jr, W. D. and Hove, E. G. (1978). Water-soluble lanthanide porphyrins: shift reagents for aqueous solution. *Journal of the American Chemical Society*, 100(14), 4386-4392.
- Horváth, O., Huszánk, R., Valicsek, Z. and Lendvay, G. (2006). Photophysics and photochemistry of kinetically labile, water-soluble porphyrin complexes. *Coordination Chemistry Reviews*, 250(13), 1792-1803.
- Horváth, O., Valicsek, Z., Harrach, G., Lendvay, G. and Fodor, M. A. (2012). Spectroscopic and photochemical properties of water-soluble metalloporphyrins of distorted structure. *Coordination Chemistry Reviews*, 256(15), 1531-1545.
- Horváth, O., Valicsek, Z. and Vogler, A. (2004). Unique photoreactivity of mercury (II) 5, 10, 15, 20-tetrakis (4-sulfonatophenyl) porphyrin. *Inorganic Chemistry Communications*, 7(7), 854-857.
- Hu, S., Maslov, K. and Wang, L. V. (2011). Second-generation optical-resolution photoacoustic microscopy with improved sensitivity and speed. *Optics Letters*, 36(7), 1134-1136.

- Hudson, M. F. and Smith, K. M. (1974). Novel mercury (II) porphyrins-II: mercury (II) chelates of meso-tetraphenylporphyrin and N-methylporphyrins. *Tetrahedron Letters*, 15(26), 2223-2226.
- Huszánk, R. and Horváth, O. (2005). A heme-like, water-soluble iron (II) porphyrin: thermal and photoinduced properties, evidence for sitting-atop structure. *Chemical Communications*, (2), 224-226.
- Huynh, E., Jin, C. S., Wilson, B. C. and Zheng, G. (2014). Aggregate enhanced trimodal porphyrin shell microbubbles for ultrasound, photoacoustic, and fluorescence imaging. *Bioconjugate Chemistry*, 25(4), 796-801.
- Huynh, E., Lovell, J. F., Helfield, B. L., Jeon, M., Kim, C., Goertz, D. E. . . . Zheng, G. (2012). Porphyrin shell microbubbles with intrinsic ultrasound and photoacoustic properties. *Journal of the American Chemical Society*, 134(40), 16464-16467.
- Huzinaga, S. (1985). Basis sets for molecular calculations. *Computer Physics Reports*, 2(6), 281-339.
- Hynninen, P. H. and Lötjönen, S. (1980). Preparation of phorbins from chlorophyll mixture utilizing the principle of selective hydrolysis. *Synthesis*, 1980(07), 539-541.
- Ichiki, T., Matsuo, Y. and Nakamura, E. (2013). Photostability of a dyad of magnesium porphyrin and fullerene and its application to photocurrent conversion. *Chemical Communications*, 49(3), 279-281.
- Inhoffen, H. H., Fuhrhop, J. H., Voigt, H. and Brockmann, H. (1966). Zur weiteren Kenntnis des Chlorophylls und des Hämins, VI. Formylierung der meso-Kohlenstoffatome von Alkyl-substituierten Porphyrinen. *European Journal of Organic Chemistry*, 695(1), 133-143.
- Ishida, M., Hwang, D., Koo, Y. B., Sung, J., Kim, D. Y., Sessler, J. L. and Kim, D. (2013). β -(Ethynylbenzoic acid)-substituted push-pull porphyrins: DSSC dyes prepared by a direct palladium-catalyzed alkynylation reaction. *Chemical Communications*, 49(80), 9164-9166.
- Ishihara, S., Labuta, J., Van Rossom, W., Ishikawa, D., Minami, K., Hill, J. P. and Ariga, K. (2014). Porphyrin-based sensor nanoarchitectonics in diverse physical detection modes. *Physical Chemistry Chemical Physics*, 16(21), 9713-9746.
- Ivanova, Y. B., Semeikin, A., Glazunov, A. and Mamardashvili, N. Z. (2010). Pyridyl-substituted porphyrins: II. Synthesis and basic properties of dipyrindylporphyrins. *Russian Journal of Organic Chemistry*, 46(6), 917-923.
- Jablonski, A. (1933). Efficiency of anti-Stokes fluorescence in dyes. *Nature*, 131(3319), 839-840.

- Jackson, A., Kenner, G. and Smith, K. (1971). Pyrroles and related compounds. Part XVII. Porphyrin synthesis through b-bilenes. *Journal of the Chemical Society C: Organic*, 502-509.
- Jacquemin, D., Perpète, E. A., Ciofini, I. and Adamo, C. (2010). Assessment of functionals for TD-DFT calculations of singlet–triplet transitions. *Journal of Chemical Theory and Computation*, 6(5), 1532-1537.
- Jacquemin, D., Perpète, E. A., Scuseria, G. E., Ciofini, I. and Adamo, C. (2008). TD-DFT performance for the visible absorption spectra of organic dyes: conventional versus long-range hybrids. *Journal of Chemical Theory and Computation*, 4(1), 123-135.
- Jaquinod, L. (2000). Functionalization of 5, 10, 15, 20-tetra-substituted porphyrins. In K. M. Kadish, K. M. Smith and R. Guilard (eds.), *The Porphyrin Handbook* (Vol. 1, pp. 45). San Diego: Academic Press.
- Jeandon, C., Bauder, C. and Callot, H. (1990). Selective acetylation of porphyrins possessing a free pyrrolic position as a tool for petroporphyrin analysis. A reinvestigation. *Energy and Fuels*, 4(6), 665-667.
- Jensen, F. (2013). Atomic orbital basis sets. *Wiley Interdisciplinary Reviews: Computational Molecular Science*, 3(3), 273-295.
- Jentzen, W., Ma, J.-G. and Shelnut, J. A. (1998). Conservation of the conformation of the porphyrin macrocycle in hemoproteins. *Biophysical Journal*, 74(2), 753-763.
- Jentzen, W., Simpson, M., Hobbs, J., Song, X., Ema, T., Nelson, N. . . . Mazzanti, M. (1995). Ruffling in a Series of Nickel (II) meso-Tetrasubstituted Porphyrins as a Model for the Conserved Ruffling of the Heme of Cytochromes c. *Journal of the American Chemical Society*, 117(45), 11085-11097.
- Jiang, J., Vairaprakash, P., Reddy, K. R., Sahin, T., Pavan, M. P., Lubian, E. and Lindsey, J. S. (2014). Hydrophilic tetracarboxy bacteriochlorins for photonics applications. *Organic & Biomolecular Chemistry*, 12(1), 86-103.
- Jiang, X.-L., Zhang, H.-L. and JIAN, W. (2006). Synthesis of diaryl ether-linked porphyrin dimers via ullmann coupling reaction. *Heterocycles*, 68(10), 2153-2160.
- Jiang, X., Gou, F. and Jing, H. (2014). Alternating copolymerization of CO₂ and propylene oxide catalyzed by C₂v-porphyrin cobalt: Selectivity control and a kinetic study. *Journal of Catalysis*, 313, 159-167.
- Johnson, A. (1978). Synthesis of Porphyrins from 1, 19-Dideoxybiladienes-ac and 1, 19-Dideoxybilenes-b. In D. Dolphin (ed.), *The Porphyrins* (Vol. 1, pp. 235-264). New York: Academic Press.

- Johnson, A. and Kay, I. (1961). 468. The formation of porphyrins by the cyclisation of bilenes. *Journal of the Chemical Society (Resumed)*, 0, 2418-2423.
- Jokerst, J. V. (2014). Bioimaging: Sensed at the gut level. *Nature Nanotechnology*, 9(8), 569-570.
- Jradi, F. M., O'Neil, D., Kang, X., Wong, J., Szymanski, P., Parker, T. C. . . . Marder, S. R. (2015). A Step Toward Efficient Panchromatic Multi-Chromophoric Sensitizers for Dye Sensitized Solar Cells. *Chemistry of Materials*, 27(18), 6305-6313.
- Jurow, M., Schuckman, A. E., Batteas, J. D. and Drain, C. M. (2010). Porphyrins as molecular electronic components of functional devices. *Coordination Chemistry Reviews*, 254(19), 2297-2310.
- Jusélius, J. and Sundholm, D. (2000). The aromatic character of magnesium porphyrins. *The Journal of Organic Chemistry*, 65(17), 5233-5237.
- Kadish, K. M., Van Caemelbecke, E., Boulas, P., D'Souza, F., Vogel, E., Kisters, M. . . . Smith, K. M. (1993). First reversible electrogeneration of triply oxidized nickel porphyrins and porphycenes. Formation of nickel (III). pi. dications. *Inorganic Chemistry*, 32(20), 4177-4178.
- Kalyanasundaram, K. (1991). *Photochemistry of polypyridine and porphyrin complexes*. London: Academic Press.
- Kaplan, W. A., Suslick, K. S. and Scott, R. A. (1991). Core size and flexibility of metallohydrophyrin macrocycles. Implications for F430 coordination chemistry. *Journal of the American Chemical Society*, 113(26), 9824-9827.
- Kasha, M. (1950). Characterization of electronic transitions in complex molecules. *Discussions of the Faraday Society*, 9, 14-19.
- Katritzky, A. R., He, H.-Y., Long, Q. and Wilcox, A. L. (2001). Preparation of 2, 6-dialkoxybenzaldehydes. *Arkivoc*, 3, 3-12.
- Kendrew, J., Dickerson, R., Strandberg, B., Hart, R., Davies, D., Phillips, D. and Shore, V. (1960). Structure of myoglobin: A three-dimensional Fourier synthesis at 2 Å. resolution. *Nature*, 185(4711), 422-427.
- Kim, C., Cho, E. C., Chen, J., Song, K. H., Au, L., Favazza, C. . . . Xia, Y. (2010). In vivo molecular photoacoustic tomography of melanomas targeted by bioconjugated gold nanocages. *ACS Nano*, 4(8), 4559-4564.
- Kinoshita, H., Tanaka, S., Nishimori, N., Dejima, H. and Inomata, K. (1992). Synthesis of 2-(substituted methyl)-3, 4-disubstituted pyrroles and their conversion into the

corresponding porphyrins. *Bulletin of the Chemical Society of Japan*, 65(10), 2660-2667.

- Knopoff, L. and Shapiro, J. (1970). Pseudo-Grüneisen parameter for liquids. *Physical Review B*, 1(10), 3893-3895.
- Kohn, W. and Sham, L. (1965). Self-consistent equations including exchange and correlation effects. *Physical Review*, 140, A1133-A1138.
- Kowalski, K., Dean, D., Hjorth-Jensen, M., Papenbrock, T. and Piecuch, P. (2004). Coupled cluster calculations of ground and excited states of nuclei. *Physical Review Letters*, 92(13), 132501(1-4).
- Kruglik, S. G., Apanasevich, P. A., Chirvony, V. S., Kvach, V. V. and Orlovich, V. A. (1995). Resonance Raman, CARS, and picosecond absorption spectroscopy of copper porphyrins: The evidence for the exciplex formation with oxygen-containing solvent molecules. *The Journal of Physical Chemistry*, 99(10), 2978-2995.
- Kumar, R. and Sankar, M. (2014). Synthesis, Spectral, and Electrochemical Studies of Electronically Tunable β -Substituted Porphyrins with Mixed Substituent Pattern. *Inorganic Chemistry*, 53(24), 12706-12719.
- Kuster, W. (1912). Information on bilirubine and haemine. *Hoppe-Seylers Zeitschrift Fur Physiologische Chemie*, 82(6), 463-483.
- Ladomenou, K., Nikolaou, V., Charalambidis, G. and Coutsolelos, A. G. (2016). "Click"-reaction: An alternative tool for new architectures of porphyrin based derivatives. *Coordination Chemistry Reviews*, 306, 1-42.
- Lakowicz, J. (1999a). *Principles of fluorescence spectroscopy*. New York: Kluwer Academic Plenum.
- Lakowicz, J. R. (1999b). Introduction to fluorescence. *Principles of Fluorescence Spectroscopy* (ed. 3rd, pp. 1-23). New York: Springer.
- Lash, T. D. (1996). Porphyrin synthesis by the "3+ 1" approach: new applications for an old methodology. *Chemistry-A European Journal*, 2(10), 1197-1200.
- Lash, T. D. (2000). Carbaporphyrinoids: Taking the Heterocycle Out of Nature's [18] Annulene. *Synlett*, 2000(03), 279-295.
- Le Maux, P., Bahri, H. and Simonneaux, G. (1991). Molecular recognition of racemic phosphines by a chiral ruthenium porphyrin. *Journal of the Chemical Society, Chemical Communications*, (19), 1350-1352.

- Le Maux, P., Bahri, H. and Simonneaux, G. (1993). Synthesis and stereochemical studies of chiral ruthenium porphyrins. *Tetrahedron*, 49(7), 1401-1408.
- Leach, A. R. (2001). *Molecular modelling: principles and applications*. (ed. 2nd). United Kingdom: Prentice Hall Harlow.
- Lee, C., Yang, W. and Parr, R. (1988a). Density-functional exchange-energy approximation with correct asymptotic behaviour. *Physical Review B*, 37, 785-789.
- Lee, C., Yang, W. and Parr, R. G. (1988b). Development of the Colle-Salvetti correlation-energy formula into a functional of the electron density. *Physical Review B*, 37(2), 785-789.
- Lewars, E. G. (2016). *Computational chemistry: introduction to the theory and applications of molecular and quantum mechanics*. Boston: Springer.
- Lewinski, N., Colvin, V. and Drezek, R. (2008). Cytotoxicity of nanoparticles. *Small*, 4(1), 26-49.
- Liao, M.-S., Watts, J. D. and Huang, M.-J. (2005). Effects of peripheral substituents and axial ligands on the electronic structure and properties of cobalt porphyrins. *The Journal of Physical Chemistry A*, 109(51), 11996-12005.
- Liao, M.-S., Watts, J. D. and Huang, M.-J. (2006). DFT/TDDFT study of lanthanide(III) mono- and bisporphyrin complexes. *The Journal of Physical Chemistry A*, 110(48), 13089-13098.
- Licha, K., Riefke, B., Ntziachristos, V., Becker, A., Chance, B. and Semmler, W. (2000). Hydrophilic Cyanine Dyes as Contrast Agents for Near-infrared Tumor Imaging: Synthesis, Photophysical Properties and Spectroscopic In vivo Characterization ¶. *Photochemistry and Photobiology*, 72(3), 392-398.
- Lin, J. J., Gerzevske, K. R., Liddell, P. A., Senge, M. O., Olmstead, M. M., Khoury, R. G. . . . Smith, K. M. (1997). Metal-catalyzed oxidative cyclizations of a, c-biladiene salts bearing 1-and/or 19-arylmethyl substituents: Macrocyclic products and their chemistry. *The Journal of Organic Chemistry*, 62(13), 4266-4276.
- Lin, V. S.-Y., DiMagno, S. G. and Therien, M. J. (1994). Highly conjugated, acetylenyl bridged porphyrins: new models for light-harvesting antenna systems. *Science*, 264(5162), 1105-1112.
- Lindsey, J. S., Schreiman, I. C., Hsu, H. C., Kearney, P. C. and Marguerettaz, A. M. (1987). Rothmund and Adler-Longo reactions revisited: synthesis of tetraphenylporphyrins under equilibrium conditions. *The Journal of Organic Chemistry*, 52(5), 827-836.

- Lindsey, J. S. and Woodford, J. N. (1995). A simple method for preparing magnesium porphyrins. *Inorganic Chemistry*, 34(5), 1063-1069.
- Littler, B. J., Miller, M. A., Hung, C.-H., Wagner, R. W., O'Shea, D. F., Boyle, P. D. and Lindsey, J. S. (1999). Refined synthesis of 5-substituted dipyrromethanes. *The Journal of Organic Chemistry*, 64(4), 1391-1396.
- Liu, C., Shen, D.-M. and Chen, Q.-Y. (2007). Practical and Efficient Synthesis of Various meso-Functionalized Porphyrins via Simple Ligand-Free Nickel-Catalyzed C–O, C–N, and C–C Cross-Coupling Reactions. *The Journal of Organic Chemistry*, 72(8), 2732-2736.
- Liu, P. P., Feng, Y. Q., Gu, C. Z., Meng, S. X. and Zhang, B. (2012). The facile synthesis of 5-formylporphyrin. *Chinese Chemical Letters*, 23(5), 505-508.
- Liu, X., Yang, G., Zhang, L., Liu, Z., Cheng, Z. and Zhu, X. (2016). Photosensitizer cross-linked nano-micelle platform for multimodal imaging guided synergistic photothermal/photodynamic therapy. *Nanoscale*, 8(33), 15323-15339.
- Ljungdahl, T., Pettersson, K., Albinsson, B. and Mårtensson, J. (2006). Solvent and base dependence of copper-free palladium-catalyzed cross-couplings between terminal alkynes and aryl iodides: Development of efficient conditions for the construction of gold (III)/free-base porphyrin dimers. *The Journal of Organic Chemistry*, 71(4), 1677-1687.
- Locos, O. B. and Arnold, D. P. (2006). The Heck reaction for porphyrin functionalisation: synthesis of meso-alkenyl monoporphyrins and palladium-catalysed formation of unprecedented meso- β ethene-linked diporphyrins. *Organic & Biomolecular Chemistry*, 4(5), 902-916.
- Longo, F. R. (1979). *Porphyrin chemistry advances*. New York: Ann Arbor Science Publishers Inc.
- Lovell, J. F., Jin, C. S., Huynh, E., Jin, H., Kim, C., Rubinstein, J. L. . . . Zheng, G. (2011). Porphysome nanovesicles generated by porphyrin bilayers for use as multimodal biophotonic contrast agents. *Nature Materials*, 10(4), 324-332.
- Luciano, M., Erfanzadeh, M., Zhou, F., Zhu, H., Bornhütter, T., Röder, B. . . . Brückner, C. (2016). In vivo photoacoustic tumor tomography using a quinoline-annulated porphyrin as NIR molecular contrast agent. *Organic & Biomolecular Chemistry*, 15(4), 972-983.
- Luguya, R., Jaquinod, L., Fronczek, F. R., Vicente, M. G. H. and Smith, K. M. (2004). Synthesis and reactions of meso-(p-nitrophenyl) porphyrins. *Tetrahedron*, 60(12), 2757-2763.

- Luo, S., Zhang, E., Su, Y., Cheng, T. and Shi, C. (2011). A review of NIR dyes in cancer targeting and imaging. *Biomaterials*, 32(29), 7127-7138.
- Luthra, A., Denisov, I. G. and Sligar, S. G. (2011). Spectroscopic features of cytochrome P450 reaction intermediates. *Archives of Biochemistry and Biophysics*, 507(1), 26-35.
- Lysenko, A. B., Thamyongkit, P., Schmidt, I., Diers, J. R., Bocian, D. F. and Lindsey, J. S. (2006). Diverse porphyrin dimers as candidates for high-density charge-storage molecules. *Journal of Porphyrins and Phthalocyanines*, 10(01), 22-32.
- MacDonald, F., Arsenault, P. and Bullock, E. (1960). Pyrromethanes and porphyrins therefrom. *Journal of American Chemical Society*, 82, 4384-4389.
- Maji, S. K., Sreejith, S., Joseph, J., Lin, M., He, T., Tong, Y. . . . Zhao, Y. (2014). Upconversion nanoparticles as a contrast agent for photoacoustic imaging in live mice. *Advanced Materials*, 26(32), 5633-5638.
- Mallidi, S., Larson, T., Tam, J., Joshi, P. P., Karpouk, A., Sokolov, K. and Emelianov, S. (2009). Multiwavelength photoacoustic imaging and plasmon resonance coupling of gold nanoparticles for selective detection of cancer. *Nano Letters*, 9(8), 2825-2831.
- Mamardashvili, N. Z. and Golubchikov, O. A. (2000). The synthesis of porphyrins from dipyrrolylmetanes. *Russian Chemical Reviews*, 69(4), 307-323.
- Markovac, A. and MacDonald, S. (1965). Syntheses with 5-dibromomethyl- and 5-formyl-pyrromethenes. *Canadian Journal of Chemistry*, 43(12), 3364-3371.
- Marques, M. A. and Gross, E. K. (2003). Time-dependent density functional theory. *Lecture Notes In Physics-New York Then Berlin-*, 144-184.
- Marques, M. A., Maitra, N. T., Nogueira, F. M., Gross, E. K. and Rubio, A. (2012). *Fundamentals of time-dependent density functional theory*. New York: Springer Science & Business Media.
- Márquez, N., Ysambertt, F. and De La Cruz, C. (1999). Three analytical methods to isolate and characterize vanadium and nickel porphyrins from heavy crude oil. *Analytica Chimica Acta*, 395(3), 343-349.
- Marten, B., Kim, K., Cortis, C., Friesner, R. A., Murphy, R. B., Ringnalda, M. N. . . . Honig, B. (1996). New model for calculation of solvation free energies: correction of self-consistent reaction field continuum dielectric theory for short-range hydrogen-bonding effects. *The Journal of Physical Chemistry*, 100(28), 11775-11788.

- Matano, Y., Fujii, D., Shibano, T., Furukawa, K., Higashino, T., Nakano, H. and Imahori, H. (2014). Covalently Linked 5, 15-Diazaporphyrin Dimers: Promising Scaffolds for a Highly Conjugated Azaporphyrin π System. *Chemistry-A European Journal*, 20(12), 3342-3349.
- Mathew, S., Yella, A., Gao, P., Humphry-Baker, R., Curchod, B. F., Ashari-Astani, N. . . . Grätzel, M. (2014). Dye-sensitized solar cells with 13% efficiency achieved through the molecular engineering of porphyrin sensitizers. *Nature Chemistry*, 6(3), 242-247.
- McGlynn, S., Azumi, T. and Kasha, M. (1964). External Heavy-Atom Spin—Orbital Coupling Effect. V. Absorption Studies of Triplet States. *The Journal of Chemical Physics*, 40(2), 507-515.
- Milgrom, L. R. and Warren, M. J. (1997). *The colours of life: an introduction to the chemistry of porphyrins and related compounds*. Oxford: Oxford University Press.
- Milroy, J. A. (1918). Observations on some Metallic Compounds of Haematoporphyrin. *Biochemical Journal*, 12(4), 318-338.
- Minaev, B. and Lindgren, M. (2009). Vibration and fluorescence spectra of porphyrin-coredbis (methylol)-propionic acid dendrimers. *Sensors*, 9(3), 1937-1966.
- Mitra, K., Singha, A. and Dey, A. (2016). Iron porphyrins with a hydrogen bonding cavity: Effect of weak interactions on their electronic structure and reactivity. *Dalton Transactions*, 45(47), 18796-18802.
- Mohr, B., Enkelmann, V. and Wegner, G. (1994). Synthesis of alkyl- and alkoxy-substituted benziles and oxidative coupling to tetraalkoxyphenanthrene-9, 10-diones. *Journal of Organic Chemistry*, 59(3), 635-638.
- Monteiro, C. J., Pereira, M. M., Vicente, M. G. H. and Arnaut, L. G. (2012). Photophysical properties of unsymmetric meso-substituted porphyrins synthesized via the Suzuki coupling reaction. *Tetrahedron*, 68(42), 8783-8788.
- Montgomery Jr, J. A., Frisch, M. J., Ochterski, J. W. and Petersson, G. A. (1999). A complete basis set model chemistry. VI. Use of density functional geometries and frequencies. *The Journal of Chemical Physics*, 110(6), 2822-2827.
- Mori, G., Shinokubo, H. and Osuka, A. (2008). Highly selective Ir-catalyzed direct sixfold borylation of peripheral aromatic substituents on hexakisaryl-substituted [28] hexaphyrin (1.1. 1.1. 1.1). *Tetrahedron Letters*, 49(13), 2170-2172.
- Naik, A., Rubbiani, R., Gasser, G. and Spingler, B. (2014). Visible-Light-Induced Annihilation of Tumor Cells with Platinum–Porphyrin Conjugates. *Angewandte Chemie International Edition*, 53(27), 6938-6941.

- Nakamura, M., Ikezaki, A. and Takahashi, M. (2013). Metal-porphyrin orbital interactions in paramagnetic iron complexes having planar and deformed porphyrin ring. *Journal of the Chinese Chemical Society*, 60(1), 9-21.
- Nappa, M. and Valentine, J. S. (1978). The influence of axial ligands on metalloporphyrin visible absorption spectra. Complexes of tetraphenylporphinatozinc. *Journal of the American Chemical Society*, 100(16), 5075-5080.
- Naruta, Y., Tani, F. and Maruyama, K. (1992). Meso-perfluorination of porphyrins with N-fluoropyridinium triflate. *Tetrahedron Letters*, 33(8), 1069-1072.
- Natali, M., Luisa, A., Iengo, E. and Scandola, F. (2014). Efficient photocatalytic hydrogen generation from water by a cationic cobalt (II) porphyrin. *Chemical Communications*, 50(15), 1842-1844.
- Nazeeruddin, M. K., De Angelis, F., Fantacci, S., Selloni, A., Viscardi, G., Liska, P. . . . Grätzel, M. (2005). Combined experimental and DFT-TDDFT computational study of photoelectrochemical cell ruthenium sensitizers. *Journal of the American Chemical Society*, 127(48), 16835-16847.
- Nelson, J. S., Roberts, W. G. and Berns, M. W. (1987). In vivo studies on the utilization of mono-L-aspartyl chlorin (NPe6) for photodynamic therapy. *Cancer Research*, 47(17), 4681-4685.
- Nemykin, V. N. and Hadt, R. G. (2010). Interpretation of the UV– vis Spectra of the meso (Ferrocenyl)-Containing Porphyrins using a TDDFT Approach: Is Gouterman's Classic Four-Orbital Model Still in Play? *The Journal of Physical Chemistry A*, 114(45), 12062-12066.
- Neugebauer, J., Baerends, E. J. and Nooijen, M. (2005). Vibronic structure of the permanganate absorption spectrum from time-dependent density functional calculations. *The Journal of Physical Chemistry A*, 109(6), 1168-1179.
- Neya, S., Quan, J., Hoshino, T., Hata, M. and Funasaki, N. (2004). Convenient synthesis of porphine from β -tetra (tert-butyl) porphyrin. *Tetrahedron Letters*, 45(47), 8629-8630.
- Neya, S., Yodo, H. and Funasaki, N. (1993). Convenient synthesis of porphine. *Journal of Heterocyclic Chemistry*, 30(2), 549-550.
- Nielsen, A. B. and Holder, A. J. (1998). *GaussView. User's reference*. Gaussian, Incorporated.
- Ol'shevskaya, V. A., Zaytsev, A. V., Savchenko, A. N., Shtil, A. A., Cheong, C.-S. and Kalinin, V. N. (2007). Boronated porphyrins and chlorins as potential anticancer drugs. *Bulletin of the Korean Chemical Society*, 28(11), 1910-1916.

- Ol'shevskaya, V. A., Zaitsev, A. V., Luzgina, V. N., Kondratieva, T. T., Ivanov, O. G., Kononova, E. G. . . . Hofmann, J. (2006). Novel boronated derivatives of 5, 10, 15, 20-tetraphenylporphyrin: synthesis and toxicity for drug-resistant tumor cells. *Bioorganic and Medicinal Chemistry*, 14(1), 109-120.
- Ono, N., Kawamura, H., Bougauchi, M. and Maruyama, K. (1990). Porphyrin synthesis from nitrocompounds. *Tetrahedron*, 46(21), 7483-7496.
- Ostrowski, S. (2005). Preparation of 2-Nitro-5, 10, 15, 20-tetraphenylporphyrin Zinc (II) Complex-post scriptum to Electrophilic Nitration of Porphyrins at the beta-Pyrrolic Position. *Polish Journal of Chemistry*, 79(7), 1169-1172.
- Osuka, A. and Shimidzu, H. (1997). meso, meso-Linked Porphyrin Arrays. *Angewandte Chemie International Edition*, 36(1-2), 135-137.
- Paine III, J. B., Kirshner, W. B., Moskowitz, D. W. and Dolphin, D. (1976). An improved synthesis of octaethylporphyrin. *The Journal of Organic Chemistry*, 41(24), 3857-3860.
- Paproski, R. J., Forbrich, A., Huynh, E., Chen, J., Lewis, J. D., Zheng, G. and Zemp, R. J. (2016). Porphyrin Nanodroplets: Sub-micrometer Ultrasound and Photoacoustic Contrast Imaging Agents. *Small*, 12(3), 371-380.
- Pereira, Simões, Tomé and Almeida Paz. (2016). Porphyrin-Based Metal-Organic Frameworks as Heterogeneous Catalysts in Oxidation Reactions. *Molecules (Basel, Switzerland)*, 21(10), 1348(1-19).
- Pereira, A. M., Alonso, C. M., Neves, M. G., Tomé, A. C., Silva, A. M., Paz, F. A. and Cavaleiro, J. A. (2008). A New Synthetic Approach to N-Arylquinolino [2, 3, 4-at] porphyrins from β -Arylaminoporphyrins. *The Journal of Organic Chemistry*, 73(18), 7353-7356.
- Pereira, M. M., Muller, G., Ordinas, J. I., Azenha, M. E. and Arnaut, L. G. (2002). Synthesis of vinylated 5, 10, 15, 20-tetraphenylporphyrins via Heck-type coupling reaction and their photophysical properties. *Journal of the Chemical Society, Perkin Transactions*, 2(9), 1583-1588.
- Perpète, E. A., Wathelet, V., Preat, J., Lambert, C. and Jacquemin, D. (2006). Toward a theoretical quantitative estimation of the λ_{max} of anthraquinones-based dyes. *Journal of Chemical Theory and Computation*, 2(2), 434-440.
- Perutz, M., Rossmann, M., Cullis, A., Muirhead, H., Will, G. and North, A. (1960). *Structure of hemoglobin*. Paper presented at the Brookhaven Symp Biol.
- Pietro, W. J., Francl, M. M., Hehre, W. J., DeFrees, D. J., Pople, J. A. and Binkley, J. S. (1982). Self-consistent molecular orbital methods. 24. Supplemented small split-

valence basis sets for second-row elements. *Journal of the American Chemical Society*, 104(19), 5039-5048.

- Pietro, W. J. and Hehre, W. J. (1983). Molecular orbital theory of the properties of inorganic and organometallic compounds. 3. STO-3G basis sets for first-and second-row transition metals. *Journal of Computational Chemistry*, 4(2), 241-251.
- Poland, C. A., Duffin, R., Kinloch, I., Maynard, A., Wallace, W. A. H., Seaton, A. . . . Donaldson, K. (2008). Carbon nanotubes introduced into the abdominal cavity of mice show asbestos-like pathogenicity in a pilot study. *Nature Nanotechnology*, 3(7), 423-428.
- Poncet, J.-L., Barbe, J.-M., Guilard, R., Oumous, H., Lecomte, C. and Protas, J. (1982). Vanadium (II) porphyrin complexes: synthesis and characterization. Crystal structure of 2,3,7,8,12,13,17,18-octaethylporphinatobis-(dimethylphenylphosphine)vanadium(II). *Journal of the Chemical Society, Chemical Communications*, (24), 1421-1422.
- Prasath, R., Butcher, R. and Bhavana, P. (2012). Nitrothienylporphyrins: Synthesis, crystal structure and, the effect of position and number of nitro groups on the spectral and electrochemical properties. *Spectrochimica Acta Part A: Molecular and Biomolecular Spectroscopy*, 87, 258-264.
- Prins, L. J., Reinhoudt, D. N. and Timmerman, P. (2001). Noncovalent synthesis using hydrogen bonding. *Angewandte Chemie International Edition*, 40(13), 2382-2426.
- Prushan, M. (2005). Absorption and Fluorescence Spectroscopy of Tetraphenylporphyrin and Metallo-Tetraphenylporphyrin (pp. 1-9).
- Radon, M. (2015). Role of Spin States in Nitric Oxide Binding to Cobalt (II) and Manganese (II) Porphyrins. Is Tighter Binding Always Stronger? *Inorganic Chemistry*, 54(12), 5634-5645.
- Rao, P. D., Dhanalekshmi, S., Littler, B. J. and Lindsey, J. S. (2000). Rational syntheses of porphyrins bearing up to four different meso substituents. *The Journal of Organic Chemistry*, 65(22), 7323-7344.
- Rassolov, V. A., Pople, J. A., Ratner, M. A. and Windus, T. L. (1998). 6-31G* basis set for atoms K through Zn. *The Journal of Chemical Physics*, 109(4), 1223-1229.
- Ricciardi, G., Rosa, A., Baerends, E. J. and van Gisbergen, S. A. (2002). Electronic structure, chemical bond, and optical spectra of metal bis (porphyrin) complexes: a DFT/TDDFT study of the bis (porphyrin) M (IV)(M= Zr, Ce, Th) series. *Journal of the American Chemical Society*, 124(41), 12319-12334.

- Rieffel, J., Chen, F., Kim, J., Chen, G., Shao, W., Shao, S. . . . Nickles, R. J. (2015). Hexamodal Imaging with Porphyrin-Phospholipid-Coated Upconversion Nanoparticles. *Advanced Materials*, 27(10), 1785-1790.
- Rillema, D., Nagle, J., Barringer Jr, L. and Meyer, T. (1981). Redox properties of metalloporphyrin excited states, lifetimes, and related properties of a series of para-substituted tetraphenylporphine carbonyl complexes of ruthenium (II). *Journal of the American Chemical Society*, 103(1), 56-62.
- Risch, N., Gauler, R. and Keuper, R. (1999). Synthesis of porphyrin dimers using a Heck-type coupling reaction with bisacrylates. *Tetrahedron Letters*, 40(15), 2925-2926.
- Rothemund, P. (1935). Formation of porphyrins from pyrrole and aldehydes. *Journal of the American Chemical Society*, 57(10), 2010-2011.
- Rothemund, P. (1939). Porphyrin studies. III. 1 The structure of the Porphine² ring system. *Journal of the American Chemical Society*, 61(10), 2912-2915.
- Rothemund, P. and Menotti, A. R. (1941). Porphyrin Studies. IV. 1 The Synthesis of α , β , γ , δ -Tetraphenylporphine. *Journal of the American Chemical Society*, 63(1), 267-270.
- Rousseau, K. and Dolphin, D. (1974). A purification of meso-tetraphenylporphyrin. *Tetrahedron Letters*, 15(48), 4251-4254.
- Rubio, M., Roos, B. O., Serrano-Andrés, L. and Merchán, M. (1999). Theoretical study of the electronic spectrum of magnesium-porphyrin. *The Journal of Chemical Physics*, 110(15), 7202-7209.
- Runge, E. and Gross, E. K. (1984). Density-functional theory for time-dependent systems. *Physical Review Letters*, 52(12), 997-1000.
- Runge, S. and Senge, M. O. (1999). Reaction of β -formylporphyrins with organometallic reagents—A facile method for the preparation of porphyrins with exocyclic double bonds. *Tetrahedron*, 55(34), 10375-10390.
- Rybicka-Jasińska, K., Shan, W., Zawada, K., Kadish, K. M. and Gryko, D. (2016). Porphyrins as photoredox catalysts: Experimental and theoretical studies. *Journal of the American Chemical Society*, 138(47), 15451-15458.
- Saltsman, I., Goldberg, I., Balasz, Y. and Gross, Z. (2007). Porphine and pyrrole-substituted porphyrin from cyclocondensation of tripyrrane with mono-substituted pyrroles. *Tetrahedron Letters*, 48(2), 239-244.
- Scales, L. (1985). *Introduction to non-linear optimization*. New York: Springer-Verlag New York, Inc.

- Schaberle, F. A., Arnaut, L. G., Serpa, C., Silva, E. F., Pereira, M. M., Abreu, A. R. and Simões, S. (2010). Infrared absorbing dyes tailored for detection and therapy of solid tumors. *Laser Applications in Life Sciences*, ed. M. Kinnunen and R. Myllylä, Oulu, 73760X.
- Schaberle, F. A., Reis, L. A., Sá, G. F., Serpa, C., Abreu, A. R., Pereira, M. M. and Arnaut, L. G. (2011). *Multi-spectral photoacoustic mapping of bacteriochlorins diffusing through the skin: exploring a new PAT contrast agent*. Paper presented at the European Conference on Biomedical Optics.
- Scheidt, W. R., Duval, H. F., Neal, T. J. and Ellison, M. K. (2000). Intrinsic structural distortions in five-coordinate (nitrosyl) iron (II) porphyrinate derivatives. *Journal of the American Chemical Society*, 122(19), 4651-4659.
- Schlegel, H. B. (1989). Some practical suggestions for optimizing geometries and locating transition states. *New Theoretical Concepts for Understanding Organic Reactions*, 267, 33-53.
- Schrödinger, E. (1926). An undulatory theory of the mechanics of atoms and molecules. *Physical Review*, 28(6), 1049-1070.
- Schwarz, M., Buehler, A., Aguirre, J. and Ntziachristos, V. (2016). Three-dimensional multispectral optoacoustic mesoscopy reveals melanin and blood oxygenation in human skin in vivo. *Journal of Biophotonics*, 9(1-2), 55-60.
- Scolaro, L. M., Romeo, A., Castriciano, M. A. and Micali, N. (2005). Unusual optical properties of porphyrin fractal J-aggregates. *Chemical Communications*, (24), 3018-3020.
- Screen, T. E., Blake, I. M., Rees, L. H., Clegg, W., Borwick, S. J. and Anderson, H. L. (2002). Making conjugated connections to porphyrins: a comparison of alkyne, alkene, imine and azo links. *Journal of the Chemical Society, Perkin Transactions*, 1(3), 320-329.
- Şen, P., Hirel, C., Andraud, C., Aronica, C., Bretonnière, Y., Mohammed, A. . . . Baryshnikov, G. (2010). Fluorescence and FTIR spectra analysis of trans-A2B2-substituted di-and tetra-phenyl porphyrins. *Materials*, 3(8), 4446-4475.
- Senge, M. O., Fazekas, M., Notaras, E. G., Blau, W. J., Zawadzka, M., Locos, O. B. and Ni Mhuirheartaigh, E. M. (2007). Nonlinear optical properties of porphyrins. *Advanced Materials*, 19(19), 2737-2774.
- Sergeeva, N. N., Scala, A., Bakar, M. A., O’Riordan, G., O’Brien, J., Grassi, G. and Senge, M. O. (2009). Synthesis of stannyl porphyrins and porphyrin dimers via stille coupling and their ¹¹⁹Sn NMR and fluorescence properties. *The Journal of Organic Chemistry*, 74(18), 7140-7147.

- Serpa, C., Schabauer, J., Piedade, A. P., Monteiro, C. J., Pereira, M. M., Douglas, P. . . . Arnaut, L. G. (2008). Photoacoustic measurement of electron injection efficiencies and energies from excited sensitizer dyes into nanocrystalline TiO₂ films. *Journal of the American Chemical Society*, 130(28), 8876-8877.
- Sessler, J. L., Johnson, M. R. and Lynch, V. (1987). Synthesis and crystal structure of a novel tripyrrane-containing porphyrinogen-like macrocycle. *The Journal of Organic Chemistry*, 52(19), 4394-4397.
- Sessler, J. L., Mozaffari, A. and Johnson, M. R. (1991). 3, 4-Diethylpyrrole and 2, 3, 7, 8, 12, 13, 17, 18-Octaethylporphyrin. *Organic Syntheses*, 68-68.
- Sessler, J. L. and Tomat, E. (2007). Transition-metal complexes of expanded porphyrins. *Accounts of Chemical Research*, 40(5), 371-379.
- Seybold, P. G. and Gouterman, M. (1969). Porphyrins: XIII: Fluorescence spectra and quantum yields. *Journal of Molecular Spectroscopy*, 31(1-13), 1-13.
- Shanmugathan, S., Johnson, C. K., Edwards, C., Matthews, E. K., Dolphin, D. and Boyle, R. W. (2000). Regioselective halogenation and palladium-catalysed couplings on 5, 15-diphenylporphyrin. *Journal of Porphyrins and Phthalocyanines*, 4(3), 228-232.
- Sharma, R. K., Ahuja, G. and Sidhwani, I. T. (2009). A new one pot and solvent-free synthesis of nickel porphyrin complex. *Green Chemistry Letters and Reviews*, 2(2), 101-105.
- Shea, K. M., Jaquinod, L. and Smith, K. M. (1998). Dihydroporphyrin synthesis: new methodology. *The Journal of Organic Chemistry*, 63(20), 7013-7021.
- Shelby, M. L., Mara, M. W. and Chen, L. X. (2014). New insight into metalloporphyrin excited state structures and axial ligand binding from X-ray transient absorption spectroscopic studies. *Coordination Chemistry Reviews*, 277, 291-299.
- Sheldon, R. A. (1994). *Metalloporphyrins in catalytic oxidations*. New York: CRC Press.
- Shelnutt, J. and Medforth, C. (1998). Nonplanar porphyrins and their significance in proteins. *Chemical Society Reviews*, 27(1), 31-42.
- Shelnutt, J. and Ortiz, V. (1985). Substituent effects on the electronic structure of metalloporphyrins: a quantitative analysis in terms of four-orbital-model parameters. *The Journal of Physical Chemistry*, 89(22), 4733-4739.
- Shelton, R. L. and Applegate, B. E. (2010). Ultrahigh resolution photoacoustic microscopy via transient absorption. *Biomedical Optics Express*, 1(2), 676-686.

- Shen, D. M., Liu, C. and Chen, Q. Y. (2007). Synthesis and Versatile Reactions of β -Azidotetraarylporphyrins. *European Journal of Organic Chemistry*, 2007(9), 1419-1422.
- Shi, B. and Boyle, R. W. (2002). Synthesis of unsymmetrically substituted meso-phenylporphyrins by Suzuki cross coupling reactions. *Journal of the Chemical Society, Perkin Transactions*, 1(11), 1397-1400.
- ShingáChan, K. and Thomas, C. (1994). Synthesis of β -aryl substituted porphyrins by palladium-catalysed cross-coupling reactions. *Journal of the Chemical Society, Chemical Communications*, (3), 271-272.
- Shoji, Y., Tashiro, K. and Aida, T. (2004). Selective extraction of higher fullerenes using cyclic dimers of zinc porphyrins. *Journal of the American Chemical Society*, 126(21), 6570-6571.
- Siri, O., Jaquinod, L. and Smith, K. M. (2000). Coplanar conjugated β -nitroporphyrins and some aspects of nitration of porphyrins with N_2O_4 . *Tetrahedron Letters*, 41(19), 3583-3587.
- Slater, J. C. (1930). Atomic shielding constants. *Physical Review*, 36(1), 57-64.
- Smith, K., Lindsey, J., Vicente, M., Jaquinod, L., Senge, M., Callot, H. and Ocampo, R. (2000). Cyclizations of a,c-Biladiene Salts to Give Porphyrins and Their Derivatives. In K. M. Kadish, K. M. Smith and R. Guilard (eds.), *The Porphyrin Handbook—Synthesis and Organic Chemistry* (Vol. 1, pp. 119-148). San Diego: Academic Press.
- Smith, K. M. (2000). Strategies for the synthesis of octaalkylporphyrin systems. In K. M. Kadish, K. M. Smith and R. Guilard (eds.), *The porphyrin handbook—Synthesis and Organic Chemistry* (Vol. 1, pp. 119-148). San Diego: Academic Press.
- Smith K. M. (Ed.). (1975). *Porphyrins and Metalloporphyrins*, Amsterdam, Elsevier
- Smith, K. M., Bisset, G. M. and Tappa, H. D. (1982). Polyformylation of copper (II) complexes of octa-alkylporphyrins. *Journal of the Chemical Society, Perkin Transactions*, 1, 581-585.
- Smith, K. M., Goff, D. A. and Abraham, R. J. (1984). The NMR spectra of porphyrins. 27—proton NMR spectra of chlorophyll-a and pheophytin-a. *Magnetic Resonance in Chemistry*, 22(12), 779-783.
- Smith, N. W. and Dzyuba, S. V. (2010). Efficient nitration of meso-tetraphenylporphyrin with nitronium tetrafluoroborate. *Arkivoc*, 7, 10-18.

- Sommer, J. R., Shelton, A. H., Parthasarathy, A., Ghiviriga, I., Reynolds, J. R. and Schanze, K. S. (2011). Photophysical properties of near-infrared phosphorescent π -extended platinum porphyrins. *Chemistry of Materials*, 23(24), 5296-5304.
- Sondheimer, F., Wolovsky, R. and Amiel, Y. (1962). Unsaturated Macrocyclic Compounds. XXIII. 1 The Synthesis of the Fully Conjugated Macrocyclic Polyenes Cyclooctadecanonaene ([18] Annulene), 2 Cyclotetracosadodecaene ([24] Annulene), and Cyclotriacontapentadecaene ([30] Annulene). *Journal of the American Chemical Society*, 84(2), 274-284.
- Soret, J. (1883). Analyse spectrale: Sur le spectre d'absorption du sang dans la partie violette et ultra-violette. *Comptes Rendus Chimie*, 97, 1269-1273.
- Sreejith, S., Huong, T. T. M., Borah, P. and Zhao, Y. (2015). Organic-inorganic nanohybrids for fluorescence, photoacoustic and Raman bioimaging. *Science Bulletin*, 60(7), 665-678.
- Sreejith, S., Joseph, J., Lin, M., Menon, N. V., Borah, P., Ng, H. J. . . . Zhao, Y. (2015). Near-infrared squaraine dye encapsulated micelles for in vivo fluorescence and photoacoustic bimodal imaging. *ACS Nano*, 9(6), 5695-5704.
- Srivastava, V., Gusain, D. and Sharma, Y. C. (2015). Critical review on the toxicity of some widely used engineered nanoparticles. *Industrial & Engineering Chemistry Research*, 54(24), 6209-6233.
- Stepien, M. and Latos-Grazynski, L. (2008). Aromaticity and tautomerism in porphyrins and porphyrinoids. In T. M. Krygowski and M. K. Cyranski (eds.), *Aromaticity in Heterocyclic Compounds* (Vol.19, pp. 84-146). Berlin: Springer.
- Strohm, E. M., Berndl, E. S. and Kolios, M. C. (2013). High frequency label-free photoacoustic microscopy of single cells. *Photoacoustics*, 1(3), 49-53.
- Sugita, N., Hayashi, S., Hino, F. and Takanami, T. (2012). Palladium-catalyzed Kumada Coupling Reaction of bromoporphyrins with silylmethyl Grignard reagents: Preparation of silylmethyl-substituted porphyrins as a multipurpose synthon for fabrication of porphyrin systems. *The Journal of Organic Chemistry*, 77(23), 10488-10497.
- Sugita, N., Hayashi, S., Ishii, S. and Takanami, T. (2013). Palladium-Catalyzed Polyfluorophenylation of Porphyrins with Bis (polyfluorophenyl) zinc reagents. *Catalysts*, 3(4), 839-852.
- Suijkerbuijk, B. M. and Klein Gebbink, R. J. (2008). Merging porphyrins with organometallics: synthesis and applications. *Angewandte Chemie International Edition*, 47(39), 7396-7421.

- Sundholm, D. (2000). Density functional theory study of the electronic absorption spectrum of Mg-porphyrin and Mg-etiochlorophyll-a. *Chemical Physics Letters*, 317(3), 392-399.
- Suslick, K. S. and Watson, R. A. (1992). The photochemistry of chromium, manganese, and iron porphyrin complexes. *New Journal of Chemistry* 16, 633-642.
- Szabo, A. and Ostlund, N. S. (2012). *Modern quantum chemistry: introduction to advanced electronic structure theory*. New York: Courier Dover Publications.
- Takanami, T. (2013). Functionalization of Porphyrins through CC Bond Formation Reactions with Functional Group-Bearing Organometallic Reagents. *Heterocycles: an International Journal for Reviews and Communications in Heterocyclic Chemistry*, 87(8), 1659-1689.
- Takanami, T., Wakita, A., Sawaizumi, A., Iso, K., Onodera, H. and Suda, K. (2008). One-pot synthesis of meso-formylporphyrins by SNAr reaction of 5, 15-disubstituted porphyrins with (2-pyridyldimethylsilyl) methylolithium. *Organic Letters*, 10(4), 685-687.
- Taniguchi, M. and Lindsey, J. S. (2012). Enumeration of isomers of substituted tetrapyrrole macrocycles: from classical problems in biology to modern combinatorial libraries *Handbook of Porphyrin Science (Volume 23) With Applications to Chemistry, Physics, Materials Science, Engineering, Biology and Medicine* (pp. 1-80): World Scientific.
- Taniguchi, S., Hasegawa, H., Nishimura, M. and Takahashi, M. (1999). A Facile Route to Tripyrrane from 2, 5-Bis (hydroxymethyl) pyrrole and the Improved Synthesis of Porphine by the. *Synlett*, 1999(01), 73-74.
- Tapia, O. and Goscinski, O. (1975). Self-consistent reaction field theory of solvent effects. *Molecular Physics*, 29(6), 1653-1661.
- Tawada, Y., Tsuneda, T., Yanagisawa, S., Yanai, T. and Hirao, K. (2004). A long-range-corrected time-dependent density functional theory. *The Journal of Chemical Physics*, 120(18), 8425-8433.
- Taylor, G. A. and Tsutsui, M. (1975). Out-of-plane metalloporphyrin complexes. *Journal of Chemical Education*, 52(11), 715-720.
- Thies, S., Bornholdt, C., Köhler, F., Sönnichsen, F. D., Näther, C., Tuzcek, F. and Herges, R. (2010). Coordination-Induced Spin Crossover (CISCO) through Axial Bonding of Substituted Pyridines to Nickel-Porphyrins: σ -Donor versus π -Acceptor Effects. *Chemistry-A European Journal*, 16(33), 10074-10083.
- Thudichum, J. (1867). Report Med. Off. Privy Council, 10, 152.

- Tirado-Rives, J. and Jorgensen, W. L. (2008). Performance of B3LYP density functional methods for a large set of organic molecules. *Journal of Chemical Theory and Computation*, 4(2), 297-306.
- To, W. P., Liu, Y., Lau, T. C. and Che, C. M. (2013). A Robust Palladium (II)–Porphyrin Complex as Catalyst for Visible Light Induced Oxidative C–H Functionalization. *Chemistry-A European Journal*, 19(18), 5654-5664.
- Tomasi, J., Mennucci, B. and Cammi, R. (2005). Quantum mechanical continuum solvation models. *Chemical Reviews*, 105(8), 2999-3094.
- Tovmasyan, A., Sheng, H., Weitner, T., Arulpragasam, A., Lu, M., Warner, D. S. . . . Batinic-Haberle, I. (2013). Design, mechanism of action, bioavailability and therapeutic effects of Mn porphyrin-based redox modulators. *Medical Principles and Practice*, 22(2), 103-130.
- Trova, M. P., Gauuan, P. J. F., Pechulis, A. D., Bubb, S. M., Bocckino, S. B., Crapo, J. D. and Day, B. J. (2003). Superoxide dismutase mimetics. Part 2: synthesis and structure–Activity relationship of glyoxylate-and glyoxamide-Derived metalloporphyrins. *Bioorganic and Medicinal Chemistry*, 11(13), 2695-2707.
- Tsuchiya, S. and Seno, M. (1989). Novel synthetic method of phenol from benzene catalysed by perfluorinated hemin. *Chemistry Letters*, 18(2), 263-266.
- Tsutsui, M. and Hrung, C. (1973). A technetium porphyrin: μ -[mesoporphyrin ix dimethyl esterato] bis [tricarbonyltechnetium (i)]. *Chemistry Letters*, 2(9), 941-942.
- Tsutsui, M., Ostfeld, D. and Hoffman, L. M. (1971). Unusual metalloporphyrins. VI. Metal shuttling between imidazole nitrogens in a ruthenium porphyrin imidazole. *Journal of the American Chemical Society*, 93(7), 1820-1823.
- Ullrich, C. A. (2011). *Time-dependent density-functional theory: concepts and applications*. Oxford: Oxford University Press.
- Urbani, M., Grätzel, M., Nazeeruddin, M. K. and Torres, T. (2014). Meso-substituted porphyrins for dye-sensitized solar cells. *Chemical Reviews*, 114(24), 12330-12396.
- Valeur, B. and Berberan-Santos, M. N. (2012). *Molecular fluorescence: principles and applications*. USA; John Wiley & Sons.
- Valicsek, Z., Eller, G. and Horváth, O. (2012). Equilibrium, photophysical and photochemical examination of anionic lanthanum (III) mono-and bisporphyrins: the effects of the out-of-plane structure. *Dalton Transactions*, 41(42), 13120-13131.

- Valicsek, Z. and Horváth, O. (2007). Formation, photophysics and photochemistry of thallium (III) 5, 10, 15, 20-tetrakis (4-sulphonatophenyl) porphyrin: New supports of typical sitting-atop features. *Journal of Photochemistry and Photobiology A: Chemistry*, 186(1), 1-7.
- Valicsek, Z. and Horváth, O. (2013). Application of the electronic spectra of porphyrins for analytical purposes: the effects of metal ions and structural distortions. *Microchemical Journal*, 107, 47-62.
- Valicsek, Z., Horváth, O. and Patonay, K. (2011). Formation, photophysical and photochemical properties of water-soluble bismuth (III) porphyrins: The role of the charge and structure. *Journal of Photochemistry and Photobiology A: Chemistry*, 226(1), 23-35.
- Valicsek, Z., Lendvay, G. r. and Horváth, O. (2008). Equilibrium, photophysical, photochemical, and quantum chemical examination of anionic mercury (II) mono-and bisporphyrins. *The Journal of Physical Chemistry B*, 112(46), 14509-14524.
- Van Gisbergen, S., Rosa, A., Ricciardi, G. and Baerends, E. (1999). Time-dependent density functional calculations on the electronic absorption spectrum of free base porphyrin. *The Journal of Chemical Physics*, 111(6), 2499-2506.
- Vasil'ev, V. and Lobanovskaya, A. (2015). Production of hydrogen in a ternary photocatalytic system based on water-soluble palladium (II) porphyrin. *Russian Journal of Applied Chemistry*, 88(2), 283-288.
- Vaz, B., Alvarez, R., Nieto, M., Paniello, A. I. and de Lera, A. R. (2001). Suzuki cross-coupling of meso-dibromoporphyrins for the synthesis of functionalized A₂B₂ porphyrins. *Tetrahedron Letters*, 42(42), 7409-7412.
- Vicente, M. (2001). Porphyrin-based sensitizers in the detection and treatment of cancer: recent progress. *Current Medicinal Chemistry-Anti-Cancer Agents*, 1(2), 175-194.
- Vicente, M. G. H. and Smith, K. M. (1990). Functionalization of alkyl substituents in octaalkylporphyrins. *Synlett*, 1990(10), 579-581.
- Vicente, M. G. H. and Smith, K. M. (1991). Vilsmeier reactions of porphyrins and chlorins with 3-(dimethylamino) acrolein to give meso-(2-formylvinyl) porphyrins: New syntheses of benzochlorins, benzoisobacteriochlorins, and benzobacteriochlorins and reductive coupling of porphyrins and chlorins using low-valent titanium complexes. *The Journal of Organic Chemistry*, 56(14), 4407-4418.

- Vydrov, O. A., Scuseria, G. E. and Perdew, J. P. (2007). Tests of functionals for systems with fractional electron number. *The Journal of Chemical Physics*, 126(15), 154109(1-9).
- Wang, B., Su, J. L., Amirian, J., Litovsky, S. H., Smalling, R. and Emelianov, S. (2010). Detection of lipid in atherosclerotic vessels using ultrasound-guided spectroscopic intravascular photoacoustic imaging. *Optics Express*, 18(5), 4889-4897.
- Wang, B., Zhao, Q., Barkey, N. M., Morse, D. L. and Jiang, H. (2012). Photoacoustic tomography and fluorescence molecular tomography: A comparative study based on indocyanine green. *Medical Physics*, 39(5), 2512-2517.
- Wang, C.-B. and Chang, C. (1979). A Convenient Synthesis of Pyrrole Precursors for Octaalkylporphyrins. *Synthesis*, 1979(07), 548-549.
- Wang, H., Zhou, D., Shen, S., Wan, J., Zheng, X., Yu, L. and Phillips, D. L. (2014). The photocatalytic activity and degradation mechanism of methylene blue over copper (ii) tetra (4-carboxyphenyl) porphyrin sensitized TiO₂ under visible light irradiation. *Rsc Advances*, 4(55), 28978-28986.
- Wang, L., Yang, P.-P., Zhao, X.-X. and Wang, H. (2016). Self-assembled nanomaterials for photoacoustic imaging. *Nanoscale*, 8(5), 2488-2509.
- Wang, L. V. and Hu, S. (2012). Photoacoustic tomography: in vivo imaging from organelles to organs. *Science*, 335(6075), 1458-1462.
- Wang, R., Brugh, A. M., Rawson, J., Therien, M. J. and Forbes, M. D. E. (2017). Alkyne-Bridged Multi[Copper(II) Porphyrin] Structures: Nuances of Orbital Symmetry in Long-Range, Through-Bond Mediated, Isotropic Spin Exchange Interactions. *Journal of the American Chemical Society*, 139(29), 9759-9762.
- Wang, T., Nandy, S., Salehi, H. S., Kumavor, P. D. and Zhu, Q. (2014). A low-cost photoacoustic microscopy system with a laser diode excitation. *Biomedical Optics Express*, 5(9), 3053-3058.
- Wang, T., Yang, Y., Alqasemi, U., Kumavor, P. D., Wang, X., Sanders, M. . . . Zhu, Q. (2013). Characterization of ovarian tissue based on quantitative analysis of photoacoustic microscopy images. *Biomedical Optics Express*, 4(12), 2763-2768.
- Weigend, F., Köhn, A. and Hättig, C. (2002). Efficient use of the correlation consistent basis sets in resolution of the identity MP2 calculations. *The Journal of Chemical Physics*, 116(8), 3175-3183.
- Weng, Y.-Q., Teng, Y.-L., Yue, F., Zhong, Y.-R. and Ye, B.-H. (2007). A new selective fluorescent chemosensor for Cu (II) ion based on zinc porphyrin-dipyridylamino. *Inorganic Chemistry Communications*, 10(4), 443-446.

- Weng, Y.-Q., Yue, F., Zhong, Y.-R. and Ye, B.-H. (2007). A Copper (II) Ion-Selective On-Off-Type Fluoroionophore Based on Zinc Porphyrin-Dipyridylamino. *Inorganic Chemistry*, 46(19), 7749-7755.
- Wiehe, A., Ryppa, C. and Senge, M. O. (2002). A practical synthesis of meso-monosubstituted, β -unsubstituted porphyrins. *Organic Letters*, 4(22), 3807-3809.
- Wijesekera, T., Dupre, D., Cader, M. S. and Dolphin, D. (1996). Porphyrins bearing halogens at the meso-phenyl and -pyrrolic positions: synthesis and spectral properties. *Bulletin-Societe Chimique De France-All Sections*, 133, 765-776.
- Wijesekera, T., Matsumoto, A., Dolphin, D. and Lexa, D. (1990). Perchlorinated and Highly Chlorinated meso-Tetraphenylporphyrins. *Angewandte Chemie International Edition*, 29(9), 1028-1030.
- Wijesekera, T. P. and Dolphin, D. (1990). 1-Bromo-19-methylbiladienes-ac; Useful precursors to porphyrins. *Synlett*, 1990(05), 235-244.
- Wijesekera, T. P. and Dolphin, D. (1994). Synthetic aspects of porphyrin and metalloporphyrin chemistry. *Metalloporphyrins in Catalytic Oxidations*, 193-239.
- Willard, H. H., Merritt Jr, L. L., Dean, J. A. and Settle Jr, F. A. (1988). *Instrumental methods of analysis*. New York: Wadsworth Publishing Company.
- Williams, A. T. R., Winfield, S. A. and Miller, J. N. (1983). Relative fluorescence quantum yields using a computer-controlled luminescence spectrometer. *Analyst*, 108(1290), 1067-1071.
- Willstätter, R. and Stoll, A. (1913). Die wirkungen der chlorophyllase. In: R. Willstätter and A. Stoll (eds.), *Untersuchungen ueber chlorophyll* (pp. 172-187). Berlin: Springer.
- Wolfram, K. and Holthausen, M. (2001). *A Chemist's Guide to Density Functional Theory*. Weinheim: Wiley-VCH Verlag, GmbH.
- Wróbel, D. and Graja, A. (2006). Modification of electronic structure in supramolecular fullerene-porphyrin systems studied by fluorescence, photoacoustic and photothermal spectroscopy. *Journal of Photochemistry and Photobiology A: Chemistry*, 183(1), 79-88.
- Wu, G.-Z., Gan, W.-X. and Leung, H.-K. (1991). Photophysical properties of meso-substituted octaethylporphines and their zinc complexes. *Journal of the Chemical Society, Faraday Transactions*, 87(18), 2933-2937.

- Wu, J. I., Fernández, I. and Schleyer, P. v. R. (2012). Description of aromaticity in porphyrinoids. *Journal of the American Chemical Society*, 135(1), 315-321.
- Xiang, L., Wang, B., Ji, L. and Jiang, H. (2013). 4-D photoacoustic tomography. *Scientific Reports*, 3, 1113.
- Xu, M. and Wang, L. V. (2006). Photoacoustic imaging in biomedicine. *Review of Scientific Instruments*, 77(4), 041101(1-22).
- Yamaguchi, T., Kimura, T., Matsuda, H. and Aida, T. (2004). Macroscopic Spinning Chirality Memorized in Spin-Coated Films of Spatially Designed Dendritic Zinc Porphyrin J-Aggregates. *Angewandte Chemie*, 116(46), 6510-6515.
- Yanai, T., Tew, D. P. and Handy, N. C. (2004). A new hybrid exchange–correlation functional using the Coulomb-attenuating method (CAM-B3LYP). *Chemical Physics Letters*, 393(1), 51-57.
- Yao, J., Wang, L., Yang, J.-M., Maslov, K. I., Wong, T. T., Li, L. . . . Wang, L. V. (2015). High-speed label-free functional photoacoustic microscopy of mouse brain in action. *Nature Methods*, 12(5), 407-410.
- Yasin, A., Jose, R. and Yusoff, M. M. (2015). Predicting larger absorption cross-section in porphyrin dyes using DFT calculations. *Journal of Porphyrins and Phthalocyanines*, 19(12), 1270-1278.
- Yeh, C.-Y., Miller, S. E., Carpenter, S. D. and Nocera, D. G. (2001). Structurally homologous β - and meso-amidinium porphyrins. *Inorganic Chemistry*, 40(14), 3643-3646.
- Yella, A., Lee, H.-W., Tsao, H. N., Yi, C., Chandiran, A. K., Nazeeruddin, M. K. . . . Grätzel, M. (2011). Porphyrin-sensitized solar cells with cobalt (II/III)-based redox electrolyte exceed 12 percent efficiency. *Science*, 334(6056), 629-634.
- Yelleswarapu, C. S. and Kothapalli, S.-R. (2010). Nonlinear photoacoustics for measuring the nonlinear optical absorption coefficient. *Optics Express*, 18(9), 9020-9025.
- Youngblood, W. J., Gryko, D. T., Lammi, R. K., Bocian, D. F., Holten, D. and Lindsey, J. S. (2002). Glaser-mediated synthesis and photophysical characterization of diphenylbutadiyne-linked porphyrin dyads. *The Journal of Organic Chemistry*, 67(7), 2111-2117.
- Yuan, Z., Wu, C., Zhao, H. and Jiang, H. (2005). Imaging of small nanoparticle-containing objects by finite-element-based photoacoustic tomography. *Optics Letters*, 30(22), 3054-3056.

- Zackrisson, S., van de Ven, S. and Gambhir, S. (2014). Light in and sound out: emerging translational strategies for photoacoustic imaging. *Cancer Research*, 74(4), 979-1004.
- Zems, Y., Moiseev, A. G. and Perepichka, D. F. (2013). Convenient synthesis of a highly soluble and stable phosphorescent platinum porphyrin dye. *Organic Letters*, 15(20), 5330-5333.
- Zhan, H., Lamare, S., Ng, A., Kenny, T., Guernon, H., Chan, W.-K. . . . Wong, W.-Y. (2011). Synthesis and photovoltaic properties of new metalloporphyrin-containing polyplatinyne polymers. *Macromolecules*, 44(13), 5155-5167.
- Zhang, D., Qi, G. B., Zhao, Y. X., Qiao, S. L., Yang, C. and Wang, H. (2015). In Situ Formation of Nanofibers from Purpurin18-Peptide Conjugates and the Assembly Induced Retention Effect in Tumor Sites. *Advanced Materials*, 27(40), 6125-6130.
- Zhang, X., Zhang, Y. and Jiang, J. (2005). Infrared spectra of metal-free, N', N-dideuterio, and magnesium porphyrins: density functional calculations. *Spectrochimica Acta Part A: Molecular and Biomolecular Spectroscopy*, 61(11), 2576-2583.
- Zhang, Y., Cai, X., Wang, Y., Zhang, C., Li, L., Choi, S. W. . . . Xia, Y. (2011). Noninvasive photoacoustic microscopy of living cells in two and three dimensions through enhancement by a metabolite dye. *Angewandte Chemie*, 123(32), 7497-7501.
- Zhao, Y. and Truhlar, D. G. (2006). Density functional for spectroscopy: no long-range self-interaction error, good performance for Rydberg and charge-transfer states, and better performance on average than B3LYP for ground states. *The Journal of Physical Chemistry A*, 110(49), 13126-13130.
- Zhao, Y. and Truhlar, D. G. (2008). The M06 suite of density functionals for main group thermochemistry, thermochemical kinetics, noncovalent interactions, excited states, and transition elements: two new functionals and systematic testing of four M06-class functionals and 12 other functionals. *Theoretical Chemistry Accounts: Theory, Computation, and Modeling (Theoretica Chimica Acta)*, 120(1), 215-241.
- Zhou, Y., Liang, X. and Dai, Z. (2016). Porphyrin-loaded nanoparticles for cancer theranostics. *Nanoscale*, 8(25), 12394-12405.
- Zhu, W., Santic, M., Ou, Z., Santic, P. J., McDonald, J. A., Brotherhood, P. R. . . . Kadish, K. M. (2009). Electrochemistry and Spectroelectrochemistry of β , β' -Fused Quinoxalinoporphyrins and Related Extended Bis-porphyrins with Co (III), Co (II), and Co (I) Central Metal Ions. *Inorganic Chemistry*, 49(3), 1027-1038.

APPENDIX A

PORPHYRINS IN NATURE

The majority of animal and plant life, existing on our planet results from porphyrins. Due to their biological importance in nature and their vivid colors, porphyrins have been named the “pigments of life. The porphyrins found in nature, are usually associated with metal ions forming metalloporphyrin derivatives and are important for biological functionalities. Representative examples of porphyrin derivatives are hemes found in hemoglobins, myoglobins, cytochromes, catalases and peroxidases; chlorophylls found in green plants; bacteriochlorophylls found in cyanobacteria; and vitamin B₁₂. All these naturally occurring porphyrins play vital roles in our life such as heme for storage and transportation of oxygen; in cytochromes for electron transfer; and in catalase enzyme; chlorophyll for photosynthesis, and vitamin B₁₂ as a physiologically active substance. In cytochromes, iron uses its +2 and +3 oxidation states while carrying out the function of electron transfer during cell respiration. In vitamin B₁₂, cobalt in its trivalent state forms a complex with corrin (a porphyrin type derivative). Whereas, chlorophyll is based on magnesium and chlorin (a reduced porphyrin) complex.

Heme

The biologically most important amongst naturally occurring porphyrins is heme, the red blood pigment (Figure 1a). The heme is the prosthetic group in haemoglobin and myoglobin containing iron(II) complex of protoporphyrin IX. Hemoglobin and myoglobin are two of the most important proteins in the body. They are high molecular weight protein systems containing the heme group (Figure 1c). In hemoglobin, iron operates as a reversible binding site for oxygen, allowing the oxygen to transport throughout the body. Its first isolation was successfully achieved from crystallization of blood by L. Teichmann [1]. Myoglobin help to store oxygen and to facilitate it for reparation process [2]. Hemoglobin binds with O₂ and transports it from the lungs to the muscle cells. Then it transfer O₂ to myoglobin which has higher affinity for O₂ than does hemoglobin. By itself, heme is not a good oxygen carrier. It must be part of a larger protein to prevent oxidation of the Fe²⁺ to Fe³⁺ in the porphyrin core.

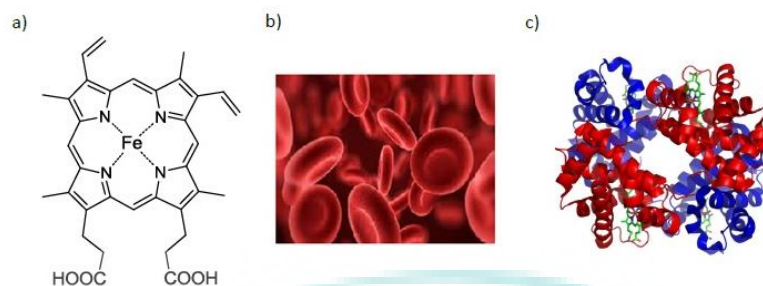


Figure 1: a) Heme b prosthetic group, the iron(II) complex of protoporphyrin-IX; b) Red blood cell, the red color is due to the presence of heme; c) Structure of hemoglobin. The red and blue are the protein α and β subunits and the green is heme groups

In heme, the coordination of iron to pyrrolic nitrogen is in its +2 oxidation state. When iron rises up to +3 state, two components, methemoglobin and metmyoglobin are formed that do not have capability to bind with dioxygen molecule. Therefore, protein in hemoglobin and myoglobin helps to stabilize the Fe(II), creating hydrophobic environment and through folded around heme. This also help in reducing chances of coordination of water molecule with heme and allow dioxygen molecule to coordinate [2, 3].

Hemoglobin is comprised of four globins (subunits), two α chains possessing 141 amino acids and the other two have 146 amino acids known as β chains [4], while myoglobin contain the protein component comprising of singlet stand of 152 amino acids [4]. Hemoglobin and myoglobin have different helical regions and these region grip the heme and oxygen binds at the distal side of porphyrin [5]. As compare to hemoglobin, myoglobin can easily be converted to oxymyoglobin at lower concentration of oxygen [6]. The detachment of oxygen molecules from hemoglobin occurs easily at low oxygen level [7, 8].

After carrying the oxygen in blood, red blood cells are transmuted to liver. In liver it degraded into two type of bile pigments, naming biliverdin and bilirubin of greenish and yellowish color respectively, by opening the porphyrin ring and releasing the iron [9, 10]. The structures of bilirubin and biliverdin are shown in Figure 2. In humans, simultaneous breakdown of heme causes the formation of bilirubin. Some bilirubin are formed by degradation of other hemoproteins such as P450 [11, 12]. Heme can also catalyze the oxidation of substrates using hydrogen peroxide in peroxidases, and catalyze the breakdown of hydrogen peroxide to water and oxygen in catalases.

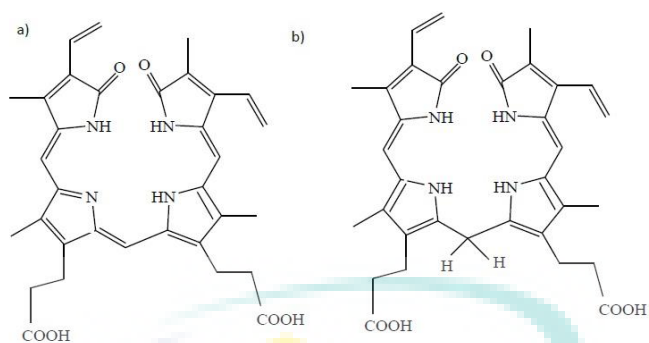


Figure 2: a) Structure of biliverdin; b) Structure of bilirubin [4]

Chlorophyll

Not less in significance are chlorophyll a (Figure 3), the green pigment involved in plant photosynthesis. In 1914 R. Willstätter [13] succeeded in the isolation of chlorophyll a and was honored only one year later with the Nobel Prize in Chemistry 1915 for his researches on plant pigments, especially chlorophyll. The Nobel Prize in Chemistry 1930 was awarded to H. Fischer for his researches into the constitution of haemin and chlorophyll and especially for his synthesis of haemin [14].

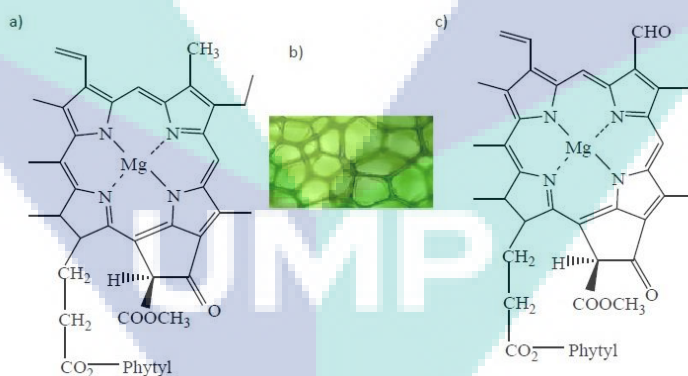


Figure 3: a) Structure of chlorophyll a; b) Chloroplast containing chlorophyll; c) Structure of chlorophyll b

Chlorophyll is the Mg(II) containing derivative of reduced porphyrin, found in subcellular structure called chloroplast in almost all plants cells. These are the molecules that give green color to stems and leaves and play a vital role to carry out the photosynthesis. Chlorophylls are capable of absorbing light at longer wavelength range [3, 15]. Various type of chlorophylls such as chlorophyll a, b, c having diverse catalytic

activity (shown in Figure 3) can be achieved by slightly changing the basic magnesium(II) porphyrin system.

Chlorophyll a is the dye that is available on earth in large amount and exist in all higher plants and algae. Photosynthesis requires chlorophyll for active reaction side. In photosynthesis, chlorophyll play their part to harvest the light energy and utilize it for the generation of reducing agents, ATP (Adenosine Triphosphate) storing energy and producing O₂ through oxidation of water [3, 4, 16, 17].

Bacteriochlorophylls

Bacteriochlorophylls, related to chlorophylls, are photosynthetic pigments found in various phototropic bacteria. Various type of bacteriochlorophylls are Mg(II)-chlorin complexes (reduced porphyrin derivatives) like chlorophylls. Bacteriochlorophylls c, d, e and f are the dihydroporphyrin (chlorin) having one reduced pyrrole ring (Figure 4) whereas bacteriochlorophylls a, b, and g are tetrahydroporphyrin (bacteriochlorins) having two reduced pyrrole rings (Figure 5). Generally, bacteriochlorophylls absorb light of a longer wavelength as compared to that of the chlorophylls. Their absorption spectra are observed to be in red or infra-red region and largely depend on the macrocycle conjugation and the protein environment.

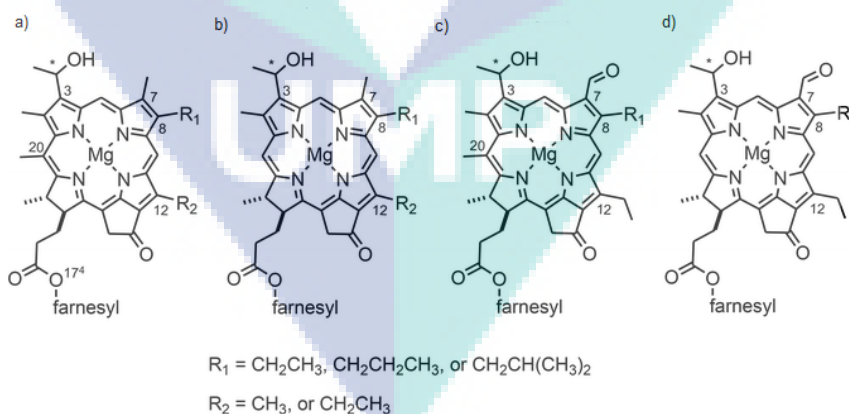


Figure 4: Structure of a) Bacteriochlorophyll c; b) Bacteriochlorophyll d; c) Bacteriochlorophyll e; and d) Bacteriochlorophyll

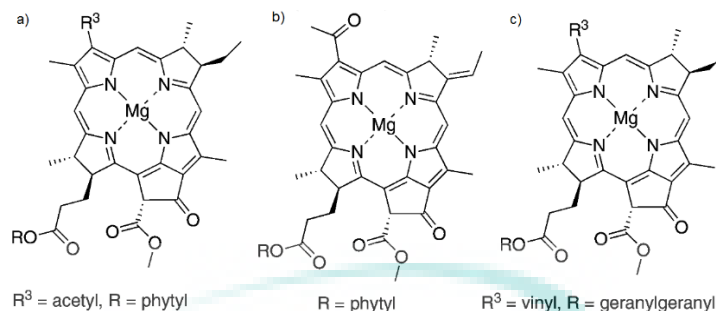


Figure 5: Structure of a) Bacteriochlorophyll a; b) Bacteriochlorophyll b; and c) Bacteriochlorophyll g

Cytochromes

The cytochromes are the kinds of metalloporphyrins that contains iron which execute different functions in animals and plants cells. Some cytochromes carried out electrons transfer reactions and some are helpful in photosynthesis and cell respiration. Other cytochromes like cytochromes c and P450 also helps in oxidation-reduction reactions [18]. Cytochromes facilitates catalytic process as well by making a reversible change between Fe (II) and Fe(III) oxidation states [19]. The connection of cytochrome c with amino acids of protein via cysteine and thio groups by covalent bonds is shown in Figure 6.

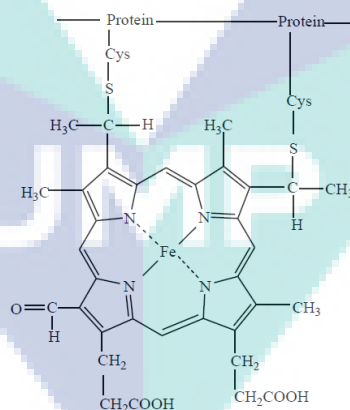


Figure 6: Structure of cytochrome c.

Co-Factor F430

Cofactor F430 is a metalloporphyrin as shown in Figure 7 and it was first attained in 1978 from MCR (methyl-coenzyme M reductase). It is a nickel-containing tetrapyrrole and acts as a prosthetic group in MCR. The behavior of this cofactor is non-fluorescent

and its color is yellow. F-430 is the name given to it because of its absorption band at 430 nm [5, 20]. Nickel ion convert its oxidation state during the process of methane generation and it play its role as catalytically active site [21]. This process results in a large, non-planarity in metal core size, which may affect its axial ligand affinity [22].

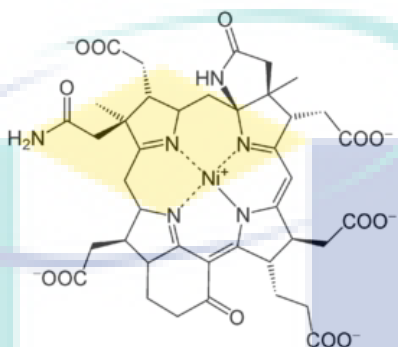


Figure 7: Structure of Co-factor F₄₃₀

Vitamin B₁₂:

In 1948, vitamin B12 was first isolated as deep red colored crystals [23]. The structure of vitamin B12 was studied by two teams, Karl Folkers from USA and Sir Alexander Todd from Britain separately. Based on their works and many other research groups, cobalt was found as central metal ion in vitamin B12 in 1953. The vitamin B12 macrocyclic ligand that contained a cobalt was firstly identified at that time [23]. The macrocycle in vitamin B12 differ from heme and chlorophyll a by absence of one CH-bridging and a reduce pyrrole ring (Figure 8), causing the loss of aromaticity in macrocycle. The resulting vitamin B12 parent ring are named as corrin (porphyrin ring derivative). Vitamin B12, the red pigment, is a trivalent cobalt-corrin complex and essential for numerous biochemically important rearrangement reactions, like cell division or hematosis. It acts as cofactors for methylation of DNA and for the production of hemoglobin. In 1972, R. B. Woodward first established the total synthesis of vitamin B12 [4, 24].

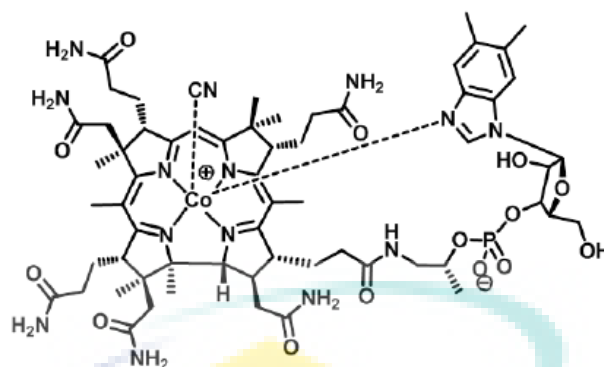


Figure 8: Structure of Vitamin B₁₂

References

1. Braunitzer, G., et al., *The hemoglobins*. Advances in protein chemistry, 1964. **19**: p. 1-71.
2. Huheey, J.E., et al., *Inorganic Chemistry: principles of structure and reactivity*. 2006: Pearson Education India.
3. Lehninger, B., *Kalyani Publishers Delhi*. 1978, India.
4. Milgrom, L.R. and M.J. Warren, *The colours of life: an introduction to the chemistry of porphyrins and related compounds*. 1997.
5. Hughes, M.N., *Inorganic Chemistry of biological processes*. 1981: J. Wiley.
6. Perutz, M., et al., *Stereochemistry of cooperative mechanisms in hemoglobin*. Accounts of Chemical Research, 1987. **20**(9): p. 309-321.
7. Bolton, W. and M. Perutz, Three dimensional Fourier synthesis of horse deoxyhaemoglobin at 2.8 Å resolution. *Nature*, 1970. **228**(5271): p. 551-552.
8. Perutz, M.F., Stereochemistry of Cooperative Effects in Haemoglobin1, in *From theoretical physics to biology*. 1973, Karger Publishers. p. 247-285.
9. Sjöstrand, T., The in vitro formation and disposal of carbon monoxide in blood. *Nature*, 1951. **168**: p. 729-730.
10. Moss, G., *Nomenclature of tetrapyrroles (Recommendations 1986)*. Pure and Applied Chemistry, 1987. **59**(6): p. 779-832.

11. Kayser, H., Die Rolle der Carotinoide und des Gallenfarbstoffs bei der Farbmodifikation der Puppen von *Pieris brassicae*. *Journal of Insect Physiology*, 1974. **20**(1): p. 89-103.
12. Tenhunen, R., et al., Enzymic degradation of heme. Oxygenative cleavage requiring cytochrome P-450. *Biochemistry*, 1972. **11**(9): p. 1716-1720.
13. Willstätter, R. and A. Stoll, *Die wirkungen der chlorophyllase*, in *Untersuchungen ueber chlorophyll*. 1913, Springer. p. 172-187.
14. Fischer, H. and K. Zeile, *Synthese des haematoporphyrins, protoporphyrins und haemins*. *European Journal of Organic Chemistry*, 1929. **468**(1): p. 98-116.
15. Seliger, H.H. and W.D. McElroy, *Light: Physical and biological action*. 2013: Academic Press.
16. Miller, S. and L. Orgel, *The origins of life on earth*. 1974. Prentice-Hall, Englewood Cliffs, New Jersey.
17. Sauer, K., *Photosynthesis-the light reactions*. *Annual Review of Physical Chemistry*, 1979. **30**(1): p. 155-178.
18. Kaim, W., B. Schwederski, and A. Klein, *Bioinorganic Chemistry--Inorganic Elements in the Chemistry of Life: An Introduction and Guide*. 2013: John Wiley & Sons.
19. Smith, E.L., *Principles of biochemistry: general aspects*. Vol. 1. 1983: McGraw-Hill.
20. Ermler, U., et al., Crystal structure of methyl-coenzyme M reductase: the key enzyme of biological methane formation. *Science*, 1997. **278**(5342): p. 1457-1462.
21. Duin, E.C. and M.L. McKee, A new mechanism for methane production from methyl-coenzyme M reductase as derived from density functional calculations. *The Journal of Physical Chemistry B*, 2008. **112**(8): p. 2466-2482.
22. Eschenmoser, A., *Chemistry of corphinoids*. *Annals of the New York Academy of Sciences*, 1986. **471**(1): p. 108-129.
23. Schneider, Z. and A. Stroinski, *Comprehensive B12: chemistry, biochemistry, nutrition, ecology, medicine*. 1987: Walter de Gruyter.
24. Vicente, M.G.H. and K.M. Smith, *Porphyrins and Derivatives Synthetic Strategies and Reactivity Profiles*. *Current Organic Chemistry*, 2000. **4**(2): p. 139-174.

APPENDIX B PORPHYRINS AS PA CONTRAST AGENTS

Table B-1 describes the literature of porphyrins and related macromolecules used as PA contrast agents.

Table B-1 Porphyrin and related macromolecules as PA contrast agents

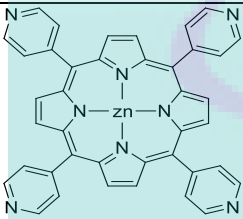
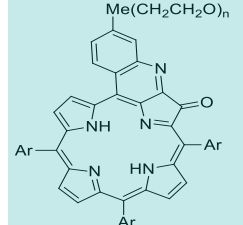
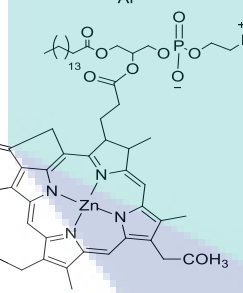

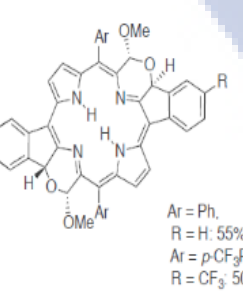
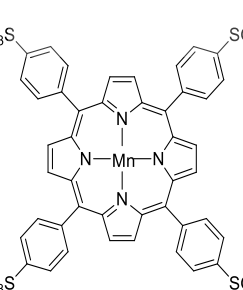
Structure	Porphyrins/applications	Techniques	Published year	Ref
	Hybrid materials of zinc tetra(4-pyridyl)porphyrin shell encapsulated the gold nanorods	Photoacoustic tomography (PAT)	2017	[1]
	Serum-soluble quinoline-annulated porphyrin derivative	Photoacoustic tomography (PAT)	2016	[2]
	Synthetic metallochlorin (reduced porphyrin) in a biocompatible lipid scaffold.	Photoacoustic imaging (PAI)	2016	[3]
	Porphyrin-containing lipid-stabilized perfluorobutane microbubbles	Photoacoustic and ultrasonic imaging	2016	[4]
	Expanded bacteriochlorin analogues (porphyrin related analogues) to morpholinobacteriochlorins	Photoacoustic imaging (PAI)	2016	[5]
	5,10,15,20-Tetrakis(4-sulfonylphenyl)porphyrin manganese(III) acetate (MnTPPS) as a contrast agent binding with serum albumin	Photoacoustic tomography (PAT)	2016	[6]

Table B-1 Continued

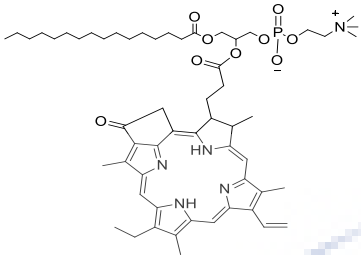
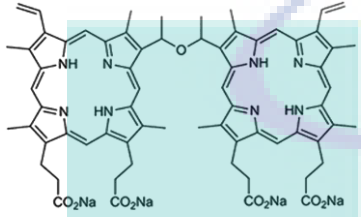
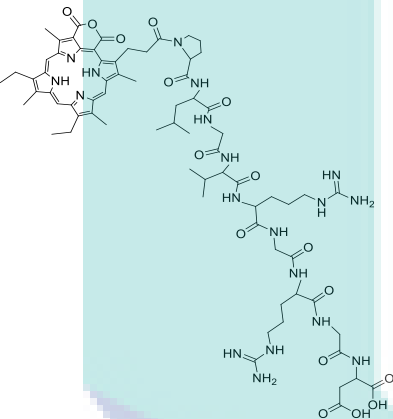
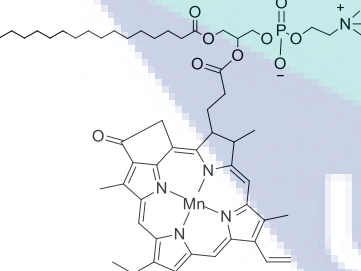
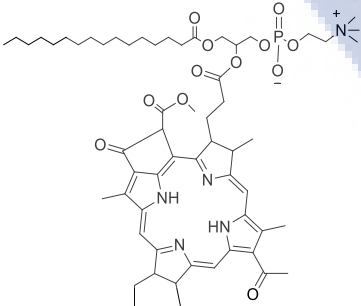

Structure	Porphyrins/applications	Techniques	Published year	Ref
	Phospholipid-porphyrin conjugates micububbles conjugated with Paclitaxel-loaded human serum albumin nanoparticles (PTX-HSA-NPs)	Photoacoustic and ultrasonic imaging (PAI and US)	2015	[7]
	Photo-theranostic platform based on sinoporphyrin sodium photosensitizer-loaded PEGylated graphene oxide (GO-PEG-DVDMS)	Photoacoustic imaging and photodynamic therapy (PAI and PDT)	2015	[8]
	Self-assembled nanofibers of P18-PLGVRGRG, consisting of purpurin 18 (P18), a chlorophyll derivative, Pro-Leu-Gly-Val-Arg-Gly (PLGVRG), and Arg-Gly-Asp (RGD).	Photoacoustic imaging (PAI)	2015	[9]
	Porphyrin-phospholipids coated upconversion nanoparticles (PoP-UCNPs)	Hexamodal imaging (FL, PA, PET, CT, CL, UC imaging)	2015	[10]
	Microbubble of a bacteriochlorophyll-lipid (porphyrin-lipid) around a perfluoropropane gas.	Multimodal imaging (US, PA and and fluorescence imaging)	2015	[11]
	The porphyrinoid analogue cyclo[1]furan[1]pyridine[4]-pyrrole in photoacoustic imaging for detecting an actinide cation	Photoacoustic imaging (PAI)	2015	[12]

Table B-1 Continued

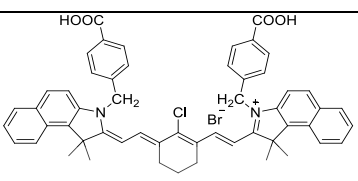
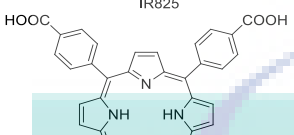
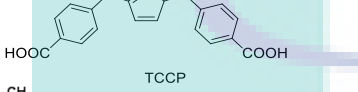
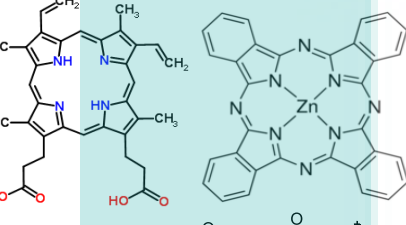
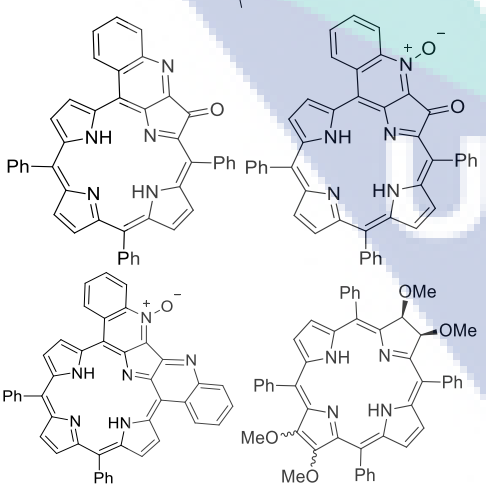
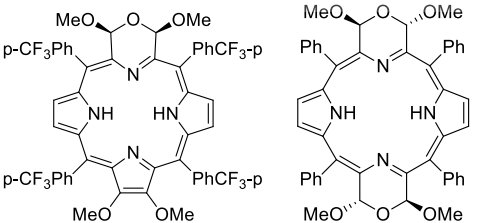
Structure	Porphyrins/applications	Techniques	Published year	Ref
	Tetrakis(4-carboxyphenyl) porphyrin (chelated with Mn^{+2}) cross-linked with P(PEGMA-co-APMA)-b-PMMA diblock copolymer loaded with IR825 multifunctional micelles (IR825@P(PEGMA-co-APMA)-b-PMMA@TCPP/ Mn^{+2})	Multimodal imaging (PA, PD, MR, and fluorescence imaging)	2014	[13]
	Photosensitizers, zinc phthalocyanine and protoporphyrin IX as photoacoustic contrast agents.	Photoacoustic imaging (PAI)	2014	[14]
				
	Microbubble including porphyrin-phospholipids (pyro-lipid) around a fluorinated gas.	Dimodal and trimodal imaging (US, PA and fluorescence imaging)	2014, 2012	[15, 16]
	Free-base tetrapyrrolic chromophores, three quinoline-annulated porphyrins and three morpholinobacteriochlorins as contrast agent for photoacoustic imaging	Photoacoustic imaging (PAI)	2013	[17]
				

Table B-1 Continued

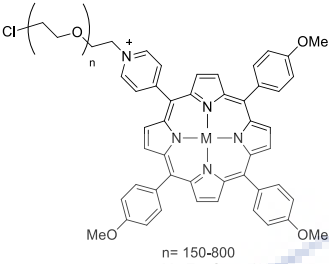
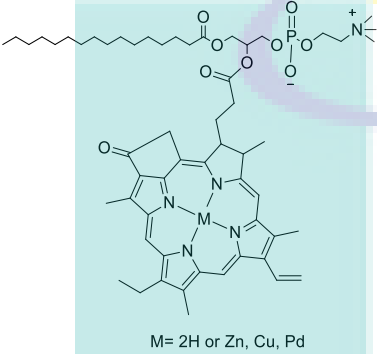
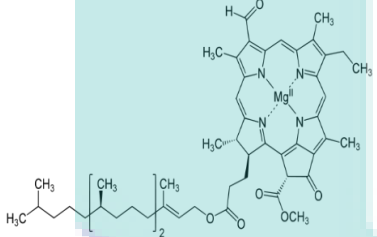
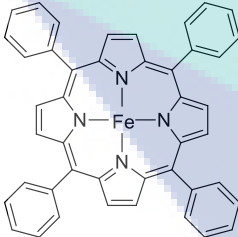
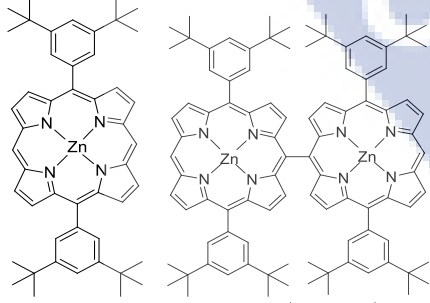
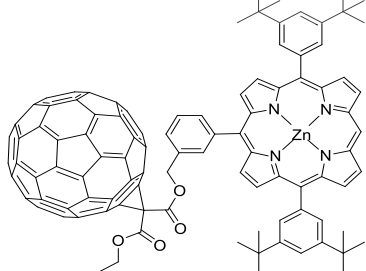
Structure	Porphyrins/applications	Techniques	Published year	Ref
 <p>n= 150-800 M= Zn, Cu or 2H</p>	Molecular aggregates of pyridyl porphyrins (zinc, copper, and free-base) covalently linked to polyethylene glycol (PEG)	Light-induced optoacoustic spectroscopy (LIOAS)	2012	[18]
 <p>M= 2H or Zn, Cu, Pd</p>	Porphysomes (porphyrin-lipid conjugates) consisted of lysophosphatidylcholine, pyropheophorbide, and a chlorophyll-derived porphyrin.	Multimodal imaging and therapeutic applications (PAI and fluorescence imaging)	2011	[19]
	A probe consisting of a derivative of chlorophyll or natural photosynthetic bacteriochlorophyll for photoacoustic imaging	Photoacoustic imaging (PAI)	2010	[20]
	Self-aggregates of metalloporphyrin on the glass substrate	Photoacoustic spectroscopy (PAS)	2007	[21]
	Characterization of fullerene-porphyrin hybrids	Steady-state photoacoustic and time-resolved optoacoustic spectroscopy (LIOAS)	2006	[22]
				

Table B-1 Continued

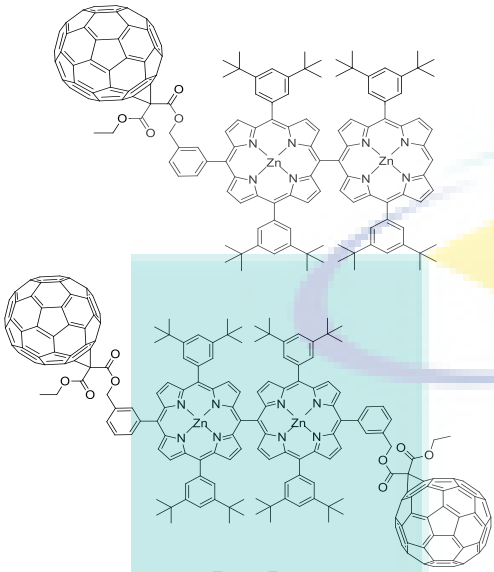
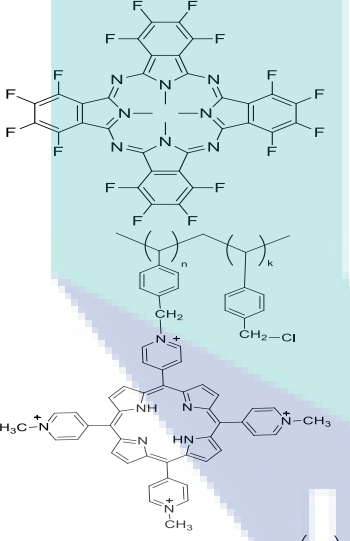
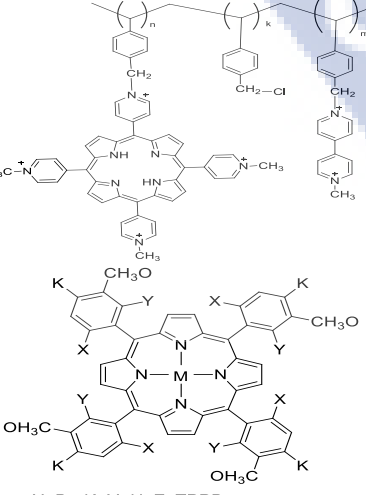
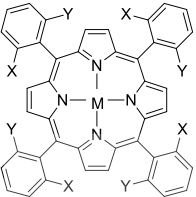
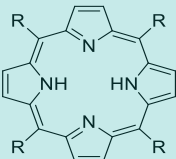
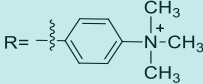
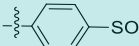
Structure	Porphyrins/applications	Techniques	Published year	Ref
	Characterization of fullerene–porphyrin hybrids	Steady-state photoacoustic and time-resolved optoacoustic spectroscopy	2006	[23]
	Characterization of polymer with tetrapyrrolyl porphyrins (PPor), copolymer with tetrapyrrolyl porphyrins and viologens (PPorV).	Steady-state photoacoustic and time-resolved optoacoustic spectroscopy (LIOAS)	2003	[24]
 <p>X=Br, K=Y=H, ZnTPPBr₄ X=K=Br, Y=H, ZnTPPBr₄(Br)₄ X=K=Y=Br, ZnTPPBr₆(Br)₄</p>	Characterization of polyhalogenated and metallated tetrakisphenylporphyrins	Photoacoustic calorimetry (PAC)	2002	[25]

Table B-1 Continued

Structure	Porphyrins/applications	Techniques	Published year	Ref
 <p> X=Y=H, M=2H, H₂TPP X=Y=H, M=Mg, MgTPP X=Y=H, M=Zn, ZnTPP X=Y=H, M=Cd, CdTPP X=Y=F, M=2H, H₂TPPF₈ X=H, Y=Cl, M=2H, H₂TPPCl₄ X=Y=Cl, M=2H, H₂TPPCl₆ X=Y=F, M=Zn, ZnTPPF₈ X=Y=Cl, M=Zn, ZnTPPCl₆ </p>  <p> R =  or  </p>	Aggregates of positively charged tetrakis(N,N,N-trimethylammonium-4-yl)porphyrin and negatively charged tetrakis(4-sulfonatophenyl)porphyrin	Photoacoustic spectroscopy (PAS).	2002	[26]

References

- Gao, F., et al., Rationally encapsulated gold nanorods improving both linear and nonlinear photoacoustic imaging contrast in vivo. *Nanoscale*, 2017. **9**(1): p. 79-86.
- Luciano, M., et al., In vivo photoacoustic tumor tomography using a quinoline-annulated porphyrin as NIR molecular contrast agent. *Organic & Biomolecular Chemistry*, 2016. **15**(4): p. 972-983.
- Ng, K.K., et al., Chlorosome-Inspired Synthesis of Templated Metallochlorin-Lipid Nanoassemblies for Biomedical Applications. *ACS Nano*, 2016. **10**(4): p. 4092-4101.
- Paproski, R.J., et al., Porphyrin Nanodroplets: Sub-micrometer Ultrasound and Photoacoustic Contrast Imaging Agents. *Small*, 2016. **12**(3): p. 371-380.
- Guberman-Pfeffer, M.J., et al., Bacteriochlorins with a Twist: Discovery of a Unique Mechanism to Red-Shift the Optical Spectra of Bacteriochlorins. *Journal of American Chemical Society*, 2017. **139**(1): p. 548-560.
- Chaves, O.A., et al., *In situ ultra-fast heat deposition does not perturb the structure of serum albumin*. *Photochemical & Photobiological Sciences*, 2016. **15**(12): p. 1524-1535.

7. Moon, H., et al., Multifunctional theranostic contrast agent for photoacoustics- and ultrasound-based tumor diagnosis and ultrasound-stimulated local tumor therapy. *Journal of Controlled Release*, 2015. **218**: p. 63-71.
8. Yan, X., et al., Optical and photoacoustic dual-modality imaging guided synergistic photodynamic/photothermal therapies. *Nanoscale*, 2015. **7**(6): p. 2520-2526.
9. Zhang, D., et al., In Situ Formation of Nanofibers from Purpurin18-Peptide Conjugates and the Assembly Induced Retention Effect in Tumor Sites. *Advanced Materials*, 2015. **27**(40): p. 6125-6130.
10. Rieffel, J., et al., Hexamodal Imaging with Porphyrin-Phospholipid-Coated Upconversion Nanoparticles. *Advanced Materials*, 2015. **27**(10): p. 1785-1790.
11. Huynh, E., et al., In situ conversion of porphyrin microbubbles to nanoparticles for multimodality imaging. *Nature Nanotechnology*, 2015. **10**(4): p. 325-332.
12. Ho, I.-T., et al., Parts per billion detection of uranium with a porphyrinoid-containing nanoparticle and in vivo photoacoustic imaging. *Analyst*, 2015. **140**(11): p. 3731-3737.
13. Liu, X., et al., Photosensitizer cross-linked nano-micelle platform for multimodal imaging guided synergistic photothermal/photodynamic therapy. *Nanoscale*, 2016. **8**(33): p. 15323-15339.
14. Ho, C.J.H., et al., Multifunctional photosensitizer-based contrast agents for photoacoustic imaging. *Scientific reports*, 2014. **4**.
15. Huynh, E., et al., Aggregate enhanced trimodal porphyrin shell microbubbles for ultrasound, photoacoustic, and fluorescence imaging. *Bioconjugate Chemistry*, 2014. **25**(4): p. 796-801.
16. Huynh, E., et al., *Porphyrin shell microbubbles with intrinsic ultrasound and photoacoustic properties*. *Journal of the American Chemical Society*, 2012. **134**(40): p. 16464-16467.
17. Abuteen, A., et al., The evaluation of NIR-absorbing porphyrin derivatives as contrast agents in photoacoustic imaging. *Physical Chemistry Chemical Physics*, 2013. **15**(42): p. 18502-18509.
18. Wróbel, D., A. Biadasz, and B. Bursa, *Triplet Thermal Relaxation Study as a Probe of Weak Interdimers of Porphyrin Derivatives*. *International Journal of Thermophysics*, 2012. **33**(4): p. 716-732.

19. Lovell, J.F., et al., Porphysome nanovesicles generated by porphyrin bilayers for use as multimodal biophotonic contrast agents. *Nature Materials*, 2011. **10**(4): p. 324.
20. Green, A.H., et al., *In vitro testing of a protease-sensitive contrast agent for optoacoustic imaging*. *Journal of Biomedical Optics*, 2010. **15**(2): p. 021315-021315-8.
21. Sathiyamoorthy, K. and C. Vijayan, Photoacoustic investigations on self-organization effects in metalloporphyrins on glass substrates. *Materials Letters*, 2007. **61**(19): p. 4156-4159.
22. Wróbel, D. and A. Graja, Modification of electronic structure in supramolecular fullerene-porphyrin systems studied by fluorescence, photoacoustic and photothermal spectroscopy. *Journal of Photochemistry and Photobiology A: Chemistry*, 2006. **183**(1): p. 79-88.
23. Wróbel, D. and A. Dudkowiak, *Porphyrins and phthalocyanines-functional molecular materials for optoelectronics and medicine*. *Molecular Crystals and Liquid Crystals*, 2006. **448**(1): p. 15/[617]-38/[640].
24. Bartczak, A., et al., *The interactions between tetrapyrrolyl porphyrin and viologen units covalently linked to polymers*. *Journal of Photochemistry and Photobiology A: Chemistry*, 2003. **159**(3): p. 259-272.
25. Azenha, E.I.G., et al., *Heavy-atom effects on metalloporphyrins and polyhalogenated porphyrins*. *Chemical Physics*, 2002. **280**(1): p. 177-190.
26. Hanyż, I. and D. Wróbel, The influence of pH on charged porphyrins studied by fluorescence and photoacoustic spectroscopy. *Photochemical & Photobiological Sciences*, 2002. **1**(2): p. 126-132.

APPENDIX C SCREEN SHORT OF OPTIMIZATION OF PORPHYRINS

Gaussian 09 Revision-B.01-SMP

File Process Utilities View Help

Existing File Job Edit

File Edit Check-Route Set-Start

C:\Users\Amina Yaseen\Desktop\comp 4 opt.gjf

Additional Steps 0

% Section %chk=C:\Users\Amina Yaseen\Desktop\comp 4 opt.chk
%mem=16GB

Route Section #p opt b3lyp/lanl2dz
scrf=(iefpcm,solvent=methanol) geom=connectivity

Title Section optimization comp 4

Charge , Multipl. 0 1

Molecule Specification			
C	-2.69320200	0.82622900	-0.47141200
C	-3.33777900	2.11771600	-0.36337000
C	-2.38699100	3.00783200	0.05476700
C	-1.14678700	2.27487000	0.20650200
N	-1.36040000	0.93836800	-0.12295100
H	-4.37650000	2.31049800	-0.58164900
H	-2.50771000	4.06334300	0.24039100

Gaussian 09 Revision-B.01-SMP

File Process Utilities View Help

Batch Data: Processing:

Active Job: C:\USERS\AMINA YASEEN\DESKTOP\COMP 4 OPT.LOG Output File: COMP 4 OPT.LOG

Run Progress: C:\G09W\1401.exe is processing...

```

GePol: Cavity volume = 2004.542 Ang**3
Leave Link 301 at Thu Jan 18 02:03:56 2018, MaxMem= 33554432 cpu:
(Enter C:\G09W\1302.exe)
NPDdir=0 NMcPBC= 1 NCell= 1 NCell= 1 NCell= 1 NCell= 1 NCell= 1
NCell= 1 NCell= 1 NCell= 1 NCell= 1 NCell= 1 NCell= 1
NCell= 1 NCell= 1 NCell= 1 NCell= 1 NCell= 1 NCell= 1
One-electron integrals computed using PRISM.
1 Symmetry operations used in ECPInt.
ECPInt: NShT= 248160 NPtT= 1839631 LenC2= 117352 LenP2D= 368915.
LDataN: DoStor=T MaxTD1= 5 Len= 102
NBasis= 1124 RedA0= T NBF= 1124
NBsUse= 1124 1.00D-06 NBFU= 1124
Precomputing XC quadrature grid using
IKGrd= 2 IRadAn= 0 IRanWt= -1 IRanGd= 0 Acc:
NRdTot= 13039 NPtTot= 1677936 NUUsed= 1738595 NTot= 1738611
NSgBfM= 838 845 848 848 848 NatAll= 197 175.
Leave Link 302 at Thu Jan 18 02:04:59 2018, MaxMem= 33554432 cpu:
(Enter C:\G09W\1303.exe)
DipDrv: MaxL=1.
Leave Link 303 at Thu Jan 18 02:05:02 2018, MaxMem= 33554432 cpu:

```

Performing the Initial MO Guess

APPENDIX D MOLECULAR STRUCTURES AND NOMENCLATURES OF DESIGNED PORPHYRINS

Porphine (parent porphine) is the preliminary porphyrins core to study several porphyrins molecules. To compute the effect of substituent in optoelectronic properties, various substituents at meso-position are added. The studied porphyrins are classified into two different sets. In set one, the effect of substituents on optoelectronic properties at mono, di, and tetra meso- positions are investigated separately, starting from the basic core (Table C-1). Whereas, in set two, tetra meso-substituted Zn(II) porphyrins are studied to compare their properties (Table C-2). Labeling of the designed porphyrin structures are shown in tables along with their IUPAC naming.

Table C-1 Porphine, Zn(II)porphyrin, mono, di and tetra substituted porphyrins (Set One)

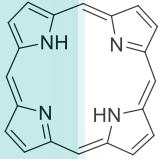
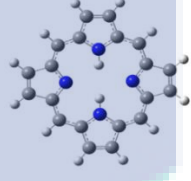
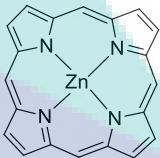
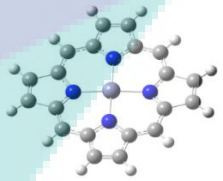
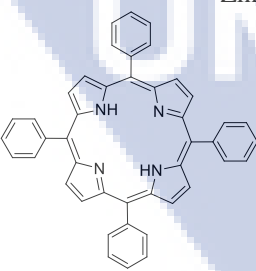
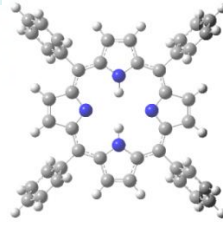
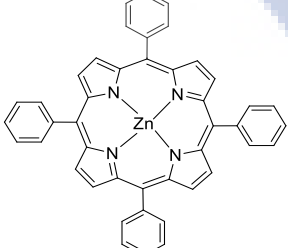
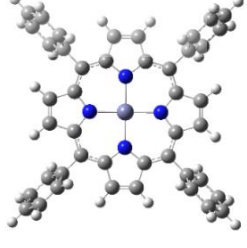
Name	Studied Porphyrins Molecules	
	ChemDraw Sketch	Optimized Structures developed by Gaussview
Porphine		
ZnP		
P-1		
ZnP-1		

Table C-1 Continued

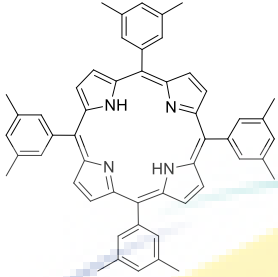
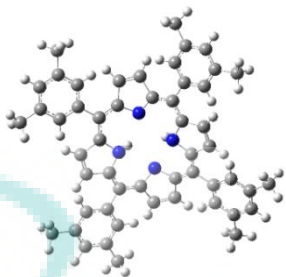
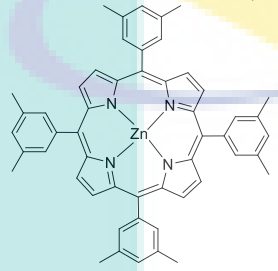
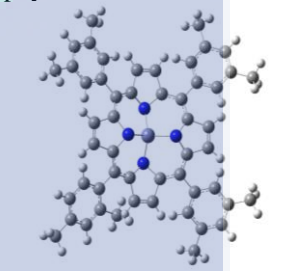
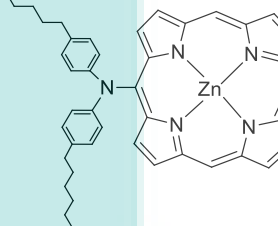
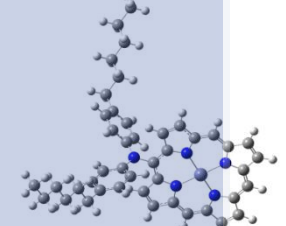
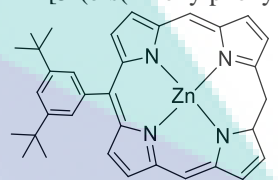
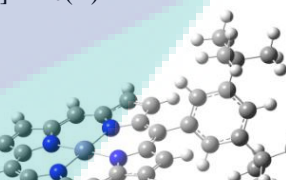
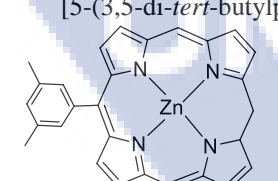
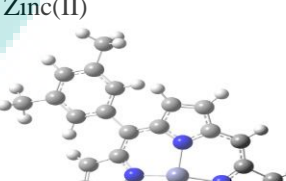
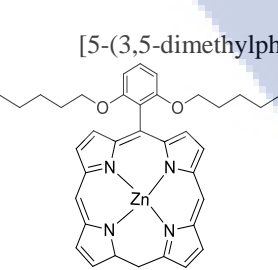
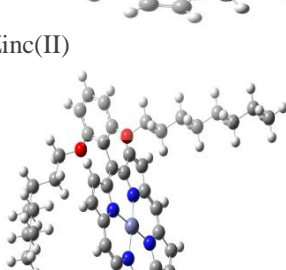
Name	Studied Porphyrins Molecules	
	ChemDraw Sketch	Optimized Structures developed by Gaussview
P-2		
ZnP-2		
ZnP(hpa)		
ZnP(tbp)		
ZnP(dmp)		
ZnP(ohp)		

Table C-1 Continued

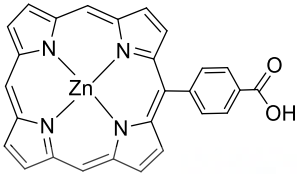

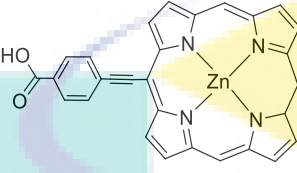
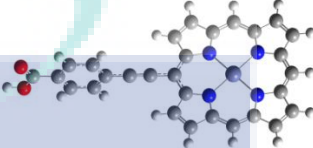
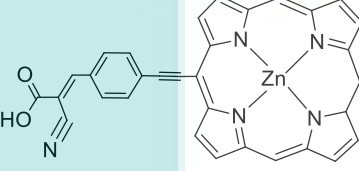
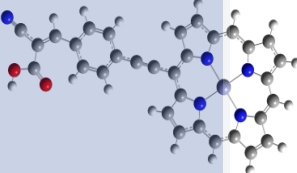
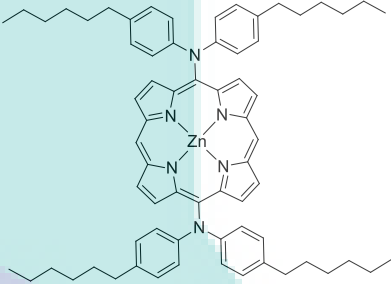
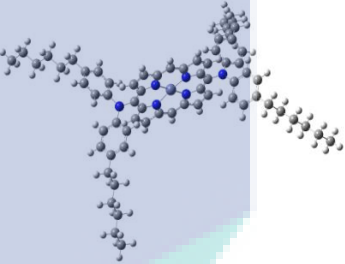
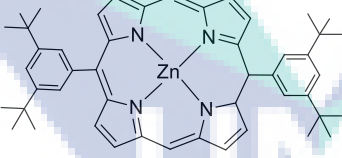
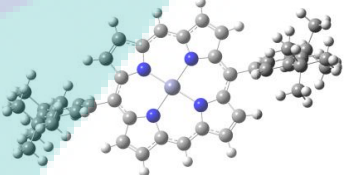
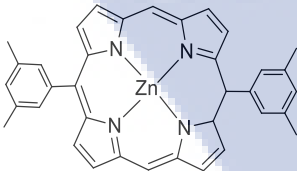
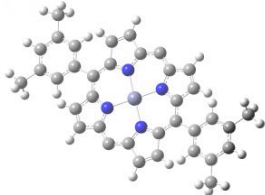
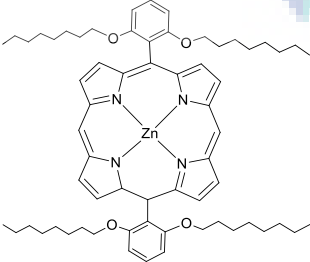
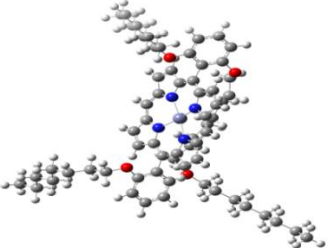
Name	Studied Porphyrins Molecules	
	ChemDraw Sketch	Optimized Structures developed by Gaussview
ZnP(cp)		
	[5-(4-carboxyphenyl)porphyrinato] Zinc(II)	
ZnP(cpe)		
	[5-(4-carboxyphenyl ethynyl)porphyrinato] Zinc(II)	
ZnP(ccpe)		
	[5-(4-(2-cyanopropenoic acid) phenyl)ethynyl)porphyrinato] Zinc(II)	
ZnP(2hpa)		
	[5,15-di(bis(4-hexylphenyl)amino)porphyrinato] Zinc(II)	
ZnP(2tbp)		
	[5,15-bis(3,5-di-tert-butylphenyl)porphyrinato] Zinc(II)	
ZnP(2dmp)		
	[5,15-bis(3,5-dimethylphenyl)porphyrinato] Zinc(II)	
ZnP(2ohp)		
	[5,15-bis(2,6-dioctoxyphenyl)porphyrinato] Zinc(II)	

Table C-1 Continued

Name	Studied Porphyrins Molecules	
	ChemDraw Sketch	Optimized Structures developed by Gaussview
ZnP(dmp&hpa)		
ZnP(2cp)		
ZnP(2cpe)		
ZnP(2ccpe)		
ZnP(cpe&ccpe)		
ZnP(hpa&cpe)		
ZnP(dmp&cp)		

Table C-1 Continued

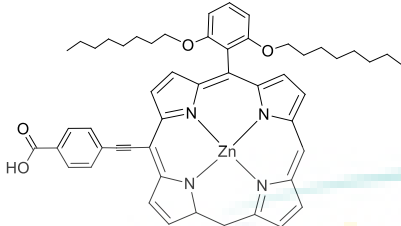
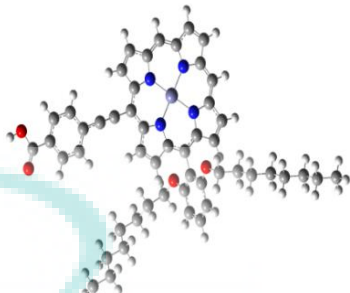
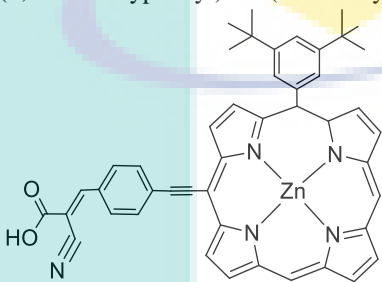
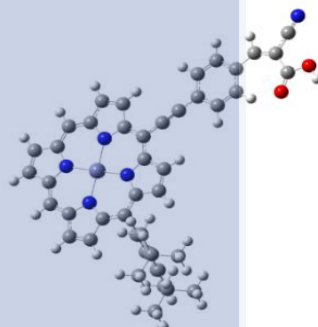
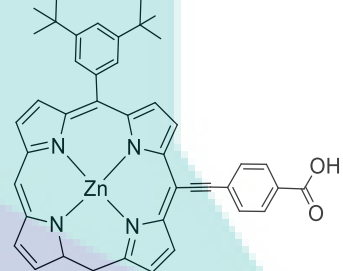
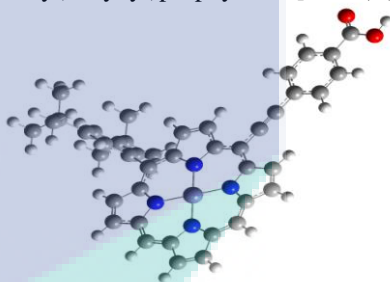
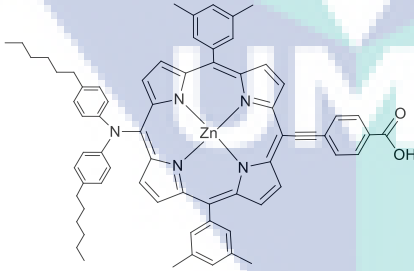
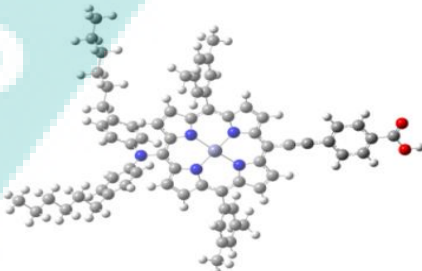
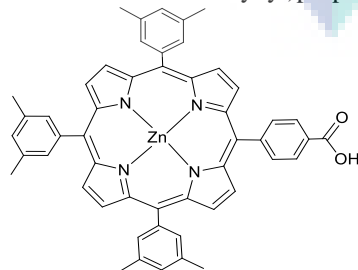
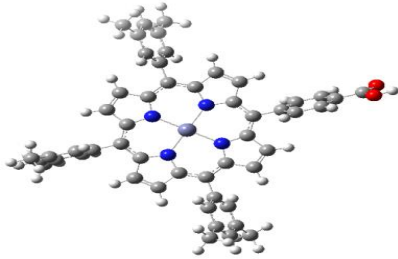
Name	ChemDraw Sketch	Optimized Structures developed by Gaussview
ZnP(ohp&cpe)		
ZnP(tbp&ccpe)		
ZnP(tbp&cpe)		
ZnP(1)		
ZnP(2)		

Table C-1 Continued

Studied Porphyrins Molecules		
Name	ChemDraw Sketch	Optimized Structures developed by Gaussview
ZnP(3)		
	[5,15-di(3,5- <i>tert</i> -butylphenyl)-10-(4-carboxyphenylethynyl)-20-(4-(2-cyanopropenoic acid) phenyl)ethynyl porphyrinato]Zn(II)	
ZnP(4)		
P-4	[5,10,15,20-tetra(4-carboxyphenylethynyl)porphyrinato]Zn(II)	
	5,10,15,20-tetra(4-carboxyphenylethynyl)porphyrin	

Table C-2 Meso-tetra substituted Zn(II)porphyrins (Set Two)

Studied Porphyrins Molecules		
Name	ChemDraw Sketch	Optimized Structures developed by Gaussview
A ₂ B ₂ (1)		
	[5,15-bis(4-carboxylphenyl)-10,20-bis(4-(2-cyanopropenoic acid)phenyl)ethynyl]porphyrinato] Zn(II).	

Table C-2 Continued

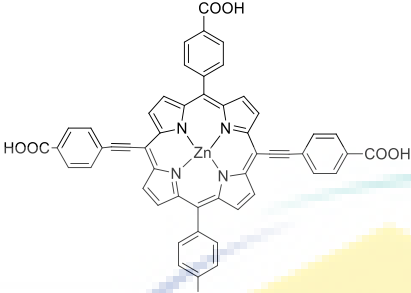
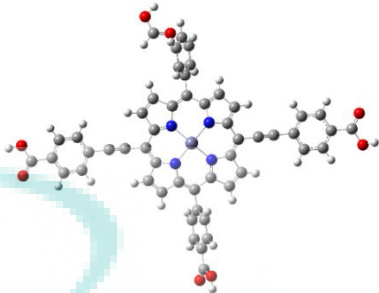
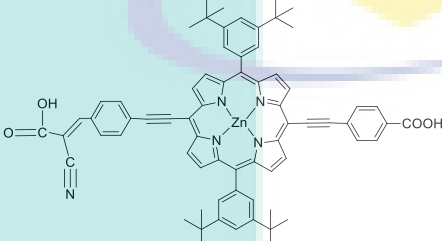
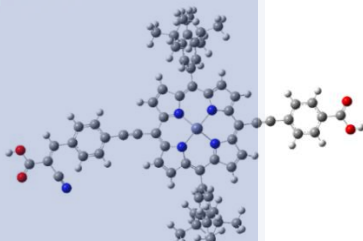
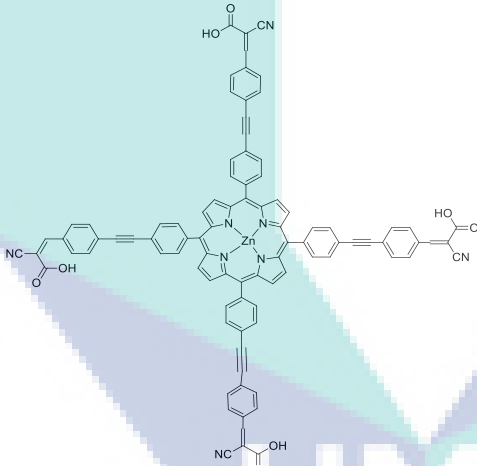
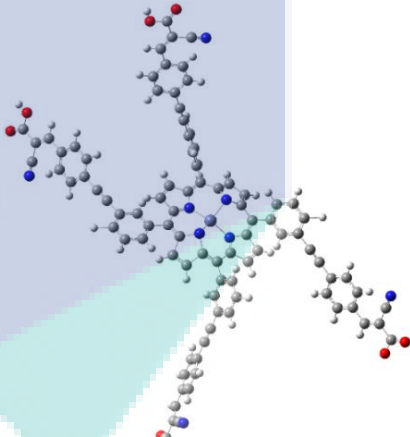
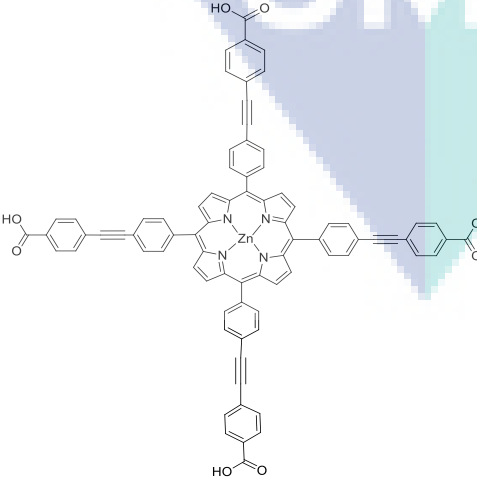
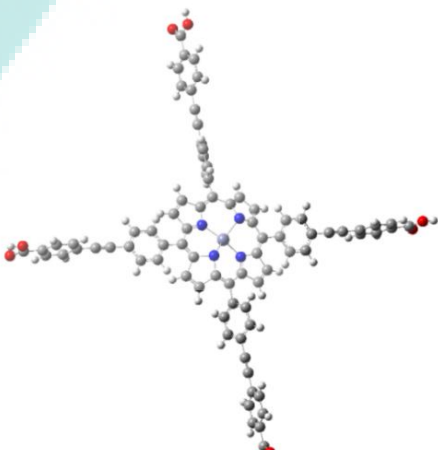
Name	ChemDraw Sketch	Studied Porphyrins Molecules	Optimized Structures developed by Gaussview
A ₂ B ₂ (2)			
A ₂ B ₂ (3)			
A ₄ (1)			
A ₄ (2)			

Table C-2 Continued

Name	ChemDraw Sketch	Optimized Structures developed by Gaussview
A ₄ (3)		
A ₂ B ₂ (4)		
A ₂ B ₂ (5)		
A ₂ B ₂ (6)		
A ₂ B ₂ (7)		

Table C-2 Continued

Name	ChemDraw Sketch	Optimized Structures developed by Gaussview
A ₂ B ₂ (8)		
A ₂ B ₂ (9)		
A ₂ B ₂ (10)		
A ₂ B ₂ (11)		
A ₂ B ₂ (12)		

Table C-2 Continued

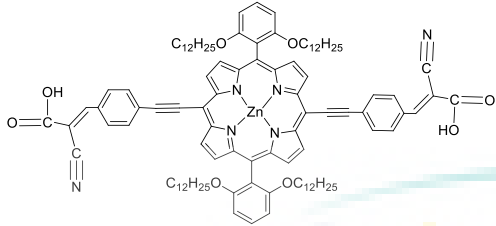
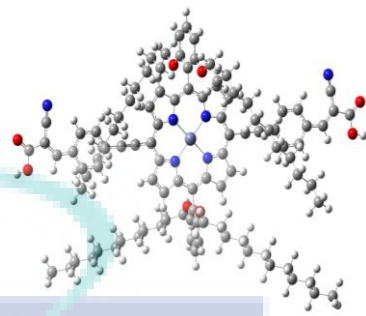
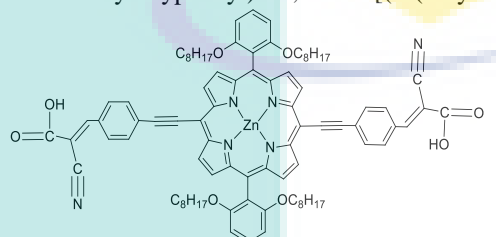
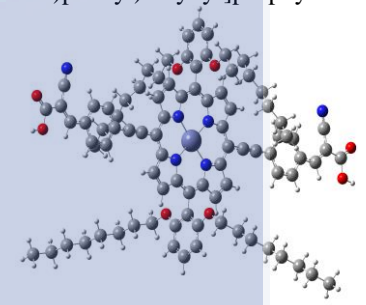
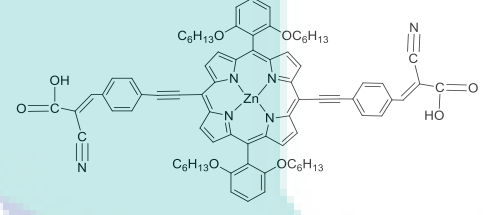
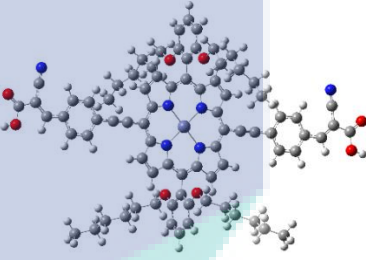
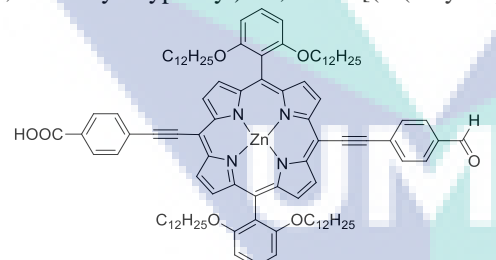
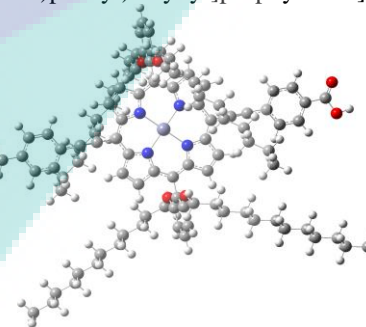
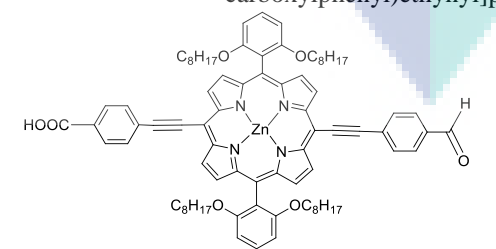
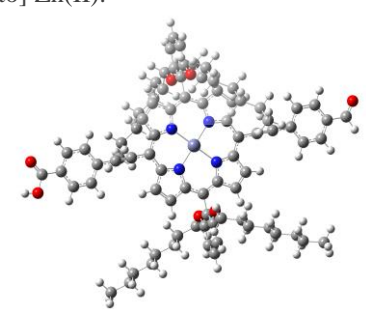
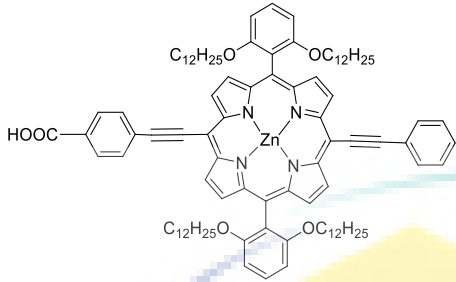
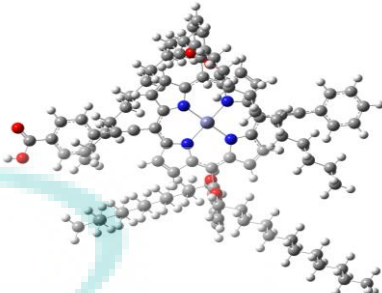
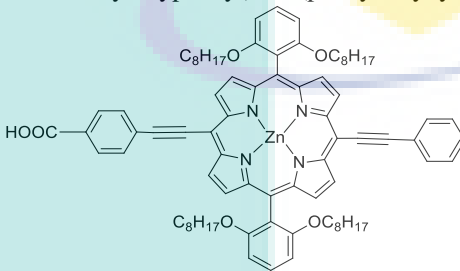
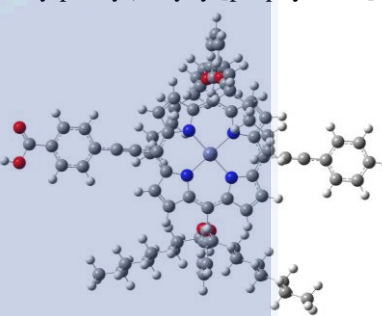
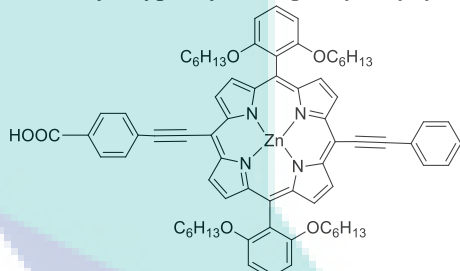
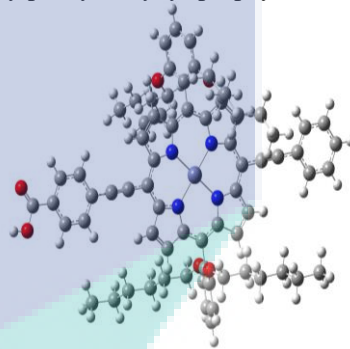
Studied Porphyrins Molecules		
Name	ChemDraw Sketch	Optimized Structures developed by Gaussview
A ₂ B ₂ (13)		
[5,15-bis(3,5-di-dodecyloxyphenyl)-10,20-bis-[(4-(2-cyanopropenoic acid)phenyl)ethynyl]porphyrinato] Zn(II). A ₂ B ₂ (14)		
[5,15-bis(3,5-di-octyloxyphenyl)-10,20-bis-[(4-(2-cyanopropenoic acid)phenyl)ethynyl]porphyrinato] Zn(II). A ₂ B ₂ (15)		
[5,15-bis(3,5-di-hexyloxyphenyl)-10,20-bis-[(4-(2-cyanopropenoic acid)phenyl)ethynyl]porphyrinato] Zn(II). A ₂ B ₂ (16)		
[5,15-bis(3,5-di-dodecyloxyphenyl)-10-[(4-formylphenyl)ethynyl]-20-[(4-carboxylphenyl)ethynyl]porphyrinato] Zn(II). A ₂ B ₂ (17)		
[5,15-bis(3,5-di-octyloxyphenyl)-10-[(4-formylphenyl)ethynyl]-20-[(4-carboxylphenyl)ethynyl]porphyrinato] Zn(II).		

Table C-2 Continued

Name	ChemDraw Sketch	Optimized Structures developed by Gaussview
A ₂ B ₂ (18)	<p>Chemical structure of Zn(II) porphyrin with substituents: 3,5-di-hexyloxyphenyl (C₆H₁₃O), 4-formylphenyl (H), and 4-carboxylphenyl (HOOC).</p>	
[5,15-bis(3,5-di-hexyloxyphenyl)-10-[(4-formylphenyl)ethynyl]-20-[(4-carboxylphenyl)ethynyl]porphyrinato] Zn(II).		
A ₂ B ₂ (19)	<p>Chemical structure of Zn(II) porphyrin with substituents: 3,5-di-dodecyloxyphenyl (C₁₂H₂₅O), 4-hydroxyphenyl (OH), and 4-carboxylphenyl (HOOC).</p>	
[5,15-bis(3,5-di-dodecyloxyphenyl)-10-[(4-hydroxyphenyl)ethynyl]-20-[(4-carboxylphenyl)ethynyl]porphyrinato] Zn(II).		
A ₂ B ₂ (20)	<p>Chemical structure of Zn(II) porphyrin with substituents: 3,5-di-octyloxyphenyl (C₈H₁₇O), 4-hydroxyphenyl (OH), and 4-carboxylphenyl (HOOC).</p>	
[5,15-bis(3,5-di-octyloxyphenyl)-10-[(4-hydroxyphenyl)ethynyl]-20-[(4-carboxylphenyl)ethynyl]porphyrinato] Zn(II).		
A ₂ B ₂ (21)	<p>Chemical structure of Zn(II) porphyrin with substituents: 3,5-di-hexyloxyphenyl (C₆H₁₃O), 4-hydroxyphenyl (OH), and 4-carboxylphenyl (HOOC).</p>	
[5,15-bis(3,5-di-hexyloxyphenyl)-10-[(4-hydroxyphenyl)ethynyl]-20-[(4-carboxylphenyl)ethynyl]porphyrinato] Zn(II).		

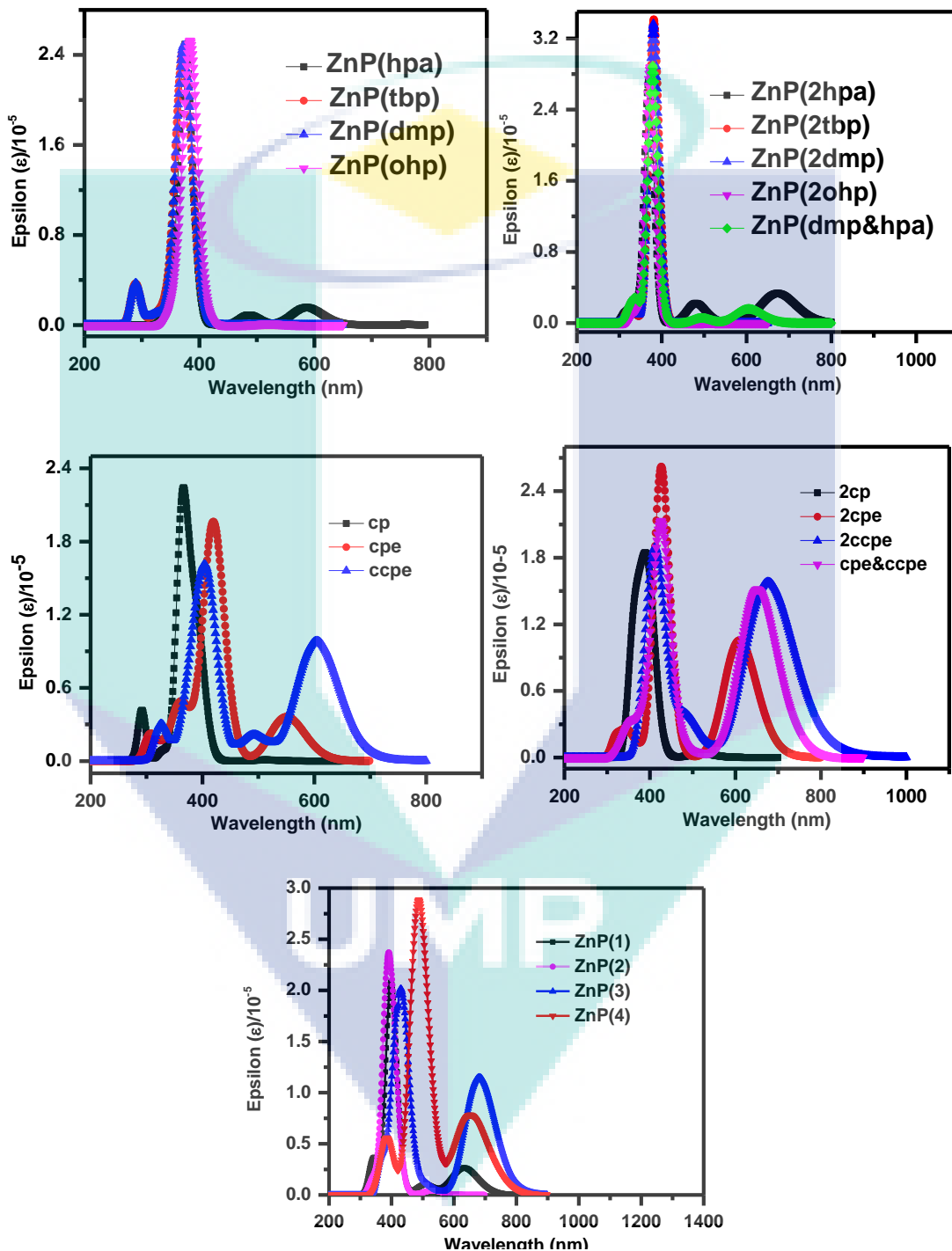
Table C-2 Continued

Name	Studied Porphyrins Molecules	
	ChemDraw Sketch	Optimized Structures developed by Gaussview
A ₂ B ₂ (22)		
[5,15-bis(3,5-di-dodecyloxyphenyl)-10-(phenylethynyl)-20-[(4-carboxylphenyl)ethynyl]porphyrinato] Zn(II). A ₂ B ₂ (23)		
[5,15-bis(3,5-di-octyloxyphenyl)-10-(phenylethynyl)-20-[(4-carboxylphenyl)ethynyl]porphyrinato] Zn(II). A ₂ B ₂ (24)		
[5,15-bis(3,5-di-hexyloxyphenyl)-10-(phenylethynyl)-20-[(4-carboxylphenyl)ethynyl]porphyrinato] Zn(II).		

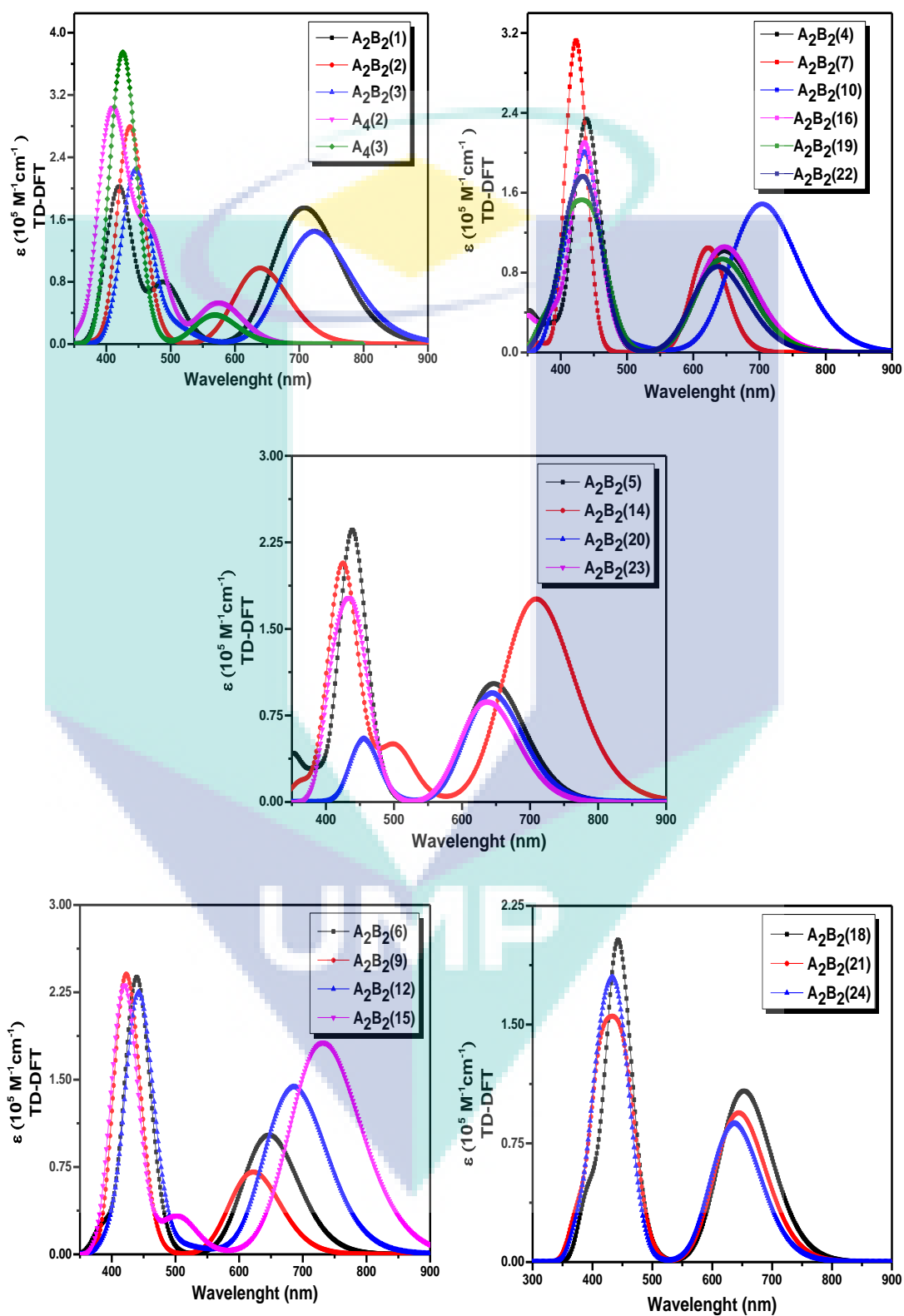
UMP

APPENDIX E UV-VIS SPECTRA OF ALL DESIGNED PORPHYRINS

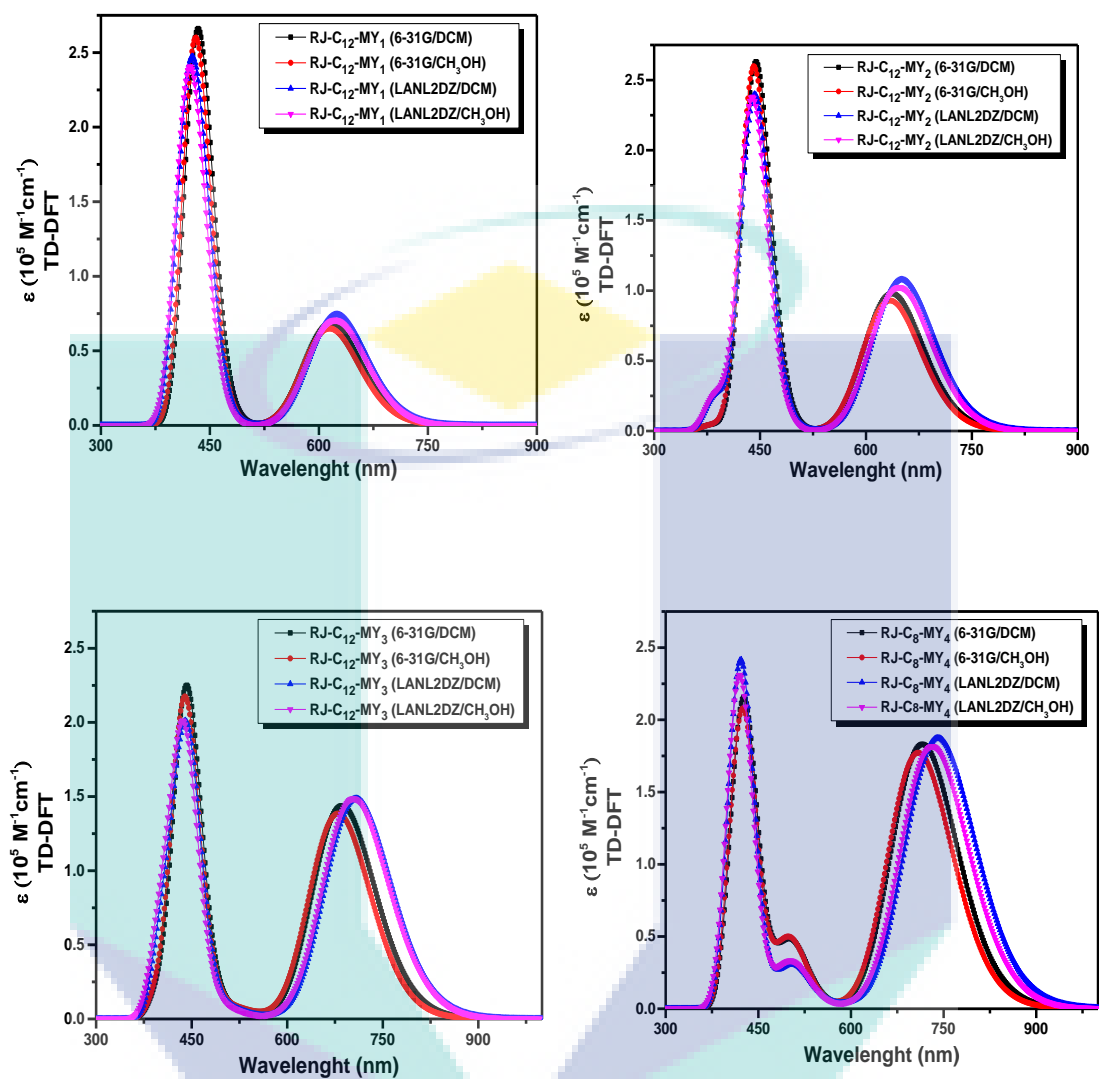
Set One: Absorption spectra of mono, di and tetra substituted porphyrins



Set Two: Absorption spectra of meso-tetra substituted Zn(II)porphyrins



Effect of solvent on absorption spectra of RJ-C_n-MY_m series of complexes



APPENDIX F NMR OF THE SYNTHESIZED PORPHYRINS

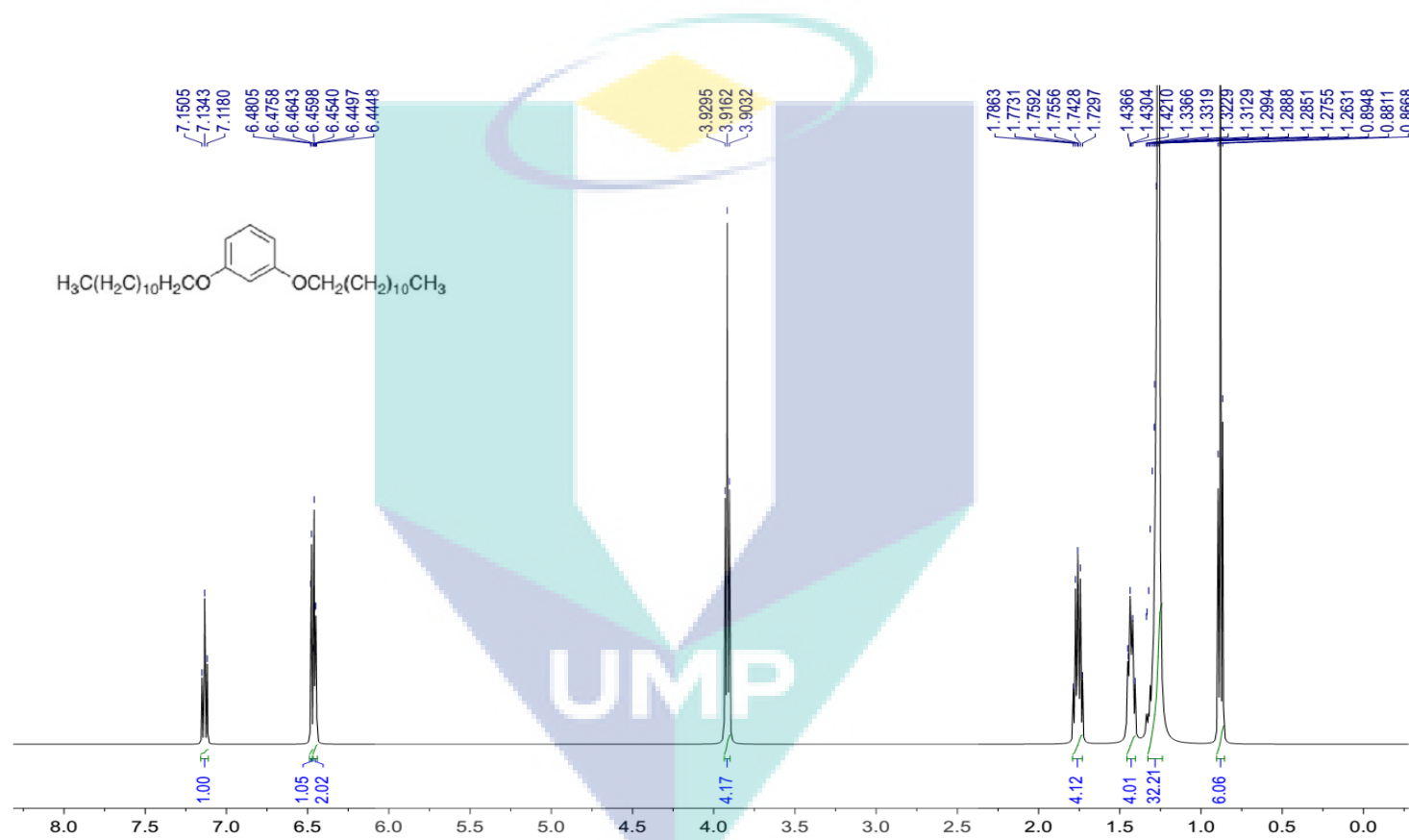


Figure S1 ¹H NMR of 1,3-di(dodecyloxy)benzene (5) in CDCl₃

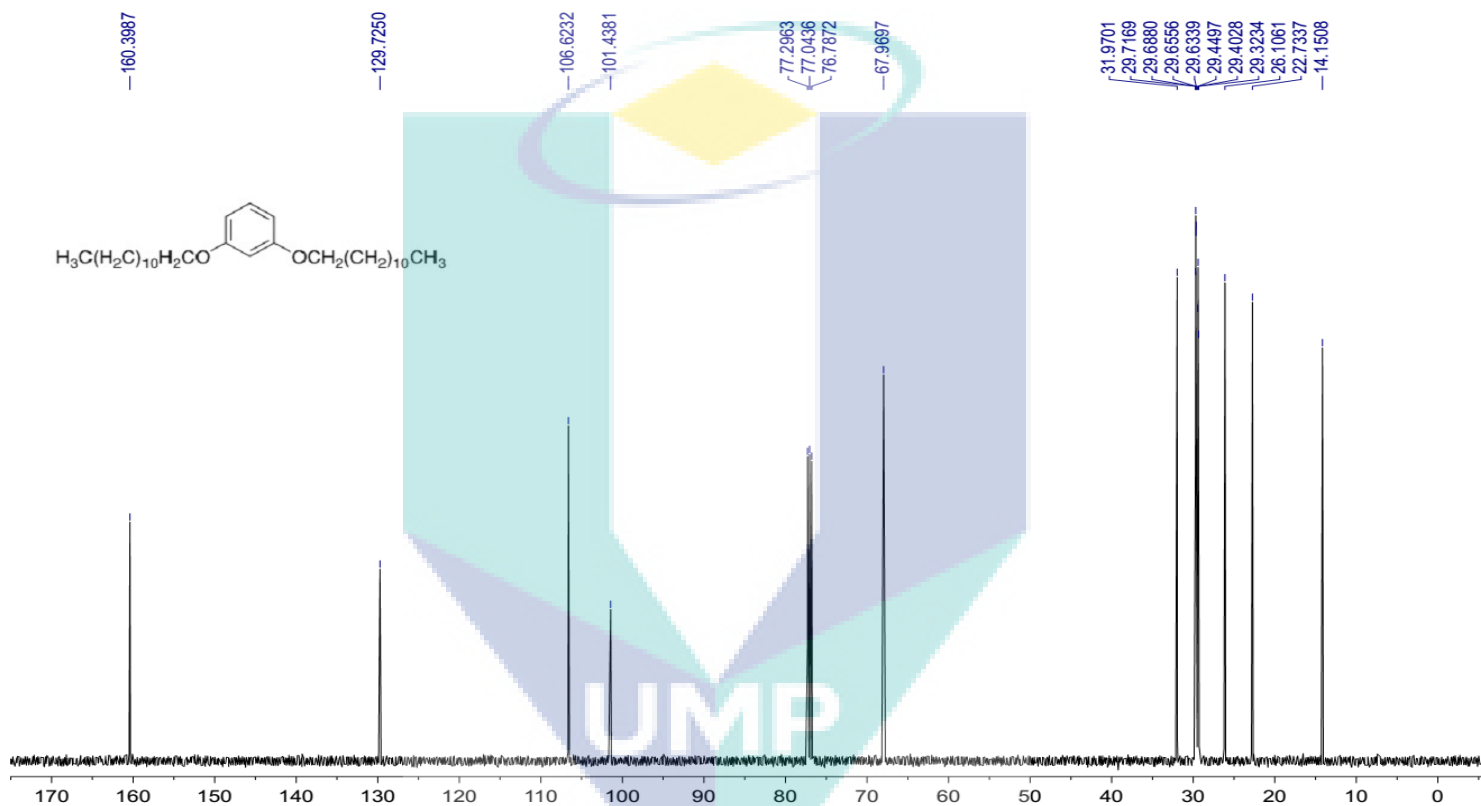


Figure S2 ^{13}C NMR of 1,3-di(dodecyloxy)benzene (5) in CDCl_3

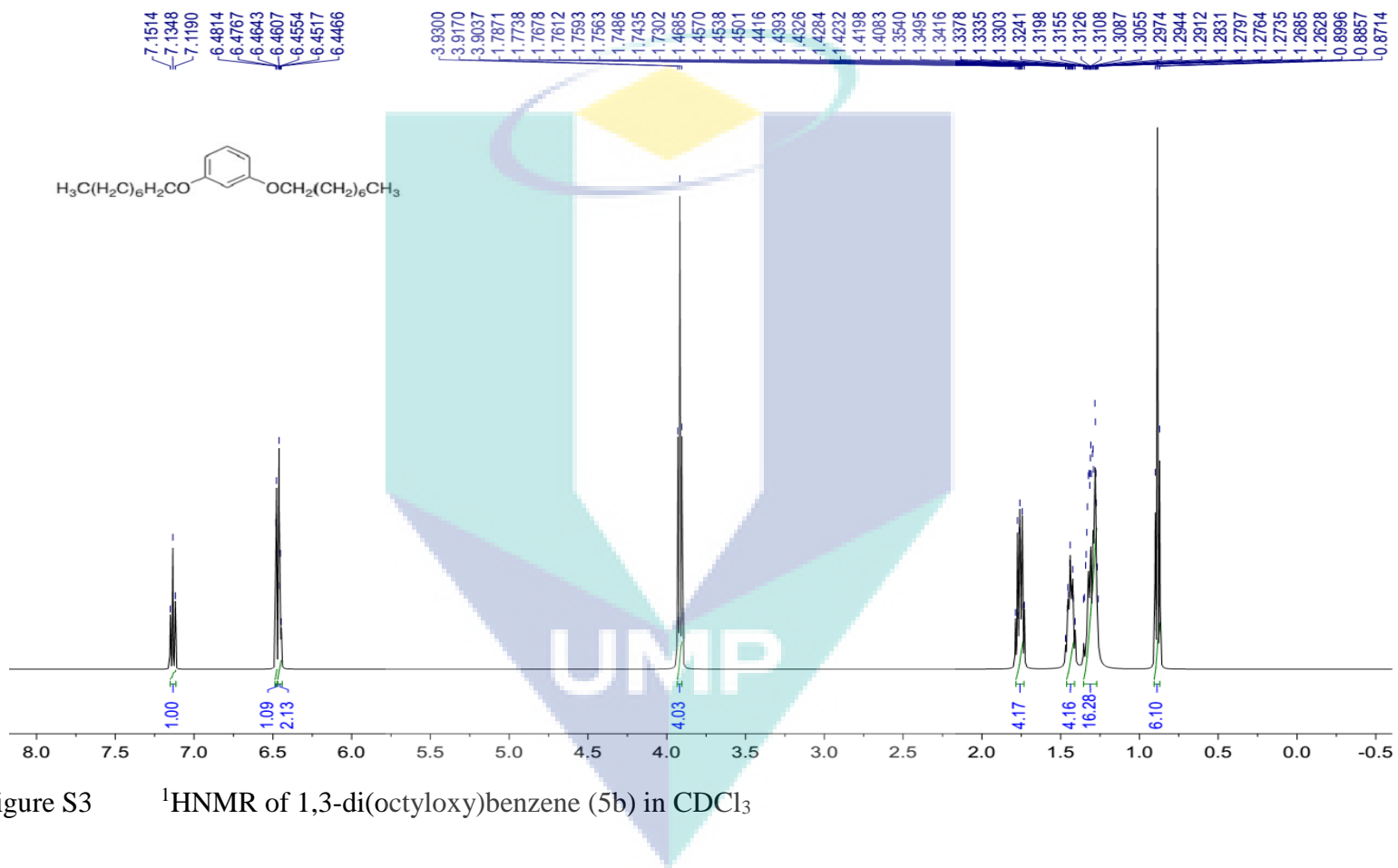


Figure S3 ^1H NMR of 1,3-di(octyloxy)benzene (5b) in CDCl_3

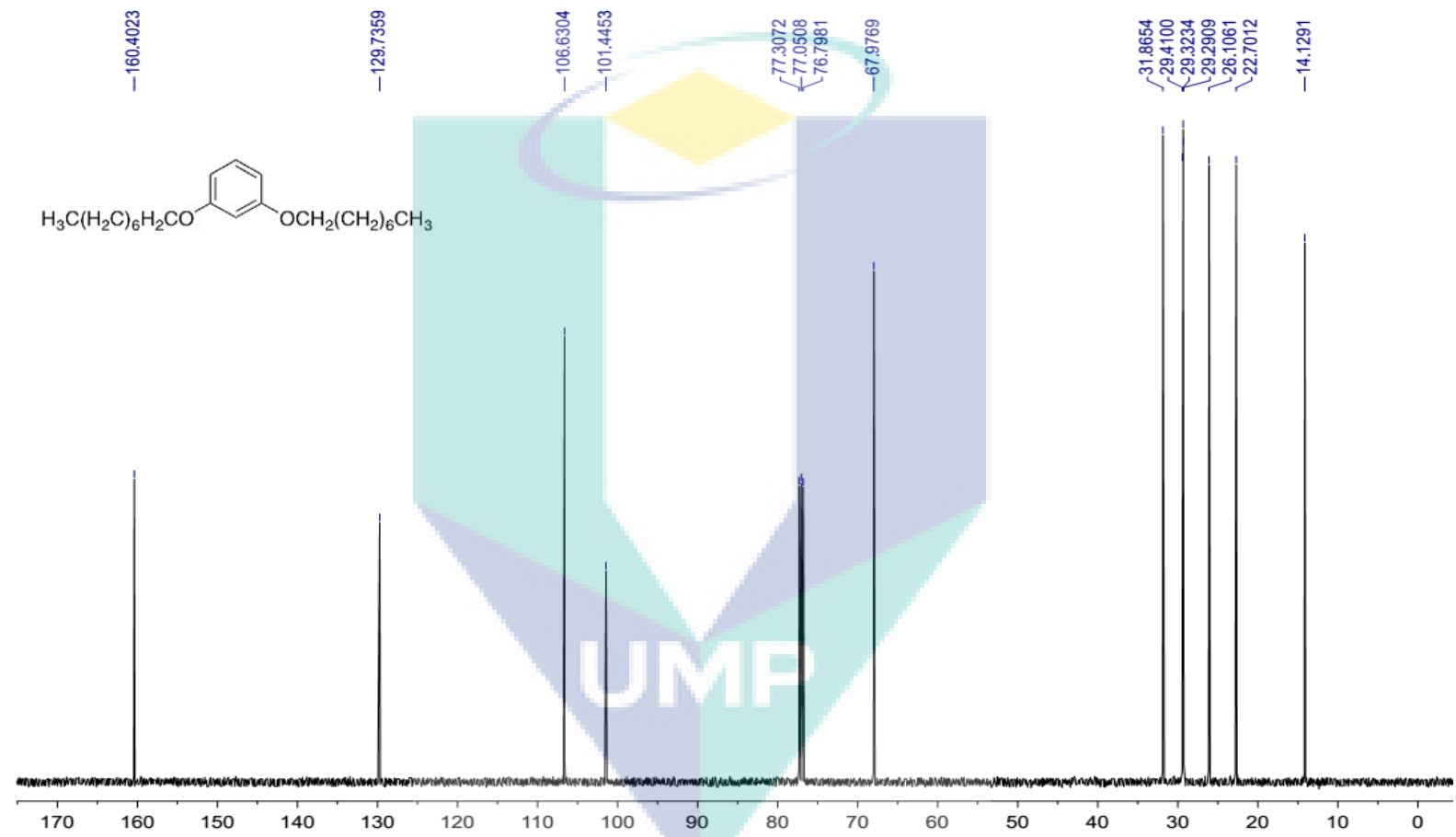


Figure S4 ^{13}C NMR of 1,3-di(octyloxy)benzene (5b) in CDCl_3

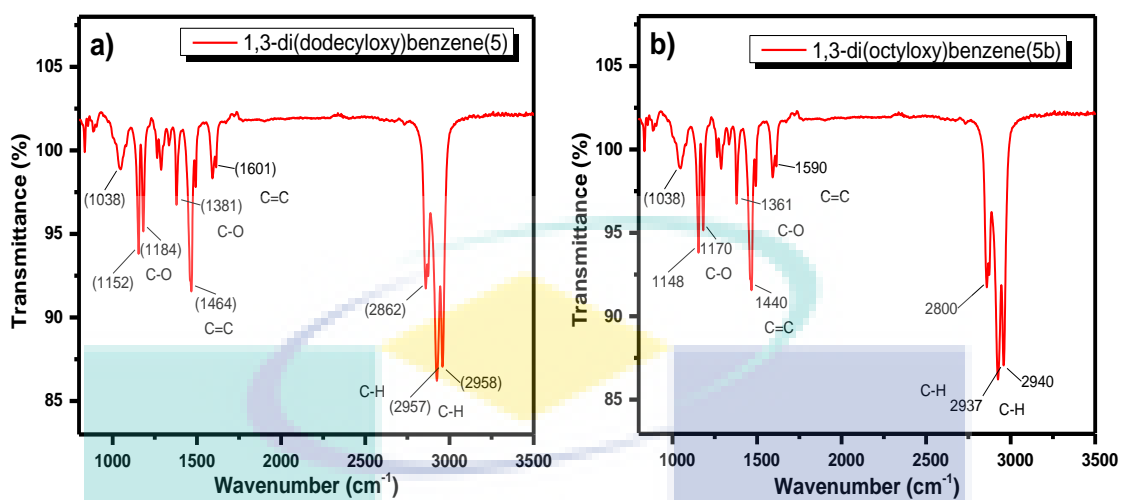


Figure S5 FTIR spectrum of a) 1,3-di(dodecyloxy)benzene (5); b) FTIR spectrum of 1,3-di(octyloxy)benzene (5b)

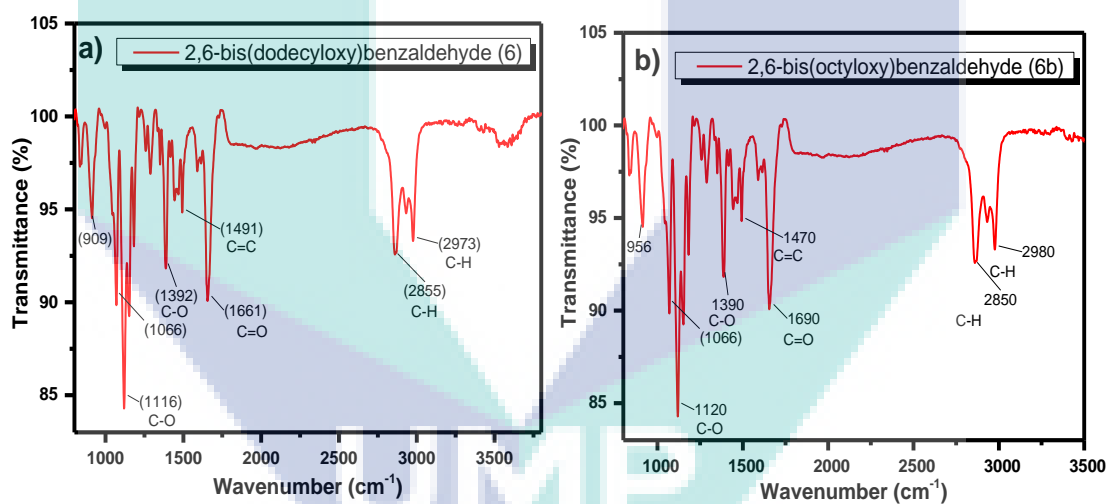


Figure S6 FTIR spectrum of a) 2,6-bis(dodecyloxy)benzaldehyde (6); b) 2,6-bis(octyloxy)benzaldehyde (6b)

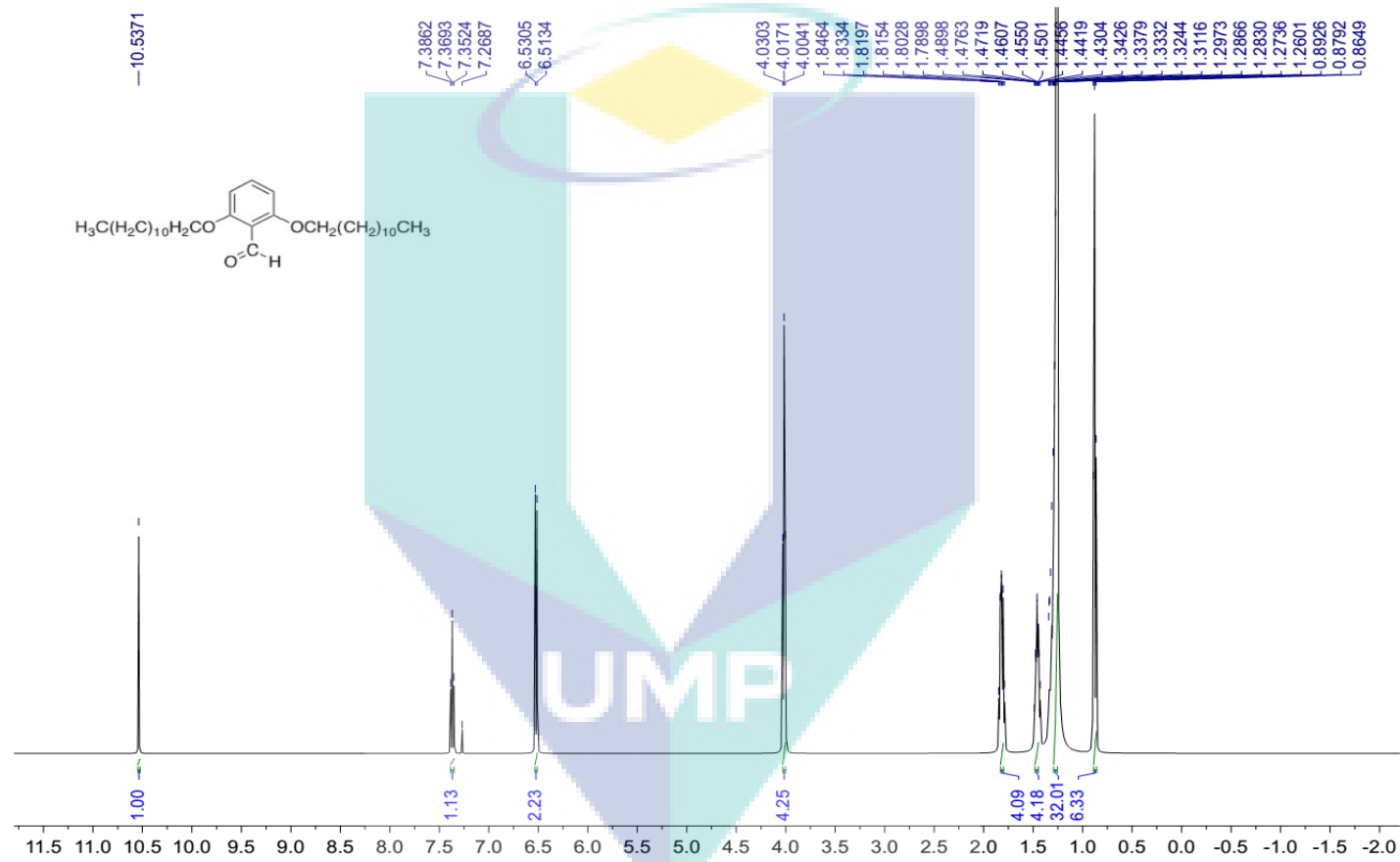


Figure S7 $^1\text{H NMR}$ of 2,6-bis(dodecyloxy)benzaldehyde (6) in CDCl_3

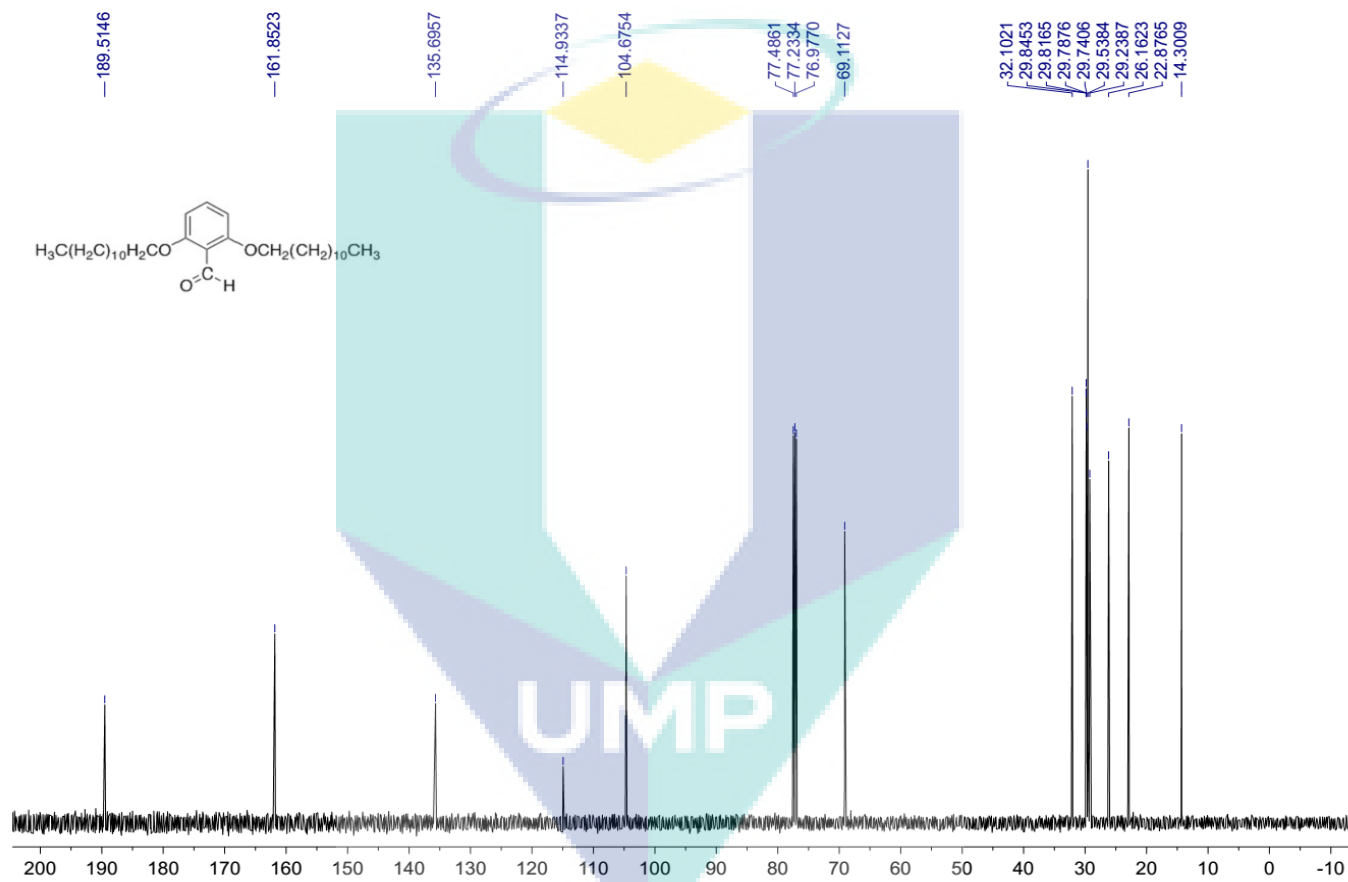


Figure S8 ^{13}C NMR of 2,6-bis(dodecyloxy)benzaldehyde (6) in CDCl_3

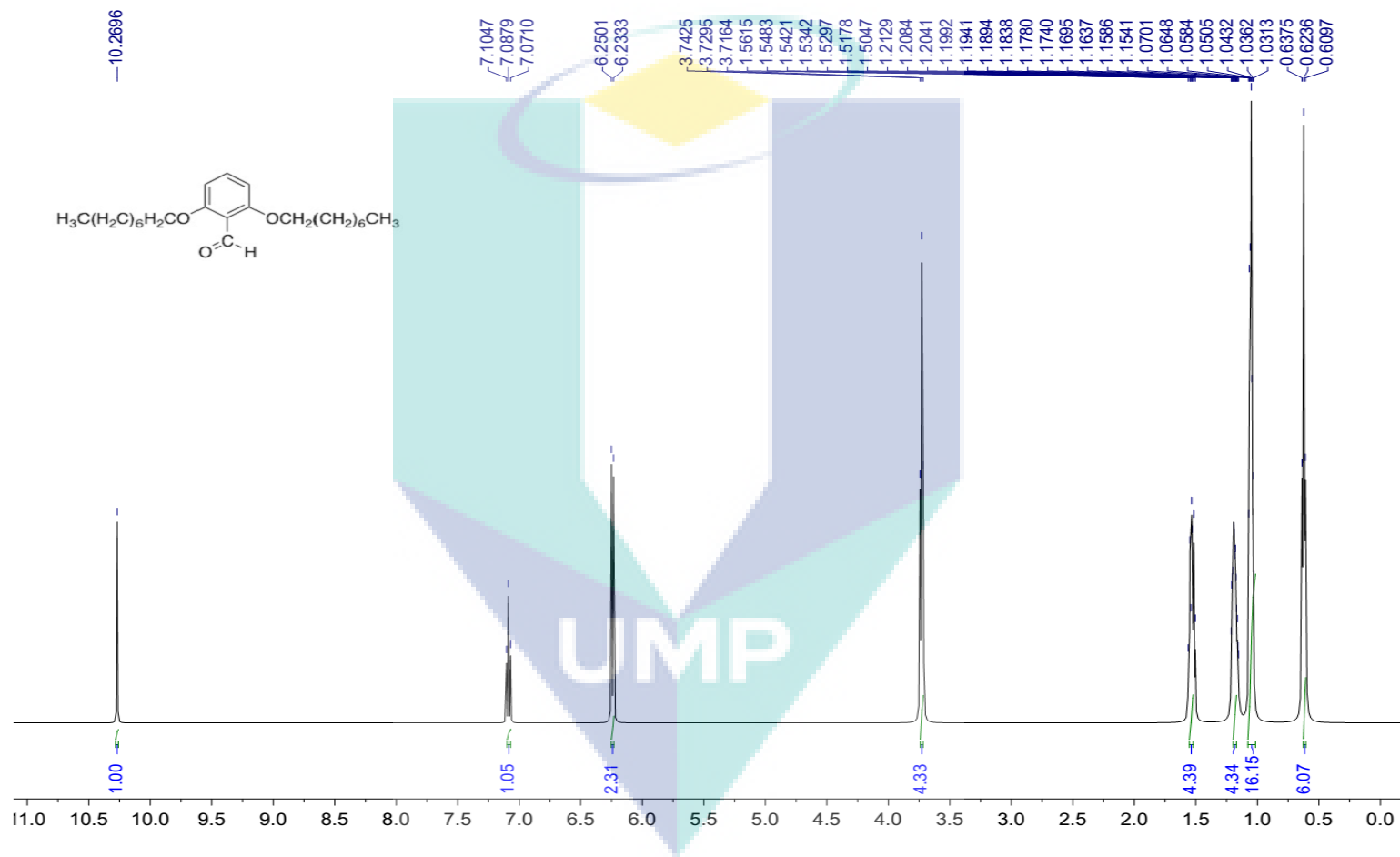


Figure S9 $^1\text{H NMR}$ of 2,6-bis(octyloxy)benzaldehyde (6b) in CDCl_3

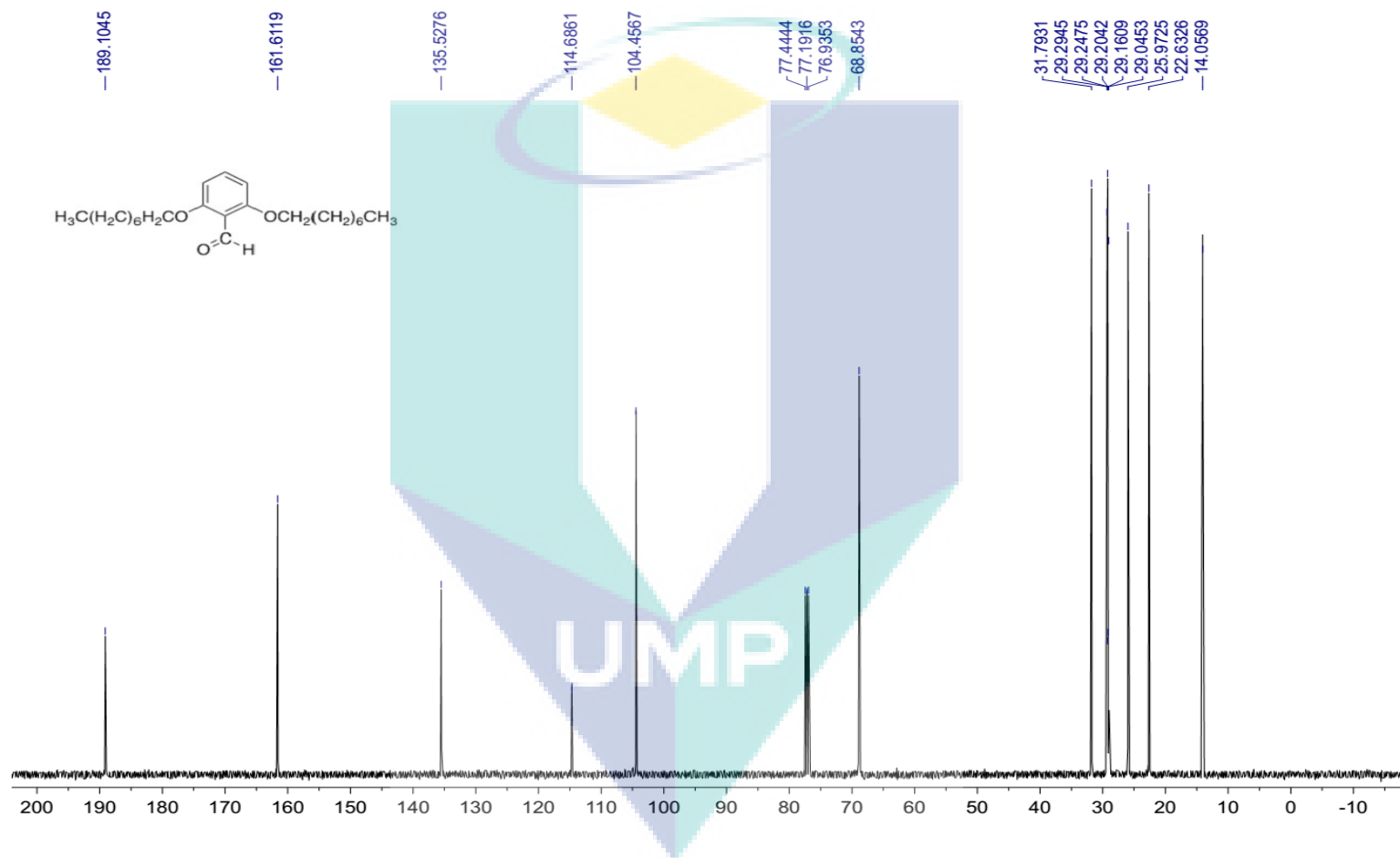


Figure S10 ^{13}C NMR of 2,6-bis(octyloxy)benzaldehyde (6b) in CDCl_3

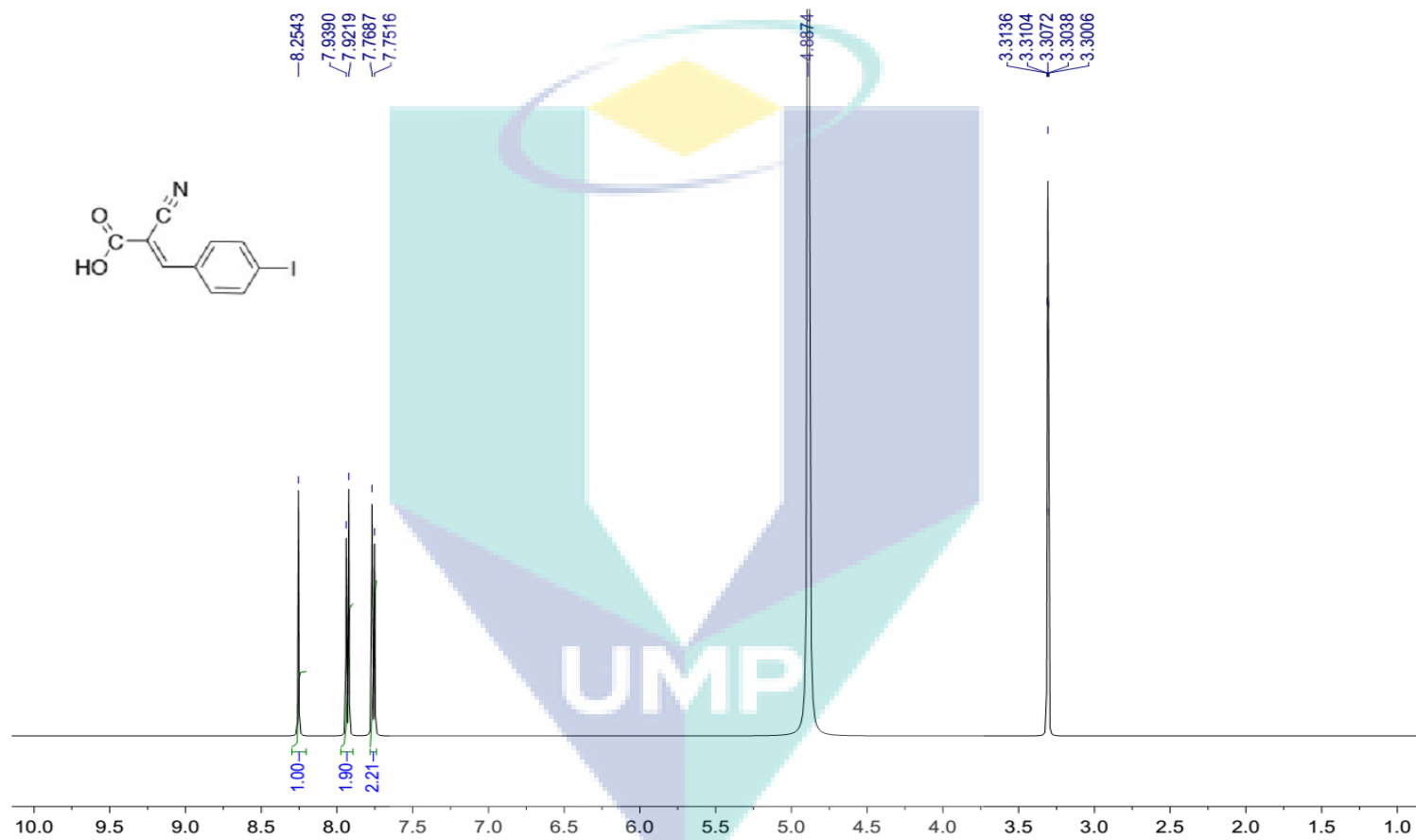


Figure S11 ¹H NMR of 2-cyano-3-(4-iodophenyl)acrylic acid (3) in CD₃OH

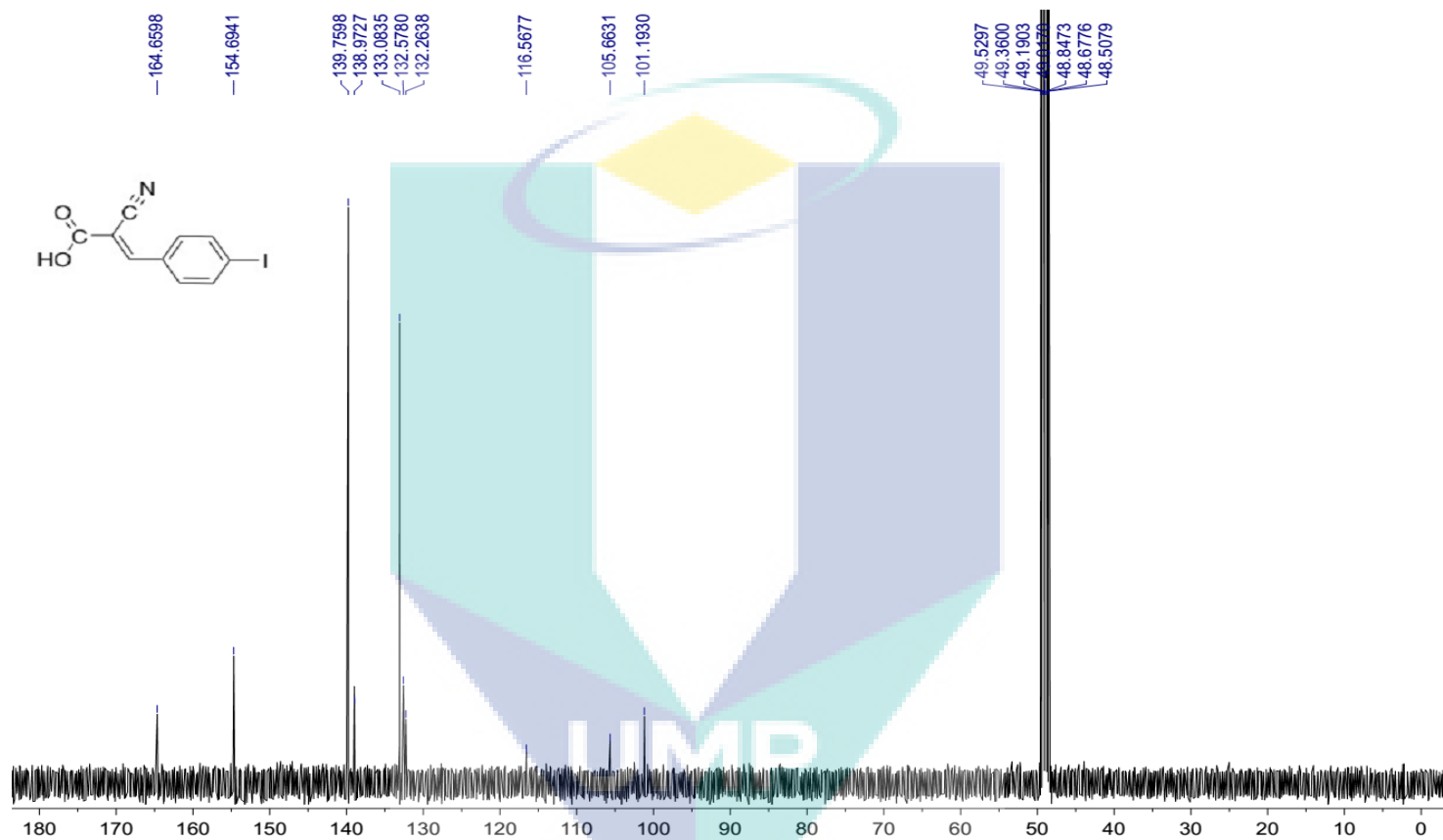


Figure S12 ^{13}C NMR of 2-cyano-3-(4-iodophenyl)acrylic acid (3) in CD_3OH

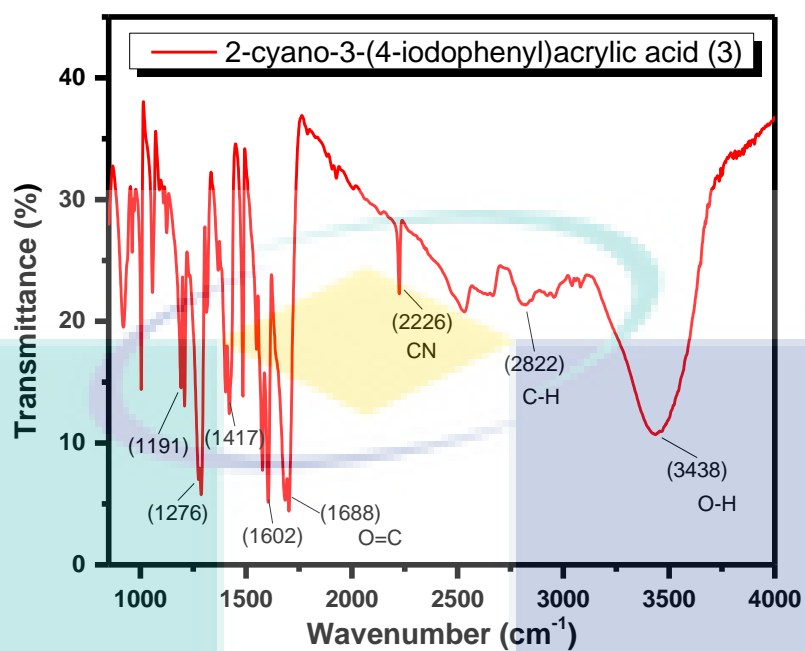


Figure S13 FTIR spectrum of 2-cyano-3-(4-iodophenyl)acrylic acid (3)

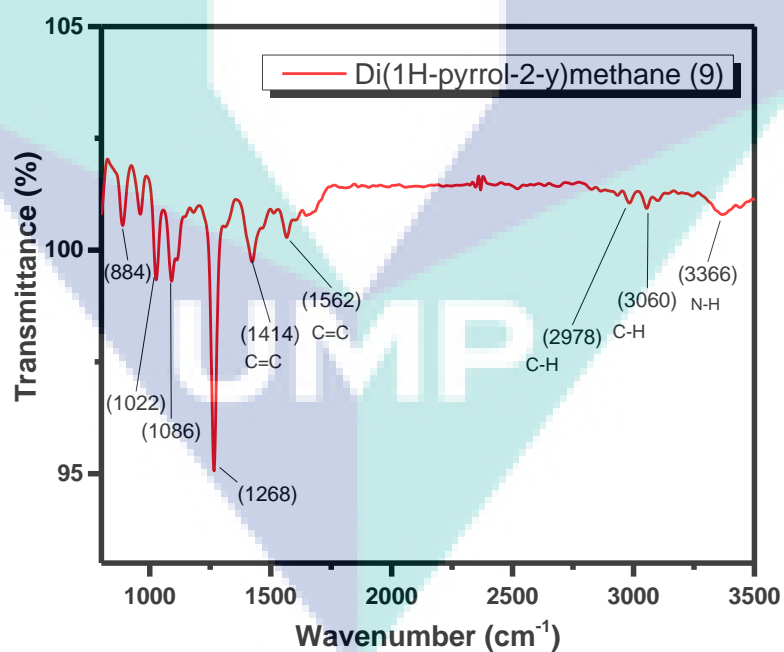


Figure S14 FTIR spectrum of di(1H-pyrrol-2-yl)methane (9)

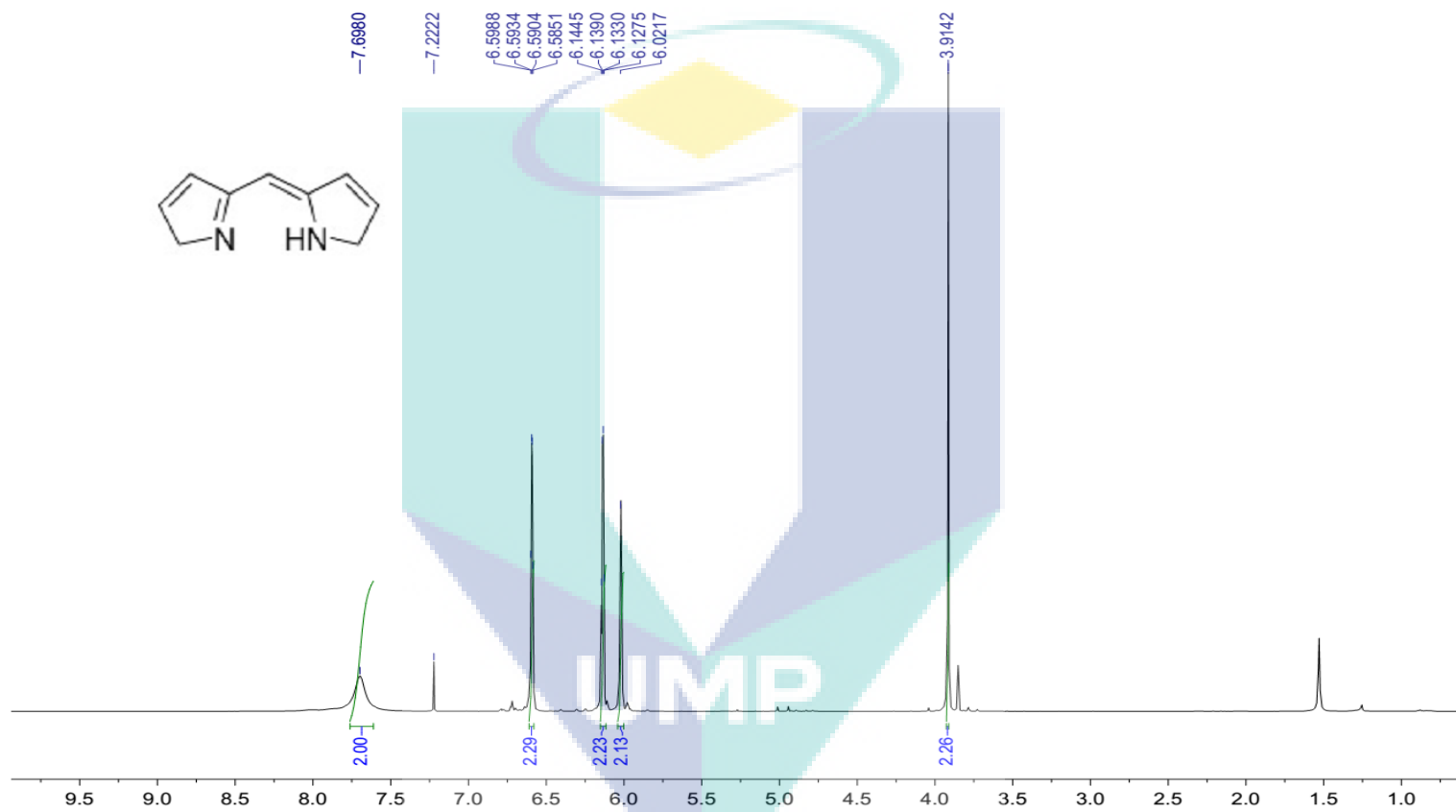


Figure S15 ¹H NMR of di(1H-pyrrol-2-yl)methane (9) in CDCl₃

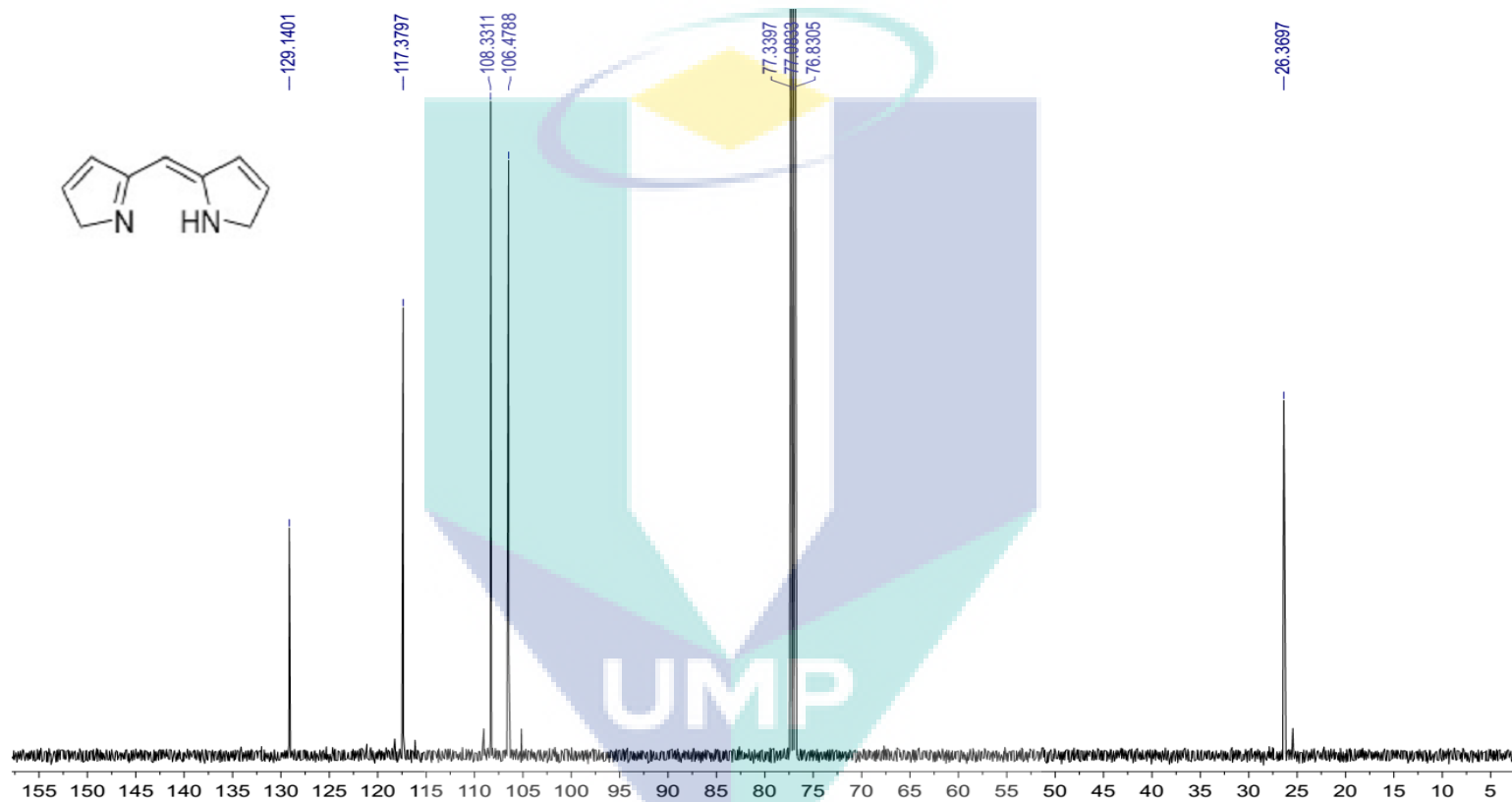


Figure S16 ^{13}C NMR of di(1H-pyrrol-2-yl)methane (9) in CDCl_3

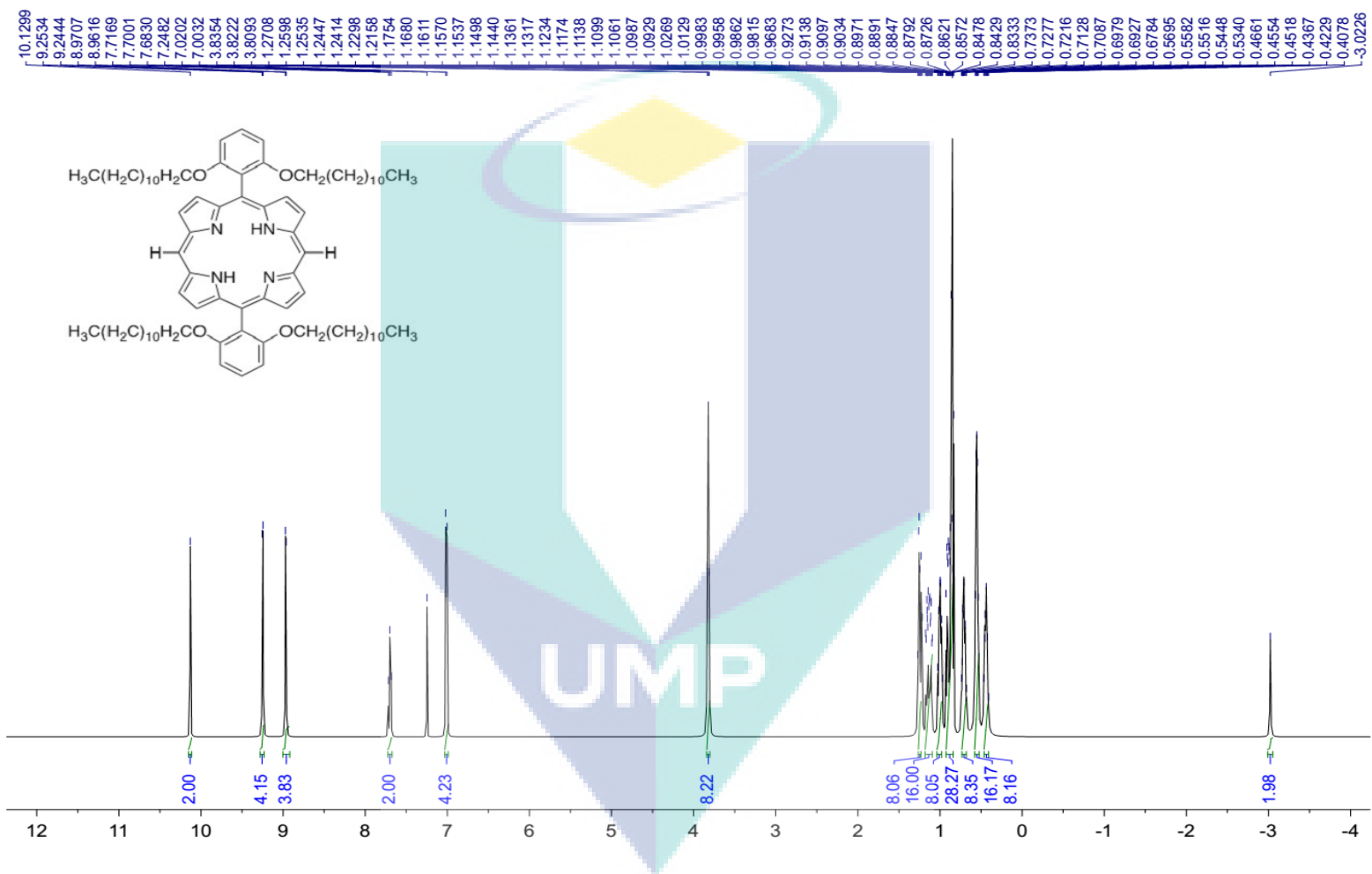


Figure S17 $^1\text{H NMR}$ of 5,15-bis(2,6-di(dodecyloxy)phenyl)porphyrin (10) in CDCl_3

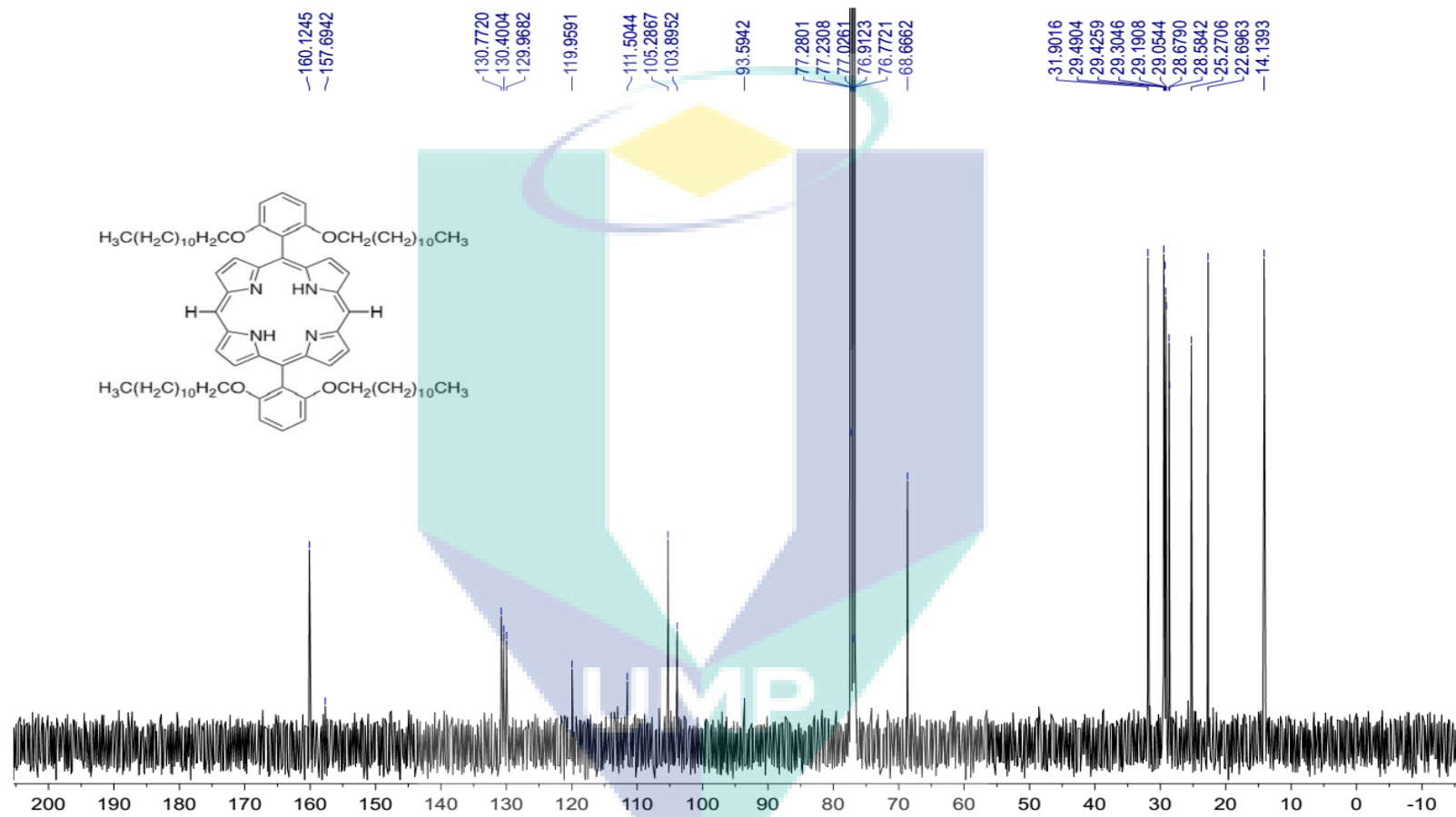


Figure S18 ^{13}C NMR of 5,15-bis(2,6-di(dodecyloxy)phenyl)porphyrin (10) in CDCl_3

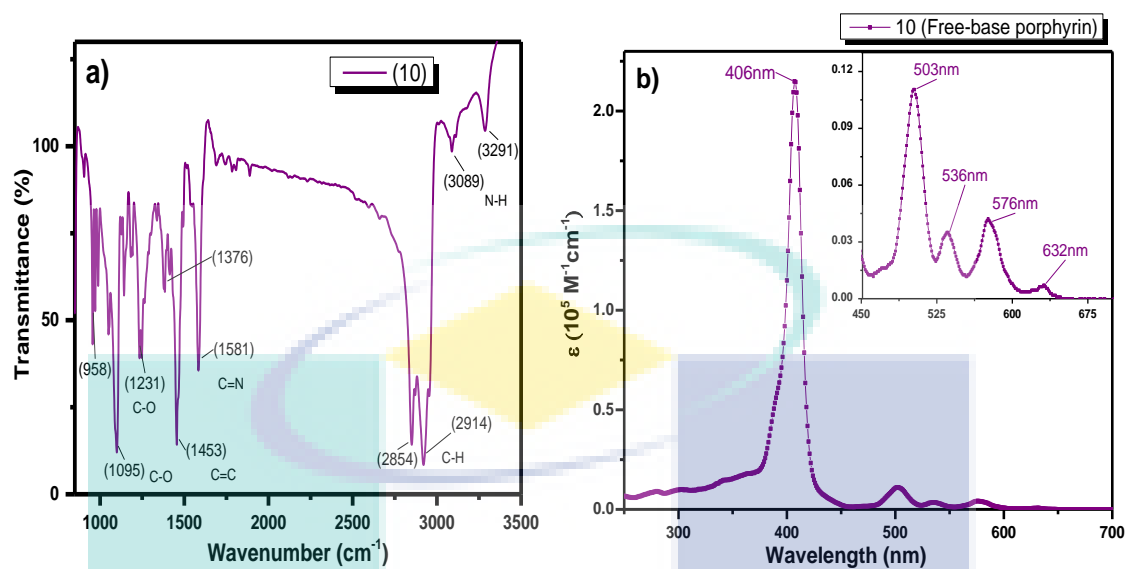


Figure S19 a) FTIR spectrum of 5,15-bis(2,6-di(dodecyloxy)phenyl)porphyrin (10); b) UV-Vis spectrum of 5,15-bis(2,6-di(dodecyloxy)phenyl)porphyrin (10)

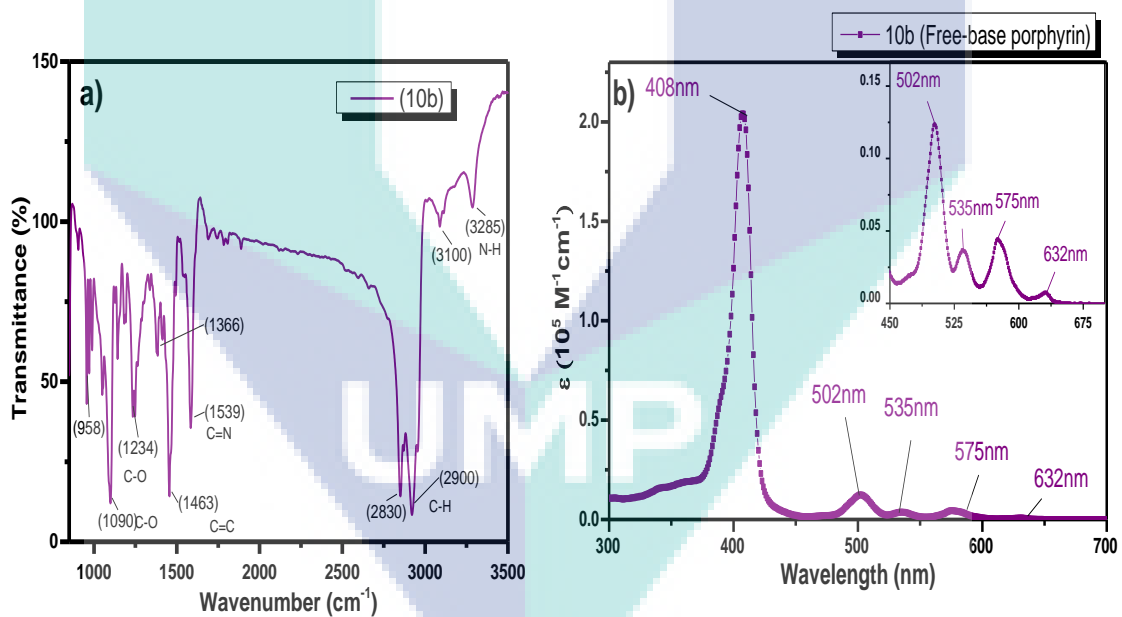


Figure S20 a) FTIR spectrum of 5,15-bis(2,6-di(octyloxy)phenyl)porphyrin (10b); b) UV-Vis spectrum of 5,15-bis(2,6-di(octyloxy)phenyl)porphyrin (10b)

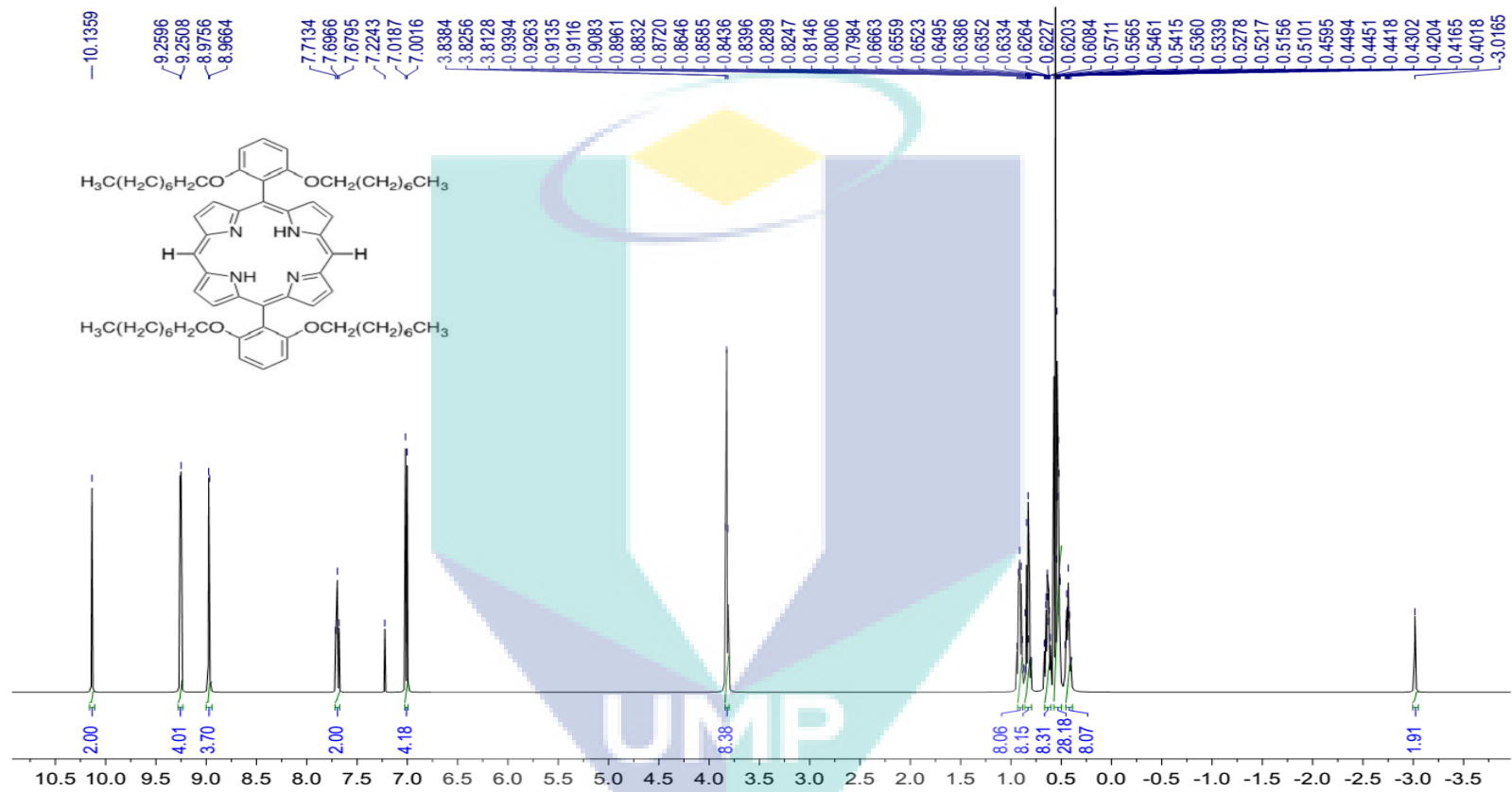


Figure S21 ¹H NMR of 5,15-bis(2,6-di(octyloxy)phenyl)porphyrin (10b) in CDCl₃

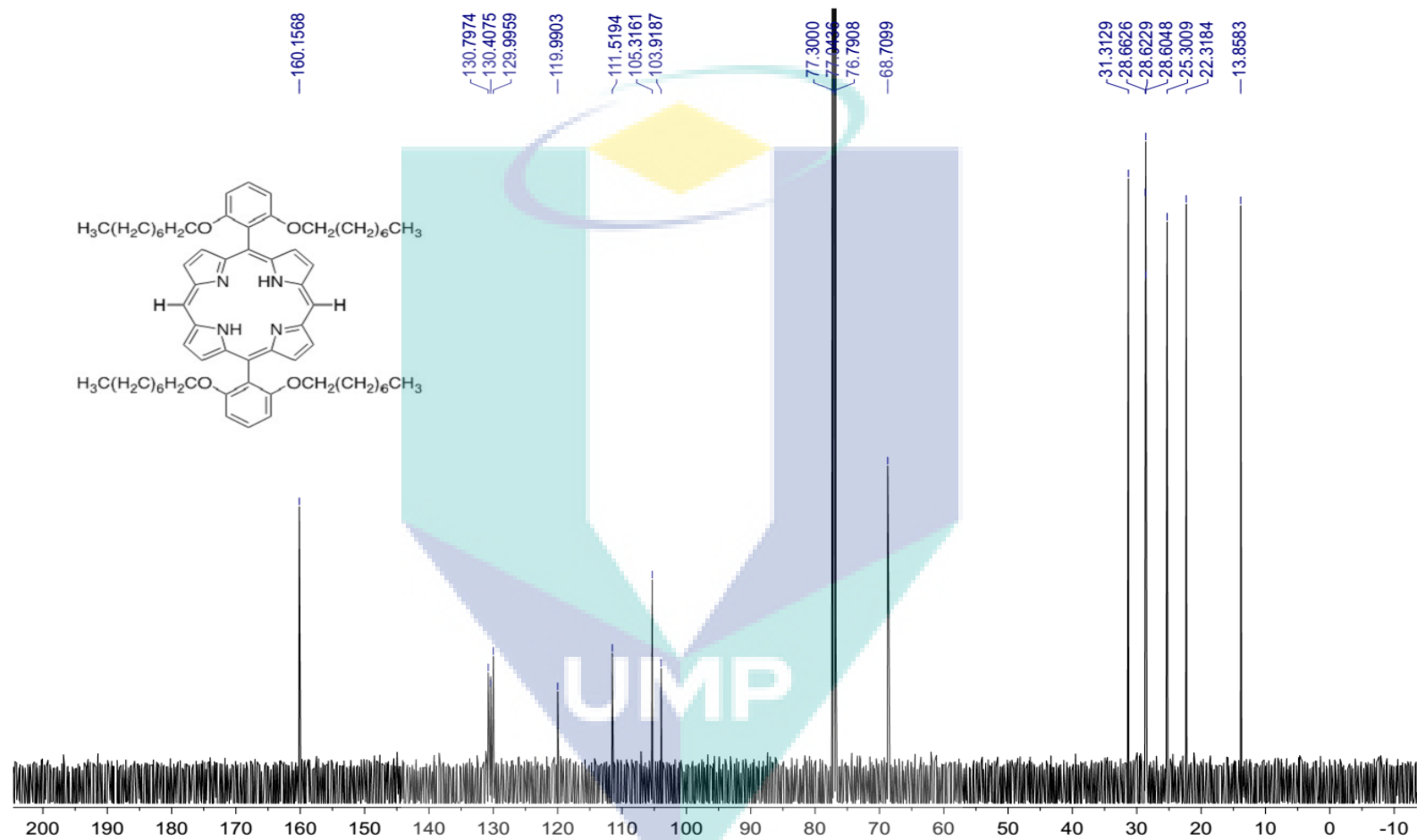


Figure S22 ^{13}C NMR of 5,15-bis(2,6-di(octyloxy)phenyl)porphyrin (10b) in CDCl_3

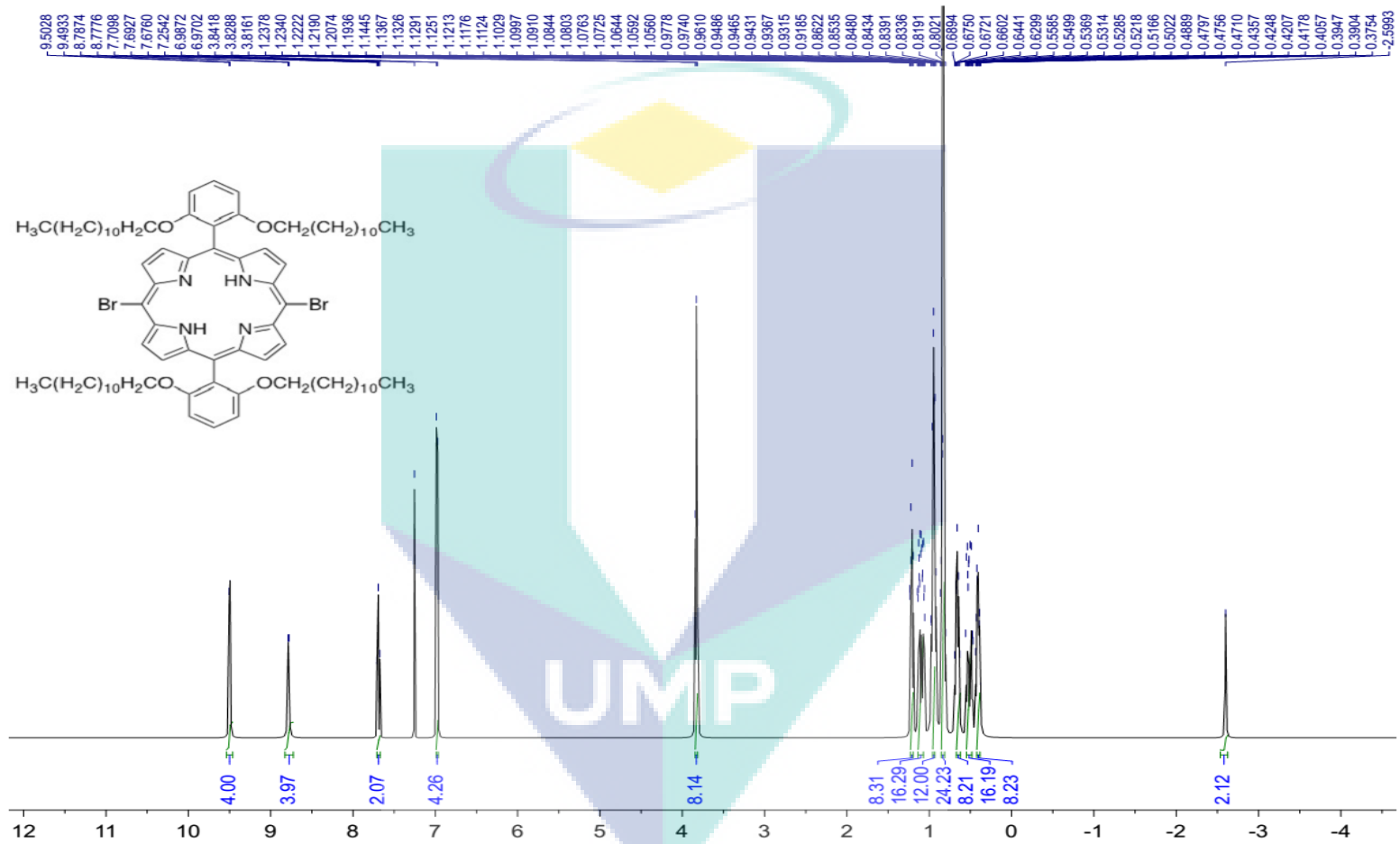


Figure S23 $^1\text{H NMR}$ of 5,15-bisbromo-10,20-bis(2,6-di(dodecyloxy)phenyl)porphyrin (11) in CDCl_3

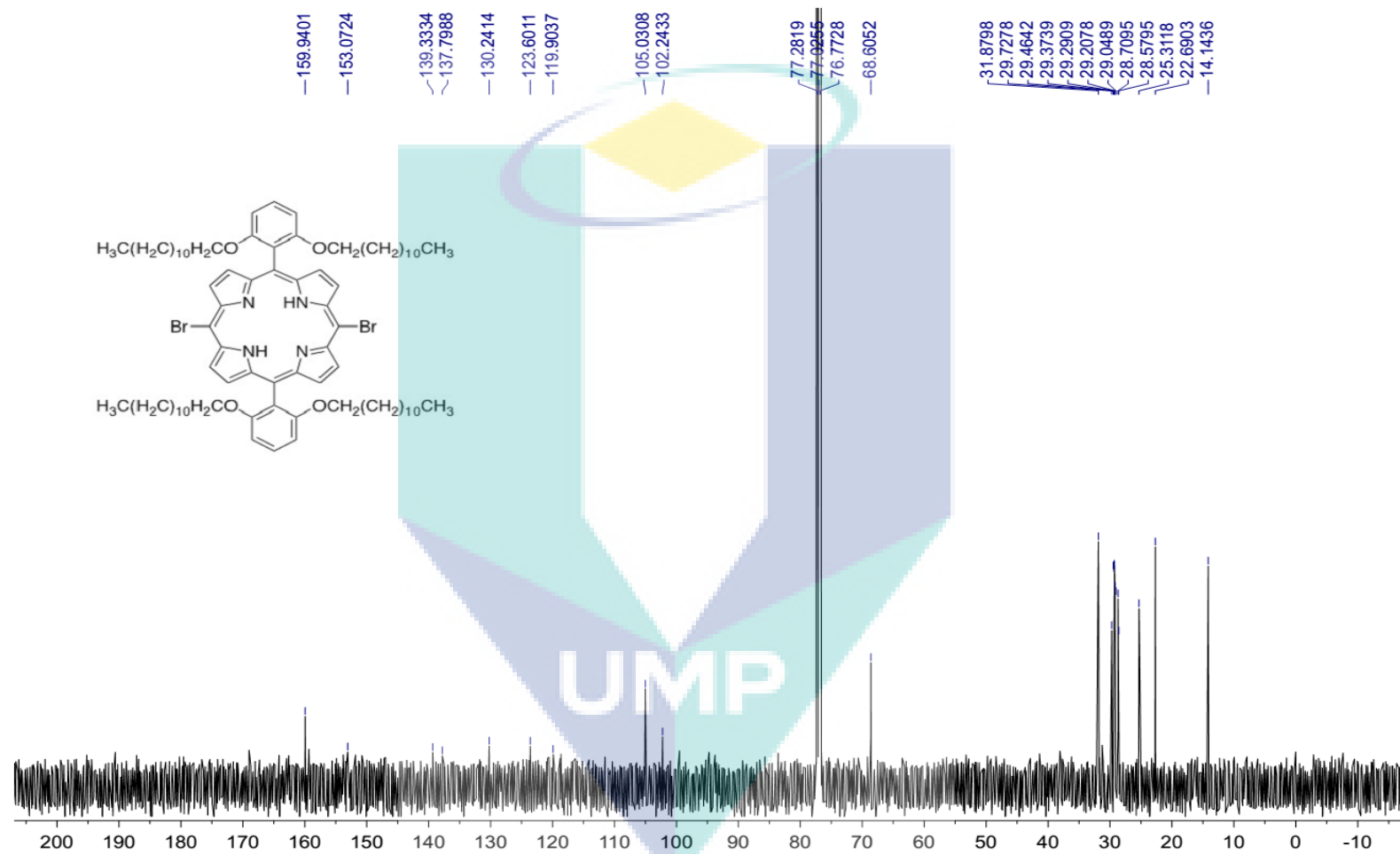


Figure S24 ^{13}C NMR of 5,15-bisbromo-10,20-bis(2,6-di(dodecyloxy)phenyl)porphyrin (11) in CDCl_3

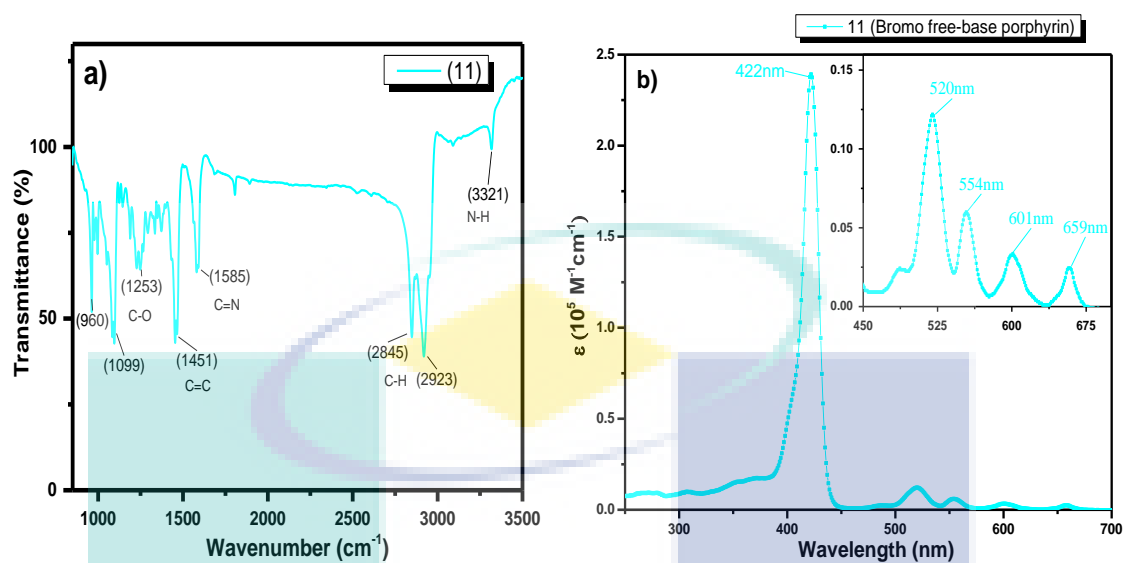


Figure S25 a) FTIR spectrum of 5,15-bisbromo-10,20-bis(2,6-di(dodecyloxy)phenyl)porphyrin (11); b) UV-Vis spectrum of 5,15-bisbromo-10,20-bis(2,6-di(dodecyloxy)phenyl)porphyrin (11)

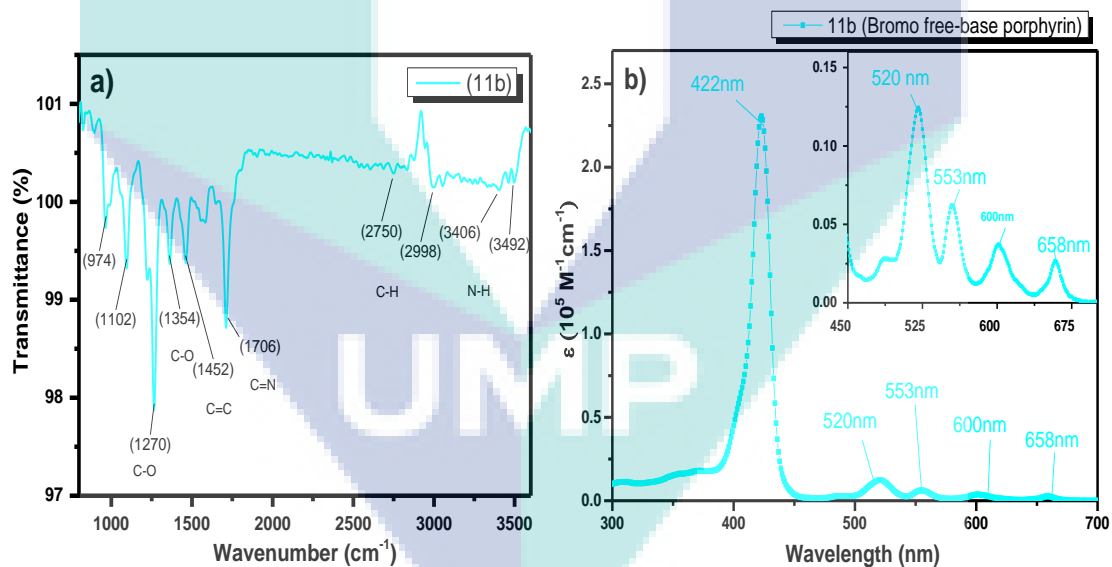


Figure S26 a) FTIR spectrum of 5,15-bisbromo-10,20-bis(2,6-di(octyloxy)phenyl)porphyrin (11b); b) UV-Vis spectrum of 5,15-bisbromo-10,20-bis(2,6-di(octyloxy)phenyl)porphyrin (11b)

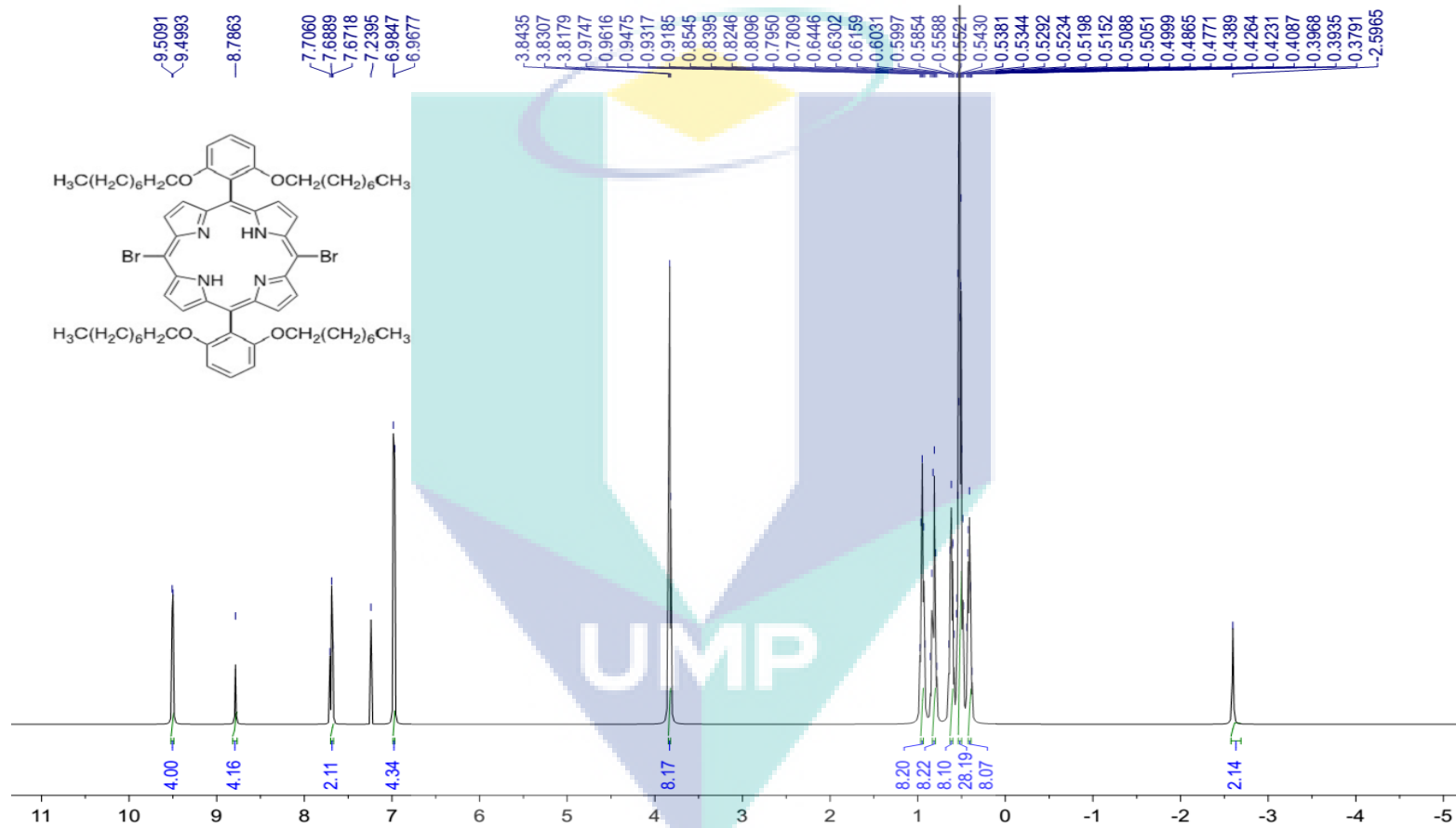


Figure S27 $^1\text{H NMR}$ of 5,15-bisbromo-10,20-bis(2,6-di(octyloxy)phenyl)porphyrin (11b) in CDCl₃

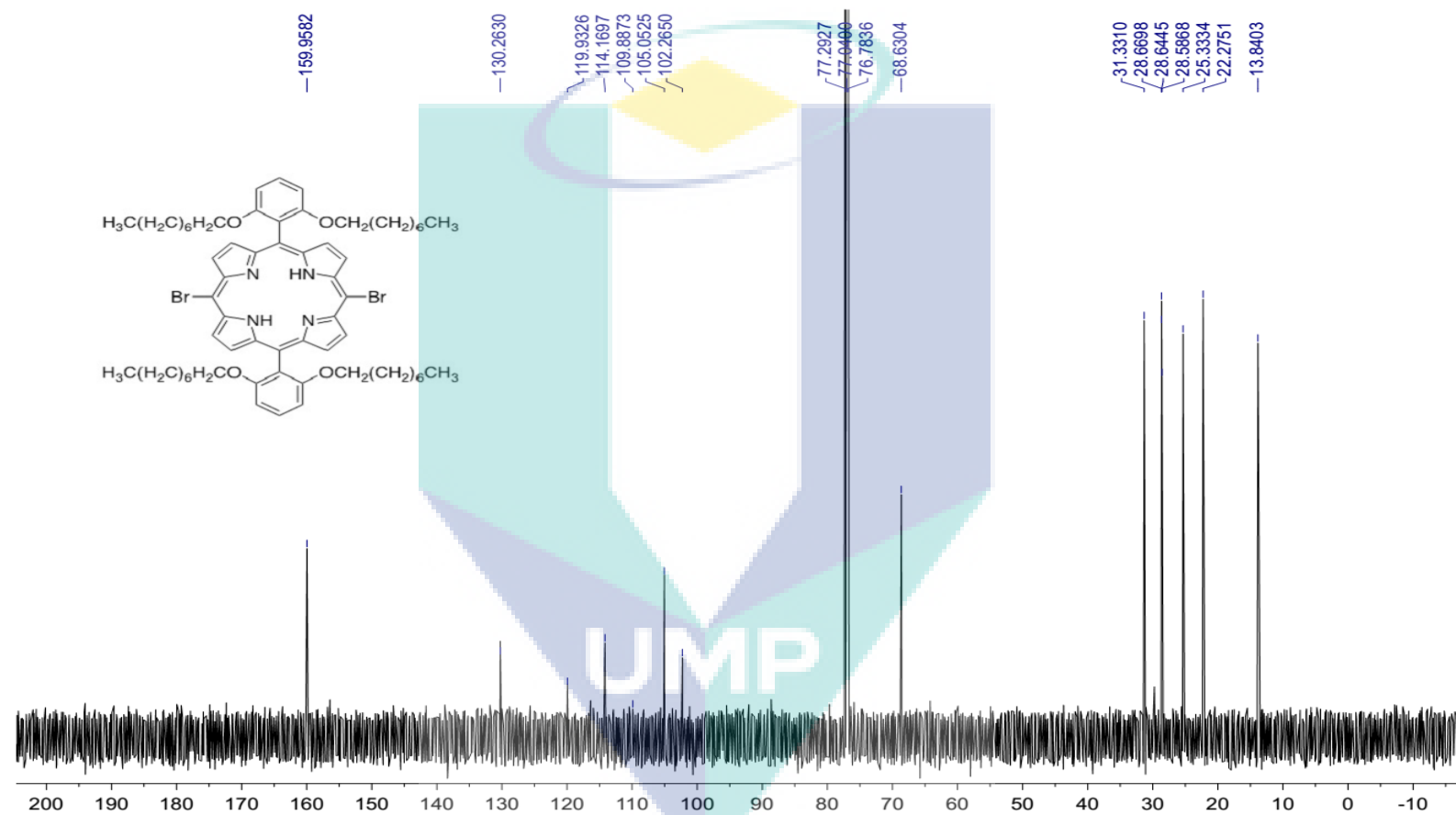


Figure S28 ^{13}C NMR of 5,15-bisbromo-10,20-bis(2,6-di(octyloxy)phenyl)porphyrin (11b) in CDCl_3

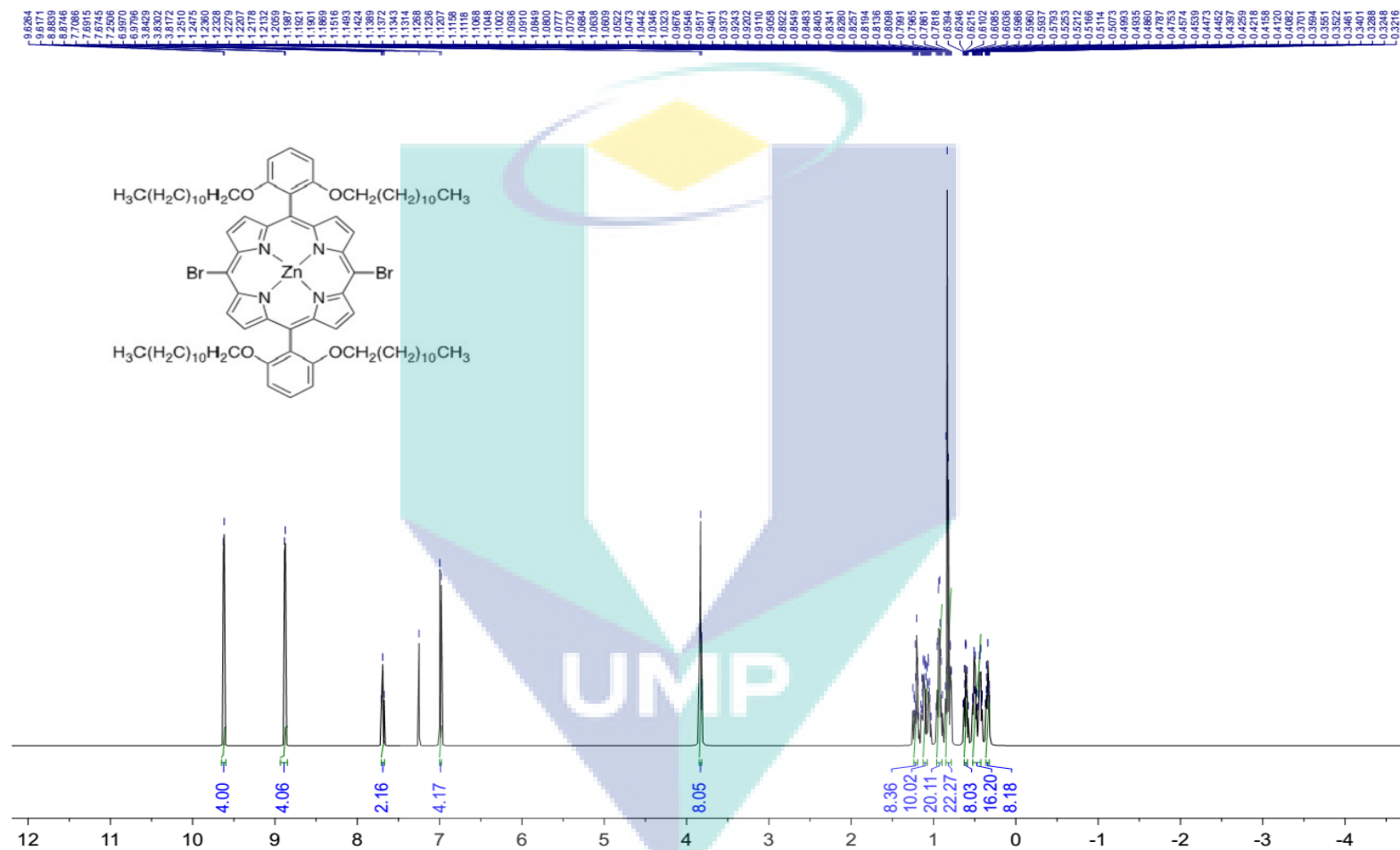


Figure S29 $^1\text{H NMR}$ of [5,15-bisbromo-10,20-bis(2,6-di(dodecyloxy)phenyl)porphinato]zinc(II) (12) in CDCl_3

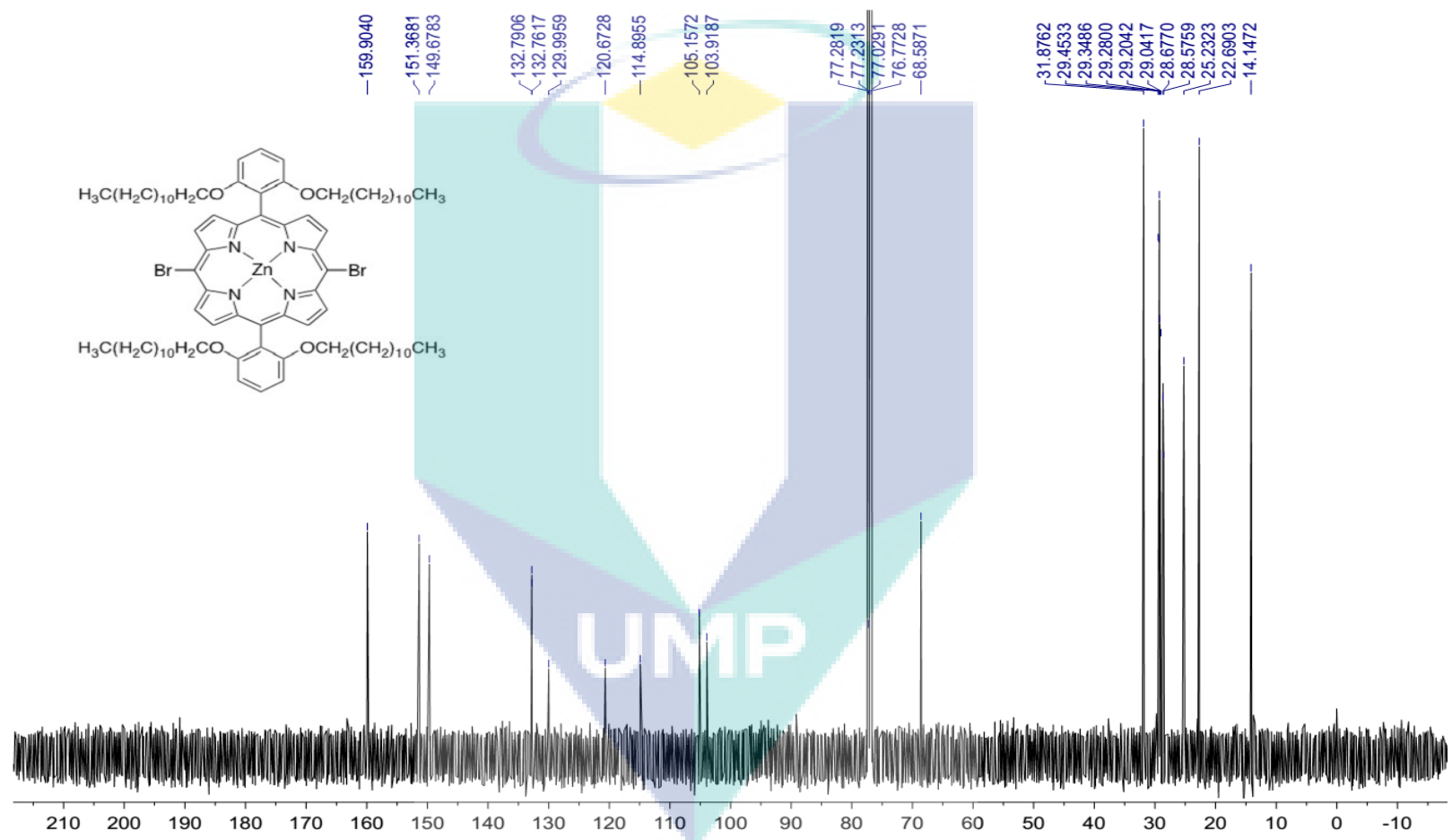


Figure S30 ^{13}C NMR of [5,15-bisbromo-10,20-bis(2,6-di(dodecyloxy)phenyl)porphinato]zinc(II) (12) in CDCl_3

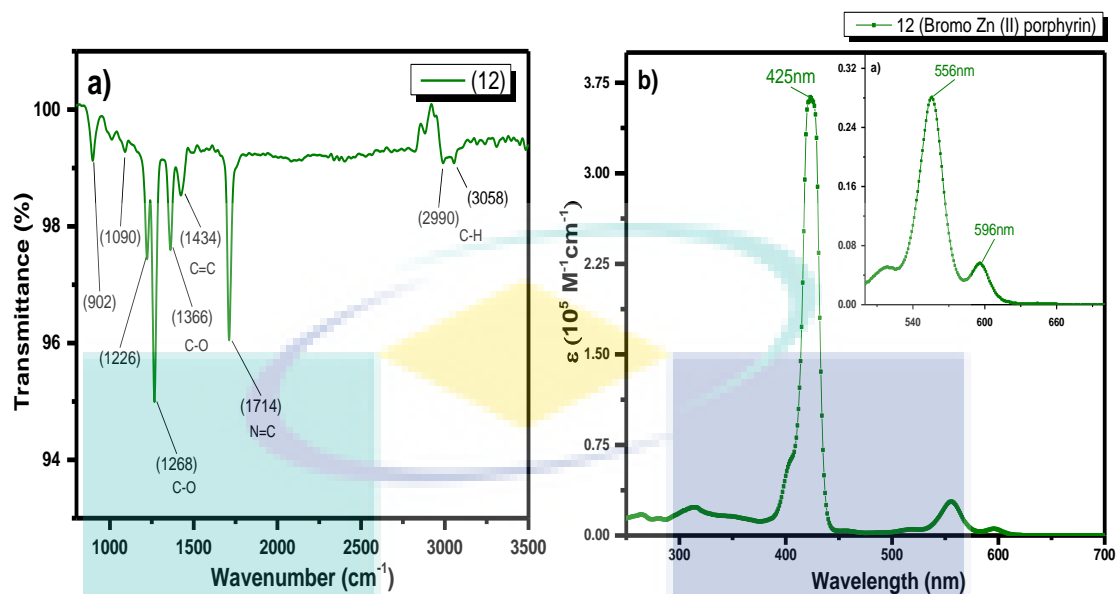


Figure S31 a) FTIR spectrum of [5,15-bisbromo-10,20-bis(2,6-di(dodecyloxy)phenyl)porphinato]zinc(II) (12); b) UV-Vis spectrum of [5,15-bisbromo-10,20-bis(2,6-di(dodecyloxy)phenyl)porphinato] zinc(II) (12)

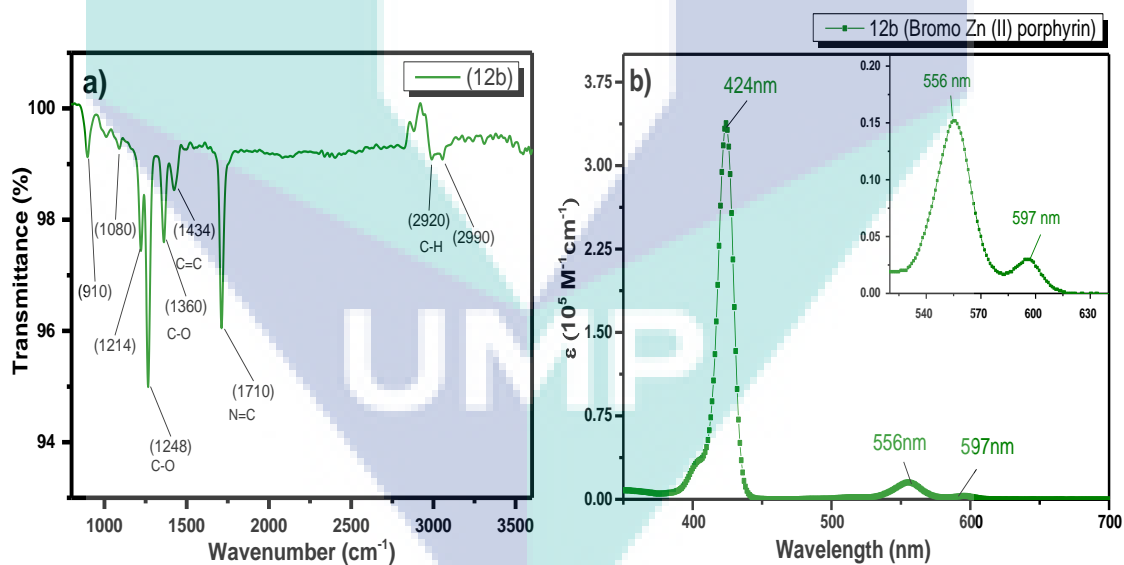


Figure S32 a) FTIR spectrum of [5,15-bisbromo-10,20-bis(2,6-di(octyloxy)phenyl)porphinato]zinc(II) (12b); b) UV-Vis spectrum of [5,15-bisbromo-10,20-bis(2,6-di(octyloxy)phenyl)porphinato]zinc(II) (12b)

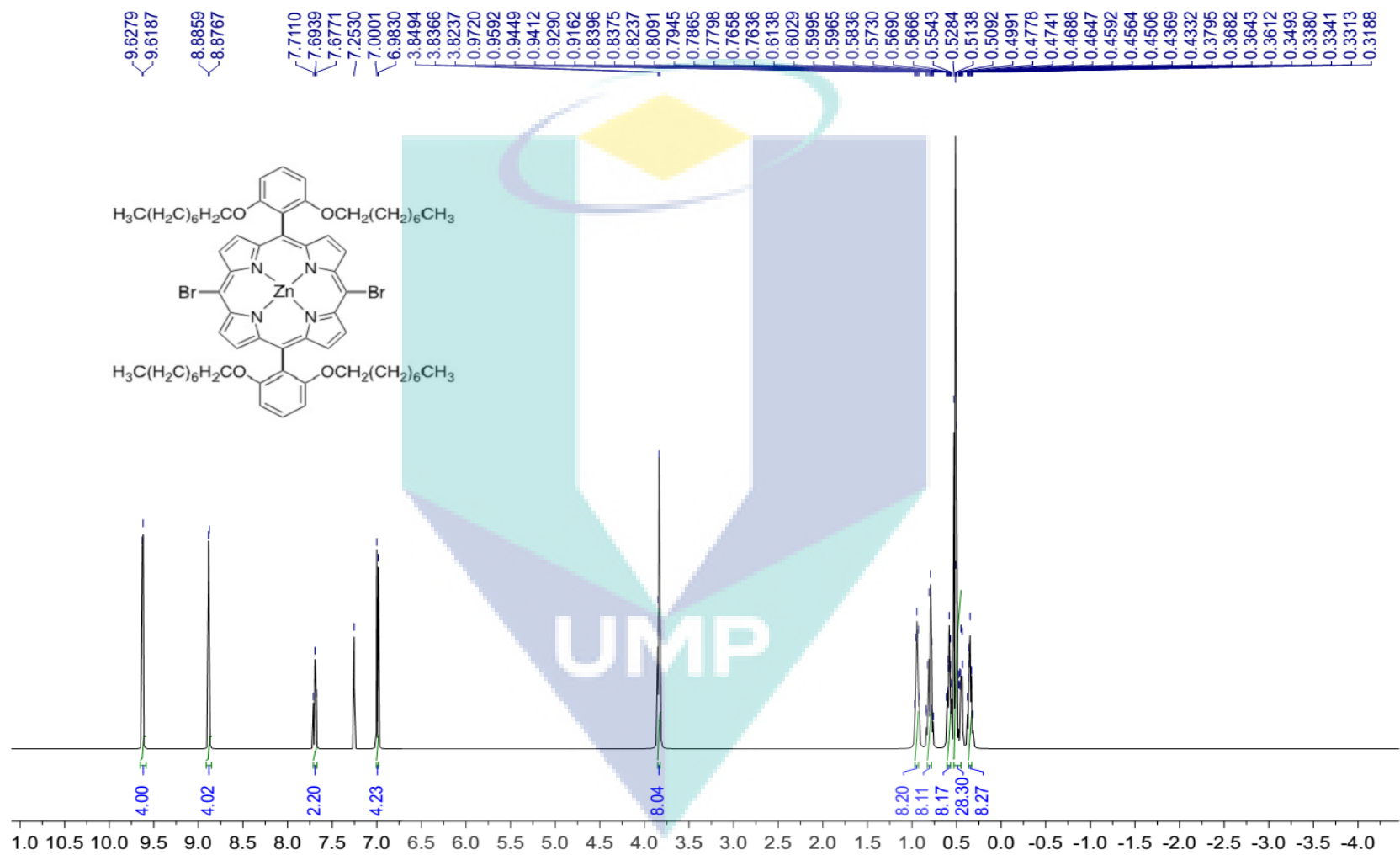


Figure S33 $^1\text{H NMR}$ of [5,15-bisbromo-10,20-bis(2,6-di(octyloxy)phenyl)porphinato]zinc(II) (12b) in CDCl₃

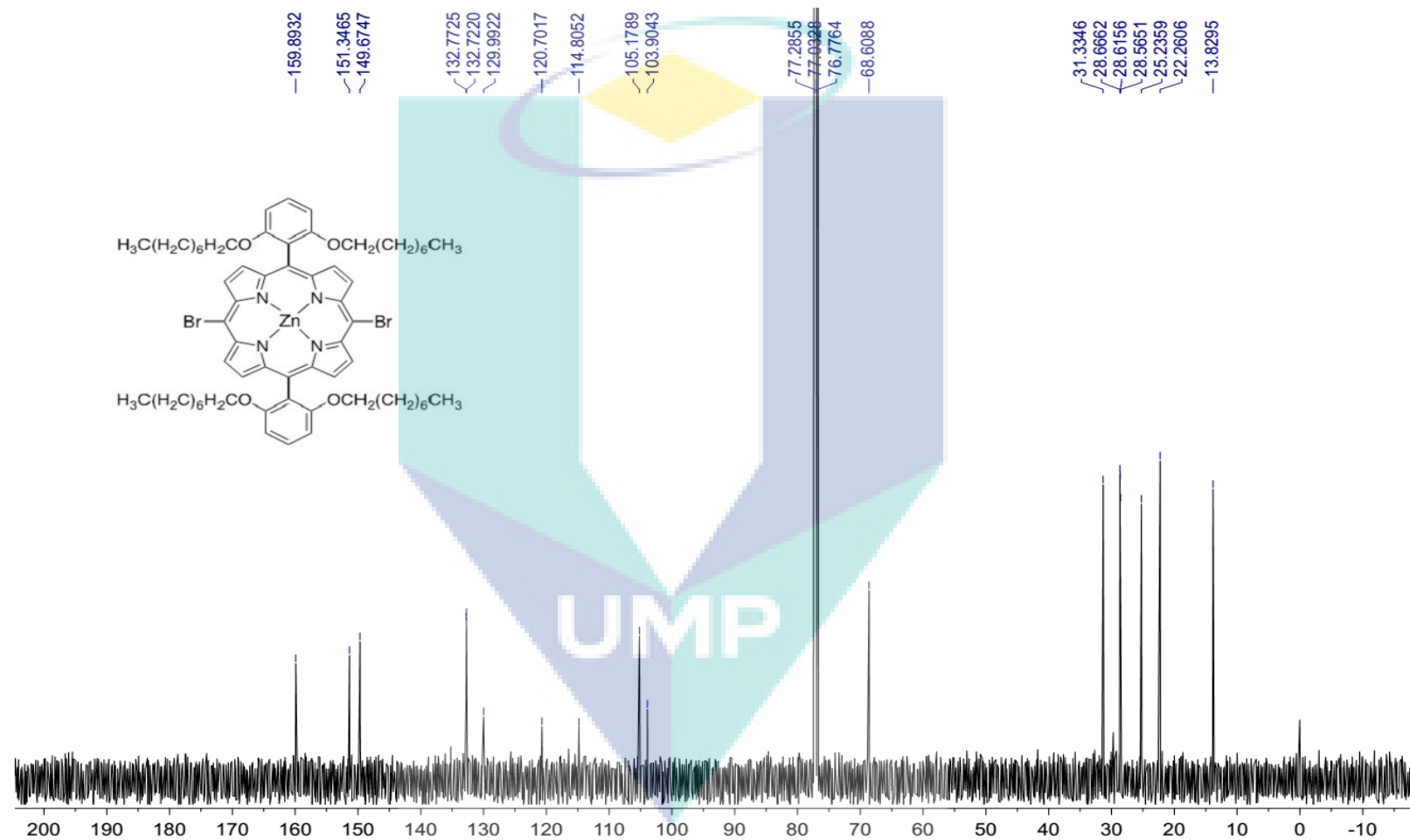


Figure S34 ^{13}C NMR of [5,15-bisbromo-10,20-bis(2,6-di(octyloxy)phenyl)porphinato]zinc(II) (12b) in CDCl_3

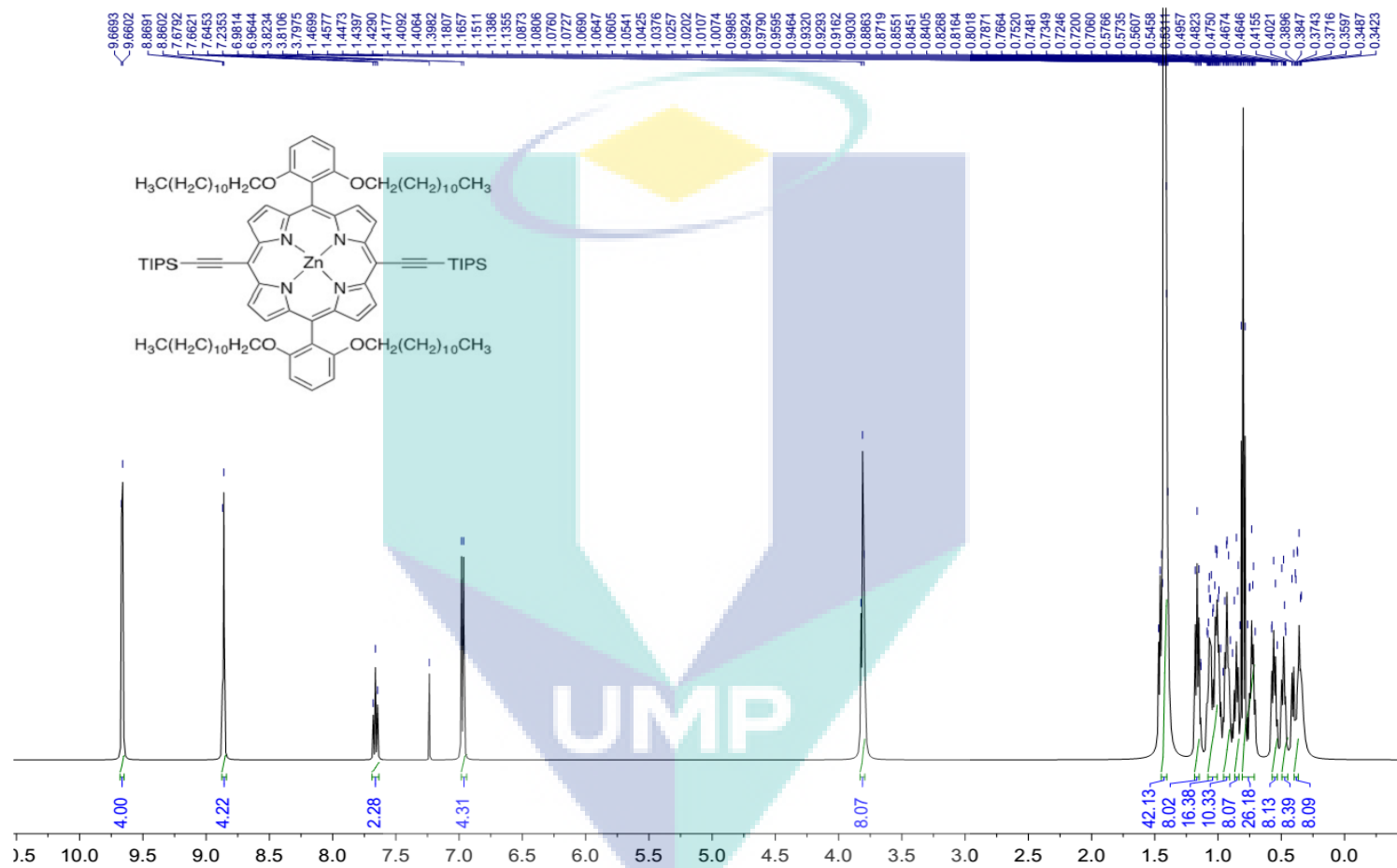


Figure S35 ¹H NMR of [5,15-bis(2,6-di(dodecyloxy)phenyl)-10,20-bis(triisopropylsilyl)ethynyl]porphinatozinc(II) (13) in CDCl₃

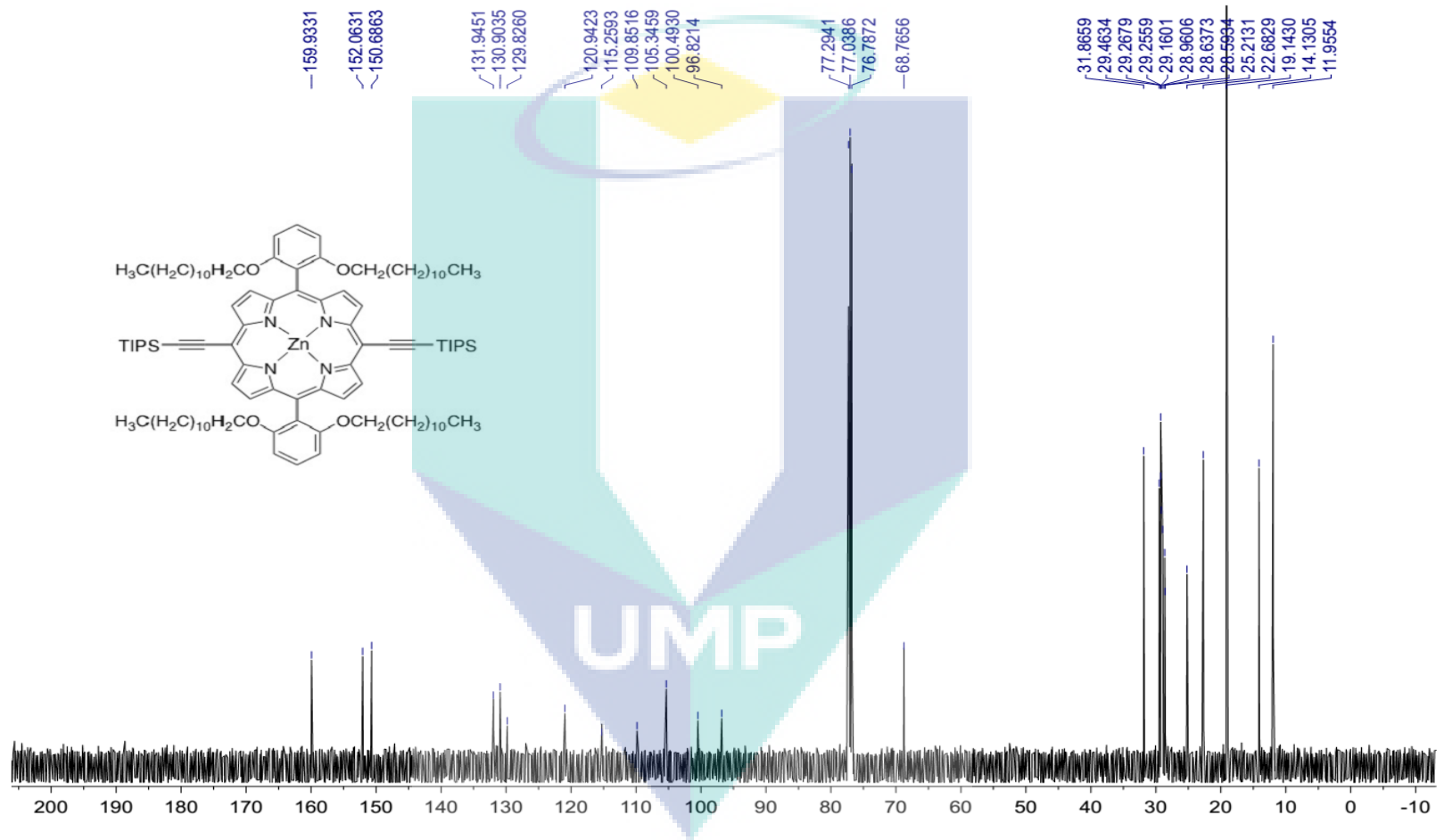


Figure S36 ^{13}C NMR of [5,15-bis(2,6-di(dodecyloxy)phenyl)-10,20-bis(triisopropylsilyl)ethynyl]porphyrinato]zinc(II) (13) in CDCl_3

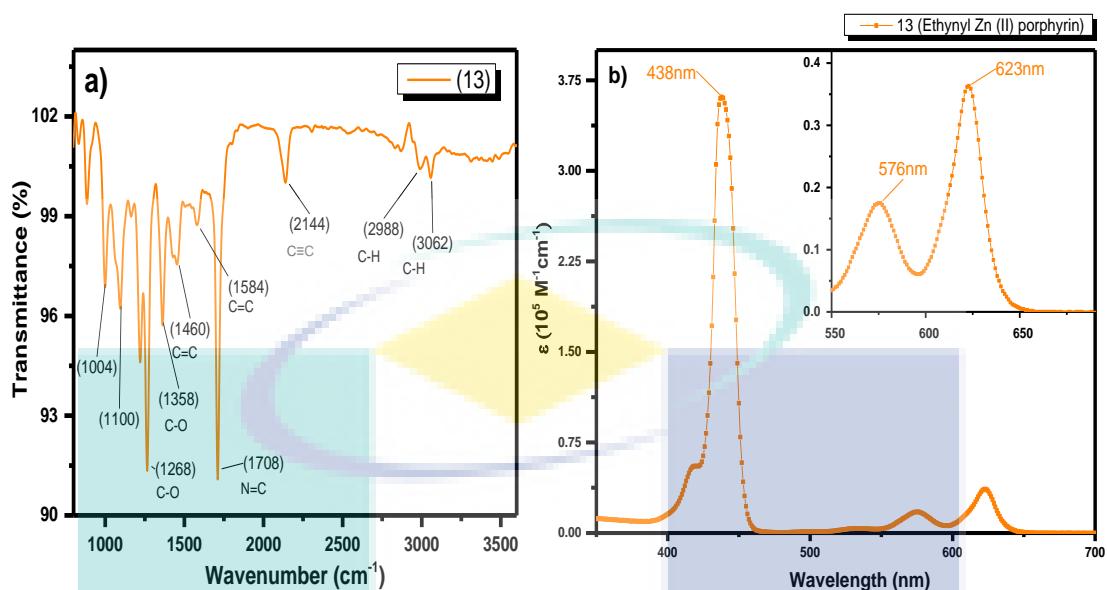


Figure S37 a) FTIR spectrum of [5,15-bis(2,6-di(dodecyloxy)phenyl)-10,20-bis(triisopropylsilyl)ethynyl] porphinato]zinc(II) (13); b) UV-Vis spectrum of [5,15-bis(2,6-di(dodecyloxy)phenyl)-10,20-bis(triisopropylsilyl)ethynyl] porphinato]zinc(II) (13)

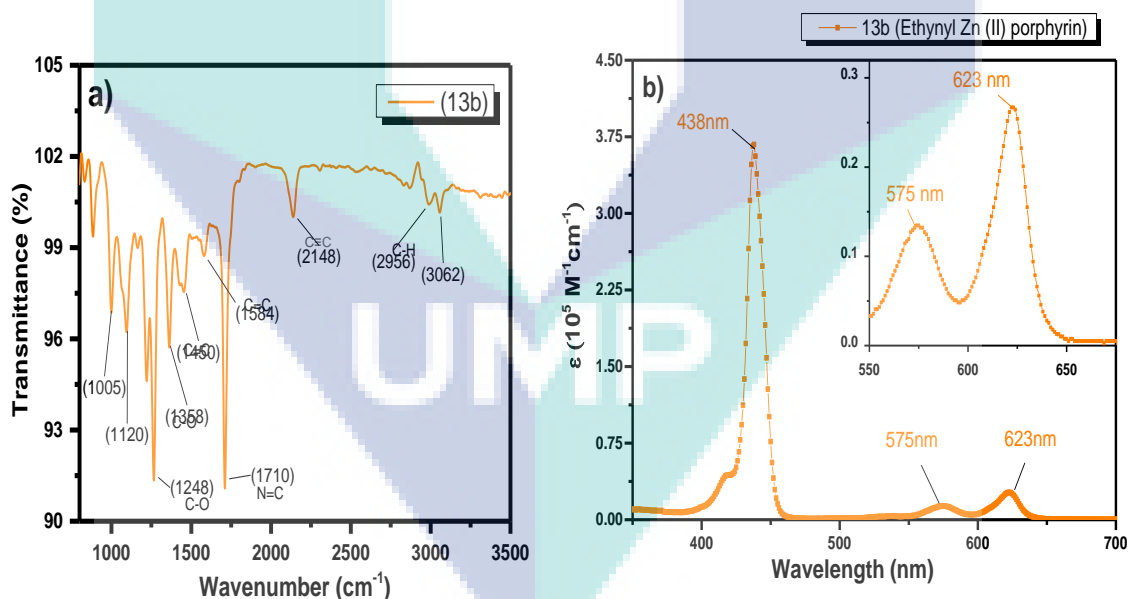


Figure S38 a) FTIR spectrum of [5,15-bis(2,6-di(octyloxy)phenyl)-10,20-bis(triisopropylsilyl)ethynyl] porphinato]zinc(II) (13b); b) UV-Vis spectrum of [5,15-bis(2,6-di(octyloxy)phenyl)-10,20-bis(triisopropylsilyl)ethynyl] porphinato]zinc(II) (13b)

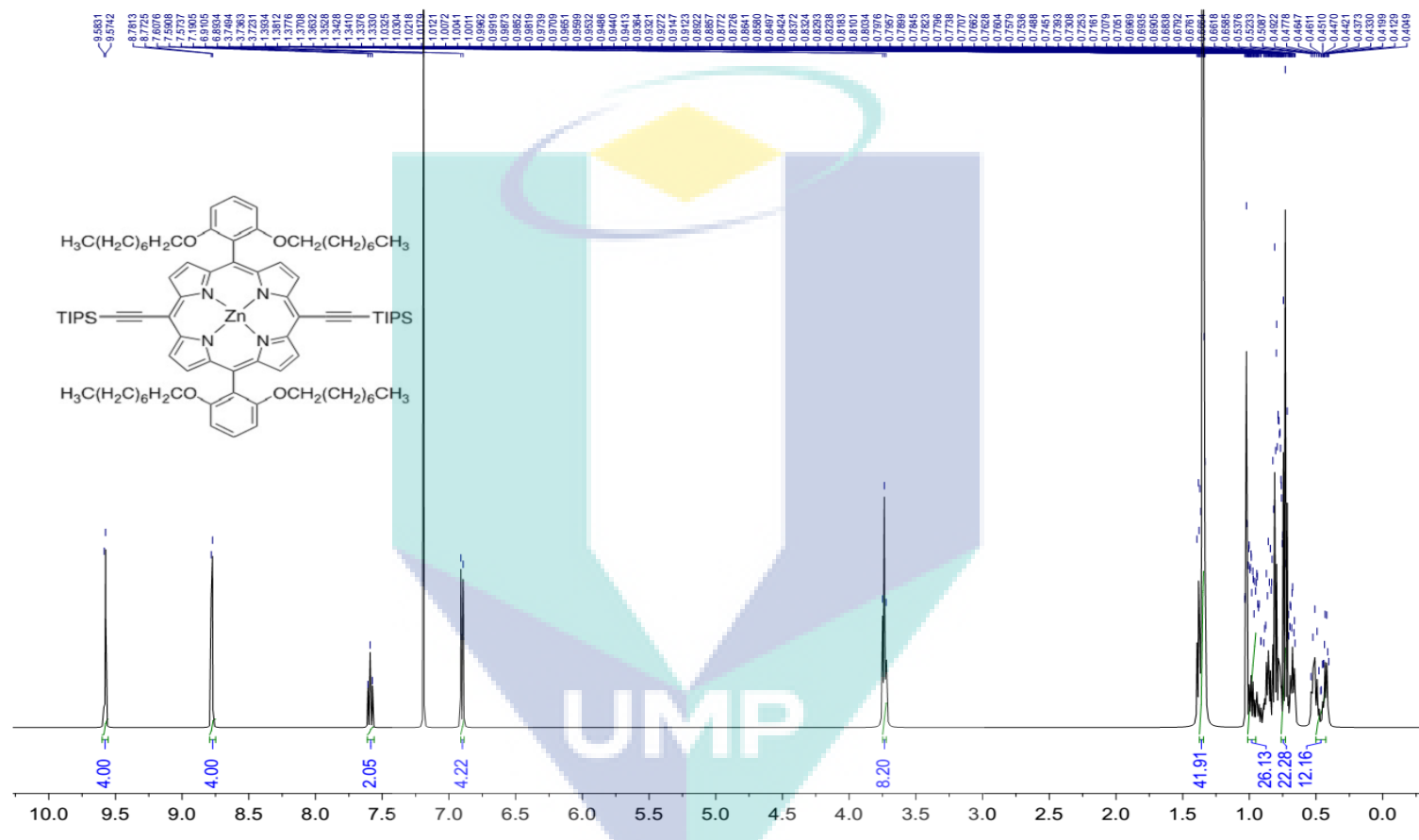


Figure S39 ¹H NMR of [5,15-bis(2,6-di(octyloxy)phenyl)-10,20-bis(triisopropylsilyl)ethynyl]porphinatozinc(II) (13b) in CDCl₃

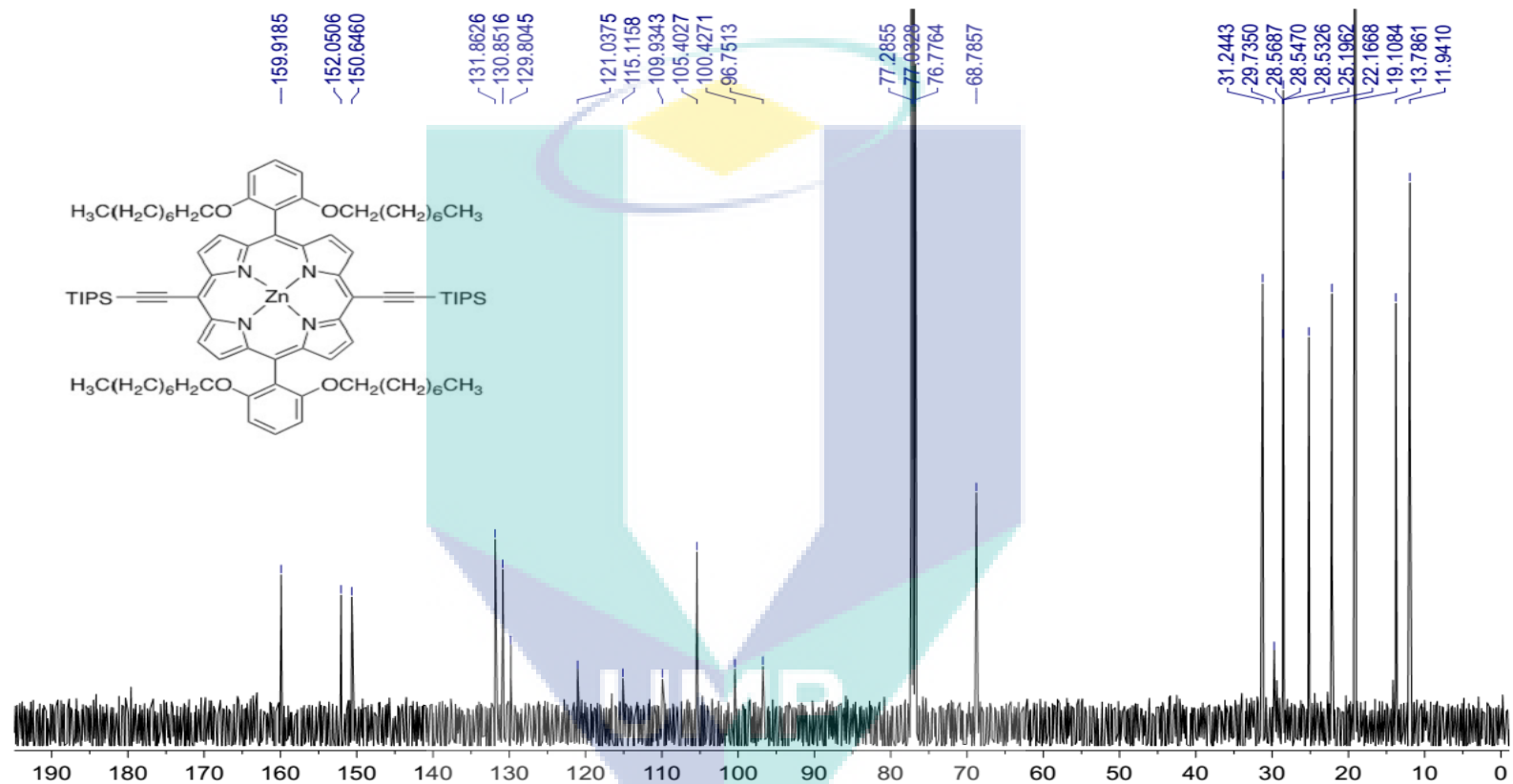


Figure S40 ^{13}C NMR of [5,15-bis(2,6-di(octyloxy)phenyl)-10,20-bis(triisopropylsilyl)ethynyl]porphinatozinc(II) (13b) in CDCl_3

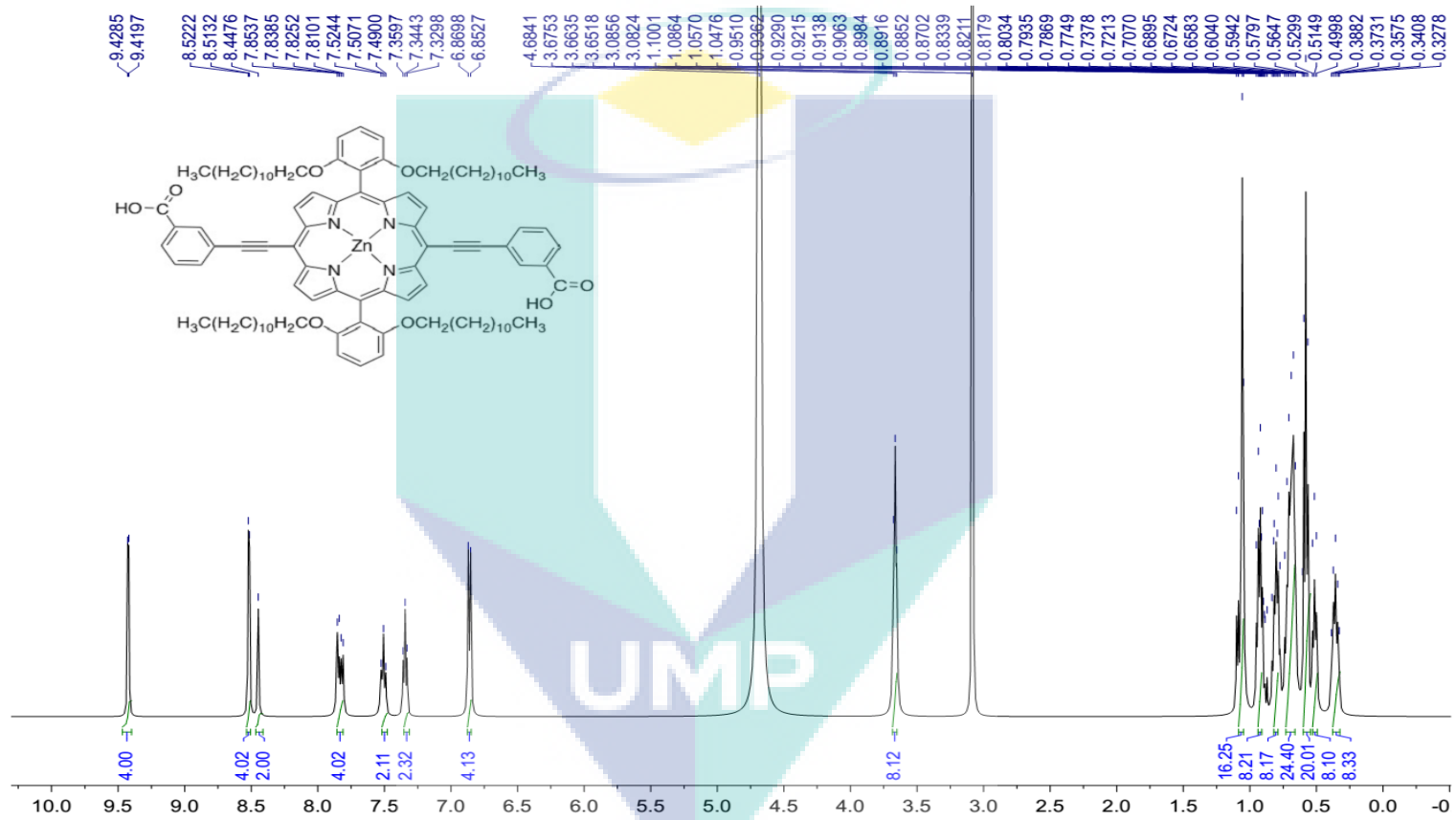


Figure S41 ¹H NMR of [5,15-bis(2,6-di(dodecyloxy)phenyl)-10,20-bis(3-carboxylphenyl) ethynyl]porphinato]zinc(II) (RJ-C₁₂-MY₁) in CD₃OH

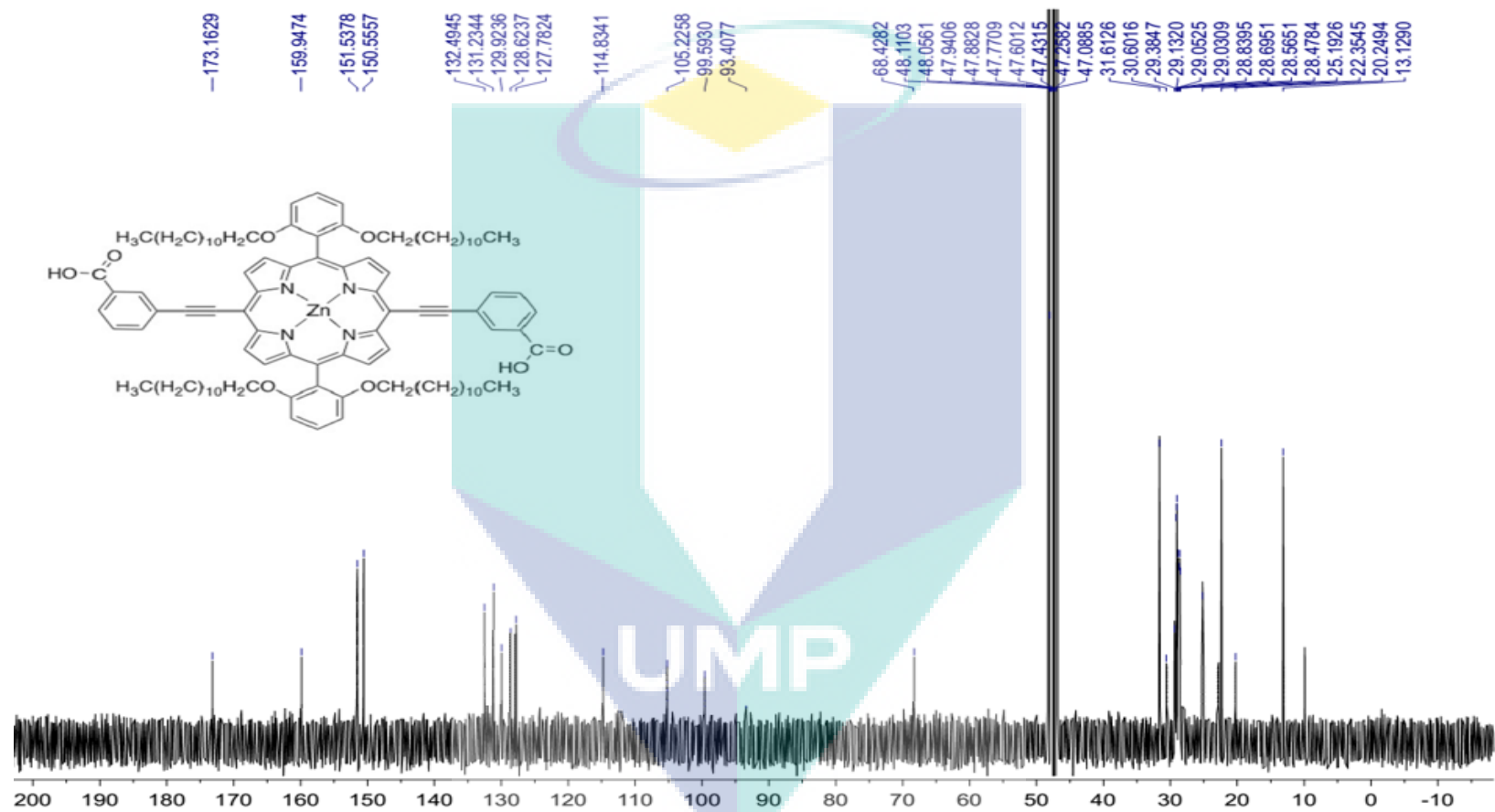


Figure S42 ^{13}C NMR of [5,15-bis(2,6-di(dodecyloxy)phenyl)-10,20-bis(3-carboxylphenyl) ethynyl]porphinato]zinc(II) (RJ-C12-MY₁) in CD₃OH

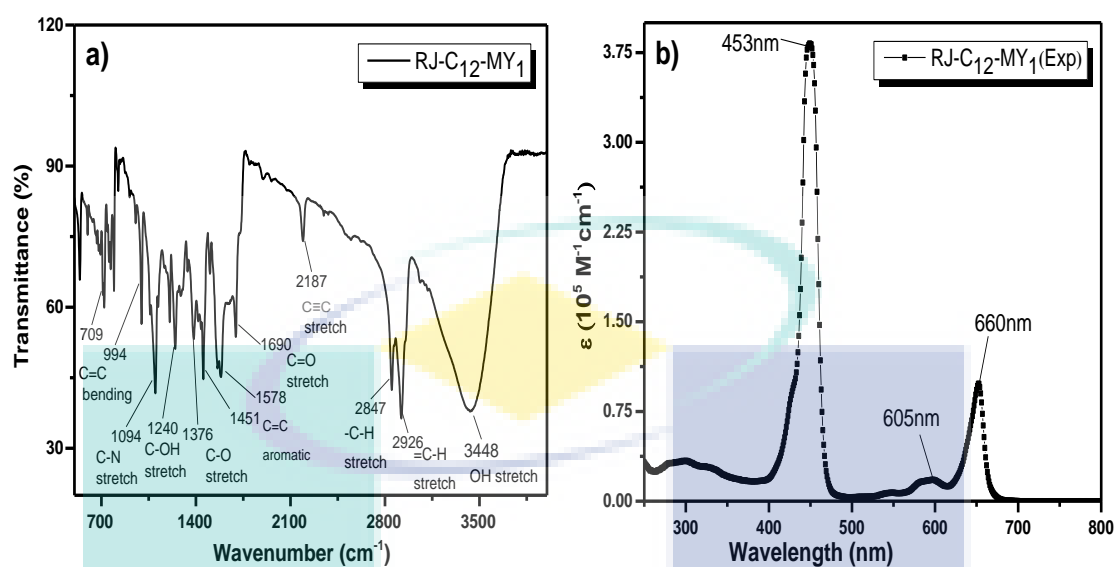


Figure S43 a) FTIR spectrum of [5,15-bis(2,6-di(dodecyloxy)phenyl)-10,20-bis(3-carboxylphenyl) ethynyl]porphinato]zinc(II) (RJ-C₁₂-MY₁); b) UV-Vis spectrum of [5,15-bis(2,6-di(dodecyloxy)phenyl)-10,20-bis(3-carboxylphenyl) ethynyl]porphinato]zinc(II) (RJ-C₁₂-MY₁)

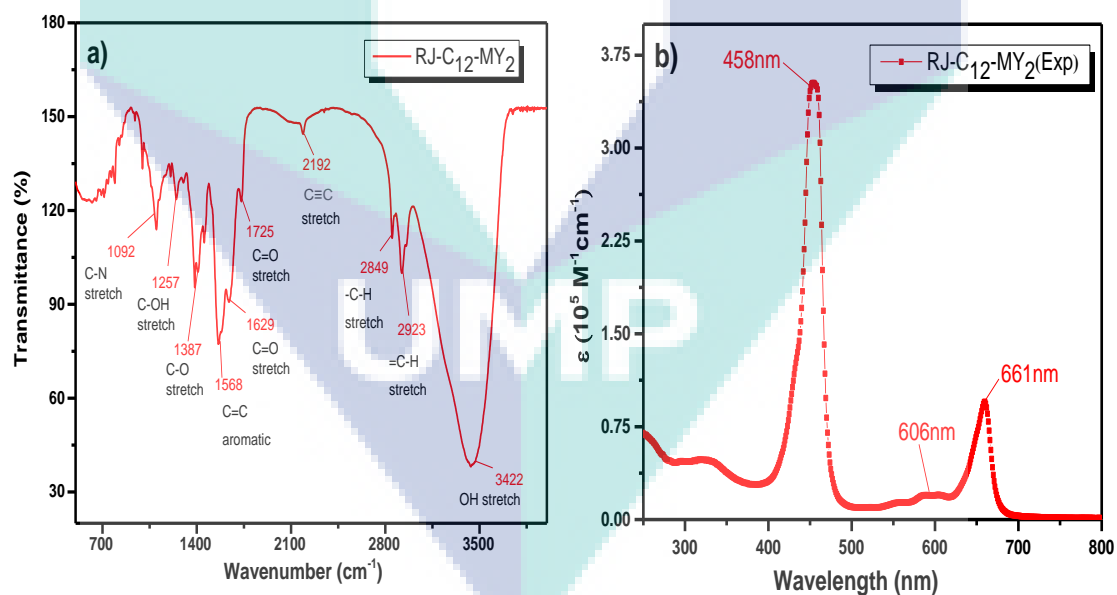


Figure S44 a) FTIR spectrum of [5,15-bis(2,6-di(dodecyloxy)phenyl)-10,20-bis(4-carboxylphenyl) ethynyl]porphyrinato]zinc(II) (RJ-C₁₂-MY₂); b) UV-Vis spectrum of [5,15-bis(2,6-di(dodecyloxy)phenyl)-10,20-bis(4-carboxylphenyl)ethynyl]porphyrinato]zinc(II) (RJ-C₁₂-MY₂)

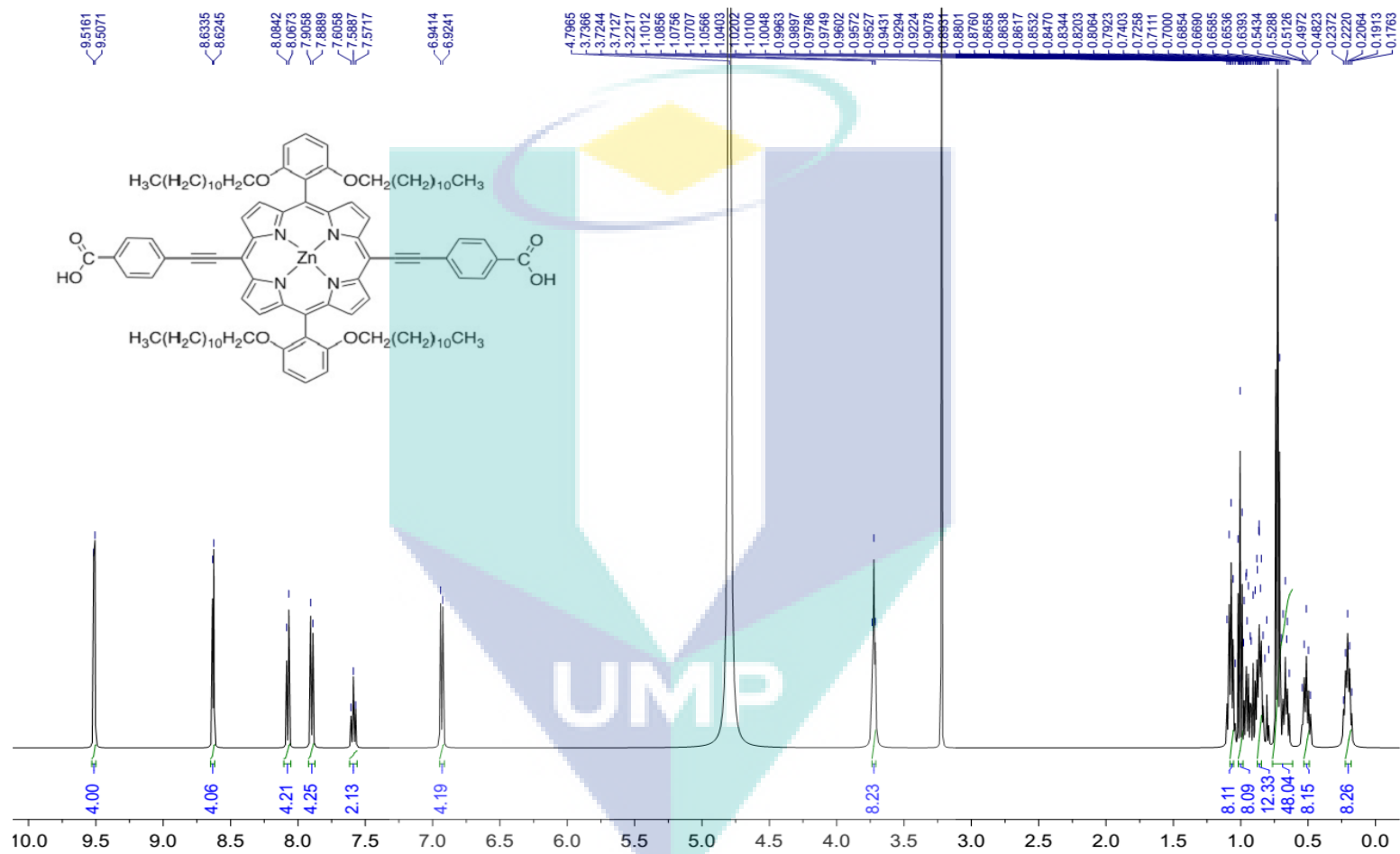


Figure S45 ¹H NMR of [5,15-bis(2,6-di(dodecyloxy)phenyl)-10,20-bis(4-carboxylphenyl) ethynyl]porphyrinato]zinc(II) (RJ-C₁₂-MY₂) in CD₃OH

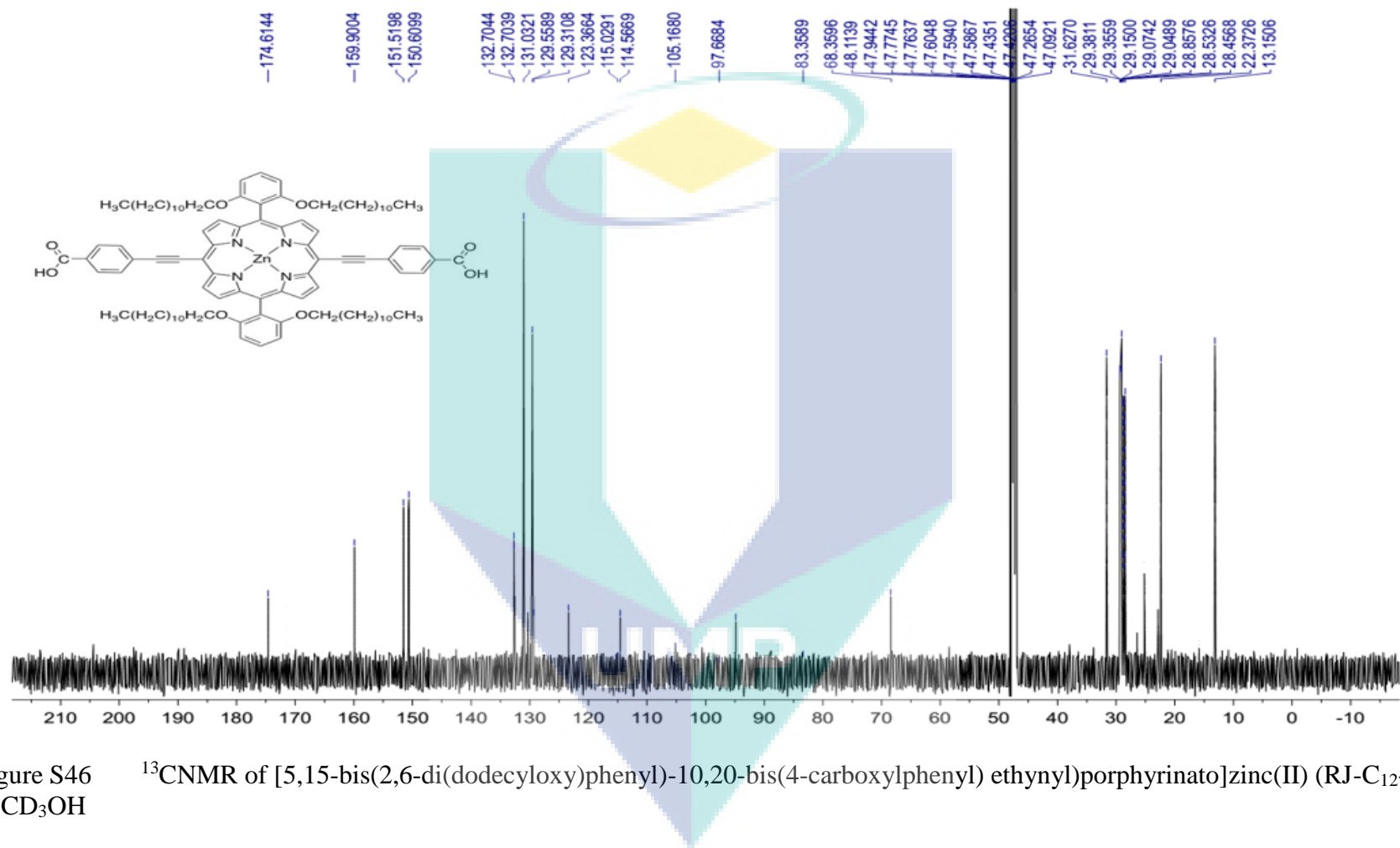


Figure S46 ¹³CNMR of [5,15-bis(2,6-di(dodecyloxy)phenyl)-10,20-bis(4-carboxylphenyl) ethynyl]porphyrinato]zinc(II) (RJ-C₁₂-MY₂) in CD₃OH

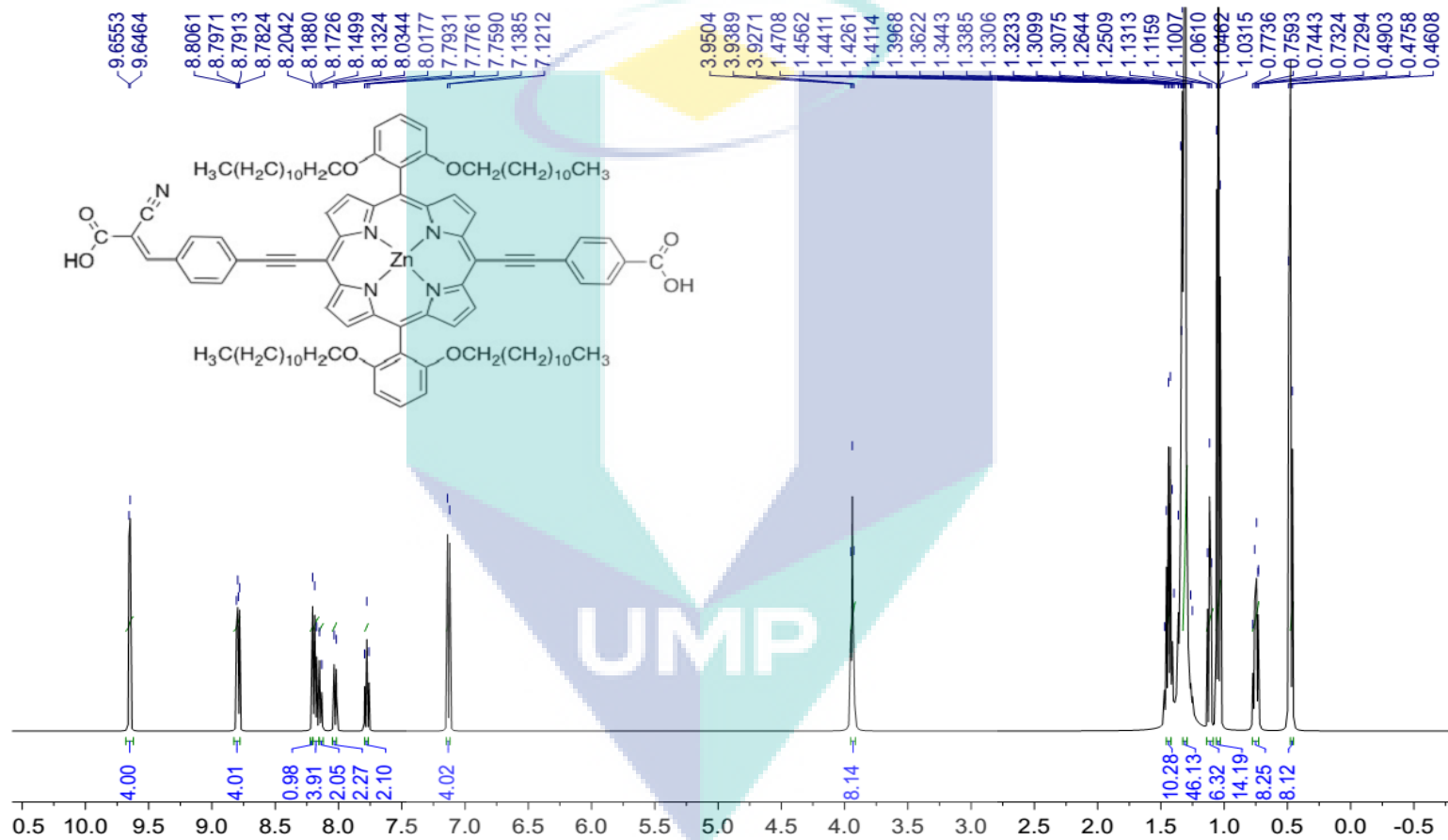


Figure S47 ¹H NMR of [5,15-bis(2,6-di(dodecyloxy)phenyl)-10-[(4-carboxylphenyl)ethynyl]-20-[(4-(2-cyanopropenoic acid)phenyl)ethynyl]porphyrinato]zinc(II) (RJ-C₁₂-MY₃) in CD₃OH

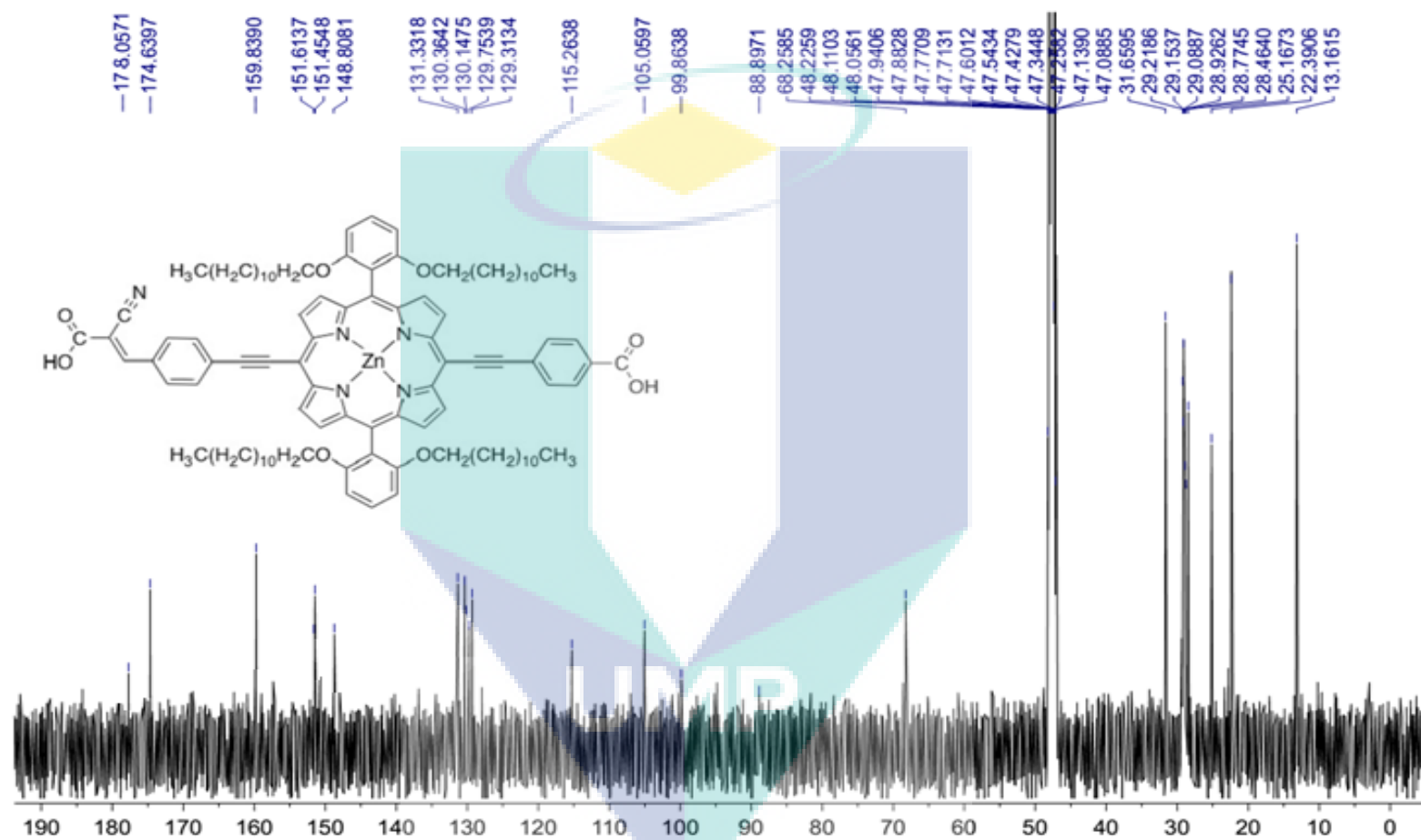


Figure S48 ¹³CNMR of [5,15-bis(2,6-di(dodecyloxy)phenyl)-10-[(4-carboxyphenyl)ethynyl]-20-[(4-(2-cyanopropenoic acid)phenyl)ethynyl]porphyrinato]zinc(II) (RJ-C₁₂-MY₃) in CD₃OH

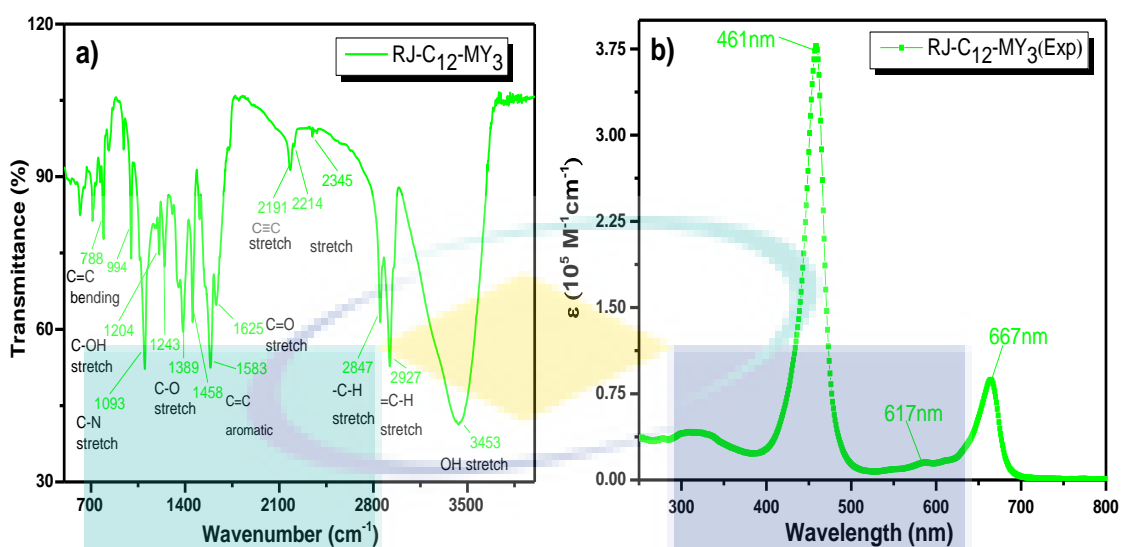


Figure S49 a) FTIR spectrum [5,15-bis(2,6-di(dodecyloxy)phenyl)-10-[(4-carboxylphenyl)ethynyl]-20-[(4-(2-cyanopropenoic acid)phenyl)ethynyl]porphyrinato]zinc(II) (RJ-C₁₂-MY₃); b) UV-Vis spectrum of [5,15-bis(2,6-di(dodecyloxy)phenyl)-10-[(4-carboxylphenyl)ethynyl]-20-[(4-(2-cyanopropenoic acid)phenyl)ethynyl]porphyrinato]zinc(II) (RJ-C₁₂-MY₃)

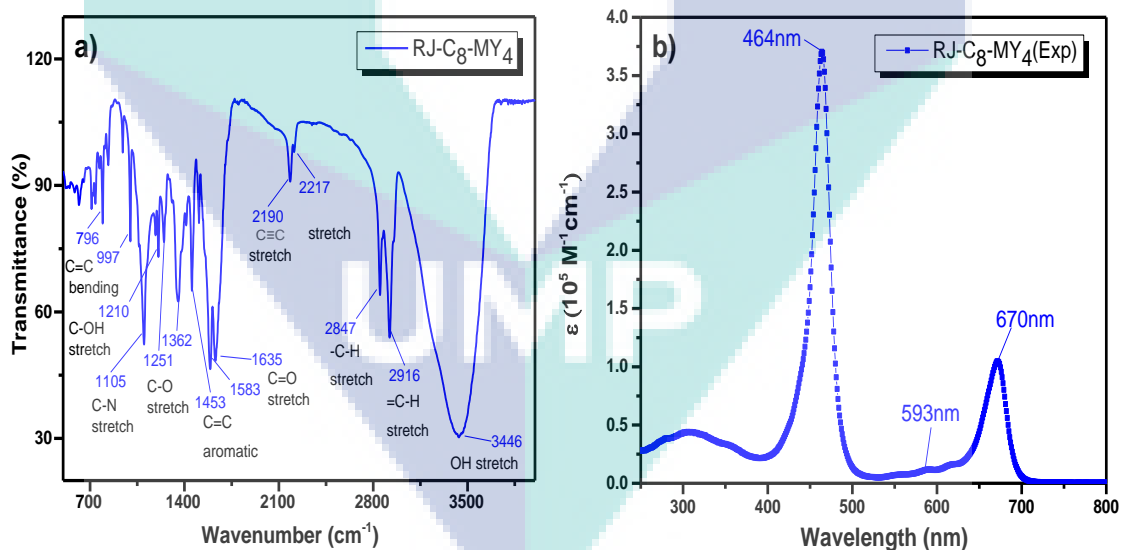


Figure S50 a) FTIR spectrum [5,15-bis(2,6-di(octyloxy)phenyl)-10,20-[(4-(2-cyanopropenoic acid)phenyl)ethynyl]porphyrinato]zinc(II) (RJ-C₈-MY₄); b) UV-Vis spectrum [5,15-bis(2,6-di(octyloxy)phenyl)-10,20-[(4-(2-cyanopropenoic acid)phenyl)ethynyl]porphyrinato]zinc(II) (RJ-C₈-MY₄)

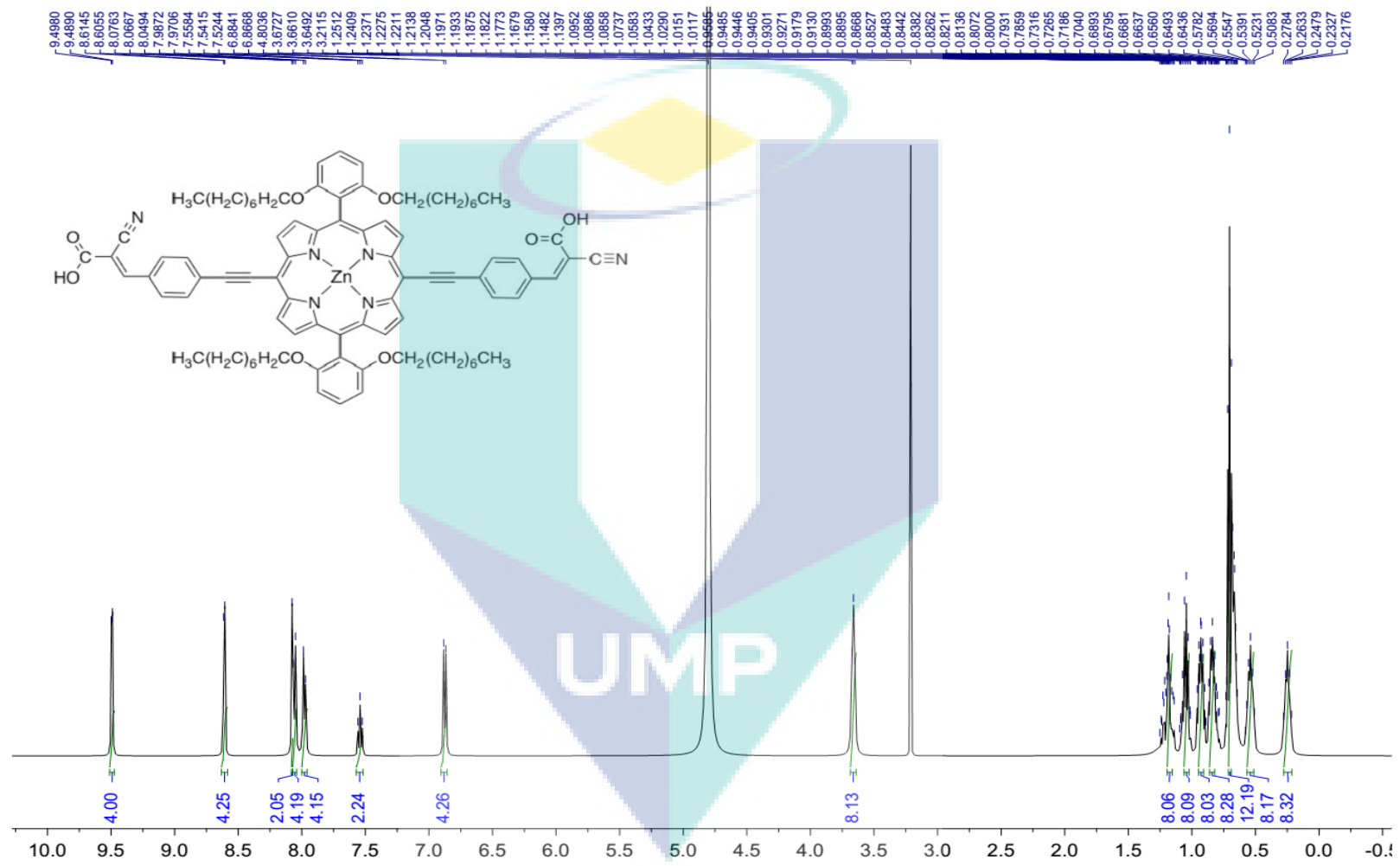


Figure S51 ¹H NMR of [5,15-bis(2,6-di(octyloxy)phenyl)-10,20-[(4-(2-cyanopropenoic acid)phenyl)ethynyl]porphyrinato]zinc(II) (RJ-C₈-MY₄) in CD₃OH

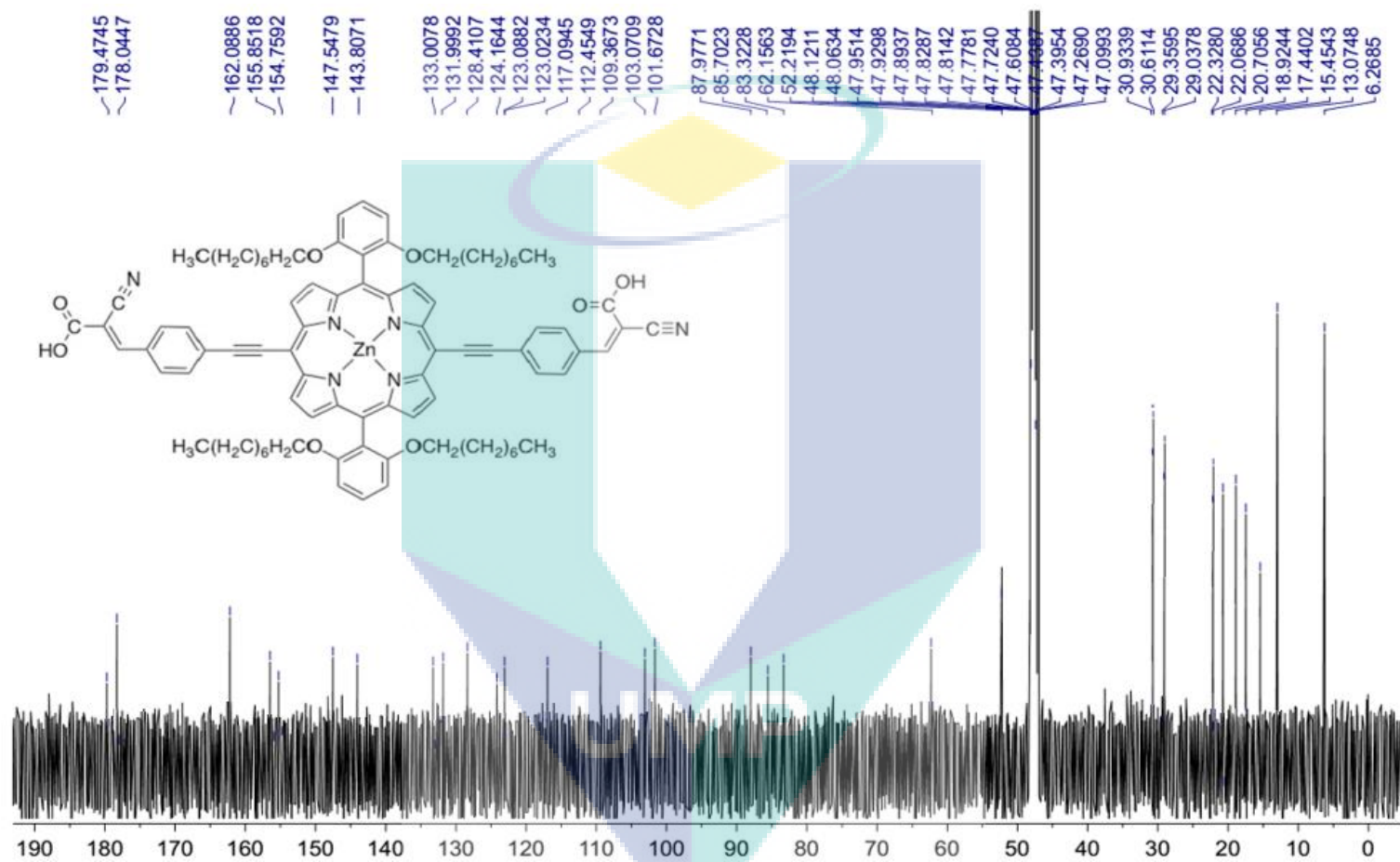


Figure S52 ^{13}C NMR of [5,15-bis(2,6-di(octyloxy)phenyl)-10,20-[(4-(2-cyanopropenoic acid)phenyl)ethynyl]porphyrinato]zinc(II) (RJ-C₈-MY₄) in CD₃OH

APPENDIX G

ENERGY-GAP LAW

One of the most fundamental laws governing energy transfer is the energy gap law (EGL). The EGL simply states that the probability of radiationless intramolecular energy transfer between two weakly coupled electronic states is inversely proportional to the exponential of the electronic energy gap (ΔE) between the two states. In other words, the first order rate constant for radiationless decay decreases exponentially as the energy gap between the two coupled states increases. This explains why the higher excited states (S_n $n>1$) in most polyatomic molecules display little or no fluorescence as the electronic states higher than S_1 tend to be closely spaced. The S_1 state on the other hand has a relatively large energy gap between itself and the ground state. For this reason, the radiationless decay from S_1 is much slower than from S_n ($n>1$) allowing S_1 fluorescence to take place before its population is depleted. The EGL applies not only to internal conversion between states of the same electron spin multiplicity but also to intersystem crossing between states of different electron spin multiplicity which means that the closer in energy the S_1 state of a polyatomic molecule is to the T_1 state the faster the rate of population of the triplet becomes [1].

Franck-Condon Principle

The second major consideration for rates of energy transfer is the Franck-Condon factor (FC). The FC is the square integral of the overlap between vibrational wavefunctions of the initial and final electronic states involved in the transition. Since a greater amount of overlap between the two states makes a transition more likely to take place, a larger FC means a faster rate of non-radiative energy transfer. The rate of non-radiative decay (k_{nr}) is related to this factor by the following equation:

$$k_{nr} \propto V^2 F$$

where V is the intramolecular electronic coupling energy and F is the density-of-vibrational states weighted Franck-Condon factor. Because this value is related to the density-of vibrational-states, as the energy gap between the initial and final electronic states (ΔE) increases and the overlap of the states decreases exponentially, the exponential decrease in F is also observed. This is where the exponential dependence on

the energy gap for non-radiative transitions comes from [1, 2]. Therefore, when a graph of the natural log of the rate of relaxation via non-radiative pathways versus ΔE is plotted a linear relationship should be evident. However, this inverse exponential dependence of non-radiative transfer rates on ΔE is only apparent in cases where the intramolecular electronic coupling energy (V) is relatively small, i.e. the weak coupling limit. The weak coupling limit, which is typical of internal conversion and intersystem crossing in aromatic hydrocarbons, is the case where

$$EM \approx h\langle\omega\rangle$$

where EM is the molecular rearrangement energy and $\langle\omega\rangle$ is the mean vibrational frequency of the state. This means that a relatively small displacement in the normal vibrational modes will take place from one electronic state to the next resulting in F having a much greater influence on k_{nr} than V^2 in equation 1.7. In cases where the weak coupling limit holds the energy gap law holds as well. The opposite case is the strong coupling limit where

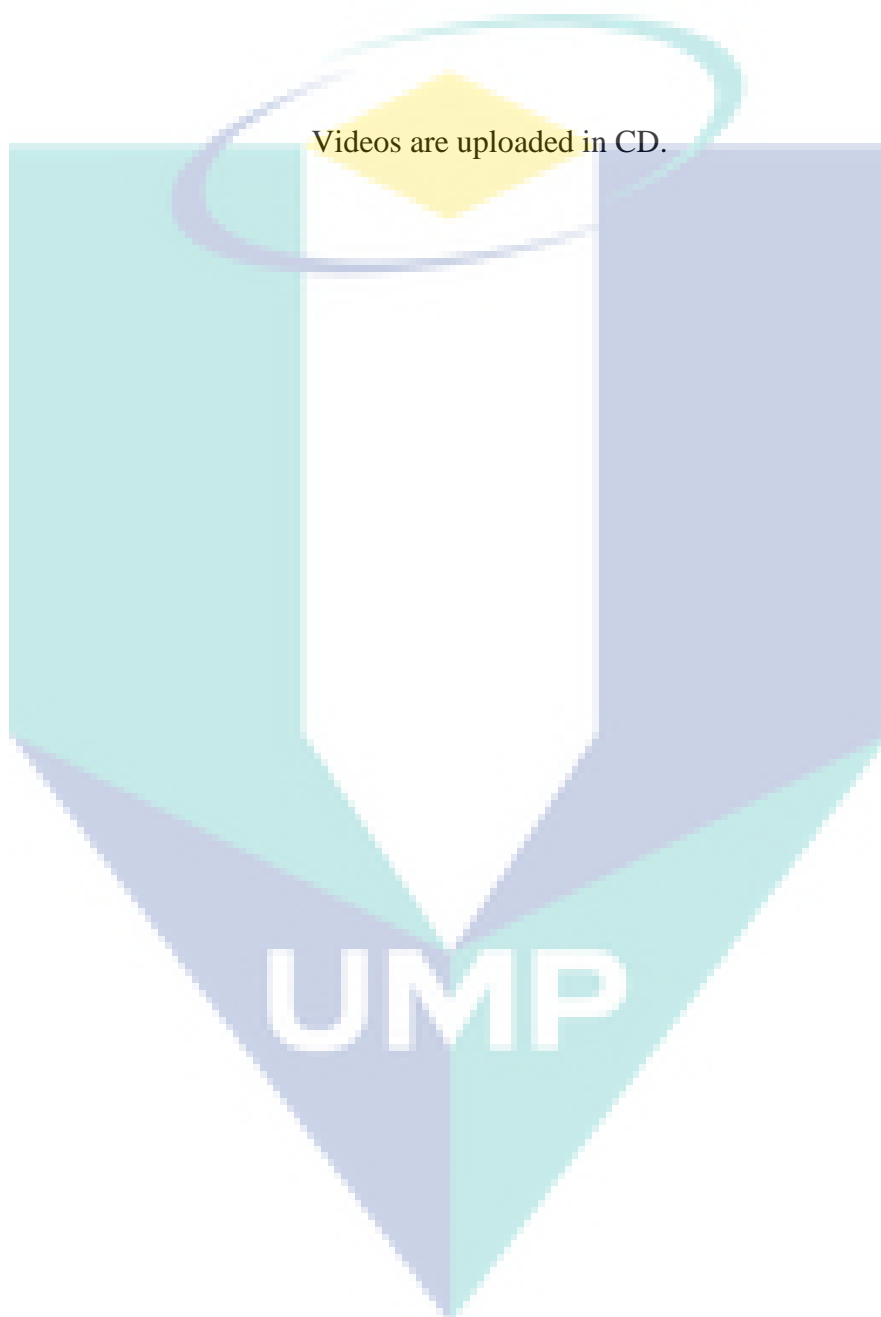
$$EM \gg h\langle\omega\rangle$$

which will lead to a large relative displacement of the energy surfaces between the initial and final electronic states involved in the transition. Transitions that fall under the strong coupling limit will not adhere to the energy gap law but will instead have a strong dependence on the activation energy required for transition and in turn the mean vibrational frequency of the molecule will strongly determine whether a transition occurs or not.

Reference

1. Lakowicz, J.R., Introduction to fluorescence, in Principles of fluorescence spectroscopy. 1999, Springer. p. 367-373.
2. Wardle, B., Principles and applications of photochemistry. 2009: John Wiley & Sons.

APPENDIX H
VISUALS OF OPTIMIZED STRUCTURES AND ALL VIBRATIONS OF RJ-C_n-
MY_m COMPLEXES



APPENDIX I
MOLECULAR ORBITAL DIAGRAMS OF THE RJ-C_n-MY_m SERIES

Table I-1 HOMO and LUMOs of the RJ-C_n-MY_m series

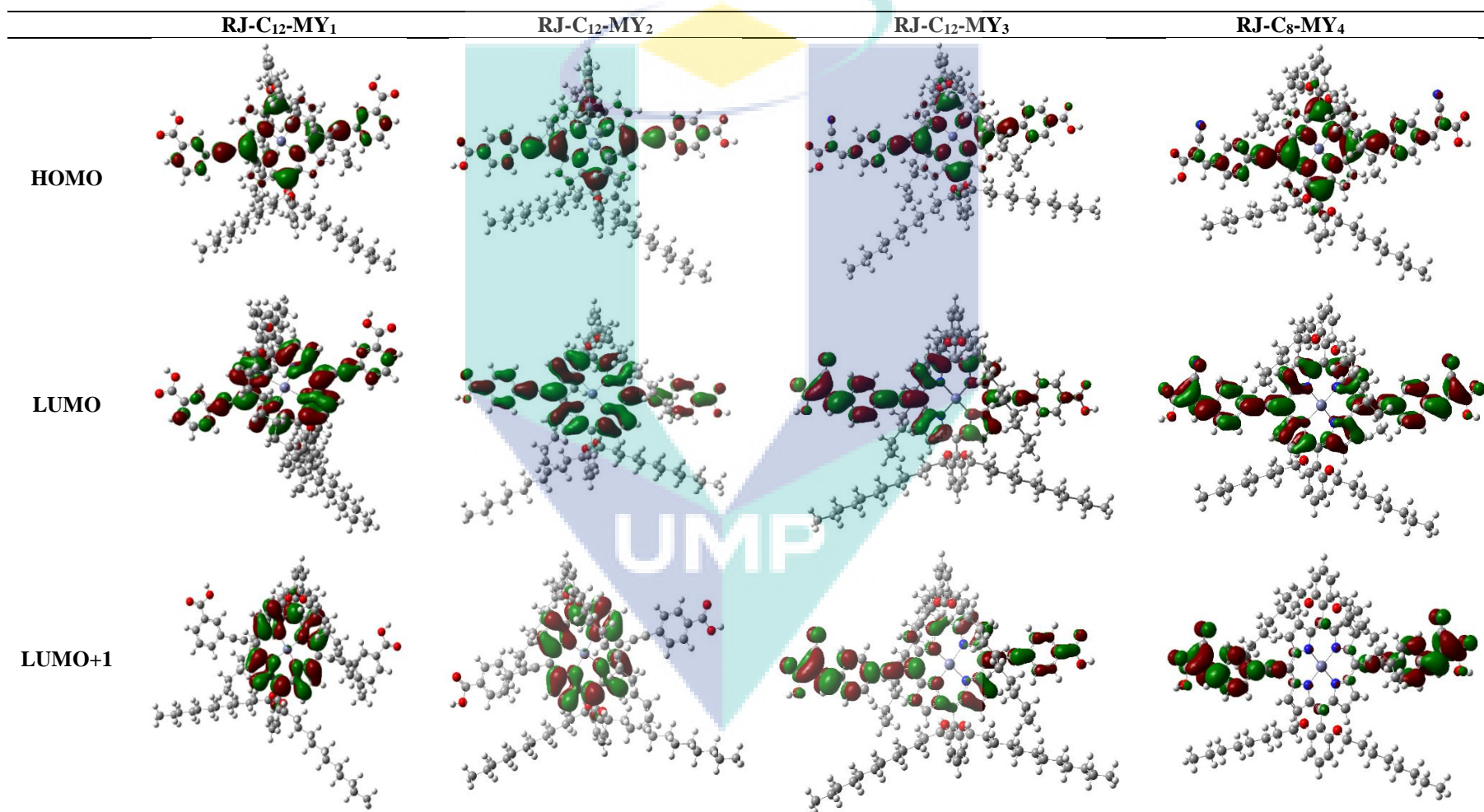
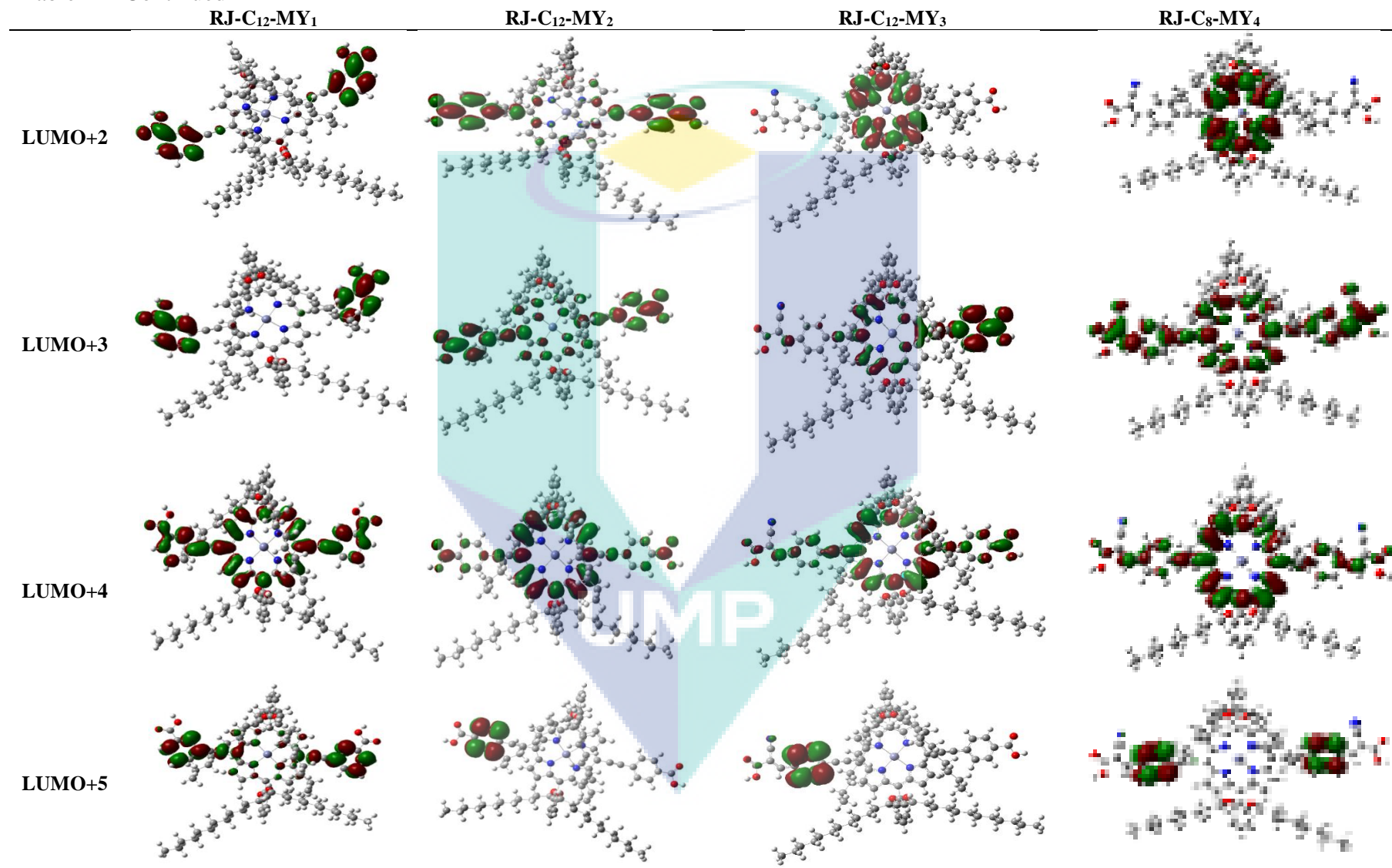


Table I-1 Continued



LIST OF PUBLICATIONS

Amina Yasin, Rajan Jose, Mashitah M. Yusoff. (2015). Predicting larger absorption cross-section in porphyrin dyes using DFT calculations. *Journal of Porphyrins and Phthalocyanines*. 19(12): 1270-1278.

Qamar Wali, Azhar Fakharuddin, Amina Yasin, Mohd Hasbi Ab Rahim, Jamil Ismail, Rajan Jose. (2015). One pot synthesis of multi-Functional tin oxide nanostructures for high efficiency dye-sensitized solar cells. *Journal of Alloys & compounds*. 646: 32-39.

CONFERENCE AND WORKSHOPS

Amina Yasin, Rajan Jose, Mashitah M. Yusoff. “DFT Studies and Synthesis of Multifunctional Porphyrin macromolecules”, *International Conference of Organic Synthesis*, 21th to 24th August 2016, Kuching Sarawak, Malaysia.

Amina Yasin, Rajan Jose, Mashitah M. Yusoff. “Evolution of electronic properties of porphyrin dyes from first principle quantum mechanical calculations”, *2nd National postgraduate Conference*, 24th to 25th January 2015, UMP Gambang, Malaysia.

Amina Yasin, Rajan Jose, Mashitah M. Yusoff. “Quantum Chemical Simulation of Molecular Structures for high efficiency solar cells”, *Malaysian Technical Universities Conference on Engineering and Technology 2013*, 3rd to 4th December 2013, Kuantan Pahang, Malaysia.

Amina Yasin (2015). Workshop on fundamentals of structural elucidation by NMR spectroscopy, 2nd and 3rd November 2015, Kulliyah of Pharmacy, International Islamic University of Malaysia, Kuantan.

Amina Yasin (2013). Workshop on fundamentals of structural elucidation by NMR & Mass spectroscopy, 17th and 19th December 2013, Central Laboratory, Universiti Malaysia Pahang, Kuantan.

OTHER AWARDS

Amina Yasin. (2014). “Zn(II)Porphyrin complexes for Dye sensitized solar cell–Enhance efficiency”, Three minute (3MT) thesis competition. *Univesiti Malaysia Pahang*

Amina Yasin. (2016). “Design and Synthesis of Porphyrins with Tailored Optical Properties”, Malaysian three minute (3MT) thesis competition. *Univesiti Malaysia Pahang*

Amina Yasin, Jose Rajan, Muhammad Shaheen Sarkar, Mashitah Mohd Yusoff. (2016). “New Multifunctional Porphyrin Molecules”, *Creation innovation, technology & research exhibition*, Universiti Malaysia Pahang. (**Bronze Medal**)

Amina Yasin, Rajan Jose, Mashitah M. Yusoff. “Quantum Chemical Simulation of Molecular Structures for high efficiency solar cells”, *Malaysian Technical Universities Conference on Engineering and Technology 2013*, 3rd to 4th December 2013, Kuantan Pahang, Malaysia. (**Best paper award**).

